

Sheffield Hallam University

Oxidation and morphology of iron and iron alloy droplets.

JACKSON, Roy.

Available from the Sheffield Hallam University Research Archive (SHURA) at:

<http://shura.shu.ac.uk/19863/>

A Sheffield Hallam University thesis

This thesis is protected by copyright which belongs to the author.

The content must not be changed in any way or sold commercially in any format or medium without the formal permission of the author.

When referring to this work, full bibliographic details including the author, title, awarding institution and date of the thesis must be given.

Please visit <http://shura.shu.ac.uk/19863/> and <http://shura.shu.ac.uk/information.html> for further details about copyright and re-use permissions.

0501
SHEFFIELD CITY
POLYTECHNIC LIBRARY
FOND STREET
SHEFFIELD S1 1WB

100214902 9

TELEPEN



Sheffield City Polytechnic Library

REFERENCE ONLY

ProQuest Number: 10697169

All rights reserved

INFORMATION TO ALL USERS

The quality of this reproduction is dependent upon the quality of the copy submitted.

In the unlikely event that the author did not send a complete manuscript and there are missing pages, these will be noted. Also, if material had to be removed, a note will indicate the deletion.



ProQuest 10697169

Published by ProQuest LLC (2017). Copyright of the Dissertation is held by the Author.

All rights reserved.

This work is protected against unauthorized copying under Title 17, United States Code
Microform Edition © ProQuest LLC.

ProQuest LLC.
789 East Eisenhower Parkway
P.O. Box 1346
Ann Arbor, MI 48106 – 1346

The Oxidation and Morphology of Molten Iron
and Iron Alloy Droplets

by

R Jackson

ABSTRACT

The oxidation characteristics of iron droplets and a range of binary iron alloy droplets have been investigated at 1600°C. The droplets were generated by a novel technique of melting the iron or iron-alloy, in the form of wire, in a levitation coil. The droplets were held for several minutes in hydrogen prior to releasing them into a mass transfer column separated from the levitation chamber by a thin plastic film. The oxidised droplets were quenched. The oxidising or reducing characteristics of various quenching media were investigated and silicone oil was selected as the quenchant.

Pure iron and a range of iron-manganese, iron-chromium and iron-silicon alloys were investigated. Whereas the iron-manganese system showed increasing oxygen pick-up with increasing manganese content, the iron-chromium and iron-silicon systems showed an inversion in oxidation behaviour after an initial increase in oxidation rate. The oxidation characteristics of these systems have been related to the surface morphology of the droplets as revealed by Scanning Electron Microscopy and to SIMS analysis of the thin surface oxide films, and mechanisms are proposed for each system.

A mathematical model has been developed which simulates the mass transfer of oxygen by forced convection to an accelerating molten iron droplet. The model generates an almost linear oxidation rate for iron, for the period of flight of the droplet and is in good agreement with the experimental work when the model is compensated for circulation within the droplet. The model predicts that temperature has a minimal effect on oxidation rate whereas droplet size is of major importance. Both of these effects were confirmed by the experimental studies.

The roles of the alloying elements in relation to the characteristics of oxide films reduced in hydrogen at 1150°C have also been considered. Reduction mechanisms are postulated to account for the morphology of the reduced droplets and the final oxygen levels in the droplets.

OXIDATION AND MORPHOLOGY OF IRON AND IRON ALLOY DROPLETS

by

ROY JACKSON BSc MSc

A thesis submitted to the Council for National Academic Awards
in partial fulfilment of the requirements for the degree of
Doctor of Philosophy

Sponsoring Establishment: Sheffield City Polytechnic

Collaborating Establishment: SKF Engineering & Research Centre
BV Nederlands

July 1987

PREFACE

The work presented in this thesis was carried out during the period January 1979 to January 1987 in the Department of Metals and Materials Engineering, Sheffield City Polytechnic.

The work described in this thesis is, to the best of my knowledge, original except where reference has been made to others, and no part of it has been submitted for an award at any college or university.

During the period of this work the author attended a course entitled "Statistics in Research".

The Oxidation and Morphology of Molten Iron

and Iron Alloy Droplets

by

R Jackson

ABSTRACT

The oxidation characteristics of iron droplets and a range of binary iron alloy droplets have been investigated at 1600°C. The droplets were generated by a novel technique of melting the iron or iron-alloy, in the form of wire, in a levitation coil. The droplets were held for several minutes in hydrogen prior to releasing them into a mass transfer column separated from the levitation chamber by a thin plastic film. The oxidised droplets were quenched. The oxidising or reducing characteristics of various quenching media were investigated and silicone oil was selected as the quenchant.

Pure iron and a range of iron-manganese, iron-chromium and iron-silicon alloys were investigated. Whereas the iron-manganese system showed increasing oxygen pick-up with increasing manganese content, the iron-chromium and iron-silicon systems showed an inversion in oxidation behaviour after an initial increase in oxidation rate. The oxidation characteristics of these systems have been related to the surface morphology of the droplets as revealed by Scanning Electron Microscopy and to SIMS analysis of the thin surface oxide films, and mechanisms are proposed for each system.

A mathematical model has been developed which simulates the mass transfer of oxygen by forced convection to an accelerating molten iron droplet. The model generates an almost linear oxidation rate for iron, for the period of flight of the droplet and is in good agreement with the experimental work when the model is compensated for circulation within the droplet. The model predicts that temperature has a minimal effect on oxidation rate whereas droplet size is of major importance. Both of these effects were confirmed by the experimental studies.

The roles of the alloying elements in relation to the characteristics of oxide films reduced in hydrogen at 1150°C have also been considered. Reduction mechanisms are postulated to account for the morphology of the reduced droplets and the final oxygen levels in the droplets.

ACKNOWLEDGEMENTS

I would like to thank my supervisors, Dr G Briggs and Mr V G Gibson for their extremely helpful discussions, guidance and patience throughout the supervision of this work. I would like to thank my industrial supervisor, Dr R Cundill, for his encouragement and discussions during the early stages of this work.

I would also like to express my thanks to colleagues for useful discussions, especially Dr A W D Hills and Dr R Acheson, and to all those members of the departmental technical staff who contributed in various ways during the course of this work. Particular thanks go to D Anderson, J Bradshaw, A Earnshaw, G Gregory, Dr B Lewis and M Muldownie. I am also indebted to Mrs Diana Cosham for her considerable patience and skill in typing this thesis.

The support of the Management of Sheffield City Polytechnic in the provision of the necessary equipment and finances and for a period of secondment to complete the work is gratefully acknowledged.

CONTENTS

Page No

List of symbols and subscripts

CHAPTER 1	INTRODUCTION	1
CHAPTER 2	LITERATURE REVIEW	3
2.1	Production of Atomised Powders	3
2.1.1	Introduction	3
2.1.2	Particle Properties	4
2.1.2(i)	Particle Size	4
2.1.2(ii)	Particle Shape	4
2.1.2(iii)	Particle Structure	7
2.1.3	The Effect of Oxygen on Properties of Atomised Powders	9
2.1.4	Parameters for Powder Forging	16
2.1.4(i)	Role of Alloying Elements	16
2.1.4(ii)	Composition Constraints	20
2.2	Single Droplet Studies	21
2.2.1	Fluidodynamic Considerations	22
2.2.2	Heat and Mass Transfer Considerations	29
2.2.2(i)	Heat and Mass Transfer in the Continuous Phase	31
2.2.2(ii)	Heat and Mass Transfer in the Dispersed Phase	36
2.2.3	Surface Phenomena	37
2.2.4	Previous Experimental Work on the Oxidation of Single Droplets	41
2.3	Oxidation and Reduction Characteristics	44
2.3.1	Oxidation Kinetics of Molten Iron and Iron Alloys	44
2.3.2	Diffusion of Oxygen in Molten Iron	46
2.3.3	Reduction of Oxide Phases in Iron Powders	47
2.4	Levitation Melting	50
2.4.1	Advantages and Disadvantages of Levitation Melting	50
2.4.2.	Electromagnetic Field in a Levitation Coil	52
2.4.3	Design Considerations	56
2.4.4	Temperature Measurement and Control	60
2.5	Quench Media	62

CHAPTER 3	EXPERIMENTAL PROCEDURE	64
3.1	Production of Iron and Iron Alloy Wires	64
3.2	Levitation Melting Rig	67
3.2.1	Power Source	67
3.2.2	Coil Design and Operating Procedure	68
3.2.3	Gas Purification System	72
3.2.4	Temperature Measurement and Control	73
3.2.5	Production of Droplets	77
3.2.6	Mass Transfer Column	79
3.3.	Chemical Analysis	80
3.3.1	Analysis for Alloying Elements	80
3.3.2	Analysis for Oxygen	81
3.4	Droplet - Quench Media Experiment	83
3.5	Thermogravimetric Studies	86
3.5.1	Introduction	86
3.5.2	Measurement of Droplet Mass Loss in Hydrogen	87
3.5.3	Measurement of Relative Humidity	88
3.6	Electron Microscopy and Surface Analysis	90
3.6.1	Scanning Electron Microscopy	90
3.6.2	Specimen Preparation for Scanning Electron Microscopy	90
3.6.3	The VG Scientific Microlab	91
3.6.4	Specimen Preparation for Surface Analysis	93
CHAPTER 4	EXPERIMENTAL RESULTS	94
4.1	Assessment of Quench Media	95
4.1.1	Introduction	95
4.1.2	Results of Initial Experiments	96
4.1.3	Reaction between Liquid Iron Droplets and Quench Oils	101
4.2	Oxidation Studies	104
4.2.1	Treatment of Results	104
4.2.2	Oxidation of Pure Iron Droplets	106
4.2.3	Oxidation of Iron-Manganese Alloy Droplets	107
4.2.4	Oxidation of Iron-Chromium Alloy Droplets	109
4.2.5	Oxidation of Iron-Silicon Alloy Droplets	112

4.3	Reduction Studies	113
4.3.1	Introduction	113
4.3.2	Reduction of Oxidised Iron Droplets	114
4.3.3	Reduction of Oxidised Iron-Manganese Alloy Droplets	115
4.3.4	Reduction of Oxidised Iron-Chromium Alloy Droplets	116
4.3.5	Reduction of Oxidised Iron-Silicon Alloy Droplets	118
4.4	Surface Morphology and Surface Analysis Studies	119
4.4.1	Surface Morphology	119
4.4.2	Surface Analysis	120
4.4.2.1	Electron Microscope Studies	120
4.4.2.2	VG Microlab Studies	122
	4.4.2.2.1 Surface Analysis	122
	4.4.2.2.2 Depth Profiles	122
CHAPTER 5	DISCUSSION	124
5.1	Accuracy and Errors of the Experimental Method	124
5.1.1	Temperature Measurement	124
5.1.2	Oxygen Analysis	124
5.1.3	Statistical Interpretation of Results	124
5.2	The Oxidation of Molten Iron Droplets in Air	125
5.2.1	Theoretical Considerations	125
	5.2.1.1 Temperature Profile of a Free-Falling Iron Droplet	125
	5.2.1.2 Model for the Oxidation of Iron Droplets	126
5.2.2	Kinetics of the Oxidation of Molten Iron Droplets	128
5.3	The Role of Alloying Elements on the Oxidation Rate of Molten Iron Droplets	131
5.3.1	Thermodynamic Considerations	131
5.3.2	The Effect of Manganese on Kinetics of Oxidation and Droplet Morphology	132
5.3.3	The Effect of Chromium on Kinetics of Oxidation and Droplet Morphology	136
5.3.4	The Effect of Silicon on Kinetics of Oxidation and Droplet Morphology	141

5.4	The Role of Alloying Elements on the Reducibility of Oxidised Iron Alloy Droplets	145
5.4.1	Thermodynamic Considerations	145
5.4.2	Reduction of Oxidised Iron Droplets	146
5.4.3	The Effect of Manganese on the Reduction of Oxidised Alloy Droplet	148
5.4.4	The Effect of Chromium on the Reduction of Oxidised Alloy Droplets	150
5.4.5	The Effect of Silicon on the Reduction of Oxidised Alloy Droplets	153
5.5	Practical Implications	154
CHAPTER 6	CONCLUSIONS	157
CHAPTER 7	SUGGESTIONS FOR FURTHER WORK	160
REFERENCES		
TABLES 1 - 127		
FIGURES 1 - 183		
PLATES 1 - 47		
APPENDICES I - IV		

SYMBOLS

A	interfacial area
A_{eff}	effective sectional area
A_p	projected surface area
a_A	activity of component A
a_S	activity of solute
b	constant
C_D	drag coefficient
C	concentration
C_δ	concentration of surface active substance
C_p	heat capacity
D	diffusion coefficient
D_0	temperature-independent factor in equation relating D to T
d	diameter
d_d	diameter of droplet
d_v	diameter of sphere of equal volume
E	activation energy for reaction
F_D	frictional or drag force
f	activity coefficient
f°	Henry's law coefficient
f	as subscript, relating to film temperature
G	Gibbs free energy
G_A°	Gibbs free energy of component A in standard state
G_A	partial molar Gibbs free energy of component A
Gr	Grashof number for heat transfer = $gd^3 (T_f - T_\infty) \left(\frac{\rho}{\mu^2 T} \right)_f$
Gr'	Grashof number for mass transfer = $gd^3 (\rho_f - \rho_\infty) \left(\frac{\rho}{\mu^2} \right)_f$

Gr''	mean Grashof number = $Gr^1 + \left(\frac{Sc}{Pr}\right)^{0.5} Gr$
g	acceleration due to gravity
H	enthalpy
h	Henryian activity
h	height
h	heat transfer coefficient
J	flux of material per unit area
K	equilibrium constant
k	thermal conductivity
k	rate constant
k _d	rate constant (droplet)
M	atomic or molecular mass
m	mass
N	dimensionless number
N _A	flux of species A
Nu	Nusselt number, $\frac{hd}{k}$
P	pressure
P _i	partial pressure of component, i
Pr	Prantl number $\left(\frac{\mu C_p}{k}\right)_f$
q	heat transfer
R	gas constant
Re	Reynold's number $\frac{u\rho d}{\mu}$
r	radius
r _v	equivalent radius
S	Entropy
Sc	Schmidt number, $\frac{\mu}{\rho D}$
Sh	Sherwood number $\frac{\beta d}{D}$

S	as subscript, surface
T	temperature
T_E	effective temperature
T_f	film temperature
t	time
u	velocity
u_t	terminal velocity
u_α	velocity of flowing liquid
V	volume
v	atomic diffusion volume
We	Weber number $\frac{d u^2 \rho}{\gamma}$
x	distance
x_A	mole or atom fraction of component A
XS	as superscript, excess
$\beta(kd)$	mass transfer coefficient
Δ	incremental change
γ	retardation coefficient
ϵ	interaction coefficient
Γ^*	interfacial concentration at equilibrium
δ	boundary layer thickness
μ	viscosity
$\mu_{c,f}$	viscosity of continuous phase
μ_d	viscosity of dispersed phase
θ	fraction of surface covered
π	product
ρ	density
ρ_f	density of surrounding phase

ρ_d	density of droplet
δ	interfacial tension
δ	Stefan-Boltzmann radiation constant
ψ	sphericity
Γ_s	excess quantity of solute s
\square_s	vacancy in surface

CHAPTER 1 INTRODUCTION

In recent years the hot forging of powder metal preforms has been receiving increasing attention as an alternative production route for low alloy steel engineering components. Iron powders are produced by a variety of techniques, notably, electrolysis, solid state reduction and atomisation. Since atomised powders are generated directly from liquid metal, more variation and control is possible compared to other types of commercial powder production processes. In atomisation the purity of the powder is a function of raw materials and melting practice. A wide range of particle shape and size is possible through variations of the atomising parameters. It is the only method of the three that can make pre-alloyed powders. Atomised powders are therefore being widely evaluated for use in steel powder compaction forging.

With powder preforms the number of factors influencing the choice of alloy composition is greater than those in traditional wrought alloy production methods. Since strength is frequently controlled by heat treatment, hardenability is of importance. The elements that are most useful in promoting hardenability at lowest cost are manganese and chromium. However, because of their affinity for oxygen, giving rise to fabrication problems, they have been replaced by molybdenum and nickel in some applications at much greater cost. In designing steels for powder forging, the over-riding factor is that of cost. Modification of the processing route in terms of high temperature pre-treatment of the pre-forms offers the possibility of closer control of oxide

formation, but the cost of the process is increased in terms of additional energy requirement. The alloy design is thus a delicate balance of the lower cost elements to promote hardenability constrained by their oxide forming tendencies as against the additions of elements with less oxygen affinity but restricted by cost and other technical factors.

The work described in this thesis was undertaken to establish the oxidation behaviour of alloying elements in molten iron. The generation of small molten metal droplets from wire in a levitation coil had previously proved successful. The behaviour of those alloying elements which have a greater affinity for oxygen than iron required investigation. In addition the effect of the amount of the alloying element in the iron on the oxygen pick-up and the effect of the alloying element present on the surface morphology of the droplet was unknown. The rate and extent of reduction of the oxides on the surface of the iron alloy droplets in terms of the distribution and nature of the retained oxides would also be of significance. Overall this study would contribute to the understanding of the influence of alloying elements on the character of iron powders.

CHAPTER 2 LITERATURE REVIEW

2.1 Production of Atomised Powders

2.1.1 Introduction

Atomisation is one of the most commonly used commercial methods for making iron powders and alloy steel powders. In this process a stream of molten metal is broken or dispersed into particles by a rapidly moving gas or liquid stream. Atomised powders have distinct advantages over powders manufactured by other routes. It is claimed that any alloy can be made, including new alloys, and systems can be designed especially and solely for powder metallurgy⁽¹⁾. All particles have the same and uniform composition; macro segregation is eliminated which results in an homogeneous grain size with improved workability and reproducibility of properties. Atomisation gives a degree of control of particle shape, size and structure; particles range from spherical to irregular. Generally the method gives higher purity metals with fewer non-metallic inclusions, *but these may be in prior crack locations.* Also associated with atomised powders is higher compressibility with improved properties and structures.

For iron and low alloy steel powders water atomisation is most widely used because it produces a somewhat irregular surface structure which is desirable for achieving a good strength in powder compacts⁽²⁾. For many other powders, which readily oxidise in contact with water or steam, inert gas atomisation is necessary⁽³⁾. Two other commercial atomisation techniques have been developed for the highly oxidation prone superalloys: the rotating electrode process and vacuum atomisation⁽⁴⁾.

The production route has a profound effect on the important characteristics of metal powders, namely, particle size, particle shape and particle structure including density.

2.1.2 Particle Properties

2.1.2(i) Particle Size

During the atomisation process atomic bonds within the liquid metal are broken in proportion to the increase in surface area, thus giving rise to an increase in total surface energy. The atomising process must supply this new energy which is proportional to the surface tension and proportional to the characteristic dimension of the drops. Considering only the parameters associated with the liquid metal, and not the atomising agent, finer particle sizes are favoured by low metal viscosity, low metal surface tension and a degree of superheat.

2.1.2(ii) Particle Shape

One of the advantages of the atomisation process is that there is a high degree of control of the particle shape; this is an important consideration in all commercial uses for metal powders. The particle shape of atomised powders can be modified from irregular to almost perfectly spherical, basically by controlling the processes that take place in the interval between disintegration of the liquid metal stream and the solidification of the drop. The particle shape is determined mainly by the surface tension of the molten metal and the cooling capacity, density, rate of flow and reactivity of the atomising agent. Water atomisation usually produces irregular shaped particles while gas atomisation usually produces spherical particles⁽¹⁾.

Rao and Tallmadge⁽⁵⁾ from photographs of atomisation processes suggest that quench atomisation can be described in terms of two sequential steps; namely the formation of droplets and the quenching of droplets. The formation zone includes the region where the liquid metal stream is broken into droplets by the atomising fluid. Some cooling occurs and the two important effects of the formation zone are the creation of a size distribution and an initial shape for each particle. In the quench zone the newly formed droplets change shape due to several forces and are cooled by convection and radiation until they freeze into the final powder shape. Rao and Tallmadge suggest that it is in the quench zone that the final particle shape variation is established. They assert that in the period between formation and freezing the forces which are primary and dominant for causing shape change of the particle are the surface tension force, internal viscous force, inertial force and an external drag force.

The surface tension of liquid metals is high and once a droplet has formed it tends to assume a spherical shape. The higher the viscosity of the medium, the greater the deformation of the droplet. Moreover, the greater the cooling rate the shorter is the time available for surface tension forces to operate to spheroidise the droplet and hence the more irregular is the particle shape. Impurities and alloying elements in the metal or surface reactions that decrease the surface energy will promote irregular particle shapes. Little is reported on the role of alloying elements on the surface tension properties of iron. Gummerson⁽¹⁾ reports on the work of Lochman who investigated the role of silicon in influencing the particle shape of atomised stainless steels. It was found that up to 1% Si addition to 18:8

and 17:13 Cr-Ni melts resulted in spherical particles while 2.5-5.0% Si additions gave irregular shaped particles.

Inert gas atomisation always produces spherical powders regardless of process variations. When oxidising gases, such as air or steam, are employed the particle shape is dependent on the formation of surface oxide films. Increasing amounts of oxygen in the atomising gas will produce increasingly irregular particle shapes in the atomisation of those metals that form tenacious, stable oxides such as aluminium and magnesium. On the other hand, metals and alloys with a high solubility for their own oxides e.g. nickel, and also those that have low melting point oxide films tend to remain spherical under oxidising conditions.

Nichiporenko et al⁽⁶⁾ suggest that the effects of an element added to a melt for alloying purposes or for the purpose of forming refractory oxides can be predicted. When the element being added to the melt has a high affinity for oxygen and the amount added is sufficient for deoxidation, the melt will become less viscous and the resultant powder particles will be more spherical.

Metal pouring temperature and degree of superheat are also of importance.

Metal pouring temperature does not appreciably affect particle shape in gas atomisation but it does affect particle shape of powders produced by water atomisation. The greater the degree of superheat then the more spherical are the resultant particles. If the pouring temperature is sufficiently high then superheat remains after the atomisation process to allow surface tension forces to create spherical particles.

It would appear that on the whole the major influence on particle shape is related to the metal surface tension, the viscosity of the atomising medium and the quenching rate.

2.1.2(iii) Particle Structure

One of the advantages of the powder metallurgy route over normal production routes is the elimination of segregation⁽¹⁾. It can be said that for all atomising processes the alloy chemistry is independent of particle size in all inert systems. In those instances where reactions can take place between the metal droplet and the atomising agent and/or the quenching medium, then the greatest effect will be on the finest particle sizes such as in oxidation reactions. These surface reactions and any concurrent changes in chemistry will increase with higher pouring temperatures, slower cooling rates and higher atomising pressures which give finer particles.

The particle structure is a function of the rate of solidification. Water or liquid atomisation will give a finer microstructure when compared with gas atomisation. A finer structure will also be given by lower metal pouring temperatures, higher atomising pressures, higher flow rate and viscosity and by shorter particle flight paths.

Grant⁽⁷⁾ has examined the dendrite arm spacing as a function of solidification rate for aluminium and copper alloys and two steels. Gas atomisation gives a solidification rate in the range 10^0 to 10^2 °C second⁻¹ and water and steam atomisation in the range 10^2 to 10^4 °C second⁻¹. The quench rate of liquid metal droplets is restricted primarily by heat flow at the surface.

Solidification rate is dependent on the heat transfer coefficient 'h'. The heat transfer equation is given by:

$$\frac{hD_0}{K_g} = 2.0 + 0.60 \frac{D_0 v^1 \rho_g}{\mu_g} Pr^{\frac{1}{3}}$$

where h = heat transfer coefficient
D₀ = diameter of liquid droplet
K_g = thermal conductivity of gas
v¹ = gas velocity relative to metal droplet
ρ_g = density of the gas
μ_g = kinematic viscosity of the gas
Pr = Prandtl number

Rapid solidification is achieved by maximising the heat transfer coefficient. This is done in practice by using higher conductivity gases, or steam or liquids.

In gas atomisation large deviations from smooth spherical particles are common⁽⁶⁾. The welding of fine droplets onto coarser particles (satellites) occurs due to repeated collisions among liquid or semi-liquid coarse particles and fine solidified particles in a turbulent atmosphere. This affects packing densities and surface area measurements become much less meaningful and increased contamination occurs. Powder particles with significantly different dendrite sizes and phase distributions are incorporated into the final product and result in negative effects on structure properties. Another major problem with gas atomisation is the entrapment of gas in the powders. If the gas is insoluble, e.g. argon, the gas becomes part of the final product. The gas pores are sealed in hot working but reform gas pockets on exposure again to high temperatures.

J B See et al⁽⁸⁾ have shown that the atomised stream initially thins out and breaks into ligaments and sheets of thin liquid metal. These thin unstable sheets flying through space reform into round particles by folding and trapping the atomising gas internally. Also at this stage, for alloys with alloying elements such as chromium, which readily oxidise to form refractory oxides, the final stage of spheroidisation into droplets is prevented or hindered and highly irregular powders form. Hence the atmosphere in the atomising chamber must be protective to minimise formation of such oxides.

The important difference between water and gas atomisation is that water has a high quench capability. Water atomisation when applied to metals and alloys which can be cleaned inexpensively of oxide surfaces, e.g. by hydrogen reduction, represents a cheaper process than gas atomisation (except when using air).

Steam atomisation offers a choice of conditions intermediate between those of gas and water atomisation. Low pressure steam, passed through geometrically arranged nozzle configurations, can be brought to resonance to produce relatively coarse powders of less than spherical shape, with a relatively high quench rate. Most classes of carbon and low alloy steels, as well as stainless steels, have been successfully and economically steam atomised⁽¹⁾⁽²⁾.

2.1.3 The Effect of Oxygen on Properties of Atomised Powders

Ferrous materials and low alloy steels, including the stainless steels, together with a number of nickel alloys can generally be air melted and atomised with water, steam or air without excessive

oxidation or other detrimental effects⁽¹⁾. Therefore these metals lend themselves to high-volume, low cost atomising techniques.

In the case of special purpose steels, inert gas atomisation may be necessary to meet stringent oxygen specifications. The sensitivity and critical applications of tool steels and high temperature alloys for most purposes preclude the use of water and air and possibly nitrogen as an atomising or cooling medium. High temperature alloys are either vacuum melted or melted under argon and are argon atomised in a dry chamber. Such practices are very expensive compared to air melting/water atomisation routes. Water atomisation is favoured, when possible, to produce very irregular particle shapes which in conventional powder metallurgy techniques require green strength and compressibility in compacts.

Water atomisation of iron alloys, particularly stainless steels, differs little from the atomisation of iron or low carbon steels except that these alloys are more sensitive to oxygen pick-up and, therefore, do not always lend themselves to subsequent economical heat treatment⁽¹⁾. Precautions are taken to prevent excessive exposure to oxygen during atomisation while the atomised particles must be irregular enough to provide compacts of good green strength from the as-atomised and dried condition. The atomising chamber can be purged with a protective atmosphere before atomisation and the flight path should be kept short for rapid quenching. Argon or nitrogen gases can be used. Nitrogen may be detrimental in the presence of chromium. In such instances, steam can sometimes be used to advantage and is cheaper than either nitrogen or argon.

Petrov et al⁽⁹⁾ examined a number of highly alloyed powders produced by argon atomisation of the liquid metal and collected in a tank containing water; the water in some experiments also containing a corrosion inhibitor. In their paper, data is given on two alloy steels, namely; an 18.5% W, 4% Cr, 1% V tool steel and an 18% Cr 15% Ni stainless steel. Determinations of the mean thickness of oxide films on the tool steel powder particles established that there is a close relationship between oxide thickness and cooling rate, Figure 1. The higher the cooling rate, the smaller^s the oxide film thickness. They argued that this is evidence that powder particles oxidise mainly while they are in the molten state. Confirmation of this conclusion is furnished by the results of experiments with various corrosion inhibitors. Several vessels were filled with liquids having varying oxidising powers (corrosion inhibitors, distilled water and ordinary water) and they were placed in the collecting tank of the atomisation unit. The distance of the nozzle to the surface of the cooling liquid was such that powder particles had sufficient time to solidify in the gaseous atmosphere. The results of the oxide film thickness and oxygen content determinations on the 18% Cr 15% Ni stainless steel, Table 1, demonstrated that the degree of oxidation of the powder in this case was not significantly affected by variations in the corrosiveness of the cooling medium.

Petrov et al concluded that the formation of an oxide film on a powder particle is affected by an aggressive environment only while the particle is in the molten state; the additional oxidation after solidification is negligible. It follows therefore, that the oxidation of atomised powder particles can be reduced by shortening their solidification time.

In the above experiments the cooling rate of the powders was measured by structural differences. From analysis of experiments using different cooling rates, Petrov and his co-workers found that the distance between the second order dendrite axes when plotted against cooling rate, using logarithmic co-ordinates, gave a straight line relationship. From this information it was then possible to determine the solidification time of a powder particle. From the relationship:

$$\text{Cooling rate of a drop, } \frac{d\theta}{dt} = \frac{\Delta\theta^+ + \Delta\theta^-}{t}$$

where $\Delta\theta^+$ represents the superheat of the drop

$\Delta\theta^-$ represents the undercooling of the drop, and

t is the solidification time

For a typical atomisation process, it may be assumed that

$$\Delta\theta^+ = 50^\circ\text{C}, \Delta\theta^- = 150^\circ\text{C} \text{ and } d\theta/dt = 2 \times 10^4 \text{ }^\circ\text{C.s}^{-1}$$

Under these conditions a drop remains in the liquid state for 0.01 seconds. The distance, s , covered by the particle before its solidification can be found from the relationship:

$$s = vt$$

where v is the flight velocity of the particle in the gaseous stream.

The flight velocity has been determined⁽¹⁰⁾ resulting in a value of the order of 20 ms^{-1} . Under these conditions, a droplet will travel 0.2 m before solidifying.

Water atomisation, on the other hand, appears to lead to increased oxidation. For example, a water atomisation unit is

described by Dunkley and Chilton⁽¹¹⁾ where conditions were such that when collecting the powder in air before settling in water the oxidation of the powder was very severe. It was necessary to purge the collecting vessel with nitrogen for three hours to reduce the oxygen level of the gas in the vessel to a reasonable figure. Under these conditions the oxygen contents of the powders quoted were: stainless steel about 1200-1500 ppm and iron 1500-2500 ppm

Grant⁽⁶⁾ has given other figures for stainless steel: 500-1500 ppm. He goes on to say that self milling of coarse powders will remove 80-90% of the surface oxides and if this is then followed by chemical treatments (not specified) the oxygen level of stainless steels can be lowered to levels of 200-400 ppm.

When an iron based VM.300 maraging steel⁽¹²⁾ was steam atomised and quenched in water the oxygen figures were between 150 and 2000 ppm. The same steel argon atomised and water quenched gave oxygen levels of 630 ppm.

Small and Bruce⁽¹³⁾ investigated the atomisation of stellite alloys. Seventy five pound charges were melted in an induction furnace and poured under conditions designed to minimise gas contamination. The initial oxygen content was 50 ppm. After atomisation each heat was blended and sampled in accordance with accepted ASTM practice. They concluded that the higher the pouring temperature, the hotter the particles after atomisation and the longer is the oxidation period. This effect was minimised with inert gas atomisation because of the limited presence of oxygen. They found that in water atomisation, increasing pressures resulted in lower oxygen levels but the opposite appeared true for inert gas

atomisation. They argued that the increased water pressure resulted in faster quenching rates which quickly cooled the powder below oxidation temperatures. The cooling rate of inert gas atomised powder is less affected by increased atomisation pressures. Instead, the increased volume of gas merely supplies additional oxygen available for pick up. However, common to both methods of atomisation, it was found that finer powders contain a proportionately higher level of oxygen. From their data, it was seen that the larger the surface area per unit mass becomes, the greater is the oxygen contamination. This, they argued, implies that the oxygen present is a result of a surface reaction though they were not able to determine whether the oxygen was present primarily as a surface oxide.

Friedman and Ansell⁽¹⁴⁾ looked at the production of super-alloy powders. They noted that water atomisation could only be applied to alloys in which the reactive elements Al, Ti or Nb are either absent of, if present, only in very low concentration. They argued that the difference between water and gas atomisation was significant, both with respect to powder chemistry and the effect on subsequent powder consolidation. The irregular particles produced by water atomisation possess relatively large surface areas compared to inert gas atomisation, and tend to contain oxides on the surface and internally. For some processes, e.g. iron powder production, the atomisation variables are deliberately controlled to promote powder oxidation, so that the particle surface area is further increased in a subsequent oxide-reduction operation. Such large surface area powders are cold compressible and are important in the press and sinter sector of the industry. In contrast, superalloys must be atomised under

conditions permitting no oxidation of the powder particle, either internally or on the surface. The reason given is that while iron and nickel oxides are easily reduced by a subsequent hydrogen anneal such is not the case for the reactive γ' formers. The stability of oxides such as TiO_2 , Al_2O_3 , Nb_2O_5 are such that once formed there is no practical way to return these oxides to the metallic state without influencing the integrity of the powder. Therefore, the superalloy compositions containing elements such as Ti, Al, Nb are usually melted in vacuum or under inert gas cover and are atomised with inert gas. The consequence of such inert gas atomisation is that the powder produced has low surface area and may be spherical in shape. The combination of low surface area and high hardness has the effect of making the inert gas atomised powders virtually incompressible at room temperature.

Oxygen levels on nickel superalloy Udimet 700 vary widely depending on the atomisation technique⁽¹⁴⁾. Atomisation with either nitrogen or argon and employing a water tank at the bottom of the atomisation chamber to quench the hot particles gave a resultant oxygen level of 700 ppm from melt stock containing 310 ppm oxygen. When the melt stock was 20 ppm and using nitrogen as the atomising gas the resultant powder had an oxygen level of 160-250 ppm. Current practice for superalloys is to atomise with argon and collect the powder in a dry chamber; powder so produced is spherical with oxygen contents ranging from 20 to 100 ppm.

2.1.4 Parameters for Powder Forging

2.1.4(i) Role of Alloying Elements

The possibility of hot working a powder preform in order to increase density, accelerate sintering and give good mechanical properties has been attractive for many years. However, serious development work only commenced from about 1970 onwards⁽¹⁵⁾. The forging of a hot preform has been shown to lead to mechanical properties which are superior to those normally produced by conventional powder metallurgy. The hot forging operation adds to the costs of the product and hence must be compared with drop forgings used as stress components. In terms of surface finish and economy of materials, powder forging is in the lead, but in terms of mechanical properties the situation is more complex. The powder forging is more isotropic than the traditional drop forging which tends to have very high mechanical properties in a longitudinal direction and poor properties in the other two directions. The ductility and impact properties of the powder forged material are intermediate between the transverse and longitudinal properties of the wrought steel. Brown⁽¹⁶⁾ suggests the answer lies with non-metallic inclusions since in the powder forged steel the inclusions present the same length of path to a propagating crack whatever the direction of testing. In wrought steel, elongated inclusions assist crack propagation in one direction and when the crack is propagating perpendicular to them in the other direction the crack is deflected. In view of this a careful assessment of the designed stress levels in components is necessary when a conventional drop forging is replaced by a powder forging.

The basic powder forge process route for steels has the following steps:

- (a) Mix iron or alloy powders with graphite to adjust carbon content.
- (b) Meter powder into die cavity; apply pressure to produce a green preform.
- (c) Heat preform in controlled atmosphere furnace.
- (d) Remove preform direct from hot zone and transfer to press or forge. It is important that the transfer time is short since no atmosphere protection is used⁽¹⁾.
- (e) Complete the densification by single stroke in a heated totally enclosed die.

Atomisation from the melt is likely to become the leading production method for forging grade powders⁽¹⁷⁾. While the particle interior of atomised powders is usually fully dense, surface texture depends to a great extent on the atomising conditions. For iron and low alloy steel powders, water atomisation is most widely used because it produces a somewhat irregular surface structure which is desirable for achieving a good strength in powder compacts. For many other powders which readily oxidise in contact with water or steam, inert gas atomisation is necessary⁽³⁾.

Brown⁽¹⁶⁾ suggests that the two principal requirements are an ability to develop an appropriate hardenability to guarantee strength and the control of fatigue performance by reference to

microstructural features and, in particular, the non-metallic inclusion count. The effect of non-metallic inclusion content on the fatigue performance of powder forged steels is shown in Figure 2. Again, from a comparison between water atomised powder and powder reduced from iron ore, only water atomised powder appears suitable for quality powder forgings because the relatively large content of non-reducible oxide inclusions in sponge iron powder causes a serious reduction of ductility or impact properties⁽¹⁸⁾.

In the powder route alloying elements can be introduced by two main techniques, namely, by prealloying or by blending followed by alloying during heating. However, it has been reported that even after sintering for one hour at relatively high temperatures, homogenisation in powder blends containing Ni, Mo, Cr and Mn is not complete⁽¹⁹⁾. This is reflected in hardenability data, see Figure 3.

In the design of an alloy for fabrication by the powder forging route, the conditions controlling optimum hardenability tend to conflict with those promoting high fatigue and ductility performance⁽¹⁶⁾. The normal steel making inclusions, which result from slag entrapment, refractory wear and deoxidation products, are atomised along with the steel. These present an angular appearance in the final microstructure. In addition, a series of complex oxides are formed during the atomisation process itself. During atomising with high pressure water jets, the environment of the first formed droplets is essentially oxidising. After atomising, the powder is separated from the water and dried in hot air. Corrosion of the product is inevitable and hence the

oxygen content is increased during this drying operation. The powder is subsequently annealed in dissociated ammonia and the thin oxide films reduced.

Guichelaar and Pehlke⁽²⁰⁾ looked at the gas metal reactions during sintering and explain in some detail oxide reduction and how it depends on sintering conditions. The graphite reacts with the oxides present on the particle surfaces to give CO and CO₂. The degree of reduction of the oxides depends on the CO/CO₂ ratio which is given by the equilibrium constant of the Boudouard reaction $C + CO_2 = 2 CO$. Above 700°C a CO/CO₂ ratio is established which is reducing even to the lowest iron oxide, wustite (FeO), according to the reaction $FeO + CO = Fe + CO_2$. As the reaction proceeds in the presence of excess carbon, the iron oxide is completely reduced to iron. At higher temperatures the CO/CO₂ equilibrium shifts further towards CO making the atmosphere even more reducing. Because of this, at very high temperatures it is possible to reduce such difficult oxides as those of manganese or chromium if excess carbon is available.

At temperatures of 1100°C the reaction kinetics are so fast^(20,21) that the reduction of iron oxides is practically complete after about three minutes total heating time.

No accurate kinetic data exist for the reduction of other than iron oxides, although it appears that nickel and molybdenum oxides are reduced under similar conditions. The modified Ellingham diagram, Figure 4, shows that the oxides of iron, molybdenum and nickel are easily reduced, whereas the oxides of manganese, chromium and silicon are more difficult. The ease of reducing the oxides formed on a Ni-Mo steel powder in practice are shown in Figure 5.

It has been shown that chromium and manganese oxides need reducing temperatures in excess of 1120°C and 1160°C respectively, see Figure 6. Heating time is a factor, not so much in relation to the reduction equilibrium but in the diffusion of the elements released. Where cost is a major controlling influence, long heating times or high temperatures (in excess of 1125°C) present a barrier.

2.1.4(ii) Composition Constraints

It is evident from previous evidence that the alloy systems chosen must produce a minimum of non-metallic inclusions⁽¹⁶⁾. However, at the same time, the alloy selection must be such as to give acceptable service properties.

Hardenability is an important factor⁽²⁾. Manganese, chromium and molybdenum are all efficient promoters of hardenability whereas nickel is not. The major constraints in any strategy would therefore seem to be cost, in the case of nickel and molybdenum, and oxide formation in the case of chromium and manganese.

Silicon is found in iron by virtue of its presence in the ore or as a deoxidation element in the refining process. Normally the level of silicon in iron is fairly low.

In powder forging alloys, the top limit for nickel is set in relation to its cost. It is usually accepted that up to 2% is a reasonable compromise between the attainment of hardenability and cost⁽¹⁶⁾. The lower end is of the order of 0.25% which gives some small degree of hardenability.

A minimum of 0.25% molybdenum is necessary to affect hardenability⁽¹⁶⁾. Up to about 0.7% is currently used but beyond

this figure molybdenum becomes too expensive and is only found in special purpose alloys.

Manganese in powder forging alloys is desirable from hardenability and cost points of view. However, this has to be equated with its affinity for oxygen and a compromise made. The current situation appears to be that to obtain a significant effect on hardenability a lower limit of 0.25% is desirable but, to restrict oxide formation, an upper limit of about 0.55% is appropriate.

Chromium strongly promotes hardenability and is desirable from this point of view. Theoretically chromium oxide is easier to reduce than manganese oxide but it forms a coherent, tenacious oxide film, and both elements appear to be additive when considering oxidation effects. Manganese, however, is first choice because of its sulphur control. Consequently, a minimum of 0.15% chromium is used to aid hardenability; the upper limit is not clearly defined but at the 0.5% chromium level there is a marked increase in inclusion content⁽¹⁶⁾.

2.2 Single Droplet Studies

The number of publications pertaining to the fluidodynamic behaviour and heat and mass transfer characteristics of single droplets in free fall through a fluid medium is considerable and it is beyond the scope of the present work to attempt a complete review. Only a general introduction with a more detailed review of that work which is pertinent to this research will be considered here. More extensive reviews of the literature already exist^(22,23).

2.2.1 Fluidodynamic Considerations

A droplet in free fall through a fluid will accelerate until the force of gravity producing the motion is exactly balanced by the buoyancy force and by the drag forces (F_D) at the surface of the droplet, tending to resist motion. From this point onward the drop will move at a constant velocity, the terminal velocity, u_t .

$$\pi \frac{d_d^3}{6} \rho_d = \pi \frac{d_d^3}{6} \rho_f + F_D$$

where d_d is the diameter of the droplet and ρ_d and ρ_f are the densities of the droplet and fluid respectively.

$$\text{Hence: } F_D = \frac{\pi d_d^3}{6} (\rho_d - \rho_f) \quad 2.1$$

The drag force acting on a freely falling droplet is quantified in terms of the dimensionless group, the drag coefficient, C_D :

$$C_D = \frac{F_D}{A_p \cdot \frac{1}{2} \rho_f u_t^2} \quad 2.2$$

where A_p is the 'projected' surface area of the droplet, such that

$$A_p = \frac{\pi d_d^2}{4} \quad 2.3$$

The drag coefficient is a function of the shape of the droplet and the Reynolds Number of the droplet

$$N_{Re} = \frac{d_d u_t \rho_f}{\mu_f} \quad 2.4$$

Graphical correlations between C_D and N_{Re} are presented in the literature, Figure 7(24).

When the Reynolds number is less than unity, creeping flow conditions pertain. Creeping flow conditions usually only apply to very small droplets, e.g. for steel droplets in slag such a condition only occurs with droplet diameters $<0.5 \text{ mm}$ (25). The droplet is so small that surface tension forces dominate its internal fluidodynamic behaviour, causing it to effectively behave as a solid sphere. Under these conditions it is found that:

$$C_D = \frac{24}{N_{Re}} \quad 2.5$$

By substituting from equations 2.2, 2.3 and 2.4 it can be shown that the drag force acting on the droplet under these conditions is given by:

$$F_D = 3\pi d_d \mu_f u_t \quad 2.6$$

This equation is known as Stoke's Law, in honour of Stokes who derived it analytically by integrating the Navier Stokes equations for the case of creeping flow(26).

The value of the terminal velocity of the droplet under creeping flow conditions may be obtained by combining equations 2.1 and 2.6

$$u_t = \frac{d_d^2 g (\rho_d - \rho_f)}{18 \mu_f} \quad 2.7$$

For droplets with a Reynold's number greater than 0.5, surface tension forces are no longer sufficient to cause the droplet to behave as a rigid sphere. The external flow of fluid over the surface of the droplet induces circulatory flow within the droplet(27), Figure 8, reducing the drag force below that predicted by Stokes' Law,

$$C_D = \frac{18.5}{N_{Re}^{0.6}} \quad 2 < N_{Re} < 10^3 \quad 2.5$$

(intermediate region, Fig.7)

The terminal velocity of the droplet is consequently greater than that predicted by Stokes' Law⁽²⁸⁾, see Figure 9.

For even larger droplets, and hence even greater N_{Re} , the droplet deforms to an oblate spheroid but the terminal velocity it reaches is below the value predicted by Stokes' Law.

The peak velocity is generally associated with increased droplet distortion and the onset of oscillations; both of which tend to reduce the velocity. Ultimately a size is reached at which the oscillations are so pronounced that surface tension is no longer sufficient to prevent the break-up of the droplet. Allied to these phenomena are changes in the flow pattern of the fluid over the external surface of the droplet. At higher Reynold numbers the boundary layer becomes separated from the rear surface of the droplet leading to the formation of a turbulent wake behind the droplet. All of these phenomena lead to a considerably enhanced, drag force on the droplet - usually referred to as the 'form drag'. Various mathematical models have been developed which attempt to predict the effect on the terminal velocity of various degrees of internal circulation and droplet oscillation^(29,30,31).

Hadamard⁽³²⁾ and Rybczynski⁽³³⁾ have derived a limiting law which predicts the effect of internal circulation. This law for laminar flow corresponds to Stokes' law for solid spheres and also gives an exact solution of the Navier Stokes equations. The boundary conditions differ from those for flow around solid particles. In the case of solid spheres the velocity at the inter-

face is zero; for the droplet it is equal in both phases, but not equal to zero. In the droplet the velocity decreases towards the centre and reaches negative values in the interior (relative to the external flow pattern). Compared to Stokes' Law the resistance is smaller i.e. the ascending velocity is larger due to the non-zero velocity at the interface. Hadamard expressed the frictional force and drag coefficient by the equations:

$$F_D = \pi d_d \mu_f u_\infty \left(\frac{2 \mu_f + 3 \mu_d}{\mu_f + \mu_d} \right) \quad 2.9$$

$$C_D = \frac{2 \mu_f}{\mu_\infty d_d \rho} \left(\frac{2 \mu_f + 3 \mu_d}{\mu_f + \mu_d} \right) \quad 2.10$$

$$C_D = \frac{8}{N_{Re}} \left(\frac{2 \mu_f + 3 \mu_d}{\mu_f + \mu_d} \right) \quad 2.11$$

Combining equations 2.1 and 2.2 gives

$$u_t = \left[\frac{4 g d_d (\rho_d - \rho_f)}{3 C_D \rho_f} \right]^{1/2} \quad 2.12$$

Combining 2.10 and 2.12 (where $u_t = u_\infty$), the terminal velocity u_t can be expressed as

$$u_t = \frac{g d_d^2 (\rho_d - \rho_f)}{6 \mu_f} \left(\frac{\mu_f + \mu_d}{2 \mu_f + \mu_d} \right) \quad 2.13$$

which is known as the Rybczynski-Hadamard equation. For droplets falling through a gaseous medium, the viscosity of the gas is very small compared to the viscosity of the droplet and can therefore be neglected: as a result Stokes' Law reapplies.

The drag coefficient of non-spherical droplets depends not only on the Reynold's number but also on a dimensionless number known as the sphericity. This factor takes into account the deviations of the droplet from a sphere. Sphericity is defined as:

$$\psi = \frac{\pi d_v^2}{A} \quad 2.14$$

where A is the droplet surface area

and d_v is the diameter calculated from the volume where

$$d_v = 2 r_v = \sqrt[3]{\frac{6v}{\pi}} \quad 2.15$$

Pettyjohn and Christiansen⁽³⁰⁾ suggest that the terminal velocity of an isometric body can be expressed by Stoke's law for low Reynold's numbers provided a correction factor κ (kappa) is introduced:

$$u_t = \frac{\kappa d_v^2 g (\rho_d - \rho_f)}{18 \mu} \quad 2.16$$

$$\text{where } \kappa = 0.843 \log \frac{\psi}{0.065} \quad 2.17$$

κ depends on sphericity. It can be seen that the terminal velocity decreases with the sphericity, which means that the resistance increases with increasing deviation from the spherical shape.

Although drag forces on small drops are often expressed in terms of Stoke's law, this is sometimes not correct⁽²⁴⁾. The conditions for flow around droplets are complicated by the influence of interfacial tension. Although a number of experimental and theoretical investigations have been made, notably

the work of Garner and Lane,⁽³¹⁾ many of the phenomena are not yet completely understood.

The influence of surface active agents on the velocity of droplets in laminar flow has been considered theoretically. According to Gibb's adsorption isotherm surface active agents accumulate in the interface⁽²⁹⁾. When the droplet moves in the surrounding fluid, the concentration of the surface active agent at the stagnation point becomes lower than the equilibrium value due to the continuous renewal of the interfaces; at the rear it increases, since the molecules present in the interface are transported to the rear by the flow. The concentration gradients so formed in turn give rise to a gradient of the interfacial tension and as such provide an additional tangential force retarding the flow along the interface. This phenomenon has been examined theoretically by a number of investigators, notably Levich⁽³⁴⁾. He put forward the following expressions for drag coefficient and terminal velocity:

$$C_D = \frac{8}{N_{Re}} \left[\frac{2 \mu_f + 3 \mu_d + 3 \gamma}{\mu_f + \mu_d + \gamma} \right] \quad 2.18$$

$$u_t = \frac{g d_d^2 (\rho_d - \rho_f)}{6 \mu_f} \left[\frac{\mu_f + \mu_d + \gamma}{2 \mu_f + 3 \mu_d + 3 \gamma} \right] \quad 2.19$$

The coefficient 'gamma' is the retardation coefficient. As γ tends to zero, equations 2.18 and 2.19 become the Rybczynski-Hadamard equations. With very large values of the retardation coefficient ($\gamma \gg \mu_f + \mu_d$), Stokes relationships are obtained.

The value of the retardation coefficient depends on the concentration gradient attained at the bounding surface; this in turn is dependent on the kinetics of the transport of the surface active agent. Levich derived three equations for the situations when either a phase boundary reaction, volume diffusion or boundary surface diffusion is the rate determining step, assuming that the surface active agent is practically insoluble in the droplet.

When reaction, i.e. adsorption is rate determining the following equation applies:

$$\gamma_1 = \frac{2 \Gamma^*}{2 k r} \left| \frac{\partial \sigma}{\partial \Gamma} \right| \quad 2.20$$

where k is the rate constant and is determined experimentally.

When volume diffusion is rate determining, i.e.

$$\gamma_2 = \frac{2 RT (\Gamma^*)^2 \delta}{3 D r C_\delta} \quad 2.21$$

For practically insoluble surface active agents the surface diffusion is rate determining, and for the retardation coefficient one can write:

$$\gamma_3 = \frac{2 \Gamma^* r RT}{3 D} \quad 2.22$$

where D is the coefficient of the interface diffusion.

For higher Reynold's numbers ($N_{Re} > 1$) the theoretical derivation of similar resistance laws is very difficult and only possible by making some simplified assumptions. A number of

derivations have been made but these are mainly associated with spherical bubbles rising through a liquid. B T Chao^(35,36) has suggested an equation applicable to droplets:

$$C_D = \frac{16 b_2}{N_{Re}} \left(1 + \frac{0.814}{N_{Re}^{1/2}} \right) \quad 2.23$$

where $b_2 =$

$$\frac{2 + \frac{3 \mu_d}{\mu_f}}{1 + \left(\frac{\rho_d \mu_d}{\mu_f \mu_f} \right)^{1/2}} \quad 2.24$$

The resistance law is only valid for spherical or nearly spherical droplets.

Hamielec and Woo⁽³⁷⁾ carried out a theoretical investigation of the effect of simultaneous free fall and forced thermal convection on fluid drag for a single sphere fixed in an unbounded fluid moving at constant velocity. Their main conclusion is that Stoke's law can be in serious error for low Reynold's number flows ($N_{Re} < 1$) when applied to estimate the terminal velocity of a sphere falling in a fluid of low Prandtl number and of different temperature. They suggest that, in particular, when $N_{Gr} N_{Re}^{-2}$ is greater than 0.5, Stoke's law is significantly in error and should only be used for rough estimations.

2.2.2. Heat and Mass Transfer Considerations

The reaction mechanism between a droplet and a gaseous atmosphere involves:

- (i) Mass transfer within the continuous, gas phase.
- (ii) Reaction at the gas-droplet interface.
- (iii) Mass transfer within the dispersed phase, i.e. the droplet.

The rate of any one or combination of these processes may *effectively* control the overall rate of the process.

The rates of mass transfer processes are influenced by the stirring conditions and the diffusion coefficients of the relevant reactive species within the continuous and dispersed phases. Interfacial reaction rates are influenced by the activation energy and the probabilities of the chemical steps involved i.e. adsorption and reaction.

Heat and mass transfer in fluid media primarily occurs by convection which may be natural or forced. The functional dependence of heat and mass transfer coefficients may be expressed in terms of dimensionless groups. Thus for mass transfer:

$$N_{Sh} \propto N_{Re}^{\alpha} \cdot N_{Sc}^{\beta} \quad \text{for forced convection}$$

and

$$N_{Sh} \propto N_{Gr}^{\alpha^1} \cdot N_{Sc}^{\beta^1} \quad \text{for natural convection}$$

Similarly, the heat transfer coefficient may be expressed:

$$N_{Nu} \propto N_{Re}^{\gamma} \cdot N_{Pr}^{\delta} \quad \text{for forced convection}$$

and

$$N_{Nu} \propto N_{Gr}^{\gamma^1} \cdot N_{Pr}^{\delta^1} \quad \text{for natural convection}$$

Radial diffusion always exists. In the limiting case of a spherical particle in a motionless fluid:

$$N_{Re} = N_{Gr} = 0$$

it has been shown⁽³⁸⁾ that $N_{Nu} = N_{Sh} = 2$ for heat/mass transfer in the continuous phase.

This is taken into consideration in the previously noted dimensionless relationships so that, for example, in the case of forced mass convection: $N_{Sh} = 2 + C N_{Re}^{\alpha} N_{Sc}^{\beta}$ where C is a constant.

A large number of investigations have been carried out to determine the values of the constant and exponents in equations of the above general type. (25,38,39,40,42)

2.2.2(i) Heat and Mass Transfer in the Continuous Phase

Natural convection occurs when $N_{Re} = 0$. Mass transfer results from the flow of the surrounding medium promoted by differences in the fluid density brought about by concentration and/or temperature gradients. High temperature differences between the sphere and the gas enhance this effect. Merk and Prins⁽³⁹⁾ analysed heat losses by natural convection from which an analogy for mass transfer can be made. Madden, Piret and co-workers^(40,41) solved, numerically, the simultaneous heat and mass transfer equations for free convection. Steinberger and Treybal⁽⁴²⁾ derived two equations depending whether $N_{Gr} N_{Sc}$ was greater or less than 10^8 .

Forced convection arises when $N_{Re} > 0$ i.e. when relative flow exists between the sphere and the bulk fluid. Differences exist in the literature as to the most appropriate form of dimensionless relationship to use. The simplest form for mass transfer in the continuous phase, for a stagnant sphere under conditions where natural convection is negligible is given:⁽⁴²⁾

$$N_{Sh} = 2 + \text{const. } N_{Re}^{\frac{1}{2}} N_{Sc}^{\frac{1}{3}} \quad 2.25$$

For high Sherwood numbers where the radial diffusion flux can be ignored:

$$N_{Sh} = \text{const. } N_{Re}^{\frac{1}{2}} N_{Sc}^{\frac{1}{3}} \quad 2.26$$

Davies and Alexander⁽²⁵⁾ suggest the constant lies between 0.6 and 0.8. This type of correlation applies only to the leading surface

of the sphere and completely ignores the wake. The contribution of the rear surface is due to turbulent transfer through the wake. Unfortunately this is not amenable to rigorous theoretical treatment. White and Churchill⁽⁴³⁾ suggested that the contribution is proportional to the Reynold's number. A more satisfactory correlation is proposed by Kinard et al⁽⁴⁴⁾ of the form:

$$N_{Sh} = \text{const. } N_{Re}^{\frac{1}{2}} N_{Sc}^{\frac{1}{3}} + \text{const. } N_{Re} N_{Sc}^{\frac{1}{3}} \quad 2.27$$

where the second term describes transfer within the wake region of the droplet surface.

Rowe, Claxton and Lewis⁽⁴⁵⁾ have reviewed published data on heat and mass transfer to spheres, and, together with experimental results, in which heat and mass transfer between air and a spherical particle was measured, arrived at the following equation:

$$N_{Sh} = 2 + 0.69 N_{Re}^{\frac{1}{2}} N_{Sc}^{\frac{1}{2}} \quad 2.28$$

The Reynold's number exponent increases slowly from about 0.4 at $N_{Re} = 1$ to about 0.6 at $N_{Re} = 10^4$ but it can be assumed constant and equal to 0.5 in the range $20 < N_{Re} < 2000$.

Hadamard⁽³²⁾ has suggested improvements to this approach and derived the equation:

$$N_{Sh} = 2 + \text{const. } Re^{\frac{1}{2}} N_{Sc}^{\frac{1}{2}} \left[N_{Sc} \left(\frac{\mu_f}{\mu_d + \mu_f} \right)^{\frac{1}{2}} \right] \quad 2.29$$

by considering the surface velocity term in viscous systems. The constant lies between 0.46 and 0.61⁽⁴⁶⁾ It is clear, from the above, that circulation and oscillation are of major importance in determining mass transfer rates

For a circulating drop, Beek and Kramers⁽⁴⁷⁾ have used the penetration theory to derive the following equation:

$$N_{Sh} = 2 + 0.80 N_{Re}^{1/2} N_{Sc}^{1/2} \left[\frac{\mu_f}{\mu_f + 1.5 \mu_d} \right] \quad 2.30$$

Richardson⁽⁴⁸⁾ quotes the dimensionless equation of Steinberger and Treybal which relates the Sherwood number to other dimensionless groups:

$$N_{Sh} = 2 + 0.5 (Gr'' N_{Sc})^{0.25} + b (N_{Re} N_{Sc})^{0.5} \quad 2.31$$

The first term, as already noted, represents the contribution from radial diffusion such as would occur in a static isothermal system. The second term is a contribution from free convection and would arise with a droplet which is hotter than the gas even without any imposed gas flow. The third term is a contribution arising from gas flow under isothermal conditions. The value of the constant, b, depends on the geometry of the system e.g. the relation between the size of the droplet to the diameter of tube in which it is supported or down which it falls. At low temperatures the first and third terms are the most important, but at high temperatures all three terms are about equally important. The Grashof number N_{Gr}^1 is a mean value of Grashof number as defined by Mathers et al⁽⁴¹⁾ instead of N_{Gr} where:

$$N_{Gr}^1 = N_{Gr_{mass}} + \left(\frac{N_{Sc}}{N_{Pr}} \right)^{0.5} N_{Gr_{heat}} \quad 2.32$$

This follows the suggestion of Baker et al⁽⁴⁹⁾ who used a mean value of Grashof number because heat and mass transfer occur

simultaneously in the very steep temperature and concentration gradients which co-exist when reacting gases at room temperature come into contact with metal which is 1500°C or hotter.

Richardson⁽⁴⁸⁾ notes that it is surprising that the three contributions in equation 2.31 should be additive but states that experiment shows this to be approximately so, whereas Kinard et al question the validity of linearly adding the contributions of radial diffusion, natural convection and forced convection to obtain the overall transfer rate.

More recently, Furuta et al⁽⁵⁰⁾ investigated the average and local mass transfer coefficients for a rotating sphere in an axial stream with rotational Reynolds number N_{Re_t} from 10^3 to 5×10^4 and four kinds of stream Reynolds number N_{Re_t} of 0, 2000, 3800 and 10,000. They used an electrochemical method and fifteen isolated electrodes were used to obtain the local mass transfer rate. The average Sherwood numbers $N_{Sh_{av}}$ were measured for a stationary sphere in the stream ($N_{Re_r} = 0$) and for a rotating sphere in a quiescent fluid ($N_{Re_t} = 0$). These were correlated as:

$$N_{Sh_{av}} = 1 + 0.570 N_{Re_t}^{\frac{1}{2}} N_{Sc}^{\frac{1}{3}} \quad 2.33$$

$$N_{Sh_{av}} = 1 + 0.453 N_{Re_r}^{\frac{1}{2}} N_{Sc}^{\frac{1}{3}} \quad 2.34$$

The local mass transfer coefficients N_{Sh_1} within the laminar boundary layer were found to increase gradually with increase of rotational speed.

Levi and Mehrabian⁽⁵¹⁾ investigated the heat flow in atomised aluminium, iron and nickel droplets using an enthalpy model. They presented equations describing the cooling of an initially super-

heated droplet and a numerical heat flow model for its subsequent solidification. Parameters such as times for initiation and completion of solidification, cooling rates and interface velocities in iron were related to the process variables governing the rate of heat extraction from the droplets. The models predicted that the average cooling rate in the liquid prior to solidification is directly proportional to the heat transfer coefficient in the gas phase, h , inversely proportional to the droplet radius, r , and independent of the initial superheat. The cooling time, t^0 , for the surface to reach the melting point, which was estimated from the analytical solution, increases with increasing superheat towards the Newtonian model prediction:

$$\frac{\alpha_b t}{r^2} = \frac{\ln(1 + \theta_0/Ste)}{3 Bi} \quad 2.35$$

Reducing the droplet radius, r , has a less pronounced effect on t^0 than the direct proportionality indicated by the Newtonian model. However, increasing the heat transfer coefficient at the droplet surface has a more pronounced effect on decreasing t^0 than the inverse proportionality predicted by Newtonian cooling.

In the continuous phase, mass transfer is faster for fully circulating drops than for rigid drops. In his work on heat transfer, Boussinesq⁽⁵²⁾ showed that the following dimensionless correlation should apply:

$$N_{Sh} = \frac{2}{\sqrt{\pi}} N_{Re}^{0.5} N_{Sc}^{0.5} \quad 2.36$$

An equation was derived by Higbie⁽⁵³⁾ who considered transfer to take place by unsteady state diffusion from elements of liquid which are formed at the front stagnation point and pass in stream-

lines over the surface until they reach the rear of the droplet. Compared with Steinberger and Treybals' equation for rigid drops, equation 2.31, the rates given by Higbie's model are some four to six times greater, depending on drop size and liquid properties. For a circulating droplet, Boussinesq⁽⁵²⁾ applied the penetration theory to continuous phase transfer and found the relationship:

$$\beta = \frac{2 D^{1/2} u^{1/2}}{\pi^{1/2} d^{1/2}} \quad 2.37$$

2.2.2(ii) Heat and Mass Transfer in the Dispersed Phase

The nature of the velocity profiles in and around a falling droplet and the intensity of any internal circulation will vary from one droplet to another depending on the duration of the fall, the size and inertia of the droplet and the presence of any adsorbed species. For the case of no circulation, there will be minimum rates of mass transfer. If the surface of the droplet is kept saturated by the continuous phase, then the fractional saturation for a drop starting from zero bulk concentration is given by⁽⁵⁴⁾

$$F = \left[1 - \exp \left(\frac{-4 \pi^2 D_d t}{d^2} \right) \right]^{1/2} \quad 2.38$$

When mass transfer in the continuous phase is rate controlling, the Steinberger and Treybal correlation, equation 2.31, can be used for most cases neglecting the free convection term.

It can be supposed that if there is full circulation within the droplet plus random radial motions caused by oscillations, these conditions will give maximum internal rates of transfer. A model to describe such a situation has been proposed by Handlos and

Baron⁽⁵⁵⁾. They assumed that transfer takes place by eddy diffusion arising from the radial motions, the speeds of which are related to the rate of circulation within the droplet which in turn is determined by the droplet size and velocity and by the viscosities of the two phases. They developed the relation:

$$k_d = \frac{0.00375 U}{1 + \frac{\mu_d}{\mu_c}} \quad 2.39$$

where U is the velocity of the drop, and

μ_c and μ_d are the viscosities of the continuous and dispersed phases respectively.

An intermediate model, between the rigid and oscillating turbulent models has been developed by Kronig and Brink⁽⁵⁶⁾. The model only considers a circulating droplet with no radial motion which would be more applicable to low Reynolds numbers. The rate of mass transfer is entirely controlled by radial diffusion within the drop. The equation for the fractional saturation for a droplet starting with zero bulk concentration has the same form as equation 2.38 except that the term D_d , the diffusion coefficient, is replaced by $2.25 D_d$. Hence the effect of the circulation is equivalent to increasing the diffusivity in the droplet by a factor of 2.25.

2.2.3 Surface Phenomena

In addition to fluidodynamic factors, mass transfer itself may lead to interfacial turbulence due to concentration or density variations, the Marangoni effect, which may further increase mass transfer rates.⁽⁵⁷⁾ Garner⁽²⁷⁾ has shown that mass transfer

coefficients in drops of water and organic liquids in a wind tunnel are highest in the first few seconds of their existence, presumably due to the high circulations induced in the droplets during their formation. Another factor is the presence of surfactants which tend to decrease mass transfer either by interfering with circulation patterns or by reducing the effective interfacial area by blocking transfer sites⁽³²⁾.

Interfacial turbulence may occur when a reaction taking place at an interface involves the transfer of a surface active substance. It arises when the eddies in the gas or liquid phase which bring reactants to the interface, give rise to local variations in the surface concentrations of these agents bringing about strong local changes in surface tension. Thus, whilst reaction is taking place, the surface tension varies from one place to another over the interface; the areas of high surface tension tend to contract whilst those of low surface tension tend to expand. Movement of the interface may then result.

Kozakevitch⁽⁵⁸⁾ has shown that oxygen, along with a number of other elements, is surface active in liquid iron and lowers the surface tension strongly. It is possible that in reactions in which oxygen is removed from or added to liquid iron, eddies in the metal (or gas) may bring about sufficiently large local changes in surface tension for interfacial turbulence to be set up. Because this effect occurs at such a critical region i.e. the interface, it may greatly enhance the mass transfer coefficient in the metal phase. However, from data presented to date it is not possible to determine how important such effects are. The effect of oxygen on the surface tension of iron is shown in Fig.10. Kozakevitch

also notes that Cr, Mo, Mn and Ni in dilute solution in iron are not surface active. Richardson⁽⁵⁹⁾ notes that although some highly active solutes such as oxygen and sulphur have strongly exothermic heats of solution, this is no guide to surface activity, because silicon and phosphorus are only weakly active in iron in spite of their high heats of solution.

The Gibbs adsorption equation has been applied⁽⁵⁸⁾ to data for oxygen in liquid iron in order to estimate the excess of solute in the surface region over and above the concentration in the bulk liquid. The Gibbs equation is:

$$\Gamma_s = - \frac{1}{RT} \left(\frac{\partial \gamma}{\partial \ln a_s} \right)_T \quad 2.40$$

where Γ_s is the excess quantity of solute s associated with unit area of interface, γ is the surface tension and a_s is the activity of the solute in the system. A plot of the surface tension of liquid iron vs $\ln \%O$ is shown in Fig.11. The slope $\frac{\partial \gamma}{\partial \ln [\%O]}$ is equal to the term in the bracket in equation 2.40 since the activity coefficient of oxygen is constant over the relevant concentration range. From such slopes the values of Γ shown in Fig.12 have been obtained.

Equation 2.40 only gives the excess solute in the interfacial region. Richardson⁽⁵⁹⁾ suggests that it is confined to one layer of atoms. If it is assumed that the limiting value of Γ represents complete coverage of the surface by the adsorbed species, the fraction of the surface covered at each concentration may be calculated⁽⁶⁰⁾ as shown in Fig.13 for oxygen in iron. If the adsorption reaction is represented as:

$$[O]_b + \square_s = [O]_s \quad 2.41$$

where \square_s is a vacancy in the surface and subscripts b and s represent bulk and surface concentrations,

$$K = \frac{[O]_s}{[O]_b \square_s} = \frac{\theta}{[O]_b (1-\theta)} \quad 2.42$$

where θ is the fraction of surface covered.

Richardson notes that in the case of oxygen in iron, $\%[O]_b$ may be written instead of $[O]_b$ because the activity coefficient is constant.

The initial slope of the curve in Fig.13 gives a value for K of 71. When the film tends to saturation the value is 780; the curve for an ideal monolayer with K equal to this value is shown by the broken line. This suggests that the activity coefficient of the oxygen in the surface layer decreases markedly as its concentration rises.

Richardson⁽⁴⁸⁾ quotes examples where high temperature reaction kinetics have been found to be chemically controlled. It seems probable that in some high temperature reactions between gases and metals adsorption of a surface active element such as oxygen may influence these kinetics.

Impurities in a metal may also exert an impeding effect by forming relatively thick films on the surfaces of metal droplets. It has been shown⁽⁶¹⁾ that when silicon is present in liquid copper at a concentration of 2 ppm it produces over the entire surface of the drop, a film of silica which impedes further

reaction. It is unlikely that very small amounts of silicon in iron could impede surface reactions as silicon is rapidly evaporated about 1500°C under oxygen pressures low enough for oxidation not to occur. On the other hand, large amounts of silicon in iron can be oxidised to form liquid slags and if these wet the metal they can cover the metal surface and so prevent direct contact between gas and metal.

Absorption of gaseous oxygen by liquid iron using a constant volume Sieverts' apparatus has been measured^(62,62). The absorption process was found to proceed in two stages. When pure oxygen came into contact with the surface of the molten iron, extremely rapid disappearance of oxygen from the gas phase accompanied by strong local superheating of the melt at the gas/metal interface was observed. The rate of oxygen uptake during this stage was found to be dependent upon oxygen pressure and gas/metal interfacial area, but essentially independent of temperature, volume and stirring conditions of the melt. This was followed by a second stage of continued absorption at a much lower rate in the presence of an oxide phase covering the melt. This rate depended on oxygen pressure. It was noted that the absorption during both stages was independent of concentration of dissolved oxygen in the melt.

2.2.4 Previous Experimental Work on the Oxidation of Single Droplets

The reaction between levitated iron droplets and flowing gases containing oxygen and of free falling iron droplets in oxygen containing atmospheres has been extensively investigated.

However, most of the work has been in relation to the decarburisation of molten iron. Baker et al⁽⁶⁴⁾ determined rates of decarburisation of levitated Fe-C droplets containing 5.5 to 0% carbon at 1660°C. They noted that with 10% or more oxygen in the gas stream and when the carbon concentration in the melt was low (less than 1% C), the rate of oxygen supply through the gas boundary layer exceeded the rate of consumption by carbon at the surface; the specimen surface became rich in oxygen and some of the excess oxygen diffused into the specimen leading to internal nucleation of CO within the droplet (i.e. mass transport control within the dispersed phase). Baker and Ward⁽⁶⁵⁾ reacted single iron droplets of about 4 mm diameter, containing between 0.8% C and 4.5% C, during free fall through oxygen. At low carbon values, less than 0.5% C, the droplets exploded due to the formation of carbon monoxide within the droplet.

Distin et al⁽⁶⁶⁾ conducted a series of experiments where iron droplets were levitated in flowing gases. One of these experiments included the oxidation of pure iron drops in carbon dioxide. However, the samples were quenched in a 3ft column of flowing water. They noted that a flaky oxide layer formed on the surface of the quenched droplets due to the reaction with the water. The flaky oxide layer was removed by light filing before the oxygen picked up during the experiment could be determined by analysis. Figure 14 shows the oxidation of iron droplets in flowing carbon dioxide.

Desforges⁽⁶⁷⁾ used a high frequency coil to melt wires to form droplets in argon. The droplet fell down a flight tube where

it was oxidised in air or oxygen prior to quenching through argon into water. A soap film was used to separate the oxidising gas and the argon at the top of the tube. The oxidising column length was controlled up to a height of 1.3 metres by means of a second soap film below which was argon directly above the water quench tank. Binary alloys of Fe-Mn up to 6.78 mass % Mn, Fe-Si up to 9.5 mass % Si and Fe-Zr up to 3.0 mass % Zr were investigated. Photographic evidence of a falling drop revealed that the droplet oscillated from spherical to prolate spheroid and in the case of Fe-3 mass % Si alloy, the frequency of oscillation was 166 Hz. An investigation into the fuming of certain alloys, notably the Fe-Mn alloys, was also made. The quenched droplets were metallographically mounted and the oxide phase examined by electron probe microanalysis. He concluded that if the oxygen flux to the droplet surface was greater than the metal vapour flux then a liquid oxide should form whilst the reverse condition should produce a vapour/gas reaction. Fe-Mn alloys exemplified the latter situation. In the case of Fe-Si alloys he concluded that a liquid oxide forms and the rate of oxidation is controlled by the rate of transfer of oxygen through the liquid oxide.

Vig and Lu⁽⁶⁸⁾ used levitation melting to study the oxidation kinetics of free-falling iron droplets. Single droplets of about 1 g were initially deoxidised by hydrogen then allowed to fall through oxidising columns of known heights and then quenched in silicone oil. The amount of oxygen picked up by a droplet, for a given height of fall was found to be dependent on its initial temperature, its size, and the composition of the

reacting gas. The effects of these parameters on oxygen pick up are shown in Figs.15-18.

Schwerdtfeger and Wepner⁽⁶⁹⁾ have suggested a model to calculate the oxidation of disintegrated steel streams by mass transfer of oxygen to the droplets. The mass transfer of oxygen into the cylindrical space occupied by droplets and gas is assumed to occur by bulk flow and diffusion. They computed the increase in oxygen content of the metal phase for a steel stream disintegrated into droplets of various sizes; the result for a steel stream of 4 cm radius falling into a cylindrical space 8 cm radius with a starting velocity of 600 cm s^{-1} is shown in Fig.19.

Baker⁽⁷⁰⁾ studied the reactions which occur when molten iron-alloy droplets fall freely in oxygen. He found that with carbon-silicon-manganese-iron alloys up to 80% of the silicon and manganese was removed during a 5 foot fall. The emphasis of the work was on carbon and sulphur removal from carbon-containing and sulphur-containing alloys. The alloys were quenched in water and no account was taken of oxygen levels in the samples so obtained.

2.3 Oxidation and Reduction Characteristics

2.3.1 Oxidation Kinetics of Molten Iron and Iron Alloys

Several authors^(71,63,72,62,73) have used a constant-volume Sievert's apparatus to measure the rate of oxygen solution in molten iron. It was noted that the volume of gaseous oxygen which initially reacts with metals is strongly dependent upon the physical nature of the oxide film which forms during the initial

stage of reaction. In the case of molten iron which forms a liquid surface oxide the initial oxygen absorption is greater than for molten nickel which forms a solid oxide⁽⁷²⁾. The absorption of liquid iron containing up to 4 mass% Si is similar to the oxidation of pure iron at 1600°C. Above this concentration of alloying element, considerable decrease in the oxidation rate occurs^(72,73). This is shown in Fig.20. Formation of a silica-rich oxide layer on the melt prevents further progress of the exothermic chemical reaction. Further, addition of diluents to oxygen markedly and continuously decreased the oxidation rate of a pure iron melt.

Filippov and Zharov⁽⁷⁴⁾ using an emf method to investigate the kinetics of gaseous oxygen absorption by liquid iron identified three process stages. In the first stage after contact of the oxidant with the liquid metal surface, self- or auto-acceleration of the process takes place in a short space of time, with a rising rate up to a maximum value. With a decrease in the rate of supply of the oxidant, the individual stages became more prolonged and the maximum rate was maintained for a considerable interval of time. The final stage was characterised by a rapid drop in rate and by retarded oxygen absorption by the metal. The activation energy in the first stage of direct oxygen absorption by the metal was determined to be about 84 kJ mol⁻¹. Filippov and Zharov concluded that the oxidation of pure iron, even in the absence of dissolved oxygen was limited by the mass transfer of oxygen to the metal surface. This conclusion was also reached by Choh⁽⁷⁵⁾.

Hosoda and his co-workers⁽⁷⁶⁾ looked at the role of silicon and manganese in liquid iron in relation to their deoxidation behaviour. Iron-oxygen alloys, of up to 0.153 mass% oxygen, were mixed with iron-silicon, iron-manganese and iron-silicon-manganese alloys respectively. The alloys were brought into contact under argon and held at 1600°C for different periods. The specimens were allowed to solidify and a chemical profile was taken through each sample. In the case of silicon alone, iron oxides were reduced by silicon in the metal and transformed to solid silica. In the case of deoxidation by silicon and manganese with a 2:1 ratio of Si:Mn the oxide phase on nucleation was iron-manganese silicate. However, it was reduced by silicon in the metal and in due time was changed to solid silica particles. In the case of deoxidation by silicon and manganese with a ratio of Mn:Si of 2.5:1, non-metallic inclusions were always iron-manganese silicates.

Choh et al⁽⁷⁷⁾ measured the rates of oxygen absorption of liquid Fe-18% Cr, Fe-18% Cr - 8% Ni and Fe-25% Cr-20% Ni alloys from O₂-Ar gas mixtures. They found that the initial rates of oxygen absorption were proportional to the partial pressure of oxygen and independent of the alloy mixture. The results were consistent with those for liquid iron⁽⁷⁵⁾.

2.3.2 Diffusion of Oxygen in Molten Iron

The diffusivity of oxygen in molten iron has been measured by a number of techniques but more recently by oxygen concentration cell technique^(78,79). Kawakami and Goto⁽⁷⁸⁾ used a Mo, MoO₂/ZrO₂.CaO/Fe(O) cell and Povolotskiy and his co-workers⁽⁷⁹⁾ used a

Mo, $\text{MoO}_2/\text{ZrO}_2\cdot\text{Y}_2\text{O}_3/\text{Fe}(0)$ cell. The first group determined a value of diffusivity of $(1.9 \pm 0.7) \times 10^{-4} \text{ cm}^2 \text{ s}^{-1}$ at 1550°C . The second group measured the diffusion coefficient in the temperature range $1550\text{--}1650^\circ\text{C}$. They also determined the activity coefficient of oxygen in iron with initial oxygen contents of $0.003 - 0.95\%$. They reported the temperature dependence of the diffusion coefficient of oxygen in liquid iron as:

$$D_o = \exp \left(-6.65 - \frac{1671.32}{T} \right)$$

It was also found that the oxygen content in liquid iron influences only slightly its diffusion coefficient:

$$D_o = \exp \left(-7.45 + 0.028 \log a_o \right)$$

Ershov and Kasatkin⁽⁸⁰⁾ have reviewed the effect of alloying elements on oxygen diffusion rate in molten iron. Of the elements of interest, nickel dissolved in molten iron increases the rate of oxygen diffusion. On the other hand, molybdenum and chromium markedly reduce the value of D_o , the reason given is that they increase the viscosity of molten iron. The effect of these alloying elements on the value of D_o is given in Fig.21.

2.3.3 Reduction of Oxide Phases in Iron Powders

Bulanov et al⁽⁸¹⁾ have used an electrolytic dissolution technique to separate the oxide phases in alloyed iron powders. In a range of alloys containing up to 1.16% Ni, 0.75% Cr and 0.95% Mn they identified Fe_2O_3 , FeO , SiO_2 , Cr_2O_3 and MnO and they were able to deduce the relative amounts of the alloying element

present as oxide and in solution. Grintsov et al⁽⁸²⁾ reduced atomised iron powders in hydrogen. Virtually complete removal of oxygen from atomised iron powders of various fractions occurred in a very dry hydrogen atmosphere (with a dewpoint not exceeding -40°C) at an end reduction temperature of 500°C . The form of silica has an effect on the reducibility of iron oxide⁽⁸³⁾. If the silica is present as crystalline particles it improves the reduction and fayalite ($2\text{FeO}\cdot\text{SiO}_2$) does not form. If it is amorphous in form it undergoes reaction with wustite (FeO) to form fayalite which results in a deceleration in the reduction rate.

Ryzhonkov⁽⁸⁴⁾ argued that the reduction rate of an oxide mixture is not an additive function of the reduction rates of individual oxide components. The presence of a second oxide affects the reduction of the first one, even in a mechanical mixture. From his work, he showed that, depending on the relative amounts of oxides in the mixture, an intensification or deceleration of the reduction process is possible. For example, the reduction of Fe_2O_3 and Cr_2O_3 mixtures is complicated by the formation of spinels by the reduced wustite with Cr_2O_3 . Chu and Rahmel⁽⁸⁵⁾ studied the reduction kinetics of chromium oxide as a function of hydrogen partial pressures, gas flow rate and temperature. They found that reduction follows a linear time law and is dependent on gas flow rate below a value of approximately 10 cm s^{-1} . At high flow rates the phase boundary reaction is rate determining and the activation energy was found to be 123 kJ mol^{-1} .

Lindskog and Grek⁽⁸⁶⁾ investigated the reduction of oxide inclusions in powder preforms prior to hot forming. For a 1% Cr 1% Mn steel they found an initial reaction at 600-700°C. The oxygen content remained constant until a temperature of 800-900°C was reached. With increasing temperature the rate of reaction increased reaching its highest value at 1120°C for a heating rate of 4° C/min. and at 1200°C for 25° C/min. There were no discontinuities in either curve, Fig.22, which indicated that the oxides form a solid solution for which there was no sharp separation between the reduction of the different components at the heating rates employed. The results indicated that equilibrium conditions were practically established at 1300°C within 5-10 minutes.

2.4 Levitation Melting

2.4.1 Advantages and Disadvantages of Levitation Melting

One of the primary advantages of levitation melting is non-contamination of the melt⁽⁸⁷⁾. Iron is a moderately reactive metal and will react with many refractories resulting in a loss of purity when crucibles are used for melting.

Levitation melting is especially suited to physico-chemical studies of gas-liquid metal systems and difficulties of interpretation due to possible side reactions with crucible materials are eliminated.

Levitation melting offers rapid heating and melting. The rapid melting cycle for small samples permits a large number of metal samples or alloys to be prepared for investigation. Alternatively, rapid heating and melting allows the variation of more parameters than would ordinarily be practical.

Homogeneity of the melt due to very efficient stirring is also achieved in levitation melting. The induced currents in the metal droplet keep the charge in a continual state of motion and the molten metal is stirred efficiently. Polonis⁽⁸⁸⁾ noted that homogeneity is also retained in the "ingot" due to the rapidity of solidification. Comenetz and Salatka⁽⁸⁹⁾ obtained greater homogeneity with levitation melting than was obtained by repeated arc melting.

Rapid attainment of equilibrium is achieved in gas-liquid metal systems and is another advantage of levitation melting. The rapid attainment of equilibrium is due to the relatively large surface area of the droplet exposed to the gas phase and also to the efficient stirring of the melt. The rate is further

enhanced when the gas flows past the molten sphere. Peifer⁽⁹⁰⁾ has reported the increase in nitrogen content of molten pure iron from 2 ppm to the equilibrium solubility level of 445 ppm in 50 seconds by levitation melting. Rapid deoxidation of iron in a hydrogen stream is possible by this technique; the time required to deoxidise a 1 g sample being of the order of two minutes⁽⁶⁹⁾.

The main disadvantage of levitation melting is the difficulty of temperature control. In the design of a levitation coil for a particular metal there is often a conflict between the electromagnetic field for levitation and the field for heating. In some cases the power required to levitate the metal is so high that too rapid heating resulted⁽⁸⁸⁾. On reduction of power to the coil the levitation force decreases but as the metal sinks further into the coil the heating effect is increased. Another disadvantage is temperature measurement. Since a thermocouple cannot be used to measure the temperature of a molten droplet within the coil temperature can only be measured by pyrometry. Here problems of surface emissivities are encountered.

Stability within the coil can also be a problem⁽⁸⁸⁾. On occasions a droplet can begin to oscillate in the field of the coil. This can often occur when a droplet has been in the coil for a period of time⁽⁸⁸⁾. The reasons are not clear, but, resonance is important and sometimes changes in the properties of the droplet, e.g. due to oxidation, may be a factor. The amplitude of the oscillation may be diminished by regulation of the power to the coil. On occasions, however, the droplet may be ejected from the coil and then interaction with the containing walls occurs.

A lesser disadvantage can be the relatively severe vapourisation of high vapour pressure elements from a melt due to the large surface area to volume ratio and due to rapid stirring. This effect is of little importance in simple alloying but can be of extreme importance in physico-chemical experiments requiring longer times. The weight of a molten charge can also be a limitation.

2.4.2 Electromagnetic Field in a Levitation Coil

A conductor when placed in an electromagnetic field will move from the stronger to the weaker portion of the field. For levitation, the field strength must decrease vertically to provide a lifting force equal to the weight of the conductor. For lateral stability, the field strength must decrease radially toward the field axis, thus providing a restoring force forward of the axis. Such a field is obtained from two coaxial coils matched to a high frequency generator. Normally variable capacitance is employed to provide the means of tuning the load to the generator for maximum power transfer to the coils.

Levitation coils, in practice, are generally unequal, carrying alternating currents with a 180 degree phase difference. In this way, a point of minimum field strength, necessary for stable levitation, is obtained between the two coils. At some point along the axis between the two coils the fields from each coil are equal and opposite such that they exactly counteract each other, producing a null point in the field. The field strength increases in all directions from this point. A conductor placed

in the magnetic field will experience a force tending to move it toward the null point. Weightless conductors would remain at this point. In practice, an equilibrium will be established between the magnetic field and gravitational forces and the final position of the conductor will lie a certain distance below the null point. Slater et al⁽⁹¹⁾ investigated the electromagnetic field configuration within a levitation coil and the effect on this field of inserting a metallic charge within the coil. They devised a Magnaflux powder technique which produced interesting visible patterns of the levitation field. The field strength along the axis of a levitation coil was measured by Hulsey⁽⁹²⁾. He measured the voltage induced on a small probe coil, 3 mm o.d. x 3 mm long, wrapped on the end of a small quartz tube. The probe coil was calibrated by measuring the induced voltages when placed inside a straight solenoid where the field strength was readily calculated.

The fundamental equations of levitation theory were first stated by Okress et al⁽⁹³⁾. They considered the important factors that determine the levitating force on a solid sphere and arrived at a complex quantitative relationship. The fundamental result of their calculations is that the metal sphere behaves as an idealised magnetic dipole loop. They demonstrated experimentally that their theoretical result for the levitating force is accurate for a 1 inch diameter bronze ball suspended between two co-axial loops with current flowing in reverse directions. The approximation they used in deriving their formula is only valid for small spheres and relatively small

magnetic field gradients. The relationship which they derived indicates that the levitation force is directly proportional to the square of the coil current and to a complex parameter which is proportional to the square root of the frequency; the higher the frequency the larger the value of the parameter. As the parameter becomes very large, the lift or force function becomes a maximum at relatively low values of the parameter whereas the heating function increases almost without bound. The significance of their formula is that for metals of moderate electrical conductivity no significant increase in the levitation force results at very high frequencies. However, the energy absorbed by the conductor becomes so large that melting results and the temperature of the melt increases; the temperature may rise beyond the desired level. It can be concluded that the maximum levitation force with minimum heating is attained at low frequencies and high field strengths and gradients. The size and nature of the metal, coupled with the temperature, will determine the value of the frequency to be used.

There has been no adequate theoretical treatment of the levitation of a liquid mass. The problem here is not only that of total levitating force but also of local support of the droplet, in particular at the lower tip of the melt. Any solution to the problem should involve surface tension and the effect of an oxide or other surface film.

Comenetz and Salatka⁽⁸⁹⁾ have investigated the force in levitation melting. While the formula they quote is restricted with several limitations it does give perspective as to the influence of some parameters. The limitations are that the

charge is spherical, homogeneous and non-magnetic and small compared to distance over which the magnetic field can be assumed linear. The operating parameters are, first of all, material, viz. density and resistivity; secondly, electrical, viz. frequency and current and thirdly, geometrical, viz. coil dimension and charge radius.

It has been noted that the stability of a liquid metal is far more complex than for solid metals. Various workers^(88,89,92,93) have suggested that surface tension and the density of the liquid metals determine whether they will drip during levitation. Hulsey⁽⁹²⁾ in his report, has derived a relationship for a condition of static equilibrium involving surface tension, density and radii of curvature of the top and bottom of the melt. In his analysis, he neglected any electromagnetic or hydrodynamic forces acting on the melt and equated the static equilibrium pressures. Rony⁽⁹⁴⁾ has suggested that these calculations may be greatly in error since the stability of a levitated metal system depends on both static and dynamic elements. Static stability results with balanced electromagnetic, gravitational and surface tensional forces while dynamic stability is concerned with the oscillations set up by these forces. It can be argued that if a melt has a high value of surface tension then any instabilities generated in the melt will be inhibited to a greater extent than in the comparable situation of a melt with a low surface tension value. In this way, surface tension is important to both static and dynamic stability.

2.4.3 Design Considerations

Much of the work to date in the design of levitation coils has been empirical⁽⁹²⁾. Most of the analyses performed on levitation forces has been directed to solid charges and little attention has been directed to the study of heating effects or to the problem of coil design. In general coils have been constructed of 6 mm diameter or less copper tubing. For a given coil current the levitating force increases with coil turns⁽⁹⁰⁾. Hence, the smallest diameter tubing is preferable to provide more turns/unit length of coil. This is important in the high gradient position and for multilayer coils. In practice, 3 mm diameter tubing is about the smallest that can be adequately cooled. In some instances larger bore tube has been taken and flattened to give it an oval shape, in this way more layers of tubing can be accommodated in a coil and there is less restriction on water flow. Small diameter coils provide higher field strengths but the volume of material that can be accommodated within the coil is restricted. Harris and Jenkins⁽⁹⁵⁾ in their coil design used 3 mm o.d. silver tubing to reduce the impedance of the coil.

Coils used for levitation melting have been of a variety of sizes and shapes. Slater et al⁽⁹¹⁾ arbitrarily determined the levitation force for various coil configurations. The coils were made by winding 3 mm diameter annealed copper tubing on wooden formers. Five conical coils were made so that the semi-cone angle varied from 0° (solenoid) to 90°. In addition, a sixth coil was made incorporating a reverse turn equal in diameter

to the top turn of the coil. From their results they concluded that the maximum levitating force occurred at or just above the smallest and lowest turn in the coil. The exception to this was the solenoid where the maximum force appeared to occur above the top turn. However, with the solenoid they found that lateral stability was absent. They found that as the conical coil semi-angle was increased the levitating force decreased to a minimum. This occurred at a cone semi-angle of 45° . They concluded that with a semi-angle of 20° to 30° optimum conditions of greatest metallic charge and ample lateral stability would be obtained. The levitating force appeared to be independent of coil semi-angle at values in excess of 60° . From investigations of the field developed in the coil, having a reverse turn at the top, it was found that the levitating force would be small until the metallic charge was well inside the top turns of the coil. This was further borne out by the measurement of the actual levitating force. However, the maximum force appeared to be at least as high as that obtained for a similar coil without a reverse turn. Slater also showed that to obtain the highest possible levitating force a coil with a few turns and with small diameter turns at the bottom is required.

Harris and Jenkins⁽⁹⁵⁾ in their designs used co-planar lower turns. This they argued was equivalent to a turn of smaller diameter and produced good stability of the liquid charge. They also adopted two co-planar reversed turns directly above the cone arguing that this produced high lateral stability

and prevented the levitated sample touching the side of the coil. Peifer⁽⁹⁰⁾ reported that cylindrical coils gave maximum levitating force but, for stability, required surmounted opposing coils or reverse turns.

The steady state temperature of a levitated charge depends upon the properties of the charge material, characteristics of the levitation system and the heat dissipated by the charge. The physical factors of importance in this connection are the electrical resistivity and the density of the specimen. Materials of greater mass or density and higher electrical resistivity levitate lower in the coil where the field strength is greater and thus are heated to a greater extent. The higher density materials require a high magnetic field strength to produce levitation and in turn a high temperature results. Decreasing the power permits the charge to drop lower into the coil with the result that the temperature increases. Since levitation force and heating of the metal are controlled, more or less, by the current control of the induction heater it follows that the high field strength required to support a high density material also often results in higher than desired temperatures. It has been noted^(90,95,96) that a separate way of cooling the levitated charge is by passing a gas of high thermal conductivity such as helium or hydrogen over the charge. This cooling effect can be significant at high flow rates. Additional means of temperature control are dependent upon adjusting the mass of the charge and/or power input. Peifer⁽⁹⁰⁾ found that the minimum temperature was obtained with a small charge.

It has been shown^(97,98) that the levitation force on a spherical charge increases with the square of the current, I , in the coil, and that the levitating force is independent of the current frequency at sufficiently high frequencies which are normally used in levitation melting. The diameter of the tubing used in the coil should be kept small to increase the number of turns which can be used in the high gradient positions. The minimum size which can be used will depend on the amount of power which must be dissipated in the cooling water.

Since the levitation force is proportional to the axial field gradient, G , the choice of adding an additional turn to the coil design depends on its effect on the ratio of G to the total tubing length. Increasing the length of the coil increases its resistance which in turn increases the power to the coil. The location of the coil turns are limited by physical restrictions. Allowance has to be made for insertion of the charge. Openings at the top and bottom generally limit the use of turns in positions which add greatly to the coil gradient, and thus reduce the levitating force and reduce the heating efficiency. The coil must also be made so that the leads can be brought out without interfering with the coil operation. The reversing connection from the upper and lower sections of the coil should be short to minimise the coil resistance and yet at the same time the field from the loop should not interfere with the magnetic field generated by the coil itself. Making this connection from the bottom turn of the upper coil to the top turn of the lower coil reduces this length and also reduces the problem of electrical

discharge between the coil sections. Another problem is due to the difficulty of bending tubing to small radii without flattening the tube and restricting the water flow.

2.4.4 Temperature Measurement and Control

Peifer⁽⁹⁰⁾ has reported that temperature control and measurement of a levitated charge has probably been the area of greatest difficulty in developing the levitation melting technique. The difficulty of control is inherent in the electrical equipment which requires that both the levitation force and the heating of the metal must be controlled, more or less, by the current control of the induction heater. Harris and Jenkins⁽⁹⁵⁾ claim that the mass of the sample levitated and its position in the coil are important factors affecting the equilibrium temperatures. The amount of energy lost by radiation at a given temperature depends on the surface area of the sample and the emissivity of the surface. For any one metal sample in the molten state, these variables are fixed and cannot be used as a means of temperature control. The heat lost by conduction depends upon the gas pressure and upon the gas composition. Variation in gas pressure from one atmosphere down to half an atmosphere increases the temperature only slightly^(90,95).

Measurement of the temperature of levitated metal droplets presents difficulties. Thermocouples have been ruled out on several grounds⁽⁹⁰⁾. Firstly, induced e.m.f's in the thermocouple from the high frequency coil give erroneous electrical

signals and also generate a heating effect in the thermocouple itself. Thermocouples would not be desirable or convenient in some respects because of possible melt contamination and, in many instances, the temperature is too high. These objections do not apply to the optical pyrometer but other difficulties arise due to the non-black conditions associated with an unenclosed body. Emslie and Blau⁽⁹⁹⁾ examined the case of an unenclosed body and concluded that, without a prior knowledge of emissivity, it was impossible to measure the temperature of such an object in the range 2 000-4 000 K with an accuracy greater than 10%. If, however, the emissivity of the body is known within 20%, the temperature can be determined within one or two percent by means of an optical pyrometer.

Jenkins et al⁽¹⁰⁰⁾ used an optical pyrometer to observe the solid-liquid junction of a molten drop formed on the end of a rod by induction heating. They measured the emissivity of the metal at this temperature i.e. at its melting point. This method was useful for reactive metals. However, they assumed that there was no appreciable change in emissivity above the melting point. This difficulty of emissivity values has been overcome to a certain extent by the use of two-colour pyrometers. The basis of this pyrometer is that the unknown quantity of emissivity can be eliminated by taking the ratio of the radiant intensities from the object at two different wavelengths, and that the emissivity is the same at the two wavelengths. However, the ratio of the emissivities at the two

wavelengths can, in practice, differ considerably from unity⁽⁹⁹⁾. Shiraishi and Ward⁽¹⁰¹⁾ modified the two-colour pyrometer technique by obtaining a linear calibration for the pyrometer against a thermocouple over the lowest part of their temperature range and extrapolated for the upper range. They considered their measurements correct to within $\pm 10^{\circ}\text{C}$. Peifer⁽⁹⁰⁾ found that emission of fume can be troublesome at high temperatures and leads to erroneous temperature measurement. Here he found the two-colour pyrometer gave correct temperature readings whilst a disappearing filament pyrometer indicated a temperature 300°C lower.

2.5 Quench Media

Different media have been used to quench reacted iron droplets. Water was used by Desforges⁽⁶⁷⁾, Baker⁽¹⁰²⁾, Distin et al.⁽⁶⁶⁾ and Vig and Lu⁽⁶⁸⁾. Liquid nitrogen and silicone oil were also examined by Vig and Lu.

Water was found to be very oxidising^(68,102). When deoxidised Armco-iron droplets, weighing about one gramme, were quenched into water without falling through an oxidising chamber an oxygen content in excess of 650 ppm resulted⁽⁶⁸⁾.

Liquid nitrogen always contains amounts of oxygen and the gas layer between the droplet and the liquid nitrogen gives a low quenching rate. Deoxidised droplets of iron when quenched into liquid nitrogen were found to contain more than 300 ppm oxygen⁽⁶⁸⁾.

Silicone oil was tested with respect to its oxidising and reducing powers on iron-oxygen droplets⁽⁶⁸⁾. The oxygen content

of deoxidised droplets quenched in 704 Dow Corning silicone oil was found to be less than 30 ppm. Specimens of Armco iron of known oxygen content (890 ppm) were levitated in an inert atmosphere and quenched into silicone oil. Droplet temperatures of 1580°C and 1638°C were used. The oxygen content of the quenched specimens was found to be within ±50 ppm of the initial values.

3.1 Production of Iron and Iron Alloy Wires

The wires used in the experiments were made from high purity materials. The iron base metal was Japanese electrolytic iron, the composition of which is given in Table 2. The iron was initially degassed by heating in vacuum for one hour at 1100°C to remove any hydrogen which may be present. The furnace was a NGN Limited Horizontal Tube Furnace, Model VTF/H3 fitted with rotary and vapour diffusion pumps and a Carbolite Furnace with a maximum temperature of 1400°C. The furnace tube was a 50 mm Recrystallised Alumina tube fitted with water cooled steel flanges at each end. The electrolytic iron was very brittle and was broken down into small pieces of approximately 0.5 cm cube. The pieces were placed in an alumina boat and put in the cold furnace. The furnace was evacuated and the temperature raised to 1100°C where it was held for one hour. The furnace took several hours to cool to room temperature when the iron was removed. During the heating and cooling periods the furnace was kept under vacuum. The iron was transferred to an A.E.I. Tungsten Electrode Flat Hearth Furnace where it was melted down. The charge, consisting of the small iron pieces plus the addition of the appropriate alloying element, was 'heaped' onto the water-cooled copper hearth in the furnace. The furnace was evacuated and flushed with high purity argon. An arc was struck between a tungsten electrode and the charge in the hearth which formed the other electrode. The charge melted down and ran into a

shallow groove in the hearth. The charge was about 50 gramme in total and formed a stick of metal about 100 mm long with cross section of approximately 7 mm x 4 mm. Whilst in the mould the alloy was melted from end to end in three passes to ensure homogeneity of the melt.

The pure iron wire was made by a difference technique. A 0.5 kg charge of iron was melted in an Electroheating 15 kVA High Frequency Induction Furnace in a zirconia crucible. The crucible was open to the air but argon gas was purged over the surface of the iron melt. When the temperature of the metal was 1600°C, vacuum sealed pyrex glass tubes were dipped into the metal. The glass melted and the iron was sucked up into the tube. The lower end of the tube was well immersed so that the surface layer of the iron was not drawn up into the tube. The sample was cooled and the glass was then removed from around the iron rod.

The samples were then swaged down to wire, the machines employed in this operation were Robertson Swaging machines. However, some of the iron samples were found to contain 'blow holes' and broke up in the swaging machine. As a result, the samples were radiographed and only sound iron 'sticks' were used. The radiography was performed on a Marconi X-Ray Unit, Type TM 4334. Prior to swaging, the surface of the iron was removed using emery paper. The metal samples were also annealed before swaging. Initially, this was carried out by sealing the iron in a mild steel capsule, in argon. The mild steel capsule was made from mild steel tubing with mild steel blanks welded on

each end. A 15 cm length of 18 mm i.d. mild steel tubing was machined from a stock length of tubing in a lathe. Two circular discs of mild steel of the same diameter as the tubing were machined from 3 mm plate. The components were cleaned and degreased in trichlorethane and the first disc was welded in position with a continuous weld run on one end of the tube. The iron was placed inside the tube and the air was displaced with argon. The second disc was welded in place on the open end, again with a continuous weld run using tungsten-argon welding. A piece of zirconium foil was placed inside the capsule to take up any oxygen which might be present. The capsule and specimen were annealed at 950°C for 1 hour and then left in the furnace whilst it cooled down. The iron alloy samples were not sealed in a capsule but placed in an alumina boat and annealed in vacuo in the NGN Horizontal Tube furnace at 1000°C for 30 minutes and furnace-cooled under vacuo.

The iron and iron alloys were swaged on the two Robertson Swaging machines. The first and larger machine, employing ten sets of dies, took the metal samples down to 3.2 mm (0.125 inches). The dies were lubricated by oil continuously pumped around the dies. The second and smaller swaging machine was then employed to reduce the diameter of the rod down to 1.5 mm (0.060 inches). In this machine the rod was dipped in oil prior to insertion in the dies for lubrication. Because of the heavy reduction in cross sectional area it was necessary to inter-stage anneal to relieve the work hardening of the material. All alloys received one anneal, some alloys required a second inter-stage anneal.

These were all carried out during the first few swaging steps. Annealing was carried out in the NGN Horizontal Tube furnace at 950°C under vacuum for 30 minutes, furnace cooling under vacuum.

The iron, iron-chromium and iron-manganese alloys were all swaged down to 1.5 mm diameter. However, difficulty was experienced with the iron-silicon alloys. Despite annealing, the rods were hard and brittle and many cracked in the dies but sufficient material was generated for the purpose of experimentation.

3.2 Levitation Melting Rig

3.2.1 Power Source

The power unit used initially in the design of the levitation coil was a 15 kVA, 350-450 kHz Electroheating power source, the power output of which is varied by the operator using a handwheel located on the front panel of the unit. As there was no output current meter on the unit, the power setting was gauged from the position of the handwheel pointer which covered a circular scale 0-7.5. A meter giving the anode current to the valve oscillator was another indication of the power being supplied to the coil. The water cooled, flexible, high frequency leads from the generator were connected to a tufnol plate which was clamped to the experimental rig. The high frequency connections from the generator to the coil were placed close together to minimise their inductance. At the tufnol plate, the 13 mm ($\frac{1}{2}$ ") water connections from the high

frequency leads were reduced down by brass couplings to 3 mm ($\frac{1}{8}$ ") copper connections.

Once the coil design had been established the experimental work was carried out on a 6 kVA, 450 kHz Radyne power source. The power output from the Radyne unit was varied by a linear rheostat. Because of the coupling of the coil the power factor was only just in excess of 50% and the delivered power was only 3 kW. By moving the position of the rheostat the power to the coil was increased. The power delivered was linear in relation to the rheostat slide position but it was delivered at two rates as can be seen in Figure 23. The initial movement delivered power at a lower rate than that of the final stages of movement. The power developed was indicated by a meter on the front of the power unit.

3.2.2 Coil Design and Operating Procedure

The objective was to build a coil which would successfully levitate iron for a period of several minutes. To this end, several designs were investigated. The initial designs were based on coils designed by other workers^(95,99). However, these designs, although giving good levitation, showed poor lateral stability. With the charge solid in the coil it would maintain a central position, but upon melting, the charge invariably contacted the wall of the glass tube. As a result the coil was designed from theoretical considerations. It has been shown⁽⁹⁷⁾ that the levitating force is proportional to G, the axial field gradient. If, therefore, the value of G can be increased then

there will be a corresponding increase in the levitating force. From theoretical considerations, the contribution of each turn to the total field strength along the axis of the coil was calculated.

By considering each turn of a levitation coil as a single turn solenoid, the contribution of each turn to the total field strength along the axis of the coil was calculated. By the principle of super-position, the total field intensity at any point on the axis of a coil could be calculated by summing the contributions from the various turns at the appropriate radius and distance along the coil axis. By convention, the upper turns make a negative contribution. Several coil designs were examined by this method and the axial field gradient determined. From these considerations it was possible to wind coils with greater magnetic field gradients and then determine how the coils behaved in practice.

The levitation coils were all made from 3.175 mm ($\frac{1}{8}$ ") diameter bright annealed copper tubing. This size of copper tubing is readily available and a small diameter tubing is preferable to provide more turns per unit length of coil. Prior to winding the coils, the copper tubing was sheathed with a close fitting insulated sheath of Vida-flex. The voltage at the coil, from valve oscillator units, can be of the order of several kV. If bare coils are used, water from the atmosphere condenses on them, and flashover may occur. The insulating braid used was of the order 0.8 mm ($\frac{1}{32}$ ") so that when coils were wound tightly, the gap between the copper tubing was of the order of 1.6 mm ($\frac{1}{16}$ "). The coils were made by winding

the sheathed copper tubing on suitably shaped metal formers. The formers were machined from aluminium in the shape of a cone. The centre of the cone was drilled to fit round glass tubing which formed the levitation chamber. The former was machined to give a semi-angle of 30° , Plate 1, Figure 24. The minimum diameter of the coil was decided by the available pyrex glass tubing in the department. The coil was placed around the glass tube and the metal charge was levitated inside the tube. In this way an inert atmosphere could be used while the sample was being levitated. Initially three sizes of glass tubing were used: 14 mm O.D., 17 mm O.D. and 22 mm O.D.

The procedure adopted was as follows. With the coil empty, the H.F. power was raised to a maximum. The specimen was placed on top of a silica rod and then gently raised and levitated in the coil. The length of time that the specimen levitated in the coil was noted. A note was also made as to whether the specimen melted or not. It was found that the mass of the metal being levitated was important, and so this parameter was also varied and investigated.

Because it was found difficult to levitate iron droplets for several minutes, an alternative technique was developed. This technique involved forming a molten droplet on the end of a wire in the high frequency coil. For this experiment 2 mm diameter mild steel rods were employed. It was found that if the rod was suspended vertically in the coil, such that the lower tip of the rod was at the same level as the lowest coil, on increasing the power supply to the coil a molten droplet

would form at the end of the rod. Under the action of surface tension and levitation forces, the droplet would climb up the rod to an equilibrium position where these forces were counter balanced by the weight of the droplet. It was possible to hold this position for several minutes. On switching off the power the molten droplet immediately fell from the end of the rod.

Figure 24 shows the coil shape and the associated field strength for the design that was finally adopted. Some of the other designs investigated showed better characteristics for levitation but these designs involved a large number of turns which restricted the water flow to the coil. Of the designs evaluated, the coil design chosen showed good lateral stability and was capable of holding iron samples for the longest period⁽⁹⁷⁾. With respect to the design, the experiments and theoretical considerations indicate that the number of turns and the position of the upper reversed coil is important. The coil creates a stable system for both solid and molten charges which can then be levitated near the top turn of the lower coil. The number of turns and spacing influence the value of the axial magnetic field gradient. In general it was found that the reverse turns must be symmetrical with and parallel to the upper turn of the lower coil.

With all of the coil designs, it was found necessary to operate at or near the maximum power level. There was a critical sample size below which stable levitation could not be achieved. This threshold value decreases with increasing power. For a spherical charge the mass is proportional to the cross sectional

area which in turn determines the amount of magnetic flux intersected. For an increase in power the same area will cross more lines of magnetic force and stable levitation results.

The technique of forming a droplet at the end of a wire or a rod and holding in the levitation coil was the technique finally adopted, Figure 29, Plates 2 and 3. The droplet sizes were reasonably consistent and, because the position of the droplet in the coil was not totally dependent on the levitation force, it was possible to adjust the temperature of the droplet to a large extent by means of the power input. Because the droplet was attached to the solid rod there would be a temperature gradient within the droplet near this point.

Since the electromagnetic field imparted a stirring action to the liquid metal this temperature gradient would be very steep and localised and its effect on the homogeneity of the droplet therefore minimal.

3.2.3. Gas Purification System

Hydrogen and argon were employed throughout the experiments. Both gases were obtained from BOC high purity cylinders and were of grade: hydrogen 99.99% minimum, argon 99.998%.

The gases were fed via a pressure regulator to a gas purification train and from thence to the levitation chamber via a variable area flowmeter. The gas train is shown diagrammatically in Fig.25. It was fabricated from Quikfit glass components. The ground glass joints were held in place by springs. The pipework was produced in 6 mm diameter copper

tubing. Connections between the glass fittings and copper tubing were made in polyethylene tubing. The polyethylene tubing was wired in position.

The first U-tube contained molecular sieve, $\frac{1}{16}$ " pellet, Type 5A, to remove any trace of oxygen from the gas. The second U-tube contained Analar grade magnesium perchlorate in the first limb to remove any trace of water vapour. The second limb was filled with silica gel. Again this acts as an absorbent for moisture but its colour gave a clear indication of how the gas train was operating. Any particulate matter was retained by 'plugs' of glass wool.

Both gases were fed into the train through a common Y-piece. The pressures were regulated at the cylinder head and the flow rate was adjusted by means of in-line valves. The gas flow rate was measured by a rotameter graduated to 2.5 litres per minute flow rate for argon. The same rotameter was also used for the measurement of the hydrogen flow rate. Hydrogen was always used at a flow rate of 1 litre per minute and the rotameter was initially calibrated for this flow rate by means of an in-line gage. The gases, after passing over the droplet, were taken away via copper tubing to an extraction system where they were vented to atmosphere.

3.2.4. Temperature Measurement and Control

The pyrometer used to measure the temperature of the levitated droplet was a Land total radiation pyrometer which employed a silicon photovoltaic cell detector, Type OQO 14/120/48B. It was fitted with a double lens system so that it focussed down

to 3 mm diameter at 25 cm focal length. This was engineered in the following way. The water-cooled, flexible high frequency leads from the generator were connected to a Tufnol Plate which, in turn, was clamped to the experimental rig. Consequently, the high frequency coil was always a fixed distance from the plate. The pyrex tube which formed the levitation chamber was clamped in the coil with its axis vertical. The iron or iron alloy wire was then fed into the chamber down the axis of the tube. The pyrometer itself was clamped to the rig, a distance of 25 cm from the axis of the tube. The pyrometer was inclined at an angle of 25° to the horizontal so that the pyrometer pointed through the gap between the upper and lower coils of the levitation furnace and focussed onto the axis in the plane of the top turn of the lower coil. The pyrometer was equipped with a viewing port at the rear of the barrel so that the pyrometer could be lined up visually, if required.

The pyrometer was calibrated using a probe as shown in Fig.26. The temperature probe consisted of an iron tip, 6 mm diameter which had been machined with a tapered point and drilled with a 2 mm diameter hole which terminated in the point. The top section of the tip had its diameter reduced so that it was an easy fit in a 23 cm long Vitreosil fused silica tube (Thermal Syndicate Limited).

A platinum-platinum 13% rhodium thermocouple sheathed in twin-bore alumina sleeves was inserted down the centre of the fused silica sheath and into the hole in the iron tip. The tip was then cemented into the silica tube using C60 refractory cement and the recrystallised alumina sleeves around the thermo-

couple where they emerged from the silica tube were also cemented in position.

The probe was lowered into the levitation coil inside the pyrex tube until the tapered tip was at the focal point of the optical pyrometer. It was firmly clamped into this position. The output from the thermocouple was taken to one of the inputs of an Oxford 3000, two-pen potentiometric recorder with one side of the thermocouple also being taken to earth. The output from the Land total radiation pyrometer was taken to the second input of the recorder. Since the pyrometer does not produce an output until it receives visible light and also because of the reduced emissivity of iron, the threshold value was at about 1100°C. Power was put into the levitation coil at six different levels. At each level the output from the pyrometer and the thermocouple were recorded. Both gave steady readings. The power was then increased until steady outputs were achieved and the power switched off. The two millivolt readings for the lower temperature from both instruments were again noted as the falling temperature passed through that point. Under these conditions of no power there would be no induced emfs to distort the true reading. This was repeated for each temperature level up to the melting point of iron.

A calibration chart for the total radiation pyrometer supplied by the manufacturers was the basis for all temperature measurements. The results of the calibration, for an emissivity value of 1, are shown in Table 3. The results for the pyrometer output with temperature for the iron probe are recorded in Table 4. It is evident from the results that the emissivity of the system,

i.e. the iron surface in the glass levitation column, approximates to a value of 0.36. The values of pyrometer output from both tables are plotted in Fig.27. The line drawn for an emissivity value of 0.36 is a good fit to the results obtained for the iron temperature probe.

It was noted when droplet studies were undertaken that the pyrex tube forming the levitation chamber was slightly darkened due to evaporation from the molten droplet and deposition on the glass. Under these circumstances the millivolt output of the pyrometer was reduced although the power level was being maintained. Account was taken of this evaporation since it obviously affected the temperature recorded for the droplet by monitoring the temperature of a droplet under ideal conditions, i.e. with a clean glass levitation column. This was repeated at different temperatures and the readings noted. A piece of plain glass and a piece of opaque glass were placed between the column and the optical pyrometer in each experiment and the new outputs of the pyrometer recorded.

Where the reading for the temperature was reduced due to darkening of the glass, the power to the coil was reduced and brought back to the operating power. Under these conditions the droplet was allowed to solidify for a few seconds and then remelted. An inflexion appeared in the pyrometer output trace at the melting point. This temperature being known, the final temperature could be related back to the melting point and hence determined.

Table 5 gives the results of the pyrometer output under the conditions when an extra piece of glass was inserted between the

levitation coil and the pyrometer to simulate darkening of the glass. Basically, the results indicate that insertion of glass lowers the emissivity value of the system. It was assumed that darkening of the glass operated in the same way. As a consequence the emissivity of the system was determined from the melting point temperature of the droplet and from this the temperature of the droplet could be deduced. The results are shown in Figure 28.

3.2.5 Production of Droplets

The stages in the generation of a droplet from wire were as follows and are indicated in Fig.29. The pyrex tubing was 17 mm O.D. and was held vertical. The levitation coil was close fitting on the glass tube and positioned as shown. The wire, which had been degreased in acetone, was lowered into the coil such that it protruded below the coil by approximately 5 mm, Fig.29(i) and Plate 2. Any air was purged from the system by passing argon through the tube in an upwards direction at a rate of 1.5 litres per minute for one minute. The power was switched on and approximately 1 kw was delivered to the coil. Under these conditions the temperature of the wire was raised to 1100°C to 1200°C. The argon gas was then replaced by hydrogen gas. On change-over the temperature of the wire dropped markedly due to the much greater thermal conductivity and specific heat capacity of hydrogen compared to those of argon, Table 6. It was necessary to raise the power to between 1.5 to 2.0 kw to maintain the temperature. This was maintained for 5 minutes to ensure any surface oxide or contaminant had been removed.

At the end of five minutes, the power was gradually raised. This resulted in an increase in temperature of the wire and, at the centre of the lower coil, melting of the wire took place. Under the action of the levitating force and surface tension the bottom section of the wire was drawn up into the coil so that a molten droplet of metal was formed at the end of the wire in the coil, stage (ii), Fig.29. The power was slowly raised further so that the droplet was raised to just below the top turn of the lower coil, stage (iii), Fig.29. The droplet was held in this position for five minutes under hydrogen at a flowrate of 1 litre per minute to ensure complete deoxidation of the metal.

At the end of this deoxidation period, the hydrogen flow was changed to argon via the valve arrangement. The argon was passed through the tube around the droplet at a flowrate of 2.5 litres per minute to ensure that the hydrogen was completely removed. The droplet position was adjusted so that it was in or just above the plane of the top turn of the coil, Fig.29(iv) and Plate 3. At the end of one minute the argon flowrate was reduced to 0.5 litres per minute, the temperature of the droplet was adjusted by means of the power to the coil, then the power was switched off. This was sufficient to release the droplet from the end of the wire as shown in Fig.29, stage (v).

Control over the mass of the droplet was exercised since the wires were swaged to the same diameter and the position of the wires in the coil was fixed. Since the droplet was attached to the wire the final position in the coil was also controlled. The final adjustment to the temperature was via the power input.

3.2.6 Mass Transfer Column

The assembled apparatus for the mass transfer experiments is shown in Fig.30 and Plate 4.

The levitation coil fitted tightly around the 17 mm O.D. pyrex tubing which formed the levitation chamber. The top of the tube was attached to a second pyrex tube with reduced bore entries in a Y-form as shown. Connection between the tubes was made with tight-fitting heavy wall rubber tubing. The side arm on the top section formed the exit for the gases. The iron wire was fed axially into the chamber as shown via a tight-fitting rubber bung. The lower end of the levitation chamber fitted via a drilled bung into a 5 cm/2 cm reduction coupling with a 5 mm diameter side arm for gas entry into the levitation chamber. The temperature of the iron droplets was measured with the pre-calibrated Land total radiation pyrometer. The reducing/inert atmosphere of the levitation chamber was separated from the oxidation chamber below by a diaphragm. The diaphragm material was polythene film which was held stretched in position using a ground glass joint. The polythene film decomposed as the hot droplet approached, leaving a neat hole in the diaphragm as the droplet passed through. The oxidation chamber was made up of 5 cm O.D. pyrex tubes 35 cm long, joined together by using ground glass joints. In this way the height of the reaction chamber could be varied. The bottom tube ended above the surface of the quenchant. The droplet, after reaction for a given distance, was quenched in the quenching medium placed in a stainless steel beaker at the bottom of the flight tube. The column was set up and the polythene diaphragm was put in place. A droplet was

generated as described in section 3.2.5. After deoxidising the droplet, the atmosphere in the levitation chamber was switched back to argon and the desired droplet temperature obtained by adjusting the power input to the coil. The droplet was released by switching off the power and it was subsequently quenched into the quench medium.

3.3 Chemical Analysis

3.3.1 Analysis for Alloying Elements

Sections of the fabricated iron wires were analysed for the relevant alloying element, namely manganese, chromium and silicon.

Manganese was determined by the Persulphate Oxidation Volumetric method⁽¹⁰³⁾. In this method following a zinc oxide separation of iron from diluted sulphuric acid solution and a fractional filtration, the manganese was oxidised in hot sulphuric-phosphoric acid solution by ammonium persulphate, catalysed by silver nitrate. The cold solution of permanganic acid was titrated with standard ferrous ammonium sulphate and potassium dichromate, using diphenylamine sodium sulphonate as indicator.

Chromium was determined by the Persulphate Oxidation method⁽¹⁰⁴⁾. After solution of the sample in sulphuric-phosphoric acid and oxidation with nitric acid, chromium and any manganese were oxidised by ammonium persulphate in the presence of silver nitrate. Excess persulphate was removed by boiling, any permanganic acid destroyed by dilute hydrochloric acid and the chromium was determined by titration with standard ferrous ammonium sulphate and potassium permanganate solutions.

Silicon was determined by the Perchloric Acid method⁽¹⁰³⁾. After decomposition of the sample in hydrochloric acid and oxidation by nitric acid, the solution was evaporated to fumes with perchloric acid. The fumed residue was extracted in hydrochloric acid and the insoluble siliceous residue was collected by filtration, ignited and weighed as SiO₂.

3.3.2 Analysis for Oxygen

The iron and iron alloy droplets were analysed for oxygen. In all cases the droplet had been quenched immediately after oxidation. Where oil had been the quenchant there was a need to remove the oil from the specimen surface prior to analysis.

The oxidised droplet was removed from the oil with a pair of tongs and immediately immersed in acetone to remove the oil. On removal from the acetone the droplet was gently wiped on a paper tissue to remove any adhering oil. It was then transferred to an ultra-sonic bath containing acetone and cleaned for two minutes to remove the reaction film. The specimen was then dried on a paper tissue and weighed. The specimen was finally stored under vacuum in a desiccator containing silica gel. All specimens were stored in this manner prior to analysis for oxygen or examination in the Scanning Electron Microscope.

Oxygen analysis of the iron and iron alloy droplets was carried out on a Strohlein Coulometric Oxygen Analyser. The principle of the operation is as follows. The iron droplet is introduced into a graphite crucible in the direct resistance furnace through a sample port. In the furnace the crucible and sample are heated to a temperature of about 1900°C. The sample

fuses in the crucible and the oxygen of the sample combines with the carbon of the crucible to form carbon monoxide. Argon carrier gas, flowing through the furnace, transfers the carbon monoxide to an oxidation column filled with Schütze reagent⁺ where the carbon monoxide is converted to carbon dioxide. The carbon dioxide then passes, together with the carrier gas, into an absorption vessel where it is absorbed in an alkaline barium perchlorate solution. Absorption of the carbon dioxide reduces the alkalinity of the solution; the solution is automatically titrated back to the original pH value with alkali generated by electrolysis. The quantity of electricity required to produce the alkali is measured accurately, the quantity of carbon dioxide is then determined, using Faraday's law, and from this, together with the sample weight, the oxygen content of the sample in ppm is determined. A counter indicates in digital form the quantity of electricity consumed to regenerate the OH⁻ ions. Each step of the counter corresponds to 2×10^{-4} mg oxygen. With the sample weights used in the experiments this gives a sensitivity better than 1 ppm.

In practice the unit was purged with high purity argon gas for 24 hours prior to use. Two or three graphite crucibles would be processed through the furnace as "blanks", this would give the background reading on the instrument. A standard steel specimen, of known oxygen content, would then be charged into a crucible in the furnace. By this technique the calibration of the machine was checked. If the result proved satisfactory the iron samples were analysed. At the end of each run, normally about twelve or fifteen samples, another standard specimen would be used to confirm the calibration.

+ Trade name

3.4 Droplet-Quench Media Experiment

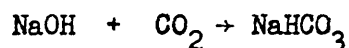
An experiment was devised to investigate the effect of the interaction between a molten oxidised iron droplet and quench media. Basically, the technique was to detect the amount of carbon dioxide given off when the droplet was quenched in a medium containing carbon. Any reduction of iron oxide from the molten droplet by the carbon based quenchant would result in the evolution of carbon monoxide and possibly some carbon dioxide.

The carbon monoxide was converted to carbon dioxide for detection.

The gases above the quenchant were bubbled through a carbon dioxide solvent which was then titrated to determine the CO₂ content. The absorber used was dimethylformamide which was then titrated with tetrabutylammonium hydroxide using thymolphthalein indicator. The amount of carbon dioxide given off was likely to be small and since carbon dioxide is present in air the apparatus was isolated from the surrounding atmosphere. The air column through which the iron droplet fell was filled with air which had been passed through soda asbestos (ascarite) to remove any carbon dioxide. To carry the gases through the absorber, high purity argon was used as carrier gas.

The experimental layout is shown in Fig.31 and Plate 5. The procedure was as follows. Column A is the levitation chamber where the iron was heated to form a droplet at the end of the wire, under argon gas. It was then heated for five minutes in hydrogen to completely deoxidise it and then gas was changed back to argon. During this time the gases entered the chamber

as shown and left via tap T1. The heating chamber A and oxidation chamber B were separated by a thin film of polyethylene. The oxidation chamber was filled with carbon dioxide free air by admitting the air through column C which was filled with soda asbestos. The CO₂ is absorbed by the reaction:

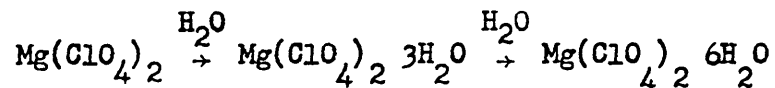


With taps T2 and T4 open, taps T3, T5 and T6 closed, the carbon dioxide free air was swept through the arrangement for about ten minutes to ensure that only carbon dioxide free air existed in the system. Near the end of this period the absorption vessel F was partly filled with methylformamide. This was the absorber used to dissolve the carbon dioxide carried over by the argon gas. The solution was made from formyldimethylamide, mon-ethanolamine and the indicator thymolphthalein in the volumetric ratio 150:5:2.

The molten iron droplet was released as described in Section 3.2.5. The argon flow rate had been adjusted to 500 ml per minute prior to this. After falling through the air column the droplet was collected in the quenchant retained in a stainless steel beaker, Q.

Immediately that the power was switched off, taps T1 and T2 were closed. The argon gas was now diverted through the polyethylene film and through the system via tap T4. Since the base of the glass tubing of the air column was seated firmly against the bottom of the beaker holding the quenchant, any gases evolved due to reaction between the droplet and the quenchant were forced into the space in the oxidation column above the

liquid surface. The gas in the system, at this point, was being both 'pushed' by the pressure of the argon supply, and 'pulled' by a small air pump at the outlet of the system. This combination maintained a constant pressure within the system and prevented pressure build ups within the apparatus with the possible loss of quenchant and entrained gas. Before entering the reaction vessel F, the gas was passed through two columns, D and E. Column D contained magnesium perchlorate to dry the gas. There is no true chemical reaction, the magnesium perchlorate just becomes hydrated, viz:



Column E contained Schütz reagent, this converts any carbon monoxide formed to carbon dioxide.

From column E the gas enters the reaction vessel F where it was bubbled through 20 ml dimethylformamide solution which absorbs the CO₂. The solution was titrated with tetrabutylammonium hydroxide to the end point at five minute intervals. This was repeated until a constant background level was reached i.e. the additions of titrant were approximately equal for each time interval. The burette was fitted with a two-way tap. As a result titrant could be delivered into the absorption cell and secondly the burette could be filled with the titrant without the admission of air. Also the tetrabutylammonium hydroxide solution was corrosive and using the tap it could be easily introduced to the burette using a reservoir and a hand pump. The air used to pressurise the reservoir was passed through a tube of soda

asbestos prior to entering the reservoir chamber to remove carbon dioxide.

The absorption cell had two side arms. One arm was used for the addition of the dimethylformamide solution, the other arm was the outlet for the gas. The gas passed through column G which was filled with activated charcoal. This filtered the gas before it passed through a flow meter and on to the small suction pump which 'pulled' the gas through the system.

3.5 Thermogravimetric Studies

3.5.1 Introduction

Oxidised droplets were reduced in hydrogen at 1150°C to simulate the conditions prevailing during annealing and sintering. The reduction of the droplets was carried out in a Stanton Massflow Thermobalance, model MF-H5. With this machine the change in weight of the specimen and the temperature are recorded simultaneously on the same chart. Consequently the temperature at which the onset of reduction of the oxides occurred could be noted. The balance would accept a sample up to several grammes mass and could be used to record a mass change of 0.10 gramme in ten steps of 10 milligramme. The furnace was capable of a maximum temperature of 1350°C and the heating rate could be varied, if desired, by a simple cam change. The balance was used to examine the effect of temperature up to 1150°C on the reducibility of oxides in hydrogen and also to monitor oxide reducibility at 1150°C with time.

3.5.2 Measurement of Droplet Mass Loss in Hydrogen

A section of the furnace arrangement of the Thermobalance is shown in Fig.32. The furnace itself could move in a vertical direction. With the furnace raised the Mullite furnace tube, with its gas tight rubber 'O' ring was removed. The oxidised droplet was carefully weighed. Weights equivalent to the gross weight of the droplet were removed from the Thermobalance tare-pot. The alumina support platform was centred and the droplet was placed centrally on the platform. Care was taken to ensure that the support system was central and cleared both thermocouple and gas inlet tube. The Mullite tube was lowered and clamped into position then the furnace itself was drawn down to gently rest on the springs. At room temperature, the system was purged with argon at a rate of 1 litre per minute for a period of one hour minimum. The gas flow was then changed to hydrogen, again at a flow rate of 1 litre per minute. Under these conditions the furnace was switched on and allowed to heat up. Heating conditions were identical in all cases, the heating rate being linear at 6°C per minute. It took just over three hours heating to reach 1150°C. Once this temperature had been reached it was maintained for 1 hour. At the end of the isothermal period the furnace was switched off and allowed to cool. When the furnace reached 500°C the hydrogen gas flow was changed to argon. When the furnace was cold the specimen was removed and reweighed. A typical trace is shown in Fig.33. The temperature is recorded by the right hand pen and the weight change by the left hand pen. Full chart width for the weight change represents 10 milligrammes.

When the pen reaches the limit of the span the operation of the periodic timing device automatically triggers a weight adjustment of 20 milligrammes. The other factor which has to be taken into account is the buoyancy effect. When the balance is used continuously over a wide range of temperature with a gas flow, it is necessary to consider buoyancy. This is indicated as a very steady drift as the temperature increases and must be allowed for in the interpretation of the chart since the buoyancy effect can be greater than the weight loss of the oxidised droplet. Because of this it was essential that the gas flow rate was maintained at a constant rate and it was impossible to change from hydrogen to argon during the measuring period since the density of the gases are different. With careful analysis of the charts the effect of the buoyancy could be compensated for and the weight change with time and temperature determined.

The gases prior to entering the furnace were passed over a molecular sieve and magnesium perchlorate arrangement similar to that described in an earlier section (3.2.3)

3.5.3 Measurement of Relative Humidity

The relative amounts of hydrogen and water vapour determine whether the atmosphere is oxidising or reducing. When the metal oxide is heated in a pure hydrogen atmosphere, the oxide and the hydrogen will react to form the metal and water vapour; the relative amount of water formed is dependent upon the temperature and pressure of the system and the relative stability of the metal oxide. The stability of the oxide can be described at

any one temperature and pressure as the ratio of hydrogen to water vapour when the reaction is at equilibrium. The H_2/H_2O ratio can also be stated in terms of the dewpoint of the hydrogen atmosphere (Fig.34).

In practice, if oxidation is to be prevented (or oxide reduced) using hydrogen as a furnace atmosphere, the dewpoint of the atmosphere in contact with the metal has to be maintained lower than the equilibrium dewpoint. This requires sufficient flow to prevent local building up of water vapour owing to leakage of air into the furnace or oxide reduction. Metal oxides become less stable as the temperature is raised: the equilibrium H_2/H_2O ratio gets smaller, equilibrium dewpoint larger.

The instrument used was an Alnor Dew Point Meter. This essentially is a portable 'fog chamber' and is based on the principle that, at a constant temperature during the adiabatic expansion of gas, the pressure change to cause condensation is related to the water vapour content of the gas. The dewpoint meter subjects the gas sample to varying adiabatic pressure changes. The pressure that just causes visible condensation in the fog chamber is recorded. To make a mist form, a condensation nucleus for each droplet must be present in the gas. Under some conditions these nuclei may not be present, so in this particular instrument they are provided by a source of α radiation (Americium 241) inside the chamber. The dewpoint is found by using a 'dewpoint' calculator and a series of curves (for different ambient temperatures) relating dewpoint to pressure change. The meter can measure a wide range of dewpoints, from

below -73°C (-100°F) to ambient temperatures.

The meter was put 'on line' to the Stanton Massflow Thermobalance where oxidised iron droplets were reduced in hydrogen. Only a few specimens were investigated using this technique.

The experimental arrangement of the Stanton Massflow Thermobalance and Alnor Dewpoint Meter are shown in Plate 6.

3.6 Electron Microscopy and Surface Analysis

3.6.1 Scanning Electron Microscopy

In the examination of droplets, two instruments were used: the Cambridge Scanning Electron Microscope and the Philips Scanning Electron Microscope, most of the work being carried out on the second machine. The advantages of the SEM over optical microscopy are two-fold in this instance. The considerable depth of focus available to the SEM is particularly valuable in looking at the morphology of the curved surfaces of the droplets and secondly, since both machines were equipped with EDX facilities identification of a range of elements was available.

3.6.2 Specimen Preparation for Scanning Electron Microscopy

At least two samples from each alloy composition were examined by Scanning Electron Microscopy. The samples were either the 50 cm fall in air and quenched and/or the 100 cm fall in air and quenched droplets and, hydrogen reduced samples which had undergone the same initial fall in air. Droplets were examined either mounted or unmounted. In the unmounted condition the drop-

let surface could be examined in the as-quenched condition. The samples were ultrasonically cleaned in acetone for two minutes prior to insertion in the Microscope. All handling procedures were carried out with fine tweezers. The droplets were held in position in the Microscope on an aluminium support by means of a conducting film of silver 'Dag' compound. When examining the surface, the beam of electrons was incident at an angle of 30° and the scattered beam produced the image.

Droplets were also examined mounted in an electrical conducting bakelite. The mounted droplets were carefully ground on 240, 400 and 600 grit wet carborundum paper. Only sufficient material was removed such that, if the droplet could be viewed in section, only a chord was removed, see Fig.35. The mounted specimens were final polished on a Selvyt cloth impregnated with $6\ \mu\text{m}$ diamond paste. Specimens were examined in the 'as-polished' state.

When examining the mounted specimens the beam of electrons was incident at 0° and identification of major elements was carried out on the section.

3.6.3 The VG Scientific Microlab

The VG Scientific Microlab Mark II offers several examination modes. The following options were used: Scanning Electron Microscopy (SEM); Scanning Auger Microscopy (SAM) and Secondary Ion Mass Spectrometry (SIMS). Provision of an energy dispersive X-ray analyser (EDX) allowed elemental analysis of the bulk to be performed concurrently with Auger Electron Spectroscopy (AES).

With the multidetector option of Microlab MkII the sensitivity of the machine is increased and it is possible to detect very low concentration elements which would otherwise be masked by background noise. Also the high sensitivity of the analyser permits the use of lower beam currents and correspondingly smaller spot sizes in the point analysis mode. With this machine, energy resolution and energy scale calibration are independent of specimen position so high resolution Auger spectra can be routinely obtained and peak positions can be accurately determined. In the AES mode it was therefore possible to identify the elements present in the surface layer.

The other mode used was the SIMS. This is one of the most sensitive techniques used in materials analysis. It detects certain elements at concentrations orders of magnitude lower than the detection limits for electron spectroscopy. The analyser in the machine is the MM12-125 quadrupole mass spectrometer which gives good sensitivity and resolution over its entire 1-800 a.m.u. mass range. Data was obtained in the Static SIMS mode. In Static SIMS a low flux of low energy (<5 keV) argon ions is used to probe the surface. Argon was used to prevent chemical interactions with the sample surface. Using beam current densities below 5 nA.cm^{-2} , analysis, each time, was obtained from a fraction of a monolayer. Under these static conditions it is necessary to avoid surface contamination during analysis so the work was carried out in ultra high vacuum. The Static SIMS provides information on elemental composition, but also chemical structure of the surface can be obtained by monitoring molecular cluster

ions which generate a characteristic fragmentation pattern in the SIMS spectrum.

The Microlab was fitted with the VGS 1000 datasystem based on the Apple II Plus Microcomputer. The datasystem allows accurate and reproducible instrument control, data acquisition and processing. Depth profiling could be performed in SIMS under datasystem control. Profiling was by sequential etch/analyse steps and data was acquired by peak switching. From this, profiles were plotted in conventional signal versus etch time (depth) format.

3.6.4 Specimen Preparation for Surface Analysis

Samples were examined in the VG Scientific Microlab Mark II described in the following subsection. A number were examined in the as-quenched condition. As before, the samples were ultrasonically cleaned in acetone, for two minutes prior to insertion in the Specimen Stage of the Microlab.

Droplets were mounted in cold-setting resin. The samples were carefully ground on 240, 400 and 600 grit wet carborundum paper. As with the other samples, only a chord of material was removed. The surface was again polished to a 6 μm diamond finish. Once the specimen had been prepared the resin mount was carefully cut with a saw and then prised away from the sectioned droplet. The prepared specimen was ultrasonically cleaned in acetone for two minutes and inserted into the Specimen Stage of the Microlab. Inside the Microlab the specimens were further cleaned by removing surface contaminants with the Argon-ion gun or Metal-ion gun. The specimens were now ready for examination.

CHAPTER 4 EXPERIMENTAL RESULTS

Before the results of the droplet oxidation studies could be verified it was necessary to examine the extent of droplet interaction with the quench media. Once this had been established, the oxidation kinetics of the iron and iron alloy droplets was determined. The same alloy range of oxidised droplets were subsequently examined for reduction by hydrogen at 1150°C. In tandem with the oxidation and reduction studies, examination of the droplet morphologies by SEM was undertaken. This work was also complemented with EDX and SIMS analysis of selected oxide films.

4.1 Assessment of Quench Media

4.1.1 Introduction

The purpose of the investigation was to simulate the oxidation conditions in the atomisation process of a molten metal droplet moving through air. To study the reaction process and the morphology of the droplet surface it was necessary to 'freeze' the process at the end of an oxidising fall in air. The only possible way to do this was to quench the droplet at the end of its flight. Quenching in a copper mould was considered but dismissed since this method involves splashing which results in the disruption of the droplet surface.

A number of liquid quench media were investigated. These included distilled water, liquid nitrogen, silicone oil, Invoil 30 and paraffin oil. However, before the effects of the quench media were investigated it was established that the droplets were completely deoxidised in the hydrogen gas whilst in the levitation coil.

The wire was exposed to hydrogen for five minutes whilst at a temperature of 1100 to 1200°C. The diffusion coefficient for hydrogen in γ -Fe has been determined⁽¹⁰⁵⁾. At 1127°C the diffusion coefficient has a value of $3.08 \times 10^{-4} \text{ cm}^2 \text{ s}^{-1}$. Using the theory of diffusion in a cylinder⁽¹⁰⁶⁾ and taking the radius of the wire to be 0.75 mm the time to penetrate the wire by hydrogen could be determined. For a cylinder, saturation is complete at a value of $(Dt/r^2)^{\frac{1}{2}}$ equal to unity, where D is the diffusion coefficient ($\text{cm}^2 \text{ s}^{-1}$), t is the time (s) and r is the radius of the wire (cm). For the values quoted above the time

required to saturate the wire with hydrogen is 18.3 seconds. This assumes that the boundary conditions are fulfilled and assumes that there is no serious violation of other assumptions involved in the diffusion theory.

Alternatively, the diffusion of oxygen out of the droplet can be calculated. The molten droplet was also held for five minutes in hydrogen. For liquid iron, the diffusion coefficient for oxygen has been established as $1.9 \times 10^{-4} \text{ cm}^2 \text{ s}^{-1}$ at 1550°C ⁽⁷⁸⁾. Assuming the droplet formed in the levitation coil is spherical, the time for oxygen to completely diffuse out of the droplet can be determined. Considering diffusion in a sphere⁽¹⁰⁶⁾, complete penetration occurs at a value of $(Dt/r^2)^{\frac{1}{2}}$ equal to 0.8. Substituting the values of D and r in this expression, the time required is 300 seconds. However, the droplet in the coil is subject to induced currents and there is continual stirring in the liquid phase. Consequently the time required for completion of the diffusion process will be much less.

A number of iron droplets were deoxidised in hydrogen by heating iron wire in the levitation coil to the temperature range $1100\text{--}1200^\circ\text{C}$, holding for five minutes and then melting the wire into a droplet and holding in this state in hydrogen for five minutes. The droplets were allowed to cool under argon; they were separated from the wire from which they were formed and analysed for oxygen. The results are given in Table 7. The figures range from 0.002 to 0.006 mass% oxygen.

4.1.2 Results of Initial Experiments

The results of the oxidation of iron droplets falling through

50 cm air and quenching in different media are recorded in Tables 8 to 13. The droplets were initially deoxidised as described in the previous section, allowed to fall through the air and were collected in a 500 ml stainless steel beaker containing the quenchant to a depth of 12 cm.

The first medium considered was 704 silicone oil. Silicone oil was selected because of the work of Vig and Lu⁽⁶⁸⁾. On quenching into the silicone oil bubbles of gas appeared at the surface of the oil. On retrieving the droplet from the oil, the droplet was coated with a black reaction film. This film had not been reported in the work previously cited⁽⁶⁸⁾. The droplets were immersed in trichloroethane and acetone to remove the oil layer and the black film. Soaking the droplet in the solvent for two minutes removed the oil but not the black film. Some of the film could be removed by wiping on a tissue. It was found that the oil and most of the film could be removed by ultrasonically cleaning the droplets in acetone for two minutes and wiping with a paper tissue. The surface of the droplet under the deposit was grey in appearance suggesting oxidation had occurred. The results of the oxygen analysis of twenty samples are given in Table 8. It can be seen that the masses of the droplets varied from 0.73 g to 1.45 g and the oxygen levels varied from 0.026 mass% to 0.074 mass%.

It was evident from the beginning that there was a wide disparity in the oxygen values recorded for the droplets and there was no direct relation between mass of droplet and oxygen level assuming all other conditions remained the same. The temperature of the droplet at fall was kept as close to 1600°C as possible in these initial experiments. Because of the wide range of values

recorded in oxygen level, a large number of droplets were generated so that a statistical analysis could be made of the oxygen levels. Initially twenty droplets, as identical as possible, were generated. The twenty samples generated, with silicone oil as quenchant, gave a mean value of 0.0457 mass% oxygen with a sample standard deviation of 0.0140 mass% oxygen.

Because of the reaction between the liquid metal and the silicone oil alternative quenchants were examined. Invoil 30 was chosen as a quenchant because it is a carbon based oil with good high temperature properties and has replaced the more expensive silicone oil in some applications. On quenching into the Invoil 30, gas bubbles appeared at the surface of the oil. The droplets were bright in appearance on removal from the oil. The droplets were degreased in trichloroethane and dried on a tissue before analysis. The results of the twenty samples are presented in Table 9. The values range from 0.0073 mass% to 0.052 mass% oxygen giving a mean value of 0.0150 mass% with a sample standard deviation of 0.0121 mass%.

A second carbon based quenchant, namely paraffin oil was also examined. The results are given in Tables 10 and 11. The cold paraffin oil was very viscous. The droplets emerged bright and clean from the oil. A second series of tests were performed with the paraffin oil at 110°C. At this temperature the oil had a similar viscosity to the silicone oil and Invoil 30. With the cold paraffin oil the values ranged from 0.011 to 0.037 mass% oxygen, with a mean value of 0.0182 mass% oxygen and a sample standard deviation of 0.0065 mass% oxygen. Ten droplets were

interacted with the hot paraffin oil and oxygen values ranged from 0.008 to 0.020 mass% oxygen. In this case the mean value was 0.0133 mass% with a sample standard deviation of 0.039 mass%.

The next quench medium considered was water. The water used was distilled water and this was deaerated by gently bubbling argon gas through the water for 30 minutes prior to use. The results for the oxygen levels in these droplets are recorded in Table 12. It can be seen that the masses of the droplets varied between 0.7 and 1.1 g and the oxygen levels across all samples varied from 0.167 to 0.431 mass%. The samples quenched in water were grey in colour indicative of oxide formation. The twenty droplets generated a mean value of 0.3182 mass% oxygen with a sample standard deviation of 0.0811 mass% oxygen.

The final quenchant considered was liquid nitrogen. The liquid nitrogen was contained in the stainless steel beaker which had been insulated. The results for the quenched droplets are given in Table 13. It was found that on retrieving six droplets from the liquid nitrogen, the droplets had broken up into smaller droplets. The reaction between the molten metal and the liquid nitrogen seemed to be more violent than with other quench media. Twenty two droplets were investigated; they gave a mean oxygen value of 0.1032 mass% with a sample standard deviation of 0.0264 mass% oxygen.

The major problem was to establish which quenchant reacted or interfered least with the oxide film established on the iron droplet surface during the fall through the mass transfer column. Vig and Lu⁽⁶⁸⁾ stated that 704 Silicone oil interfered least

with the droplet surface. However, they did not report the presence of a reaction film which was evident in these investigations. The main question was to determine whether the reaction between the droplet and the oil altered the absolute value of the oxygen content of a droplet. From the foregoing results it is certain that water and liquid nitrogen raise the level of the oxygen in the droplet. It is well known that during the first stages of quenching in water a hot object is surrounded by a gas envelope as a result of localised boiling of the water. A steam atmosphere would be oxidising to iron under these conditions. The case of liquid nitrogen is more difficult to explain. Any reaction with liquid nitrogen would leave a nitrogen gas envelope around the droplet. However, the reaction was so violent it could be possible that a secondary reaction with air at the liquid nitrogen-air interface results. Certainly the oxygen levels recorded in the iron droplets when quenched in liquid nitrogen, although not as high as those quenched in water, are considerably higher than those quenched in any of the oils. Here the oxygen levels in the silicone oil quenched droplets were less than half the levels recorded in the liquid nitrogen quenched droplets on average. The carbon based oils gave the lowest levels of oxygen in the iron. The droplets were also clean and bright. Under the conditions of the tests it would be expected that the surfaces of the droplets would be dulled by the presence of an oxide film. Since these droplets recorded lower oxygen levels than similar droplets quenched in the silicone oil it was necessary to determine whether carbon based quenchants were reducing to iron oxides under the conditions of

the experiment and whether silicone oil was reducing or oxidising to the oxidised iron droplets.

4.1.3 Reaction between Liquid Iron Droplets and Quench Oils

In this preliminary experiment fifteen iron droplets were quenched in three different oils (five per oil). The quench oils examined were Invoil 30, Paraffin oil and Silicon oil. The results of the titrations are given in Tables 14 to 23 and in Figs.36 to 50.

The titration with the tetrabutylammonium hydroxide was carried out to the end point at five minute intervals. The titration was repeated until a constant background level was reached. This was necessary because the argon purge rate was 500 ml per minute and the volume of the system was of the order of three litres. The argon flow rate was the maximum rate possible without forcing gas round the liquid seal in the stainless steel beaker at the bottom of the mass transfer column. To ensure that all of the carbonaceous gases had been carried over to the absorption vessel the gas was swept through for many minutes. As a result, the titration was carried out several times. The solution itself aged with the result that the end point went out of adjustment and it was necessary to take this into account in the final analysis. In all of the titrations, Figs.36 to 50 it can be seen that there is a gradient to the titration-time graph in each case after the initial high titration value at 5 minutes. In some cases the carrier gas was carried over for one hour to confirm the titration-time gradient after this period of time. The gradients in each figure are constant within each separate titration but vary slightly over the fifteen

separate experiments. This deviation is probably attributable to slight variations in the concentrations of the absorbent or the titrant or could perhaps be a temperature factor. This ageing contribution had to be accommodated for the period of the first five minutes before the titration was carried out. To take this into account the graph was drawn and the best fit line was projected back to the volume of titrant axis i.e. at zero time and this value was the value attributed to the carbon dioxide in the absorbent dimethylformamide. It can be seen from the graphs drawn that this figure is usually very close to the value obtained at the first titration after five minutes.

The information from the graphs is put together in Table 29. The volume of titrant required to neutralise the carbon dioxide generated (i.e. the zero time value) is recorded in column 4. The volume of titrant can be readily converted to the mass of oxygen reduced from a knowledge of the molarity of the titrant. This figure can then be converted to mass per cent oxygen by reference to the mass of the droplet.

In relation to the Invoil 30 quenchant the volume of titrant varied from 1.66 to 3.3 ml. The residual oxygen in the droplets was measured by chemical analysis and the values recorded; these values ranged from 0.0032 to 0.0053 mass% oxygen. When corrected, by the addition of the oxygen collected from the reaction with the Invoil 30, the values range from 0.0625 to 0.0935 mass% oxygen.

The paraffin oil quenchant produced a closer range of values for titrant volume for 2.00 to 2.60 ml. However, the residual oxygen figures for these five samples were more wide ranging,

varying from 0.0046 to 0.0124 mass%. When corrected, the values of oxygen level for the droplets varied from 0.0688 to 0.0806 mass%.

The volume of titrant required to neutralise the carbon dioxide generated from the silicone oil quenched samples ranged from 0.25 to 0.90 ml. The residual oxygen values were much higher than the previous samples ranging from 0.0336 to 0.0531 mass%. The corrected values increased the oxygen levels to the range 0.040 to 0.0636 mass%.

It can be seen that the volumes of titrant required to neutralise the carbon dioxide generated by reaction of oxidised droplets with the carbon based quenchants, Invoil 30 and paraffin oil are similar and considerably higher than the volumes recorded against the silicone oil. Further the measured oxygen levels of the droplets after quenching in the oils vary widely. In comparison with the silicone oil quenched droplets the Invoil 30 and paraffin oil quenched droplets are very low in oxygen, in many cases by an order of magnitude.

It would seem that there is a definite reaction between the carbon based quenchants and the oxidised iron droplets. The residual oxygen values in many cases are comparable with the values recorded for deoxidised droplets, cf Table 7.

The position with the silicone oil quenched droplets is more difficult to determine. The volume of titrant required in each case is very much less than the carbon based quenchants and as a consequence the impact on the final corrected figure is much less. Evidently, if there is a reaction between the oxidised droplet and the silicone oil it is very limited.

Of the five quenching media examined, silicone oil interfered least with the oxygen figures. On this basis silicone oil was used to quench the droplets in the main part of the programme.

4.2 Oxidation Studies

4.2.1 Treatment of Results

From the initial results it was evident that there was a large scatter in oxygen values obtained and that a statistical interpretation of the results would have to be made. Assuming the quench media did not appreciably alter the oxygen values the only other parameters to be considered were those of temperature and droplet size. As far as possible, all tests were carried out at 1600°C. There was difficulty in maintaining a constant 1600°C and in ensuring that the droplet was at 1600°C when it fell from the coil. Most of the iron droplets were released from the coil at 1600°C \pm 20°C. The results are recorded in Table 30 and presented in Figure 51. The results do not show any definable trend and the values are within the experimental error of the oxygen analysis.

The effect of the droplet size on oxygen pick-up was also considered. Again the figures quoted are for pure iron. The results are recorded in Table 31 and presented in Fig.52. It can be seen from the data that surface area is a factor to be considered in relation to oxygen pick-up. The data indicates that the smaller the mass of the droplet the higher the oxygen pick-up. The mass per cent oxygen figure is directly related to the volume of the droplet and the oxygen pick-up will be related to the surface area

presented to the oxidising atmosphere. The smaller droplets have the greater surface area to volume ratio and should therefore record the higher oxygen figures when presented in mass per cent values. This is in fact so. To confirm this trend the exercise was repeated for the Fe-0.25% Cr alloy droplets. The results are recorded in Table 32 and Fig.53. These results confirm the earlier findings with the iron droplets.

The results also confirmed that some form of standardisation of the results in relation to size was required as it was not possible to compare oxygen figures for different alloy systems if the droplet size values varied widely. A survey was made of the droplet sizes for each of the alloy systems considered. These are presented in Table 33 and Fig.54. The information is presented as a histogram with the number of droplets as ordinate and the mass of the droplets as abscissae. The masses of the droplets were grouped in half-gramme units and the values quoted on the histogram are the figures shown ± 0.25 gramme. It can be seen that the size distribution approaches a normal distribution centred on 0.7 g mass. In view of this all the results were 'normalised' to a 0.7 g droplet. The normalising was carried out in the following manner. The radius of any particular droplet was determined from the mass of the droplet assuming a value of 7.08 g cm^{-3} for the density of liquid iron at 1600°C (107). The value of the radius, in cm, so obtained was then divided by 0.287 cm, the radius of a 0.7 g iron droplet at 1600°C , and the quotient was multiplied by the value of the mass% oxygen figure for the droplet to give the normalised oxygen figure i.e. for a 0.7 g droplet. These values are the ones used in the presentation of the results for the pure iron and each of the alloy systems.

The results are presented in two ways, viz, as mass% oxygen against height of fall in air and as mass% oxygen against time of fall in air. The height of fall was directly measured in the experimental arrangement. The time of fall in air was calculated for the prevailing experimental conditions. The droplets fell 15 cm from the levitation coil in argon before entering the air column so it was already accelerating when it contacted the air. A plot of height of fall in air versus time of fall in air for 0.7 g droplet is shown in Fig.55.

4.2.2 Oxidation of Pure Iron Droplets

The oxidation of the iron droplets is recorded in Tables 34 to 39. Each table records the height and time of fall in air for the iron droplets. Against each droplet, its mass, temperature at fall and its oxygen analysis, are recorded. From the mass of the droplet the radius was determined and the oxygen value for a 0.7 g equivalent droplet was determined and recorded. The number of droplets varied for each height of fall and the data for each group of droplets was analysed statistically. For each group of droplets the sample mean was determined and the sample standard deviation calculated. The standard deviation or standard error of the mean was calculated by dividing the sample standard deviation by the square root of the sample size. The 95 per cent confidence interval for the mean value was determined by reference to the t-distribution. The mean value was plotted on the graph by a circle and the limits of the 95 per cent confidence interval were recorded by a bar. It can be seen that using this technique the spread of the confidence interval tends to be inversely related

to the number of samples taken. Graphs were drawn for oxygen pick-up in mass% versus height of fall in air, Fig.56, and for oxygen pick-up versus time of fall in air, Fig.57. It can be seen that the confidence limits for the 59 cm and 100 cm fall in air are much closer to the mean than those for the 37 cm and 90 cm fall in air values. The number of samples for the former were twenty and twenty-four respectively, whilst for the latter six and four respectively. The results from eighty-three droplets were used to compute the two graphs. A line of best fit was drawn through the oxygen pick-up versus height of fall in air points, originating at the zero of the graph. In the case of the oxygen pick-up versus time of fall in air graph the best fit through the points was a straight line. Extrapolating the line back to the zero time axis the line did not pass through the origin but intercepted the mass per cent oxygen axis at about 0.005 mass% oxygen.

The rate of oxidation of iron at 1600°C over the measured interval suggests that the reaction is zero order. The rate constant, k , is then simply given by mass% oxygen per unit time. Taken from the graph this gives 0.215 mass% oxygen per second. If the rate is related to the mass of oxygen picked up per unit area per unit time this value becomes 7.6 mg oxygen per cm² of iron surface per second.

4.2.3 Oxidation of Iron-Manganese Alloy Droplets

Three iron-manganese alloys were investigated, Fe-0.5% Mn, Fe-0.7% Mn and Fe-1.0% Mn. The 0.5% Mn alloy was investigated over five different heights in air and the results are recorded

in Tables 40 to 44. These results are plotted in Figs.58 and 59. It can be seen that when oxygen pick-up is plotted against height of fall in air the form of the graph is similar to that for pure iron. In fact the values for the 75 cm, 100 cm and 118 cm fall in air are almost identical to the values recorded for the iron droplets. The difference is with the 37 cm and 50 cm values which are larger for the manganese alloy. When the results are plotted against time, the best fit is again a straight line through the points, again suggesting a zero order reaction over the time interval investigated. The rate constant for the alloy, k , is 0.173 mass% oxygen per second or 6.10 mg oxygen per cm^2 of iron alloy surface per second.

It is evident that the initial rate, compared to that of iron, is higher. The first point on the graph is at 37 cm or 0.15 second. If a line is drawn from the origin to this first point at 0.15s, this would give the minimum value of the initial rate constant. In this case it is 0.30 mass% oxygen per second or 10.6 mg oxygen per cm^2 surface per second.

The second iron-manganese alloy, 0.7 mass% Mn, was investigated over six different fall heights in air. The results are recorded in Tables 45 to 50 and Figs.60 and 61. Compared to the Fe-0.5% Mn alloy, the oxygen pick-up at each height interval for the Fe-0.7% Mn alloy is marginally greater, except for the 118 cm fall. As in the previous cases, the best fit for the rate of oxidation is a straight line. The rate constant over the measured distance is 0.15s mass% oxygen per second or 5.50 mg oxygen per cm^2 iron alloy surface per second. Again the minimum initial rate constant from zero time

to 0.15s was calculated by measuring the slope of the line connecting the two points: this gave a value of 0.34 mass% oxygen per second or 12.0 mg oxygen per cm² surface per second.

The third iron-manganese alloy, 1.0 mass% Mn, was investigated over five different fall heights in air. The results are recorded in Tables 51 to 55 and Figs. 62 and 63. The 37 cm and 50 cm oxygen values are very similar to the Fe-0.7% Mn values and the two systems only really diverge above these levels. The curve of oxygen pick-up against height of fall in air is very similar to the previous curves and the three manganese curves are plotted together in Fig. 64 for comparison.

The best fit through the points of the Fe-1.0% Mn rate of oxidation is again a straight line. The measured value of the rate constant over the distance investigated is 0.22 mass% oxygen per second or 7.8 mg per cm² per second, with a minimum initial rate constant of 0.34 mass% oxygen per second or 12.0 mg oxygen per cm² of surface per second. The oxidation rates for the three manganese alloys are presented in Fig. 65. These show only small differences over the range studied compared to iron.

4.2.4 Oxidation of Iron-Chromium Alloy Droplets

Four iron-chromium alloys were investigated, Fe-0.17% Cr, Fe-0.25% Cr, Fe-0.8% Cr and Fe-1.46% Cr. The 0.17 mass% Cr alloy was investigated over six different heights in air and the results are recorded in Tables 56 to 61 and in Figs. 66 and 67. Fifty droplets were examined in this particular alloy programme. However, the scatter amongst the results was greater than for pure iron droplets and for the three iron-manganese alloys examined.

This is exemplified by the wider confidence interval on each point and the poorer fit of the line through the points. Deviation is particularly marked in the 100 cm and 118 cm points. For the rate of oxidation of the Fe-0.17% Cr alloy the best fit through the first five points has been taken. Examination of the results for the 118 cm fall in air shows that the results are effectively in two groups; the lower group of five results clustering around 0.10 mass% oxygen and the top group of four clustering around 0.17 mass% oxygen.

The value of the rate constant is 0.18 mass% oxygen per second or 6.4 mg per cm² per second. In comparison with the pure iron and iron-manganese results the oxygen pick-up is much higher especially with the 37 cm fall in air droplet, the first height of fall measured in each of the series. The value of oxygen pick-up for the 0.17% chromium alloy is 0.072 ± 0.024 mass% compared with 0.051 ± 0.011 mass% for the 1% manganese alloy. This suggests that the initial rate of oxygen pick-up is considerably higher in this alloy. Adopting the procedure outlined earlier, the minimum initial rate constant works out at 0.48 mass% oxygen per second or 17.0 mg oxygen per cm² surface per second.

The 0.25 mass% chromium alloy results for six heights of fall in air are given in Tables 62 to 67, and in Figs. 68 and 69. As with the previous group, there was more degree of uncertainty about the results, apart from the 37 cm fall in air, which can be seen by the width of the bars around each point. Again there is an increase in oxygen pick-up as recorded by the first measured point: a value of 0.10 mass% oxygen is recorded for the 37 cm

fall in air. The rate constant over the measured range is 0.18 mass% oxygen per second or 6.4 mg per cm² per second. The minimum initial rate constant for this alloy is 0.67 mass% oxygen per second or 23.6 mg oxygen per cm² surface per second.

The results for the Fe-0.8 mass% Cr alloy are given in Tables 68 to 73 and Figs.70 and 71. The results are very similar to the 0.25% Cr alloy system being just marginally higher. A straight line fit seemed the best approach to the rate of oxidation points. The slope of the line gave a rate constant of 0.25 mass% oxygen per second or 8.8 mg oxygen per cm² per second. Since the 37 cm point was almost identical with the 0.25 mass% chromium alloy 37 cm point, the minimum initial rate constant was the same at 0.67 mass% oxygen per second or 23.6 mg oxygen per cm² surface per second.

Whereas in the previous chromium alloys, increasing the level of chromium in the alloy increased the oxygen pick-up there was a reversal at the 1.46% Cr level. The results for this alloy are given in Tables 74 to 79 and Figs.72 and 73. A total of 45 droplets over six different heights of fall in air were examined. There is a scatter around each point but the trend is evident. The level of oxygen pick-up is reduced at all points and the values are nearer the 0.17 mass% chromium values than the rest. The rate constant over the range 0.15 to 0.35s is 0.17 mass% oxygen per second or 6.0 mg per cm² per second and the minimum initial rate constant is 0.44 mass% oxygen per second or 15.6 mg per cm² surface per second.

Figures 74 and 75 show the results for the four chromium alloys together. The oxygen pick-up for each level of chromium in the iron is clearly seen.

4.2.5 Oxidation of Iron-Silicon Alloy Droplets

Three iron-silicon alloys were investigated, Fe-0.3 mass% Si, Fe-0.75 mass% Si and Fe-1.33 mass% Si. The 0.3 mass% silicon alloy was examined over five different heights of fall and the results are presented in Tables 80 to 84 and Figs. 76 and 77. It has been noted earlier that the silicon alloys were difficult to prepare into wire and as a result there was not much material suitable for melting as wire in the levitation coil. There were a minimum of five droplets at each height of fall in air but because of the small number of samples the scatter at each point is correspondingly high. The line of best fit has been drawn through the points and again it has been assumed a linear rate of oxygen pick-up. The slope of the oxygen pick-up versus time of fall in air has a value of 0.25 mass% oxygen per second or 8.8 mg oxygen per cm² surface per second. Since the line extrapolates back to zero the minimum initial rate constant is also 0.25 mass% oxygen per second or 8.8 mg oxygen per cm² per second.

The Fe-0.75 mass% Si alloy was only investigated over three heights of fall, namely 50, 75 and 100 cm. The results are given in Tables 85 to 87 and Figs. 78 and 79. In all three heights the results are very similar, and almost identical. Furthermore, the values of oxygen pick-up are very low and although only fifteen droplets were examined the scatter in the results is less than in many earlier runs. The only possible line through the points is a straight line, parallel to the time axis suggesting that after falling 50 cm in air there is no further oxygen pick-up i.e. a rate constant of zero with a minimum initial rate of 0.15 mass% oxygen per second or 5.4 mg oxygen per cm² surface per second.

The Fe-1.33% Si alloys were examined at five heights of fall in air and the results are collected in Tables 88 to 92 and Figs. 80 and 81. A total of thirty four droplets were analysed for oxygen. The results are extremely consistent despite the small number in each sample. Again, as with the Fe-0.75% Si alloys, the oxygen pick-up is low and beyond the 37 cm fall in air the figures remain static suggesting that once an initial oxygen level is reached there is no further oxidation. Hence the rate constant over the time the droplet fell in air would be zero with a maximum initial rate of 0.14 mass% oxygen per second or 5.0 mg oxygen per cm² surface per second.

The results for all the silicon alloys are compared in Figs. 82 and 83. These clearly show the marked reduction in oxygen pick-up with increasing silicon content in the alloy.

4.3 Reduction Studies

4.3.1 Introduction

In the reduction experiments it was assumed that the change in mass was attributable only to loss of oxygen and the loss of oxygen could be determined as mass per cent by reference to the mass of the sample. Hence the per cent oxygen loss with temperature could be determined. Further if the final oxygen analysis on the hydrogen reduced droplet was known it was then possible to work backwards from this final oxygen figure to determine the original oxygen figure and record how the level of oxygen in the sample had changed with temperature and time. Where these figures have been determined they are plotted with mass per cent

oxygen as ordinate and temperature/time as abscissa. Since the heating rate was the same in all the reduction runs, i.e. 6°C per minute, the graphs were plotted such that the temperature intervals corresponded approximately to the time intervals so that, if required, the total heating time could be easily determined.

Of interest from the graphs are the final oxygen figures of the reduced droplet and the temperature at which onset of reduction occurs.

4.3.2 Reduction of Oxidised Iron Droplets

Oxidised iron droplets were reduced in hydrogen and the data is presented in Tables 93 and 94 and Figs. 84 and 85. Sample number A.304 had been oxidised by falling 100 cm through air prior to reduction in hydrogen. There was no change in mass till about 500°C when there was a slight inflexion and no further change till 690°C. Again this was a single inflexion and there was no further change till 870°C. From this point there was a continual reduction in oxygen level with increasing temperature to 1150°C. The specimen now held isothermal at 1150°C continued to be reduced but at a reduced level until after 30 minutes no further reduction occurred. The final oxygen figure was 0.038 mass% (for 0.7 g droplet).

Sample number A.307 was similarly oxidised by a 100 cm fall in air. There was a minor inflexion before 800°C at about 570°C but, as in the previous sample, the major reduction of the oxide commenced at 800°C and continued to 1150°C and for about 20 minutes at 1150°C. The final oxygen figure was 0.043 mass% (for 0.7 g droplet).

A number of dewpoint measurements were taken during the heating up cycle of a sample similarly oxidised to the above two samples. Values ranging from $-20^{\circ}\text{C}(-4^{\circ}\text{F})$ to $-25^{\circ}\text{C}(-13^{\circ}\text{F})$ were recorded.

4.3.3 Reduction of Oxidised Iron-Manganese Alloy Droplets

Six iron-manganese alloy droplets, after oxidation in air, were reduced in hydrogen; four samples were Fe-0.5 mass% Mn and two samples Fe-0.7 mass% Mn. The results are recorded in Tables 95 to 100 and Figs.86 to 91.

Sample number D.77, Fe-0.5% Mn, (Table 96, Fig.87) was oxidised by allowing it to fall through 50 cm of air before quenching. The onset of reduction was around the 800°C temperature mark. Once reduction commenced it proceeded fairly rapidly and the specimen was still losing oxygen at 1150°C , the maximum temperature although the rate was beginning to slow down. However, some reduction occurred up to about 30 minutes at 1150°C .

A similar graph is given by specimen number D.53 (Table 95, Fig.86). This droplet, of the same composition, was oxidised by falling through 100 cm air. The onset of reduction was about 800 to 820°C . Again once reduction had started it proceeded fairly quickly and by 1150°C was slowing down. Some reduction occurred up to about 20 minutes at 1150°C . Taking the mass loss figures for these two samples and projecting back to an initial oxygen figure, in both cases, gives a level which is somewhat higher than the rest of the samples in the same group.

Two other samples of the same composition and similar oxygen level, D.92 (Table 97, Fig.88) and D.94 (Table 98, Fig.89) are

presented. Although no final oxygen figure is available both show the onset of reduction near 800°C with the highest reduction rate at the commencement of the reduction process.

Samples D.11 (Table 99, Fig.90) and D.32 (Table 100, Fig.91), both Fe-0.7% Mn, with falls in air of 50 cm and 100 cm respectively, gave similar results. Sample D.11 was an 'overshoot' situation and the sample reached a temperature of 1300°C before the furnace was switched off. Reduction of the oxide continued up to 1300°C, from the mass-loss figures, and ceased immediately the cooling process commenced. Reduction appeared to commence at about 840°C. Sample D.32 showed a threshold temperature of 820°C for reduction; the reduction rate was greatest immediately after the onset and this rate reduced as temperature increased. Some reduction at 1150°C appeared to occur for a few minutes.

4.3.4 Reduction of Oxidised Iron-Chromium Alloy Droplets

Eleven iron-chromium alloy droplets were reduced in hydrogen. Three samples containing 0.17% Cr were investigated and the results are given in Tables 101 and 102 and Fig.92. Sample C.109 (Table 101, Fig.92) indicates that reduction commenced at about 750°C. The reduction rate appeared fairly constant up to 1100°C when the rate decreased, however, there was a sharp decrease in oxygen level after 30 minutes at 1150°C which is unusual. Table 102 gives the results of two samples reduced at the same time. Perhaps the only important feature here is the threshold temperature for reduction, 780°C. The oxygen mass loss recorded in the table is an average for the two samples since there was no means of establishing the rate of reduction of each sample.

Four samples at the 0.25% chromium composition were reduced in hydrogen. Sample number C.54 was oxidised by falling through 50 cm air prior to reduction, the other three samples were oxidised by falling through 100 cm air prior to reduction. The information can be found in Tables 103 to 106 and Figs.93 to 96. All these samples, prior to reduction, would have relatively high oxygen content. Sample number C.54 (Table 103, Fig.93) showed a rapid reduction in oxygen from a threshold at about 850°C; the final oxygen level being 0.069 mass%.

The three samples also showed thresholds at which reduction began at about 840°C and, as in the previous sample, the final oxygen levels all ended up at about 0.07 mass%. Two samples, C.65 (Table 105, Fig.95) and C.91 (Table 106, Fig.96), showed considerable reduction at 1150°C during the isothermal period. It was estimated that the oxygen level in both of these samples was of the order of 0.09 mass% at 1150°C.

Only one sample containing 0.8% Cr was reduced in hydrogen. This was sample C.214 (Table 107, Fig.97) which had been oxidised by falling through 100 cm of air. The final oxygen was not known so that only the oxygen mass loss could be plotted.

The data suggests that reduction commences at about 800°C and that some reduction occurs during the isothermal period at 1150°C.

Three samples containing 1.46 mass% chromium and oxidised by falling through 100 cm of air prior to quenching were reduced in the thermobalance. The results are recorded in Tables 108 to 110 and Figs.98 to 100. The threshold temperature at which appreciable reduction of the oxide occurs in sample number C.168 (Table 108, Fig.98) is difficult to determine. Again the thresh-

hold temperatures vary from about 770°C through to 900°C. Reduction of the oxides occurs, as in previous chromium alloys, during the isothermal period. The final oxygen figures for the three specimens are lower than for the other chromium alloys investigated, the samples being reduced to 0.028 mass% oxygen.

4.3.5 Reduction of Oxidised Iron-Silicon Alloy Droplets

Four iron-silicon alloys, all oxidised by falling 100 cm in air, were reduced in hydrogen. Two Fe-0.3% Si alloy droplets were investigated. Both gave a threshold temperature for reduction of about 930°C, see Tables 111 and 112 and Figs.101 and 102. Both samples had a final oxygen figure of about 0.038 mass%. Sample E.2 (Table 111, Fig.101), starting from an initial higher oxygen level continued the reduction process during the 1150°C isothermal period until this figure was reached. Sample number E.3, (Table 112, Fig.102), starting from a lower oxygen level was almost at the final oxygen figure at 1150°C with the result that very little reduction occurred during the isothermal period.

Table 113 and Fig.103 give the results for the reduction of sample number E.62, Fe-0.75% Si alloy. The temperature at which reduction commenced was more difficult to determine because of the small overall mass change in the specimen. It was of the order of 900°C and the final oxygen figure was 0.017 mass%.

One sample, number E.4, with the highest silicon content, 1.33 mass% was reduced in hydrogen; the results are recorded in Table 114 and Fig.104. The threshold temperature at which reduction commenced, as indicated by mass loss, was about 925°C. However, the sample continued to lose mass after 1150°C was

reached and the mass loss up to 40 minutes in the isothermal region was fairly constant. This specimen was reduced to the lowest oxygen figure of all the samples, viz. 0.009 mass%. When the mass loss was converted back to oxygen loss (assuming the mass loss was entirely oxygen) the starting level was calculated to be 0.049 mass% oxygen which is considerably higher than other oxygen figures recorded for this alloy.

The results for all the reduction experiments are collected together in Table 115. The onset of reduction for iron-manganese alloys is in the range 780-820°C, approximately the same as pure iron specimens. The 0.17 mass% chromium alloy is also in this category. However, it appears that increasing the chromium level to 0.25 mass% and above raises the onset of reduction temperature to the range 800 to 850°C. Iron-silicon alloys all have a higher threshold temperature at 900°C plus.

4.4 Surface Morphology and Surface Analysis Studies

4.4.1 Surface Morphology

Examination of the surfaces of iron droplets and iron-alloy droplets was carried out by means of scanning electron microscopy. Four or five droplets from each of the eleven alloy systems were examined. Both oxidised droplets and oxidised and reduced droplets were examined. Characteristic features of each group were observed, noted and recorded on 35 mm film. The main features identified are presented in Plates 7 to 47.

Features of iron droplets being recorded in Plates 7 to 13.

Features of iron-manganese droplets being recorded in Plates 14 to 27.

Features of iron-chromium droplets being recorded in Plates 28 to 37.

Features of iron-silicon droplets being recorded in Plates 38 to 47.

4.4.2 Surface Analysis

4.4.2.1 Electron Microscope Studies

Seven droplets, mounted in bakelite and polished to a 6 μm diamond finish, with a chord of material removed, were examined in the electron microscope. Progressive point scans were made from the oxidised surface into the body of the droplet to determine the extent of change in alloying element. Two manganese alloys, (the 0.3 mass% and 1.0 mass%) two chromium alloys, (the 0.25 mass% and the 1.46 mass%) and three silicon alloys, (the 0.3 mass%, 0.75 mass% and 1.33 mass%) were examined in this manner.

Fe-0.3% Mn

Two different samples were analysed. In both cases there were exceptionally high silicon figures. The silicon was present from reaction of the droplet with the quench media. Any reaction with the oxygen and formation of oxide phases would have occurred prior to any reaction with the silicone oil. The value of the silicon was removed from the figures and the iron and manganese figures adjusted to 100% total. In the first sample the manganese figures are higher than expected, Table 116.

The second sample gives background manganese figures which are low; the manganese could have been removed from the sample by volatilisation whilst it was held in the levitation coil. The manganese profile is shown in Figs.105 and 106.

Fe-1.0% Mn

A small chord section was traversed from edge to edge. The results are recorded in Table 117 and the manganese profiles illustrated in Figs.107 and 108.

Fe-0.25% Cr

The results from two areas of the same specimen are recorded in Table 118 and Figs.109 and 110. A small chord section was traversed from edge to edge in the first area examined. In the second area random analyses were taken from the surface and from the centre of the polished region. In the latter zone EDX analysis was performed using a spot beam (highly localised) and also a square beam where analysis over quite a wide area is taken and averaged by computation.

Fe-1.46% Cr

The results of a few spot analyses are recorded in Table 119 and Fig.111.

Fe-0.3% Si

The results of three spot analyses are given in Table 120. The extent to which the reaction with the silicone oil affect the figures is not easily seen. This factor obscures the results of all the silicon alloy analyses.

Fe-0.75% Si

The results of three spot analyses are given in Table 121.

Fe-1.33% Si

The results of a traverse across a chord section from the edge to the centre are given in Table 122.

4.4.2.2 VG Microlab Studies

4.4.2.2.1 Surface Analysis

The surface of a chord section was analysed in the VG Microlab. The specimen was Fe-1.46% Cr and the section traversed was from the edge of the specimen to a hole in the interior of the specimen. It is shown diagrammatically in Fig.112. Seven equidistant points were analysed after the polished surface had been cleaned by iron bombardment. The results of the Positive and Negative SIMS analysis are shown in Figs.113 to 134. Analysis of the peaks from the figures for iron, chromium and oxygen are presented in Table 123 and Figs.135 and 136.

4.4.2.2.2 Depth Profiles

Three samples, namely Fe-1.0% Mn, Fe-1.46% Cr and Fe-1.33% Si were investigated by depth profiling the oxide surface in both the positive and negative SIMS mode. Successive layers of material were removed by etching the surface by gallium ion bombardment and then analysing each layer revealed.

Fe-1.0% Mn

Two areas of the oxide surface were profiled and reported as RJMN1 and RJMN2. Penetration of the oxide film was not complete. The results are shown in Figs.137 to 144 and Table 124.

Fe-1.46% Cr

One area of the oxide surface was profiled and reported as RJ1P. Penetration of the oxide film was not complete. The results are given in Figs.145 to 149 and Table 125.

Fe-1.33% Si

Two areas of the oxide surface were profiled, one in the positive SIMS mode and the other in the negative SIMS mode. As before, penetration of the oxide film was not complete. The results are given in Figs.150 to 154 and Table 126.

Fe-0.3% Mn

To obtain an oxygen profile through a surface oxide a specimen with 0.3 mass% manganese and oxidised by falling through 100 cm air and reduced in hydrogen at 1150°C was examined. This is reported as D.92.3.P. Figure 155 shows the oxygen profile through the surface oxide.

CHAPTER 5 DISCUSSION

5.1 Accuracy and Errors of the Experimental Method

5.1.1 Temperature Measurement

The temperature measurements given by the platinum-platinum rhodium thermocouple in the temperature probe gave reproducible results as established in Section 3.2.4. The emissivity of the iron was determined at 0.36 up to the melting point. This is in good agreement with recorded data⁽¹⁰⁵⁾. The biggest margin for error was in the situation where fume condensed on the glass of the levitation chamber. However, with the technique adopted of allowing the droplet to freeze and remelt and noting the inflexion on the millivolt output of the pyrometer the final temperature of the droplet could be determined to probably within $\pm 10^{\circ}\text{C}$.

5.1.2 Oxygen Analysis

The instrument used for the oxygen analysis claimed to give a sensitivity better than 1 ppm. Over the course of the project several hundred analyses were undertaken. By reference to the values obtained for the standard samples used to calibrate the instrument a more realistic sensitivity would be 20 ppm or 0.002 mass%. This value is still well within the scatter obtained on all groups of samples for each alloy system investigated.

5.1.3 Statistical Interpretation of Results

The results of the 50 cm fall in air and silicone oil quench medium are examined in Appendix I. The limits for a 95% confidence interval are given for the 'raw' results and the same

results normalised to 0.7 g droplet equivalent mass. The number of samples observed was 20. It can be seen from the spread of the results that to obtain a 99% confidence interval the number of observations required was 32 and 25 for the 'raw' and normalised respectively. For a 98% confidence interval the respective numbers were 8 and 6.

These figures refer to single points. In the final analysis the points were not examined as separate entities but were correlated in graphical form (Figures 56 to 81). Consequently not as many observations would be required for each individual point on the graph. The figures obtained for the 50 cm fall in air, quoted above, suggest that the values would be covered by the 98% confidence interval. However, the number of droplets examined at each height of fall in most instances was lower than twenty so the 95% confidence interval was chosen.

5.2 The Oxidation of Molten Iron Droplets in Air

5.2.1 Theoretical Considerations

5.2.1.1 Temperature Profile of a Free-Falling Iron Droplet

The temperature profile associated with a droplet as it falls through the mass transfer column is of interest. Vig and Lu⁽⁶⁸⁾ estimated that the temperature of the droplet fell by 10°C during its fall of 17.8 cm in the levitation chamber and about 15°C in the oxidation chamber of 84 cm.

The temperature change of a falling droplet with height of fall was determined theoretically. The temperature will be affected in two major ways, viz:

- (1) thermal losses by convection and radiation, and
- (2) thermal effects due to the enthalpy of the oxidation reaction.

In isolation the first effect will result in a fall in temperature of the droplet whereas the second effect will result in a rise in the temperature since all of the oxidation reactions are exothermic.

The theoretical considerations and calculations are set out in Appendix II.

The results of the computer programmes are plotted in Figure 156. It can be clearly seen that the iron droplet was molten throughout its flight. Even with no heat of reaction added the droplets were still approximately 40°C above the freezing point of iron for the 120 cm fall in air. When the heat of reaction was added the fall in temperature was sharply arrested and the fall was only of the order of 14°C for a 0.7 g droplet falling through 120 cm air. These values apply to the heat of reaction when FeO is formed; the heat liberated in the case of manganese and chromium would be fifty per cent higher and in the case of silicon seventy five per cent higher for the same oxygen values.

5.2.1.2 Model for the Oxidation of Iron Droplets

Since the oxidation of the liquid iron droplet involves reaction between the oxygen in the air and the liquid metal the following reaction steps should occur:

- (i) transfer of oxygen to the gas/metal interface from bulk gas,
- (ii) chemical reaction at the interface, and

- (iii) transfer of the dissolved oxygen to the interior of the droplet

When the reaction commences, the deoxidised iron and oxygen are in direct contact at high temperature. The chemical reaction rate is probably so high under these conditions that the overall rate is controlled by one of the transport processes (i) or (iii). Of these two transport processes, (i) is most likely in the initial stages as (iii), the diffusion of ions through the oxide film, may be important in the later stages of reaction.

To test this hypothesis, a mathematical model was developed to calculate the rate of mass transfer by forced convection from the gaseous phase to accelerating droplets. Using this model, the rate of oxidation of liquid iron was calculated assuming that the equilibrium value of partial pressure of oxygen at the interface is negligible compared with that of the bulk gas. The model is developed in Appendix III. A number of differential equations were generated and these were solved by computer programmes. The results of the mathematical model are drawn in Figs.157 to 164. The figures clearly show that droplet size is an important factor in oxygen pick-up i.e. the smaller the mass of the droplet the greater the oxygen pick-up at any particular oxidation time, indicating that the oxygen concentration in a droplet is directly related to the surface area to volume ratio.

In the experiments carried out on the oxidation of iron droplets it was found that the temperature of the droplet did not have a pronounced effect. The temperature of the droplets were kept, as far as possible at 1600°C. Small variations in tempera-

ture, mainly within the band $\pm 20^{\circ}\text{C}$, occurred. Vig and Lu⁽⁶⁸⁾ performed their oxidation studies over a greater range of temperatures and noted that the oxidation rate increased with increasing temperatures, however, this increase was also only small.

The results from the mass transfer model indicate that the effect of temperature on the oxidation rate is not great. Increasing the film temperature from 800°C to 1600°C only increases the oxygen level from 0.047% to 0.052%, after 0.3 seconds or 1 metre fall in air, according to the model. Although the value of film temperature is incorporated in the formula there are a number of temperature dependent factors such as diffusion coefficient, density and viscosity of air which tend to outweigh the temperature effect.

5.2.2 Kinetics of the Oxidation of Molten Iron Droplets

The mathematical model generates an almost linear oxidation rate for iron. For the six values generated in the experimental arrangement the best fit for the results is a straight line.

The oxidation of free falling iron droplets as carried out by Vig and Lu⁽⁶⁸⁾ for the 1580°C and 1638°C temperatures are reported in Table 127. Adopting the same basis of normalising (see Section 4.2.1) the oxygen pick-up for a 0.7 g mass equivalent droplet was determined from Vig and Lu's results. Their figures were the mean of as many as ten values obtained by analysing quenched specimens reacted under the same conditions. They did not indicate the range of values obtained for each result quoted. Their normalised values are plotted in Fig.165. It can be seen that there is good agreement between their normalised values and the ones determined in this experiment.

The residence time in the air was only up to 0.35 seconds. It has been noted⁽⁶²⁾ that when liquid iron is exposed to an oxidising atmosphere the absorption process occurs in two distinct stages. The first stage is one of rapid absorption where the volume absorbed is dependent on oxygen pressure and gas/metal interfacial area. This stage involves rapid exothermic chemical reaction between oxygen gas and the melt. This gives way to a second stage observed to consist of two competing processes, that is, growth of the oxide layer and simultaneous dissolution of oxygen in the melt at the oxide-metal interface. Choh and Inouye⁽⁷⁵⁾ confirmed that oxygen absorption from the gas phase is represented by a model where most of the gaseous oxygen dissolves into the liquid iron through the oxide free interface although some oxygen forms iron oxide at the interface and this in turn dissolves into the liquid iron.

For this work, it is evident that the results obtained from the oxidation of iron in air relate to the first stage of rapid absorption and are characterised by a linear rate. As the droplet falls through the air, the deoxidised metal surface at 1600°C will absorb oxygen from the air. Chemical reaction rate under these conditions would be expected to be very high and transfer of oxygen to the gas-metal interface from the bulk gas or transfer of the dissolved oxygen to the interior of the droplet could be rate controlling.

The mathematical model predicts the rate of mass transfer by forced convection from the gaseous phase to accelerating iron droplets. Figure 166 shows the experimental results and those

predicted by the model at 1600°C for droplets of 0.7 g mass for oxidation in air. The calculated rate line is of the same form and slope as the experimental line but lies below it. The experimental line is a factor of approximately 1.6 greater than the line predicted by the model. Such a line is drawn in and it can be seen that the lines are almost coincident, just starting to diverge at the 0.2s level. The divergence can be explained on the basis that, as the droplets accelerate, the turbulence in the gas surrounding the droplet increases and consequently mass transfer to the droplet increases.

The increased rate of oxidation of the experimental values compared to those predicted by the model can be explained in terms of circulation within the droplet. Internal circulation can promote oxidation in two ways. Firstly, it has been shown⁽¹⁰⁷⁾ that internal circulation in liquid drops raises the effective diffusivity to a value equal to 2.25 times the molecular diffusivity. It is difficult to estimate mass transfer coefficients for the interior of a droplet because there is no way of knowing precisely the degree of circulation set up within the drop either during levitation or in free fall. Secondly, it is known that oxygen is surface active in molten iron and lowers the surface tension strongly^(108,109). It is therefore quite feasible that in these studies, eddies in the metal may bring about sufficiently large local changes in surface tension for interfacial turbulence to be set up and promote mass transfer in this way.

The morphology of the oxidised iron droplets is shown in Plates 10 and 11. At low magnification the surface shows a

rippled effect. This effect is shown in more detail in Plate 11 where it can be seen that most of the surface presents a rounded, smooth effect. There are slight hollows in this topography where a second surface feature presenting a rough, more uneven type of oxide can be seen.

5.3 The Role of Alloying Elements on the Oxidation Rate of Molten Iron Droplets

5.3.1 Thermodynamic considerations

The Gibbs Free Energy of a chemical reaction is a measure of the spontaneity of the reaction or the driving force behind the reaction and is a useful criterion when considering oxidising and reducing operations. The standard Ellingham diagram gives the standard free energies of formation of oxides i.e. the free energy for the conversion of the reactants into products, all components being in the Raoultian standard state of pure condensed phases and gases at one atmosphere partial pressure.

The free energy change under non-standard conditions, ΔG , is obtained from the standard free energy change, ΔG° , by the Vant Hoff isotherm:

$$\Delta G = \Delta G^\circ + RT \ln \left(\frac{\pi_a \text{ products}}{\pi_a \text{ reactants}} \right)$$

Each of the alloy systems were examined and modified Ellingham diagrams generated. These gave a clearer indication of the oxidising potential of the alloy elements dissolved in iron. The theoretical considerations and calculations are set out in Appendix IV. The results are presented in Figs.167-170 for the

systems MnO , Cr_2O_3 , SiO_2 and for the three systems relative to FeO . It can be readily seen that in solution the elements only have a free energy value marginally more negative than iron. There is very little difference between the manganese and chromium oxides; the oxide of silicon does lie below these.

5.3.2 The Effect of Manganese on Kinetics of Oxidation and Droplet Morphology

The oxidation behaviour of the three iron-manganese alloys investigated showed a very similar pattern to that of pure iron. The initial rate of oxidation was higher for the iron-manganese alloys and the level of oxygen picked up by the droplets increased with increasing manganese content.

The iron-manganese equilibrium diagram, Fig.171, shows complete solubility in both the solid and liquid phases, and manganese (m.pt $1244^\circ C$) forms an almost ideal solution in liquid iron (m.pt $1535^\circ C$). Manganese oxide MnO is thermodynamically much more stable than wustite, $Fe_{1-x}O$, at all temperatures and at $1600^\circ C$ there is a difference in standard free energy of approximately 195 kJ. However, it has been shown (Appendix IV) that when dissolved in iron, at the composition levels encountered in these experiments, the manganese oxide is only marginally more stable than pure wustite when oxidised in air ($P_{O_2} = 0.2$). At $1600^\circ C$, for the 0.5% Mn, 0.7% Mn and 1.0% Mn dissolved in iron the Gibbs free energy differences are approximately 30, 40 and 50 kJ.

The reaction product between manganese and oxygen dissolved in liquid iron can be either a solid or liquid oxide, depending on the composition of the liquid and the temperature. At $1600^\circ C$

the product is liquid with up to about 0.2 mass% Mn and is a solid at higher concentrations⁽¹¹⁰⁾.

In the Fe-O system there exists a composition range in which two immiscible liquids co-exist in equilibrium, Fig.172. Iron is the primary crystalline phase in this region and the wustite-iron eutectic is on the oxygen side of the two liquid region. The Mn-O system probably has a phase diagram with a two liquid region⁽¹¹¹⁾. The system iron oxide-manganese oxide in air is shown in Fig.173. A very flat minimum appears on the liquidus and solidus curves and extensive solid solution formation takes place among the various oxides which are stable at temperatures below the solidus.

At the onset of oxidation of these iron-manganese alloys, i.e. with up to 1% manganese, the oxide will separate out as a liquid phase while a large proportion of the metal is liquid. The manganese content would have to be considerably higher before the oxide phase separated out as solid FeO-MnO crystals. Hence the situation is very similar to that of pure iron. Oxygen both reduces the surface tension and viscosity of iron and will assist in promoting interfacial turbulence. Manganese has a negligible effect on surface tension⁽¹¹²⁾. Compared to the iron droplets, the only major difference is the presence of manganese in the iron with a greater chemical potential for oxide formation.

EDX Analysis carried out on a small chord section of a Fe-0.3% Mn and on a section of a Fe-1.0% Mn sample showed a change in the manganese profile across the specimens, Figs.105 and 107. In the case of the 0.3 mass% Mn sample, the manganese level in the zone adjacent to the oxidised edge was increased. For the 1.0 mass%

Mn sample, the manganese level in the iron, again in the zone adjacent to the oxidised edge, had been reduced. It was evident that some migration of manganese in these regions had occurred. This migration could occur in two ways. Firstly, by diffusion in the iron-manganese alloy. Secondly, depletion of the sub-surface layers of the alloy could occur by evaporation of manganese or a combination of both processes. It has been reported that at low oxygen concentrations and high manganese contents, evaporation occurs⁽⁶⁷⁾. This condition was possible in this work when the droplets were held molten in the levitation coil under hydrogen gas. Further, the manganese level in the oxide film formed on the surface was considerably higher than the initial alloy composition (Table 124). It must be noted that the actual manganese and iron concentrations were considerably higher than the figures quoted in Table 124. The figures, taken from Figs. 140 and 142, were distorted by the presence of silicon (present due to interaction of the droplet with the silicone oil quenchant). The important factor was the Fe/Mn ratio. For a 1% Mn alloy the original ratio was 99:1. However, from SIMS analysis, the ratios in the oxide were between 2.1:1 and 0.4:1 (Table 124). The highest ratio was 2.1:1 at the air-oxide interface. It is well known that between 700°C and 1200°C iron oxidises in air to give a sequence of three layers⁽¹¹³⁾. The inner wustite (Fe_{1-x}O) occupies about 0.95 of the thickness, intermediate magnetite (Fe_3O_4) with the spinel structure about 0.045, and outer hematite (Fe_2O_3) with the rhombohedral structure about 0.005. The ratio of 2 Fe(Fe_2O_3) to 1 Mn(MnO) is 2.02:1; the ratio of 2 Mn to 1 Fe is 0.50:1. This

suggests a spinel structure between $(\text{Fe,Mn})_2\text{O}_3$ and $(\text{Fe,Mn})\text{O}$ occurs immediately behind the air/oxide interface. Beyond this region the Fe/Mn ratio is approximately 1:1 and is indicative of $(\text{Fe,Mn})\text{O}$ oxide. The oxygen profile, Fig.144, only extended to one third of the depth analysed for Mn and Fe. After the initial surface contamination the oxygen profile was constant.

The oxide film on the surface of the Fe-0.5% Mn droplet, Plate 14, appeared two-phased. The dominant feature was the stria which appeared directional. However, amongst the stria were pockets of an oxide with a wavy texture. Plate 15, at higher magnification, shows this in more detail. A mounted and sectioned sample shows a region of porosity behind the surface, Plate 18.

The duplex nature of the oxide on the surface of a Fe-0.7% Mn droplet is shown in Plate 20. The striated surface is not evident now and is replaced by the 'sif' pattern more resembling the pure iron specimen.

The 1.0% Mn sample shows some of the stria similar to that of the 0.5% Mn sample, Plate 24. At higher magnification the oxide appears to be duplex in nature, Plate 25.

The oxide formed on the surface of a molten metal must be amorphous in nature since a molten metal can only offer short range order. Further the melt is cooled very rapidly and it is unlikely that the constituent atoms have time to rearrange into a crystalline structure having long range order and no extensive network structure. Crystallisation of the oxide film will probably be related to the metal structure immediately beneath it on cooling. In this type of oxide no large channels are likely to exist for anion transport and the cations would be only weakly bound. Hence

cation transport is to be expected in this type of film. This is borne out by the SIMS analysis of the Fe-1.0% Mn sample.

The formation of the oxide in all cases took only a fraction of a second and the addition of up to 1% Mn to iron did not appreciably alter the morphology. The main effect of increasing additions of manganese was to reinforce the duplex nature of the oxide, namely wustite and spinel type oxides; it has been reported that manganese stabilises wustite⁽¹¹⁴⁾.

5.3.3 Effect of Chromium on kinetics of Oxidation and Droplet Morphology

The oxidation behaviour of the four iron-chromium alloys was markedly different from the behaviour of pure iron and the iron-manganese alloys and the behaviour was different within the group itself. In general the level of oxygen increased with increasing chromium content up to the 0.8% Cr level. The initial rate of oxidation was also much higher again to the 0.8% Cr level when compared to iron. At the 1.46% Cr level there was a decrease in the initial rate, Fig.75.

The iron-chromium equilibrium diagram shows complete solubility in both the solid and liquid phases, Fig.174, and chromium forms an almost ideal solution in liquid iron. Chromium oxide, Cr_2O_3 , is thermodynamically more stable than wustite Fe_{1-x}O at all temperatures and at 1600°C there is a difference in standard free energy of approximately 160 kJ mol⁻¹ oxygen. However, when dissolved in iron, at the compositions in these experiments, the chromium oxide is only marginally more stable than wustite when oxidised in air. At 1600°C, for the 0.17% Cr, 0.25% Cr, 0.80% Cr and 1.46% Cr dissolved in iron the free energy differences are approximately 35, 45, 65 and 75 kJ.

The phase relations in the system iron-oxide-Cr₂O₃ in air are shown in Fig.175. The notable features of the diagram are the marked increase in liquidus and solidus temperatures with increasing Cr₂O₃ content, and the strong stabilising effect of Cr₂O₃ on the corundum type structure of hematite relative to the spinel type structure of magnetite.

Oxygen reduces both the surface tension and viscosity of iron. Chromium has little effect on surface tension and it is not altered by up to several per cent addition of Cr⁽¹¹²⁾. The viscosity of iron is lowered with additions of Cr up to ~1% Cr after which the viscosity starts to rise again⁽¹¹⁵⁾, Fig.176. It was noticed that the lowest Cr alloy, Fe 0.17% Cr, generated spherical droplets, the 0.25% Cr droplets generated prolate spheroids and the 0.8% Cr and 1.46% Cr droplets generated prolate spheroids with diameters greater than the 0.25% Cr samples in general. This change of shape could have a two-fold effect. First of all, the oblate shape would give an increased surface area available for oxidation. Secondly the drag forces on the droplet would be increased and this would increase the residence time in the oxidising atmosphere. Both factors would contribute to an increase in the oxygen content of the droplet.

EDX Analysis of traverses across polished droplets showed an increase at the surface in both the Fe-0.25% Cr and Fe-1.46% Cr samples examined. In the case of the 0.25% Cr (Table 118) samples examined, surface analyses came out at about 0.5% Cr, and in the case of the 1.46% Cr sample examined (Table 119) the surface analysis came out at about 2.1% Cr.

The SIMS analysis of the section of a 1.46% Cr sample (Figs.135, 136) from a surface to the edge of a hole in the droplet revealed some important details. The chromium levels increased, at the surface and at the edge of the hole. The actual surface values could not be determined accurately since the obtuse angle of the surface scattered the electrons and these were not picked up by the detector.

Immediately behind the surface the chromium and oxygen counts were increasing. However, the chromium and oxygen levels at the hole were also high indicating that the droplet had been oxidised internally. Oxidation could only occur at a surface of the droplet which, in turn, had been folded in towards the centre. This could only occur by the droplet changing shape during its fall. Desforges⁽⁶⁷⁾ noted a similar effect, although in Fe-3% Si droplets whilst falling through 80 cm air.

SIMS analysis of the oxide surface on Fe-1.46% Cr alloy (Table 125) showed an Fe:Cr ratio of 2.3:1 immediately at the air-oxide interface and 0.4:1 and 0.5:1 well into the oxide. The ratio of Fe:Cr from atomic masses is 1.08:1 suggesting the surface is 2 Fe atoms:1 Cr atom. The ratio of FeO to Cr₂O₃ gives a ratio of Fe/Cr of 0.53:1.

Chromium dissolves in the alloy phase and in the spinel oxide but does not dissolve appreciably in wustite. Alloying elements that do not dissolve in wustite but do alloy with iron and dissolve in spinel, e.g. Cr, lower the thermodynamic activity of iron in the alloy and in the spinel relative to wustite⁽¹¹³⁾. With sufficient chromium added, wustite can be avoided entirely, but lesser amounts of chromium reduce the stable range of concen-

tration of wustite and reduce its growth rate correspondingly.

Examination of the morphology of the Fe-Cr alloys showed an interesting sequence, these are shown schematically in Fig.177. Plate 28, which is the oxide on the Fe-0.17% Cr alloy revealed a duplex structure. The structure appeared as rounded smooth islands of oxide, evenly distributed, standing in a matrix of finer wavy oxide. Analysis revealed that the rounded areas were low in chromium, suggesting this was wustite, Fig.177(i).

This SEM micrograph revealed the first stages in the simultaneous growth of the two immiscible oxides FeO and Cr₂O₃. The chromium oxide is more stable than the wustite but the wustite grows faster.

The SEM micrograph of the Fe-0.25% Cr, Plate 31, showed the same duplex structure as in the previous alloy. The rounded wustite phase stood even more proud from the surface. Figure 177(ii).

There was a marked increase in oxygen level in this alloy compared to the 0.17% Cr alloy which in turn showed a marked increase in oxidation rate over pure iron. Pure iron oxide is 95% wustite and a large volume of these Fe-Cr alloy oxides was wustite. The second phase was Cr₂O₃ spinel and, because Cr has a higher valency than iron, there would be an increased oxygen level associated with the spinel. Further the cation vacancy level in wustite is of the order of 10%; it is possible that there may be some doping of the wustite by Cr³⁺ but SEM analysis suggested that the chromium level in the wustite was low. If this process occurred it would yield a higher oxygen level. However, it is difficult to relate the large increase in oxygen in

in these samples to the above mechanism. It is more probable that surface distortion and oscillation in flight brought about the increase in surface area to generate these oxygen levels.

The Fe-0.8% Cr micrographs revealed a variety of spheroid sizes of wustite in a matrix of Cr_2O_3 spinel. There are a number of possibilities for the formation of this structure. It is probable that with the higher chromium level in the alloy, the spinel would cover a larger surface area and the wustite growth would be localised, Figs.177(iii) and (iv).

It has been reported that fractures that extend through an oxide film, exposing fresh alloy directly to the air, are more frequent when spinel is the fastest growing phase than when wustite is the fastest growing phase⁽¹¹⁵⁾ After depletion of chromium from the metal adjacent to the spinel the surface composition may support wustite nucleation and growth. Such a sequence of events is shown in Figs.177(v) to (vii).

In the Fe-1.46% Cr alloy the structure was uniform, Plate 34, and the smooth rounded wustite phase was absent. From the SIMS analysis this suggested that the spinel covered the surface. Surface irregularities had been removed and the surface oxide had formed a closely knit network which reflected the surface underneath. With the absence of the faster growing wustite phase the surface was now covered with a uniform thin covering of spinel, FeO , Cr_2O_3 . Under these conditions the level of oxygen associated with the oxide film was reduced.

5.3.4 The Effect of Silicon on the Kinetics of Oxidation and Droplet Morphology

The oxidation behaviour of the three iron-silicon alloys investigated showed a very different pattern to the other systems considered. The behaviour of the Fe-0.3% Si alloy was similar to that of iron but with an enhanced oxidation rate. The higher silicon alloys, namely Fe-0.75% Si and Fe-1.33% Si showed a completely different behaviour; after an initial oxidation period the rate was reduced to zero and no further oxidation occurred.

The iron-silicon equilibrium diagram shows that alloys have complete liquid solubility at 1600°C, Fig.178, for the alloys investigated and silicon shows pronounced negative deviation from Raoult's law at this temperature. Silicon oxide SiO_2 is thermodynamically much more stable than wustite Fe_{1-x}O at all temperatures and at 1600°C there is a difference in standard free energy of about 260 kJ. However, when dissolved in iron, the free energy difference is much reduced. At 1600°C, for air, for the 0.30% Si, 0.75% Si and 1.33% Si dissolved in iron the free energy differences are 74, 91 and 100 kJ respectively.

The Fe-Si-O system is complicated especially when considering the silicon dissolved in the iron. At the iron rich surface the condensed phases during oxidation would appear to be wustite and silica, Fig.178. Both have negligible solubility in each other. At the air-rich surface there is a tendency for the higher oxides of iron to form as well as silica.

Silicon lowers the surface tension of iron at 1600°C⁽¹¹⁶⁾ and silica lowers the surface tension of wustite⁽¹¹²⁾. Compared with the other systems considered, silicon is tetravalent, and silica is the most stable oxide.

Silicon forms three dimensional random networks having five or six member rings. Within the silica structure cations should be tightly bound because the oxide bond strength is very high.

EDX Analysis of small chord sections for Fe-0.3% Si, Fe-0.75% Si and Fe-1.33% Si samples all showed an increase in silicon content of the surface compared to the interior. However, as the extent of contamination by quenching into silicone oil could not be determined no attempt has been made to evaluate this effect. SIMS analysis of the surface oxide on a Fe-1.33% Si sample oxidised by falling through 1 m of air at 1600°C is given in Table 126. Most of the results gave a Fe/Si ratio of 0.33. This was a mass ratio, and when adjusted for relative atomic masses, this gave an atomic ratio of about 6 silicon atoms to each iron atom in the oxide film. The corresponding oxygen profile was constant through the oxide apart from the surface contamination, Fig.154.

Examination of the morphology of the oxide surfaces on the Fe-Si alloys showed surface features quite different to the previous alloys systems examined. Plates 38 and 39 show the details typical of the Fe-0.3% Si droplets. The overall affect at low magnification was a smooth network of oxide over the surface. However, at high magnification, the oxide does stand out in relief over the sub-surface. It can clearly be seen that the oxide was not continuous. It will have been a continuous liquid phase when originally formed on the droplet. It is well known that the network formed by silica is broken down by the addition of a basic oxide. The basic oxide enters the network and separates the corners of two tetrahedra. It has been suggested⁽¹¹⁷⁾ that discrete SiO_4^{4-} units for liquids

more basic than the orthosilicate ($2 \text{FeO} \cdot \text{SiO}_2$) composition (i.e. when sufficient oxygen ions are available to satisfy all the charges on the Si^{4+} ions) are replaced by two dimensional chains and rings and so on up to the three dimensional network of pure silica.

Although the first alloy only contained 0.3% Si the oxidation rate was continuous and linear over the oxidation period investigated. It would seem that the silica network is broken and there would be oxidation of both silicon and iron. At the orthosilicate composition all silica tetrahedra links would be broken and this would give an oxygen:silicon ratio of 4:1. The value of this ratio would fall to 2:1 at the silica composition. It was concluded that at 0.3% Si in iron, the network formed would again be broken and as such would have the capacity to take up oxygen, hence a linear rate of oxidation in excess of that of pure iron would result, Fig.179. This is confirmed by the results, Figs.57 and 77.

The Fe-0.75% Si alloy, Plate 41, showed similar morphology to the Fe-0.3% Si alloy but this time the surface oxide was much finer. The broken structure had disappeared and discontinuities in the oxide film were less and very small, suggesting almost 100% coverage of the surface by oxide film. The morphology fitted in with the oxidation figures. After an initial oxidation period of the surface, the surface was covered by an impervious oxide film. Under these conditions the metal surface was isolated from the oxidising atmosphere. These droplets were intermediate between spherical and prolate spheroid.

The Fe-1.33% Si alloy droplets, Plates 44 and 45, were almost identical to the previous alloy composition with total coverage of

the droplet surface by a dense oxide 'matting'. Examination at higher magnification showed the dense nature of the oxide completely covering the droplet surface. The two lower silicon content alloys in flight formed prolate spheroids, whereas the Fe-1.33% Si alloy droplets remained spherical.

The oxidation behaviour of these iron-silicon alloys at 1600°C is in conflict with other authors. Emi and Pehlke⁽⁷³⁾, from their work, concluded that the formation and growth of an iron oxide layer on the surface of iron-silicon alloys were not significantly affected by the presence of silicon up to 3%. i.e. enrichment of silica in the iron oxides formed was not marked when silicon concentrations in the melt were limited. They noted that for higher silicon concentrations selective oxidation of silicon took place to form a silica enriched oxide layer on the melt surface. Oxygen pick-up, in their system, suddenly decreased for pure-oxygen-Fe-Si system at about 4% Si. Robertson and Jenkins⁽¹¹⁸⁾ observed a transition in reaction behaviour from burning to passive at about 3.6 pct. Si for pure oxygen- Fe-Si systems at 1660°C. Baker⁽⁷⁰⁾ dropped different sized droplets of Fe-Si-C alloys through oxygen. The silicon removal curve suggests initiation of selective oxidation above 3% Si. All the above experiments were carried out in pure oxygen atmosphere. The former^(73,118) used a stagnant pool of metal. Only Baker approached the conditions prevailing in this experiment. The different roles of pure oxygen and carbon in the droplet is difficult to assess. However, the results of 46 Fe-Si droplets in this work confirm that some degree of passivation occurs at about 0.75% Si in iron. The droplets used in this experiment

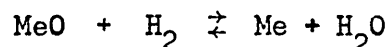
were much larger than those in Baker's experiments. Further, there was vigorous stirring within the droplet at the point when it fell from the wire. It is clear that the level of silicon in the oxide is very much greater than in the original metal. The stirring would certainly enhance the diffusion rate and under these circumstances would have maintained a constant renewing of silicon in the metal at the metal/oxide interface. Desforge⁽⁶⁷⁾ in his work noted that Fe-Si droplets burned brightly when falling through oxygen. With a Fe-9% Si alloy, he found it was not possible to oxidise alloy droplets under any conditions up to 100% oxygen. The droplets had uniform bright surfaces and there was a marked increase of silicon content in surface, with the silicon content of the shell varying from 35-45%. It should be noted that Desforges⁽⁶⁷⁾ quenched into water which would alter the surface oxidation conditions appreciably. However, the effect of silicon from the silicone oil cannot be satisfactorily accounted for in this work.

5.4 The Role of Alloying Elements On the Reducibility of Oxidised Iron Alloy Droplets

5.4.1 Thermodynamic Considerations

In the industrial process, the reducibility of oxides, formed in the powder production stage, by hydrogen during the sintering process is of paramount importance in relation to the properties of the final product.

The reducibility of an oxide is related to the H_2/H_2O ratio in equilibrium with the oxide and the metal:



By consideration of the hydrogen/water vapour ratios at a particular temperature the extent of reduction (or oxidation) of a specific metal oxide (or metal) can be determined. These ratios were determined from dewpoint measurements and the analysis is given in Appendix IV. The H_2/H_2O ratios were drawn on the free-energy temperature curve for the different alloy systems, Fig.180. The equilibrium gas composition versus temperature for the iron-hydrogen-oxygen system is reproduced in Fig.181. The reduction of magnetite and wustite at temperatures below $650^\circ C$ is shown to be thermodynamically possible.

5.4.2 Reduction of Oxidised Iron Droplets

The main objective was to determine the extent to which the oxides which had formed could be reduced and to determine the residual oxygen. In this work, reduction of a thin coherent oxide film on the surface of a droplet, generated whilst the droplet was molten, was the subject of examination. Hydrogen flow rate can have a profound effect on the rate of reduction of iron oxides⁽¹¹⁹⁾. Throughout all the tests the hydrogen flow rate was maintained at one litre per second. The rate of heating in hydrogen was maintained constant throughout these tests; the maximum temperature of $1150^\circ C$ (the industrial powder sintering temperature) was also maintained throughout the reduction investigations and the time at $1150^\circ C$ was one hour in most cases.

When oxidised droplets of iron were reduced, the oxygen level was reduced from about 0.08 mass% to give a final oxygen figure of about 0.04 mass% (for 0.7 g droplets), Figs. 84 and 85. The temperature for the onset of reduction was probably of the order

of 800°C, although one sample showed the possible onset as low as 680°C. Most of the reduction had occurred during the heating up period and very little reduction took place at 1150°C.

The SEM micrographs of the reduced iron droplets are shown, Plates 12 and 13. At low magnification it is possible to see the 'sif' type of topography even though the surface layers have been removed. A feature of these reduced surfaces was the formation of pits and the faceted nature of the reduced surface. Turkdogan and Vinters⁽¹¹⁹⁾ during the hydrogen reduction of hematite ore observed faceted surfaces on the reduced iron; they considered the reduced iron required a sufficient level of oxygen in solid solution to give rise to faceting since the feature disappeared on longer anneals (1 to 3 hours at 1200°C). Apart from the pits in evidence, it would appear that removal of the oxide film has been fairly uniform. If the oxide formed on the surface of the molten iron is compact, then the reducing hydrogen molecules cannot penetrate the oxide layer to any appreciable extent and consequently reaction can initially occur only at the oxide surface. However, as the reduction progresses and oxygen atoms are being removed from the oxide lattice, an interstitial microporosity is created through which the hydrogen can diffuse and reach the oxide molecules beneath the surface layer. However, it cannot advance any further, because its diffusion, across the coherent oxide layer, can occur only by movement of atoms or ions, both of which are relatively slow processes.

Since wustite constitutes the major iron oxide formed then reduction of wustite should give a uniform rate of removal of the oxide film. Reduction of Fe_3O_4 would proceed at a similar rate to

the wustite since both magnetite and wustite have fcc structures, the lattice change from Fe_3O_4 to FeO proceeds with no volume change and no distortion to the oxide film. However, reduction of Fe_2O_3 to Fe_3O_4 involves different structures and leads to a 25% increase in volume⁽¹²⁰⁾ which opens up the structure, albeit in his case on single crystals. Reduction of Fe_2O_3 to iron is faster than magnetite and wustite and this could give rise to the 'pits' in an otherwise uniform oxide field of wustite. A possible mechanism is schematically shown in Fig.182. The mechanism relies on an initial faster reduction of the Fe_2O_3 phase and the production of an iron phase locally within the pit. This in turn generates a local oxygen diffusion gradient. Reduction is rapid at the Fe/FeO-hydrogen interface leading to a deepening of the pit. The mechanism is hypothetical but it does offer an explanation of the number of small isolated pits found in the reduced oxide surface.

5.4.3 The Effect of Manganese on the Reduction of Oxidised Alloy Droplets

Six iron-manganese droplets were reduced in hydrogen. The oxygen levels in the six samples were reduced, in each case, by about 0.05 mass% (compared to 0.3-0.4 mass% for iron). Two samples Figs.87 and 90 were reduced to a final oxygen level of about 0.03 mass% and two were reduced to a final figure of about 0.05 mass% oxygen, Figs.86 and 91. The original oxygen levels in the droplets were increased by the addition of manganese to the iron, Figs.57 and 65. Onset of reduction in these alloys appeared to commence at about 800°C, approximately the same temperature for iron. However, the manganese alloys were characterised by a

faster reduction rate over the heating range 800°C to 1150°C.

The main feature of the Fe-0.5% Mn samples, Plates 16 and 17, are the large number of pits which are in evidence. The pits are relatively close together and in places have joined up to form a surface crack. It has already been noted that FeO and MnO are miscible in all proportions in the liquid state; further, MnO also forms a continuous solid solution with wustite. Hence the oxidation and reduction characteristics would be expected to be not too dissimilar to that of iron. SEM and SIMS analysis have indicated that there were concentration gradients of manganese within the metal and preferential consumption of manganese by the growing oxide. On reduction of the oxide there would be a manganese-rich layer at the surface. Manganese has a relatively high vapour pressure and under the conditions of low oxygen potential at 1150°C during the reduction process some removal of manganese via the vapour phase could occur. The pitting of the surface, as seen in the pure iron droplets, plus manganese removal could enhance the formation of pits in the surface.

The Fe-0.7% Mn alloy at low magnification, Plate 22, revealed a two-phase structure of smooth rounded areas set in a more uneven matrix, Plate 22. The phases were indicative of wustite and spinel-type structures. Both were in evidence in the as-oxidised samples. Removal of the oxide phase appeared to be more uniform in this alloy but higher magnification revealed the presence of small pits in the spinel-type structure. The detailed micrograph also revealed what appears to be the emergence of the metal phase (small, isolated white particles) from the oxide.

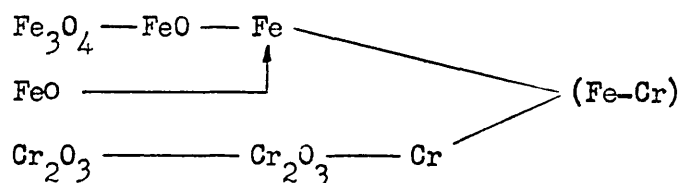
Fe-1.0% Mn alloy was characterised not only by a large number of pits in the oxide film but also by extensive cracking of the film which seems to follow grain boundaries, Plate 26. Increasing the manganese level in iron to 1% markedly reduces the solubility of oxygen in iron⁽¹²¹⁾. Rejection of oxygen by the metal will reinforce the oxide film but it also suggests a discontinuity at the oxide-metal interface. The manganese droplets retained an almost spherical shape throughout the experiments; oxidation would provide a thin oxide shell around a metal core. The oxide film, also fluid during its formation, would freeze along with the metal when quenched. If the oxide formed is assumed to be FeO or MnO the thickness of the oxide film can be readily calculated. For a one metre fall in air the oxide film thickness would be of the order of 3 microns. Such a thin film would form a coherent surface oxide on cooling. During heating, at the hydrogen reduction stage, the oxide film would be likely to crack due to the greater coefficient of expansion of the metal relative to the oxide (α metal/ α oxide = 1.25 for the Fe-FeO system⁽¹²²⁾).

5.4.4 The Effect of Chromium on the Reduction of Oxidised Alloy Droplets

The final oxygen figures for the reduced droplets over the complete alloy range gave a discernable trend, viz: the higher the initial oxidation the higher the final oxygen value. Generally the onset of reduction was in the range 800-850°C, somewhat higher than for the manganese alloys. The other point of note was that most of these alloys continued to be reduced at 1150°C whereas the pure iron and iron-manganese alloys had generally ceased to record

a weight loss after 1150°C. The highest chromium alloy, Fe-1.46% Cr, was not oxidised to the same extent as the lower chromium content alloys and the final reduced level was considerably lower.

Plate 29 revealed that the wustite areas of the Fe-0.17% Cr oxide had been reduced and much of the chromium oxide had been reduced as well. There were a few pockets, reduced in size, of the sesquioxide and the formation of pits in the surface was in evidence. In H_2/H_2O mixtures Cr_2O_3 can be reduced at 1400 K if $\log (P_{H_2}/P_{H_2O}) = 3.29^{(123)}$, i.e. up to 500 ppm water vapour in the hydrogen. Plate 29 suggests that reduction of wustite and the spinel phase were concurrent with the mechanism shown schematically in Fig.183. Plate 29 suggests that the spinel resides in pockets in the wustite. Examination of the plate revealed a large number of hollows in different stages of advancement. In some the spinel had disappeared and a rounded gentle hollow resulted. Others showed hollows of varying depth with spinel in residence; these tended to confirm a mechanism similar to that suggested in Fig.182. However, this evidence was in conflict with the work of Gurevich et al⁽¹²⁴⁾ who reduced a mixture of iron and chromium oxides in hydrogen at temperatures up to 1500 K. They concluded that at 1100°C the reduction of the oxide mixture was:



They did admit that simultaneous reduction of iron and chromium oxides could occur at higher temperatures (not specified).

Plate 32 showed the nature of the surface of the Fe-0.25% Cr alloy after oxidation followed by reduction in hydrogen. This specimen had been oxidised by falling through 50 cm air. The original oxide film would be relatively thin and the micrograph showed the surface in an 'advanced' reduced stage. The wustite/spinel type of oxide had been completely removed. A few pits left in the surface and a number of grain boundaries were in evidence and a large number of 'rosettes' could be seen. These are characteristic of iron formation from the reduced oxide⁽¹¹⁹⁾.

Plate 37 showed the structure of Fe-1.46% Cr after it had been oxidised in 100 cm fall through air at 1600°C followed by reduction in hydrogen. The oxide was still evident with holes or depressions formed in it. Gulbrausen and Jansson⁽¹²³⁾ concluded that $\text{Cr}_{(g)}$ may exert its vapour pressure when $\text{Cr}_{(s)}$ or an alloy containing Cr is covered by an oxide layer of $\text{Cr}_2\text{O}_{3(s)}$. Thermochemical data gives a value of $\log P_{\text{Cr}}$ to be ~ -7 at 1150°C.

Plate 36 showed the reduced structure of a droplet of Fe-1.46% Cr which had been originally oxidised by a 50 cm fall through air at 1600°C. The original oxide film would not be so thick and consequently the structure revealed was almost denuded of oxide. A massive crack was evident in the surface. The crack may have been generated in the heating or cooling in the hydrogen furnace when it was possible that stresses would be set up in the brittle oxide layer. Adherence of the oxide to the alloy beneath may have been affected by composition change or by change in interfacial morphology. Chromium also has a volume oxide to volume metal ratio of 2.03:1 and increasing amounts of chromium in the alloy could generate stresses within the oxide from volume increase.

5.4.5 The Effect of Silicon on the Reduction of Oxidised Alloy Droplets

Four iron-silicon alloy droplets were reduced in hydrogen. The 0.3% Si alloy was reduced to just below 0.04 mass% oxygen whereas the higher silicon alloys, which had formed a passive film, were reduced to very low oxygen levels. The onset of reduction in the silicon alloy range was between 900°C and 930°C, these temperatures being higher than the other alloy systems considered and in accordance with the thermochemical data presented for the stability of the alloys (Section 4.2.5).

The Fe-0.3% Si alloy reduced in hydrogen, is recorded in the SEM micrograph, Plate 40. The silica network was still evident and there was little change from the oxidised state in the morphology of the droplet. The appearance of a number of small pits was evident. The Fe-0.75% Si droplet which had been oxidised and reduced is shown in Plates 42 and 43. The fine network of oxide had disappeared and a large number of holes perforating the reduced oxide film were in evidence. The surface, when shown in detail, exhibited a mottled effect which looked like sub-surface blisters. The oxide film appeared to be very thin in places. When the Fe-1.33% Si alloy droplet, after oxidation, was reduced, the fine oxide network had disappeared to give a very irregular surface. Enlargement of this area as revealed in Plate 47, showed stratified nature of the surface after exposure to hydrogen at 1150°C. The surface had effectively been "thermally etched" with the removal of metal as well as the oxide film. Thermochemical data suggests that hydrogen having a water vapour concentration of ~100 ppm and a dewpoint of -40°C, then the $\text{SiO}_{(g)}$ pressure at

1150°C is of the order of 10^{-6} atm. Hence transfer of silicon and oxygen would result at this temperature under these conditions. Further it is difficult to reduce $\text{SiO}_2(\text{s})$ to $\text{Si}(\text{s})$ at 1150°C in hydrogen since the equilibrium gas mixture has a log $(P_{\text{H}_2}/P_{\text{H}_2\text{O}}) \approx 6$ i.e a dewpoint between -60 and -70°C. Such gas mixtures are very difficult to maintain in practice. Hence, reduction of the silica has occurred by vaporisation of $\text{SiO}(\text{g})$ which has reduced the oxygen level to very low figures and left the surface in a highly active state.

5.5 Practical Implications

The oxidation and reduction processes revealed for the binary systems provide an insight into the differing behaviour of the different components in the systems. The oxidation kinetics are very dependent on the alloying element present in the iron.

When manganese is added to iron, in additions up to 1 mass%, the oxygen pick-up is directly related to the amount of manganese in the iron and to the residence time of the droplet in air. This would have the consequence of promoting highly oxidised powders in atomisation directly related to the manganese content. When considering the iron-chromium system, additions of chromium at modest levels i.e. up to 0.8 mass%, results in a large increase in oxygen pick-up, hence resulting in severe oxidation of atomised powders in this range of composition. However, on further increasing the chromium to the 1.46 mass% level, there is a reduction in the amount of oxygen picked up in air. This change coincides with a change in the nature of the oxide on the surface. Consequently, high chromium alloy powders would not present the same difficulties as those with a lower chromium content. It is evident that small

amounts of silicon in iron increase the oxidation rate. Normally the levels of silicon in iron powders are low, silicon not being added as an alloying element but being present only from the original ore or being added as a deoxidation element in the refining process. This work has shown that increasing the silicon level to about 0.75 mass% results in a passive film being formed at the surface and further oxidation is stifled. Clearly there is scope for using high silicon alloy powders as a result of these findings, e.g. the fabrication of iron-silicon low hysteresis alloys by powder rolling route is a possibility.

It has been shown to be possible to reduce the oxygen level in the droplets to levels comparable with those in reduced iron droplets in the iron-manganese system. However it would appear that the final oxygen figure is related to the original oxygen figure, the higher the initial value the higher the final value. This may cause problems because of the volume changes occurring during the reduction of the compacts. As the reduction the oxide phases formed on the higher chromium alloys appears to be easier at 1150°C, when compared to lower chromium alloys, and lower oxygen values can be attained, use of higher chromium levels to promote hardenability in powder compacts could be beneficial from the point of view of surface oxide reduction provided the problem of inclusion content is not severe. With the appropriate dewpoint, reduction of oxides formed on iron-silicon alloys, with relatively high silicon contents, in hydrogen at 1150°C can be achieved leaving the surface in an active state. If levels of silicon of the order of 0.75 mass% can be tolerated in an alloy without other deleterious effects, its presence may be beneficial to the sintering stage.

The evidence presented suggests that all the binary iron alloys can be effectively reduced in hydrogen at 1150°C. It is important to note that the threshold temperatures for reduction vary for the differing alloying elements. Manganese and chromium oxides in iron have a threshold temperature about 800°C whereas silicon oxide in iron has a threshold temperature at about 900°C. This suggests that in the event of short term treatments, reduction of manganese and chromium oxides would be more attainable than reduction of silica. The temperature at which onset of reduction occurs is directly related to the free energy of formation of the oxide phase of the alloying element dissolved in iron. With a standard heating time in hydrogen the extent of removal of the oxygen is related to the initial oxygen level of the droplet.

The industrial process is clearly more complex since compaction of the powder particles will result in surface disruption and a reduction in the surface area presented to the reducing gas. Also the oxides formed in systems with more than one alloying element will be more complex. It is well known that considerable interaction can occur between elements in solution.

The findings of this work, for the binary iron systems, provide a useful basis of understanding. Consideration of ternary and more complex alloys by similar study is now possible based on the technique developed.

CHAPTER 6 CONCLUSIONS

A method has been devised to generate liquid metal droplets in a levitation coil from wire. The combination of levitation force and surface tension between the droplet and the wire gives good lateral stability and temperature control of the droplet.

Carbon based quenchants reduce the oxide film formed on molten oxidised iron droplets to low oxygen values. Water and liquid nitrogen quenchants increase the oxygen levels in iron droplets on quenching. Silicone oil has very little effect on the oxygen level of the iron droplets.

The oxidation of iron droplets falling through air approximates to a linear rate up to an oxidation time of 0.35 seconds. The oxygen concentration in a droplet rises more rapidly for smaller droplets and is directly related to the surface area to volume ratio.

A mathematical model has been developed which simulates the mass transfer by forced convection of oxygen from air to an accelerating iron droplet. The model generates oxidation rates similar to the experimentally derived values. The experimental values are greater than the theoretical by a factor of 1.6. The model takes no account of circulation within the droplet and its effect is equivalent to increasing the diffusivity in the droplet. The model allows for an initial fall under non-oxidising conditions during which the droplet is accelerating and Reynolds' number is increasing. The model indicates that increasing the temperature of the droplet only marginally increases the oxidation rate of the droplet.

Increasing manganese levels in iron up to 1.0 mass% increases the oxygen pick-up in free falling droplets. The rates of oxidation are similar to the rates of oxidation of iron droplets but there is a higher initial rate with the manganese alloys. The mechanism is related to the higher thermodynamic stability of manganese compared to iron.

Increasing chromium levels in iron up to 0.8 mass% increases the oxygen pick-up by free falling droplets. However, the addition of 1.46 mass% chromium reduces the oxidation rate to below that of the 0.17 mass% chromium alloy. These alloys are characterised by a rapid initial oxidation rate compared to iron. The higher oxidation rate is attributed to two processes; firstly, physical factors such as surface tension and viscosity which are altered by additions of oxygen and chromium so that the area presented to the oxidising atmosphere is increased, and secondly, chemical factors where the formation of oxygen-rich spinels are in competition with wustite.

Addition of 0.3 mass% silicon to iron enhances the oxidation rate of iron by 15%. However, additions of silicon in excess of 0.75 mass%, after a slight initial oxidation, reduce the oxidation rate to zero. The oxidation of the iron-silicon alloys cease when a network of silica covers the droplet surface.

The morphology of the oxidised droplet surface is related to the alloying element. Manganese has little effect on the surface characteristics of the oxide film. Chromium has a marked effect; competing oxides at low chromium levels have an influence on the oxygen level in the alloy, at higher chromium levels a single spinel covers the surface restricting oxygen pick-up. Silicon

forms an oxide network over the surface and the extent of the network determines the level of oxidation of the alloy.

Reduction of iron, iron-manganese (up to 1 mass% Mn), iron-chromium (up to 1.46 mass% Cr) and iron-silicon (up to 1.33 mass% Si) alloys occurs to differing extents after exposure to hydrogen at 1150°C for one hour. The onset of reduction is considerably higher, in excess of 900°C, for iron-silicon alloys, than for the other alloys which mainly occurs between 800 and 850°C. In most cases, the final oxygen level, in the reduced droplets, was related to the initial oxygen level.

CHAPTER 7 SUGGESTIONS FOR FURTHER WORK

The work carried out in this project could be profitably extended in three ways:

1. Extension of the iron-manganese alloy range to 2 or 3 mass% to completely determine the oxidation characteristics of the system.

Examination of the iron-chromium alloys intermediate between 0.8 mass% and 1.46 mass% Cr to determine the inflexion point in the oxygen pick-up, and the precise nature of the oxide film on the surface, plus extension of the range to 2 or 3 mass% Cr.

Examination of iron-silicon alloys intermediate between 0.3 mass% and 0.75 mass% Si to determine the inflexion point in the oxygen pick-up. A survey of silicon levels below 0.3 mass% which are normally found in steel powders would be useful.

2. To investigate industrially significant iron-ternary systems to determine the oxidation behaviour of the different combinations, and then the reduction behaviour of the oxide films so formed.
3. The work in (2) to be followed by an examination of the oxidation potential of different environments, notably steam/air mixtures and water to give a complete

picture of the role of these elements in the atomisation process of iron and iron alloy powders.

REFERENCES

1. P U Gummeson. Powder Metallurgy, 1972, 15, (29), p67.
2. W J Huppmann and M Hirschvogel. Int. Met. Rev., 1978, 5, p209.
3. G H Gessinger and M J Bamford. Int. Met. Rev., 1974, 19, p51.
4. J M Wentzell. J. Vac. Sci. Technol., Nov/Dec. 1974, 11, (6), p1035
5. P Rao and J A Tallmadge. Proc. Fall Powder Met. Conf., Oct.1971, p252.
6. O S Nichiporenko, Y I Naida and A B Medvedovskii. Poroshkovaya Metallurgiya, Dec.1972, No.12, (120), p64-68.
7. N J Grant. Rapid Solidification Technology, 1985, p243.
8. J B See, J C Runkle and T B King. Metall. Trans., Nov. 1973, 4, p2669.
9. A K Petrov et al. Sov. Powder Metall., Met. Ceram., Jan.1973, 12, (1), p13.
10. Yu I Naida and O S Nichiporenko. Poroshkovaya Met., 1968, No.4 (6).
11. J J Dunkley and A C Chilton. The Metallurgist and Mat. Tech., Vol.6, No.11, 1974, p480.
12. P A Joly and R Mehrabian. J. Met. Sci., 1974, 9, p1446.
13. S Small and T J Bruce. Int. Journal Powder Met., 1968, 4, (3), p7.
14. G I Friedman and G S Ansall. Powder Met. for Superalloys, 1972, p427.

15. A R E Singer. Powder Metallurgy, 1976, No.1, p4.
16. G T Brown. Metallurgia and Metal Forming, March 1976, p73.
17. R R Holmes. Int. Journal Powder Met., 1975, 11, p161.
18. W J Huppman. Powder Metall., 1977, 20, 36.
19. H F Fischmeister, L Olsson and K E Easterling. Powder Metall. Int., 1974, 6, p30.
20. P J Guichelaar and R D Pehlke. 1971 Fall Powder Met. Conf. (ed. S Mocarski), 109, 1972, New York, Metal Pwdr Ind. Fed.
21. J P Cook. Oxidation, reduction and decarburisation of metal powder preforms, 1972, Riverton N J Hoeganaes Corporation.
22. P B Crimes. PhD Thesis, U. of London, 1968.
23. S M Aeron. PhD Thesis, U. of London, 1971.
24. G E Lapple. Chem. Eng. Handbook, J H Perry ed, 1963, p1018.
25. M W Davies and J Alexander. Kinetics of Metallurgical Processes in Steelmaking Int. Conf., Octo.1970, Aachen, p246.
26. H Schlichting. Houndary Layer Theory, Pergamon, N.Y., 1955.
27. F H Garner. Trans. Inst. Chem. Eng., 28, 1950, p88.
28. F D Richardson. Met. Trans., 1971, 2, p2747.
29. K Schwerdtfeger. Kinetics of Metallurgical Processes in Steelmaking Int. Conf., Oct.1970, Aachen, p192.
30. E S Pettyjohn and E B Christiansen. Chem. Eng. Prog., 44, 1948, p157.
31. F H Garner and J J Lane. Trans. Inst. Chem. Eng., 37, 1959, p162.

32. J S Hadamard. Seances. Acad. Sci., 152, 1911, pl735.
33. W Rybczynski. Bull. Acad. Sci., Cracovic, Series A, 1911, p40.
34. V G Levich. Physicochemical Hydrodynamics, New York, 1962.
35. B T Chao. Phys. Fluids, 5, 1962, p69.
36. S Winnikow and B T Chao. Phys. Fluids, 9, 1966, p50.
37. A E Hamielec and S W Woo. Kinetics of Metallurgical Processes in Steelmaking, Int. Conf., Oct.1970, Aachen, p235.
38. I Langmuir. Phys. Rev., 1913, 12, p368.
39. H J Merk and J A Prinz. App. Sci. Res., 1954, A4, 11, p195.
40. J R Kyte, A J Madden and E L Piret. Chem. Eng. Prog., 1953, 49, p653.
41. W G Mathers, A J Madden and E L Piret. Ind. Eng. Chem., 1957, 49, p961.
42. R L Steinberger and R E Treybal. A.I.Ch.E.J., 1960, 6, p226.
43. R R White and S W Churchill. A.I.Ch.E.J., 1959, 5, p354.
44. G E Kinerd, F S Manning and P W Manning. Brit. Chem. Eng., May 1963, i, No.5, p326.
45. P N Rowe, K T Claxton and J B Lewis. Trans. Int. Chem. Eng., 1965, 43, pT14.
46. D M Ward, O Trass and A I Johnson. Canad. J. Chem. Eng., 40, 1962, pl64.
47. Book and Kramers. Ch. Eng. Sc., 1962, 17, p90.

48. F D Richardson. Kinetics of Metallurgical Processes in Steelmaking Int. Conf., Oct.1970, Aachen, p279.
49. L A Baker, N A Warner and A E Jenkins. Trans. A.I.M.E., 239, 1967, p857.
50. T Furuta et al. J. Chem. Eng. Jap., 8, No.6, 1975, p456.
51. C G Levi and R Mahrabian. Trans A.I.M.E., 11B, 1980, p21.
52. M J Bouasinesq. J. Maths., Ser.6, 1, 1905, p285.
53. R Higbie. Trans. Am. Inst. Chem. Engrs, 31, 1935, p365.
54. T Vermulen. Ind. Engg. Chem., 45, 1958, p1664.
55. A E Handles and T Baron. A.I.Ch.E.J., 3, 1957, p127.
56. R Kronig and J C Brink. Appl. Scient. Res., A2, 1950, p142.
57. F D Richardson. Jerhkort Ann., 153, 1969, p359.
58. P Kozakevitch. Surface Phenomena of Metals. Soc. Chem. Ind. monograph, 28, 1968, p223.
59. F D Richardson. Physical Chemistry of Melts in Metallurgy, Vol.2, 1974, p430.
60. J H Swisher and E T Turkdogan. Trans. Metall. Soc., A.I.M.E. 239, 1967, p602.
61. C G Glen and F D Richardson. Heterogeneous kinetics at elevated temperatures, ed. G R Belton and W L Worrell, Plenum, 1970, p369.
62. T Emi, W M Boorstein and R DPehlke. Metallurgical Trans., Vol.5, 1974, p1959.
63. R H Radzilowski and R D Pehlke. Met. Trans. B., Vol.9B, 1978, p129.

64. L A Baker, N A Warner and A E Jenkins. Trans. A.I.M.E., Vol.239, June 1967, p857.
65. L A Baker and R G Ward. J.I.S.I., July 1967, p714.
66. P A Distin, G D Hallet and F D Richardson, J.I.S.I., Aug.1968, p821.
67. C D Desforges. PhD Thesis, Cambridge, Dec.1964.
68. S K Vig and W K Lu. J.I.S.I., Aug.1971, p630.
69. K Schwerdtfeger and W Wepner. Met. Trans. B., Vol.8B, June 1977, p287.
70. R Baker. J.I.S.I., June 1967, p637.
71. R D Pehlke and R H Radzilowski. Physical Chem. of Steelmaking, Versailles, Oct.1978, p119.
72. S Banya and J D Shim. J.I.S.I., Japan, Oct.1980., Vol.66, p1631.
73. T Emi and R D Pehlke. Mat. Trans. Vol.6B, Mar.1975, p95.
74. S I Fillippov and A A Zharov. Steel in the USSR., 1976, (2), p27.
75. T Choh and M Inouye. Trans. I.S.I.J., Vol.20, 1980, p768.
76. H Hosoda, N Sans and Y Matsushita. Trans. I.S.I.J., Vol.16, 1976, p115.
77. T Choh, Y Naganawa and M Inouye. Trans. I.S.I.J., Vol.20, 1980, p776.
78. M Kawakami and K S Goto. Trans. I.S.I.J., Vol.16, 1976, p204.
79. D Y Povolotskiy, O K Tokovoy and A P Fedulov. Russ. Metall. 1981, (6), p52.

80. G S Ershov and A A Kasatkin. Steel in USSR, June 1978, p328.
81. V Bulanov, A K Muskin et al. Poroshkovaya Metall. No.3, (147), Mar.1975, p15.
82. A S Griatsov et al. Poroshkovaya Metall. No.10 (166) Oct.1976, pl.
83. A A El Gassy et al. Iron & Steel Int., Oct. 1977, p329.
84. D I Ryzhoukov. Scand. J. Met., (11) 1982, p135.
85. W F Chu and A Rahmel. Met. Trans., Vol.10B, Sept.1979, p401.
86. P Lindskog and S E Grek. Proc. Int. Powder Met. Conf., 1973, Vol.7, p285.
87. J Foryst and W Przylo. Mikrochimica Acta. Wien, Suppl. 10, 1983, p337.
88. D H Polonis et al. Research, 1954, Vol.7, p273.
89. G Comenetz and J W Salatka. J. Electrochem. Soc., 1958, Vol.105, p673.
90. W A Peifer. J. of Metals, May 1965, p487.
91. W J Slater et al. Science & Industry, Vol.7, No.3, 1960, p89.
92. W J Hulsey. A E C Report, Y-1413, 1963, Oak Ridge.
93. E C Okress et al. J. App. Phys., 1952, Vol.23, 1413, p545.
94. P R Rony. U.C.R.L. Report 11411, 1964, Berkeley, Calif.
95. B Harris and A E Jenkins. J. Sci. Inst., Vol.36, May 1959, p238.
96. S Jahanshahi and J H E Jeffes. Trans. I.M.M., 90(C), Dec.1981, p138.

97. R Jackson. MSc Project, S.C.P., 1977.
98. L M Holmes. J. App. Phys., 49(6), June 1978, p3102.
99. A G Emslie and H H Blau. J. Elec. Soc., 106, 1959, p877.
100. A E Jenkins, et al. Met. Soc. AIME Conf., Vol.122, 1964, p23.
101. S Y Shiraishi and R G Ward. Can. Met. Quart., 1964, Vol.3, p118.
102. R Baker. J.I.S.I., 1967, 205, p714.
103. G H Davison. Standard Methods of Analysis, United Steels Co., Ltd., 5th Ed., 1961.
104. T S Harrison. Handbook of Analytical Control of Iron and Steel Production.
105. C J Smithells. Metals Reference Book, 4th Ed., 1967, Butterworths, p666
106. J Crank. The Mathematics of Diffusion, 1970, Oxford, p72.
107. P H Calderbank and I J O Korchinski. Chem. Eng. Sci., 1956, 6, p65.
108. P Kozakevitch and G Urbain. Memoires Scientifiques, Rev. Met., LVIII, No.7, 1961, p517.
109. V S Tsepelev et al. Izv. V.U.Z., Chernaya Metall., 1984, (1), 1-4.
110. C Bodsworth and H B Bell. Physical Chemistry of Iron and Steel Manufacture, Longman, 1972.
111. A Muan and E F Osborn. Phase Equilibria among Oxides in Steelmaking, Pergamon, 1965.
112. P Kozakevitch and G Urbain. Mem. Sci. Rev. Metall. LVIII, No.7, 1961, p517.

113. F C M Driessens. Ber Bunsenges, Phys. Chem., 72, 1968, p754.
114. V S Tsepelev. Izv. V.U.Z. Chernaya Metall., 1984, (1), 1-4.
115. C E Birchenall. Oxidation of Metals and Alloys, A.S.M., 1971.
116. Y Kawai. Proc. ICSTIS Suppl. Trans. I.S.I.J., Vol.11, 1971, 387.
117. J O'M Bokris and D C Lowe. Proc-Roy. Soc., Ser A, 1954, 226, 423.
118. D G C Robertson and A F Jenkins. Proc. Int. Conf. Heterogeneous Kinetics at Elevated Temps., Philadelphia, 1970, p393.
119. E T Turkdogen and J V Vintners. Met. Trans., Vol.2, Nov.1971, 3175.
120. J O Edstrom. J.I.S.I., 1953, Vol.175, p289.
121. A M Averbukh and L A Smirnov. Steel in USSR, Mar.1981, p123.
122. D L Douglas. Proc. Int. Conf., Heterogeneous Kinetics at Elevated Temps., Philadelphia, 1970, p153.
123. E A Gulbranssen and S A Jansson. Proc. Int. Conf. Heterogeneous Kinetics at Elevated Temps., Philadelphia, 1970, p63.
124. Y G Gurevich et al. Poroshkovaya Metall., 1, 145, Jan.1975, p16.
125. A Hellawell. Inst. Met. Ann. Equ. Diag., No.26.
126. M Hansen and K Anderko. Binary Alloys, McGraw Hill, 1958.
127. A Muan and S Somiya. Am. J. Sci., 1962, V260, p230.

128. A Muan and S Somiya. J. Am. Ceram. Soc., 43, 4, 1960, 207.
129. W Koster and T Godecke. Z. Metallk., 1968, 59, 602.

TABLE 1 Effect of Cooling Medium on Oxidation of
Khl8N15 Steel Powder Particles (9)

Cooling medium	Heat No. 1		Heat No. 2	
	O ₂ %	mean oxide	O ₂ %	mean oxide
		film		film
		thickness		thickness
		μm		μm
Solution of corrosion inhibitor No.1	0.79	3.00	0.24	1.07
Solution of corrosion inhibitor No.2	0.78	3.24	0.21	1.01
Distilled water	0.78	2.71	0.20	1.00
Ordinary water	0.77	3.00	0.21	1.07

TABLE 2 Composition of Japanese Electrolytic Iron

Element	Mass%
Carbon	0.005
Phosphorus	0.004
Sulphur	0.005
Silicon	0.005
Manganese	0.005
Copper	0.004
Nickel	<0.005
Molybdenum	<0.002
Chromium	0.002-0.004
Iron	balance

**TABLE 3 Calibration for Land Total Radiation Pyrometer
Emissivity of radiating surface = 1**

Temperature °C	Output of pyrometer mV
1100	0.245
1150	0.364
1200	0.528
1250	0.748
1300	1.039
1350	1.416
1400	1.897
1450	2.503
1500	3.254
1550	4.178
1600	5.296
1650	6.639
1700	8.235
1750	10.120

**TABLE 4 Pyrometer Output with Temperature for
Iron Temperature Probe**

Thermocouple Output mV	Temperature °C	Pyrometer Output mV	Emissivity Value
13.92	1250	0.38	0.508
15.12	1335	0.47	0.360
15.61	1370	0.68	0.422
16.10	1405	0.75	0.383
16.60	1440	0.87	0.365
17.94	1535	1.41	0.361

TABLE 5 Pyrometer Output with Temperature for Different Emissivity Conditions

Pyrometer Output		Temperature C
Clean Glass Levitation Column	Glass Inserted between Pyrometer and Coil	
2.40	1.86	1655
1.41	1.10	1535
0.90	0.70	1450
1.90	1.06	1595
1.40	0.80	1535
0.95	0.50	1460
1.40	0.58	1535
2.38	0.98	1650

TABLE 6 Physical Properties of Hydrogen and Argon Gases

	Specific heat capacity J kg ⁻¹ K ⁻¹	Thermal conductivity W m ⁻¹ K ⁻¹
Hydrogen	14 300	1 684
Argon	524	162

TABLE 7 Analysis for oxygen - blank samples

Samples heated to 1100-1200°C for 5 minutes in hydrogen followed by heating in the molten state at 1600°C for 5 minutes in hydrogen

Material	Oxygen analysis mass%
Fe	0.0060
	0.0040
	0.0020
	0.0056
Fe-1.5% Cr	0.0050
	0.0050

TABLE 8 Effect of Quenchant on Oxygen Content

Height of fall in air: 50 cm
 Quenchant: Silicone oil

Droplet mass g	Oxygen content %
0.811	0.038
0.783	0.032
0.974	0.039
0.753	0.074
0.867	0.040
0.787	0.050
0.938	0.036
0.937	0.026
0.738	0.032
0.831	0.059
0.782	0.040
1.254	0.064
0.956	0.050
0.967	0.046
0.831	0.056
1.457	0.066
0.922	0.065
0.846	0.030
0.871	0.038
0.811	0.033

TABLE 9 Effect of Quenchant on Oxygen Content

Height of fall in air: 50 cm
 Quenchant: Invoil 30

Droplet mass g	Oxygen content %
1.164	0.044
1.300	0.052
1.156	0.020
1.109	0.011
1.060	0.015
1.177	0.0093
1.209	0.0080
1.079	0.0080
1.024	0.0080
1.062	0.0148
1.027	0.0073
1.069	0.0076
0.948	0.0153
0.939	0.0083
1.072	0.0076
0.981	0.0110
1.156	0.0090
0.908	0.0130
1.051	0.0093
1.204	0.023

TABLE 10 Effect of Quenchant on Oxygen Content

Height of fall in air: 50 cm
 Quenchant: Paraffin oil (cold)

Droplet mass g	Oxygen content %
0.959	0.029
1.121	0.024
0.654	0.025
1.021	0.020
1.438	0.017
1.315	0.037
0.944	0.0181
1.025	0.0167
1.005	0.0150
0.816	0.0134
1.079	0.011
1.120	0.011
1.096	0.014
0.889	0.017
0.762	0.021
1.068	0.019
0.762	0.016
0.816	0.014
0.805	0.014
1.031	0.011

TABLE 11 Effect of Quenchant on Oxygen Content

Height of fall in air: 50 cm
 Quenchant: Paraffin oil (at 110°C)

Droplet mass g	Oxygen content %
0.729	0.014
0.931	0.013
1.005	0.010
1.074	0.010
0.926	0.008
0.790	0.016
0.933	0.014
0.749	0.020
1.057	0.018
0.813	0.010

TABLE 12 Effect of Quenchant on Oxygen Content

Height of fall in air: 50 cm
 Quenchant: De-aerated distilled water

Droplet mass g	Oxygen content %
0.907	0.264
0.876	0.431
0.709	0.396
0.777	0.277
1.045	0.217
0.758	0.324
0.708	0.220
0.681	0.200
0.799	0.167
0.786	0.377
1.126	0.431
0.903	0.340
1.097	0.367
0.777	0.396
1.010	0.363
0.944	0.373
0.984	0.394
1.041	0.299
1.036	0.300
1.091	0.228

TABLE 13 Effect of Quenchant on Oxygen Content

Height of fall in air: 50 cm
 Quenchant: Liquid nitrogen

Droplet mass g	Oxygen content %
0.780	0.149
0.682	0.135
0.949	0.175*
0.943	0.103
0.752	0.096*
0.854	0.098
1.075	0.146*
1.073	0.098
0.913	0.094*
1.007	0.079
0.783	0.075
1.083	0.093*
0.998	0.088
0.773	0.107
1.027	0.096*
0.834	0.075
1.081	0.071
0.674	0.097
0.542	0.120
1.018	0.094
0.959	0.093
1.001	0.089

* Droplet broken up into a number of smaller droplets

TABLE 14 Determination of the extent of reduction
of oxidised iron droplets by the quench medium

Sample 1

Absorber	Dimethylformamide
Titrant	Tetrabutylammonium hydroxide
Quench medium	Invoil 30
Mass of sample	0.8969 g
Oxygen content	0.0039 mass %

Time	Burette Reading	Volume Titrant	Volume ΔV
min.	ml	ml	ml
0	0	0	0
5	2.15	2.15	2.15
10	2.50	2.50	0.35
15	2.80	2.80	0.30
20	3.05	3.05	0.25
25	3.20	3.20	0.15
30	3.40	3.40	0.20

(Figure 36)

TABLE 15 Determination of the extent of reduction
of oxidised iron droplets by the quench medium

Sample 2

Absorber	Dimethylformamide
Titrant	Tetrabutylammonium hydroxide
Quench medium	Invoil 30
Mass of sample	0.9182 g
Oxygen content	0.0046 mass %

Time	Burette Reading	Volume Titrant	Volume ΔV
min.	ml	ml	ml
0	0.42	0	0
5	2.10	1.68	1.68
10	2.42	2.00	0.32
15	2.62	2.20	0.20
20	2.74	2.32	0.12
25	2.91	2.49	0.17
30	3.04	2.62	0.13

(Figure 37)

TABLE 16 Determination of the extent of reduction of oxidised iron droplets by the quench medium

Sample 3

Absorber	Dimethylformamide
Titrant	Tetrabutylammonium hydroxide
Quench medium	Invoil 30
Mass of sample	0.9155 g
Oxygen content	0.0032 mass %

Time	Burette Reading	Volume of Titrant	ΔV
min.	ml	ml	ml
0	2.72	0	0
5	4.72	2.00	2.00
10	5.02	2.30	0.30
15	5.25	2.53	0.23
20	5.42	2.70	0.17
25	5.62	2.90	0.20
30	5.85	3.13	0.23

(Figure 38)

TABLE 17 Determination of the extent of reduction of oxidised iron droplets by the quench medium

Sample 4

Absorber	Dimethylformamide
Titrant	Tetrabutylammonium hydroxide
Quench medium	Invoil 30
Mass of sample	1.1972 g
Oxygen content	0.0053 mass %

Time	Burette Reading	Volume of Titrant	ΔV
min.	ml	ml	ml
0	1.18	0	0
5	4.28	3.10	3.10
10	4.72	3.54	0.44
15	4.95	3.77	0.23
20	5.12	3.94	0.17
25	5.30	4.12	0.18
30	5.42	4.24	0.12
55	6.16	4.98	0.74

(Figure 39)

TABLE 18 Determination of the extent of reduction
of oxidised iron droplets by the quench medium

Sample 5

Absorber	Dimethylformamide
Titrant	Tetrabutylammonium hydroxide
Quench medium	Invoil 30
Mass of sample	0.9783 g
Oxygen content	0.0043 mass %

Time min.	Burette Reading ml	Volume Titrant ml	ΔV ml
0	4.30	0	0
5	6.81	2.51	2.51
10	7.26	2.96	0.45
15	7.60	3.30	0.34
20	7.94	3.64	0.34
25	8.12	3.82	0.18
30	8.36	4.06	0.24
50	9.36	5.06	1.00
60	10.10	5.80	0.74

(Figure 40)

TABLE 19 Determination of the extent of reduction
of oxidised iron droplets by the quench medium

Sample 6

Absorber	Dimethylformamide
Titrant	Tetrabutylammonium hydroxide
Quench medium	Paraffin oil
Mass of sample	1.0555 g
Oxygen content	0.0124 mass %

Time min.	Burette Reading ml	Volume Titrant ml	ΔV ml
0	2.40	0	0
5	4.58	2.18	2.18
10	5.10	2.70	0.52
15	5.40	3.00	0.30
20	5.60	3.20	0.20
25	5.82	3.42	0.22
30	6.04	3.64	0.22
55	7.16	4.76	1.12

(Figure 41)

TABLE 20 Determination of the extent of reduction
of oxidised iron droplets by the quench medium

Sample 7

Absorber	Dimethylformamide
Titrant	Tetrabutylammonium hydroxide
Quench medium	Paraffin oil
Mass of sample	1.1518 g
Oxygen content	0.0046 mass %

Time min.	Burette Reading ml	Volume Titrant ml	ΔV ml
0	3.94	0	0
5	6.66	2.72	2.72
10	7.15	3.21	0.49
15	7.41	3.47	0.26
20	7.64	3.70	0.23
25	7.92	3.98	0.28
30	8.11	4.17	0.19
40	8.73	4.79	0.62

(Figure 42)

TABLE 21 Determination of the extent of reduction
of oxidised iron droplets by the quench medium

Sample 8

Absorber	Dimethylformamide
Titrant	Tetrabutylammonium hydroxide
Quench medium	Paraffin oil
Mass of sample	0.9851 g
Oxygen content	0.0064 mass %

Time min.	Burette Reading ml	Volume Titrant ml	ΔV ml
0	2.03	0	0
5	4.26	2.23	2.23
10	4.81	2.78	0.55
15	5.05	3.02	0.24
20	5.40	3.37	0.35
25	5.70	3.67	0.30
30	5.95	3.92	0.25
50	7.15	5.12	1.20

(Figure 43)

TABLE 22 Determination of the extent of reduction of oxidised iron droplets by the quench medium

Sample 9

Absorber	Dimethylformamide
Titrant	Tetrabutylammonium hydroxide
Quench medium	Paraffin oil
Mass of sample	0.8794 g
Oxygen content	0.0051 mass %

Time	Burette Reading	Volume of Titrant	ΔV
min.	ml	ml	ml
0	3.47	0	0
5	5.66	2.19	2.19
10	6.26	2.79	0.60
15	6.50	3.03	0.24
20	6.90	3.43	0.40
25	7.16	3.69	0.26
30	7.52	4.05	0.36
45	8.34	4.87	0.82
90	10.87	7.40	2.53

(Figure 44)

TABLE 23 Determination of the extent of reduction of oxidised iron droplets by the quench medium

Sample 10

Absorber	Dimethylformamide
Titrant	Tetrabutylammonium hydroxide
Quench medium	Paraffin oil
Mass of sample	1.1167 g
Oxygen content	0.0115 mass %

Time	Burette Reading	Volume of Titrant	ΔV
min.	ml	ml	ml
0	4.66	0	0
5	6.80	2.14	2.14
10	7.52	2.86	0.72
15	7.95	3.29	0.43
20	8.30	3.64	0.35
25	8.70	4.04	0.40
30	9.18	4.52	0.48
65	11.80	7.14	2.62

(Figure 45)

TABLE 24 Determination of the extent of reduction
of oxidised iron droplets by the quench medium

Sample 11

Absorber	Dimethylformamide
Titrant	Tetrabutylammonium hydroxide
Quench medium	Silicone oil
Mass of sample	1.1034 g
Oxygen content	0.0375 mass %

Time min.	Burette Reading ml	Volume Titrant ml	ΔV ml
0	3.56	0	0
5	4.40	0.84	0.84
10	4.90	1.34	0.50
15	5.06	1.50	0.16
20	5.26	1.70	0.20
25	5.44	1.88	0.18
30	5.61	2.05	0.17

(Figure 46)

TABLE 25 Determination of the extent of reduction
of oxidised iron droplets by the quench medium

Sample 10

Absorber	Dimethylformamide
Titrant	Tetrabutylammonium hydroxide
Quench medium	Silicone oil
Mass of sample	1.1285 g
Oxygen content	0.0455 mass %

Time min.	Burette Reading ml	Volume Titrant ml	ΔV ml
0	3.45	0	0
5	4.24	0.79	0.79
10	4.85	1.40	0.61
15	5.20	1.75	0.35
20	5.60	2.15	0.40
25	5.95	2.50	0.35
30	6.32	2.87	0.37

(Figure 47)

TABLE 26 Determination of the extent of reduction
of oxidised iron droplets by the quench medium

Sample 13

Absorber	Dimethylformamide
Titrant	Tetrabutylammonium hydroxide
Quench medium	Silicone oil
Mass of sample	1.1515 g
Oxygen content	0.0336 mass %

Time min.	Burette Reading ml	Volume Titrant ml	ΔV ml
0	1.64	0	0
5	2.58	0.94	0.94
10	2.86	1.22	0.28
15	3.09	1.45	0.14
20	3.32	1.68	0.12
25	3.54	1.90	0.22
30	3.73	2.09	0.19

(Figure 48)

TABLE 27 Determination of the extent of reduction
of oxidised iron droplets by the quench medium

Sample 14

Absorber	Dimethylformamide
Titrant	Tetrabutylammonium hydroxide
Quench medium	Silicone oil
Mass of sample	0.8607 g
Oxygen content	0.0531 mass %

Time min.	Burette Reading ml	Volume Titrant ml	ΔV ml
0	2.14	0	0
5	2.94	0.80	0.80
10	3.32	1.18	0.38
15	3.48	1.34	0.16
20	3.75	1.61	0.27
25	4.06	1.92	0.31
30	4.34	2.20	0.28

(Figure 49)

TABLE 28 Determination of the extent of reduction
of oxidised iron droplets by the quench medium

Sample 15

Absorber	Dimethylformamide
Titrant	Tetrabutylammonium hydroxide
Quench medium	Silicone oil
Mass of sample	1.1480 g
Oxygen content	0.0330 mass %

Burette		Volume	
Time	Reading	Titrant	ΔV
min.	ml	ml	ml
0	2.06	0	0
5	2.50	0.44	0.44
10	2.70	0.64	0.20
15	2.91	0.85	0.21
20	3.10	1.04	0.19
25	3.32	1.26	0.22
30	3.49	1.43	0.17

(Figure 50)

TABLE 29

Figure Number	Sample Number	Quench Medium	Volume of titrant to neutralise the CO ₂ generated ml	Mass of oxygen reduced g	Mass of droplet g	Mass of oxygen reduced from droplet mass%	Measured oxygen level of droplet mass%	Corrected content of droplet mass%
35	1	Invoil 30	2.00	6.4 x 10 ⁻⁴	0.8969	0.0714	0.0039	0.0753
36	2	Invoil 30	1.66	5.31 x 10 ⁻⁴	0.9182	0.0579	0.0046	0.0625
37	3	Invoil 30	1.90	6.08 x 10 ⁻⁴	0.9155	0.0664	0.0032	0.0696
38	4	Invoil 30	3.30	10.56 x 10 ⁻⁴	1.1972	0.0882	0.0053	0.0935
39	5	Invoil 30	2.40	7.68 x 10 ⁻⁴	0.9783	0.0785	0.0043	0.0828
40	6	Paraffin Oil	2.25	7.20 x 10 ⁻⁴	1.0555	0.0682	0.0124	0.0806
41	7	Paraffin Oil	2.60	8.32 x 10 ⁻⁴	1.1518	0.0722	0.0046	0.0768
42	8	Paraffin Oil	2.15	6.88 x 10 ⁻⁴	0.9851	0.0698	0.0064	0.0762
43	9	Paraffin Oil	2.10	6.72 x 10 ⁻⁴	0.8794	0.0764	0.0051	0.0815
44	10	Paraffin Oil	2.00	6.40 x 10 ⁻⁴	1.1167	0.0573	0.0115	0.0688
45	11	Silicone Oil	0.90	2.88 x 10 ⁻⁴	1.1034	0.0261	0.0375	0.0636
46	12	Silicone Oil	0.60	1.92 x 10 ⁻⁴	1.1285	0.0170	0.0455	0.0625
47	13	Silicone Oil	0.80	2.56 x 10 ⁻⁴	1.1515	0.0222	0.0336	0.0558
48	14	Silicone Oil	0.50	1.60 x 10 ⁻⁴	0.8607	0.0186	0.0531	0.0717
49	15	Silicone Oil	0.25	0.80 x 10 ⁻⁴	1.1480	0.0070	0.0330	0.0400

TABLE 30 Effect of Temperature on Oxygen Pick-up for Pure Iron (0.7 g Droplet Equivalent)

Height of Fall in Air cm	Time of Fall in Air s	Mass% Oxygen for Different Temperatures		
		< 1580°C	1581 - 1619°C	> 1620°C
37	0.150	-	0.029	0.035 ± 0.008
50	0.185	0.041 ± 0.002	0.049 ± 0.014	0.044 ± 0.014
75	0.250	0.092	0.069 ± 0.013	0.068 ± 0.008
90	0.285	0.064 ± 0.006	0.058	0.080
100	0.305	0.076 ± 0.023	0.072 ± 0.012	0.077
118	0.345	0.073	0.077 ± 0.021	0.083 ± 0.007

TABLE 31 Effect of Droplet Size on Oxygen Pick-up for Pure Iron

Height of Fall in Air cm	Time of Fall in Air s	Mass% Oxygen for Different Droplet Sizes		
		< 0.6 g	0.6 - 0.8 g	> 0.8 g
37	0.150	-	0.032 ± 0.005	0.039 ± 0.016
50	0.185	0.074	0.043 ± 0.013	0.043 ± 0.012
75	0.250	0.071	0.065 ± 0.014	-
90	0.285	-	0.069 ± 0.016	0.059 ± 0.005
100	0.305	0.086 ± 0.019	0.073 ± 0.013	0.061 ± 0.017
118	0.345	-	0.080 ± 0.014	0.081 ± 0.013

TABLE 32**Effect of Droplet Size on Oxygen Pick-up for Fe-0.25% Cr**

Height of Fall in Air cm	Time of Fall in Air s	Mass% Oxygen for Different Droplet Sizes		
		<0.4 g	0.5 - 0.7 g	>0.7 g
37	0.150	0.147 ± 0.016	0.109 ± 0.009	0.092 ± 0.006
50	0.185	0.185 ± 0.009	0.110 ± 0.025	0.061 ± 0.010
75	0.250	0.206	0.132 ± 0.001	0.125 ± 0.016
90	0.285	0.173 ± 0.020	0.146 ± 0.029	0.114 ± 0.018
100	0.305	0.185 ± 0.044	0.137 ± 0.040	0.092
113	0.344	-	0.139 ± 0.028	0.131

TABLE 33 Distribution of Droplet Size for each system

Size Range of Droplets	<0.475g	0.475-0.525g	0.525-0.575g	0.575-0.625g	0.625-0.675g	0.675-0.725g	0.725-0.775g	0.775-0.825g	0.825-0.875g	0.875-0.925g	>0.925g
No. of Droplets in Range											
Pure Fe	2	1	2	2	5	18	21	11	10	3	9
Fe-Cr alloys	13	2	7	38	58	67	12	4	4	0	0
Fe-Mn alloys	2	0	3	4	6	26	30	24	25	7	4
Fe-Si alloys	2	0	1	0	3	0	3	14	18	16	19
Totals	19	3	13	44	72	111	66	53	57	26	32

TABLE 34 Oxidation Rate In Air

Material: Pure iron
 Height of fall in air: 37 cm
 Time of fall in air: 0.15 s

Sample No	Mass of Droplet g	Radius of Droplet cm	Temperature of Droplet °C	Oxygen Pick-up mass %	0.7 g Droplet Equivalent Oxygen Pick-up mass %
A 290	0.8390	0.304	1640	0.028	0.029
A 291	0.7243	0.289	1600	0.029	0.029
A 292	0.7041	0.287	N/A	0.038	0.038
A 293	0.9526	0.317	1670	0.036	0.040
A 294	0.8950	0.311	N/A	0.024	0.026
A 295	1.0055	0.323	N/A	0.057	0.064

Statistical Data: (0.7 g Droplet Equivalent)

Sample size, $n = 6$
 Sample mean, $\bar{x} = 0.0377$
 Sample standard deviation, $s = 0.0140$
 Standard error = 0.0057
 95% confidence interval = $0.0377 \pm 2.57 \times 0.0057$
 = 0.0377 ± 0.0146

N/A Temperature not available

TABLE 35 **Oxidation Rate in Air**

Material: Pure iron
 Height of fall in air: 50 cm
 Time of fall in air: 0.185 s

Sample No	Mass of Droplet g	Radius of Droplet cm	Temperature of Droplet °C	Oxygen Pick-up mass %	0.7 g Droplet Equivalent Oxygen Pick-up mass %
A 52	0.8112	0.301	1580	0.038	0.040
A 53	0.7825	0.297	1600	0.032	0.033
A 54	0.9740	0.319	1580	0.039	0.043
A 55	0.3763	0.233	N/A	0.074	0.059
A 56	0.8666	0.307	1590	0.040	0.043
A 57	0.7869	0.298	1600	0.050	0.052
A 58	0.9383	0.316	1580	0.036	0.040
A 59	0.9371	0.315	N/A	0.026	0.029
A 60	0.7380	0.291	1590	0.032	0.033
A 61	0.8310	0.303	1610	0.059	0.062
A 62	0.7817	0.297	1600	0.040	0.041
A 77	1.2541	0.348	N/A	0.044	0.053
A 78	0.9557	0.317	1600	0.050	0.055
A 79	0.9670	0.319	1610	0.046	0.051
A 80	0.8307	0.303	1620	0.056	0.059
A 81	0.7207	0.289	1600	0.066	0.067
A 82	0.9221	0.313	1610	0.065	0.071
A 83	0.8460	0.305	1620	0.030	0.032
A 84	0.8705	0.308	1620	0.038	0.041
A 85	0.8112	0.301	1600	0.033	0.035

Statistical Data: (0.7 g Droplet Equivalent)

Sample size, $n = 20$
 Sample mean, $\bar{x} = 0.0470$
 Sample standard deviation, $s = 0.0124$
 Standard error = 0.0028
 95% confidence interval = $0.0470 \pm 2.09 \times 0.0028$
 = 0.0470 ± 0.0058

N/A Temperature not available

TABLE 37 **Oxidation Rate in Air**

Material: Pure iron
Height of fall in air: 90 cm
Time of fall in air: 0.285 s

Sample No	Mass of Droplet g	Radius of Droplet cm	Temperature of Droplet °C	Oxygen Pick-up mass %	0.7 g Droplet Equivalent Oxygen Pick-up mass %
A 63	0.8595	0.306	1610	0.055	0.058
A 64	0.7655	0.295	1570	0.057	0.059
A 65	0.9131	0.313	1580	0.062	0.068
A 300	0.6944	0.285	1625	0.080	0.080

Statistical Data: (0.7 g Droplet Equivalent)

Sample size, $n = 4$
Sample mean, $\bar{x} = 0.0663$
Sample standard deviation, $s = 0.0102$
Standard error = 0.0051
95% confidence interval = $0.0663 \pm 3.18 \times 0.0051$
= 0.0463 ± 0.0162

TABLE 38 Oxidation Rate in Air

Material: Pure Iron
 Height of fall in air: 100 cm
 Time of fall in air: 0.305 s

Sample No	Mass of Droplet g	Radius of Droplet cm	Temperature of Droplet °C	Oxygen Pick-up mass %	0.7 g Droplet Equivalent Oxygen Pick-up mass %
A 237	0.7397	0.291	1590	0.069	0.070
A 238	0.8000	0.299	1615	0.073	0.076
A 239	0.7655	0.295	1590	0.067	0.069
A 240	0.6809	0.284	1580	0.103	0.101
A 241	0.6076	0.273	1590	0.091	0.086
A 242	0.6624	0.281	N/A	0.121	0.118
A 243	0.7291	0.290	1600	0.085	0.086
A 244	0.5424	0.263	N/A	0.088	0.081
A 245	0.6897	0.285	N/A	0.063	0.062
A 246	0.7186	0.289	N/A	0.075	0.076
A 273	0.7511	0.293	N/A	0.063	0.065
A 274	0.8070	0.300	1600	0.081	0.085
A 275	0.6693	0.282	1590	0.090	0.088
A 276	0.5914	0.271	N/A	0.066	0.063
A 277	0.8116	0.301	1580	0.052	0.055
A 278	0.6550	0.280	1580	0.074	0.072
A 279	0.9831	0.320	N/A	0.050	0.056
A 280	0.6652	0.281	1600	0.067	0.066
A 281	0.7349	0.291	1615	0.067	0.068
A 283	0.7585	0.294	1605	0.049	0.050
A 297	0.6789	0.283	1605	0.062	0.061
A 298	0.1695	0.178	1605	0.103	0.064
A 299	0.7298	0.290	1620	0.076	0.077
A 304*	0.7666	0.295	1610	0.037	0.038/0.078
A 307*	0.5701	0.268	1620	0.046	0.043/0.077

Statistical Data: (0.7 g Droplet Equivalent)

Sample size, n = 24

Sample mean, \bar{x} = 0.0721

Sample standard deviation, s = 0.0121

Standard error = 0.0025

95% confidence interval = $0.0721 \pm 2.07 \times 0.0025$
 = 0.0721 ± 0.0051

N/A Temperature not available

* Sample reduced in hydrogen

TABLE 39 **Oxidation Rate in Air**

Material: Pure Iron
Height of fall in air: 118 cm
Time of fall in air: 0.344 s

Sample No	Mass of Droplet g	Radius of Droplet cm	Temperature of Droplet °C	Oxygen Pick-up mass %	0.7 g Droplet Equivalent Oxygen Pick-up mass %
A 257	0.8591	0.306	N/A	0.092	0.098
A 258	0.8060	0.300	N/A	0.087	0.090
A 259	0.7054	0.287	1590	0.063	0.063
A 260	0.7511	0.293	1595	0.111	0.113
A 261	0.7796	0.296	1585	0.070	0.072
A 262	0.7703	0.295	1585	0.073	0.075
A 263	0.8309	0.303	1575	0.069	0.073
A 284	0.7296	0.290	1600	0.068	0.063
A 285	0.7323	0.291	1640	0.078	0.079
A 286	0.8560	0.306	1620	0.071	0.075
A 287	0.8057	0.300	N/A	0.092	0.096
A 288	0.7030	0.286	1620	0.084	0.092
A 289	0.7695	0.295	1630	0.082	0.084

Statistical Data: (0.7 g Droplet Equivalent)

Sample size, n = 13
Sample mean, \bar{x} = 0.0825
Sample standard deviation, s = 0.0147
Standard error = 0.0041
95% confidence interval = $0.0825 \pm 2.18 \times 0.0041$
= 0.0825 ± 0.0089

N/A Temperature not available

TABLE 40 **Oxidation Rate in Air**

Material: Fe-0.50% Mn
Height of fall in air: 37 cm
Time of fall in air: 0.15 s

Sample No	Mass of Droplet g	Radius of Droplet cm	Temperature of Droplet °C	Oxygen Pick-up mass %	0.7 g Droplet Equivalent Oxygen Pick-up mass %
D 81	0.6004	0.273	N/A	0.047	0.045
D 82	0.6556	0.281	1580	0.048	0.047
D 83	0.7032	0.287	1610	0.046	0.046
D 84	0.6805	0.284	1620	0.040	0.039
D 85	0.6864	0.285	1610	0.053	0.052
D 86	0.6604	0.281	1625	0.053	0.052
D 87	0.6832	0.285	1600	0.030	0.030
D 88	0.6972	0.287	1590	0.051	0.051

Statistical Data: (0.7 g Droplet Equivalent)

Sample size, n = 8
Sample mean \bar{x} = 0.0453
Sample standard deviation, s = 0.0076
Standard error = 0.0027
95% confidence interval = $0.0453 \pm 2.36 \times 0.0027$
= 0.0453 ± 0.0062

N/A Temperature not available

TABLE 41 Oxidation Rate in Air

Material: Fe-0.50% Mn
Height of fall in air: 50 cm
Time of fall in air: 0.185 s

Sample No	Mass of Droplet g	Radius of Droplet cm	Temperature of Droplet °C	Oxygen Pick-up mass %	0.7 g Droplet Equivalent Oxygen Pick-up mass %
D 70	0.8086	0.301	1670	0.046	0.048
D 71	0.8143	0.302	1630	0.031	0.032
D 72	0.6857	0.285	1600	0.041	0.041
D 73	0.7915	0.299	1630	0.054	0.056
D 74	0.7574	0.295	1635	0.055	0.057
D 75	0.6927	0.286	1620	0.042	0.042
D 76	0.6080	0.274	N/A	0.081	0.077
D 77	0.7347	0.292	1640	0.031	0.032/0.085*
D 78	0.6985	0.287	1590	0.044	0.044
D 79	0.7597	0.295	1615	0.053	0.055
D 80	0.6808	0.284	1605	0.056	0.056
D 81	0.6004	0.273	N/A	0.052	0.050

Statistical Data: (0.7 g Droplet Equivalent)

Sample size, n = 12
Sample mean \bar{x} = 0.0536
Sample standard deviation, s = 0.0149
Standard error = 0.0043
95% confidence interval = $0.0536 \pm 2.20 \times 0.0043$
= 0.0536 ± 0.0094

N/A Temperature not available

* Sample reduced in hydrogen

TABLE 42 **Oxidation Rate in Air**

Material: Fe-0.50% Mn
Height of fall in air: 75 cm
Time of fall in air: 0.250 s

Sample No	Mass of Droplet g	Radius of Droplet cm	Temperature of Droplet °C	Oxygen Pick-up mass %	0.7 g Droplet Equivalent Oxygen Pick-up mass %
D 62	0.5555	0.266	N/A	0.073	0.067
D 63	0.7277	0.291	1580	0.066	0.067
D 64	0.6857	0.285	1620	0.052	0.052
D 65	0.7436	0.293	1580	0.062	0.063
D 66	0.6940	0.286	1580	0.058	0.057
D 67	0.7595	0.295	1660	0.067	0.069
D 68	0.7710	0.296	1650	0.058	0.059
D 69	0.6555	0.281	N/A	0.087	0.085

Statistical Data: (0.7 g Droplet Equivalent)

Sample size, $n = 8$
Sample mean, $\bar{x} = 0.0649$
Sample standard deviation, $s = 0.0100$
Standard error = 0.0035
95% confidence interval = $0.0649 \pm 2.36 \times 0.0035$
= 0.0649 ± 0.0082

N/A Temperature not available

TABLE 43 Oxidation Rate in Air

Material: Fe-0.50% Mn
 Height of fall in air: 100 cm
 Time of fall in air: 0.305 s

Sample No	Mass of Droplet g	Radius of Droplet cm	Temperature of Droplet °C	Oxygen Pick-up mass %	0.7 g Droplet Equivalent Oxygen Pick-up mass %
D 51	0.8331	0.304	1600	0.056	0.060
D 52	0.7816	0.298	1620	0.065	0.067
D 53	0.7311	0.291	1630	0.051	0.051/0.102*
D 54 (i)	0.3591	0.230	1590	0.098	0.079
D 54(ii)	0.2352	0.200	1590	0.098	0.068
D 55	0.7655	0.296	1600	0.071	0.073
D 56	0.7357	0.292	1610	0.067	0.068
D 57	0.5943	0.272	N/A	0.053	0.050
D 58	0.5621	0.267	N/A	0.093	0.086
D 59	0.6731	0.283	N/A	0.061	0.060
D 60	0.8586	0.307	1585	0.073	0.078
D 61	0.7540	0.294	1600	0.067	0.069

Statistical Data: (0.7 g Droplet Equivalent)

Sample size, n = 12

Sample mean, \bar{x} = 0.0717

Sample standard deviation, s = 0.0135

Standard error = 0.0039

95% confidence interval = $0.0717 \pm 2.20 \times 0.0039$
 = 0.0717 ± 0.0085

N/A Temperature not available

* Sample reduced in hydrogen

TABLE 44 Oxidation Rate in Air

Material: Fe-0.50% Mn
Height of fall in air: 118 cm
Time of fall in air: 0.344 s

Sample No	Mass of Droplet g	Radius of Droplet cm	Temperature of Droplet °C	Oxygen Pick-up mass %	0.7 g Droplet Equivalent Oxygen Pick-up mass %
D 45	0.7152	0.289	N/A	0.082	0.083
D 46	0.8275	0.303	1655	0.093	0.098
D 47	0.9452	0.317	1610	0.061	0.067
D 48	0.8384	0.305	1605	0.069	0.073
D 49	0.8415	0.305	1620	0.078	0.083
D 50	0.8697	0.309	1650	0.070	0.075

Statistical Data: (0.7 g Droplet Equivalent)

Sample size, $n = 6$
Sample mean, $\bar{x} = 0.0798$
Sample standard deviation, $s = 0.0108$
Standard error = 0.0044
95% confidence interval = $0.0798 \pm 2.57 \times 0.0044$
= 0.0798 ± 0.0113

N/A Temperature not available

TABLE 45 Oxidation Rate in Air

Material: Fe-0.70% Mn
Height of fall in air: 37 cm
Time of fall in air: 0.150 s

Sample No	Mass of Droplet g	Radius of Droplet cm	Temperature of Droplet °C	Oxygen Pick-up mass %	0.7 g Droplet Equivalent Oxygen Pick-up mass %
D 1	0.7206	0.290	1630	0.053	0.054
D 2	0.7667	0.296	1575	0.034	0.035
D 3	0.6108	0.274	1600	0.045	0.043
D 4	0.7785	0.297	1585	0.046	0.048
D 5	0.9053	0.313	1590	0.058	0.063
D 6	0.7522	0.294	1590	0.049	0.051

Statistical Data: (0.7 g Droplet Equivalent)

Sample size, $n = 6$
Sample mean, $\bar{x} = 0.0490$
Sample standard deviation, $s = 0.0096$
Standard error = 0.0039
95% confidence interval = $0.0490 \pm 2.57 \times 0.0039$
= 0.0490 ± 0.0100

TABLE 46 Oxidation Rate in Air

Material: Fe-0.70% Mn
Height of fall in air: 50 cm
Time of fall in air: 0.185 s

Sample No	Mass of Droplet g	Radius of Droplet cm	Temperature of Droplet °C	Oxygen Pick-up mass %	0.7 g Droplet Equivalent Oxygen Pick-up mass %
D 7	0.8530	0.307	N/A	0.059	0.063
D 8	0.6911	0.286	1580	0.067	0.067
D 9	0.8262	0.303	1650	0.062	0.065
D 10	0.8266	0.303	1630	0.053	0.055
D 11	0.7454	0.293	1600	0.028	0.028/0.081*
D 12	0.7062	0.288	1600	0.048	0.048
D 13	0.7583	0.295	1590	0.045	0.047
D 14	0.7804	0.298	1595	0.051	0.053
D 15	0.8051	0.301	1620	0.051	0.054

Statistical Data: (0.7 g Droplet Equivalent)

Sample size, n = 9
Sample mean, \bar{x} = 0.0592
Sample standard deviation, s = 0.0108
Standard error = 0.0036
95% confidence interval = $0.0592 \pm 2.30 \times 0.0036$
= 0.0592 ± 0.0083

N/A Temperature not available
* Sample reduced in hydrogen

TABLE 47 **Oxidation Rate in Air**

Material: Fe-0.70%Mn

Height of fall in air: 75 cm

Time of fall in air: 0.250 s

Sample No	Mass of Droplet g	Radius of Droplet cm	Temperature of Droplet °C	Oxygen Pick-up mass %	0.7 g Droplet Equivalent Oxygen Pick-up mass %
D 16	0.7366	0.292	1635	0.072	0.074
D 17	0.7490	0.294	1600	0.055	0.057
D 18	0.7099	0.288	1605	0.067	0.068
D 19	0.6861	0.285	1625	0.069	0.069
D 20	0.7126	0.289	1605	0.066	0.066
D 21	0.8434	0.305	1590	0.061	0.065

Statistical Data: (0.7 g Droplet Equivalent)

Sample size, $n = 6$

Sample mean, $\bar{x} = 0.0665$

Sample standard deviation, $s = 0.0056$

Standard error = 0.0023

95% confidence interval = $0.0665 \pm 2.57 \times 0.0023$
= 0.0665 ± 0.0059

TABLE 48 Oxidation Rate in Air

Material: Fe-0.70%Mn
Height of fall in air: 90 cm
Time of fall in air: 0.285 s

Sample No	Mass of Droplet g	Radius of Droplet cm	Temperature of Droplet °C	Oxygen Pick-up mass %	0.7 g Droplet Equivalent Oxygen Pick-up mass %
D 22	0.7896	0.299	1620	0.074	0.077
D 23	0.6641	0.282	1605	0.074	0.073
D 24	0.8354	0.304	N/A	0.059	0.062
D 25	0.8107	0.301	1570	0.065	0.068
D 26	0.7794	0.298	1600	0.066	0.069

Statistical Data: (0.7 g Droplet Equivalent)

Sample size, $n = 5$
Sample mean, $\bar{x} = 0.0698$
Sample standard deviation, $s = 0.0056$
Standard error = 0.0025
95% confidence interval = $0.0698 \pm 2.77 \times 0.0025$
= 0.0698 ± 0.0069

N/A Temperature not available

TABLE 49 Oxidation Rate in Air

Material: Fe-0.70% Mn
Height of fall in air: 100 cm
Time of fall in air: 0.305 s

Sample No	Mass of Droplet g	Radius of Droplet cm	Temperature of Droplet °C	Oxygen Pick-up mass %	0.7 g Droplet Equivalent Oxygen Pick-up mass %
D 27	0.6972	0.287	1650	0.075	0.075
D 28	0.8081	0.301	1620	0.073	0.077
D 29	0.8299	0.304	1600	0.079	0.084
D 30	0.8833	0.310	1610	0.069	0.075
D 31	0.6901	0.286	1600	0.066	0.066
D 32	0.7434	0.293	1615	0.056	0.057/0.104*
D 33	0.8285	0.304	1610	0.054	0.057
D 34	0.8502	0.306	1575	0.087	0.093
D 35	0.8029	0.300	1630	0.077	0.081
D 36	0.7765	0.297	1605	0.070	0.072
D37	0.6918	0.286	1600	0.064	0.064

Statistical Data: (0.7 g Droplet Equivalent)

Sample size, n = 11
Sample mean, \bar{x} = 0.0771
Sample standard deviation, s = 0.0133
Standard error = 0.0040
95% confidence interval = $0.0771 \pm 2.22 \times 0.0040$
= 0.0771 ± 0.0088

* Samples reduced in hydrogen

TABLE 50 Oxidation Rate in Air

Material: Fe-0.70% Mn
 Height of fall in air: 118 cm
 Time of fall in air: 0.344 s

Sample No	Mass of Droplet g	Radius of Droplet cm	Temperature of Droplet °C	Oxygen Pick-up mass %	0.7 g Droplet Equivalent Oxygen Pick-up mass %
D 38	0.6536	0.281	1625	0.083	0.082
D 39	0.7428	0.293	1590	0.061	0.063
D 40	0.8731	0.309	1605	0.074	0.080
D 41	0.8036	0.301	1605	0.073	0.077
D 42	0.8268	0.303	1595	0.078	0.083
D 43	0.7564	0.295	N/A	0.082	0.085
D 44	0.6820	0.285	1630	0.083	0.082

Statistical Data: (0.7 g Droplet Equivalent)

Sample size, $n = 7$
 Sample mean, $\bar{x} = 0.0789$
 Sample standard deviation, $s = 0.0074$
 Standard error = 0.0028
 95% confidence interval = $0.0789 \pm 2.45 \times 0.0028$
 = 0.0789 ± 0.0069

N/A Temperature not available

TABLE 51 Oxidation Rate in Air

Material: Fe - 1.0% Mn
Height of fall in air: 37 cm
Time of fall in air: 0.150 s

Sample No	Mass of Droplet g	Radius of Droplet cm	Temperature of Droplet °C	Oxygen Pick-up mass %	0.7 g Droplet Equivalent Oxygen Pick-up mass %
D 107	0.8634	0.308	1580	0.029	0.031
D 108	0.8713	0.309	1650	0.040	0.043
D 109	0.6865	0.285	1625	0.060	0.059
D 110	0.7773	0.297	1610	0.058	0.060
D 111	0.7808	0.298	1620	0.059	0.061
D 112	0.7757	0.297	1625	0.059	0.061
D 113	0.7424	0.293	1590	0.041	0.042

Statistical Data: (0.7 g Droplet Equivalent)

Sample size, $n = 7$
Sample mean, $\bar{x} = 0.0510$
Sample standard deviation, $s = 0.0122$
Standard error = 0.0046
95% confidence interval = $0.0510 \pm 2.45 \times 0.0046$
= 0.0510 ± 0.0113

TABLE 53 Oxidation Rate in Air

Material: Fe - 1.0% Mn
Height of fall in air: 75 cm
Time of fall in air: 0.250 s

Sample No	Mass of Droplet g	Radius of Droplet cm	Temperature of Droplet °C	Oxygen Pick-up mass %	0.7 g Droplet Equivalent Oxygen Pick-up mass %
D 122	0.8182	0.302	1600	0.061	0.064
D 123	0.8914	0.311	1600	0.079	0.085
D 124	0.9350	0.316	N/A	0.059	0.065
D 125	0.9194	0.314	1640	0.062	0.068
D 126	0.8450	0.306	1595	0.071	0.076
D 127	0.8325	0.304	N/A	0.084	0.089

Statistical Data: (0.7 g Droplet Equivalent)

Sample size, n = 6
Sample mean, \bar{x} = 0.0745
Sample standard deviation, s = 0.0106
Standard error = 0.0043
95% confidence interval = $0.0745 \pm 2.57 \times 0.0043$
= 0.0745 ± 0.0110

N/A Temperature not available

TABLE 54 Oxidation Rate in Air

Material: Fe - 1.0% Mn
 Height of fall in air: 100 cm
 Time of fall in air: 0.305 s

Sample No	Mass of Droplet g	Radius of Droplet cm	Temperature of Droplet °C	Oxygen Pick-up mass %	0.7 g Droplet Equivalent Oxygen Pick-up mass %
D 89	0.6864	0.285	1590	0.069	0.069
D 90	0.7355	0.292	1605	0.074	0.075
D 97	0.7412	0.293	1615	0.071	0.073
D 98	0.7559	0.294	1615	0.043	0.044 *
D 99	0.7616	0.295	1590	0.083	0.085
D 100	0.8655	0.308	1620	0.099	0.106
D 101	0.7908	0.299	1605	0.086	0.090
D 102	0.8345	0.304	1615	0.079	0.084
D 103	0.8888	0.311	1640	0.072	0.078
D 104	0.7971	0.300	1625	0.075	0.078
D 105	0.8098	0.301	1620	0.080	0.084
D 106	0.9184	0.314	1600	0.089	0.097

Statistical Data: (0.7 g Droplet Equivalent)

Sample size, n = 11
 Sample mean, \bar{x} = 0.0835
 Sample standard deviation, s = 0.0109
 Standard error = 0.0033
 95% confidence interval = $0.0835 \pm 2.22 \times 0.0033$
 = 0.0835 ± 0.0073

* Reduced in hydrogen

TABLE 55 Oxidation Rate in Air

Material: Fe - 1.0% Mn
 Height of fall in air: 118 cm
 Time of fall in air: 0.344 s

Sample No	Mass of Droplet g	Radius of Droplet cm	Temperature of Droplet °C	Oxygen Pick-up mass %	0.7 g Droplet Equivalent Oxygen Pick-up mass %
D 128	0.7339	0.292	1620	0.108	0.110
D 129	0.9063	0.313	1615	0.100	0.110
D 130	0.8047	0.301	1595	0.100	0.106
D 131	0.7559	0.294	1600	0.064	0.066
D 132	0.9726	0.320	1630	0.069	0.077
D 133	0.7822	0.298	1615	0.078	0.081
D 134	0.9335	0.316	1635	0.094	0.104
D 135	0.8441	0.305	1610	0.090	0.096

Statistical Data: (0.7 g Droplet Equivalent)

Sample size, $n = 8$

Sample mean, $\bar{x} = 0.0938$

Sample standard deviation, $s = 0.0169$

Standard error = 0.0060

95% confidence interval = $0.0938 \pm 2.36 \times 0.0060$
 = 0.0938 ± 0.0142

TABLE 56 **Oxidation Rate in Air**

Material: Fe-0.17% Cr
Height of fall in air: 37 cm
Time of fall in air: 0.15 s

Sample No	Mass of Droplet g	Radius of Droplet cm	Temperature of Droplet °C	Oxygen Pick-up mass %	0.7 g Droplet Equivalent Oxygen Pick-up mass %
C 103	0.7004	0.287	1590	0.045	0.045
C 104	0.6124	0.274	1590	0.053	0.051
C 105	0.6609	0.281	1560	0.061	0.060
C 114	0.6284	0.277	1600	0.090	0.086
C 115	0.6057	0.273	1570	0.109	0.104
C 116	0.6530	0.280	1600	0.086	0.084

Statistical Data: (0.7 g Droplet Equivalent)

Sample size, $n = 6$
Sample mean, $\bar{x} = 0.0717$
Sample standard deviation, $s = 0.0231$
Standard error = 0.0094
95% confidence interval = $0.0717 \pm 2.57 \times 0.0094$
= 0.0717 ± 0.0241

TABLE 57 Oxidation Rate in Air

Material: Fe-0.17% Cr
Height of fall in air: 50 cm
Time of fall in air: 0.185 s

Sample No	Mass of Droplet g	Radius of Droplet cm	Temperature of Droplet °C	Oxygen Pick-up mass %	0.7 g Droplet Equivalent Oxygen Pick-up mass %
C 95	0.5975	0.272	1575	0.071	0.067
C 96	0.6838	0.285	1590	0.106	0.105
C 97	0.7205	0.290	1560	0.072	0.073
C 98	0.7490	0.293	1570	0.072	0.074
C 99	0.7385	0.292	1575	0.048	0.049*
C 100	0.5693	0.268	1620	0.131	0.122
C 101	0.5324	0.262	N/A	0.064	0.058
C 102	0.6530	0.280	1570	0.068	0.066
C 136	0.7175	0.289	1570	0.071	0.071
C 138	0.7087	0.288	1600	0.049	0.049*
C 211	0.7213	0.290	1590	0.068	0.069
C 212	0.7286	0.291	1590	0.071	0.072

Statistical Data: (0.7 g Droplet Equivalent)

Sample size, n = 10

Sample mean, \bar{x} = 0.0777

Sample standard deviation, s = 0.0198

Standard error = 0.0063

95% confidence interval = $0.0777 \pm 2.26 \times 0.0063$
= 0.0777 ± 0.0142

* Droplets reduced in hydrogen
Results not included in data

N/A Temperature not available

TABLE 58 Oxidation Rate in Air

Material: Fe-0.17% Cr
 Height of fall in air: 75 cm
 Time of fall in air: 0.250 s

Sample No	Mass of Droplet g	Radius of Droplet cm	Temperature of Droplet °C	Oxygen Pick-up mass %	0.7 g Droplet Equivalent Oxygen Pick-up mass %
C 123	0.6595	0.281	1575	0.074	0.073
C 124	0.6962	0.286	1625	0.072	0.072
C 125	0.6324	0.277	1600	0.110	0.106
C 126	0.6315	0.277	1630	0.110	0.106
C 127	0.6357	0.278	1575	0.108	0.104
C 209	0.6941	0.286	1595	0.075	0.075
C 210	0.8298	0.304	1600	0.087	0.092

Statistical Data: (0.7 g Droplet Equivalent)

Sample size, $n = 7$

Sample mean, $\bar{x} = 0.0897$

Sample standard deviation, $s = 0.0161$

Standard error = 0.0061

95% confidence interval = $0.0897 \pm 2.45 \times 0.0061$
 = 0.0897 ± 0.0149

TABLE 59 **Oxidation Rate in Air**

Material: Fe-0.17% Cr
Height of fall in air: 90 cm
Time of fall in air: 0.285 s

Sample No	Mass of Droplet g	Radius of Droplet cm	Temperature of Droplet °C	Oxygen Pick-up mass %	0.7 g Droplet Equivalent Oxygen Pick-up mass %
C 128	0.7201	0.290	1600	0.084	0.086
C 129	0.6486	0.280	1600	0.115	0.112
C 130	0.6423	0.279	1570	0.092	0.090
C 131	0.6086	0.274	1580	0.087	0.084
C 132	0.6273	0.277	1590	0.119	0.116
C 207	0.6323	0.277	1625	0.079	0.076
C 208	0.6264	0.276	1590	0.093	0.089

Statistical Data: (0.7 g Droplet Equivalent)

Sample size, $n = 7$

Sample mean, $\bar{x} = 0.0933$

Sample standard deviation, $s = 0.0149$

Standard error = 0.0056

95% confidence interval = $0.0933 \pm 2.45 \times 0.0056$
= 0.0933 ± 0.0137

TABLE 60 Oxidation Rate in Ar

Material: Fe-0.17% Cr
 Height of fall in air: 100 cm
 Time of fall in air: 0.305 s

Sample No	Mass of Droplet g	Radius of Droplet cm	Temperature of Droplet °C	Oxygen Pick-up mass %	0.7 g Droplet Equivalent Oxygen Pick-up mass %
C 106	0.6232	0.276	1610	0.073	0.071
C 107	0.6088	0.274	1570	0.090	0.086
C 108	0.5566	0.266	1580	0.135	0.125
C 109	0.6288	0.277	1590	0.043	0.042/0.097*
C 110	0.6831	0.285	1580	0.131	0.130
C 111	0.5639	0.267	1575	0.131	0.122
C 112	0.6013	0.273	1595	0.117	0.111
C 113	0.5990	0.272	1605	0.135	0.128
C 133	0.6984	0.287	1560	0.050	0.050 [^]
C 134	0.6185	0.275	1590	0.079	0.076
C 135	0.2621	0.206	N/A	0.186	0.134
C 205	0.6212	0.275	1600	0.04	0.038 [^]
C 206	0.7387	0.292	1610	0.104	0.106

Statistical Data: (0.7 g Droplet Equivalent)

Sample size, n = 11
 Sample mean, \bar{x} = 0.1078
 Sample standard deviation, s = 0.0225
 Standard error = 0.0068
 95% confidence interval = $0.1078 \pm 2.23 \times 0.0068$
 = 0.1078 ± 0.0151

* Droplets reduced in hydrogen. Where the original oxygen level has been calculated, this figure is included in the data.

[^] Figure not included in data.

N/A Temperature not available

TABLE 61 Oxidation Rate in Air

Material: Fe-0.17% Cr
Height of fall in air: 118 cm
Time of fall in air: 0.344 s

Sample No	Mass of Droplet g	Radius of Droplet cm	Temperature of Droplet °C	Oxygen Pick-up mass %	0.7 g Droplet Equivalent Oxygen Pick-up mass %
C 117	0.6005	0.273	1620	0.153	0.145
C 118	0.2557	0.205	N/A	0.224	0.160
C 119	0.5426	0.264	1650	0.191	0.176
C 120	0.5198	0.259	1640	0.218	0.196
C 121	0.6441	0.279	1590	0.118	0.115
C 122	0.7390	0.292	1575	0.098	0.100
C 203	0.6714	0.283	1580	0.088	0.087
C 204	0.6373	0.278	1575	0.097	0.094
C 202	0.6310	0.277	1600	0.099	0.096

Statistical Data: (0.7 g Droplet Equivalent)

Sample size, $n = 9$
Sample mean, $\bar{x} = 0.1299$
Sample standard deviation, $s = 0.0403$
Standard error = 0.0134
95% confidence interval = $0.1299 \pm 2.30 \times 0.0134$
= 0.1299 ± 0.0308

N/A Temperature not available

TABLE 62 **Oxidation Rate in Air**

Material: Fe-0.25% Cr
Height of fall in air: 37 cm
Time of fall in air: 0.150 s

Sample No	Mass of Droplet g	Radius of Droplet cm	Temperature of Droplet °C	Oxygen Pick-up mass %	0.7 g Droplet Equivalent Oxygen Pick-up mass %
C 56	0.3265	0.222	N/A	0.135	0.105
C 57	0.5986	0.272	1620	0.119	0.113
C 58	0.6581	0.281	1630	0.098	0.096
C 59	0.1454	0.170	N/A	0.158	0.093
C 60	0.6168	0.275	1610	0.111	0.107
C 61	0.6100	0.274	1615	0.108	0.104
C 62	0.6997	0.287	1620	0.096	0.096
C 194	0.7233	0.290	1620	0.088	0.089

Statistical Data: (0.7 g Droplet Equivalent)

Sample size, $n = 8$
Sample mean, $\bar{x} = 0.1004$
Sample standard deviation, $s = 0.0081$
Standard error = 0.0029
95% confidence interval = $0.1004 \pm 2.36 \times 0.0029$
= 0.1004 ± 0.0068

N/A Temperature not available

TABLE 63 Oxidation Rate in Air

Material: Fe-0.25% Cr
 Height of fall in air: 50 cm
 Time of fall in air: 0.185 s

Sample No	Mass of Droplet g	Radius of Droplet cm	Temperature of Droplet °C	Oxygen Pick-up mass %	0.7 g Droplet Equivalent Oxygen Pick-up mass %
C 50	0.6429	0.279	1640	0.130	0.126
C 51	0.2587	0.206	N/A	0.191	0.137
C 51	0.2857	0.213	N/A	0.179	0.133
C 52	0.6042	0.273	1600	0.071	0.067/0.116*
C 53	0.5872	0.271	1580	0.120	0.113
C 54	0.5986	0.272	1580	0.069	0.065/0.135*
C 55	0.6638	0.282	1680	0.117	0.115
C 93	0.6958	0.286	N/A	0.067	0.067
C 94	0.7138	0.289	1610	0.043	0.043*
C 195	0.6218	0.276	1600	0.074	0.071
C 196	0.7565	0.295	1600	0.054	0.056

Statistical Data: (0.7 g Droplet Equivalent)

Sample size, n = 10

Sample mean, \bar{x} = 0.1069

Sample standard deviation, s = 0.0305

Standard error = 0.0096

95% confidence interval = $0.1069 \pm 2.26 \times 0.0096$
 = 0.1069 ± 0.0217

N/A Temperature not available

* Sample reduced in hydrogen

TABLE 64 **Oxidation Rate in Aire**

Material: Fe-0.25% Cr
Height of fall in air: 75 cm
Time of fall in air: 0.250 s

Sample No	Mass of Droplet g	Radius of Droplet cm	Temperature of Droplet °C	Oxygen Pick-up mass %	0.7 g Droplet Equivalent Oxygen Pick-up mass %
C 76	0.7046	0.288	1600	0.116	0.116
C 77	0.6052	0.273	1620	0.131	0.125
C 78	0.1574	0.174	N/A	0.206	0.125
C 79	0.5678	0.268	1630	0.133	0.124
C 80	0.7431	0.293	1640	0.116	0.118
C 81	0.7122	0.289	1580	0.143	0.144

Statistical Data: (0.7 g Droplet Equivalent)

Sample size, n = 6
Sample mean, \bar{x} = 0.1253
Sample standard deviation, s = 0.0099
Standard error = 0.0040
95% confidence interval = $0.1253 \pm 2.57 \times 0.0040$
= 0.1253 ± 0.0103

N/A Temperature not available

TABLE 65 Oxidation Rate in Air

Material: Fe-0.25% Cr
Height of fall in air: 90 cm
Time of fall in air: 0.285 s

Sample No	Mass of Droplet g	Radius of Droplet cm	Temperature of Droplet °C	Oxygen Pick-up mass %	0.7 g Droplet Equivalent Oxygen Pick-up mass %
C 82	0.6739	0.283	1570	0.154	0.151
C 83	0.7369	0.292	1620	0.130	0.132
C 85	0.5904	0.271	1660	0.174	0.164
C 86	0.8022	0.300	1580	0.117	0.122
C 87	0.2087	0.192	N/A	0.187	0.125
C 88	0.6941	0.286	1600	0.152	0.151
C 89	0.6615	0.281	1560	0.104	0.102
C 90	0.2463	0.203	N/A	0.159	0.113
C 197	0.7307	0.291	1600	0.095	0.096

Statistical Data: (0.7 g Droplet Equivalent)

Sample size, n = 9
Sample mean, \bar{x} = 0.1284
Sample standard deviation, s = 0.0233
Standard error = 0.0078
95% confidence interval = $0.1284 \pm 2.30 \times 0.0078$
= 0.1284 ± 0.0179

N/A Temperature not available

TABLE 66 Oxidation Rate in Air

Material: Fe-0.25% Cr
 Height of fall in air: 100 cm
 Time of fall in air: 0.305 s

Sample No	Mass of Droplet g	Radius of Droplet cm	Temperature of Droplet °C	Oxygen Pick-up mass %	0.7 g Droplet Equivalent Oxygen Pick-up mass %
C 63	0.6979	0.287	1620	0.069	0.069/0.111*
C 64	0.5904	0.271	1650	0.169	0.159
C 65	0.6113	0.274	1620	0.073	0.070/0.137*
C 66	0.6049	0.273	1680	0.162	0.154
C 67	0.4081	0.240	1640	0.207	0.173
C 68	0.2762	0.210	N/A	0.135	0.099
C 69	0.1054	0.153	N/A	0.214	0.114
C 70	0.6163	0.275	1660	0.167	0.160
C 91	0.6407	0.279	1580	0.071	0.069/0.134*
C 92	0.6991	0.287	1600	0.092	0.092
C 198	0.5619	0.267	1605	0.092	0.086
C 199	0.6537	0.281	1585	0.093	0.091

Statistical Data: (0.7 g Droplet Equivalent)

Sample size, $n = 12$

Sample mean, $\bar{x} = 0.1262$

Sample standard deviation, $s = 0.0313$

Standard error = 0.0090

95% confidence interval = $0.1262 \pm 2.20 \times 0.0090$
 = 0.1262 ± 0.0197

N/A Temperature not available

* Sample reduced in hydrogen

TABLE 67 Oxidation Rate in Air

Material: Fe-0.25% Cr
Height of fall in air: 118 cm
Time of fall in air: 0.344 s

Sample No	Mass of Droplet g	Radius of Droplet cm	Temperature of Droplet °C	Oxygen Pick-up mass %	0.7 g Droplet Equivalent Oxygen Pick-up mass %
C 71	0.7006	0.287	1630	0.131	0.131
C 72	0.6941	0.286	1650	0.171	0.170
C 73	0.6457	0.279	1620	0.167	0.162
C 74	0.6883	0.285	1600	0.111	0.111
C 75	0.6685	0.282	1620	0.118	0.116
C 200	0.6878	0.285	1590	0.118	0.117
C 201	0.6866	0.285	1570	0.126	0.125

Statistical Data: (0.7 g Droplet Equivalent)

Sample size, $n = 7$
Sample mean, $\bar{x} = 0.1331$
Sample standard deviation, $s = 0.0235$
Standard error = 0.0089
95% confidence interval = $0.1331 \pm 2.45 \times 0.0089$
= 0.1331 ± 0.0218

TABLE 68 Oxidation Rate in Air

Material: Fe-0.80% Cr
 Height of fall in air: 37 cm
 Time of fall in air: 0.150 s

Sample No	Mass of Droplet g	Radius of Droplet cm	Temperature of Droplet °C	Oxygen Pick-up mass %	0.7 g Droplet Equivalent Oxygen Pick-up mass %
C 13	0.6210	0.276	1625	0.105	0.101
C 14	0.7195	0.289	1725	0.110	0.111
C 15	0.6219	0.276	1610	0.111	0.107
C 16	0.6305	0.277	1690	0.100	0.097
C 187	0.6035	0.273	1620	0.084	0.081

Statistical Data: (0.7 g Droplet Equivalent)

Sample size, $n = 5$
 Sample mean, $\bar{x} = 0.0994$
 Sample standard deviation, $s = 0.0116$
 Standard error = 0.0052
 95% confidence interval = $0.0994 \pm 2.77 \times 0.0052$
 = 0.0994 ± 0.0144

TABLE 69 Oxidation Rate in Air

Material: Fe-0.80% Cr
 Height of fall in air: 50 cm
 Time of fall in air: 0.185 s

Sample No	Mass of Droplet g	Radius of Droplet cm	Temperature of Droplet °C	Oxygen Pick-up mass %	0.7 g Droplet Equivalent Oxygen Pick-up mass %
C 1	0.6795	0.284	1750	0.138	0.137
C 2	0.6512	0.280	1650	0.177	0.173
C 18	0.6904	0.286	1770	0.126	0.125
C 19	0.6605	0.281	1710	0.130	0.127
C 20	0.6054	0.273	1640	0.067	0.064*
C 33	0.6474	0.279	N/A	0.076	0.074
C 34	0.6784	0.284	1650	0.110	0.109
C 35	0.6708	0.283	N/A	0.105	0.104
C 36	0.6632	0.282	1630	0.122	0.120
C 188	0.7015	0.287	1600	0.067	0.067
C 189	0.6435	0.279	1585	0.075	0.073

Statistical Data: (0.7 g Droplet Equivalent)

Sample size, n = 10
 Sample mean, \bar{x} = 0.1109
 Sample standard deviation, s = 0.0331
 Standard error = 0.0105
 95% confidence interval = $0.1109 \pm 2.26 \times 0.0105$
 = 0.1109 ± 0.0237

N/A Temperature not available
 * Reduced in hydrogen

TABLE 70 Oxidation Rate in Air

Material: Fe-0.80% Cr
Height of fall in air: 75 cm
Time of fall in air: 0.250 s

Sample No	Mass of Droplet g	Radius of Droplet cm	Temperature of Droplet °C	Oxygen Pick-up mass %	0.7 g Droplet Equivalent Oxygen Pick-up mass %
C 3	0.6778	0.284	1610	0.141	0.140
C 4	0.6720	0.283	1620	0.131	0.130
C 28	0.7272	0.291	1705	0.057	0.058*
C 29	0.6193	0.275	1620	0.130	0.125
C 30	0.7207	0.290	1620	0.129	0.130
C 31	0.7590	0.295	1660	0.129	0.133
C 32	0.7598	0.295	1670	0.103	0.106
C 37	0.6105	0.274	N/A	0.145	0.138
C 38	0.7111	0.288	1680	0.130	0.130
C 39	0.6400	0.278	1660	0.129	0.125
C 40	0.6680	0.282	N/A	0.132	0.130

Statistical Data: (0.7 Droplet Equivalent)

Sample Size, $n = 10$
Sample mean, $\bar{x} = 0.1287$
Sample standard deviation, $s = 0.0093$
Standard error = 0.0029
95% confidence interval = $0.1287 \pm 2.26 \times 0.0029$
= 0.1287 ± 0.0066

N/A Temperature not available
* Sample reduced in hydrogen

TABLE 71 Oxidation Rate in Air

Material: Fe-0.80% Cr

Height of fall in air: 90 cm

Time of fall in air: 0.285 s

Sample No	Mass of Droplet g	Radius of Droplet cm	Temperature of Droplet °C	Oxygen Pick-up mass %	0.7 g Droplet Equivalent Oxygen Pick-up mass %
C 8	0.7196	0.290	1630	0.140	0.141
C 9	0.6680	0.282	1640	0.130	0.128
C 10	0.6139	0.275	1570	0.134	0.128
C 11	0.6904	0.286	1680	0.156	0.156
C 12	0.6709	0.283	1650	0.150	0.148
C 41	0.7185	0.289	1620	0.129	0.130
C 42	0.8532	0.306	1625	0.110	0.117
C 190	0.7188	0.289	1580	0.104	0.105

Statistical Data: (0.7 g Droplet Equivalent)

Sample size, $n = 8$ Sample mean, $\bar{x} = 0.1316$ Sample standard deviation, $s = 0.0165$

Standard error = 0.0058

95% confidence interval = $0.1316 \pm 2.36 \times 0.0058$ = 0.1316 ± 0.0137

TABLE 72 Oxidation Rate in Air

Material: Fe-0.80% Cr
 Height of fall in air: 100 cm
 Time of fall in air: 0.305 s

Sample No	Mass of Droplet g	Radius of Droplet cm	Temperature of Droplet °C	Oxygen Pick-up mass %	0.7 g Droplet Equivalent Oxygen Pick-up mass %
C 01	0.7172	0.289	N/A	0.142	0.143
C 02	0.6374	0.278	N/A	0.158	0.153
C 03	0.6005	0.273	N/A	0.148	0.141
C 04	0.6796	0.284	N/A	0.114	0.113
C 23	0.6654	0.282	1595	0.048	0.047*
C 25	0.7130	0.289	1620	0.050	0.050*
C 27	0.7028	0.287	1620	0.066	0.066*
C 43	0.6096	0.274	1640	0.165	0.158
C 45	0.6388	0.278	1640	0.140	0.136
C 47	0.7294	0.291	1640	0.165	0.167
C 191	0.8659	0.307	1580	0.089	0.096
C 192	0.6605	0.281	1600	0.086	0.084*

Statistical Data: (0.7 g Droplet Equivalent)

Sample size, n = 8
 Sample mean, \bar{x} = 0.1384
 Sample standard deviation, s = 0.0236
 Standard error = 0.0083
 95% confidence interval = $0.1384 \pm 2.36 \times 0.0083$
 = 0.1384 ± 0.0196

N/A Temperature not available

* Reduced in hydrogen

TABLE 73 Oxidation Rate in Air

Material: Fe-0.8% Cr

Height of fall in air: 118 cm

Time of fall in air: 0.344 s

Sample No	Mass of Droplet g	Radius of Droplet cm	Temperature of Droplet °C	Oxygen Pick-up mass %	0.7 g Droplet Equivalent Oxygen Pick-up mass %
C 5	0.6651	0.282	1550	0.137	0.135
C 6	0.6114	0.274	1690	0.165	0.158
C 7	0.6379	0.278	1700	0.168	0.163
C 48	0.7241	0.290	1570	0.159	0.161
C 49	0.6510	0.280	1590	0.161	0.157
C 193	0.6753	0.283	1620	0.148	0.146

Statistical Data: (0.7 g Droplet Equivalent)

Sample size, $n = 6$ Sample mean, $\bar{x} = 0.1533$ Sample standard deviation, $s = 0.0107$

Standard error = 0.0044

95% confidence interval = $0.1533 \pm 2.57 \times 0.0044$ = 0.1533 ± 0.0113

TABLE 74 Oxidation Rate in Air

Material: Fe-1.46% Cr
Height of fall in air: 37 cm
Time of fall in air: 0.150 s

Sample No	Mass of Droplet g	Radius of Droplet cm	Temperature of Droplet °C	Oxygen Pick-up mass %	0.7 g Droplet Equivalent Oxygen Pick-up mass %
C 139	0.7166	0.289	1600	0.051	0.052
C 140	0.8256	0.303	1580	0.063	0.067
C 141	0.6047	0.273	1640	0.113	0.107
C 142	0.6865	0.284	1570	0.046	0.046
C 143	0.6665	0.282	1650	0.067	0.066
C 144	0.6668	0.282	1610	0.065	0.064

Statistical Data: (0.7 g Droplet Equivalent)

Sample size, $n = 6$
Sample mean, $\bar{x} = 0.0670$
Sample standard deviation, $s = 0.0213$
Standard error = 0.0087
95% confidence interval = $0.0670 \pm 2.57 \times 0.0087$
= 0.0670 ± 0.0223

TABLE 75 Oxidation Rate in Air

Material: Fe-1.46% Cr
 Height of fall in air: 50 cm
 Time of fall in air: 0.185 s

Sample No	Mass of Droplet g	Radius of Droplet cm	Temperature of Droplet °C	Oxygen Pick-up mass %	0.7 g Droplet Equivalent Oxygen Pick-up mass %
C 145	0.6593	0.281	1580	0.097	0.095
C 146	0.6351	0.278	1580	0.083	0.080
C 147	0.6761	0.284	1575	0.070	0.070
C 148	0.6428	0.279	1590	0.115	0.111
C 149	0.6946	0.286	1595	0.058	0.058
C 150	0.6151	0.275	1600	0.051	0.049
C 151	0.6461	0.279	1630	0.084	0.082
C 152	0.8448	0.306	1680	0.102	0.108
C 182	0.2969	0.216	N/A	0.117	0.087
C 183	0.6649	0.282	1600	0.048	0.047
C 184	0.7146	0.289	1600	0.028	0.028/0.112*

Statistical Data: (0.7 g Droplet Equivalent)

Sample size, n = 11
 Sample mean, \bar{x} = 0.0817
 Sample standard deviation, s = 0.0237
 Standard error = 0.0071
 95% confidence interval = $0.0817 \pm 2.23 \times 0.0071$
 = 0.0817 ± 0.0158

N/A Temperature not available
 * Sample reduced in hydrogen

TABLE 76 Oxidation Rate in Air

Material: Fe-1.46% Cr
Height of fall in air: 75 cm
Time of fall in air: 0.250 s

Sample No	Mass of Droplet g	Radius of Droplet cm	Temperature of Droplet °C	Oxygen Pick-up mass %	0.7 g Droplet Equivalent Oxygen Pick-up mass %
C 153	0.7020	0.287	1620	0.062	0.062
C 154	0.6856	0.285	1650	0.096	0.096
C 155	0.6186	0.275	1610	0.086	0.083
C 156	0.6427	0.279	1590	0.077	0.075
C 157	0.6089	0.274	1625	0.086	0.083
C 158	0.7792	0.297	1680	0.103	0.106

Statistical Data: (0.7 g Droplet Equivalent)

Sample size, $n = 6$
Sample mean, $\bar{x} = 0.0840$
Sample standard deviation, $s = 0.0155$
Standard error = 0.0063
95% confidence interval = $0.0840 \pm 2.57 \times 0.0063$
= 0.0840 ± 0.0162

TABLE 77 Oxidation Rate in Air

Material: Fe-1.46% Cr
Height of fall in air: 90 cm
Time of fall in air: 0.285 s

Sample No	Mass of Droplet g	Radius of Droplet cm	Temperature of Droplet °C	Oxygen Pick-up mass %	0.7 g Droplet Equivalent Oxygen Pick-up mass %
C 159	0.6643	0.282	1600	0.086	0.085
C 160	0.6993	0.286	1570	0.079	0.079
C 161	0.6255	0.276	1630	0.117	0.113
C 162	0.6249	0.276	1590	0.082	0.080
C 163	0.6631	0.282	1570	0.089	0.088
C 164	0.6909	0.286	1580	0.111	0.111

Statistical Data: (0.7 g Droplet Equivalent)

Sample size, $n = 6$
Sample mean, $\bar{x} = 0.0927$
Sample standard deviation, $s = 0.0153$
Standard error = 0.0062
95% confidence interval = $0.0927 \pm 2.57 \times 0.0062$
= 0.0927 ± 0.0159

TABLE 78 Oxidation Rate in Air

Material: Fe-1.46% Cr
Height of fall in air: 100 cm
Time of fall in air: 0.305 s

Sample No	Mass of Droplet g	Radius of Droplet cm	Temperature of Droplet °C	Oxygen Pick-up mass %	0.7 g Droplet Equivalent Oxygen Pick-up mass %
C 165	0.6927	0.286	1610	0.095	0.095
C 166	0.7274	0.291	1660	0.124	0.126
C 167	0.7108	0.289	1610	0.111	0.112
C 168	0.6780	0.284	1590	0.028	0.028/0.110*
C 169	0.6730	0.283	1600	0.090	0.089
C 170	0.4667	0.251	1595	0.113	0.099
C 171	0.6785	0.284	1600	0.085	0.084
C 172	0.6890	0.285	1580	0.086	0.085
C 173	0.6531	0.280	1580	0.096	0.093
C 185	0.7191	0.290	1615	0.097	0.098
C 186	0.7245	0.290	1600	0.045	0.045/0.119*

Statistical Data: (0.7 g Droplet Equivalent)

Sample size, $n = 11$
Sample mean, $\bar{x} = 0.1009$
Sample standard deviation, $s = 0.0140$
Standard error = 0.0042
95% confidence interval = $0.1009 \pm 2.23 \times 0.0042$
= 0.1009 ± 0.0093

* Sample reduced in hydrogen

TABLE 79 Oxidation Rate in Air

Material: Fe-1.46% Cr
Height of fall in air: 118 cm
Time of fall in air: 0.344 s

Sample No	Mass of Droplet g	Radius of Droplet cm	Temperature of Droplet °C	Oxygen Pick-up mass %	0.7 g Droplet Equivalent Oxygen Pick-up mass %
C 174	0.6008	0.273	1625	0.101	0.097
C 175	0.6697	0.283	1600	0.094	0.093
C 176	0.7843	0.298	1600	0.100	0.104
C 177	0.6568	0.281	1620	0.092	0.091
C 178	0.8137	0.302	1625	0.098	0.103

Statistical Data: (0.7 g Droplet Equivalent)

Sample size, n = 5
Sample mean, \bar{x} = 0.0976
Sample standard deviation, s = 0.0058
Standard error = 0.0026
95% confidence interval = $0.0976 \pm 2.77 \times 0.0026$
= 0.0976 ± 0.0072

TABLE 80 Oxidation Rate in Air

Material: Fe - 0.30% Si
Height of fall in air: 37 cm
Time of fall in air: 0.150 s

Sample No	Mass of Droplet g	Radius of Droplet cm	Temperature of Droplet °C	Oxygen Pick-up mass %	0.7 g Droplet Equivalent Oxygen Pick-up mass %
E 47	0.4333	0.244	N/A	0.055	0.047
E 48	1.3646	0.358	1590	0.015	0.019
E 49	0.5377	0.262	N/A	0.052	0.047
E 50	1.3966	0.360	1615	0.034	0.043
E 51	1.5462	0.373	1600	0.021	0.027

Statistical Data: (0.7 g Droplet Equivalent)

Sample size, $n = 5$
Sample mean, $\bar{x} = 0.0366$
Sample standard deviation, $s = 0.0128$
Standard error = 0.0057
95% confidence interval = $0.0366 \pm 2.77 \times 0.0057$
= 0.0366 ± 0.0157

N/A Temperature not available

TABLE 81 Oxidation Rate in Air

Material: Fe - 0.30% Si
Height of fall in air: 50 cm
Time of fall in air: 0.185 s

Sample No	Mass of Droplet g	Radius of Droplet cm	Temperature of Droplet °C	Oxygen Pick-up mass %	0.7 g Droplet Equivalent Oxygen Pick-up mass %
E 52	1.3051	0.352	1595	0.023	0.028
E 53	1.3798	0.369	1650	0.023	0.029
E 54	0.8774	0.309	1580	0.034	0.036
E 55	0.6706	0.282	1670	0.047	0.046
E 56	0.6420	0.278	N/A	0.050	0.048

Statistical Data: (0.7 g Droplet Equivalent)

Sample size, $n = 5$
Sample mean, $\bar{x} = 0.0374$
Sample standard deviation, $s = 0.0093$
Standard error = 0.0042
95% confidence interval = $0.0374 \pm 2.77 \times 0.0042$
= 0.0374 ± 0.0115

N/A Temperature not available

TABLE 82**Oxidation Rate in air**

Material: Fe - 0.3% Si
 Height of fall in air: 75 cm
 Time of fall in air: 0.25 s

Sample No	Mass of Droplet g	Radius of Droplet cm	Temperature of Droplet °C	Oxygen Pick-up mass %	0.7 g Droplet Equivalent Oxygen Pick-up mass %
E 57	1.0768	0.330	1575	0.042	0.048
E 58	0.8088	0.300	1570	0.075	0.078
E 59	0.8987	0.311	1660	0.050	0.054
E 60	0.8276	0.303	1615	0.051	0.054
E 61	0.8718	0.308	1595	0.030	0.033

Statistical Data: (0.7 g Droplet Equivalent)

Sample size, $n = 5$
 Sample mean, $\bar{x} = 0.0534$
 Sample standard deviation, $s = 0.0162$
 Standard error = 0.0072
 95% confidence interval = $0.0534 \pm 2.77 \times 0.0072$
 = 0.0534 ± 0.0200

N/A Temperature not available

TABLE 83 Oxidation Rate in Air

Material: Fe - 0.30% Si
 Height of fall in air: 100 cm
 Time of fall in air: 0.0305 s

Sample No	Mass of Droplet g	Radius of Droplet cm	Temperature of Droplet °C	Oxygen Pick-up mass %	0.7 g Droplet Equivalent Oxygen Pick-up mass %
E 36	0.8102	0.300	1630	0.087	0.091
E 37	0.8045	0.300	1600	0.071	0.074
E 38	0.7881	0.298	1580	0.082	0.085
E 39	0.7821	0.297	1590	0.069	0.072
E 40	0.8101	0.300	1580	0.091	0.095
E 1	0.8560	0.306	1625	0.037	0.039
E 2	0.8422	0.304	1595	0.040	0.042/0.090*
E 3	0.7946	0.299	1570	0.040	0.042/0.062*

Statistical Data: (0.7 g Droplet Equivalent)

Sample size, $n = 8$
 Sample mean, $\bar{x} = 0.0760$
 Sample standard deviation, $s = 0.0187$
 Standard error = 0.0066
 95% confidence interval = $0.0760 \pm 2.36 \times 0.0066$
 = 0.0760 ± 0.0156

N/A Temperature not available
 * Sample reduced in hydrogen

TABLE 84 Oxidation Rate in Air

Material: Fe - 0.30% Si
 Height of fall in air: 118 cm
 Time of fall in air: 0.344 s

Sample No	Mass of Droplet g	Radius of Droplet cm	Temperature of Droplet °C	Oxygen Pick-up mass %	0.7 g Droplet Equivalent Oxygen Pick-up mass %
E 41	0.8529	0.306	N/A	0.085	0.091
E 42	0.8388	0.304	1604	0.079	0.084
E 43	0.8162	0.301	1575	0.091	0.096
E 44	0.6315	0.277	1580	0.068	0.066
E 45	0.1768	0.181	1580	0.167	0.105
E 46	0.7618	0.294	1615	0.073	0.075

Statistical Data: (0.7 g Droplet Equivalent)

Sample size, n = 6
 Sample mean, \bar{x} = 0.0862
 Sample standard deviation, s = 0.0142
 Standard error = 0.0058
 95% confidence interval = $0.0862 \pm 2.57 \times 0.0058$
 = 0.0862 ± 0.0149

N/A Temperature not available

TABLE 85 Oxidation Rate in Air

Material: Fe - 0.75% Si
 Height of fall in air: 50 cm
 Time of fall in air: 0.185 s

Sample No	Mass of Droplet g	Radius of Droplet cm	Temperature of Droplet °C	Oxygen Pick-up mass %	0.7 g Droplet Equivalent. Oxygen Pick-up mass %
E 68	1.7461	0.388	1650	0.018	0.024
E 69	1.1388	0.337	1625	0.018	0.021
E 70	1.1678	0.339	1585	0.025	0.030
E 71	1.2977	0.352	1610	0.023	0.028
E 72	0.9762	0.320	1600	0.034	0.038

Statistical Data: (0.7 g Droplet Equivalent)

Sample size, $n = 5$

Sample mean, $\bar{x} = 0.0282$

Sample standard deviation, $s = 0.0065$

Standard error = 0.0029

95% confidence interval = $0.0282 \pm 2.77 \times 0.0029$
 = 0.0282 ± 0.0080

TABLE 86 Oxidation Rate in Air

Material: Fe - 0.75% Si
Height of fall in air: 75 cm
Time of fall in air: 0.25 s

Sample No	Mass of Droplet g	Radius of Droplet cm	Temperature of Droplet °C	Oxygen Pick-up mass %	0.7 g Droplet Equivalent Oxygen Pick-up mass %
E 73	0.7616	0.294	1610	0.015	0.015
E 74	0.8097	0.300	1610	0.025	0.026
E 75	0.9144	0.313	1640	0.025	0.027
E 76	0.9436	0.316	1590	0.028	0.031

Statistical Data: (0.7 g Droplet Equivalent)

Sample size, $n = 4$
Sample mean, $\bar{x} = 0.0248$
Sample standard deviation, $s = 0.0069$
Standard error = 0.0034
95% confidence interval = $0.0248 \pm 3.18 \times 0.0034$
= 0.0248 ± 0.0109

TABLE 87 Oxidation Rate in Air

Material: Fe - 0.75% Si
Height of fall in air: 100 cm
Time of fall in air: 0.305s

Sample No	Mass of Droplet g	Radius of Droplet cm	Temperature of Droplet °C	Oxygen Pick-up mass %	0.7 g Droplet Equivalent Oxygen Pick-up mass %
E 62	0.8618	0.307	1585	0.017	0.019/0.033*
E 63	0.8975	0.311	1580	0.025	0.027
E 64	1.0159	0.324	1610	0.023	0.026
E 65	0.8881	0.310	1630	0.025	0.027
E 66	1.4264	0.363	1640	0.026	0.033
E 67	1.5251	0.371	1590	0.018	0.023

Statistical Data: (0.7 g Droplet Equivalent)

Sample size, $n = 6$
Sample mean, $\bar{x} = 0.0282$
Sample standard deviation, $s = 0.0040$
Standard error = 0.0016
95% confidence interval = $0.0282 \pm 2.57 \times 0.0016$
= 0.0282 ± 0.0042

* Sample reduced in hydrogen

TABLE 89 **Oxidation Rate in air**

Material: Fe - 1.33% Si

Height of fall in air: 50 cm

Time of fall in air: 0.185 s

Sample No	Mass of Droplet g	Radius of Droplet cm	Temperature of Droplet °C	Oxygen Pick-up mass %	0.7 g Droplet Equivalent Oxygen Pick-up mass %
E 24	0.8191	0.302	1620	0.016	0.017
E 25	0.8585	0.306	1605	0.021	0.023
E 26	0.7944	0.299	1640	0.025	0.026
E 27	0.9263	0.314	1590	0.018	0.020
E 28	0.8559	0.306	1600	0.018	0.019
E 29	0.8622	0.307	1605	0.021	0.023

Statistical Data: (0.7 g Droplet Equivalent)

Sample size, $n = 6$ Sample mean, $\bar{x} = 0.0213$ Sample standard deviation, $s = 0.0033$

Standard error = 0.0013

95% confidence interval = $0.0213 \pm 2.57 \times 0.0013$
= 0.0213 ± 0.0033

TABLE 90 **Oxidation Rate in Air**

Material: Fe-1.33% Si
Height of fall in air: 75 cm
Time of fall in air: 0.25 S

Sample No	Mass of Droplet g	Radius of Droplet cm	Temperature of Droplet °C	Oxygen Pick-up mass %	0.7 g Droplet Equivalent Oxygen Pick-up mass %
E 18	0.9144	0.313	1600	0.020	0.022
E 19	0.8176	0.301	1620	0.021	0.022
E 20	0.7896	0.298	1605	0.021	0.022
E 21	0.8276	0.303	1595	0.022	0.023
E 22	0.8660	0.307	1600	0.016	0.017
E 23	0.8944	0.311	1595	0.030	0.032

Statistical Data: (0.7 g Droplet Equivalent)

Sample size, $n = 6$

Sample size, $\bar{x} = 0.0230$

Sample standard deviation, $s = 0.0049$

Standard error = 0.0020

95% confidence interval = $0.0230 \pm 2.57 \times 0.0002$
= 0.0230 ± 0.00051

TABLE 92 Oxidation Rate in Air

Material: Fe-1.33% Si

Height of fall in air: 118 cm

Time of fall in air: 0.344 s

Sample No	Mass of Droplet g	Radius of Droplet cm	Temperature of Droplet °C	Oxygen Pick-up mass %	0.7 g Droplet Equivalent Oxygen Pick-up mass %
E 12	0.8179	0.301	1630	0.016	0.017
E 13	0.8612	0.307	1615	0.023	0.025
E 14	0.8014	0.299	1585	0.022	0.023
E 15	0.9736	0.319	1615	0.015	0.017
E 16	0.8754	0.308	1595	0.024	0.026
E 17	0.9177	0.313	1605	0.029	0.032

Statistical Data: (0.7 g Droplet Equivalent)

Sample size, $n = 6$ Sample size, $\bar{x} = 0.0233$ Sample standard deviation, $s = 0.0058$

Standard error = 0.0023

95% confidence interval = $0.0233 \pm 2.57 \times 0.0023$ = 0.0233 ± 0.0060

TABLE 93 Reduction in Hydrogen

Sample No: A 304
Material: Pure Fe
Height of fall in air: 100 cm
Time of fall in air: 0.305 s
Final oxygen figure: 0.037 mass %

Temperature	Mass loss mg	Oxygen loss mass %	Oxygen mass %
340	0	0	0.076
440	0	0	0.076
460	0	0	0.076
540	0.02	0.003	0.073
660	0.02	0.003	0.073
690	0.05	0.007	0.069
700	0.06	0.008	0.070
740	0.05	0.007	0.069
750	0.05	0.007	0.069
800	0.05	0.007	0.069
870	0.05	0.007	0.069
920	0.09	0.012	0.064
950	0.14	0.018	0.058
1000	0.20	0.026	0.050
1100	0.22	0.029	0.047
1150	0.24	0.031	0.045
Time 20 min	0.28	0.037	0.039
30	0.29	0.038	0.038
40	0.30	0.039	0.037
60	0.30	0.039	0.037

TABLE 94 Reduction in Hydrogen

Sample No: A 307
Material: Pure Fe
Height of fall in air: 100 cm
Time of fall in air: 0.305 s
Final oxygen figure: 0.046 mass %

Temperature °C	Mass loss mg	Oxygen loss mass %	Oxygen mass %
400	0	0	0.082
570	0.02	0.002	0.080
660	0.02	0.003	0.079
700	0.03	0.004	0.078
750	0.02	0.003	0.079
800	0.02	0.003	0.079
820	0.04	0.006	0.076
870	0.05	0.007	0.075
940	0.10	0.013	0.069
980	0.12	0.016	0.066
1030	0.15	0.019	0.063
1050	0.14	0.018	0.064
1150	0.16	0.021	0.061
1150	0.20	0.026	0.056
Time 20 min	0.26	0.034	0.048
40	0.27	0.035	0.047
60	0.28	0.036	0.046

TABLE 95 Reduction in Hydrogen

Sample No: D 53
Material: Fe-0.50% Mn
Height of fall in air: 100 cm
Time of fall in air: 0.305 s
Final oxygen figure: 0.051 mass %

Temperature	Mass loss mg	Oxygen loss mass %	Oxygen mass %
300	0	0	0.102
400	0	0	0.102
500	0	0	0.102
600	0	0	0.102
700	0	0	0.102
765	0	0	0.102
800	0	0	0.102
815	0.01	0.001	0.101
850	0.01	0.001	0.101
880	0.03	0.004	0.098
915	0.09	0.012	0.090
950	0.10	0.014	0.088
980	0.18	0.025	0.077
1010	0.22	0.030	0.072
1035	0.24	0.033	0.069
1060	0.30	0.041	0.061
1090	0.30	0.041	0.061
1120	0.30	0.041	0.061
1150	0.32	0.044	0.058
Time 10 min	0.35	0.048	0.054
20	0.37	0.050	0.052
30	0.37	0.050	0.052
40	0.38	0.051	0.051
50	0.38	0.051	0.051
60	0.38	0.051	0.051

TABLE 96 Reduction in Hydrogen

Sample No: D 77
Material: Fe-0.50% Mn
Height of fall in air: 50 cm
Time of fall in air: 0.185 s
Final oxygen figure: 0.031 mass %

Temperature	Mass loss mg	Oxygen loss mass %	Oxygen mass %
400	0	0	0.085
500	0.02	0.003	0.082
600	0	0	0.085
700	0	0	0.085
750	0	0	0.085
780	0	0	0.085
810	0.02	0.003	0.082
835	0.04	0.005	0.080
860	0.08	0.011	0.074
900	0.11	0.015	0.070
920	0.16	0.022	0.063
950	0.20	0.027	0.058
985	0.25	0.034	0.051
1015	0.27	0.036	0.049
1050	0.28	0.038	0.047
1075	0.31	0.042	0.043
1100	0.33	0.044	0.041
1150	0.33	0.045	0.040
Time 10 min	0.33	0.045	0.040
20	0.35	0.047	0.038
30	0.38	0.051	0.034
40	0.40	0.054	0.031
50	0.40	0.054	0.031
60	0.40	0.054	0.031

TABLE 97 Reduction in Hydrogen

Sample No: D 92
Material: Fe-0.50% Mn
Height of fall in air: 100 cm
Time of fall in air: 0.305 s
Final oxygen figure: Unknown

Temperature °C	Mass loss mg	Oxygen loss mass %
600	0	
700	0	
800	0	
830	0.03	0.004
860	0.06	0.008
880	0.09	0.012
920	0.12	0.016
950	0.15	0.020
970	0.17	0.022
1000	0.22	0.029
1030	0.26	0.034
1060	0.29	0.038
1090	0.30	0.039
1120	0.32	0.042
1150	0.34	0.044
Time 10 min	0.38	0.049
20	0.40	0.052
30	0.42	0.054

TABLE 98 Reduction in Hydrogen

Sample No: D 94
Material: Fe-0.50% Mn
Height of fall in air: 100 cm
Time of fall in air: 0.305 s
Final oxygen figure: Unknown

Temperature °C	Mass loss mg	Oxygen loss mass %
500	0	
550	0.02	0.002
600	0.02	0.002
650	0.02	0.002
720	0	0
750	0	0
780	0.04	0.005
810	0.04	0.005
840	0.03	0.004
870	0.06	0.008
900	0.08	0.010
930	0.11	0.014
970	0.13	0.017
1000	0.17	0.022
1030	0.19	0.025
1050	0.23	0.030
1080	0.25	0.032
1110	0.26	0.034
1150	0.31	0.040
Time 10 min	0.36	0.046

TABLE 99 Reduction in Hydrogen

Sample No: D 11
Material: Fe-0.7% Mn
Height of fall in air: 50 cm
Time of fall in air: 0.185 s
Final oxygen figure: 0.028 mass %

Temperature	Mass loss mg	Oxygen loss mass %	Oxygen mass %
400	0	0	0.084
500	0	0	0.084
600	0	0	0.084
700	0	0	0.084
780	0	0	0.084
810	0	0	0.084
840	0.01	0.001	0.083
870	0.04	0.005	0.079
900	0.08	0.011	0.073
935	0.12	0.016	0.068
965	0.16	0.021	0.063
995	0.22	0.030	0.054
1030	0.24	0.032	0.052
1060	0.29	0.039	0.045
1085	0.32	0.043	0.041
1115	0.34	0.046	0.038
1140	0.35	0.047	0.037
1170	0.36	0.048	0.036
1200	0.37	0.049	0.035
1245	0.38	0.051	0.033
1270	0.42	0.056	0.028
1300	0.42	0.056	0.028
1220	0.40	0.053	0.031
1110	0.40	0.053	0.031
1040	0.40	0.053	0.031

TABLE 100 Reduction in Hydrogen

Sample No: D 32
Material: Fe-0.7% Mn
Height of fall in air: 100 cm
Time of fall in air: 0.305 s
Final oxygen figure: 0.056 mass %

Temperature	Mass loss mg	Oxygen loss mass %	Oxygen mass %
300	0	0	0.105
400	0	0	0.105
500	0	0	0.105
600	0	0	0.105
700	0	0	0.105
800	0	0	0.105
820	0.02	0.003	0.102
850	0.04	0.005	0.100
885	0.08	0.010	0.095
915	0.14	0.019	0.086
950	0.15	0.020	0.085
980	0.18	0.024	0.081
1010	0.23	0.031	0.074
1040	0.25	0.034	0.071
1070	0.26	0.035	0.070
1100	0.28	0.038	0.067
1125	0.28	0.038	0.067
1150	0.30	0.040	0.065
Time 10 min	0.35	0.047	0.058
20	0.37	0.049	0.056
30	0.37	0.049	0.056
40	0.37	0.049	0.056
50	0.37	0.049	0.056
60	0.37	0.049	0.056

Table 101 Reduction in Hydrogen

Sample No: C 109
Material: Fe-0.17% Cr
Height of fall in air: 100 cm
Time of fall in air: 0.305 s
Final oxygen figure: 0.043 mass %

Temperature °C	Mass loss mg	Oxygen loss mass %	Oxygen mass %
200	0		0.097
300	0		0.097
400	+0.09		0.106
500	+0.03		0.099
600	0.02	0.003	0.094
700	0	0	0.097
790	0.04	0.006	0.091
830	0.06	0.009	0.088
910	0.07	0.011	0.086
940	0.09	0.014	0.083
1000	0.12	0.019	0.078
1030	0.16	0.025	0.072
1060	0.19	0.030	0.064
1090	0.20	0.032	0.062
1150	0.20	0.032	0.062
Time 10 min	0.23	0.037	0.059
20	0.26	0.041	0.056
30	0.34	0.054	0.043

Table 102 Reduction in Hydrogen

Sample Nos: C 133 & C 138
Material: Fe-0.17% Cr
Height of fall in air: 50 & 100 cm
Time of fall in air: 0.185 & 0.305 s
Final oxygen figure: 0.053 & 0.049 mass %

Temperature °C	Mass loss mg	Oxygen loss mass %
400	0	0
500	0	0
600	0	0
700	0	0
750	0	0
780	0.03	0.002
810	0.05	0.004
840	0.06	0.004
870	0.08	0.006
900	0.15	0.011
920	0.18	0.013
960	0.22	0.016
1010	0.35	0.025
1050	0.43	0.031
1090	0.47	0.033
1125	0.54	0.038
1150	0.56	0.040
Time 10 min	0.58	0.041
20	0.62	0.044
30	0.63	0.045
40	0.62	0.044

TABLE 103 Reduction in Hydrogen

Sample No: C54
Material: Fe-0.25% Cr
Height of fall in air: 50 cm
Time of fall in air: 0.185 s
Final oxygen figure: 0.069 mass%

Temperature °C	Mass loss mg	Oxygen loss mass %	Oxygen mass %
300	0	0	0.139
400	0.01	0.002	0.137
500	0.02	0.003	0.136
600	0.02	0.003	0.136
700	0.01	0.002	0.137
800	0	0	0.139
850	0	0	0.139
900	0.01	0.002	0.137
920	0.04	0.006	0.133
950	0.10	0.016	0.123
990	0.15	0.025	0.114
1020	0.24	0.040	0.099
1050	0.30	0.050	0.089
1075	0.34	0.057	0.082
1110	0.35	0.059	0.080
1140	0.38	0.064	0.075
1150	0.40	0.069	0.070
Time 10 min	0.40	0.069	0.070
20	0.41	0.069	0.070
30	0.42	0.070	0.069
40	0.42	0.070	0.069
50	0.40	0.069	0.070
60	0.42	0.070	0.069

Table 104 **Reduction in Hydrogen**

Sample No: C 63
Material: Fe-0.25% Cr
Height of fall in air: 100 cm
Time of fall in air: 0.305 s
Final oxygen figure: 0.069 mass %

Temperature °C	Mass loss mg	Oxygen loss mass %	Oxygen mass %
300	0.02	0.003	0.108
400	0.02	0.003	0.108
500	0	0	0.111
600	0	0	0.111
680	0	0	0.111
740	-0.01	+0.001	0.112
770	0.02	0.003	0.108
800	0	0	0.111
850	0	0	0.111
920	0.01	0.001	0.110
950	0.09	0.013	0.098
980	0.12	0.017	0.094
1010	0.17	0.024	0.087
1040	0.20	0.029	0.082
1070	0.23	0.033	0.078
1100	0.26	0.037	0.074
1130	0.28	0.040	0.071
1160	0.30	0.042	0.069
1190	0.30	0.042	0.069

Table 105 Reduction in Hydrogen

Sample No: C 65
Material: Fe-0.25% Cr
Height of fall in air: 100 cm
Time of fall in air: 0.305 s
Final oxygen figure: 0.073 mass %

Temperature °C	Mass loss mg	Oxygen loss mass %	Oxygen mass %
300	0	0	0.142
400	0	0	0.142
500	0	0	0.142
600	0	0	0.142
700	0	0	0.142
800	0	0	0.142
840	0	0	0.142
870	0.02	0.004	0.138
930	0.04	0.007	0.135
960	0.07	0.011	0.131
990	0.09	0.016	0.126
1020	0.16	0.026	0.116
1055	0.20	0.032	0.110
1080	0.23	0.038	0.104
1110	0.28	0.046	0.096
1130	0.30	0.048	0.094
1150	0.31	0.051	0.091
Time 10 min	0.35	0.057	0.085
20	0.40	0.064	0.078
30	0.41	0.067	0.075
40	0.42	0.069	0.073
50	0.41	0.067	0.075
60	0.42	0.069	0.073

Table 106 Reduction in Hydrogen

Sample No: C 91
Material: Fe-0.25% Cr
Height of fall in air: 100 cm
Time of fall in air: 0.305 s
Final oxygen figure: 0.071 mass %

Temperature °C	Mass loss mg	Oxygen loss mass %	Oxygen mass %
200	0	0	0.137
300	0.01	0.002	0.135
400	0.01	0.002	0.135
500	0	0	0.137
600	0	0	0.137
700	0	0	0.137
800	0	0	0.137
840	0.01	0.002	0.135
870	0.01	0.002	0.135
900	0.03	0.005	0.132
930	0.07	0.011	0.126
960	0.14	0.022	0.115
990	0.20	0.031	0.106
1025	0.24	0.037	0.100
1050	0.26	0.041	0.096
1080	0.25	0.040	0.097
1110	0.26	0.041	0.096
1150	0.28	0.044	0.093
Time 10 min	0.32	0.050	0.087
20	0.36	0.056	0.081
30	0.40	0.062	0.075
40	0.42	0.066	0.071
50	0.42	0.066	0.071
60	0.42	0.066	0.071

TABLE 107 **Reduction in Hydrogen**

Sample No: C 214
Material: Fe-0.8% Cr
Height of fall in air: 100 cm
Time of fall in air: 0.305 s
Final oxygen figure: Unknown

Temperature	Mass loss mg	Oxygen loss mass %
500	0	
600	0	
700	0	
730	0	
760	0.03	0.004
790	0.03	0.004
820	0.05	0.007
850	0.05	0.007
880	0.05	0.007
910	0.08	0.012
940	0.11	0.017
970	0.15	0.023
1000	0.19	0.029
1030	0.23	0.035
1060	0.25	0.038
1085	0.27	0.041
1120	0.30	0.046
1150	0.30	0.046
Time 10 min	0.35	0.053
20	0.40	0.060
30	0.39	0.059
40	0.40	0.060
50	0.36	0.055
60	0.37	0.056

Table 108**Reduction in Hydrogen**

Sample No: C 168

Material: Fe- 1.46% Cr

Height of fall in air: 100 cm

Time of fall in air: 0.305 s

Final oxygen figure: 0.028 mass %

Temperature °C	Mass loss mg	Oxygen loss mass %	Oxygen mass %
300	-0.04	0.006	0.116
400	-0.08	0.012	0.122
500	-0.04	0.006	0.116
600	-0.02	0.003	0.113
650	-0.02	0.003	0.113
680	0	0	0.110
720	0	0	0.110
770	0.03	0.004	0.106
800	0.05	0.007	0.103
830	0.03	0.004	0.106
900	0.06	0.009	0.101
920	0.10	0.015	0.095
960	0.20	0.030	0.080
980	0.26	0.038	0.072
1010	0.29	0.043	0.067
1040	0.34	0.050	0.060
1075	0.36	0.053	0.057
1110	0.39	0.058	0.052
1150	0.46	0.068	0.042
Time 10 min	0.45	0.066	0.044
20	0.46	0.068	0.042
30	0.49	0.072	0.038
40	0.54	0.079	0.031
50	0.55	0.081	0.029
60	0.56	0.082	0.028

Table 109**Reduction in Hydrogen**

Sample No: C 184

Material: Fe-1.46% Cr

Height of fall in air: 50 cm

Time of fall in air: 0.185 s

Final oxygen figure: 0.028 mass %

Temperature °C	Mass loss mg	Oxygen loss mass %	Oxygen mass %
300	0	0	0.112
400	-0.04	0.006	0.106
500	-0.04	0.006	0.106
600	0.02	0.003	0.109
700	0	0	0.112
800	0	0	0.112
870	0	0	0.112
910	0	0	0.112
920	0	0	0.112
960	0.04	0.006	0.106
1000	0.10	0.014	0.098
1025	0.16	0.022	0.090
1050	0.22	0.031	0.081
1080	0.24	0.034	0.078
1110	0.26	0.036	0.076
1150	0.30	0.042	0.070
Time 10 min	0.45	0.063	0.049
20	0.52	0.073	0.039
30	0.55	0.076	0.036
40	0.54	0.075	0.037
50	0.60	0.084	0.028
60	0.60	0.084	0.028

Table 110 Reduction in Hydrogen

Sample No: C 186
Material: Fe-1.46% Cr
Height of fall in air: 100 cm
Time of fall in air: 0.305 s
Final oxygen figure: 0.045 mass %

Temperature °C	Mass loss mg	Oxygen loss mass %	Oxygen mass %
300	0	0	0.119
400	0.01	0	0.118
500	0	0	0.119
600	0	0	0.119
700	0	0	0.119
800	0	0	0.119
850	0.06	0.008	0.111
880	0.08	0.011	0.108
950	0.18	0.025	0.094
1010	0.30	0.041	0.078
1070	0.36	0.050	0.069
1130	0.40	0.055	0.064
1150	0.47	0.065	0.054
Time 10 min	0.48	0.066	0.053
20	0.52	0.072	0.047
30	0.55	0.075	0.044
40	0.56	0.077	0.042
50	0.54	0.074	0.045
60	0.54	0.074	0.045

TABLE 111 Reduction in Hydrogen

Sample No: E 2
Material: Fe-0.3% Si
Height of fall in air: 100 cm
Time of fall in air: 0.305 s
Final oxygen figure: 0.038 mass %

Temperature	Mass loss	Oxygen loss	Oxygen
	mg	mass %	mass %
500	0	0	0.085
630	0	0	0.085
690	0	0	0.085
780	0	0	0.085
810	0	0	0.085
860	0	0	0.085
890	0	0	0.085
930	0.01	0.001	0.084
960	0.02	0.002	0.083
990	0.06	0.007	0.078
1020	0.10	0.012	0.073
1050	0.15	0.018	0.067
1080	0.18	0.021	0.064
1120	0.20	0.024	0.061
1145	0.23	0.027	0.058
1150	0.24	0.028	0.057
Time 10 min	0.30	0.035	0.050
20	0.31	0.036	0.049
30	0.35	0.041	0.044
40	0.39	0.046	0.039
50	0.40	0.047	0.038
60	0.40	0.047	0.038

TABLE 112 Reduction in Hydrogen

Sample No: E 3
Material: Fe-0.3% Si
Height of fall in air: 100 cm
Time of fall in air: 0.305 s
Final oxygen figure: 0.040 mass %

Temperature	Mass loss mg	Oxygen loss mass %	Oxygen mass %
500	0	0	0.059
630	0.01	0.002	0.057
690	0	0	0.059
720	0	0	0.059
800	0	0	0.059
860	0	0	0.059
890	0	0	0.059
930	0	0	0.059
960	0.01	0.001	0.058
990	0.04	0.005	0.054
1020	0.06	0.007	0.052
1050	0.08	0.010	0.049
1080	0.08	0.010	0.049
1120	0.10	0.013	0.046
1150	0.12	0.015	0.044
Time 10 min	0.13	0.017	0.042
20	0.13	0.017	0.042
30	0.14	0.018	0.041
40	0.14	0.018	0.041
50	0.15	0.019	0.040
60	0.16	0.020	0.039

TABLE 113 Reduction in Hydrogen

Sample No: E 62
Material: Fe-0.75% Si
Height of fall in air: 100 cm
Time of fall in air: 0.305 s
Final oxygen figure: 0.021 mass %

Temperature °C	Mass loss mg	Oxygen loss mass %	Oxygen mass %
600	0		0.031
700	0		0.031
800	0		0.031
850	0		0.031
880	0.01	0.001	0.030
920	0.01	0.001	0.030
950	0.15	0.002	0.029
1000	0.30	0.003	0.028
1020	0.04	0.005	0.026
1050	0.04	0.005	0.026
1080	0.05	0.006	0.025
1100	0.05	0.006	0.025
1120	0.08	0.009	0.022
1150	0.09	0.010	0.021
Time 10 min	0.11	0.013	0.018
20	0.12	0.014	0.017
30	0.125	0.014	0.017
40	0.125	0.014	0.017
60	0.12	0.014	0.017

TABLE 114 Reduction in Hydrogen

Sample No: E 4
Material: Fe-1.33% Si
Height of fall in air: 100 cm
Time of fall in air: 0.305 s
Final oxygen figure: 0.009 mass %

Temperature	Mass loss mg	Oxygen loss mass %	Oxygen mass %
500	0	0	0.049
600	0.02	0.002	0.047
700	0.02	0.002	0.047
800	0	0	0.049
870	0.01	0.001	0.048
900	0	0	0.049
925	0.01	0.001	0.048
960	0.04	0.004	0.045
1000	0.08	0.008	0.041
1030	0.10	0.010	0.039
1060	0.12	0.012	0.037
1090	0.15	0.015	0.034
1115	0.17	0.017	0.032
1150	0.18	0.018	0.031
Time 10 min	0.23	0.023	0.026
20	0.30	0.030	0.019
30	0.34	0.034	0.015
40	0.38	0.038	0.011
50	0.40	0.040	0.009
60	0.40	0.040	0.009

TABLE 115

Reduction Data for Alloy Droplets

Alloy System	Sample No	Temperature-Onset of Reduction °C	Oxygen loss mass %	Oxygen Content Mass %	
				Initial	Final
<u>Pure Iron</u>	A 304	680/800	0.040	0.078	0.038
	A 307	800	0.034	0.077	0.043
<u>Iron-Manganese</u>					
Fe-0.5% Mn	D 77	780/810	0.053	0.085	0.032
	D 53	820	0.051	0.102	0.051
	D 92	800	0.054		
	D 94	780	0.046		
Fe-0.7% Mn	D 11	820/840	0.056	0.084	0.028
	D 32	820	0.047	0.104	0.057
<u>Iron-chromium</u>					
Fe-0.17% Cr	C 109	750	0.054	0.097	0.043
	C 133/	780			0.053/
	C 138				0.049
Fe-0.25% Cr	C 54	850/900	0.070	0.139	0.069
	C 63	840/900	0.039	0.108	0.069
	C 65	840/850	0.069	0.142	0.073
	C 91	820/840	0.066	0.137	0.071
Fe-0.8% Cr	C 214	780/800	0.056		
Fe-1.46% Cr	C 168	770/830	0.088	0.116	0.028
	C 184	850/900	0.084	0.112	0.028
	C 186	800	0.074	0.119	0.045
<u>Iron-Silicon</u>					
Fe-0.3% Si	E 2	930	0.047	0.085	0.038
	E 3	930	0.020	0.059	0.039
Fe-0.75% Si	E 62	900	0.014	0.031	0.017
Fe-1.33% Si	E 4	925			0.009

TABLE 116 SEM EDAX Analysis

Material: Fe-0.3% Mn
 All values in mass %

Sample 1

	Surface	60 from surface	120 from surface	Centre			
Elements as analysed							
Fe	96.169	96.720	95.160	99.410	100.785	98.099	100.880
Mn	0.415	0.499	0.453	0.296	0.386	0.494	0.385
Si	1.055	0.716	0.562	0.764	0.540	1.052	0
Total	97.639	97.935	96.175	100.470	101.711	99.645	101.265
Elements corrected to 100% total with Si removed from figures							
Fe	99.570	99.487	99.526	99.703	99.618	99.499	99.620
Mn	0.430	0.513	0.474	0.297	0.382	0.501	0.380
Total	100.000	100.000	100.000	100.000	100.000	100.000	100.000
Fe/Mn	231	194	210	336	260	199	262

Sample 2

	Surface 1	Surface 2	Centre 1	Centre 2
Fe	97.298	97.376	96.906	96.484
Mn	0.308	0.134	0.190	0.227
Si	1.331	1.059	0.740	0.713
Total	98.938	98.569	97.836	97.424
Elements corrected to 100% total with Si removed from figures				
Fe	99.684	99.863	99.804	99.765
Mn	0.316	0.137	0.196	0.235
Total	100.000	100.000	100.000	100.000
Fe/Mn	315	729	509	425

TABLE 117 SEM EDX Analysis

Material: Fe-1.0% Mn
 All values in mass %

Element	Distance from edge μm									
	Edge	22	44	66	88	66	44	22	Edge	Edge
Fe	94.753	99.937	98.992	93.524	96.505	95.532	94.799	94.117	97.974	101.119
Mn	0.884	0.628	0.547	0.883	0.879	0.800	0.629	0.654	0.757	0.782
Si	0.688	0.571	0.750	0.398	0.717	0.895	1.298	0.928	1.070	1.390
Total	96.325	101.136	100.290	94.804	98.101	97.227	96.726	95.699	99.801	103.292
Elements corrected to 100% total with Si removed from figures*										
Fe	99.076	99.376	99.450	99.065	99.097	99.170	99.341	99.310	99.233	99.233
Mn	0.924	0.624	0.550	0.935	0.903	0.830	0.659	0.690	0.767	0.767
Total	100.000	100.000	100.000	100.000	100.000	100.000	100.000	100.000	100.000	100.000
Fe/Mn	107	159	181	106	110	119	151	141	129	129

TABLE 118**SEM EDX Analysis**

Material: Fe-0.25% Cr

All values in mass %

Element	Distance from edge μm							
	0	65	105	155	275	355	Sfce 2 (515)	
Fe	87.905	83.961	96.565	99.853	99.282	96.474	96.861	90.693
Cr	0.391	0.313	0.484	0.259	0.377	0.327	0.506	0.532
Si	4.703	7.408	0.739	0.936	1.039	0.871	0.664	0.663
Total	92.998	91.682	97.788	101.047	100.698	97.671	98.030	91.887
Corrected values (0% silicon)								
Fe	99.560	99.629	99.500	99.740	99.622	99.662	99.480	99.417
Cr	0.440	0.371	0.500	0.260	0.378	0.338	0.520	0.583
Total	100.000	100.000	100.000	100.000	100.000	100.000	100.000	100.000
Fe/Mn	225	269	200	386	263	295	191	171

Element	Surface			Centre				
	Spot	Spot	Spot	Spot	Square	Square	Spot	Spot
Fe	96.929	97.870	94.181	94.503	99.186	99.492	103.636	99.893
Cr	0.474	0.445	0.455	0.459	0.321	0.330	0.362	0.469
Si	0.869	0.573	0.782	0.700	0.129	0.605	0.142	0.159
Total	98.272	98.887	95.418	100.663	99.635	100.426	104.139	100.522
Corrected values (0.14% Si)								
Fe	99.372	99.408	99.379	99.400	99.548	99.530	99.488	99.374
Cr	0.486	0.452	0.480	0.459	0.322	0.330	0.347	0.466
Si	0.142	0.140	0.141	0.141	0.130	0.140	0.165	0.159
Total	100.000	100.000	100.000	100.000	100.000	100.000	100.000	100.000
Fe/Cr	205	220	207	217	309	302	287	213

TABLE 119 SEM EDX Analysis

Material: Fe-1.46% Cr
 All values in mass %

	Surface 1 within 10 of edge	Surface 2 within 10 of edge	Surface 3 20 from edge	Centre 1	Centre 2
Elements as analysed					
Fe	99.362	100.769	88.595	102.979	104.498
Cr	2.156	1.961	1.177	1.337	1.276
Si	0.757	1.142	0.141	0.341	0.115
Total	102.274	103.872	89.913	104.913	105.889
Elements corrected to 100% total					
Fe	97.152	97.013	98.534	98.397	98.686
Cr	2.108	1.888	1.309	1.278	1.205
Si	0.740	1.099	0.157	0.325	0.109
Total	100.000	100.000	100.000	100.000	100.000
Elements corrected to 100% total with Si adjusted					
Fe	97.778	97.993	98.583	98.619	98.686
Cr	2.122	1.907	1.310	1.281	1.205
Si	0.100	0.100	0.107	0.100	0.109
Total	100.000	100.000	100.000	100.000	100.000
Fe/Cr	46.1	51.4	75.2	77.0	81.9

TABLE 120 SEM EDX Analysis

Material: Fe-0.3% Si
All values in mass %

	Surface 1	Surface 2	Centre
Elements as analysed			
Fe	90.469	90.634	91.633
Si	3.647	3.524	0.679
Total	94.116	94.158	92.312
Fe/Si	24.8	25.7	135

TABLE 121 SEM EDX Analysis

Material: Fe-0.75% Si
All values in mass%

	Surface 1	Surface 2	Centre
Elements as analysed			
Fe	78.745	80.105	91.507
Si	7.289	5.138	1.107
Total	86.034	85.243	92.613
Fe/Si	11	15.6	83

TABLE 122 **SEM EDX Analysis**

Material: Fe-1.33% Si
All values in mass %

Element	Distance from edge μm						
	0	60	120	200	240	300	Centre
Elements as analysed							
Fe	82.927	84.867	85.173	81.744	85.321	87.564	99.061
Si	6.398	5.358	5.280	6.505	5.435	4.474	1.504
Total	89.325	90.225	90.453	88.249	90.756	92.038	100.565
Fe/Si	13	15.8	16.1	12.6	15.7	19.6	66

TABLE 123 SIMS Analysis of Area of 1.46% Cr Alloy

(i) Positive SIMS Analysis

Sample No	Height of peak mm		No of Counts		Fe/Cr Ratio
	Cr	Fe	Cr	Fe	
RJ 0	0.1	0.2	256	512	2.0
RJ 1	3.25	9.90	802	2444	3.05
RJ 2	3.10	14.10	132	600	4.55
RJ 3	4.40	14.10	136	437	3.21
RJ 4	2.75	14.10	401	2056	5.13
RJ 5	3.50	14.10	574	2312	4.03
RJ 6	2.35	14.10	798	4787	6.00
RJ 7	4.90	11.30	2185	4039	2.31

(ii) Negative SIMS Analysis

Sample No	Height of peak mm	No of Counts
	Oxygen	Oxygen
RJ 1-	14.1	14362
RJ 3-	6.6	813
RJ 4-	14.1	1025
RJ 5-	14.1	1337
RJ 6-	14.1	837
RJ 7-	14.1	7300
RJ 7-R	14.1	2850
RJ 7-R1	14.1	2000
RJ 7-R2	14.1	1725

TABLE 124**Oxide Film Analysis RJMN.1 and RJMN.2**

RJMN.1 (Fe-1.0% Mn)

Etch Time s	Concentration, mass%		Fe/Mn Ratio
	Fe	Mn	
0	14.1	6.75	2.1
925	13.5	7.7	1.8
1850	13.5	12.3	1.1
2770	14.7	18.4	0.8
3700	14.7	30.0	0.5
4625	16.0	33.1	0.5
5550	25.8	25.8	1.0
6475	28.2	20.2	1.4
7400	26.4	23.9	1.1
8325	26.4	28.2	0.9
9247	26.4	32.5	0.8

RJMN.2 (Fe-1.0% Mn)

Etch Time s	Concentration, mass%		Fe/Mn Ratio
	Fe	Mn	
0	14.1	9.8	1.4
746	12.9	11.7	1.1
1492	14.7	14.7	1.0
2240	14.7	16.0	0.9
2984	14.7	17.8	0.8
3730	14.7	18.4	0.8
4480	14.1	19.6	0.7
5220	16.0	25.8	0.6
5970	15.3	28.8	0.5
6715	14.1	33.1	0.4
7462	14.1	35.3	0.4

TABLE 125 Oxide Film Analysis RJ.1P

RJ.1P (Fe-1.46% Cr)

Etch Time s	Concentration, mass%		Fe/Cr Ratio
	Fe	Cr	
0	9.8	4.3	2.3
1260	7.4	12.3	0.6
2520	9.2	17.8	0.5
3768	12.3	24.5	0.5
5024	13.5	29.4	0.5
6280	14.7	33.1	0.4
7540	16.0	36.2	0.4
8792	16.0	38.7	0.4
10050	16.6	39.3	0.4
11306	16.5	38.7	0.4
12562	18.4	37.4	0.5

TABLE 126 Oxide Film Analysis RJ.S1.P

RJ.S1.P (Fe-1.33% Si)

Etch Time s	Concentration, mass%		Fe/Mn Ratio
	Fe	Si	
0	1.2	9.8	0.1
773	9.2	22.1	0.4
1546	13.5	30.1	0.45
2320	11.7	35.0	0.33
3092	13.5	36.8	0.37
3865	10.4	31.9	0.33
4640	12.9	36.2	0.36
5411	12.3	41.7	0.30
6184	13.5	39.3	0.34
6957	15.3	39.3	0.39
7732	8.6	50.9	0.17

TABLE 127 **Oxidation Data (Vig and Lu)(68)**

(i) Rate of Oxidation at 1580°C for 1 g droplets of iron

Time of fall in air s	Oxygen Pickup, mass %	
	1 g droplet	0.7 g droplet (equiv)
0.075	0.025	0.028
0.115	0.034	0.038
0.194	0.045	0.051
0.265	0.055	0.062
0.30	0.060	0.0675

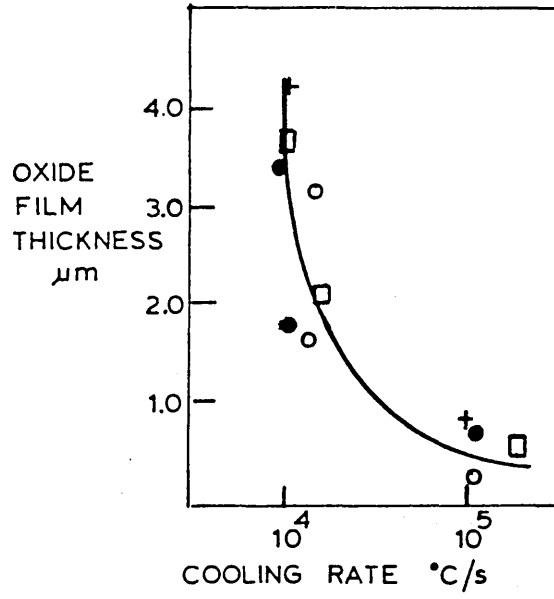
(ii) Rate of Oxidation at 1638°C for 1 g droplets of iron

Time of fall in air s	Oxygen Pickup, mass %	
	1 g droplet	0.7 g droplet (equiv)
0.075	0.023	0.026
0.115	0.032	0.036
0.194	0.045	0.051
0.265	0.055	0.062
0.296	0.060	0.0675

(iii) Rate of Oxidation at 1638°C for Different Sized Droplets

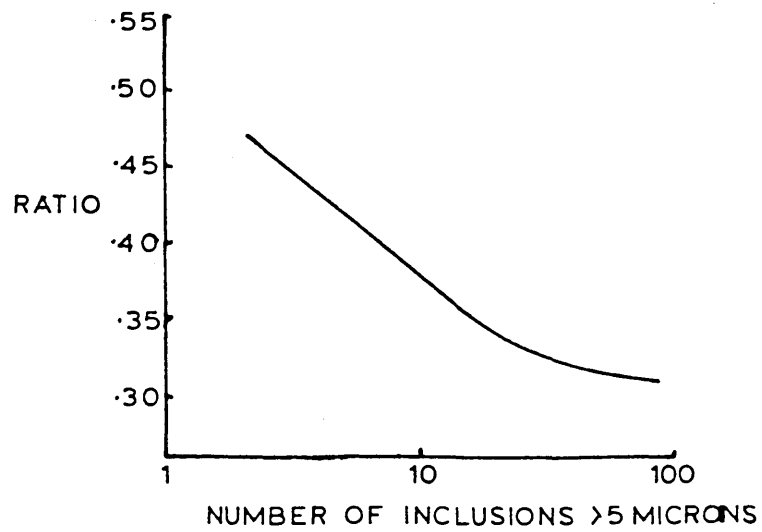
Time of fall in air s	Oxygen Pickup, mass % (0.7 g (equiv))			
	0.87 g	1.08 g	1.22 g	1.45 g
0.075	0.023(0.025)	0.022(0.025)		0.017(0.022)
0.120	0.034(0.037)	0.030(0.035)	0.027(0.033)	
0.200	0.048(0.052)	0.043(0.050)	0.041(0.050)	0.038(0.049)
0.268	0.060(0.065)	0.056(0.065)		0.048(0.062)
0.300	0.069(0.075)	0.061(0.071)	0.058(0.070)	0.053(0.068)

Figure 1



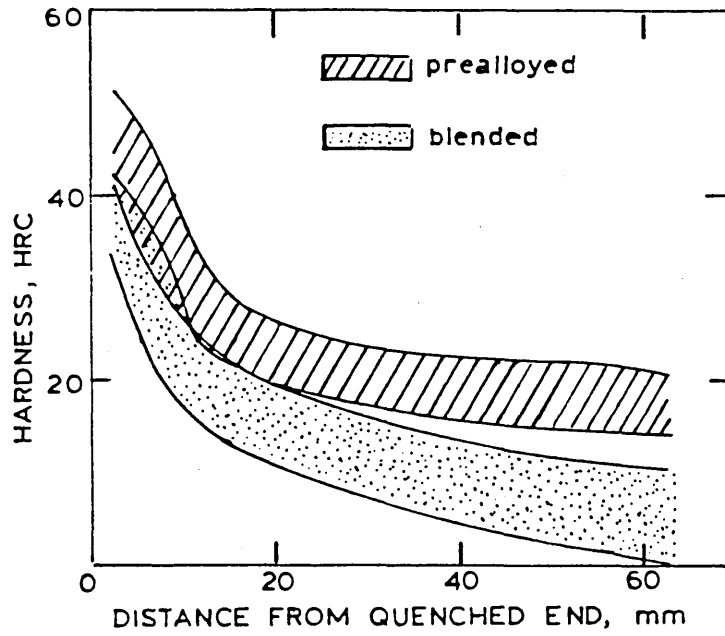
Variation of oxide film thickness with cooling rate.⁽⁹⁾

Figure 2



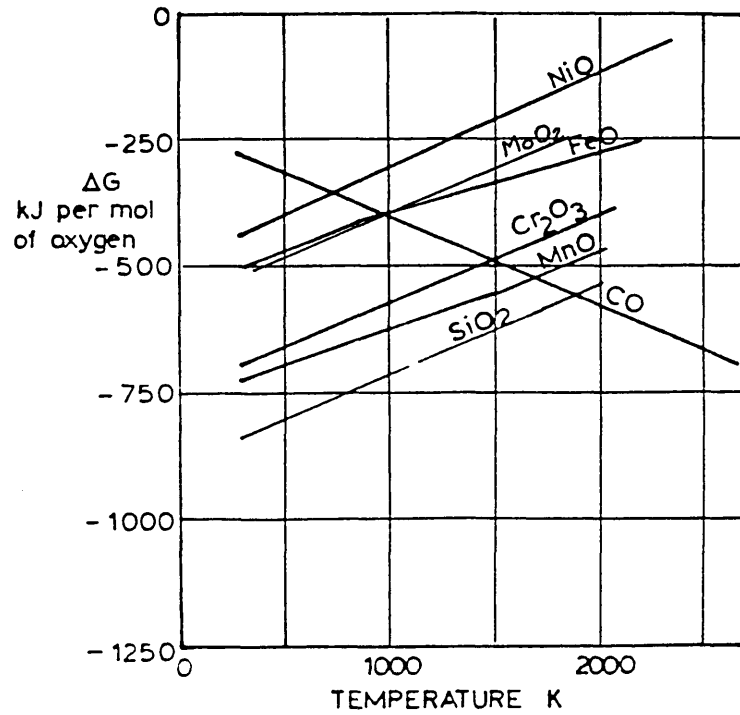
Relationship of inclusions to elastic limit/fatigue ratio of powder forged steels.⁽¹⁶⁾

Figure 3



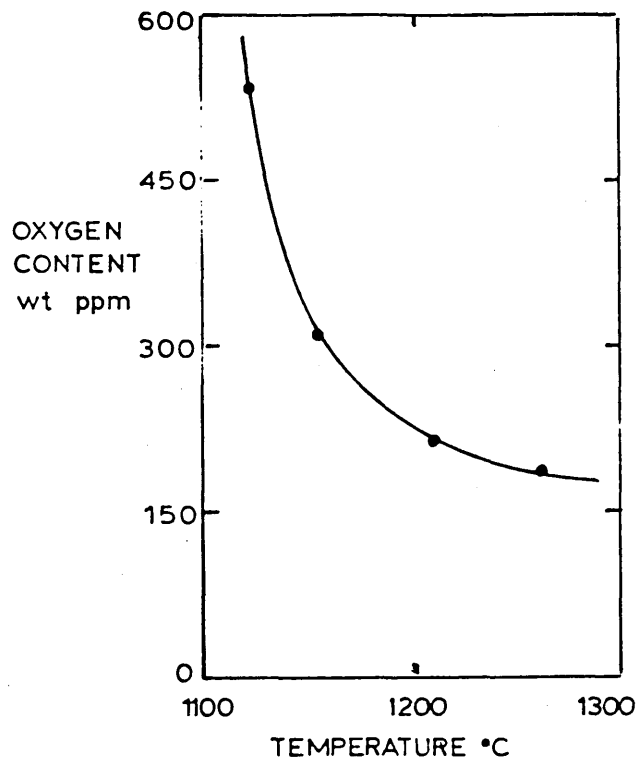
Jominy end quench hardenability data for hot forged steel preforms⁽²⁾

Figure 4



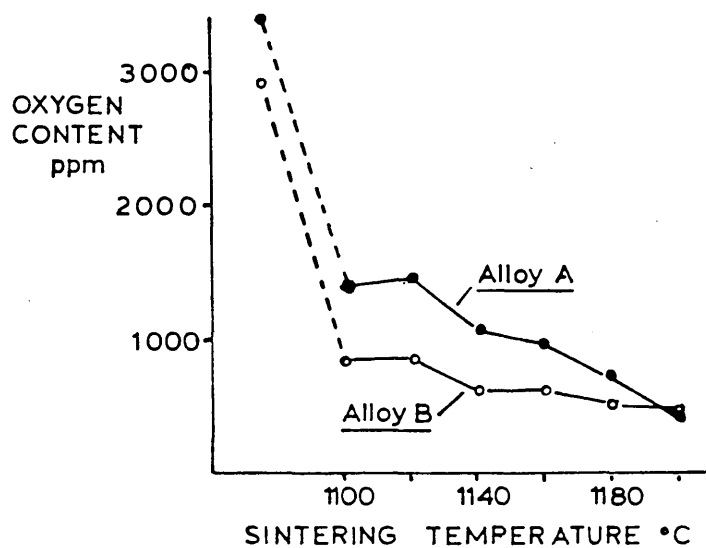
Oxygen Potentials In Oxide Systems

Figure 5



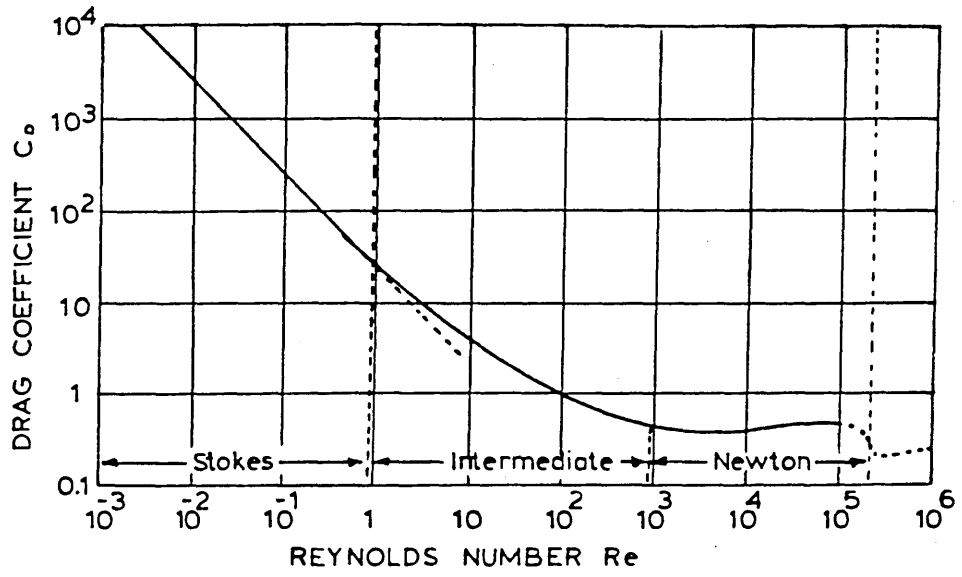
Oxide reduction:
Oxygen content of forged
Fe 0.3C 0.5Ni 0.5Mo blend
decreases as sintering temperature
increases. $t = 60\text{min}^{(2)}$

Figure 6



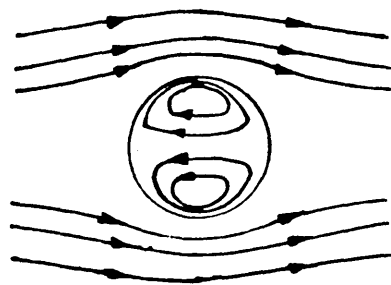
Oxygen content as a function of
sintering temperature.⁽¹⁶⁾
Hydrogen atmosphere.
Alloy A : 1.22% Mn, 0.36% Cr
Alloy B : 0.47% Mn, 0.23% Cr

Figure 7



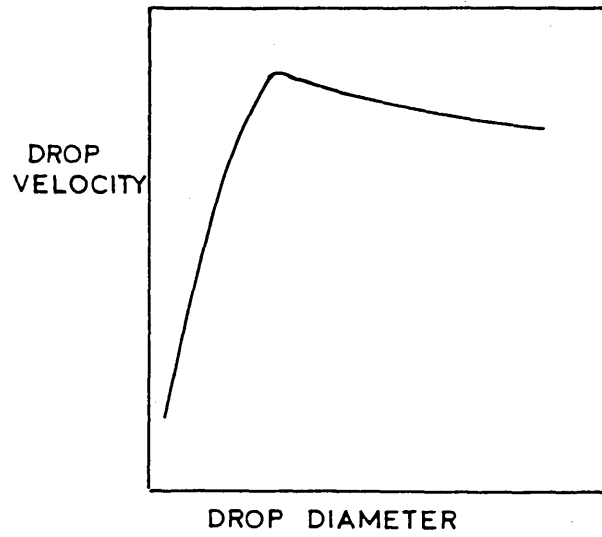
Drag coefficient for spherical particles as a function of Reynolds number.⁽²⁴⁾

Figure 8



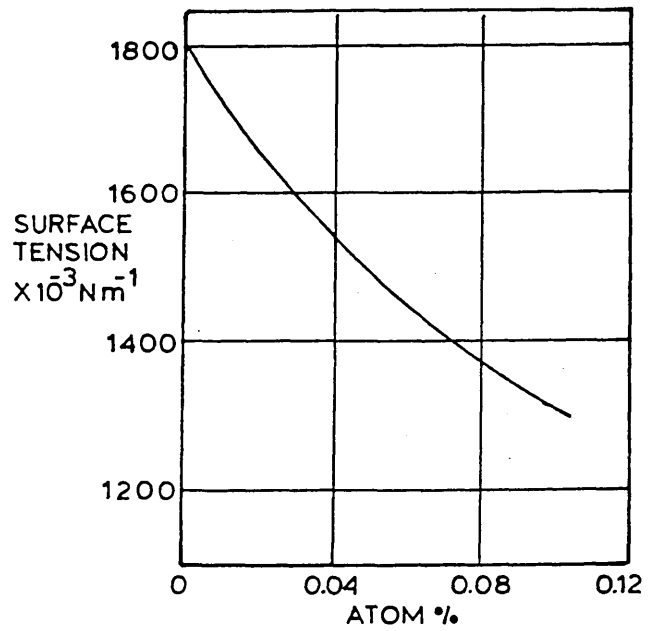
Stream lines around droplets (Rybczynski-Hadamard)⁽²⁹⁾

Figure 9



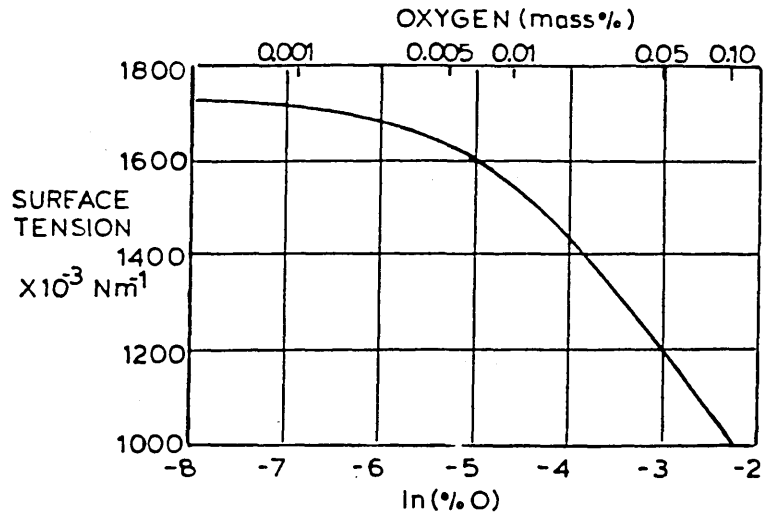
Relationship between Terminal Velocity and Droplet Diameter (24)

Figure 10



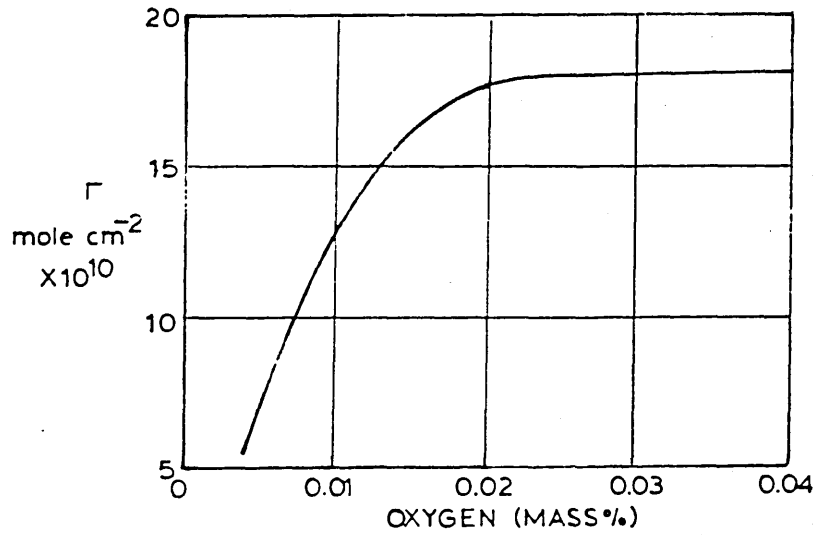
Surface tension for the solution of O in liquid iron at 1550°C. (58)

Figure 11



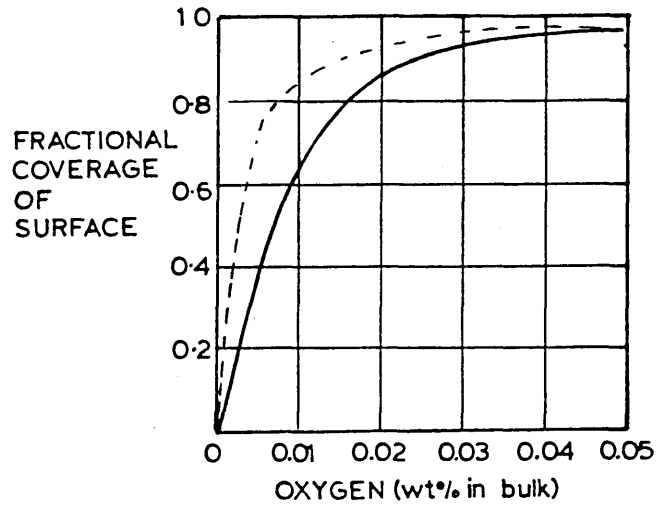
The surface tension of liquid Fe+O solutions at 1550°C. (60)

Figure 12



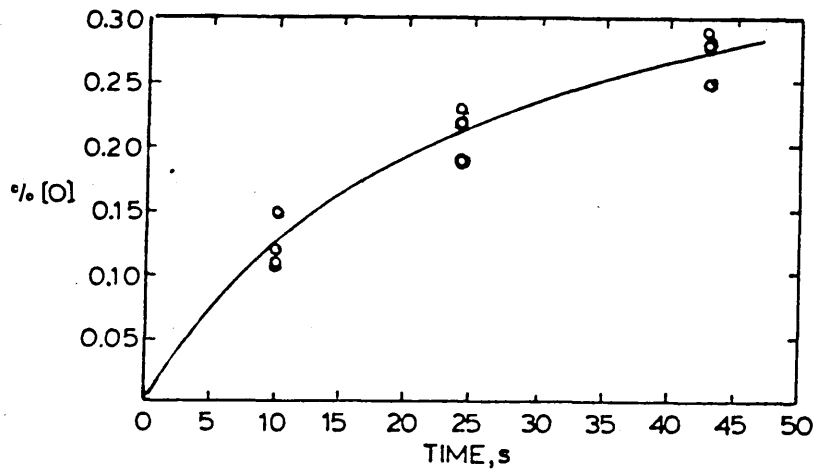
Excess oxygen per unit area of interface for Fe+O solutions at 1550°C. (58)

Figure 13



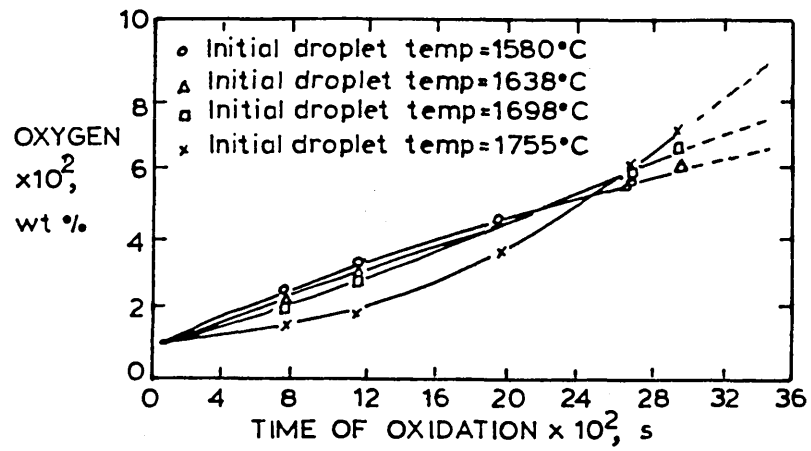
Oxygen absorption isotherm for liquid iron at 1550°C as calculated by Swisher and Turkdogan (60)

Figure 14



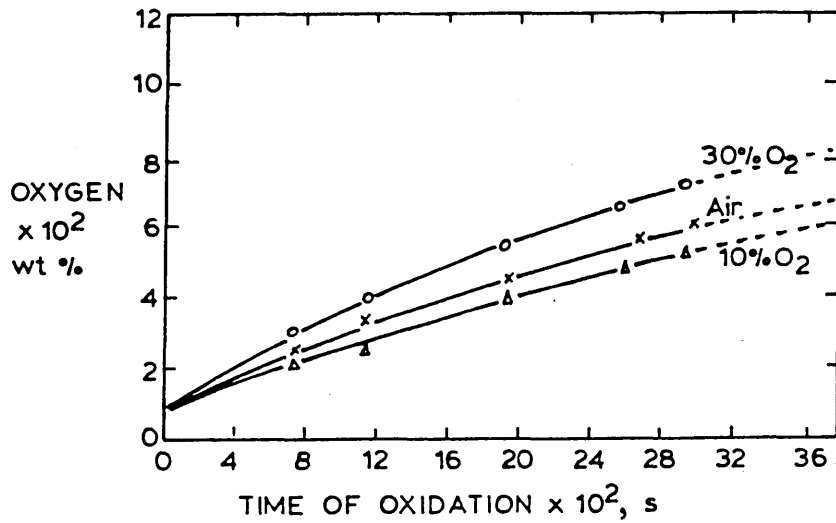
Course of oxidation of 1g specimens of pure iron held in Ar + 25% CO₂ : flowing at 100 cc. min.⁻¹ (66)

Figure 15



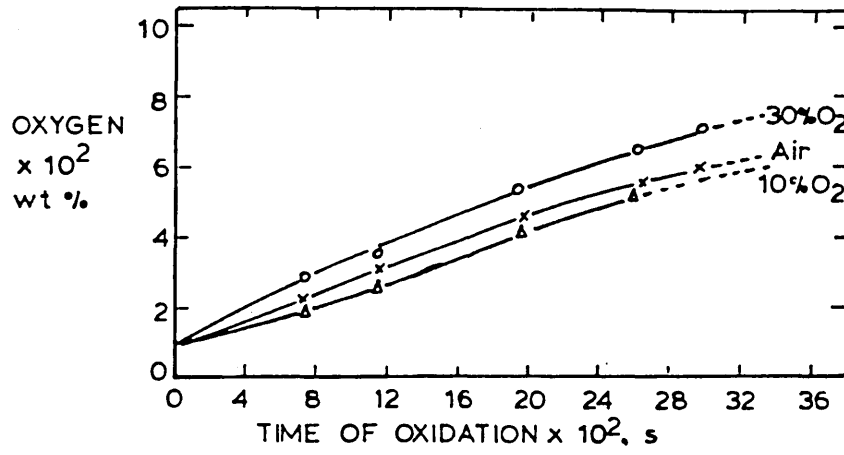
Rate of oxidation in air (68)

Figure 16



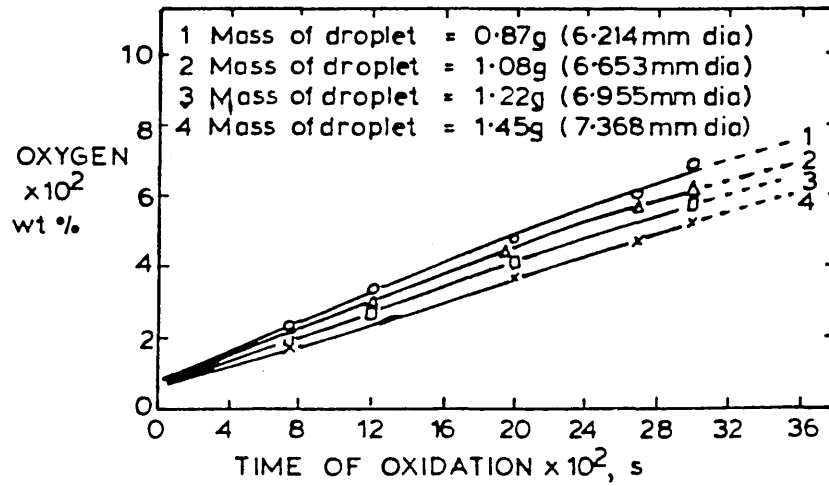
Rate of oxidation at 1580°C (68)

Figure 17



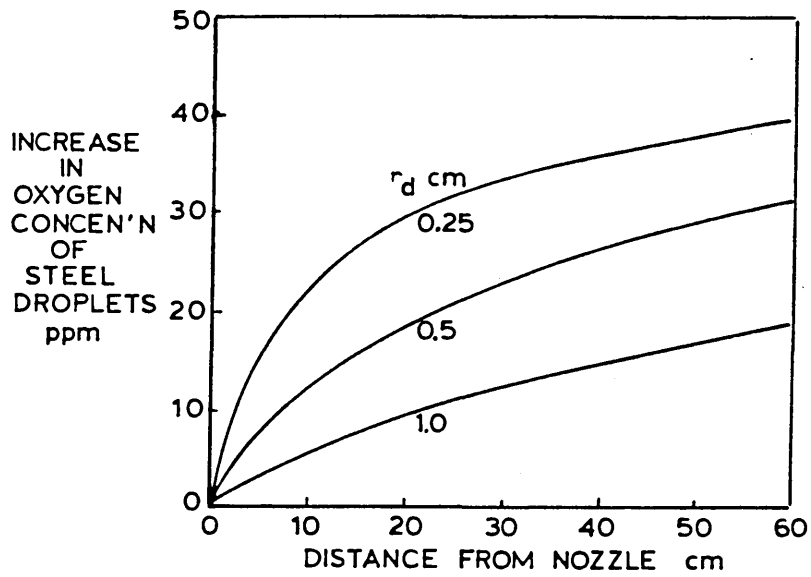
Rate of oxidation at 1638°C (68)

Figure 18



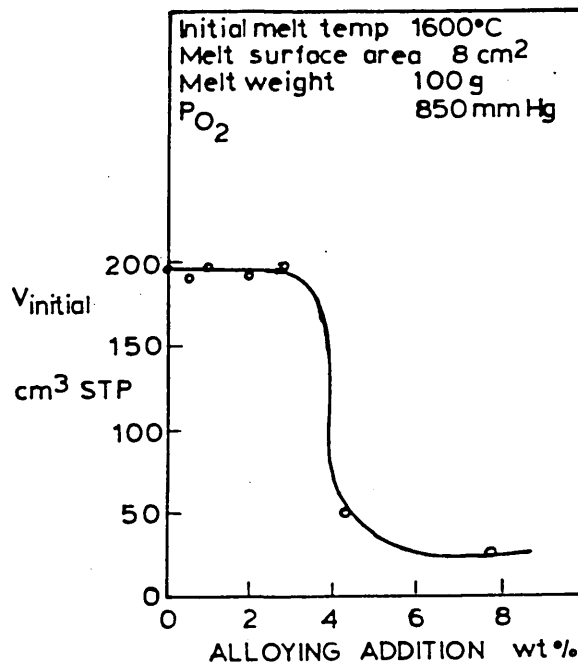
Size effect of oxidation rate in air at 1638°C (68)

Figure 19



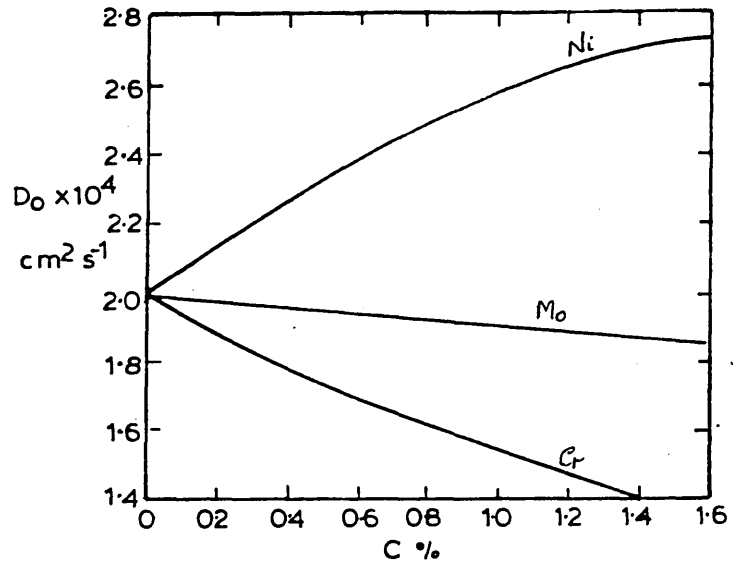
Increase of oxygen concentration in the steel⁽⁶⁹⁾

Figure 20



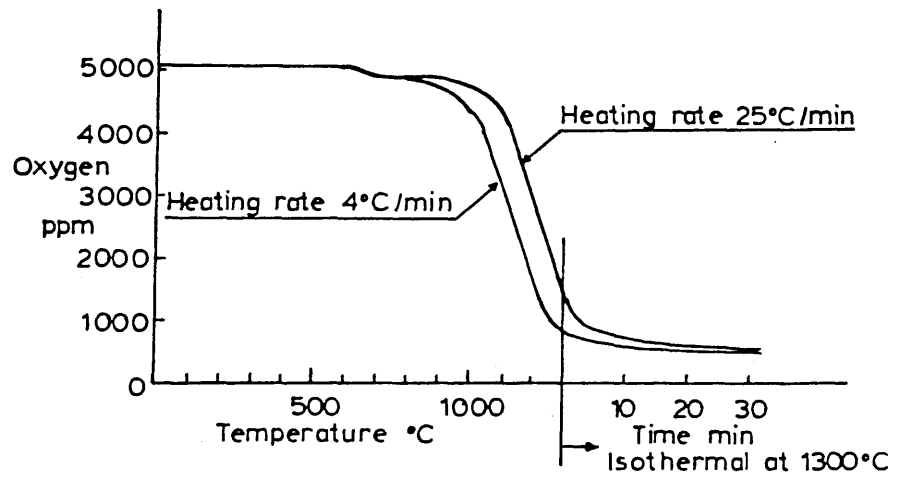
Effect of silicon addition on the initial volume of oxygen taken up by liquid binary iron alloy.⁽⁷¹⁾

Figure 21



Effect of concentration of alloying elements on coefficient of oxygen diffusion in molten iron at 1600°C (80)

Figure 22



Oxygen content calculated from weight change as a function of temperature and time at 1300°C (86)

Power Developed in Levitation Coil as a Function of Rheostat Movement.

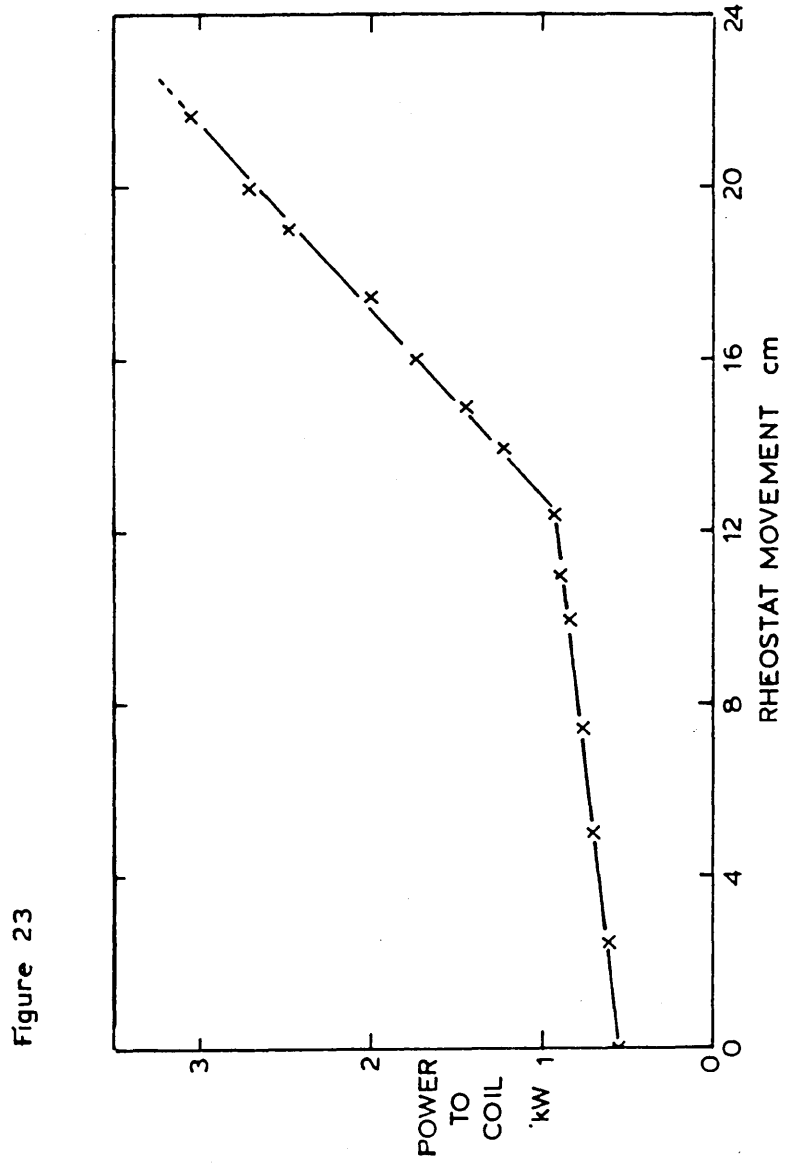
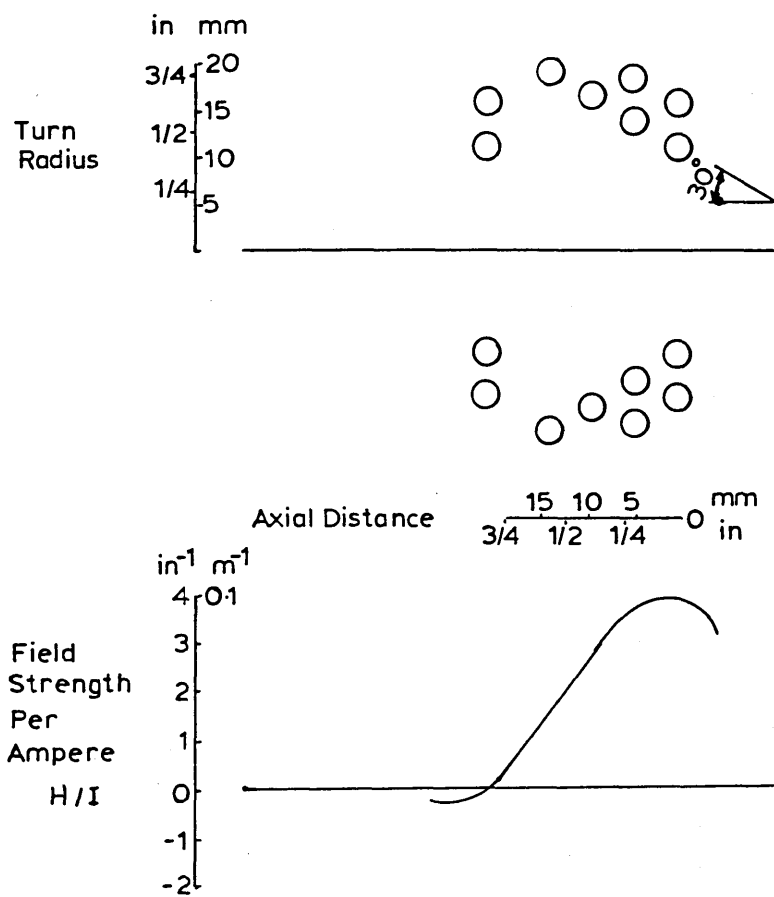


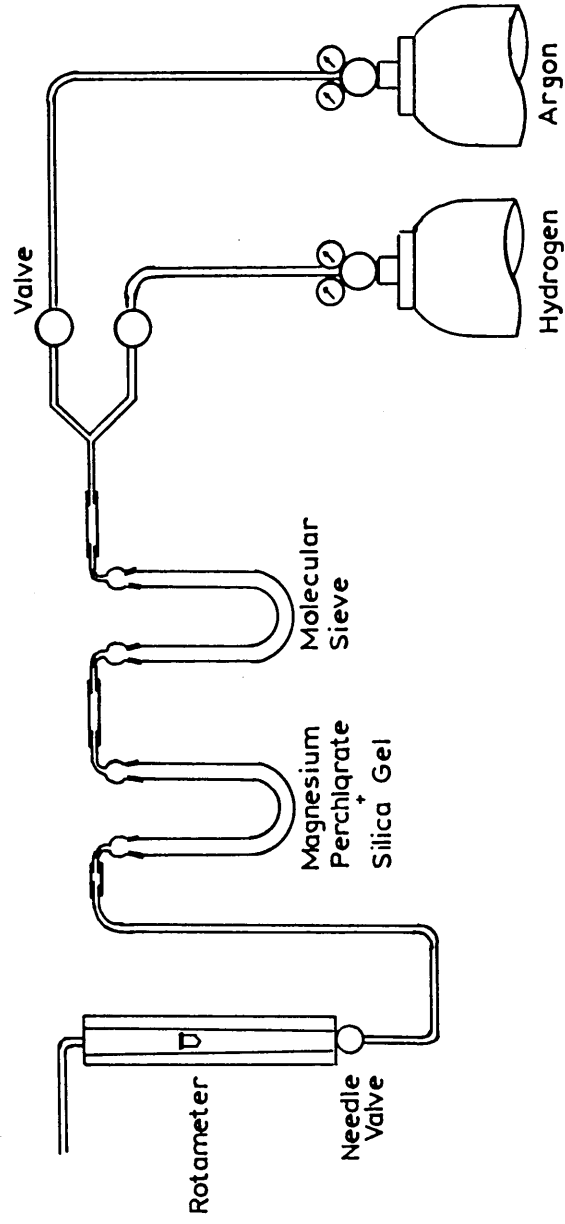
Figure 23

Figure 24



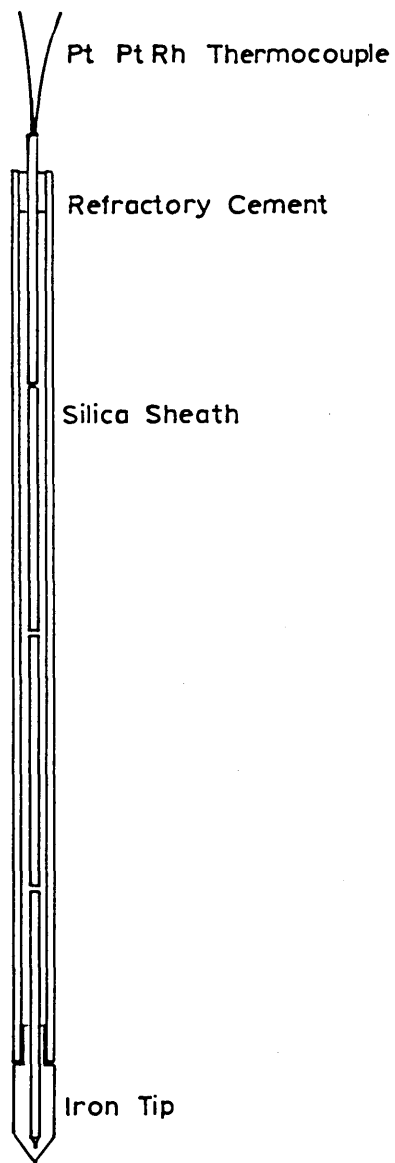
COLL SHAPE AND FIELD STRENGTH

Figure 25



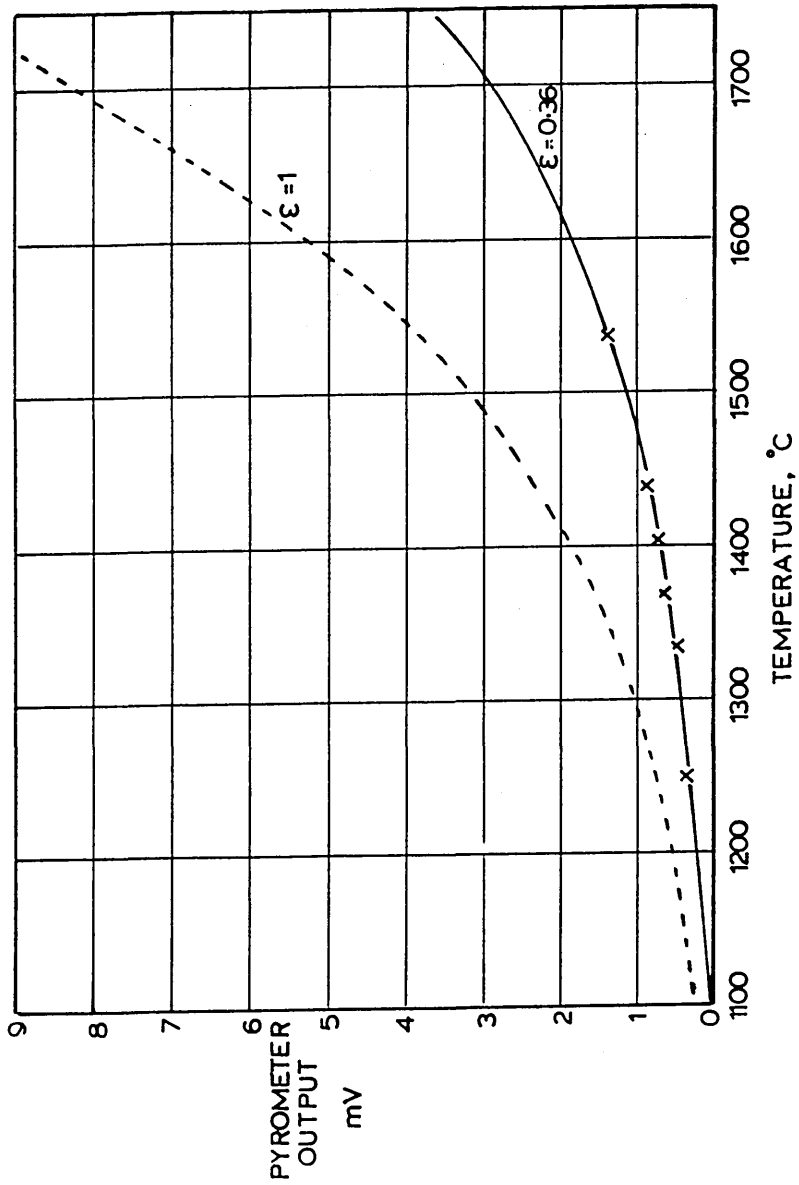
Gas Purification Train.

Figure 26



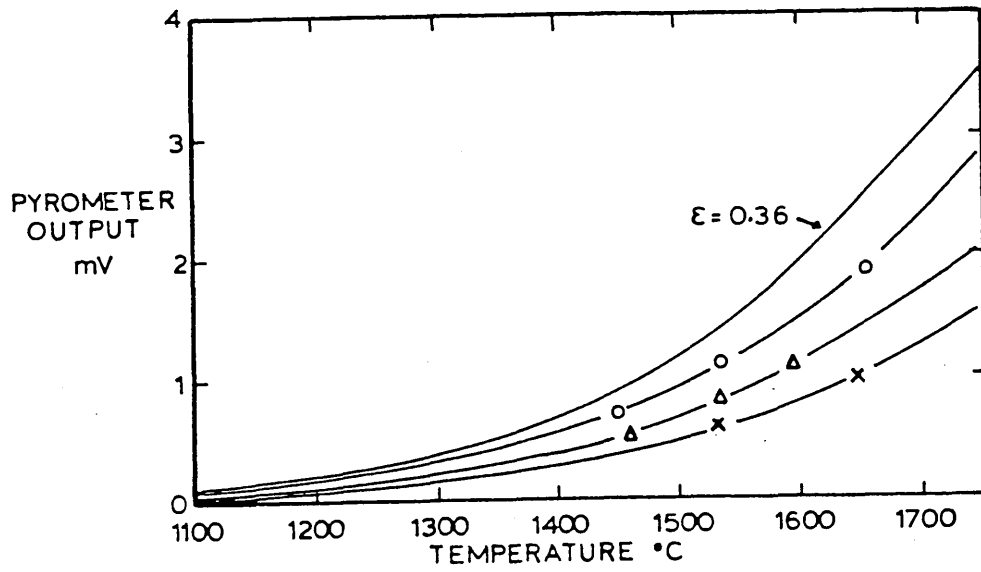
Temperature Probe.

Figure 27



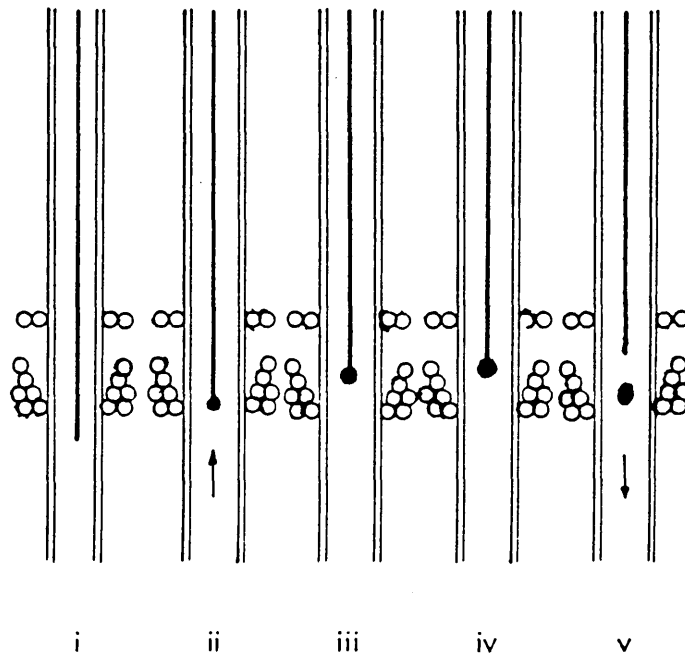
Pyrometer Output versus Temperature for Pure Iron.

Figure 28



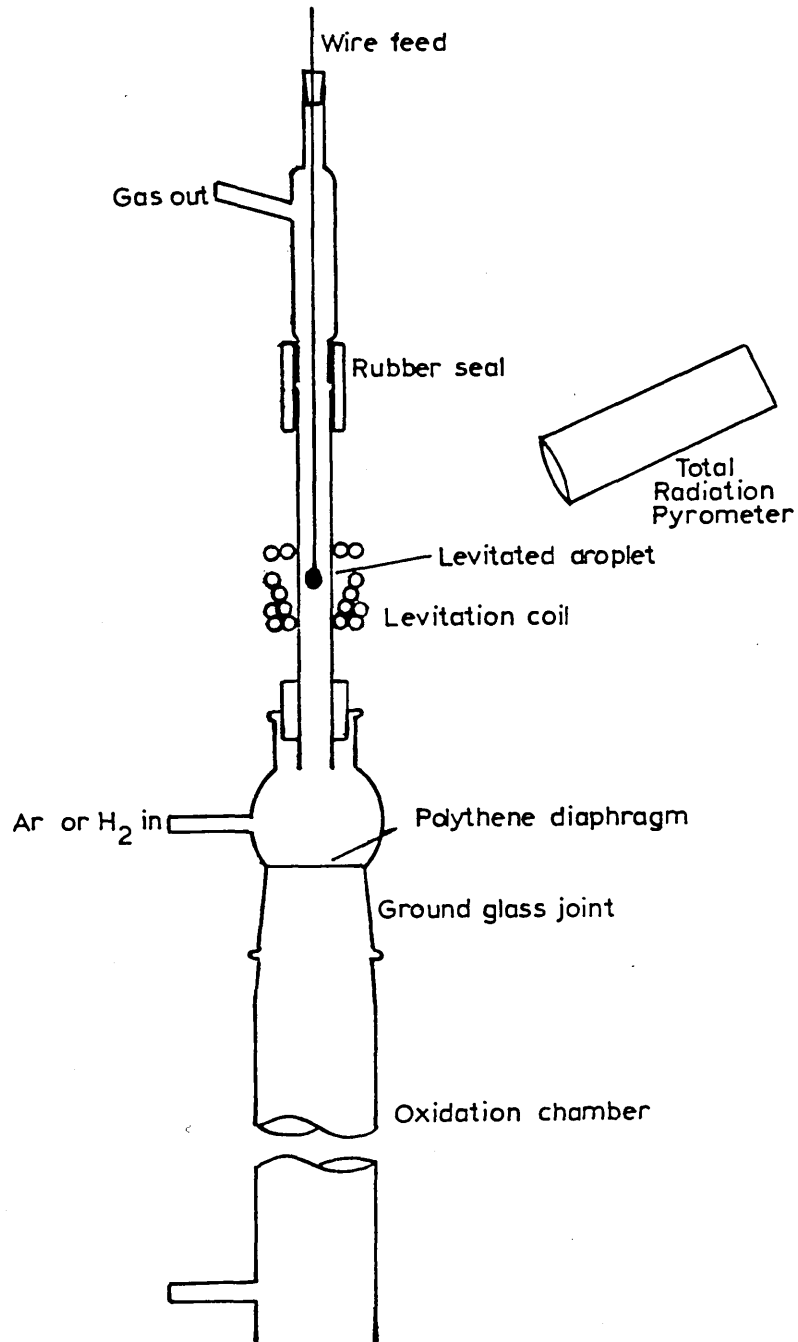
Pyrometer Output vs Temperature for Different Emissive Conditions

Figure 29



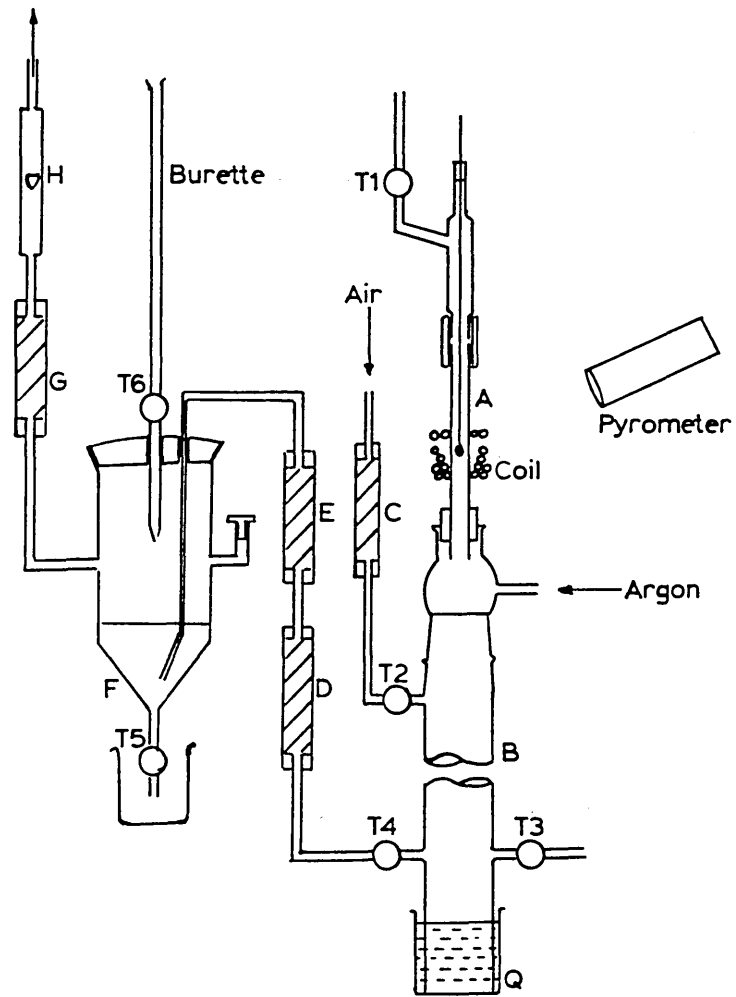
Stages in the Generation of a Droplet from Wire.

Figure 30



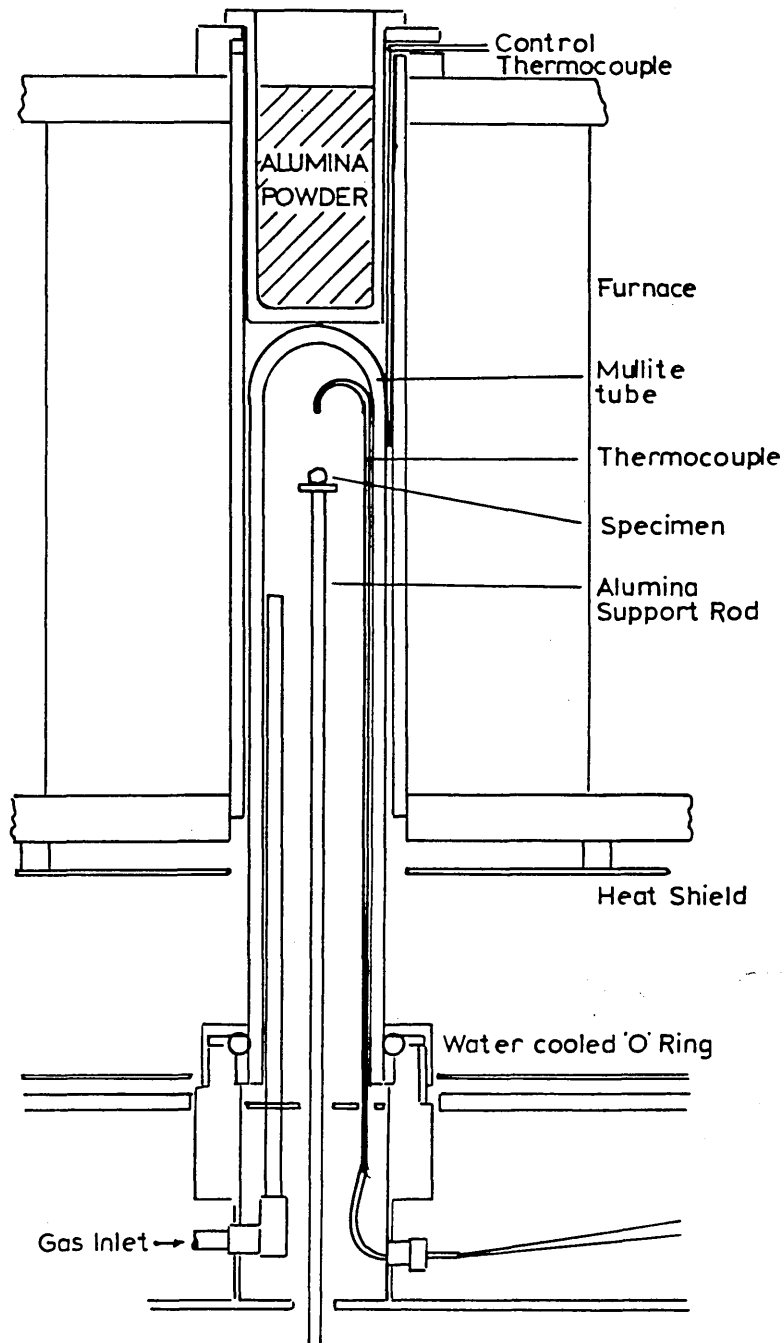
EXPERIMENTAL APPARATUS

Figure 31



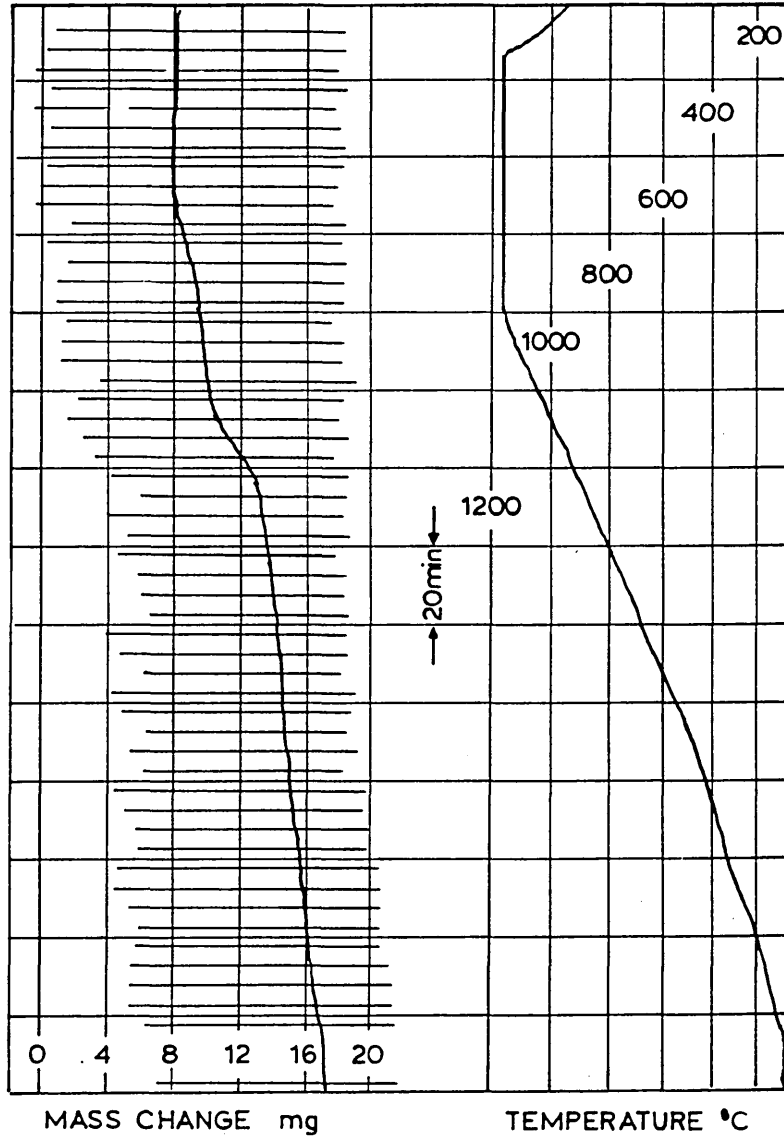
Equipment to Study Iron Droplet - Quench Medium Interactions.

Figure 32



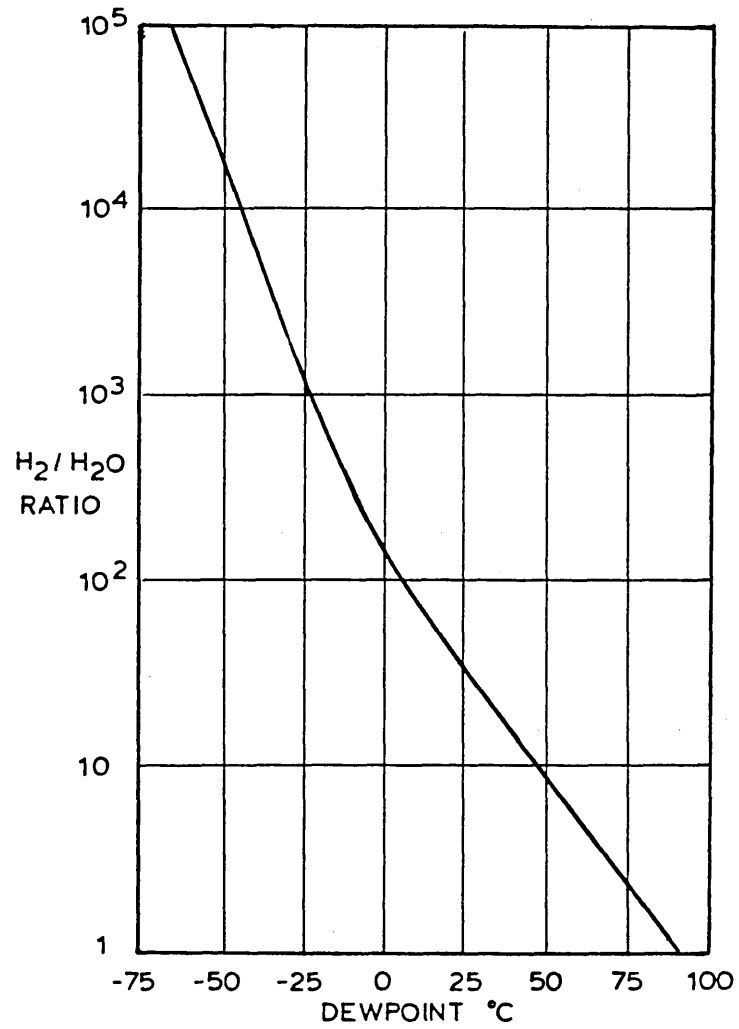
STANTON MASSFLOW THERMOBALANCE

Figure 33



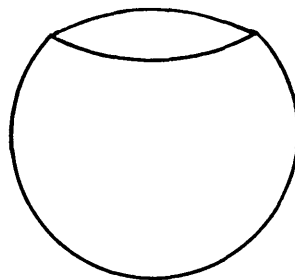
The Massflow Balance Chart.

Figure 34



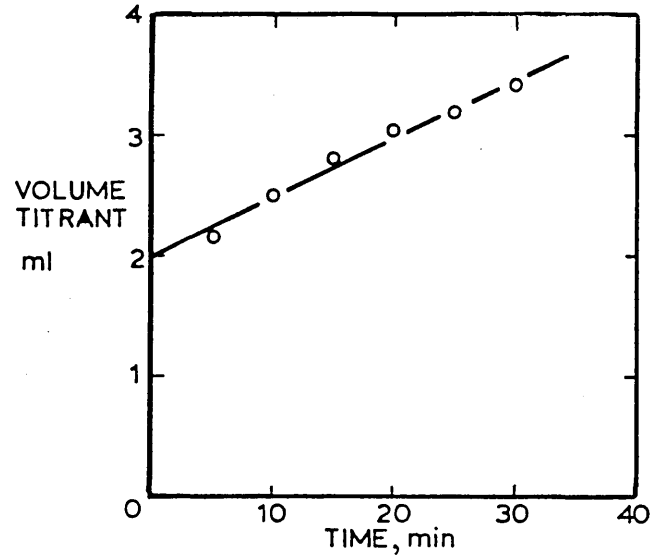
Relation Between Dew Point and H₂/H₂O Ratio

Figure 35



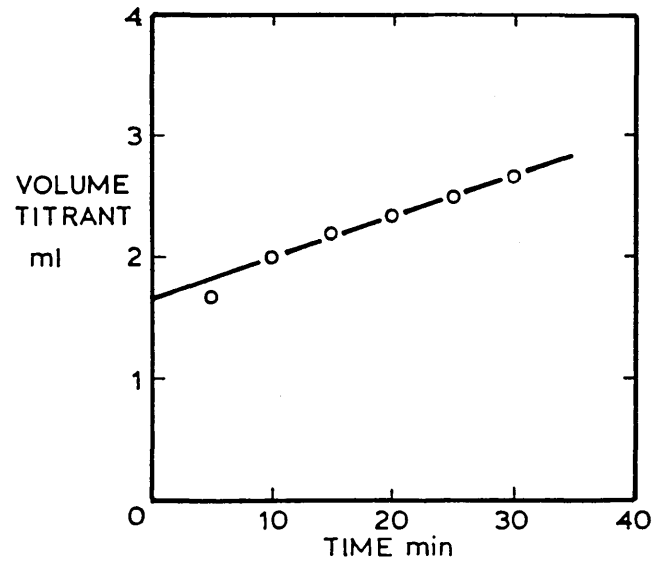
Droplet Chord Section

Figure 36



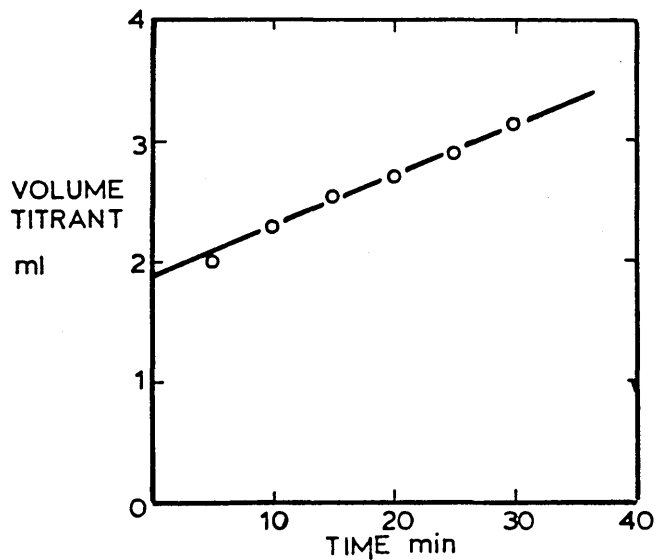
Volume of Titrant added with Time
Sample 1 (Invoil 30)

Figure 37



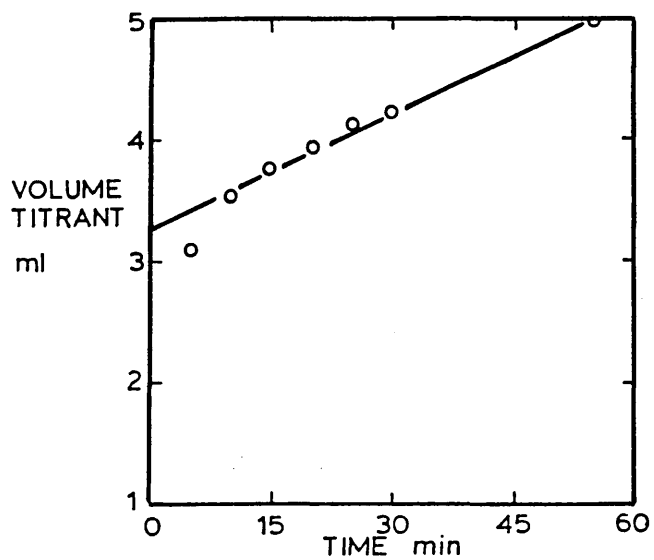
Volume of Titrant added with Time
Sample 2 (Invoil 30)

Figure 38



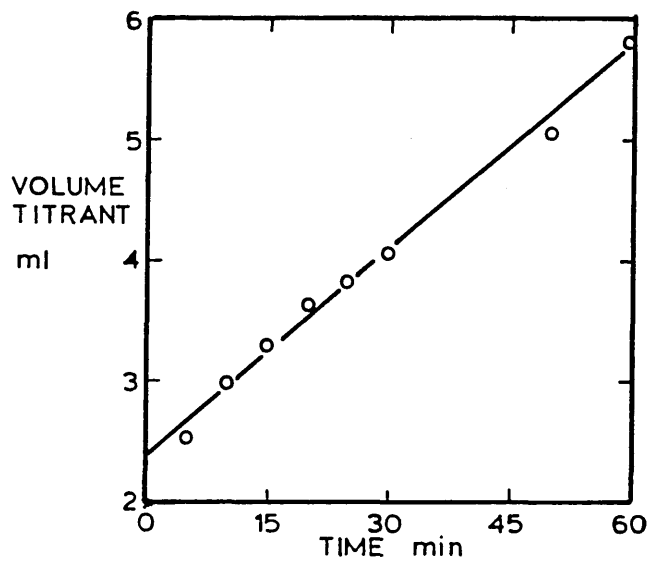
Volume of Titrant added with time
Sample 3 (Invoil 30)

Figure 39



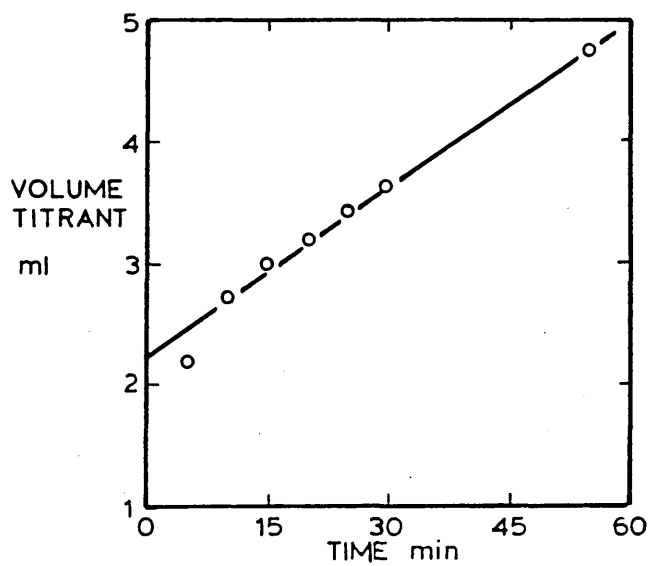
Volume of Titrant added with Time
Sample 4 (Invoil 30)

Figure 40



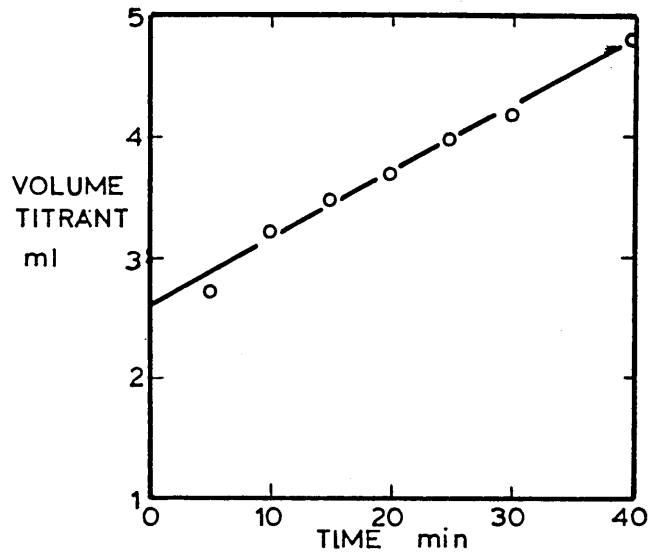
Volume of Titrant added with Time
Sample 5 (Invoil 30)

Figure 41



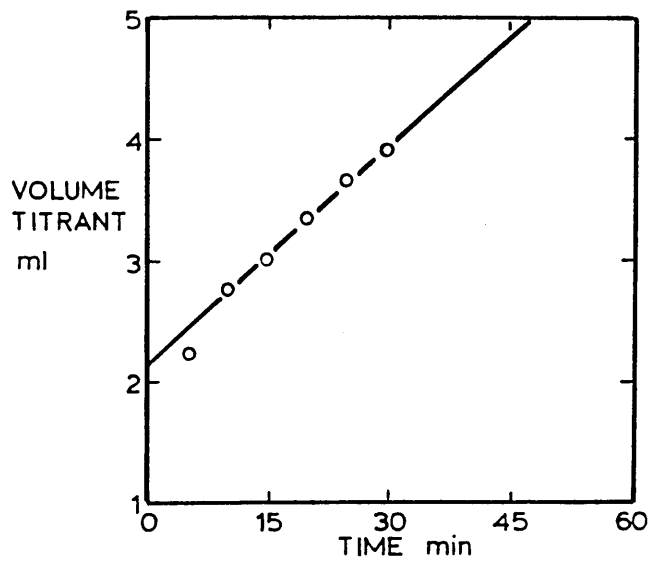
Volume of Titrant added with Time
Sample 6 (Paraffin oil)

Figure 42



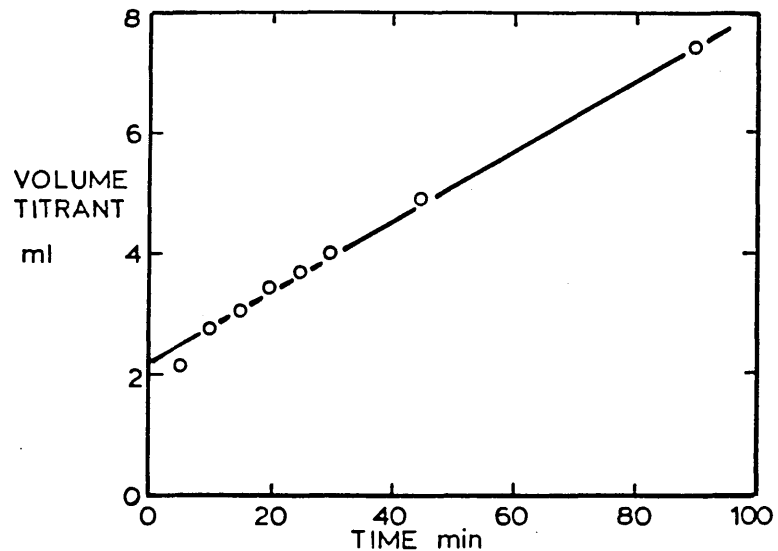
Volume of Titrant added with Time
Sample 7 (Paraffin oil)

Figure 43



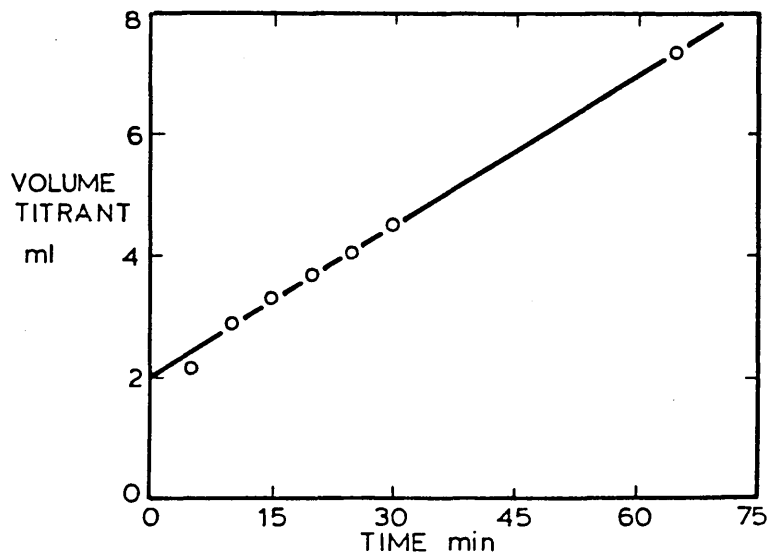
Volume of Titrant added with Time
Sample 8 (Paraffin oil)

Figure 44



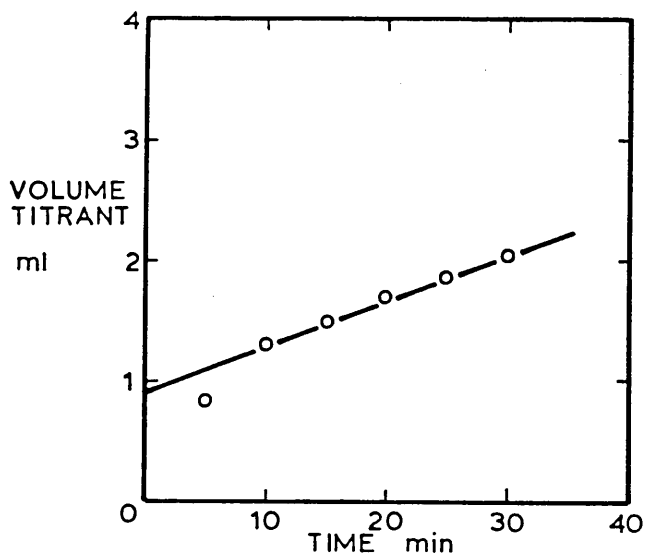
Volume of Titrant added with Time
Sample 9 (Paraffin oil)

Figure 45



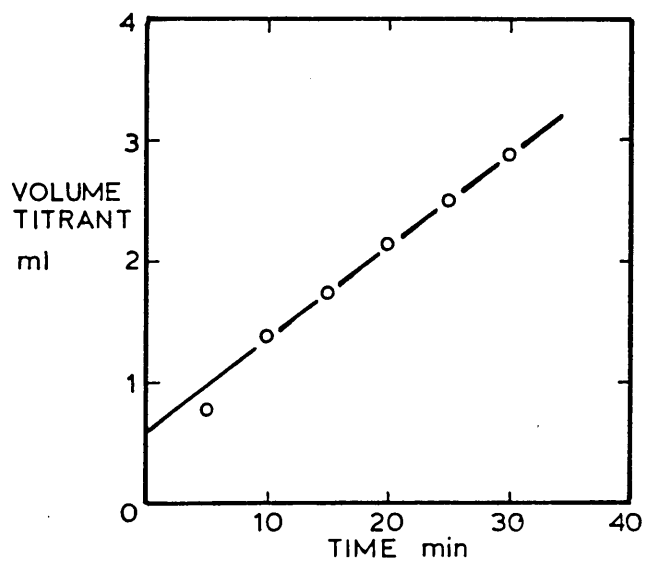
Volume of Titrant added with Time
Sample 10 (Paraffin oil)

Figure 46



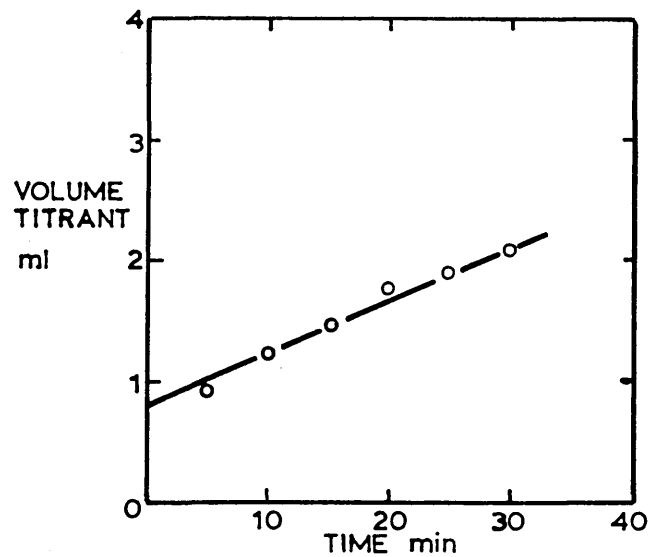
Volume of Titrant added with Time
Sample 11 (Silicone oil)

Figure 47



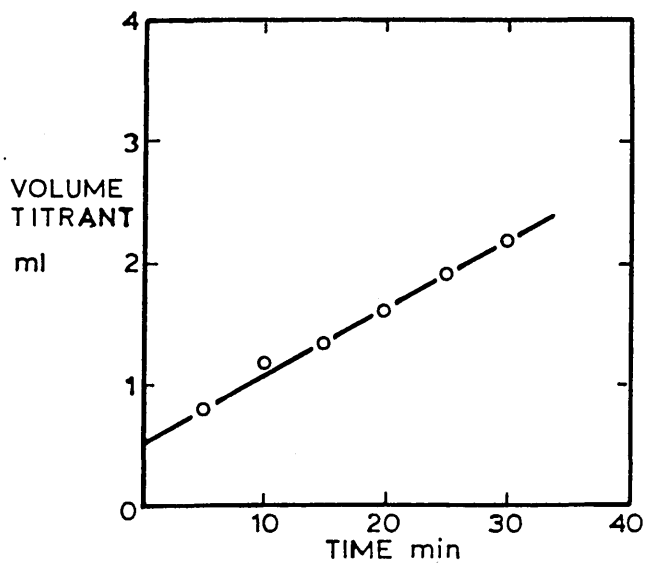
Volume of Titrant added with Time
Sample 12 (Silicone oil)

Figure 48



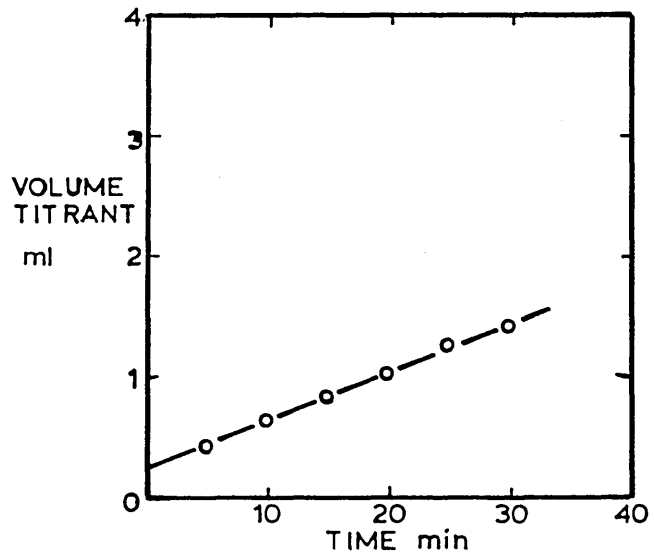
Volume of Titrant added with Time
Sample 13 (Silicone oil)

Figure 49



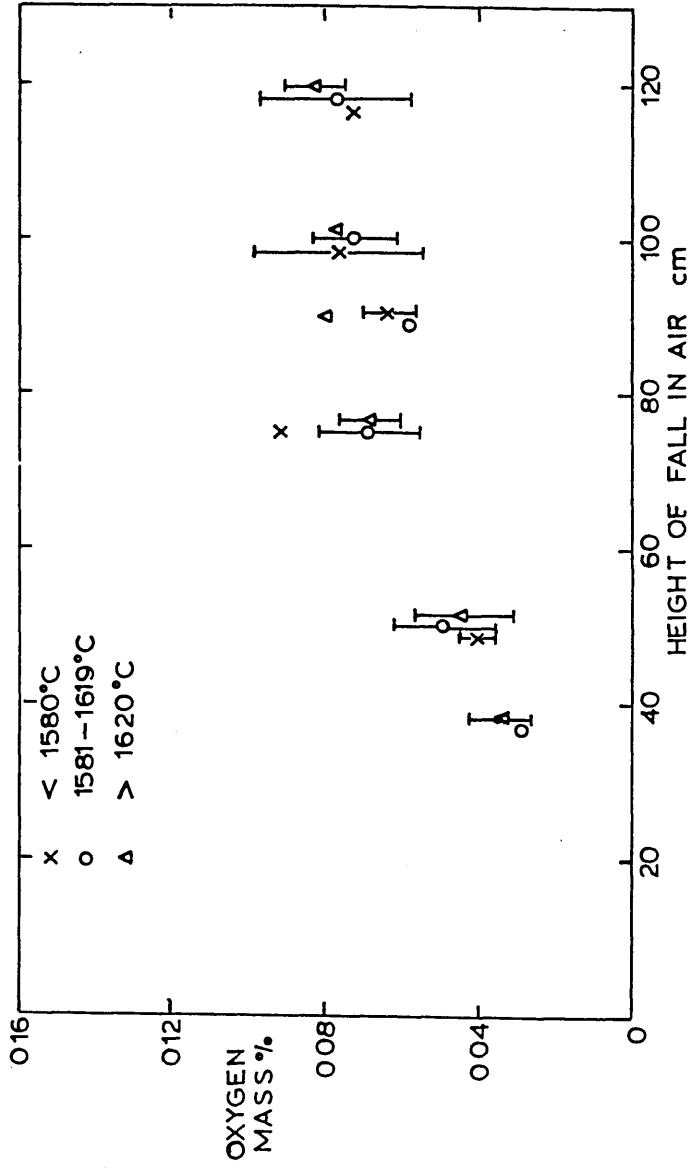
Volume of Titrant added with Time
Sample 14 (Silicone oil)

Figure 50



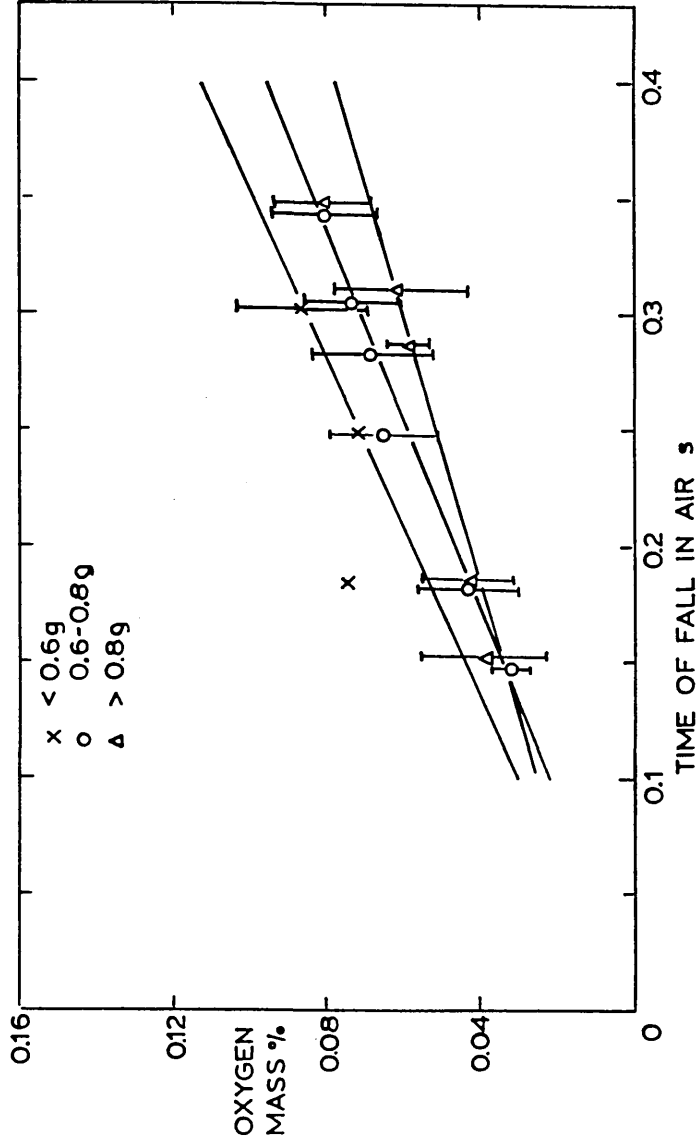
Volume of Titrant added with Time
Sample 15 (Silicone oil)

Figure 51



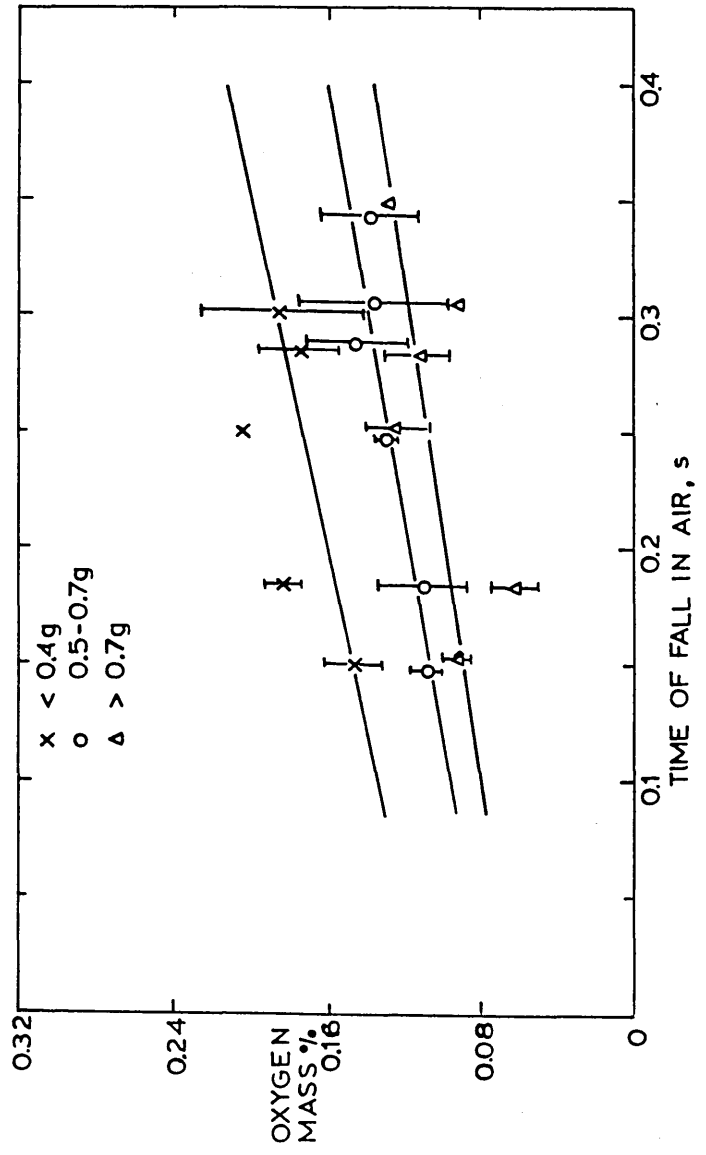
The Effect of Droplet Temperature on Oxygen Pick-up (Iron)

Figure 52



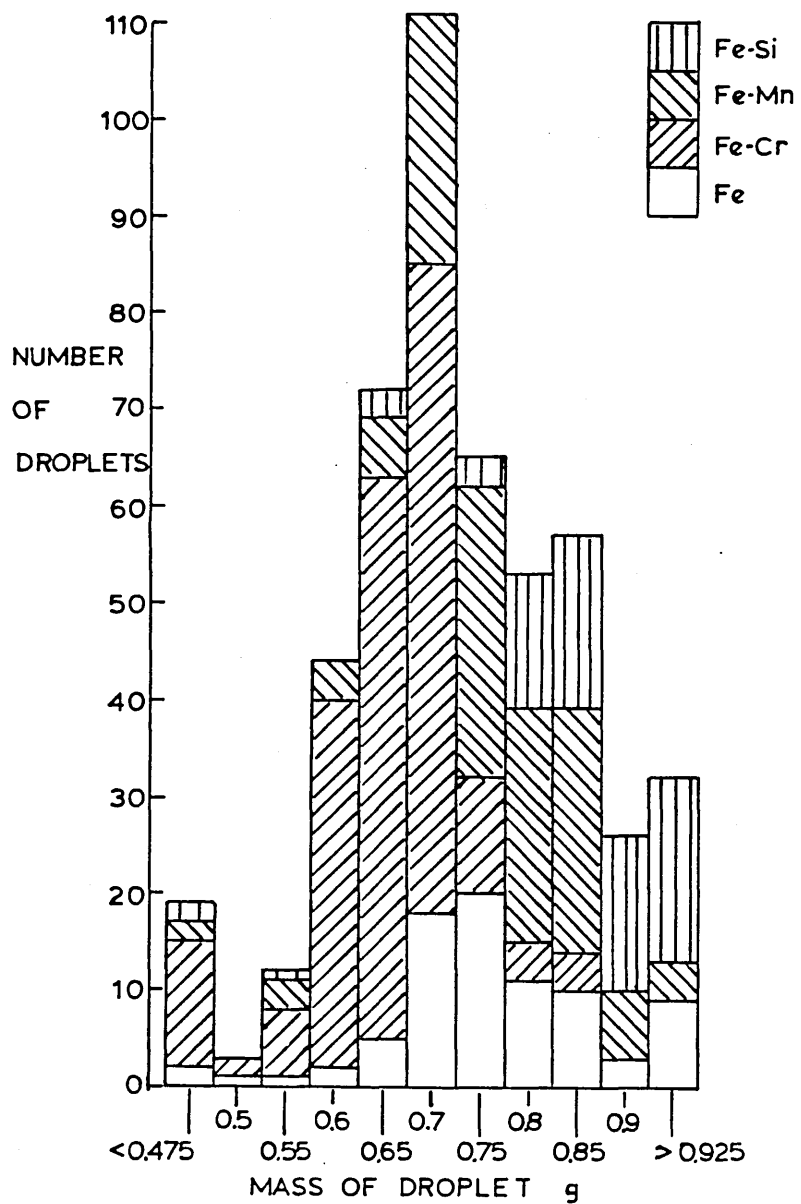
Effect of Size of Droplet on Oxygen Pick up (Iron)

Figure 53



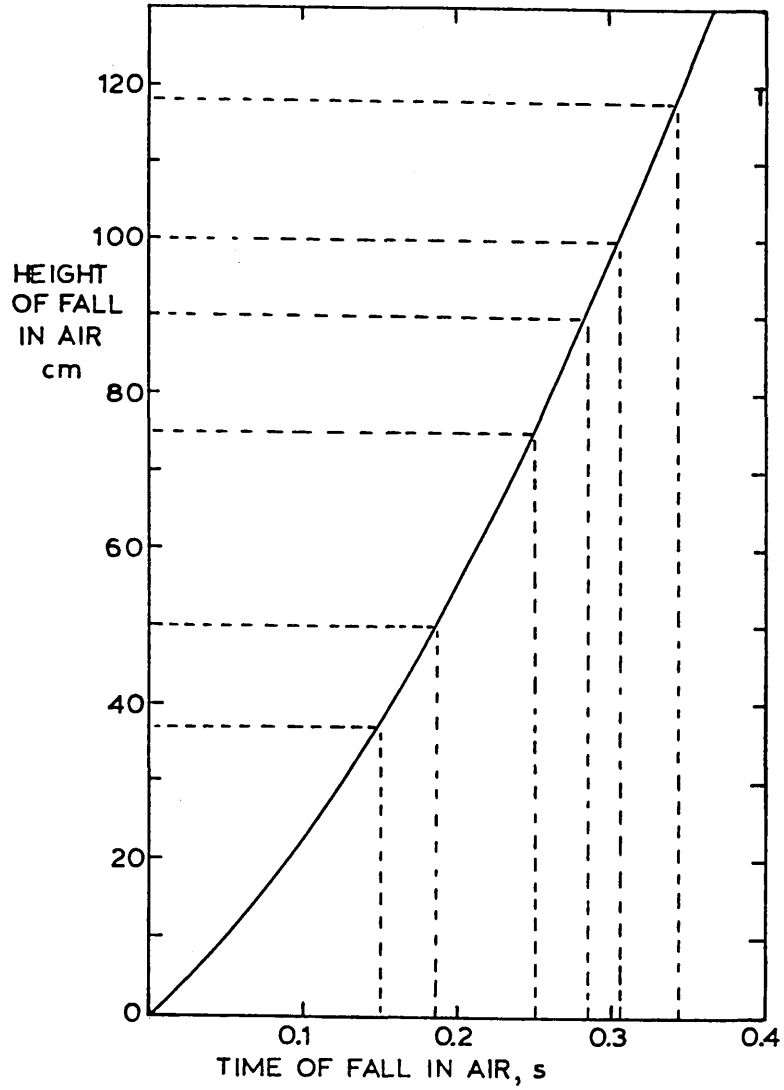
Effect of Size of Droplet on Oxygen Pick up (Fe-0.25%Cr)

Figure 54



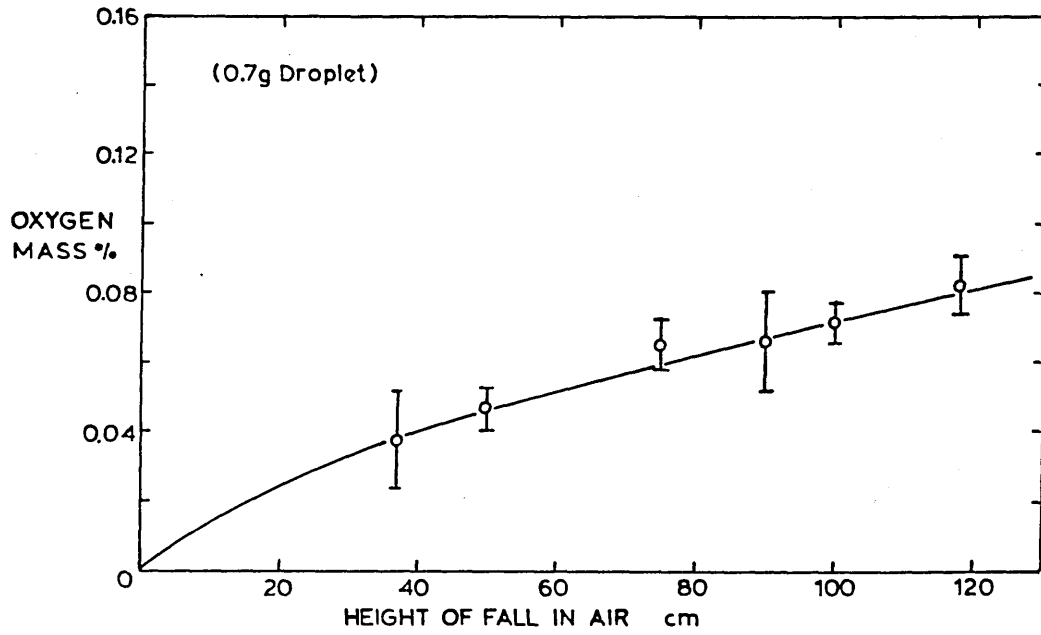
The Distribution of Droplet Sizes

Figure 55



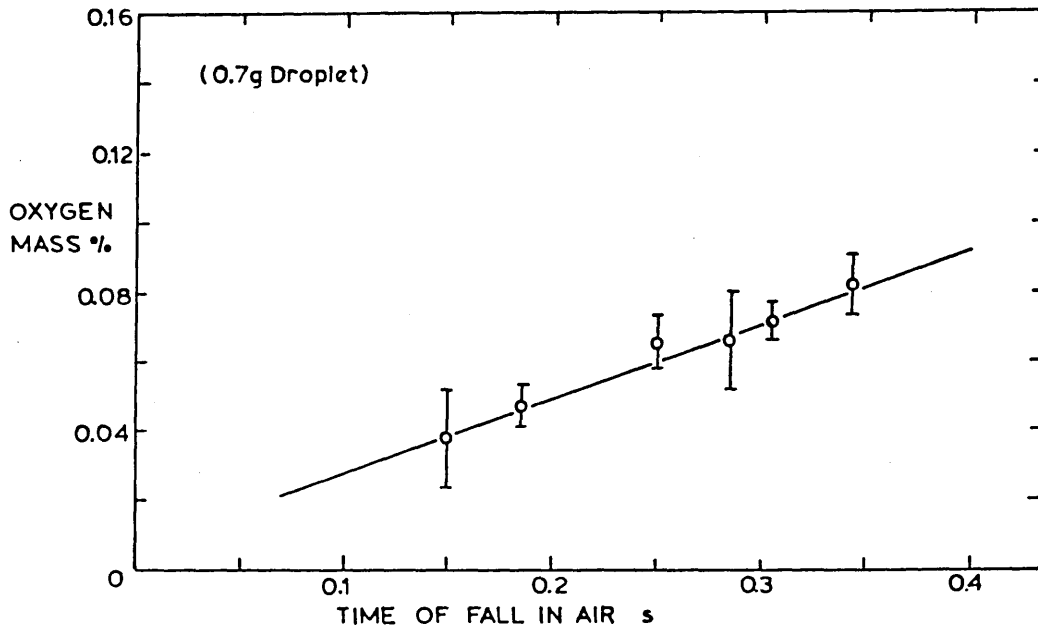
Height of fall vs Time of fall in air for 0.7g Droplet Under the Experimental Conditions.

Figure 56



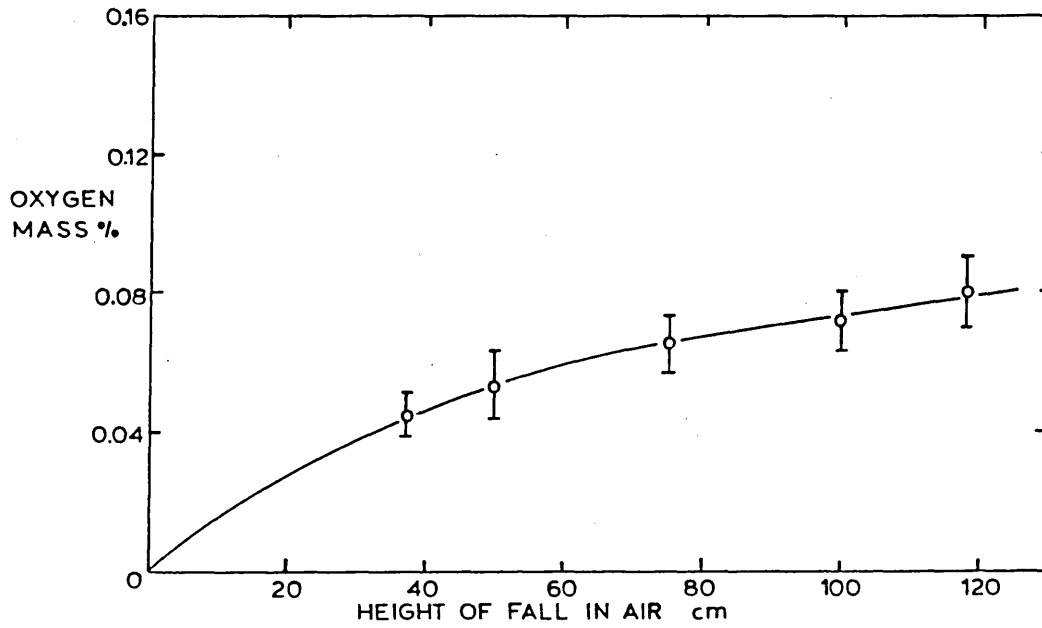
The Oxidation of Iron at 1600°C

Figure 57



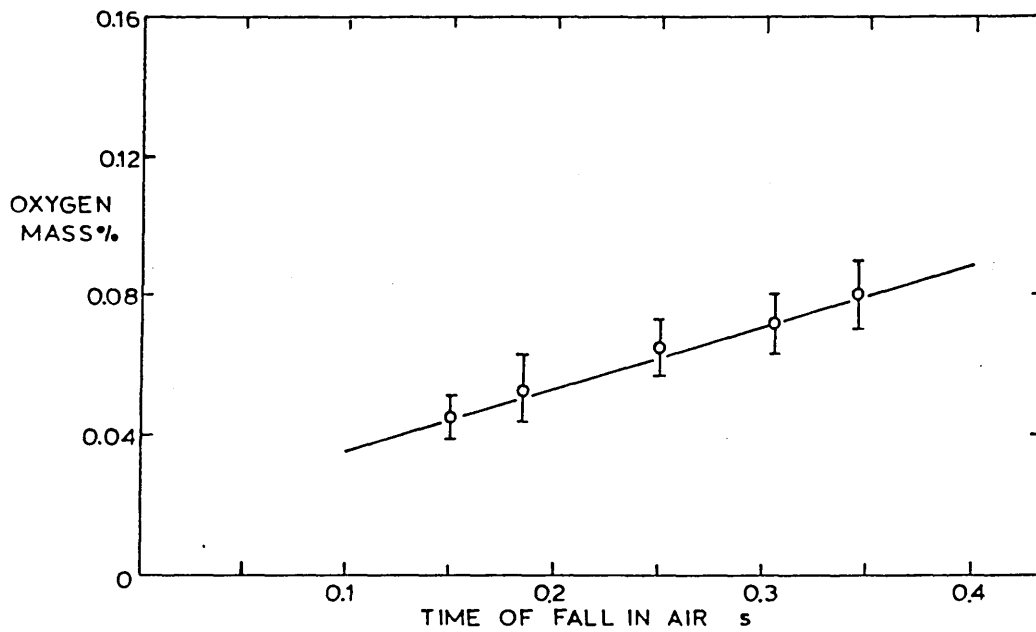
The Rate of Oxidation of Iron at 1600°C

Figure 58



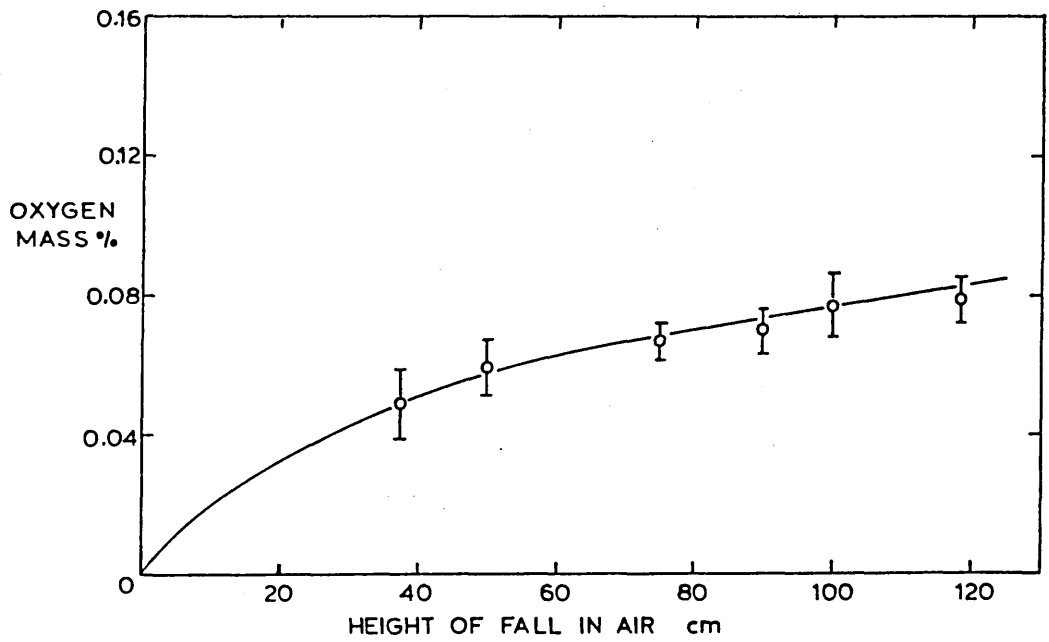
The Oxidation of Fe-0.5% Mn Droplets at 1600°C

Figure 59



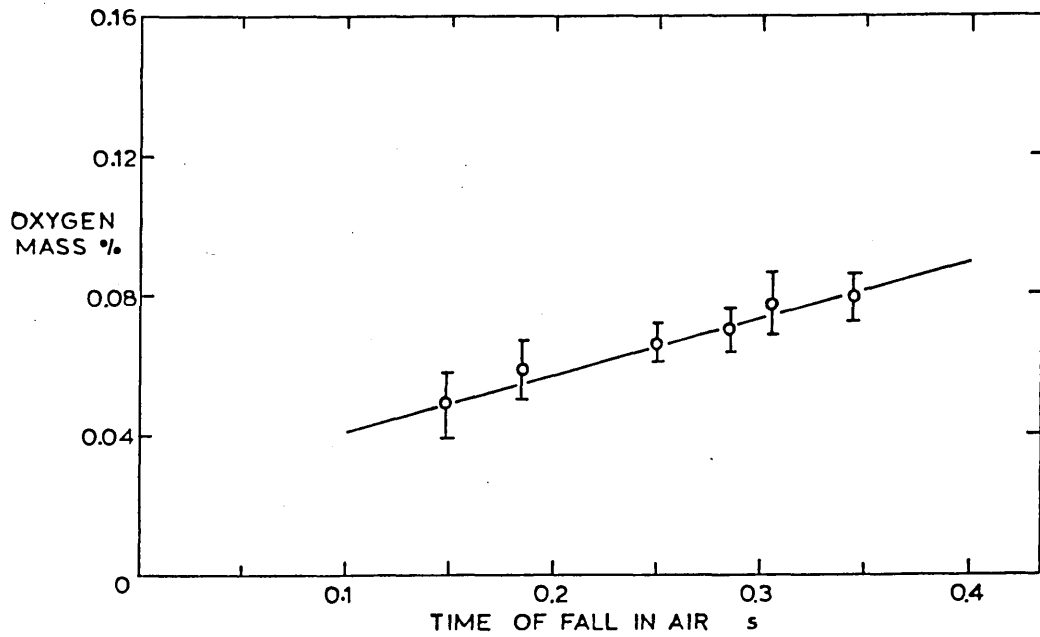
The Rate of Oxidation of Fe-0.5% Mn Droplets at 1600°C

Figure 60



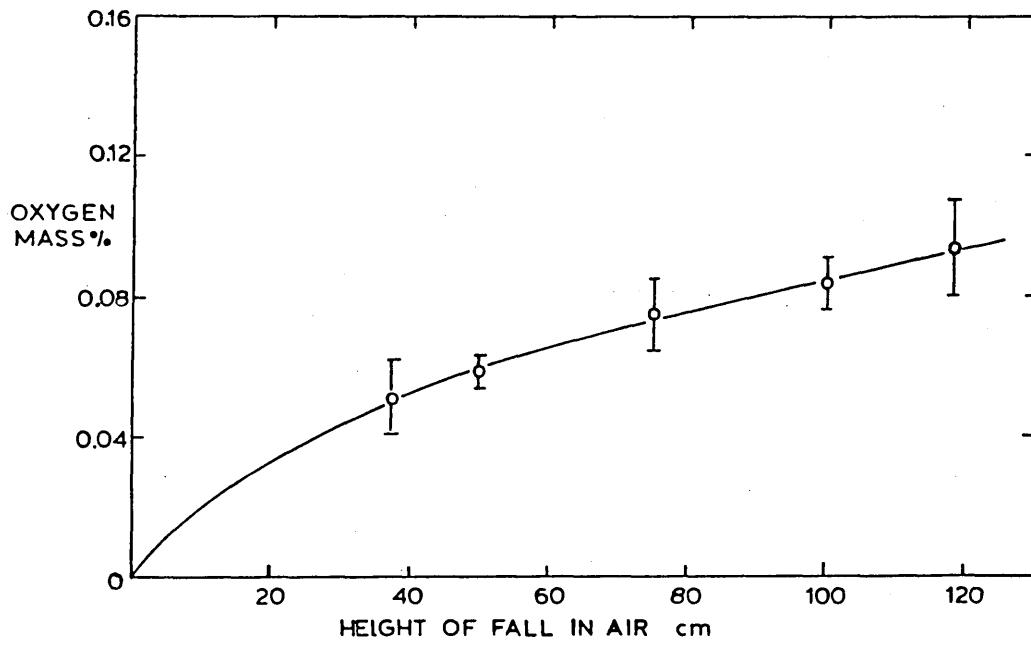
The Oxidation of Fe-0.7% Mn Droplets at 1600°C

Figure 61



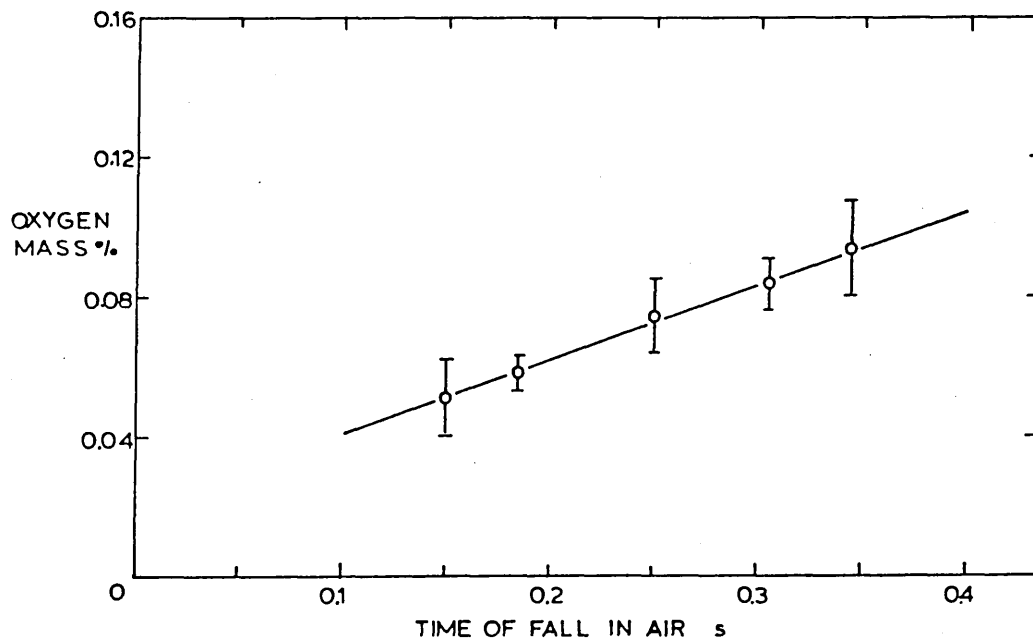
The Rate of Oxidation of Fe-0.7% Mn Droplets at 1600°C

Figure 62



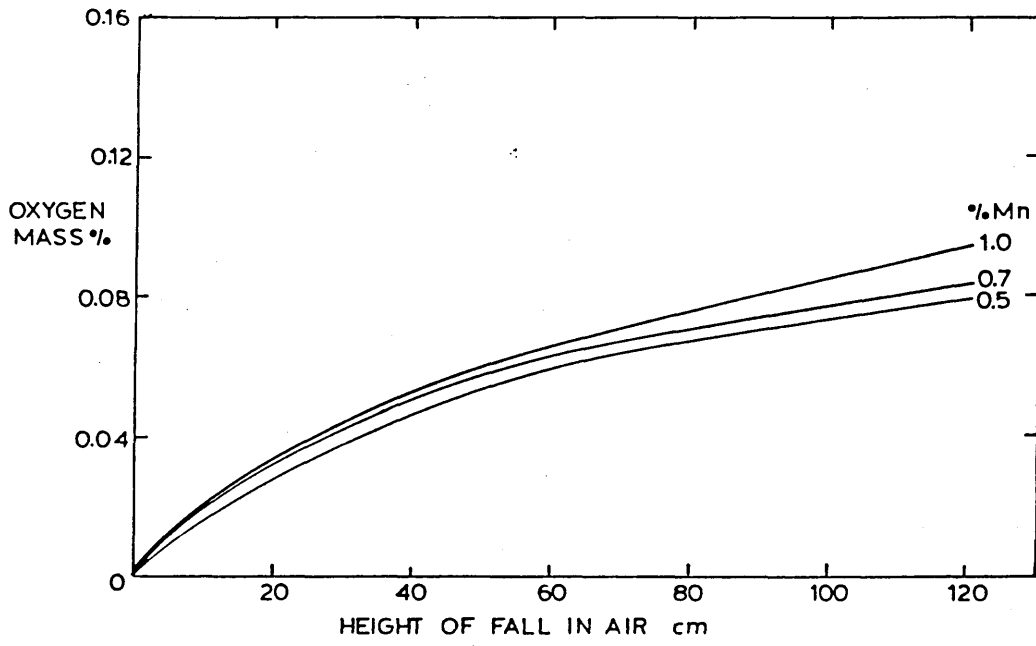
The Oxidation of Fe-1.0%Mn Droplets at 1600°C

Figure 63



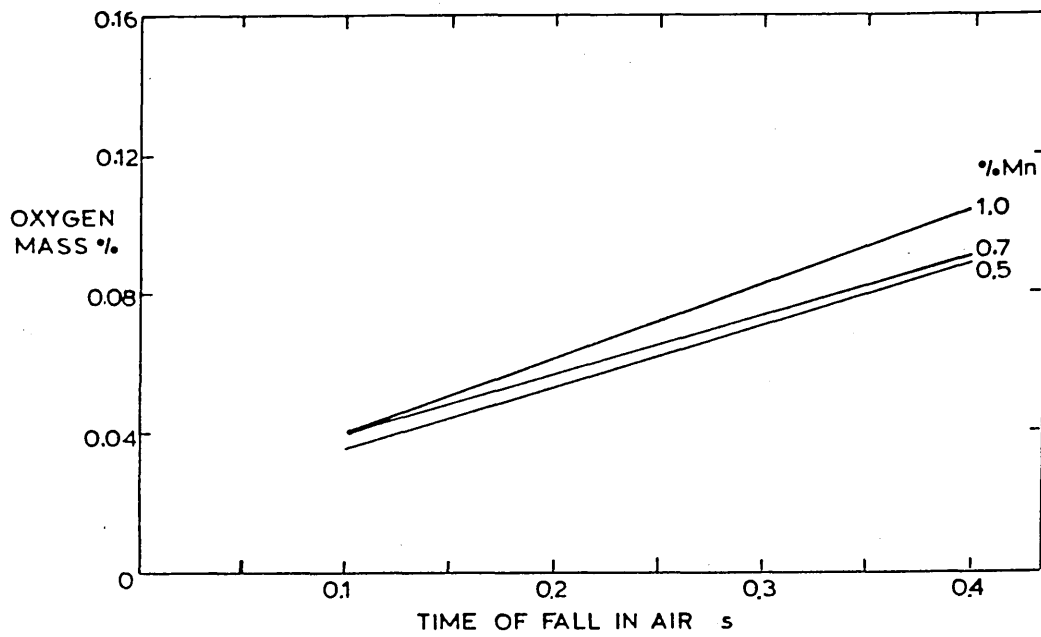
The Rate of Oxidation of Fe-1.0%Mn Droplets at 1600°C

Figure 64



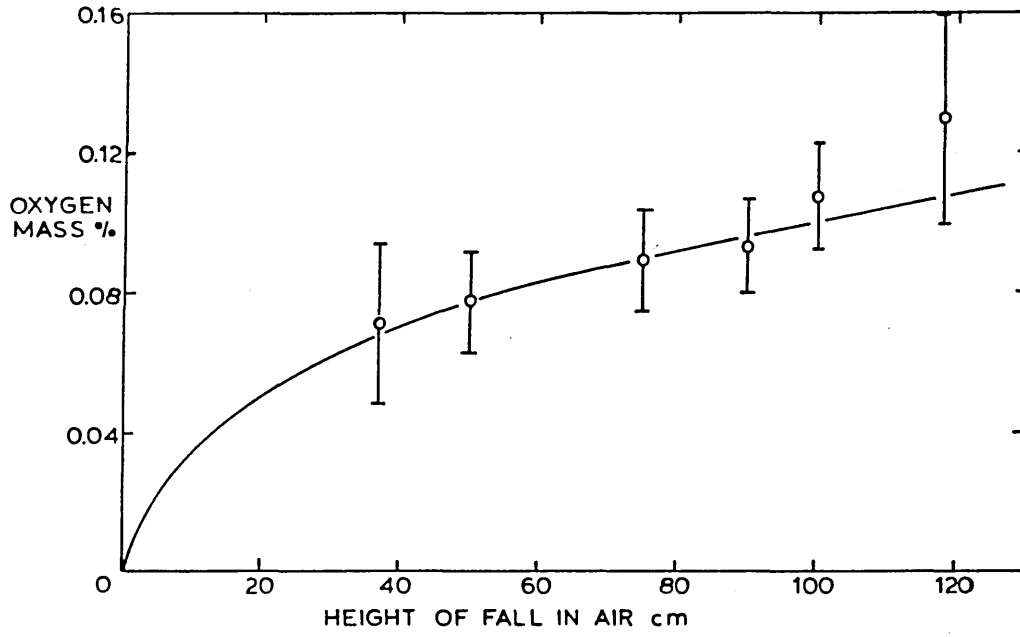
The Oxidation of Fe-Mn Droplets at 1600°C

Figure 65



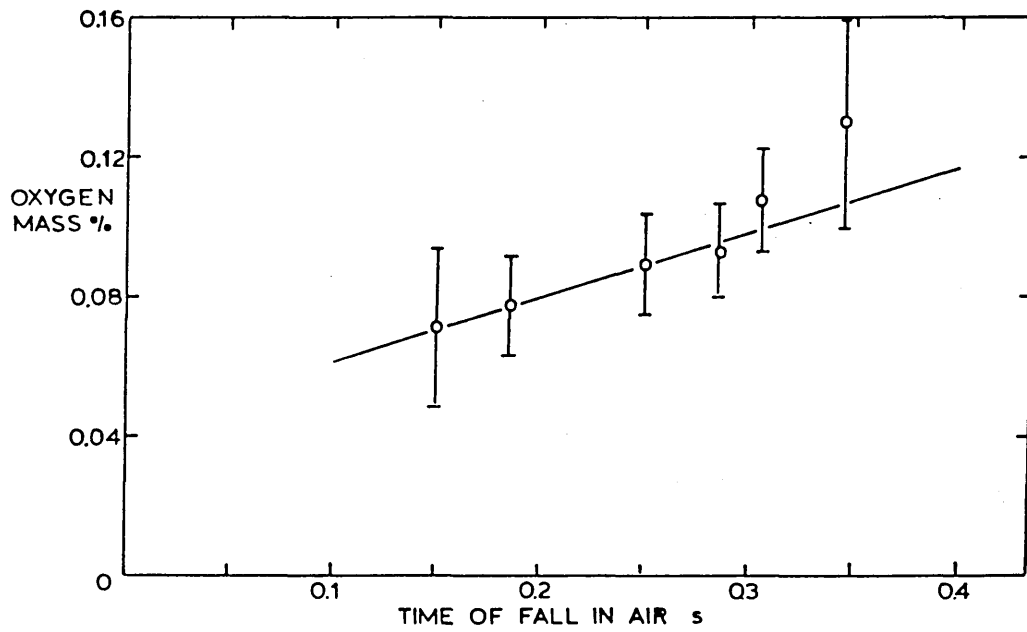
The Rate of Oxidation of Fe-Mn Droplets at 1600°C

Figure 66



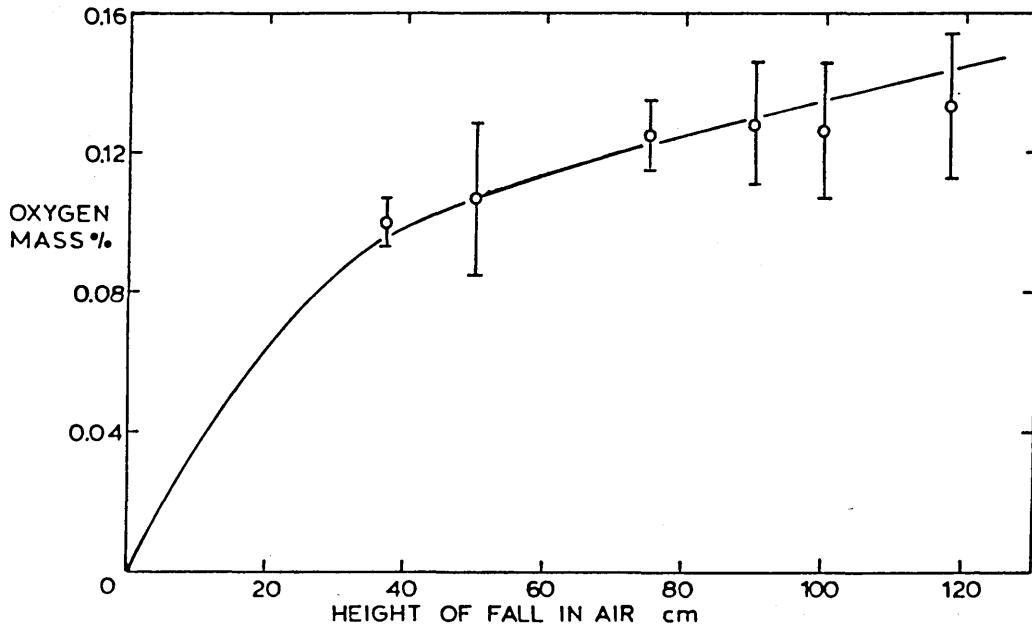
The Oxidation of Fe-0.17%Cr Droplets at 1600°C

Figure 67



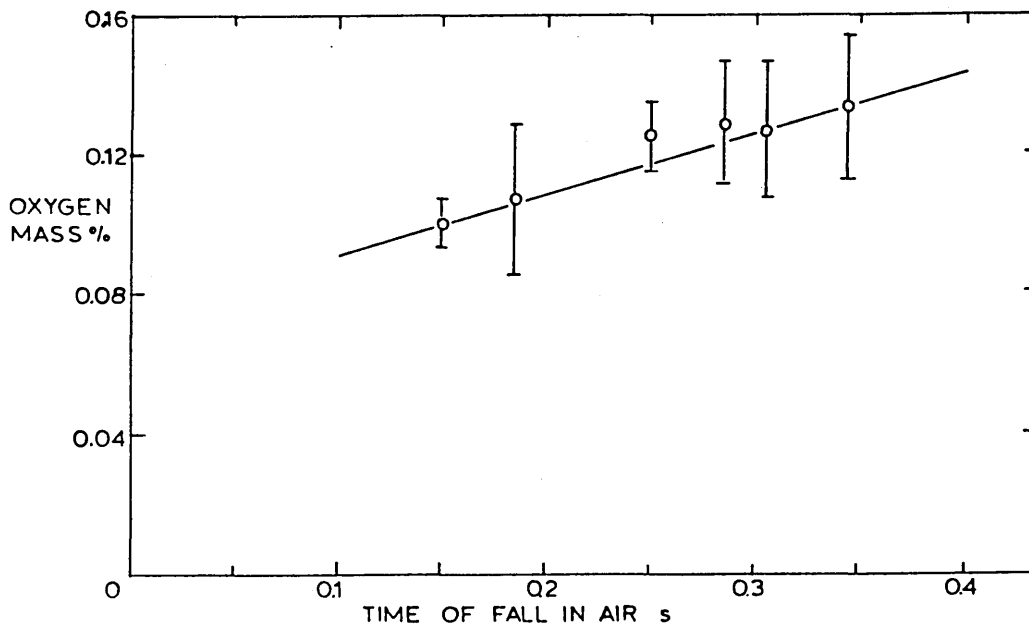
The Rate of Oxidation of Fe-0.17%Cr Droplets at 1600°C

Figure 68



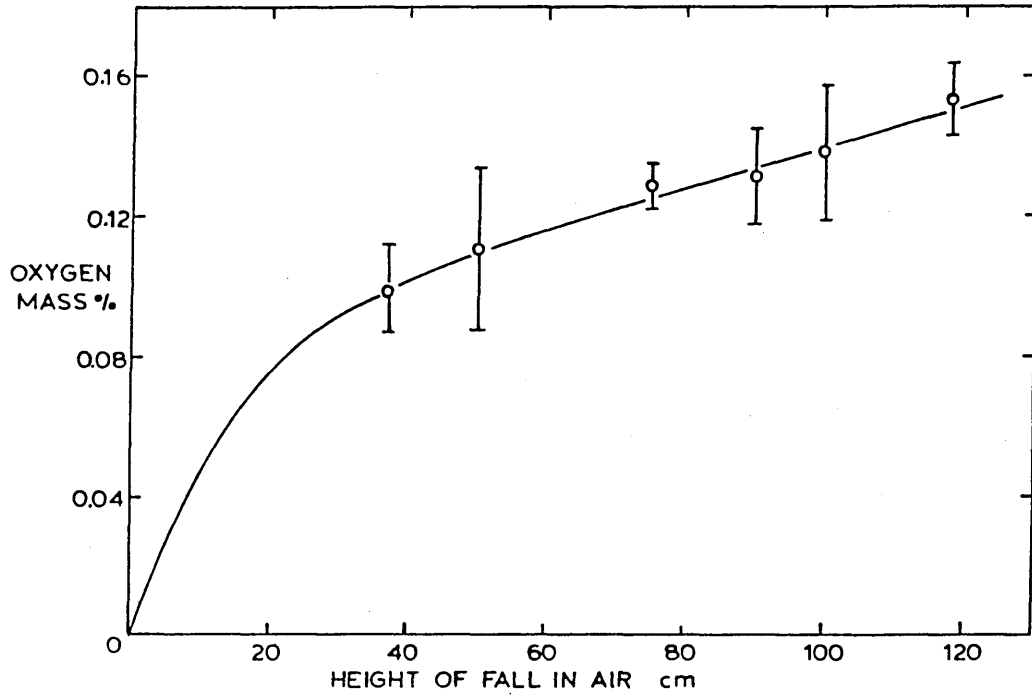
The Oxidation of Fe-0.25%Cr Droplets at 1600°C

Figure 69



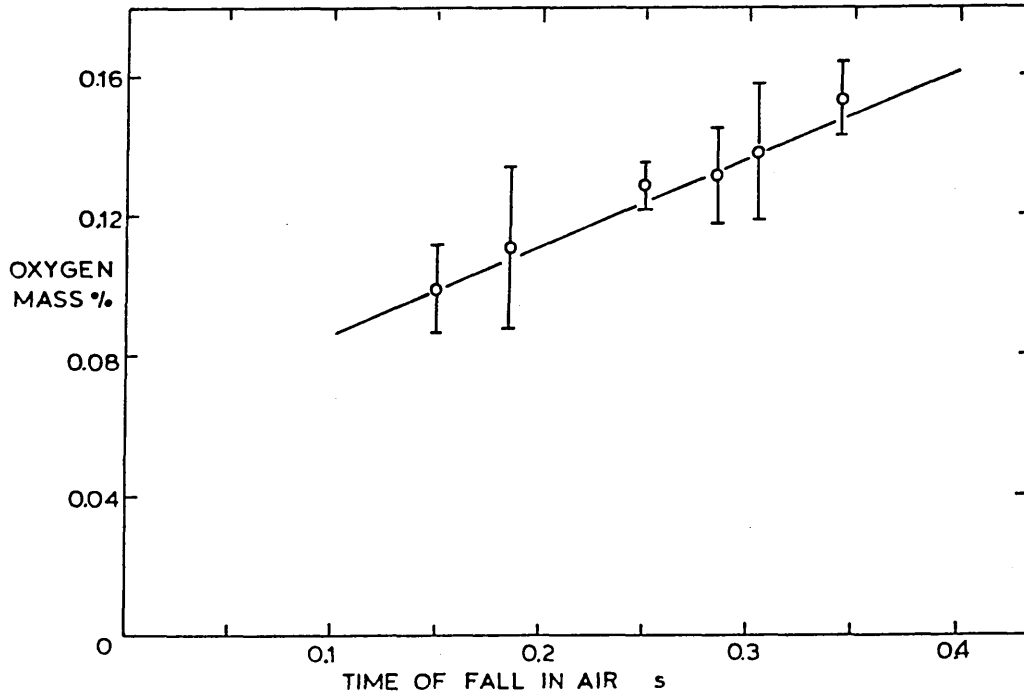
Rate of Oxidation of Fe-0.25%Cr Droplets at 1600°C

Figure 70



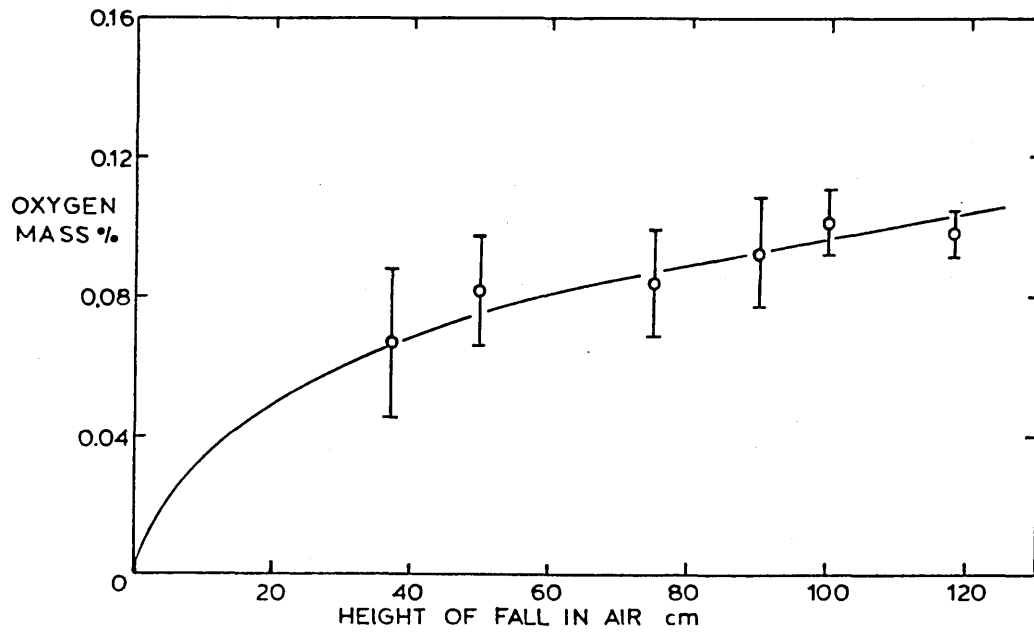
The Oxidation of Fe-0.8%Cr Droplets at 1600°C

Figure 71



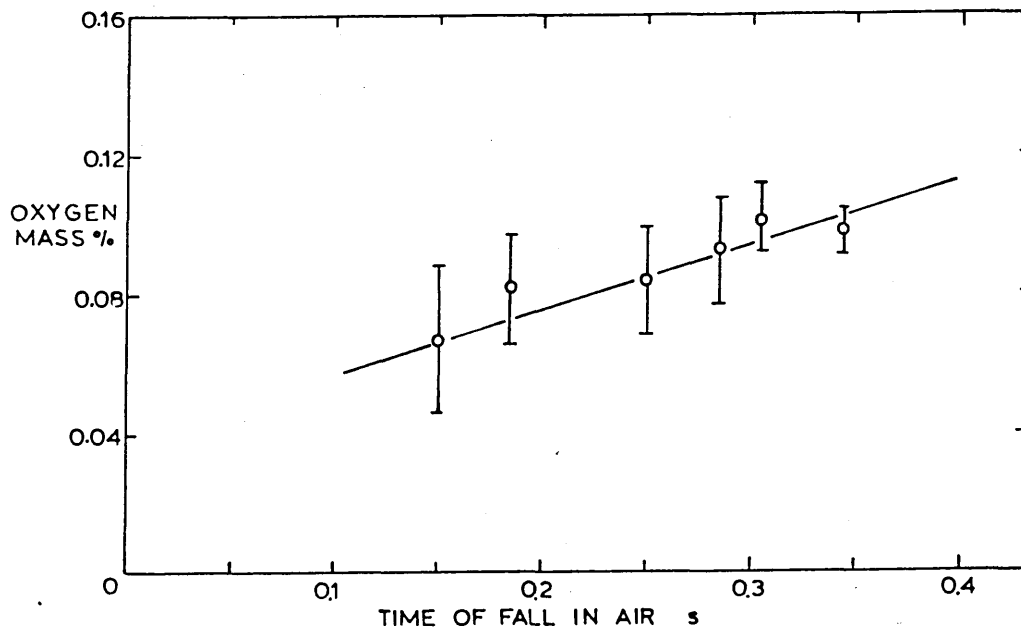
The Rate of Oxidation of Fe-0.80%Cr Droplets at 1600°C

Figure 72



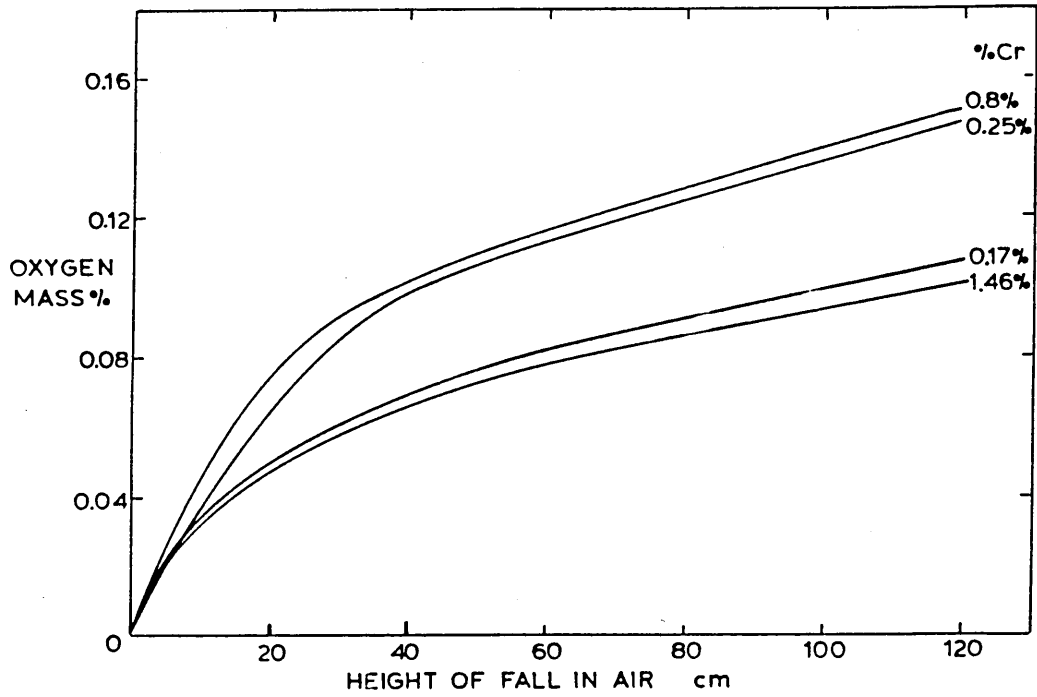
The Oxidation of Fe-1.46%Cr Droplets at 1600°C

Figure 73



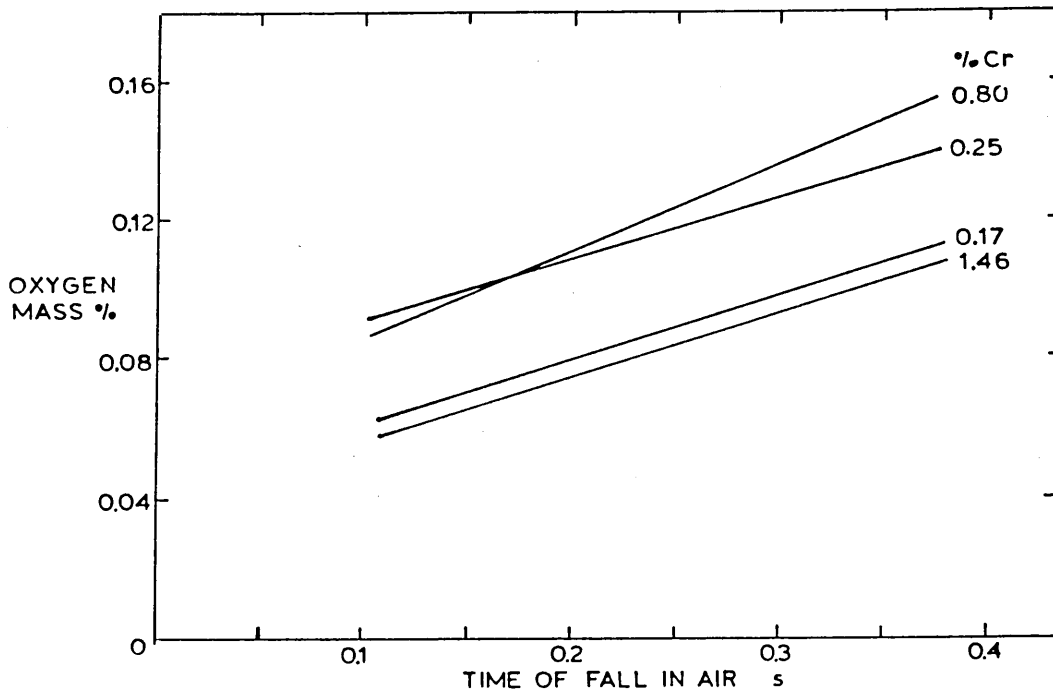
The Rate of Oxidation of Fe-1.46%Cr Droplets at 1600°C

Figure 74



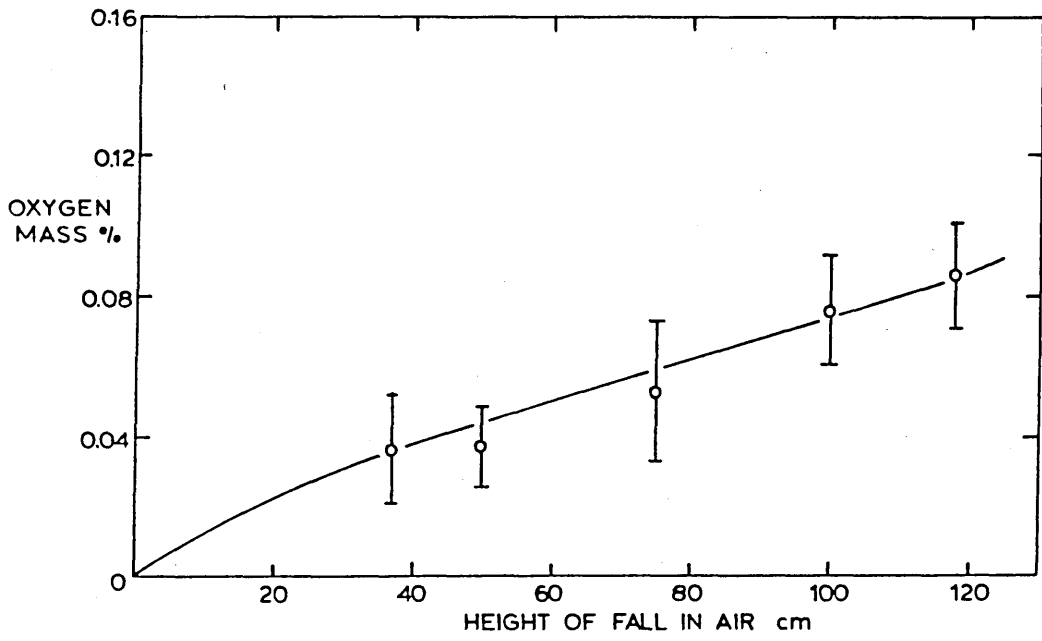
The Oxidation of Fe-Cr Droplets at 1600°C

Figure 75



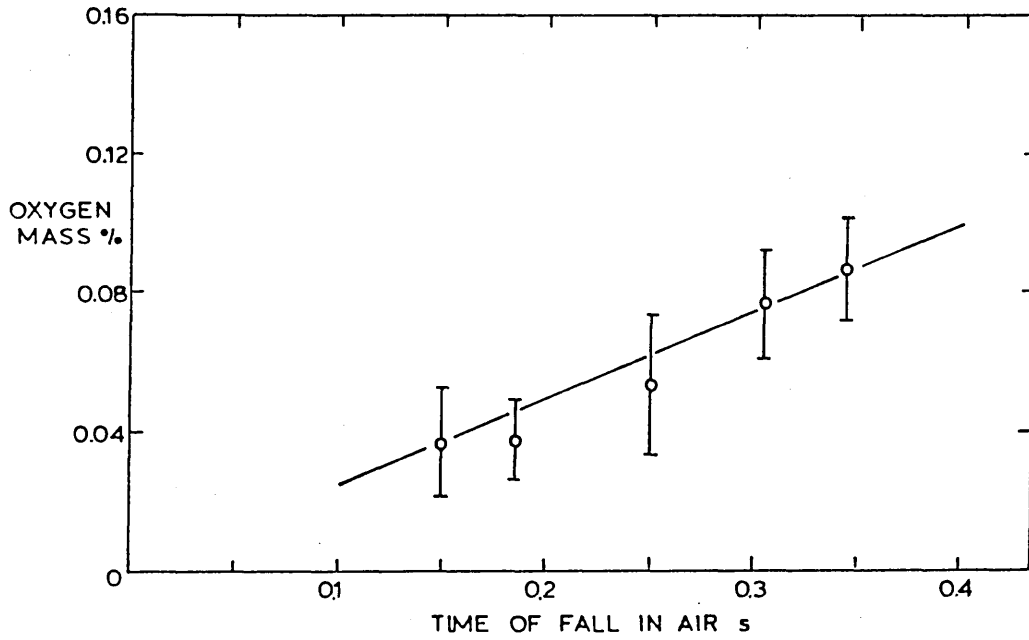
The Rate of Oxidation of Fe-Cr Droplets at 1600°C

Figure 76



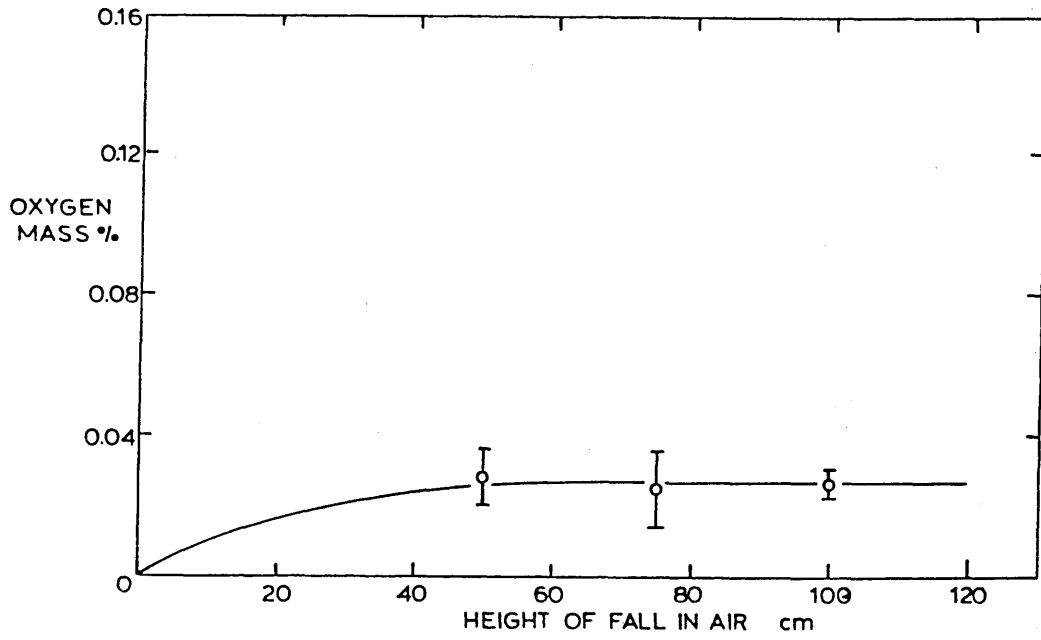
The Oxidation of Fe-0.3%Si Droplets at 1600°C

Figure 77



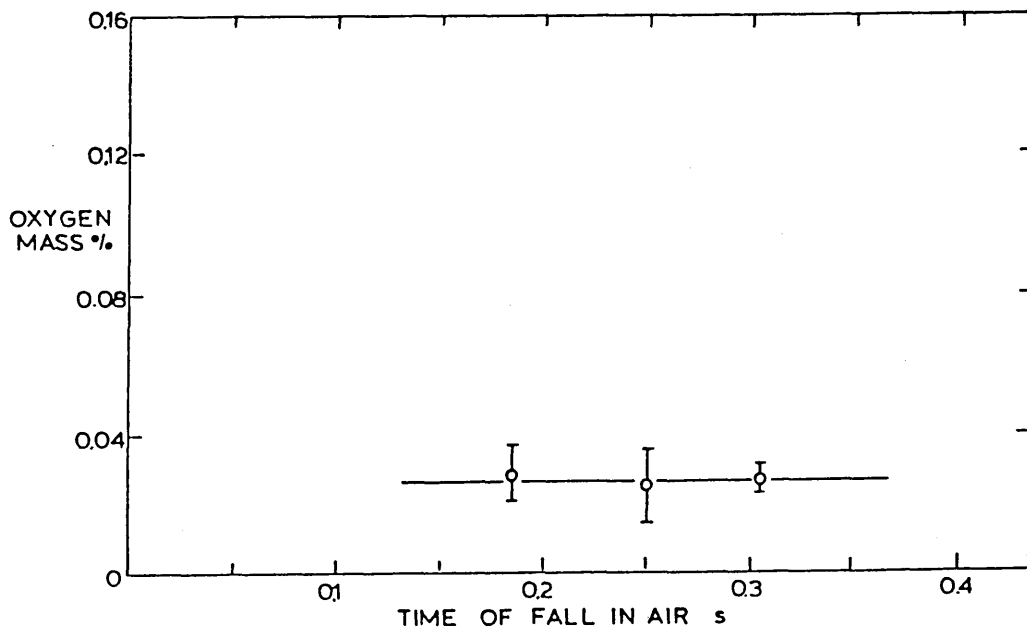
The Rate of Oxidation of Fe-0.3%Si Droplets at 1600°C

Figure 78



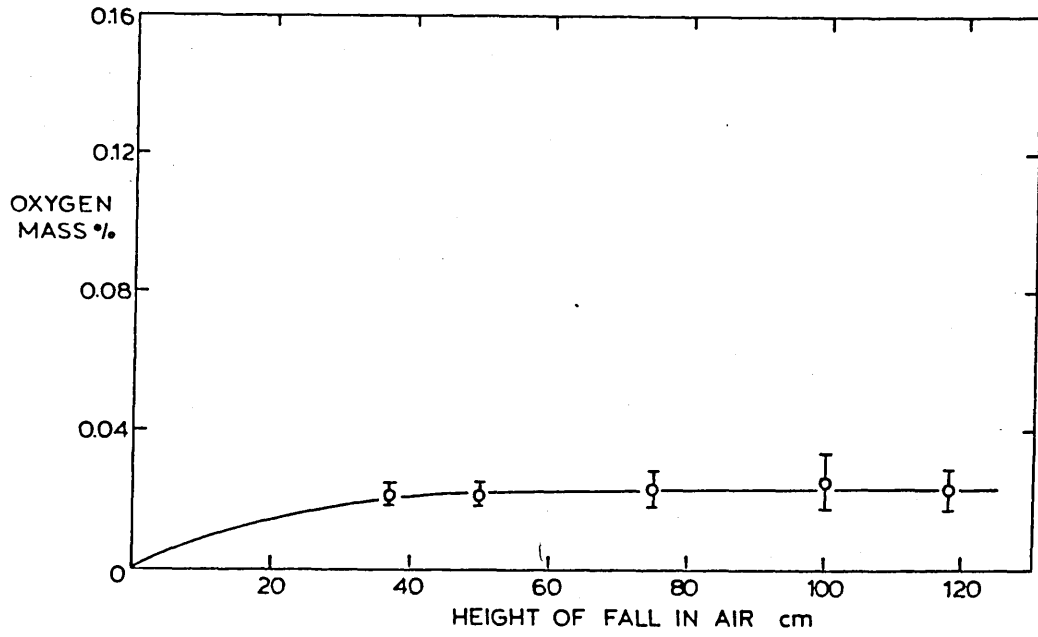
The Oxidation of Fe-0.75%Si Droplets at 1600°C

Figure 79



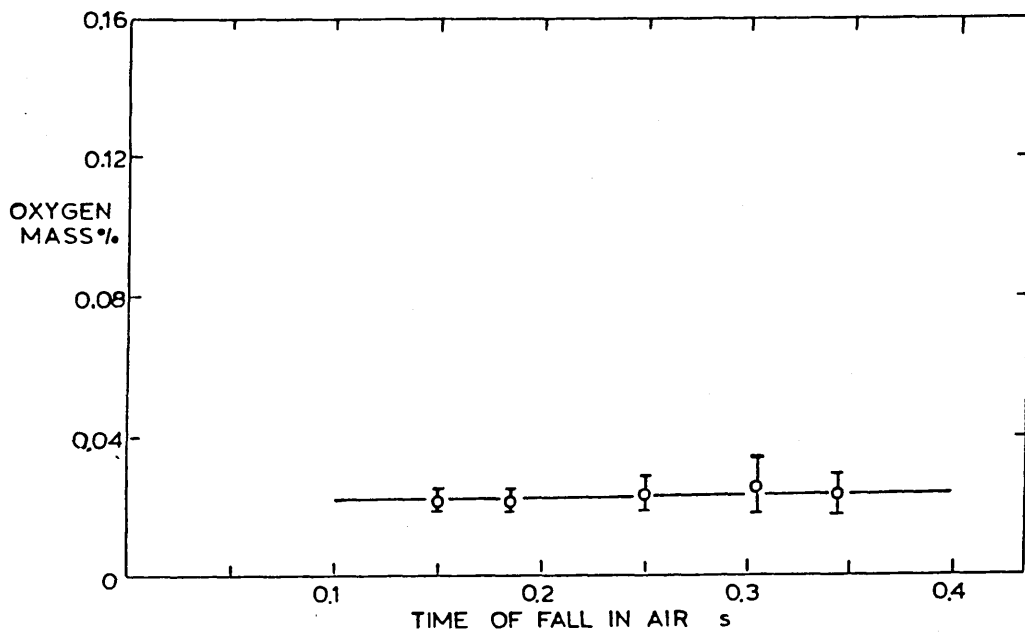
The Rate of Oxidation of Fe-0.75%Si Droplets at 1600°C

Figure 80



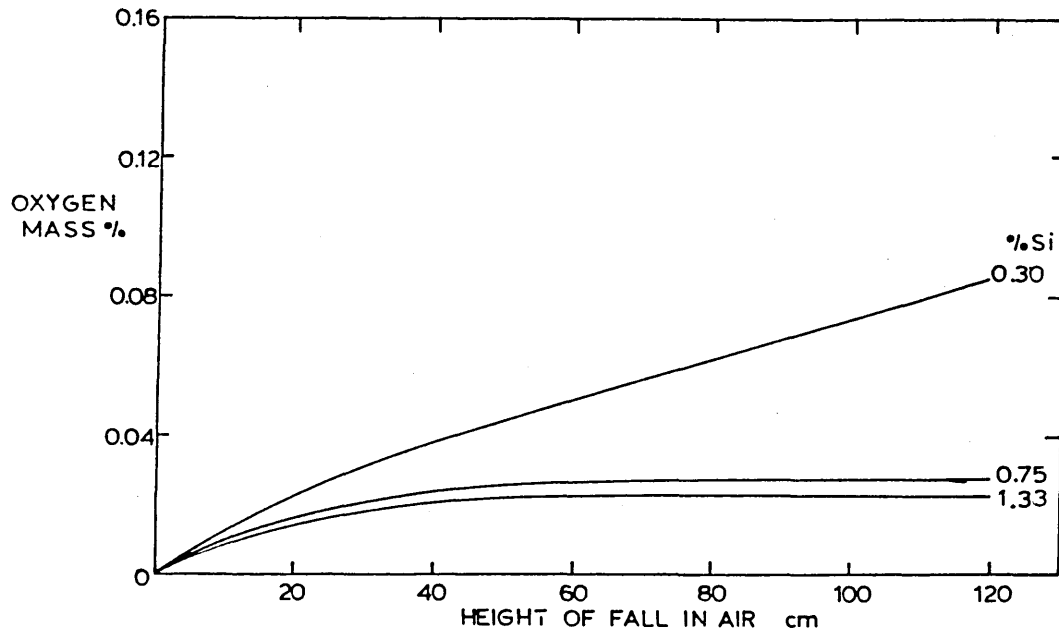
The Oxidation of Fe-1.33%Si Droplets at 1600°C

Figure 81



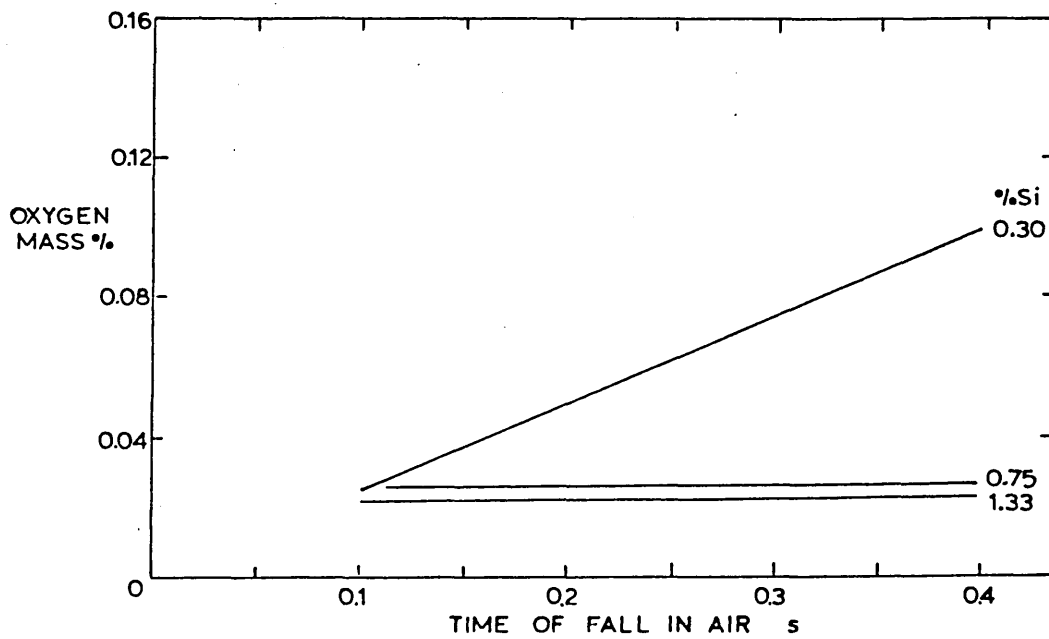
The Rate of Oxidation of Fe-1.33%Si Droplets at 1600°C

Figure 82



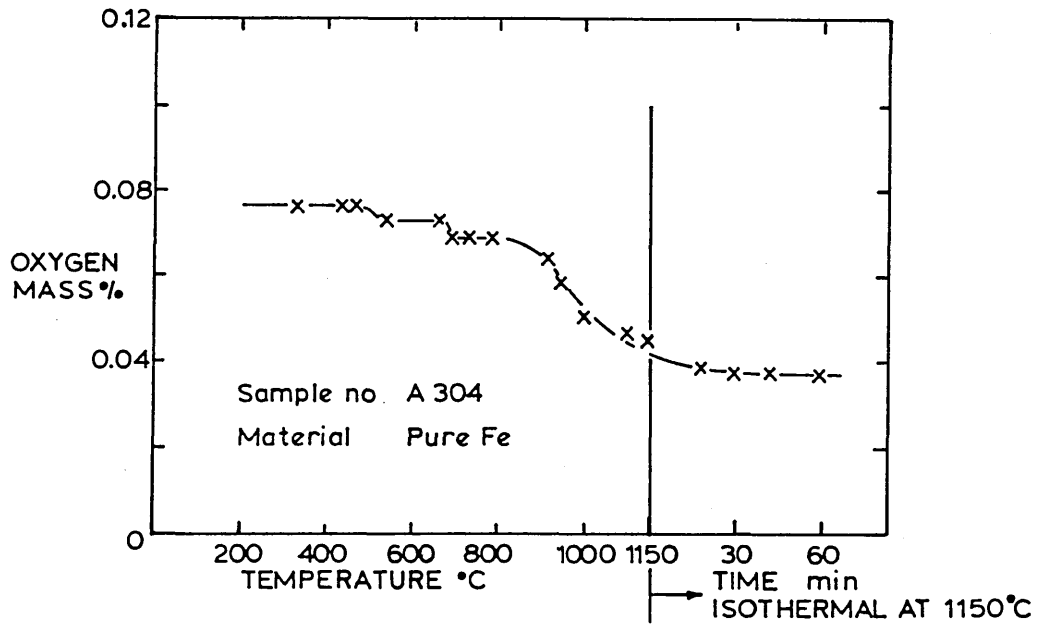
The Oxidation of Fe-Si Droplets at 1600°C

Figure 83



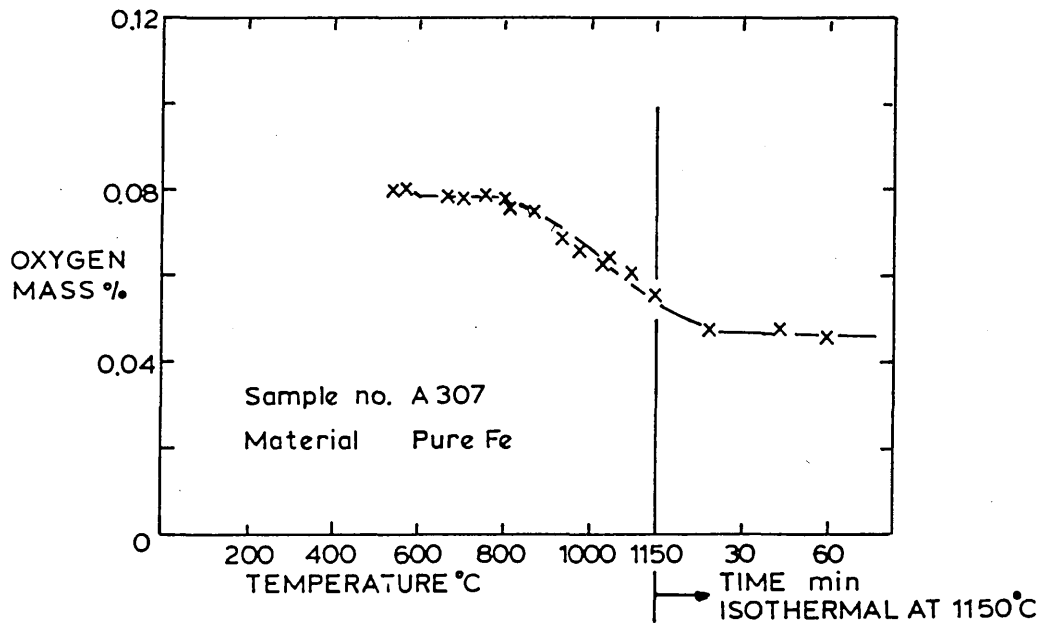
The Rate of Oxidation of Fe-Si Droplets at 1600°C

Figure 84



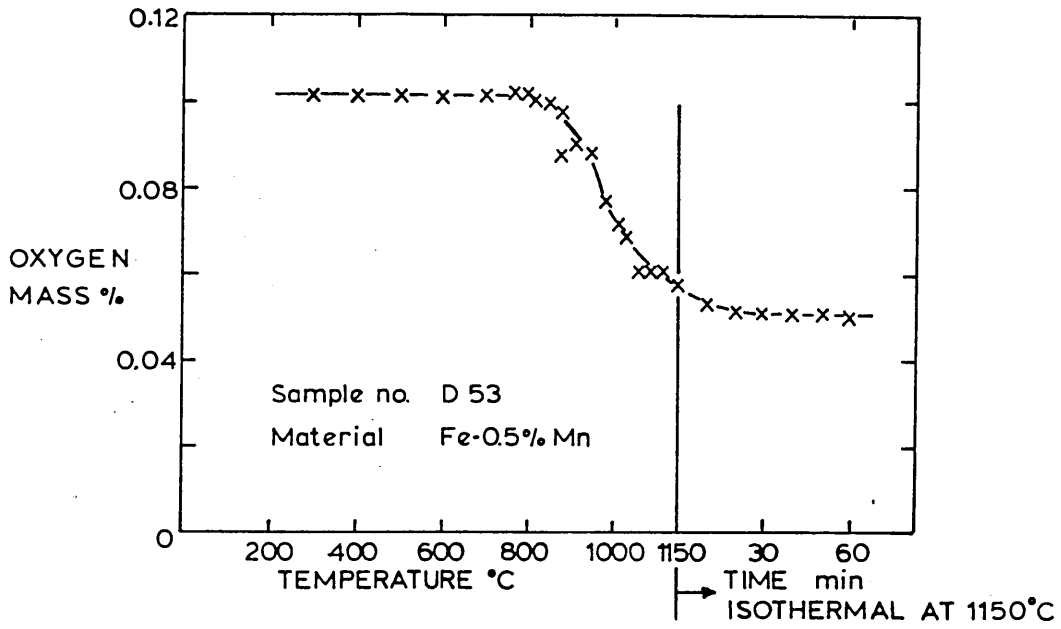
Oxygen Content Calculated from Weight Change as a Function of Temperature and Time at 1150°C

Figure 85



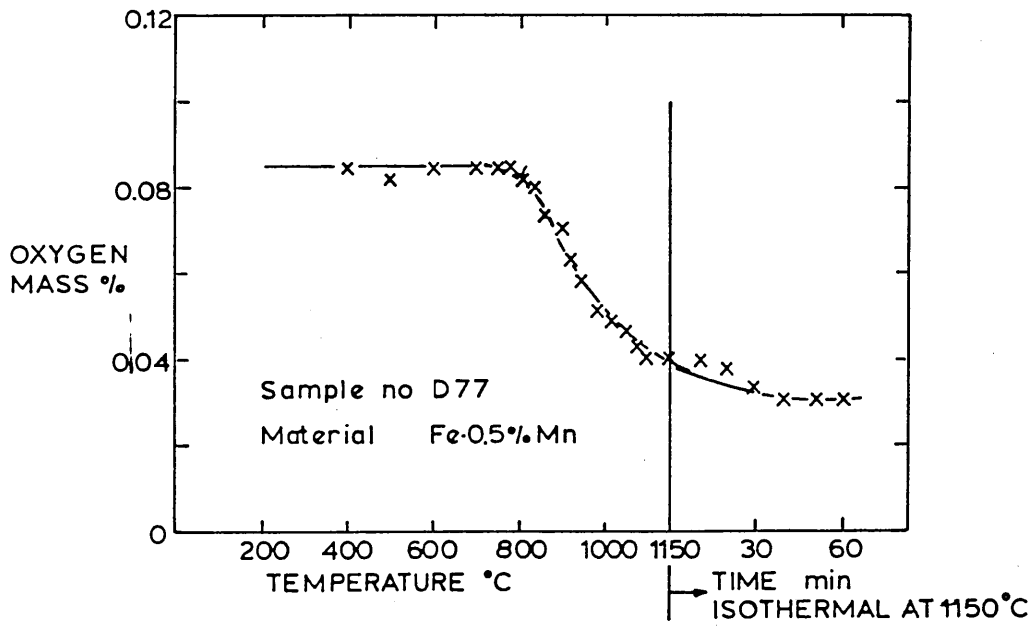
Oxygen Content Calculated from Weight Change as a Function of Temperature and Time at 1150°C

Figure 86



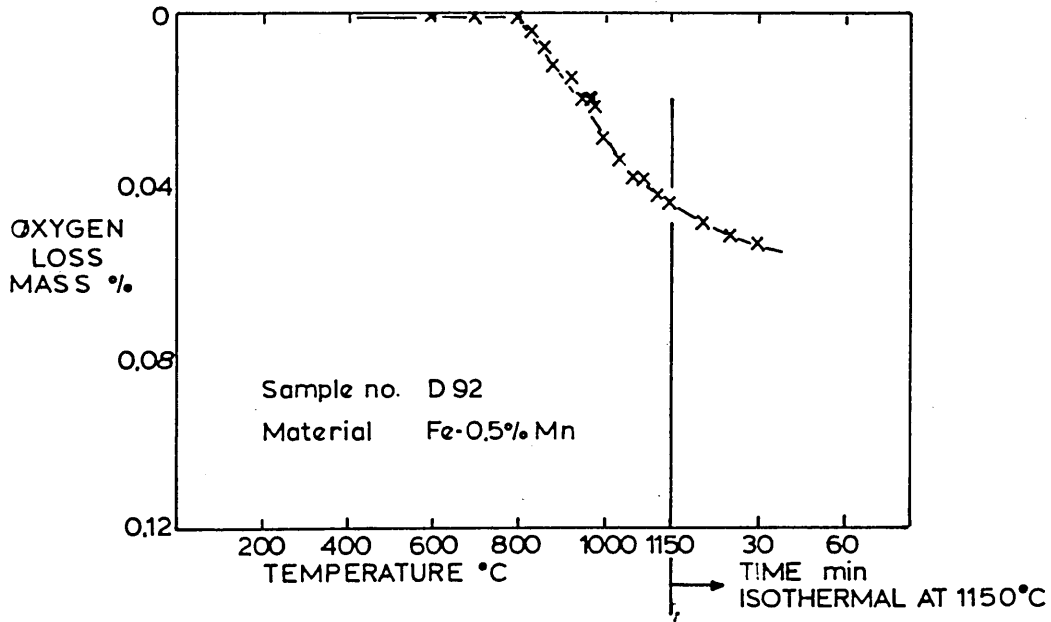
Oxygen Content Calculated from Weight Change as a Function of Temperature and Time at 1150°C.

Figure 87



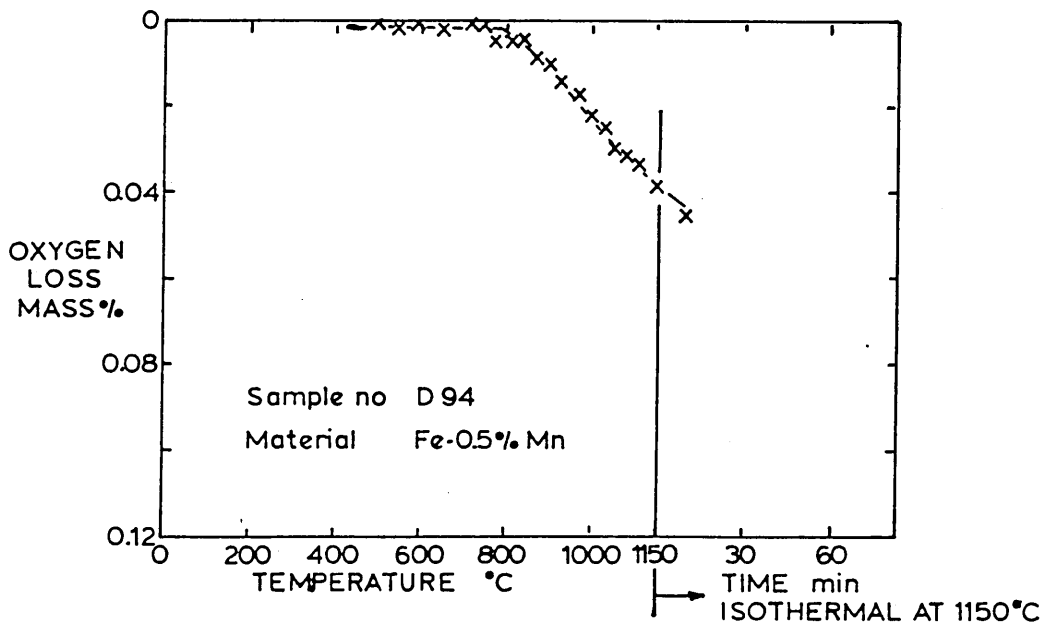
Oxygen Content Calculated from Weight Change as a Function of Temperature and Time at 1150°C

Figure 88



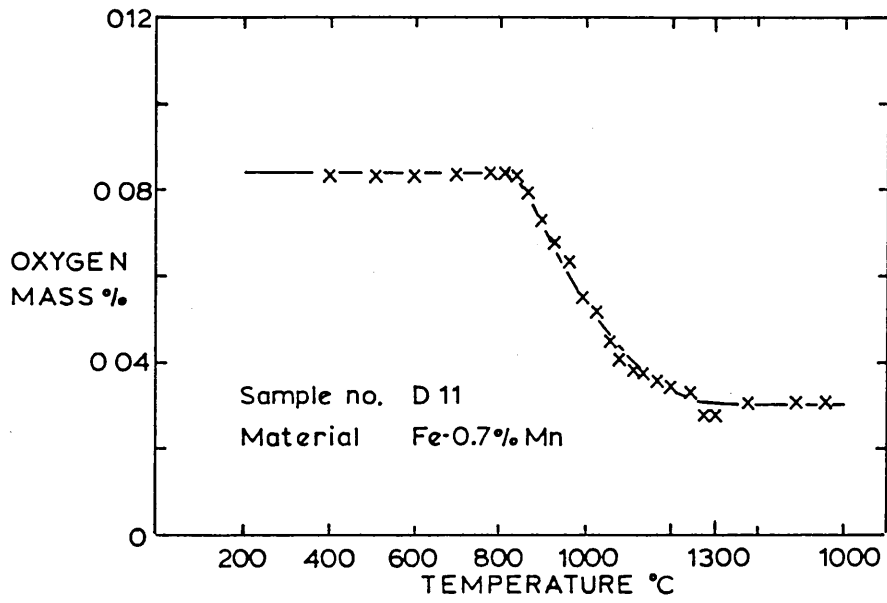
Oxygen Loss Calculated from Weight Change as a Function of Temperature and Time at 1150°C

Figure 89



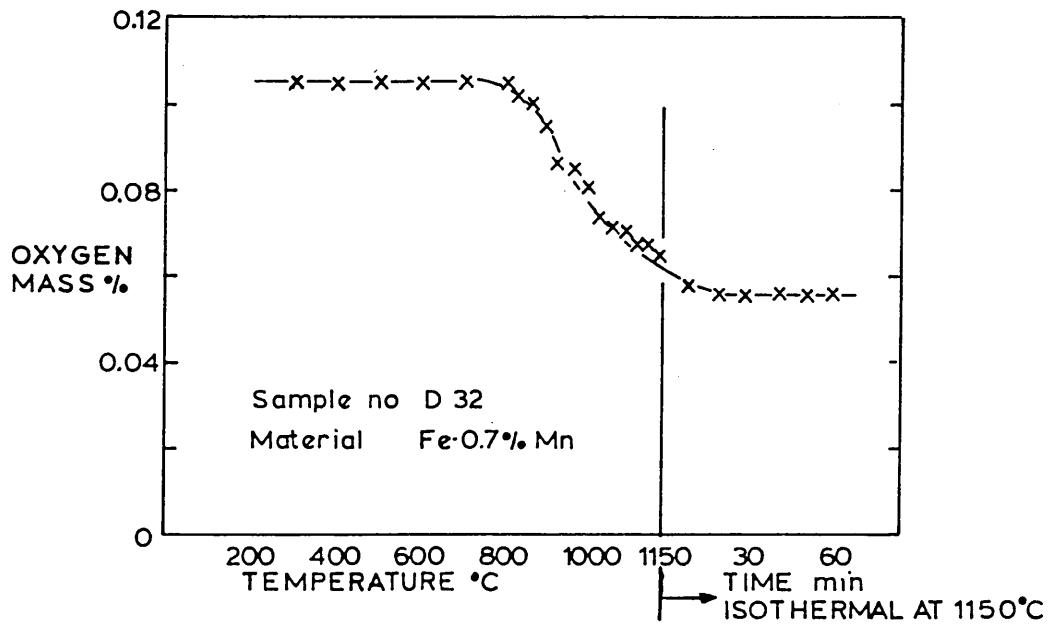
Oxygen Loss Calculated from Weight Change as a Function of Temperature and Time at 1150°C

Figure 90



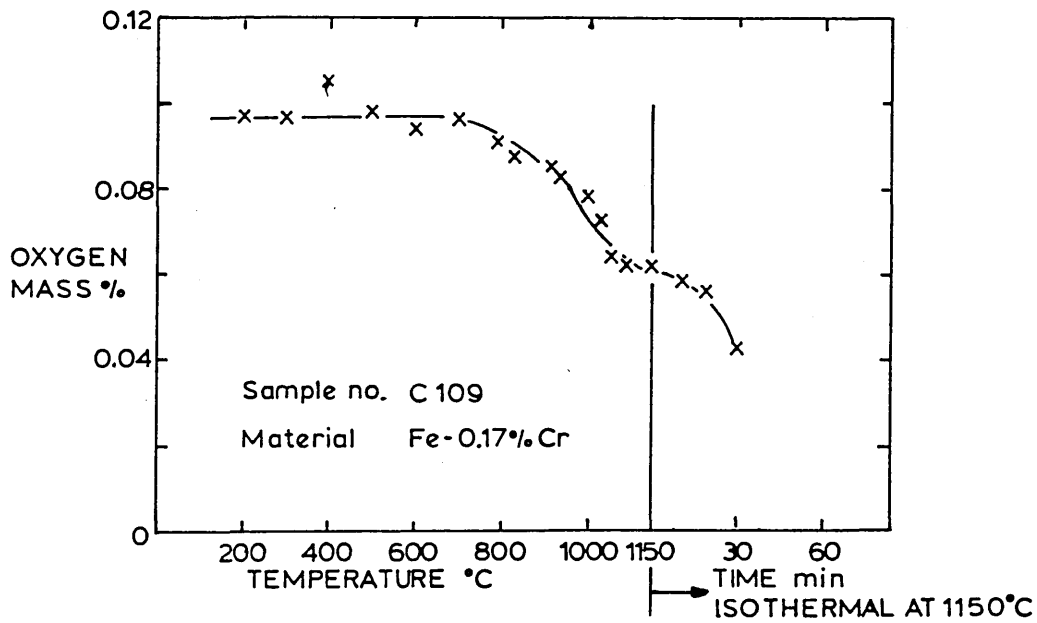
Oxygen Content Calculated from Weight Change as a Function of Temperature.

Figure 91



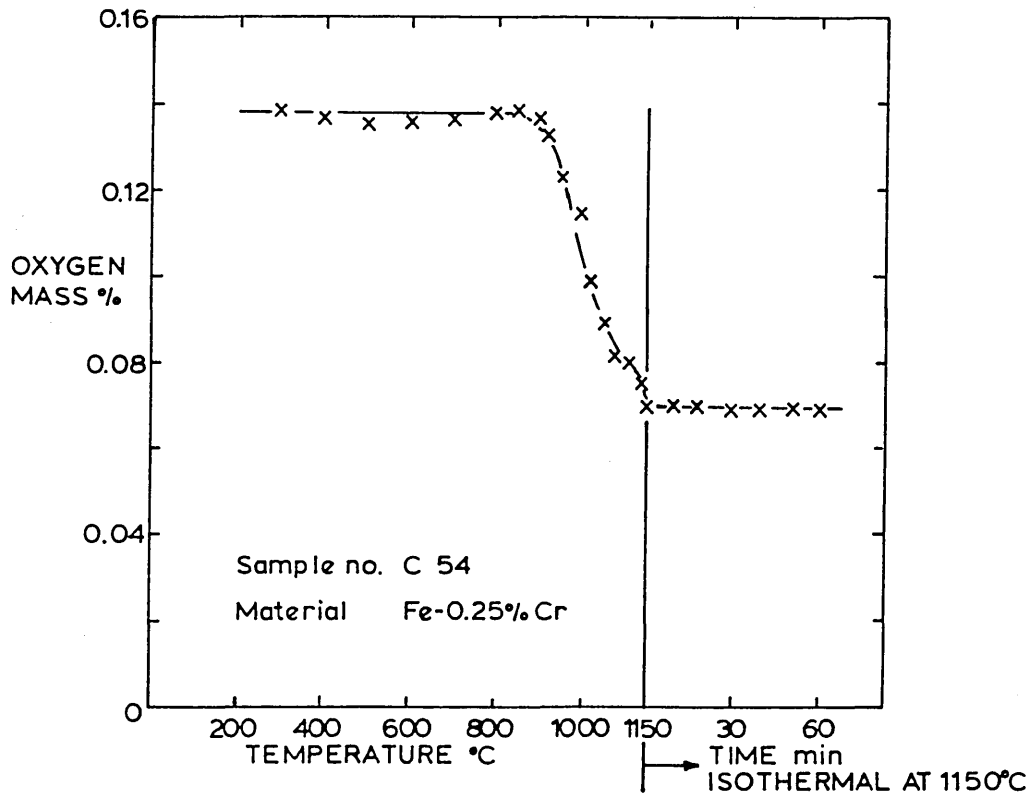
Oxygen Content Calculated from Weight Change as a Function of Temperature and Time at 1150°C

Figure 92



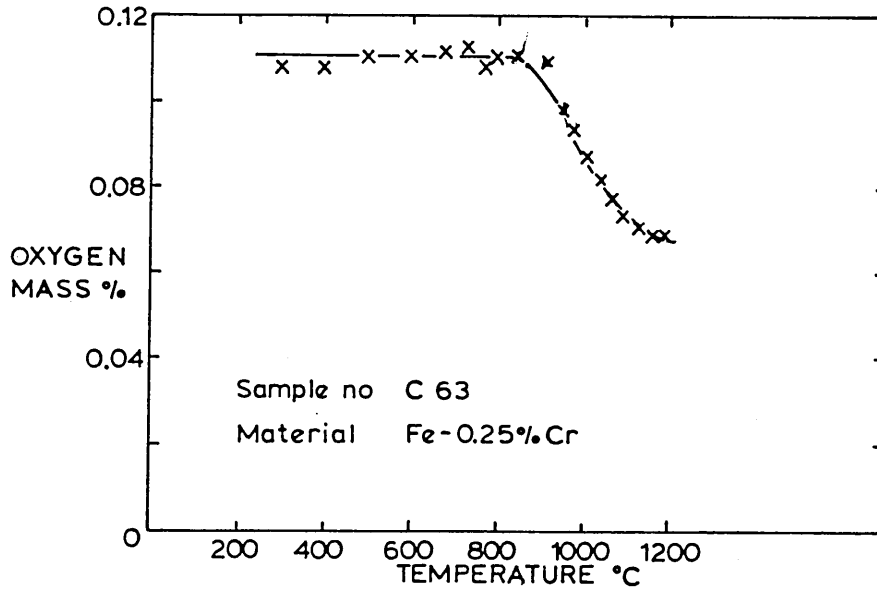
Oxygen Content Calculated from Weight Change as a Function of Temperature and Time at 1150°C

Figure 93



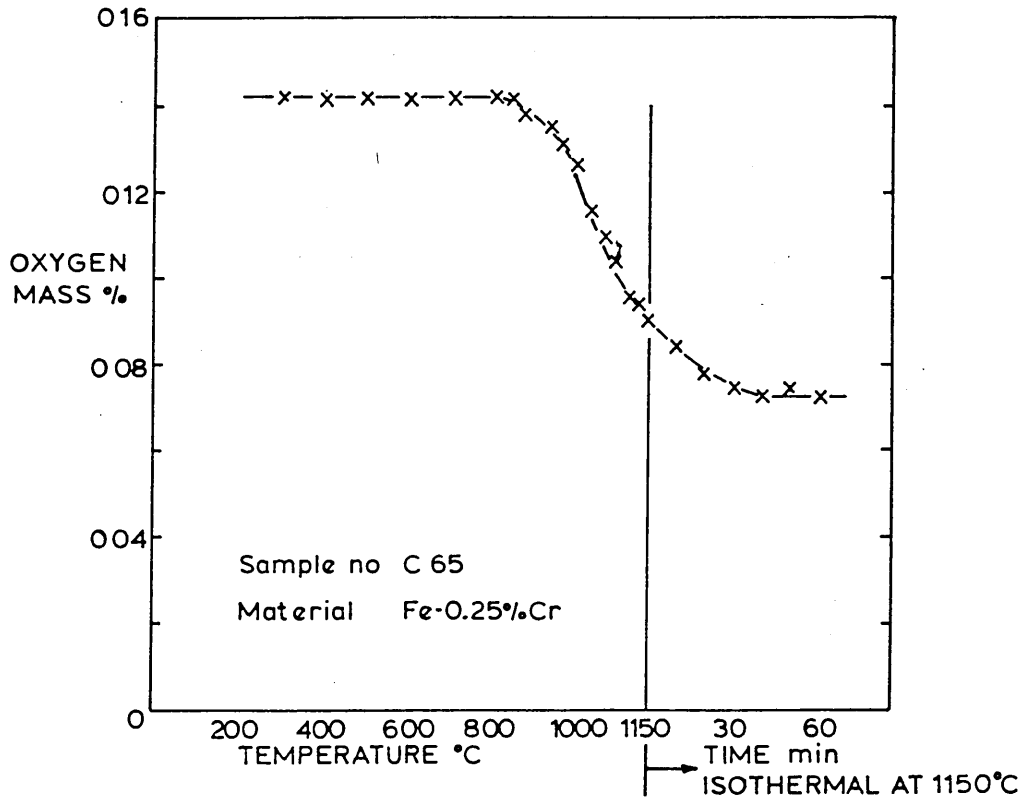
Oxygen Content Calculated from Weight Change as a Function of Temperature and Time at 1150°C

Figure 94



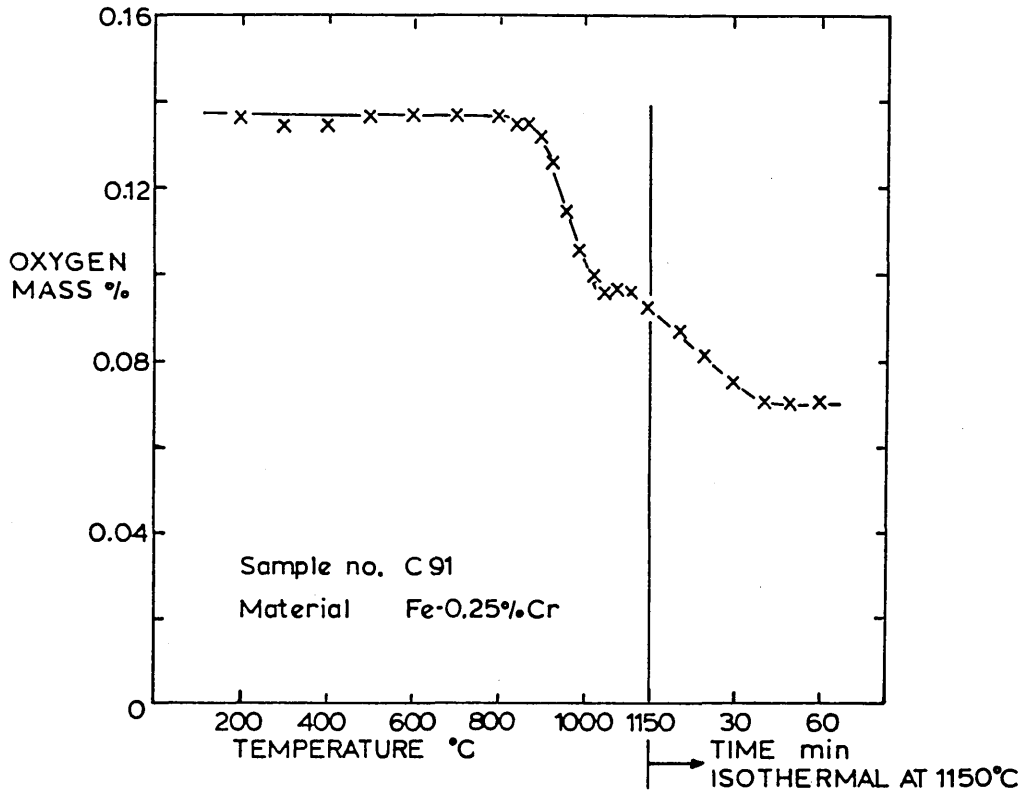
Oxygen Content Calculated from Weight Change as a Function of Temperature

Figure 95



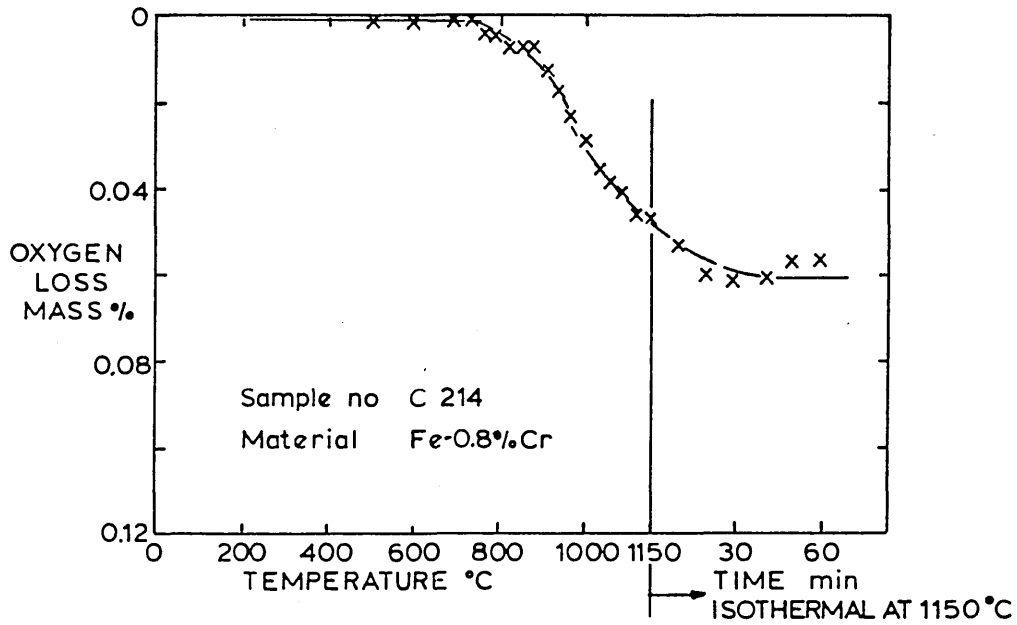
Oxygen Content Calculated from Weight Change as a Function of Temperature and Time at 1150°C

Figure 96



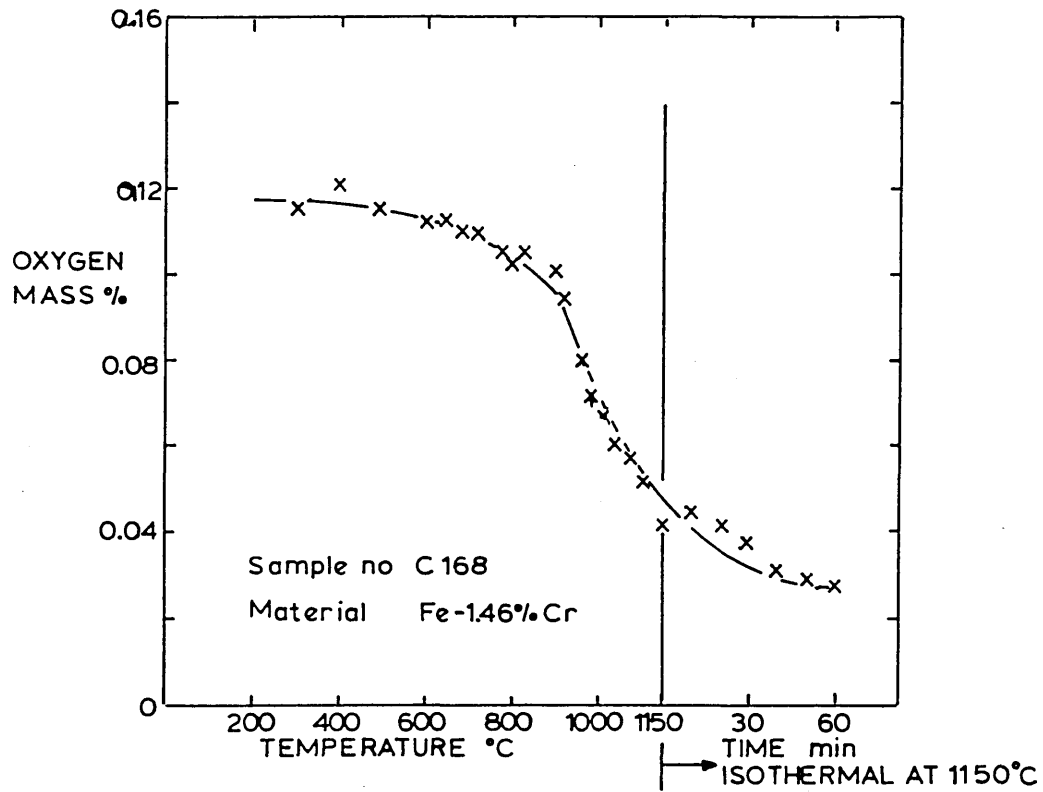
Oxygen Content Calculated from Weight Change as a Function of Temperature and Time at 1150°C

Figure 97



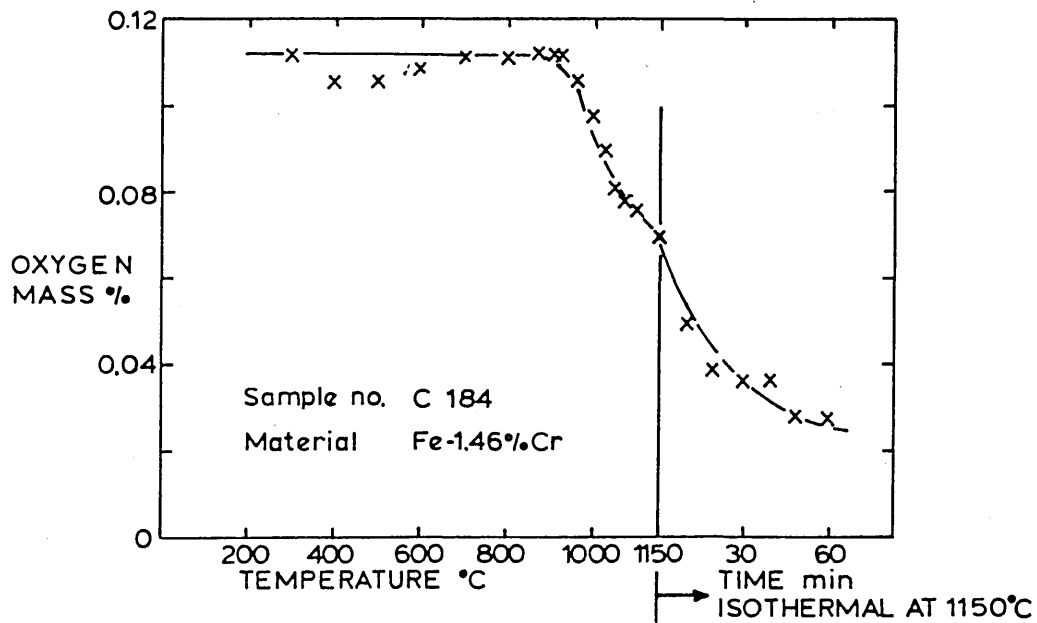
Oxygen Loss Calculated from Weight Change as a Function of Temperature and Time at 1150°C

Figure 98



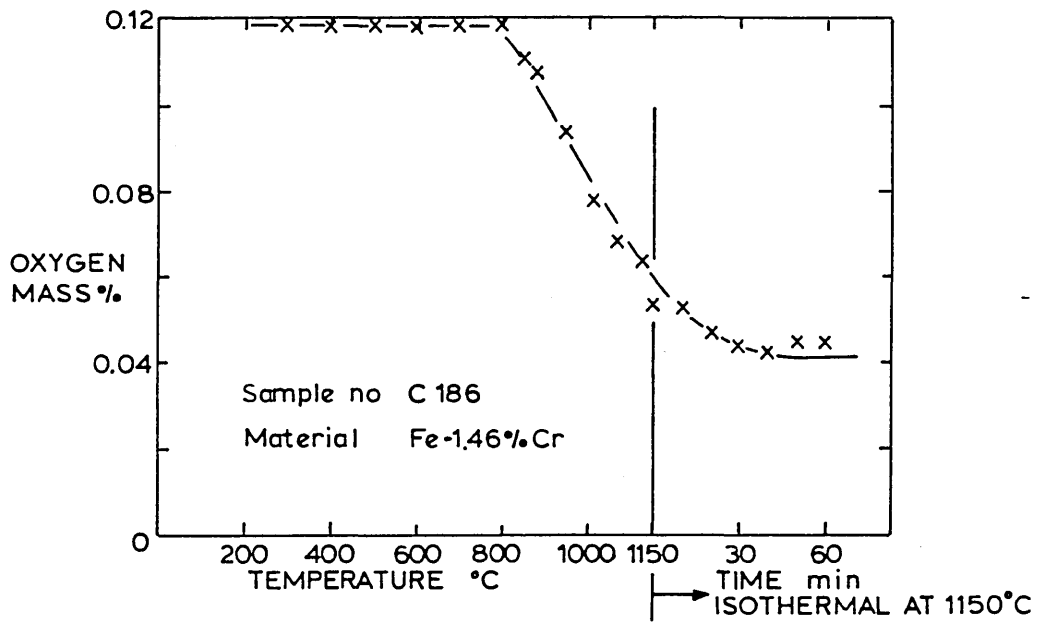
Oxygen Content Calculated from Weight Change as a Function of Temperature and Time at 1150°C

Figure 99



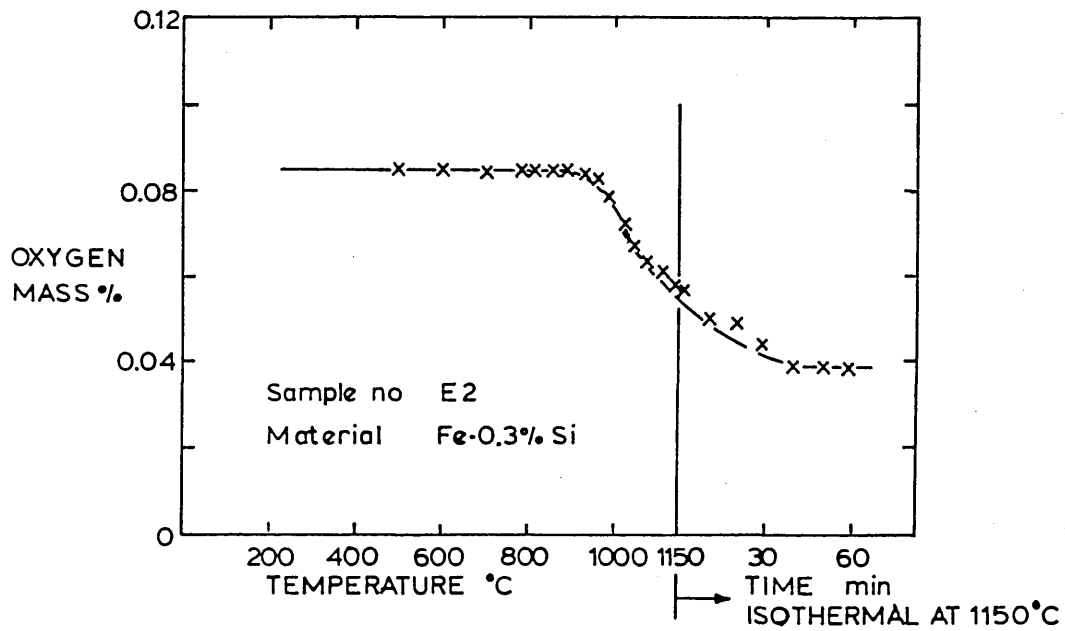
Oxygen Content Calculated from Weight Change as a Function of Temperature and Time at 1150°C

Figure 100



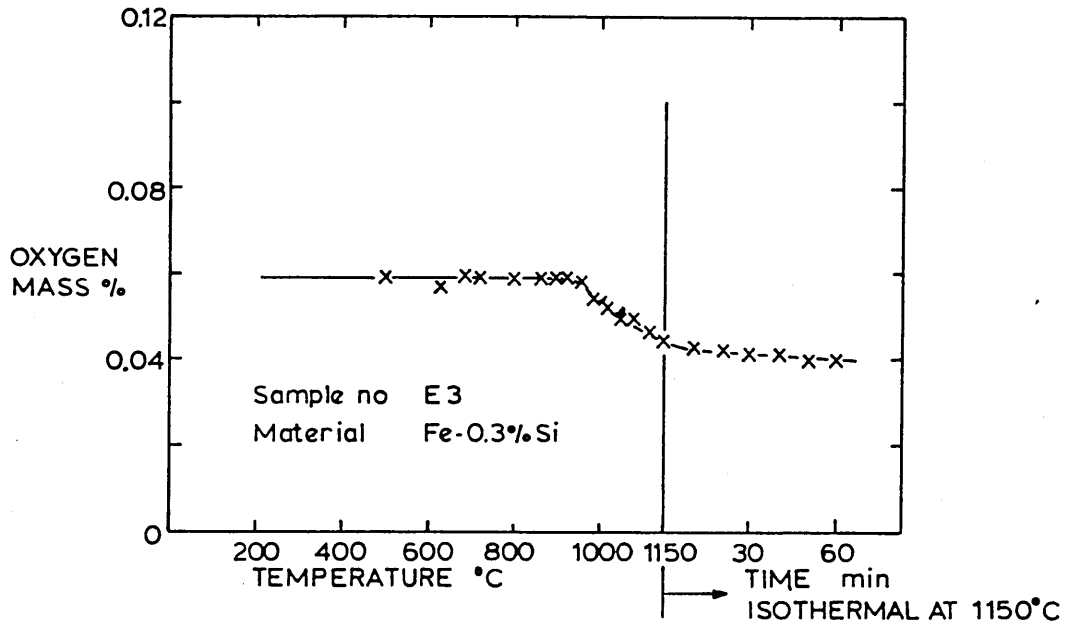
Oxygen Content Calculated from Weight Change as a Function of Temperature and Time at 1150°C

Figure 101



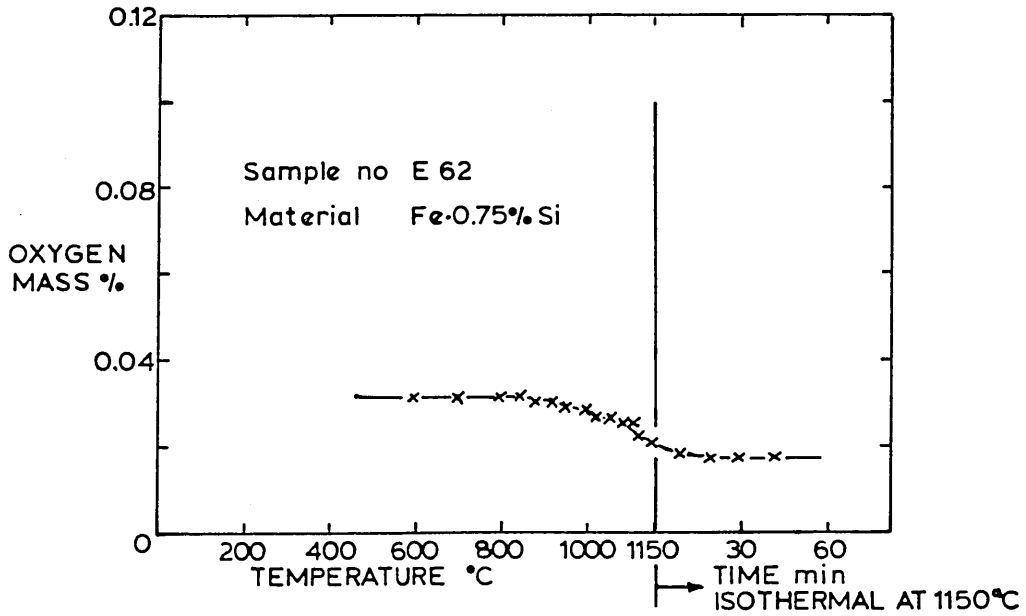
Oxygen Content Calculated from Weight Change as a Function of Temperature and Time at 1150°C

Figure 102



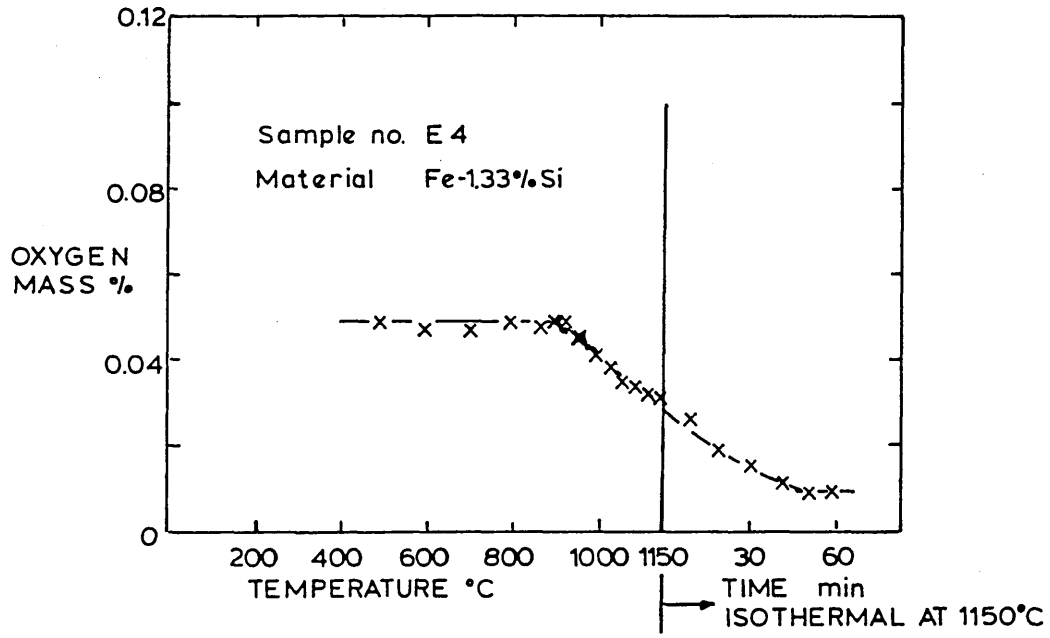
Oxygen Content Calculated from Weight Change as a Function of Temperature and Time at 1150°C

Figure 103



Oxygen Content Calculated from Weight Change as a Function of Temperature and Time at 1150°C

Figure 104



Oxygen Content Calculated from Weight Change as a Function of Temperature and Time at 1150°C

Figure 105

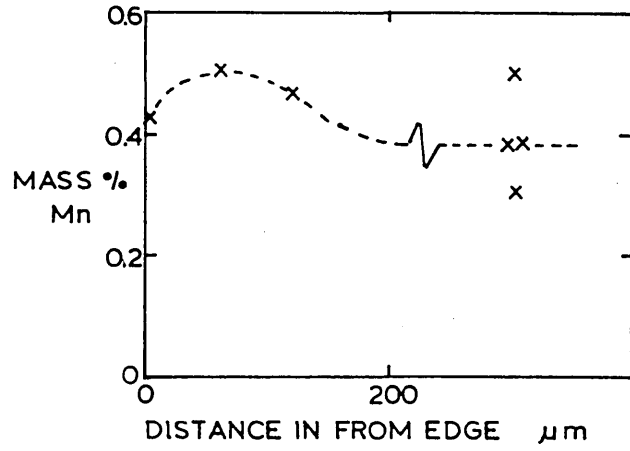
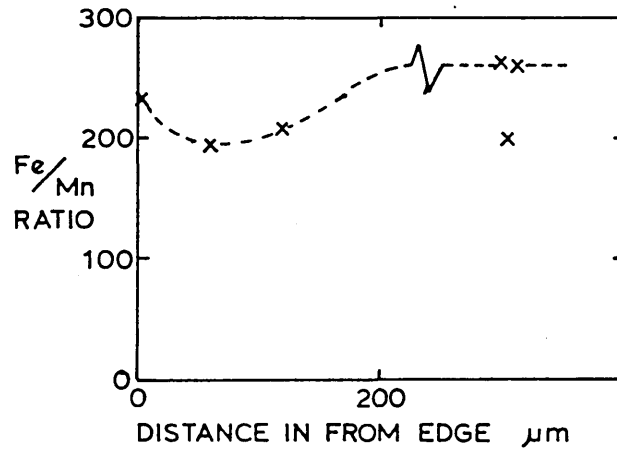


Figure 106



EDX Analysis for Fe-0.3%Mn Sample

Figure 107

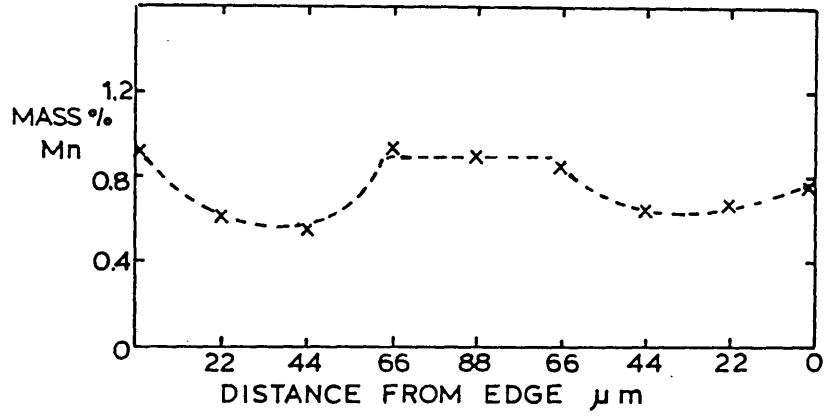
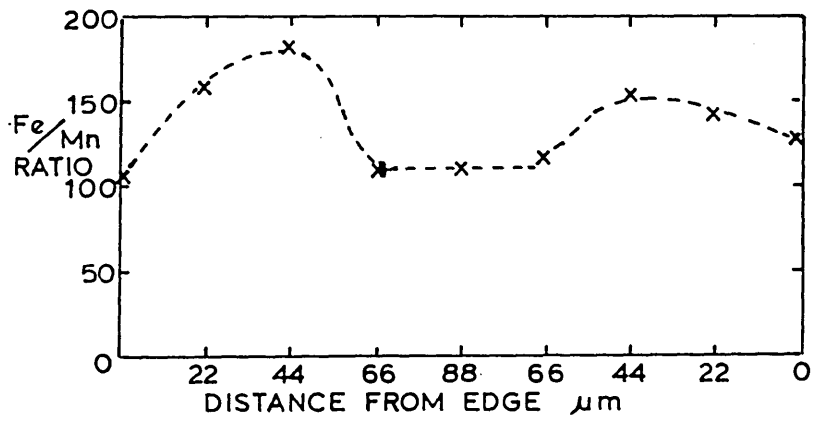


Figure 108



EDX Analysis for Fe-1.0% Mn Sample

Figure 109

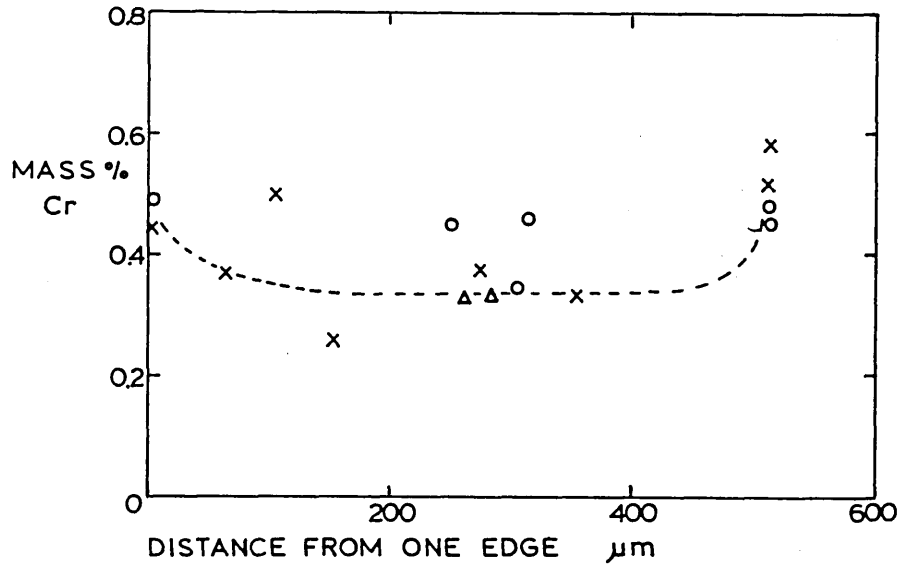
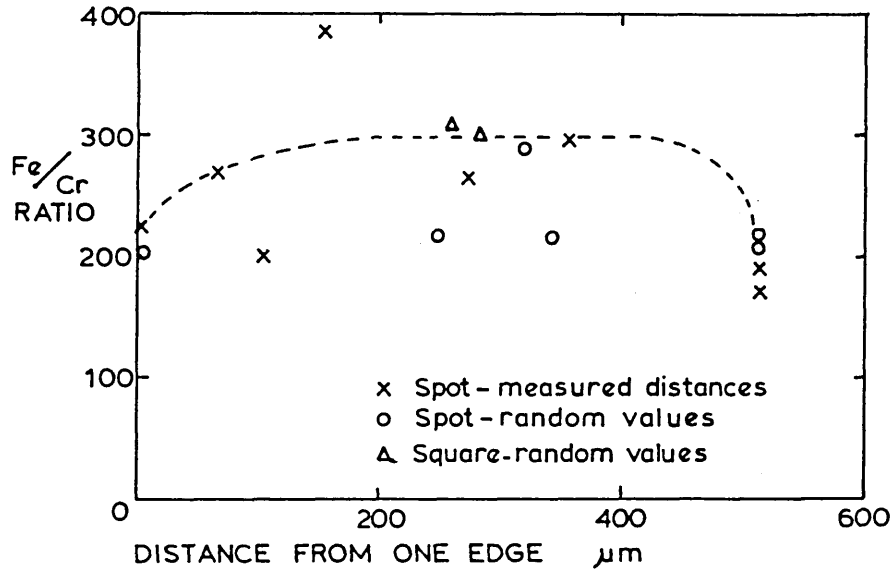
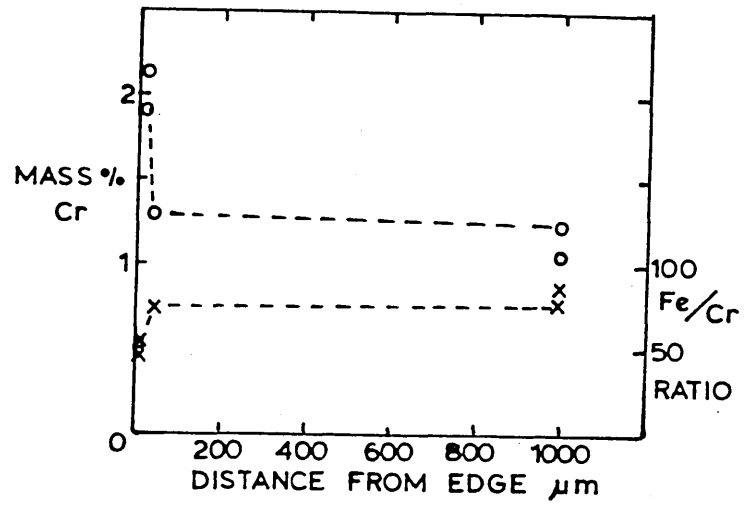


Figure 110



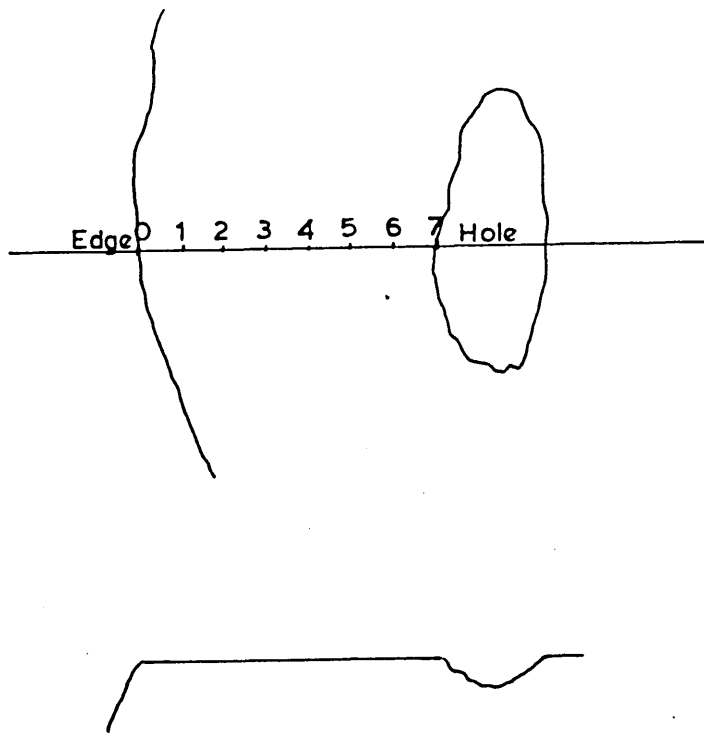
EDX Analysis for Fe-0.25%Cr Sample.

Figure 111



EDX Analysis for Fe-1.46%Cr Sample

Figure 112

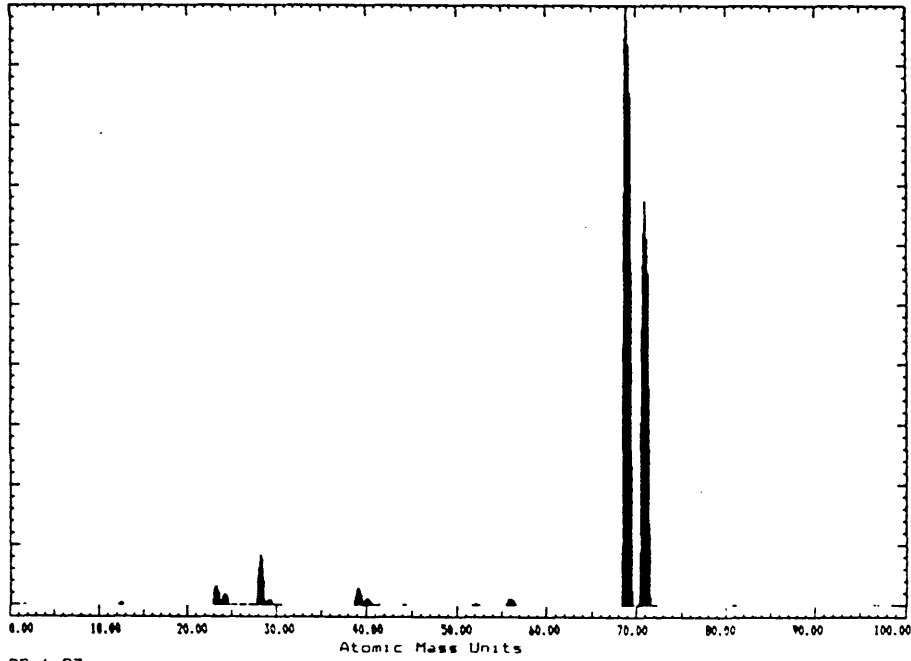


Fe-1.46%Cr Sectioned Sample

RJO Region 1 SVY

VG SCIENTIFIC

Positive SIMS. Target Bias 59.0 V Max Count Rate = 36125
Step Size = 0.050 AMU Time = 160.00 secs x 2 Scans

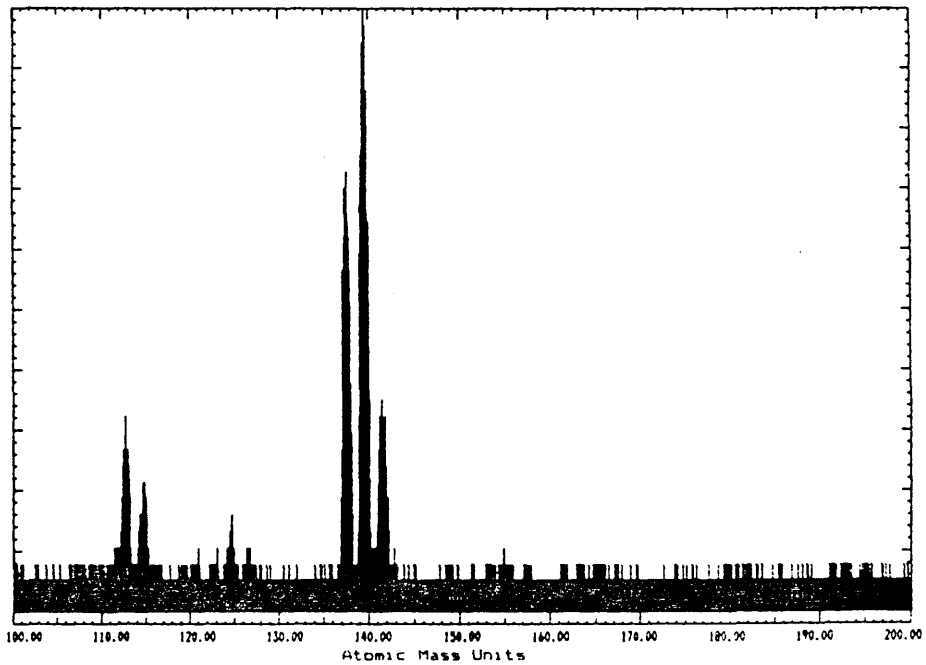


29:1:87
OXIDE LAYER

RJO Region 2 SVY

VG SCIENTIFIC

Positive SIMS. Target Bias 59.0 V Max Count Rate = 462
Step Size = 0.025 AMU Time = 160.00 secs x 2 Scans



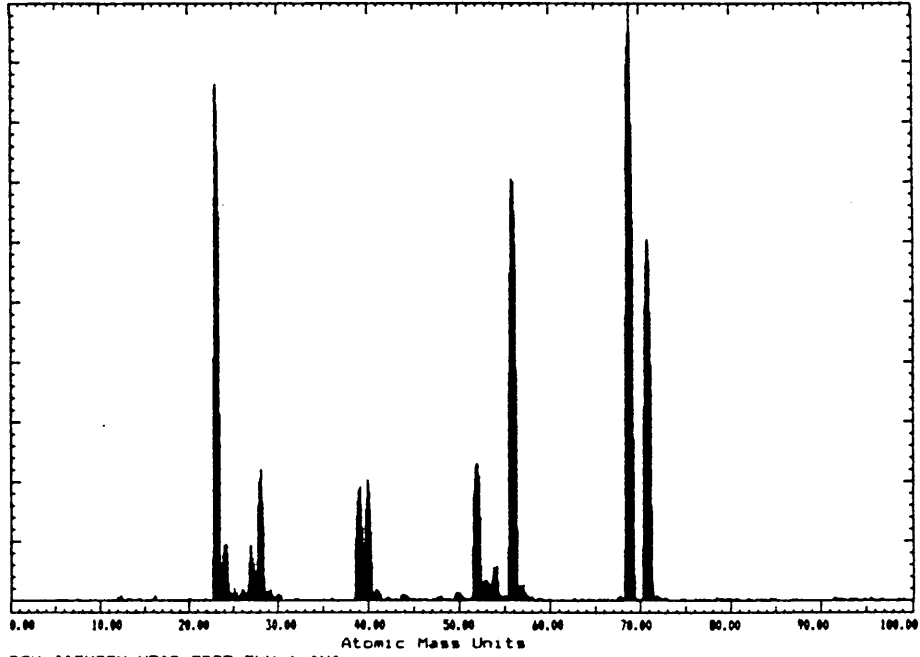
29:1:87
OXIDE LAYER

Figs.113 & 114 SIMS Analysis of Fe-1.46% Cr
Sectioned Sample

RJ1 Region 1 SVY

VG SCIENTIFIC

Positive SIMS. Target Bias 59.0 V Max Count Rate = 3481
Step Size = 0.050 AMU Time = 160.00 secs x 2 Scans

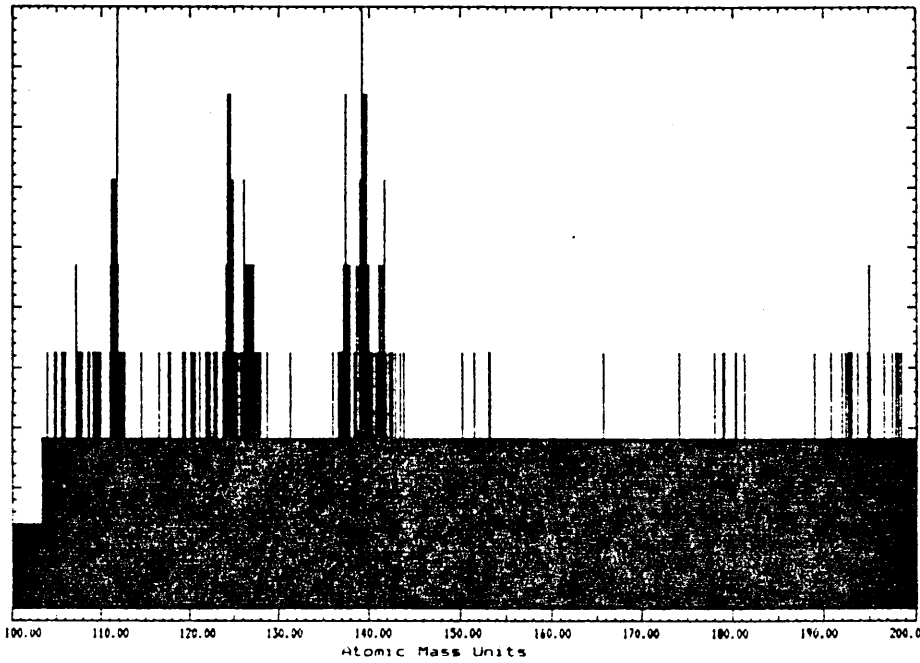


ROY JACKSON NEAR EDGE 5KV 1.0NA
20X MAG TV AREA
29/1/87

RJ1 Region 2 SVY

VG SCIENTIFIC

Positive SIMS. Target Bias 59.0 V Max Count Rate = 87
Step Size = 0.025 AMU Time = 160.00 secs x 2 Scans



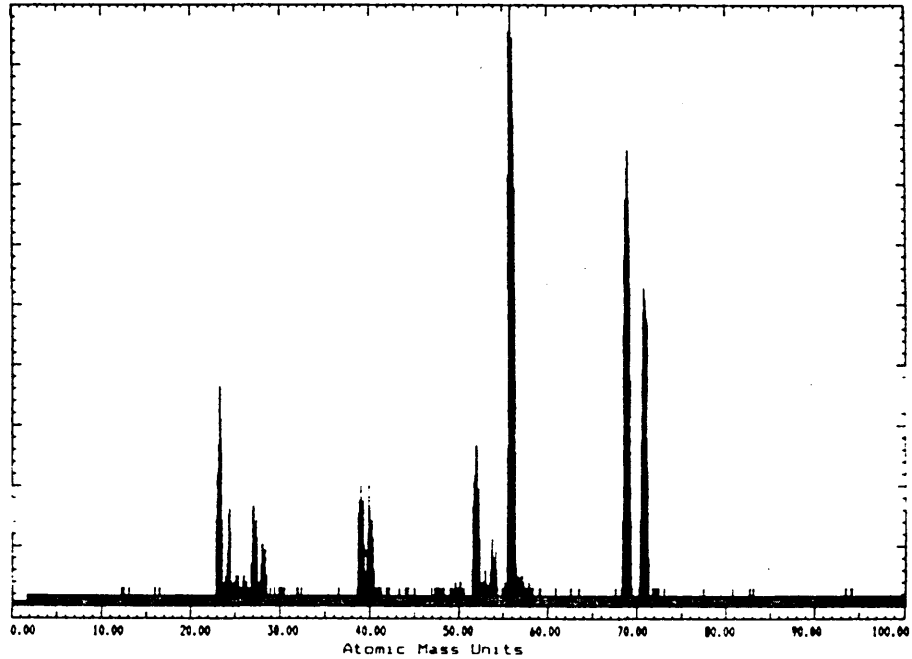
ROY JACKSON NEAR EDGE 5KV 1.0NA
20X MAG TV AREA
29/1/87

Figs.115 & 116. SIMS Analysis of Fe-1.46% Cr
Sectioned Sample

RJ2 Region 1 SVY

VG SCIENTIFIC

Positive SIMS. Target Bias 59.0 V Max Count Rate = 600
Step Size = 0.050 AMU Time = 160.00 secs x 2 Scans

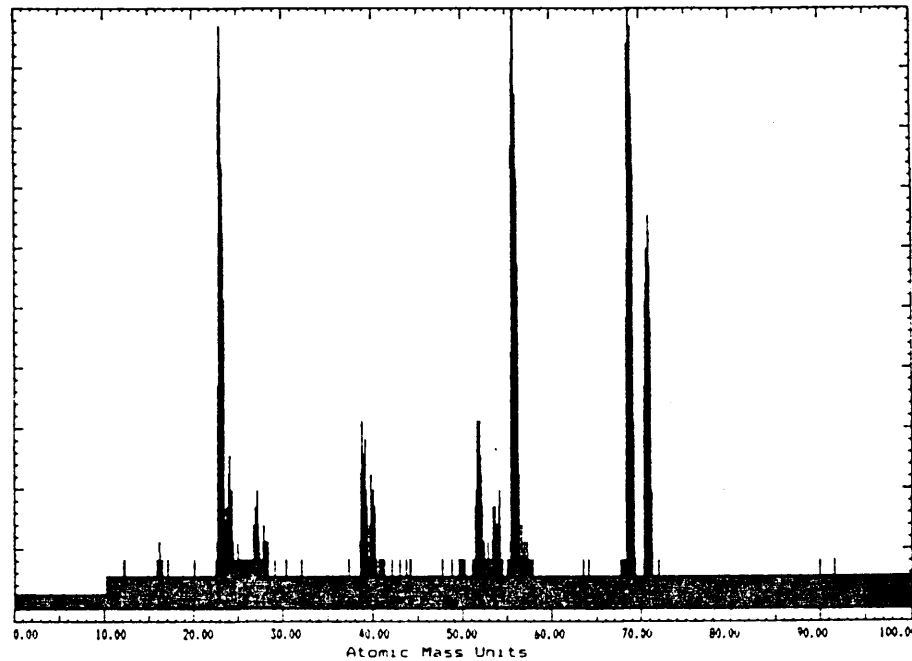


FURTHER IN THAN RJ1
SAME CONDITIONS
29/1/87

RJ3 Region 1 SVY

VG SCIENTIFIC

Negative SIMS. Target Bias 70.5 V Max Count Rate = 477
Step Size = 0.025 AMU Time = 160.00 secs x 2 Scans



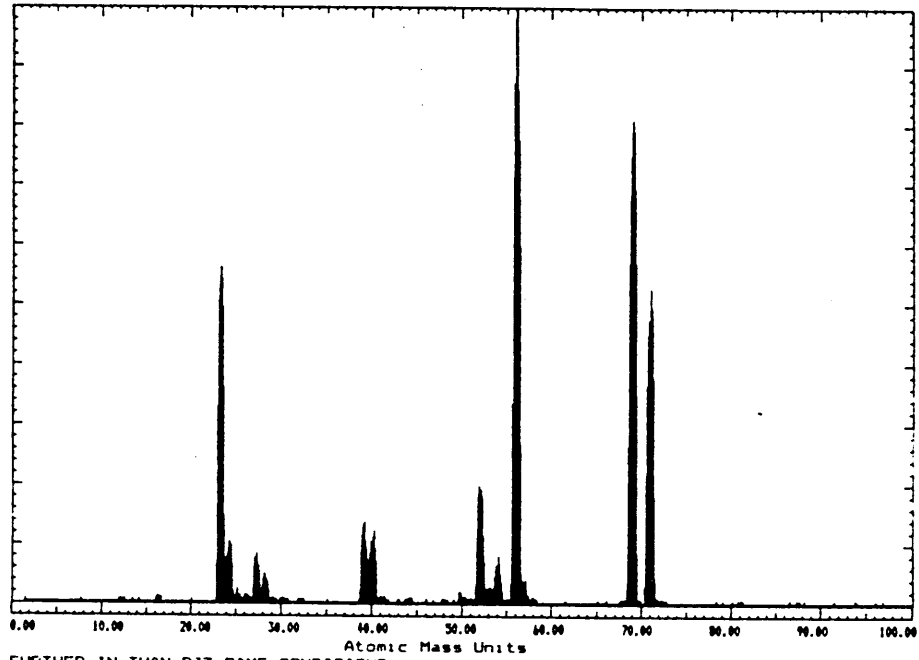
SAME AS RJ2 FURTHER IN SAME CONDITIONS
29/1/87

Figs.117 & 118. SIMS Analysis of Fe-1.46% Cr
Sectioned Sample

RJ4 Region 1 SVY

VG SCIENTIFIC

Positive SIMS. Target Bias 59.0 V Max Count Rate = 2056
Step Size = 0.050 AMU Time = 160.00 secs x 2 Scans

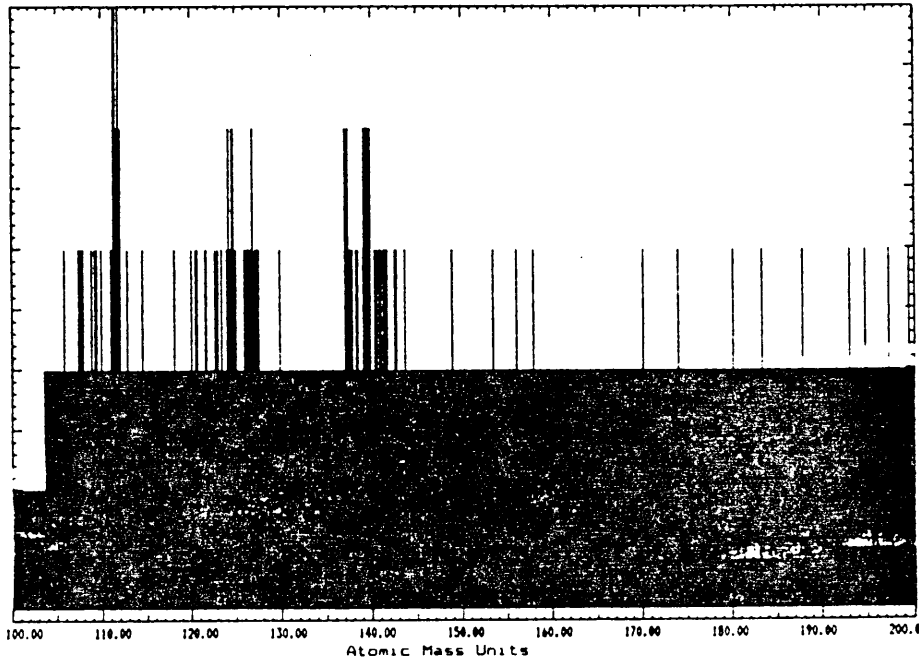


FURTHER IN THAN RJ3 SAME CONDITIONS
29/1/87

RJ4 Region 2 SVY

VG SCIENTIFIC

Positive SIMS. Target Bias 59.0 V Max Count Rate = .62
Step Size = 0.025 AMU Time = 160.00 secs x 2 Scans



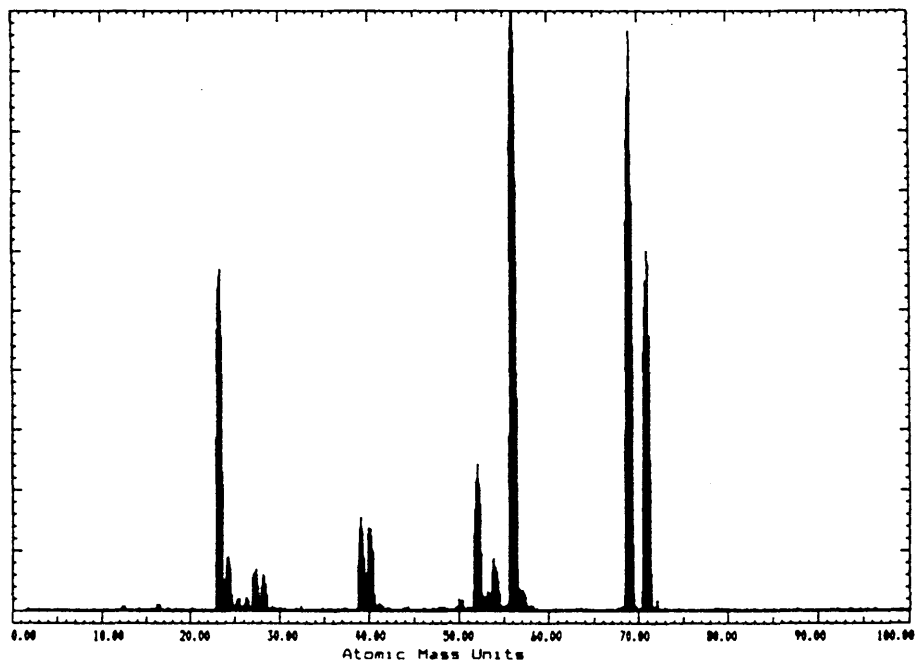
FURTHER IN THAN RJ3 SAME CONDITIONS
29/1/87

Figs.119 & 120. SIMS Analysis of Fe-1.46% Cr
Sectioned Sample

RJ5 Region 1 SVY

VG SCIENTIFIC

Positive SIMS. Target Bias 59.0 V Max Count Rate = 2312
Step Size = 0.050 AMU Time = 160.00 secs x 2 Scans



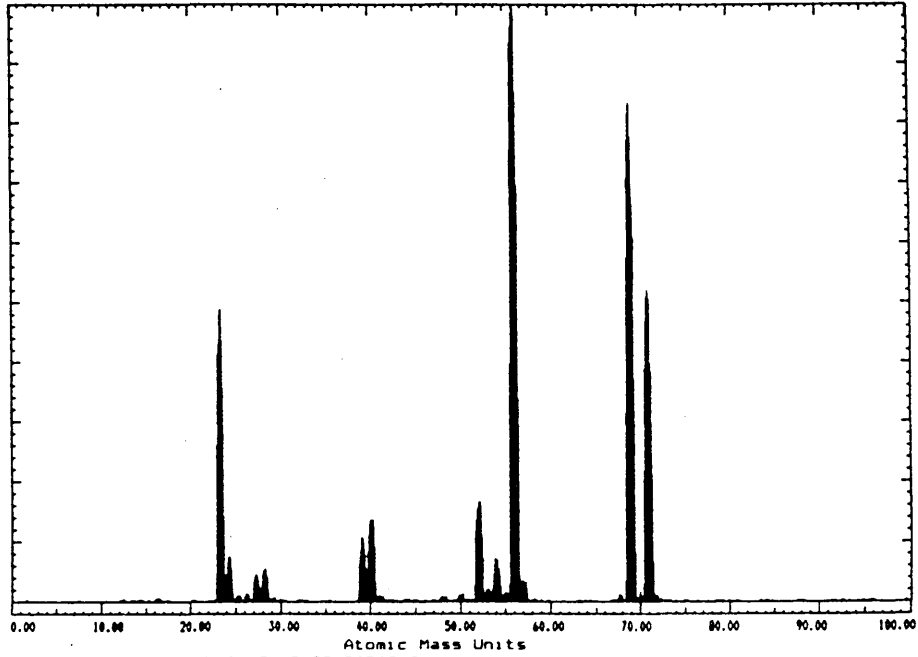
FURTHER IN SAME AS RJ4 SAME CONDITIONS
29/1/87

Fig.121. SIMS Analysis of Fe-1.46% Cr
Sectioned Sample

RJ6 Region 1 SVY

VG SCIENTIFIC

Positive SIMS. Target Bias 59.0 V Max Count Rate = 4787.
Step Size = 0.050 AMU Time = 160.00 secs x 2 Scans

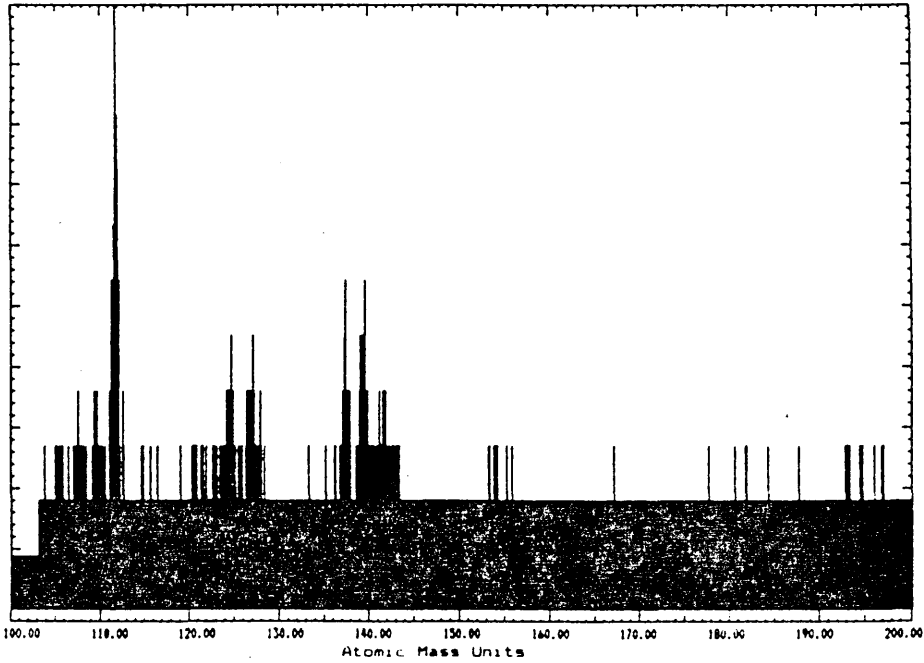


SAME AS RJ5 FURTHER IN SAME CONDITIONS
29/1/87

RJ6 Region 2 SVY

VG SCIENTIFIC

Positive SIMS. Target Bias 59.0 V Max Count Rate = 127
Step Size = 0.025 AMU Time = 160.00 secs x 2 Scans



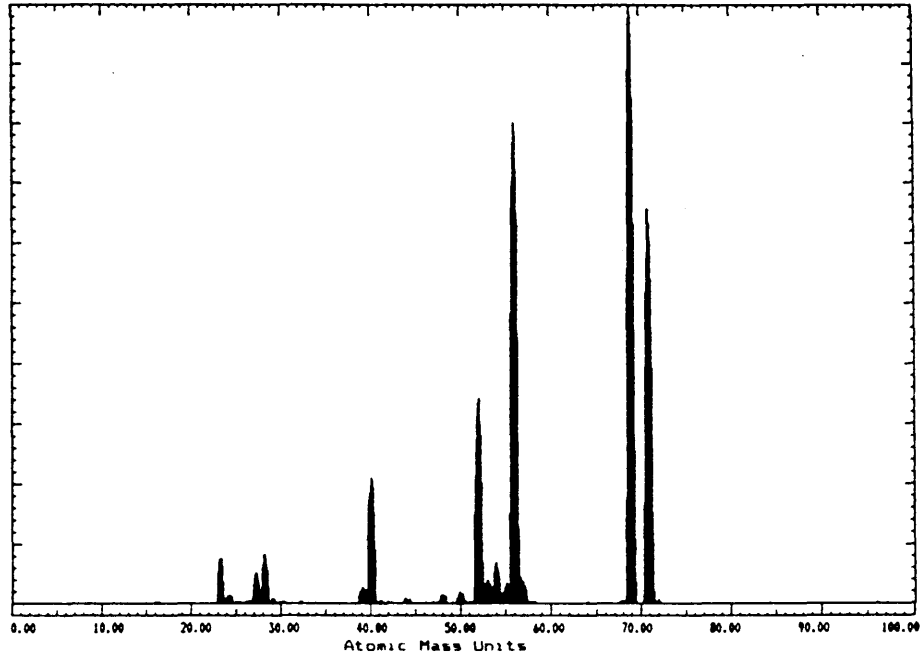
SAME AS RJ5 FURTHER IN SAME CONDITIONS
29/1/87

Figs.122 & 123. SIMS Analysis of Fe-1.46% Cr
Sectioned Sample

RJ7 Region 1 SVY

VG SCIENTIFIC

Positive SIMS. Target Bias 59.0 V Max Count Rate = 6287
Step Size = 0.050 AMU Time = 160.00 secs x 2 Scans

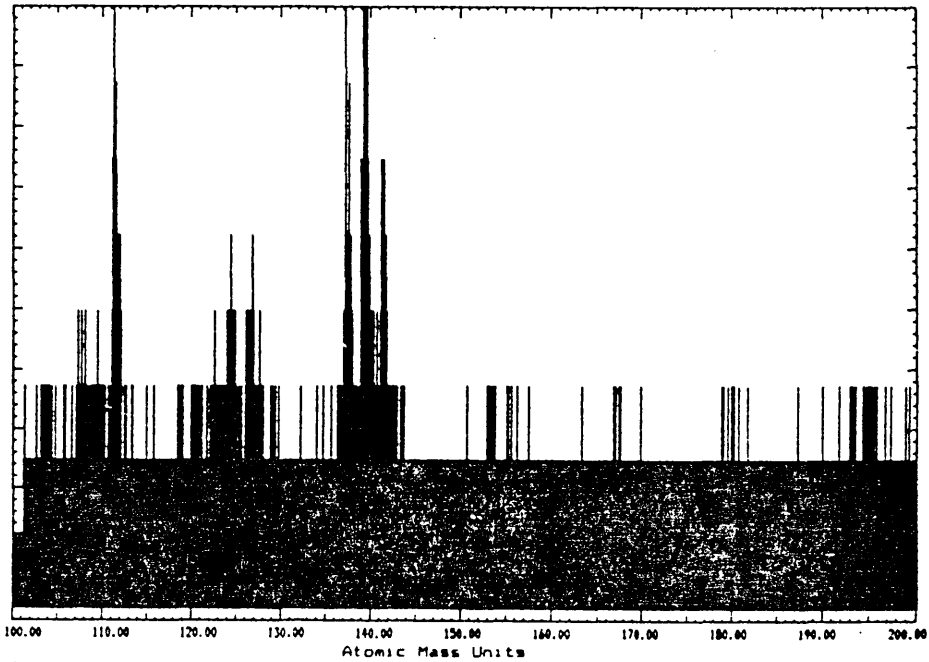


IN SMALL VOID SAME CONDITIONS
29/1/87

RJ7 Region 2 SVY

VG SCIENTIFIC

Positive SIMS. Target Bias 59.0 V Max Count Rate = 100
Step Size = 0.025 AMU Time = 160.00 secs x 2 Scans



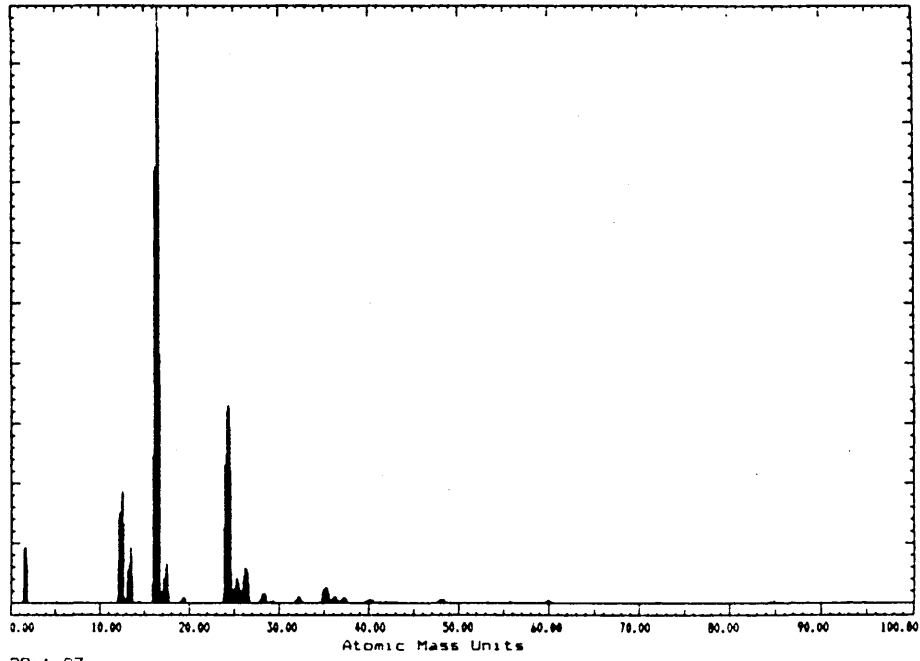
IN SMALL VOID SAME CONDITIONS
29/1/87

Figs.124 & 125. SIMS Analysis of Fe-1.46% Cr
Sectioned Sample

RJ1- Region 1 SVY

VG SCIENTIFIC

Negative SIMS. Target Bias 65.0 V Max Count Rate = 142e2
Step Size = 0.025 AMU Time = 160.00 secs x 2 Scans

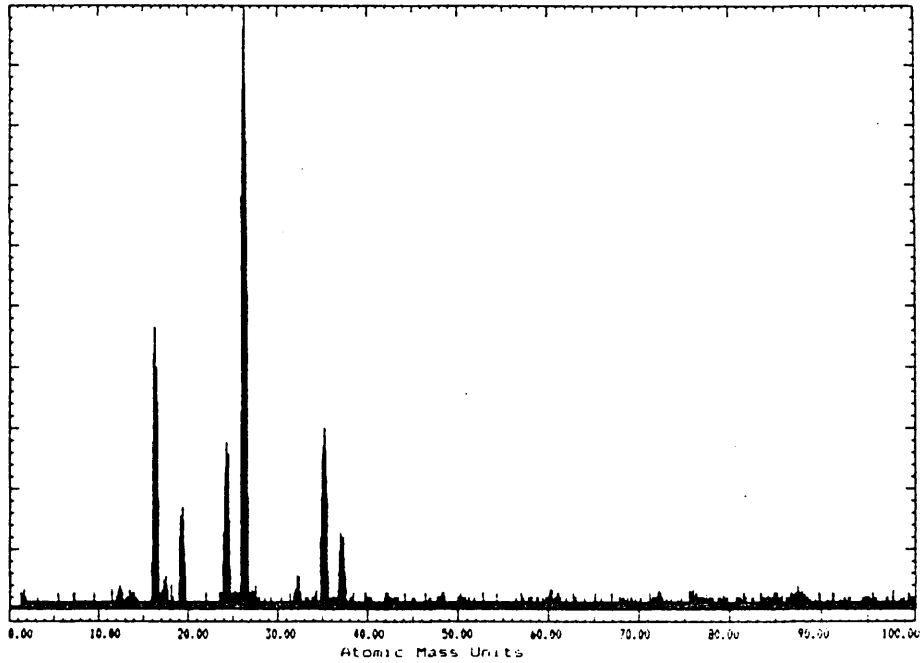


29:1:87
OXIDE LAYER

RJ2- Region 1 SVY

VG SCIENTIFIC

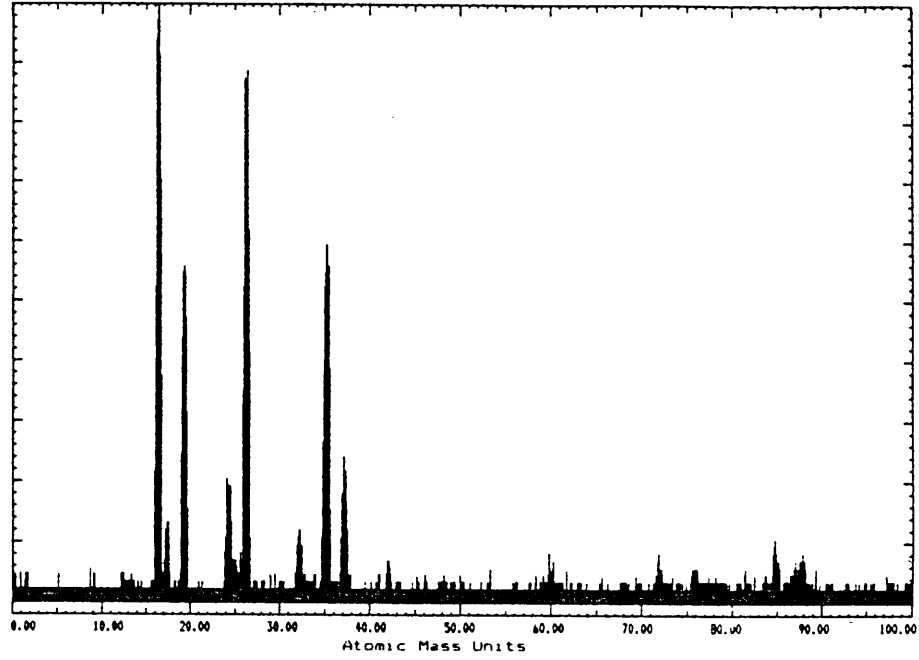
Negative SIMS. Target Bias 65.0 V Max Count Rate = 1777
Step Size = 0.025 AMU Time = 160.00 secs x 2 Scans



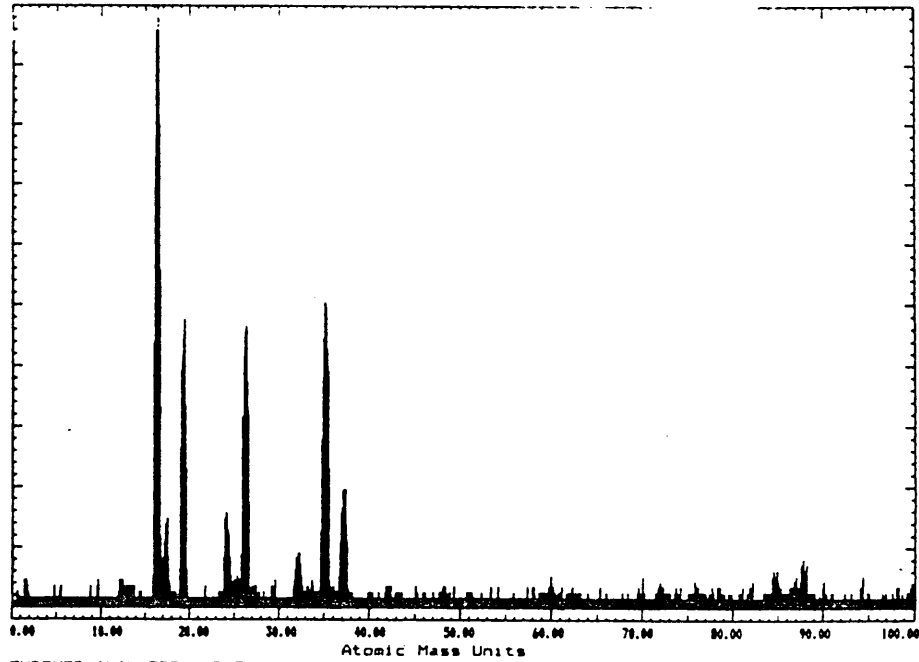
29:1:87
FURTHER AWAY FROM HOLE

Figs.126 & 127. SIMS Analysis of Fe-1.46% Cr Sectioned Sample

Negative SIMS. Target Bias 65.0 V Max Count Rate = 1025
Step Size = 0.025 AMU Time = 160.00 secs x 2 Scans



Region 1 SVY
Negative SIMS. Target Bias 65.0 V Max Count Rate = 1025
Step Size = 0.025 AMU Time = 160.00 secs x 2 Scans



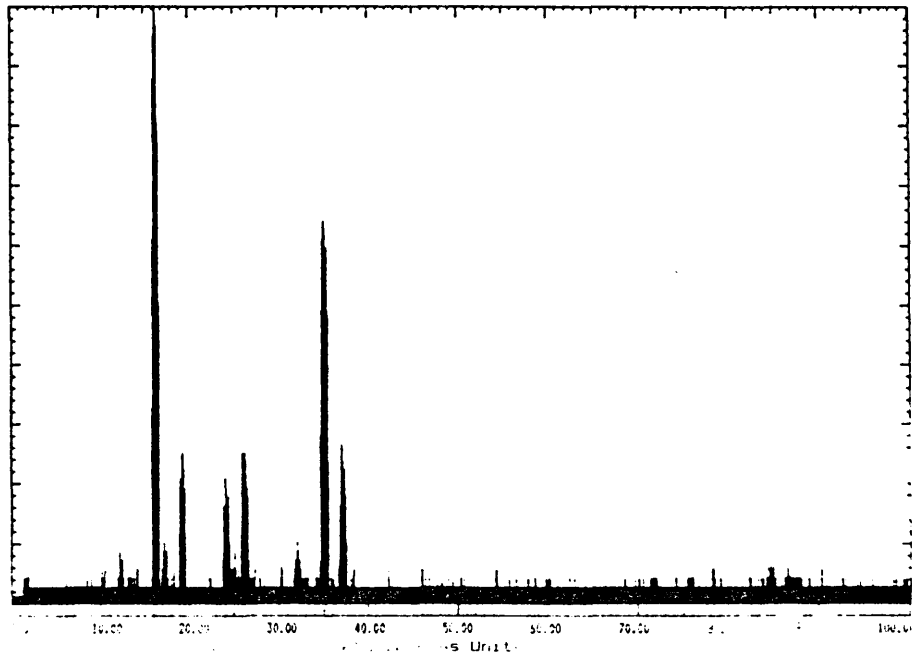
FURTHER AWAY FROM HOLE
29:11:87

Figs.128 & 129. SIMS Analysis of Fe-1.46% Cr Sectioned Sample

RJ6- Region 1 SVY

VG SCIENTIFIC

Negative SIMS. Target Bias 65.0 V Max Count Rate = 877
Step Size = 0.025 AMU Time = 160.00 secs x 2 Scans

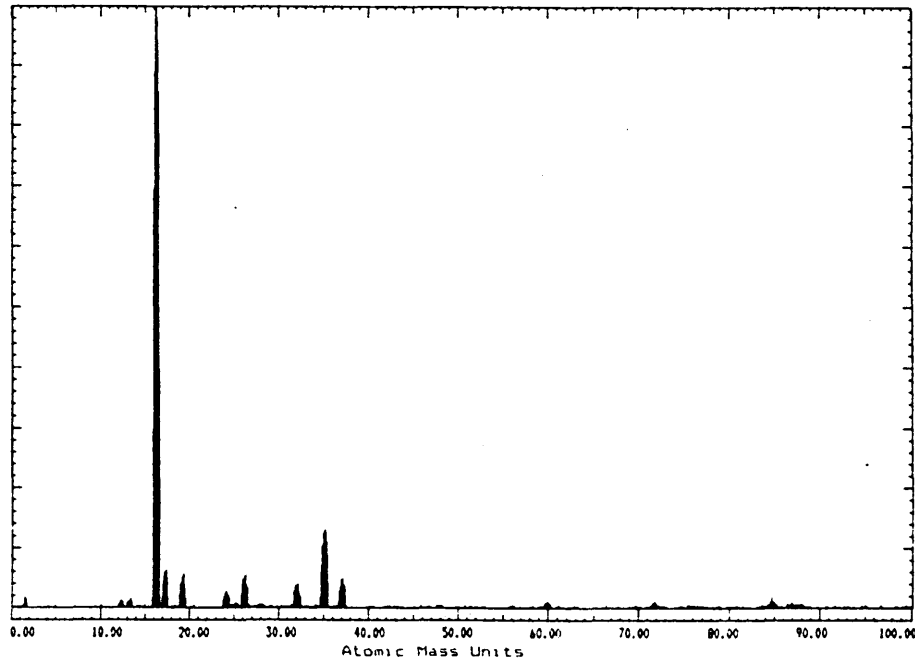


0.00 10.00 20.00 30.00 40.00 50.00 60.00 70.00 80.00 90.00 100.00
Atomic Mass Units

RJ7- Region 1 SVY

VG SCIENTIFIC

Negative SIMS. Target Bias 65.0 V Max Count Rate = 7500
Step Size = 0.025 AMU Time = 160.00 secs x 2 Scans

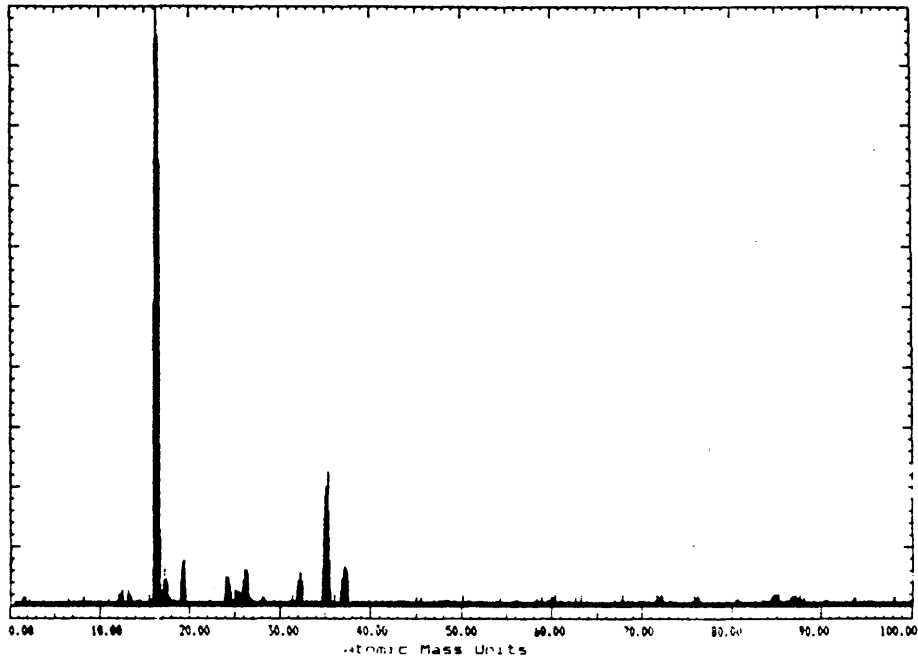


0.00 10.00 20.00 30.00 40.00 50.00 60.00 70.00 80.00 90.00 100.00
Atomic Mass Units

-VE OF RJ7
29/1/87

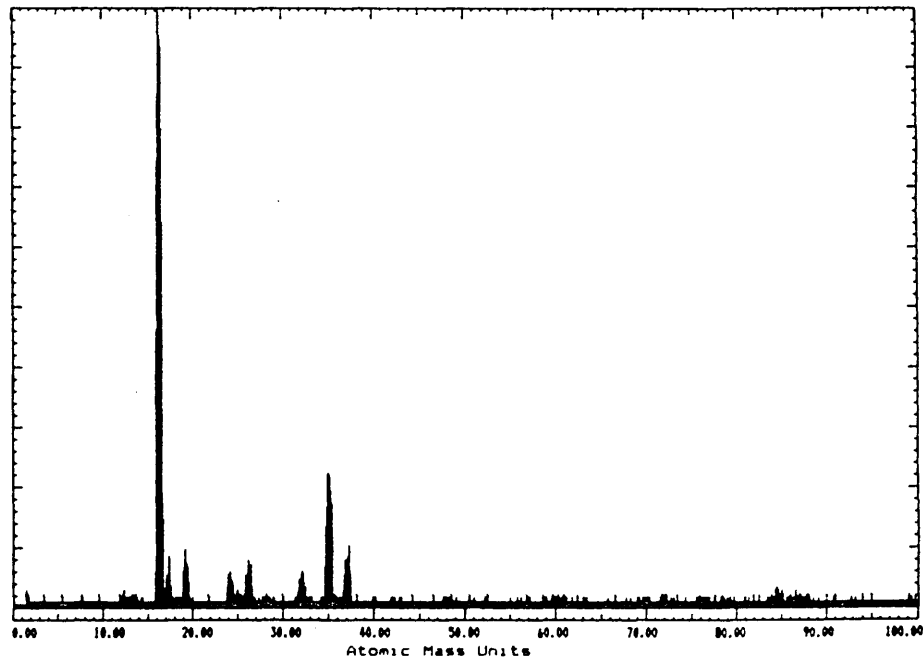
Figs.130 & 131. SIMS Analysis of Fe-1.46% Cr
Sectioned Sample

Negative SIMS. Target Bias 65.0 V Max Count Rate = 2850
Step Size = 0.025 AMU Time = 160.00 secs x 2 Scans



29:11:87
RJ7- REPEATED SAME AREA

Negative SIMS. Target Bias 65.0 V Max Count Rate = 2850
Step Size = 0.025 AMU Time = 160.00 secs x 2 Scans



REPEAT OF RJ7-R SAME AREA

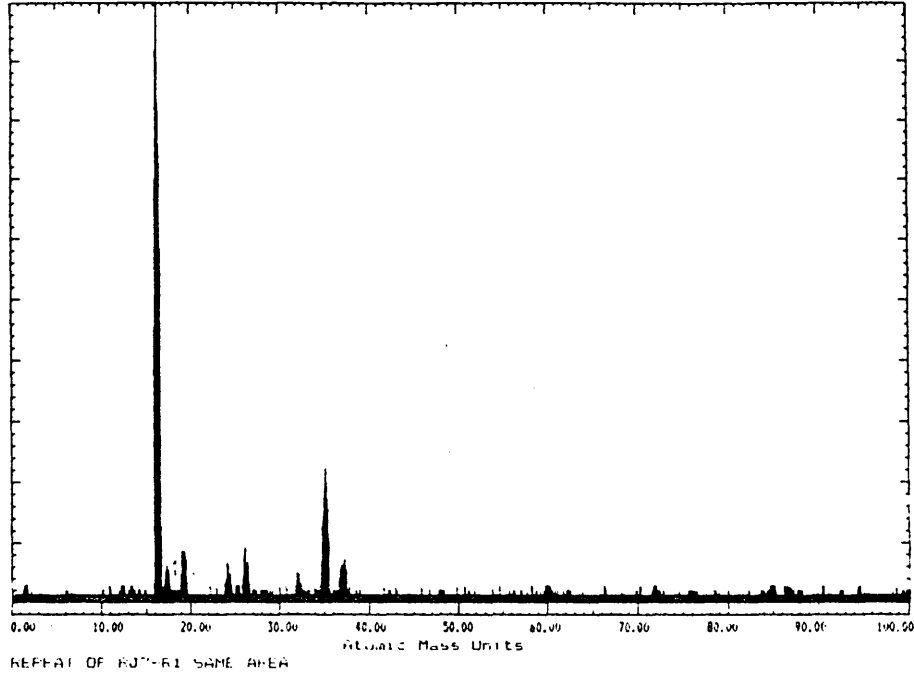
29:11:87

Figs.132 & 133. SIMS Analysis of Fe-1.46% Cr Sectioned Sample

RJ7-R2 Region 1 SVY

VG SCIENTIFIC

Negative SIMS. Target Bias 65.0 V Max Count Rate = 1725
Step Size = 0.025 AMU Time = 160.00 secs x 2 Scans



0.000000

Fig.134. SIMS Analysis of Fe-1.46% Cr
Sectioned Sample

Figure 135

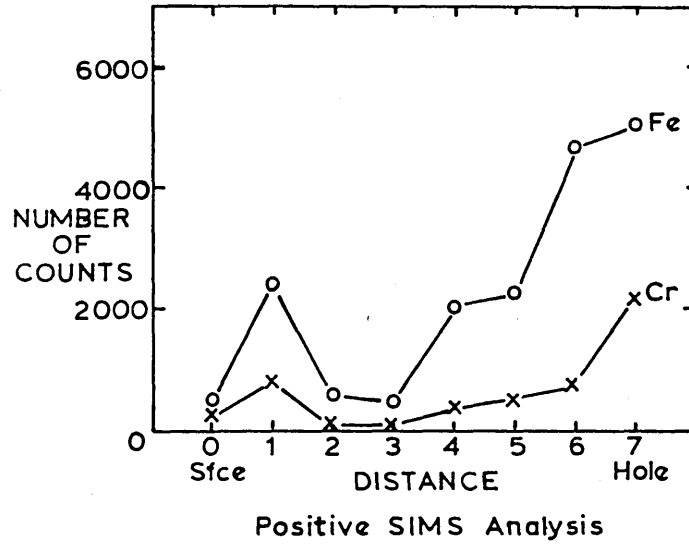
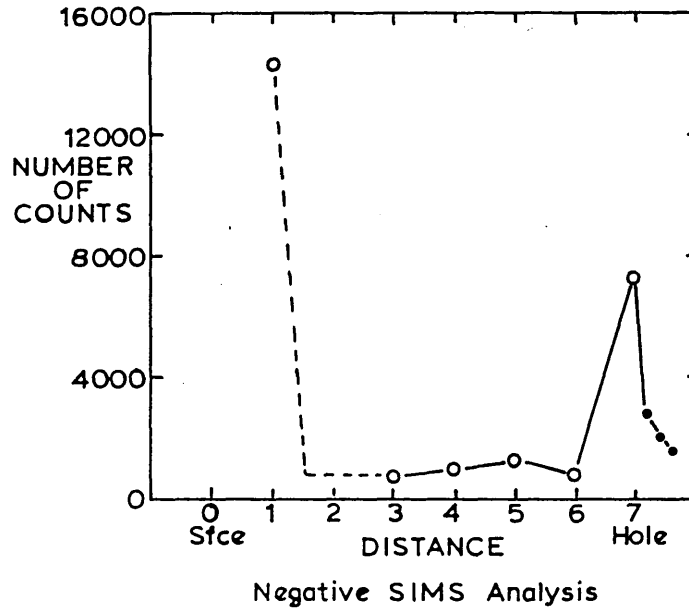
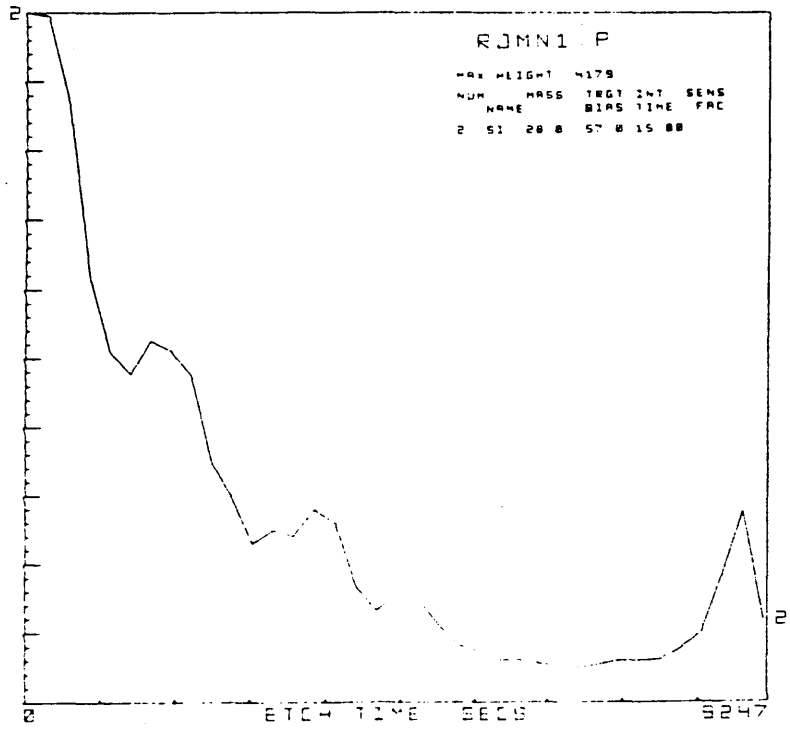
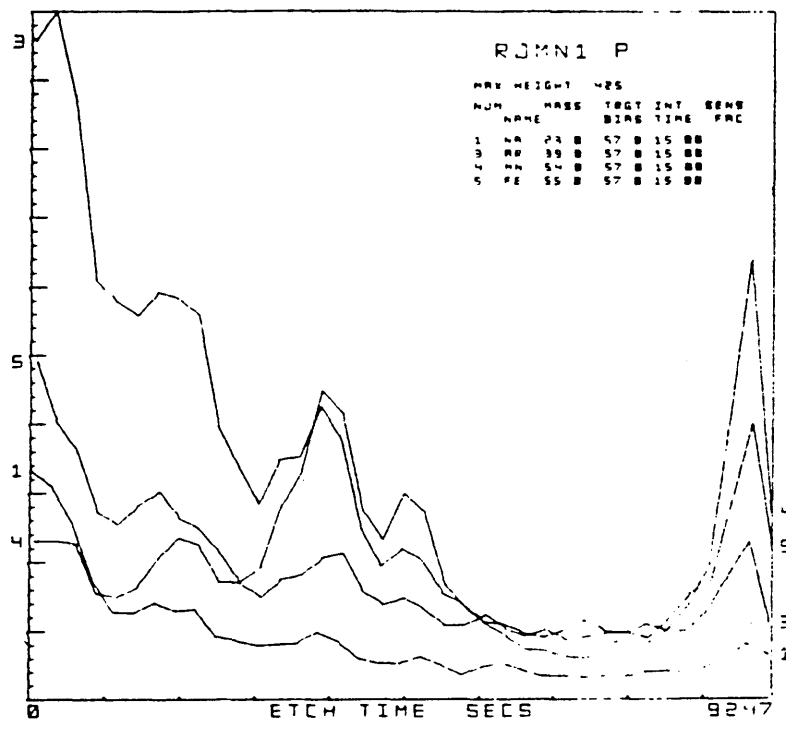


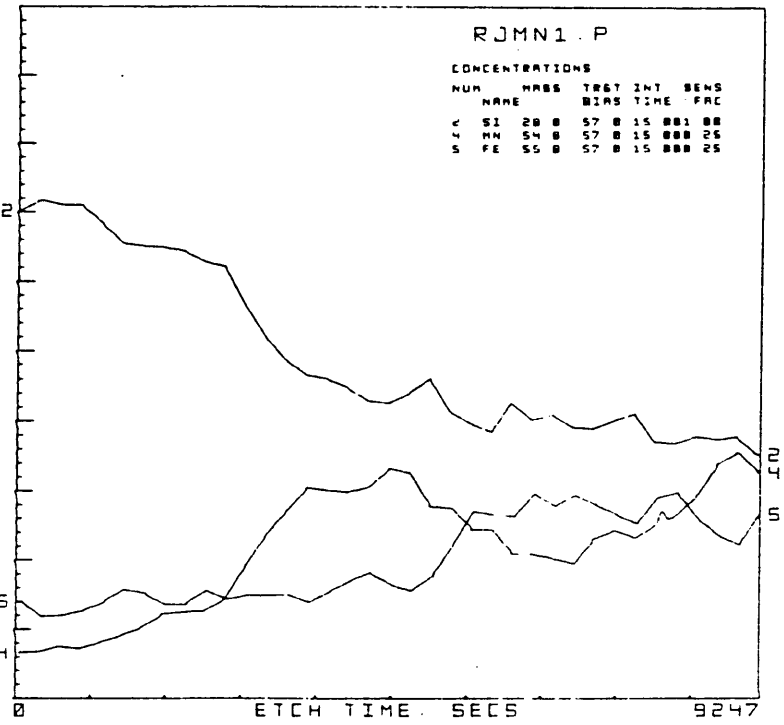
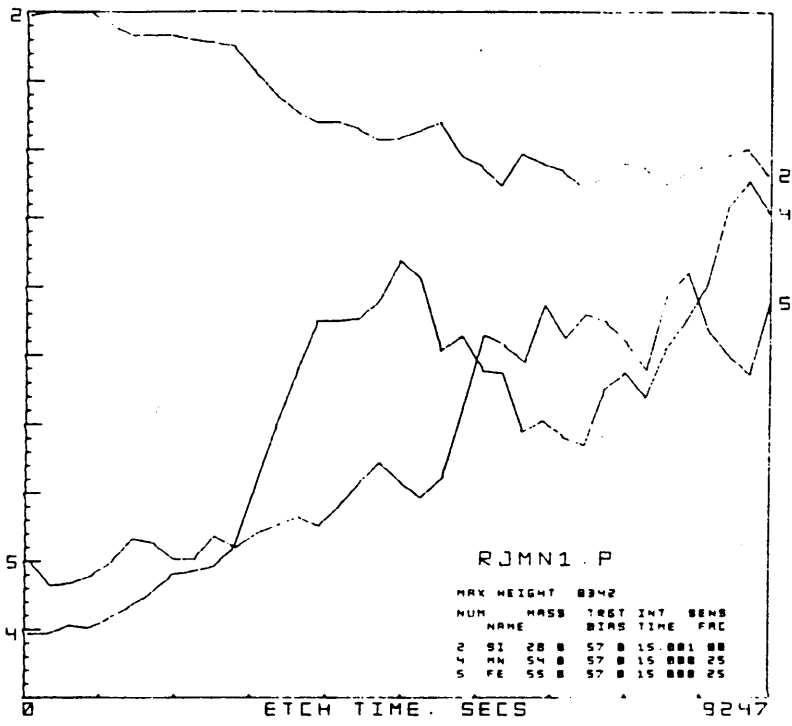
Figure 136



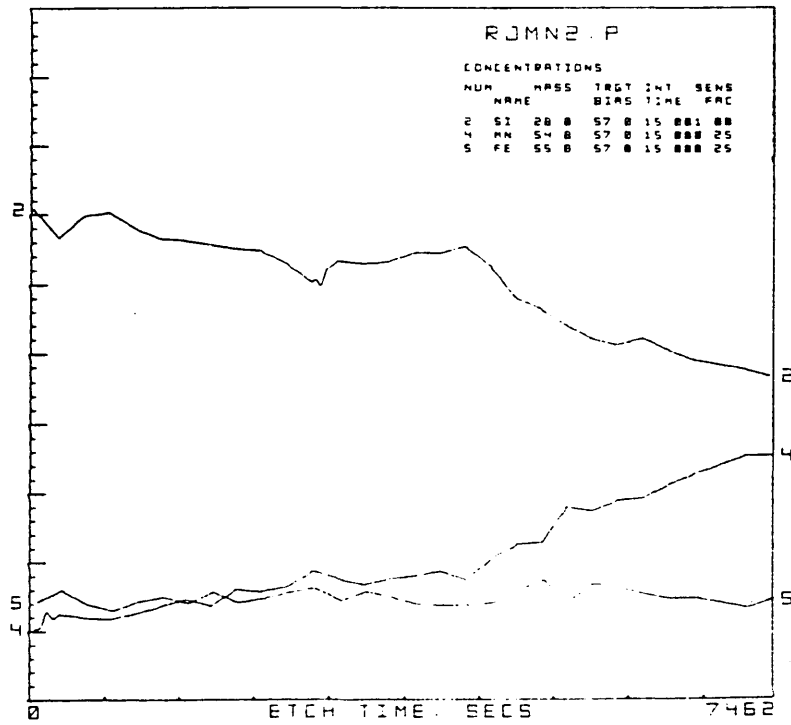
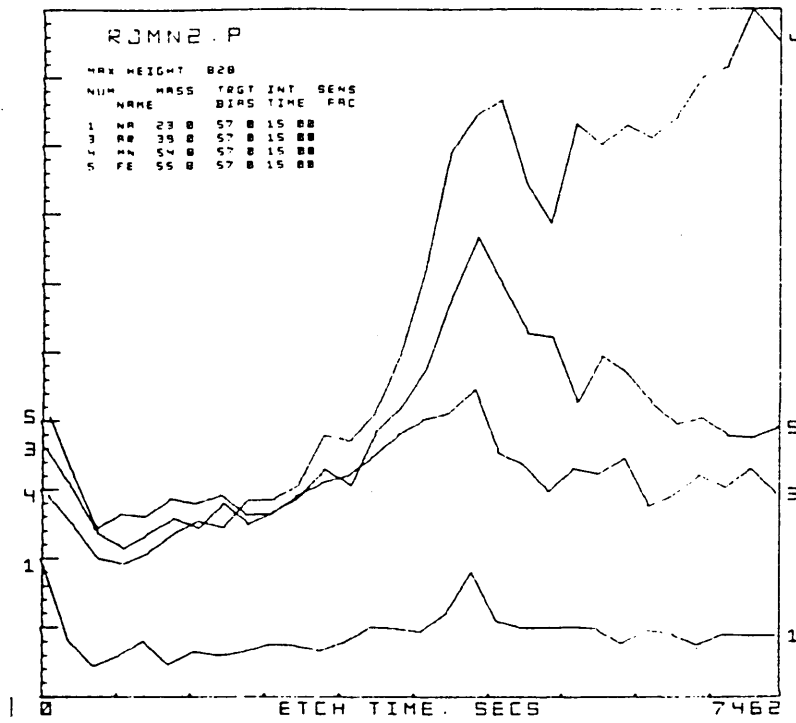
SIMS Analysis of an Area of 1.46% Cr Alloy



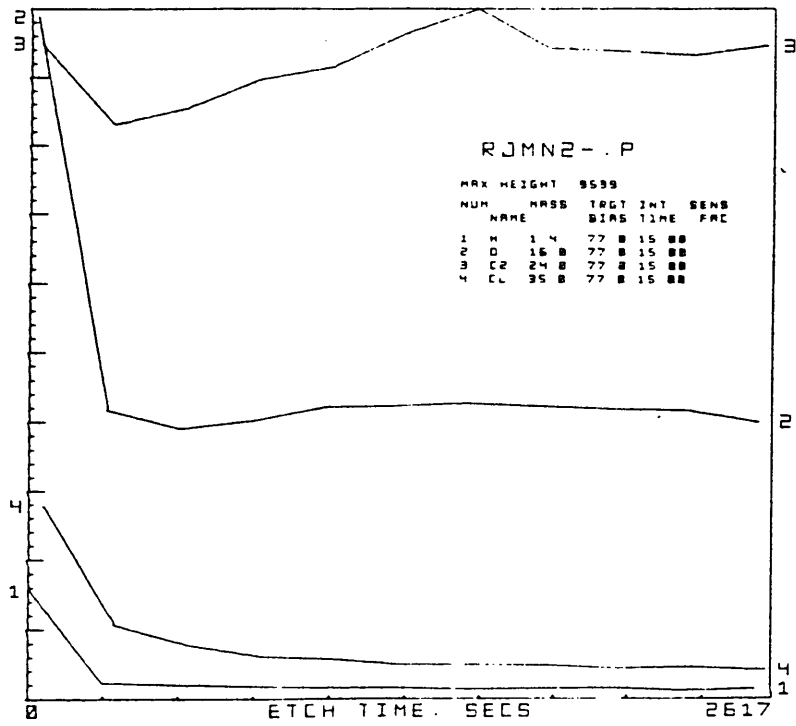
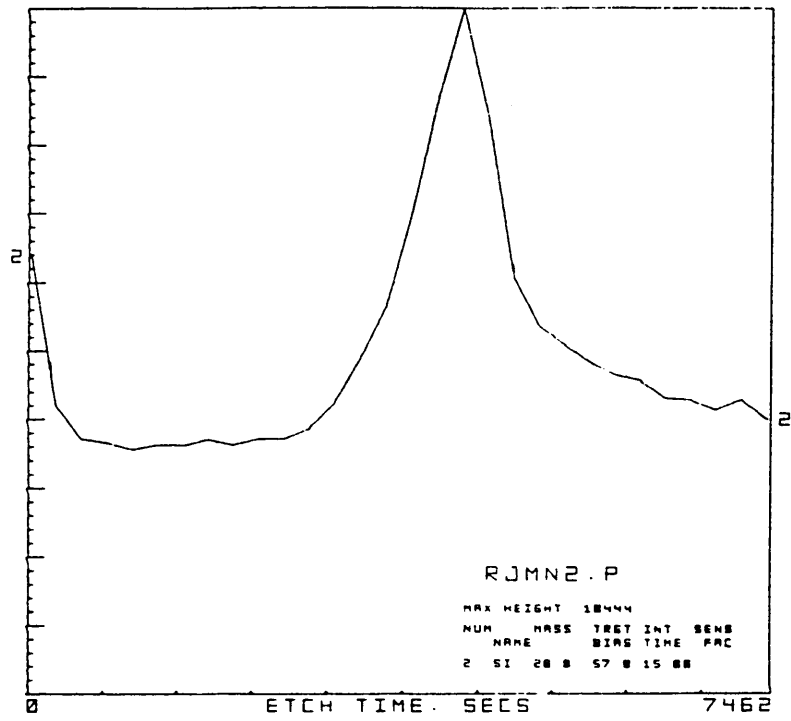
Figs.137 & 138. SIMS Analysis of Oxide Film Depth Profile, Fe-1.0% Mn



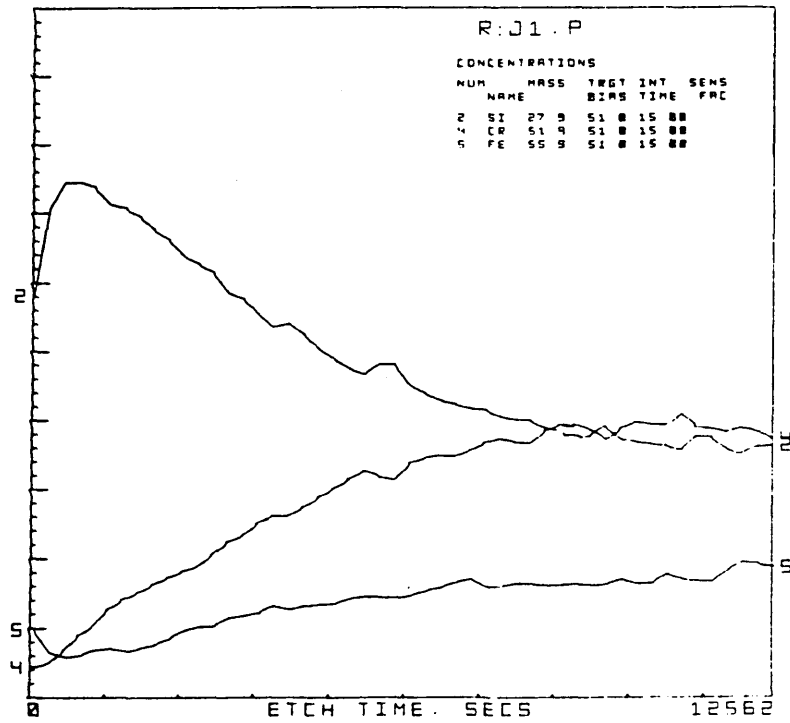
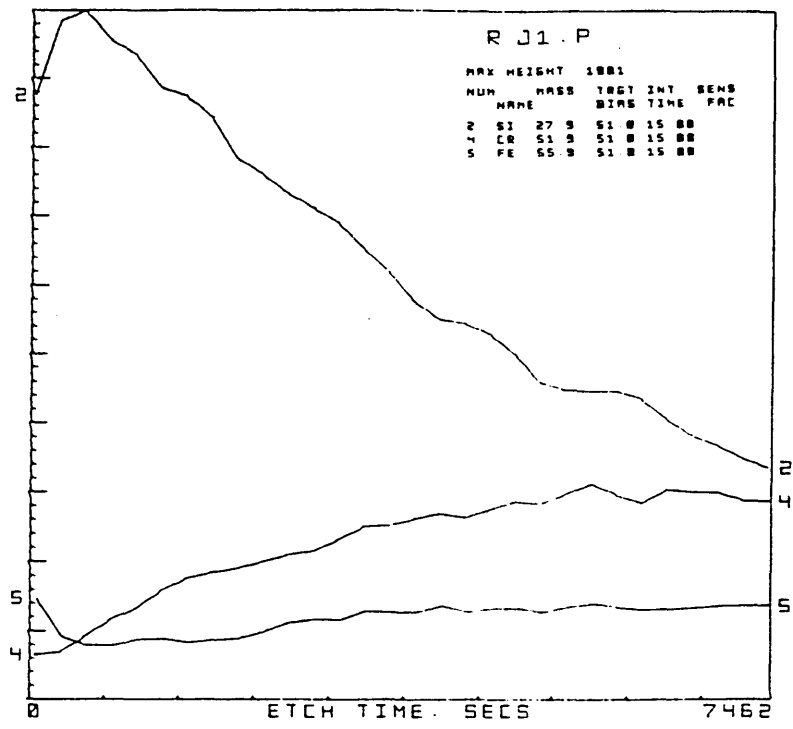
Figs.139 & 140. SIMS Analysis of Oxide Film Depth Profile, Fe-1.0% Mn



Figs.141 & 142. SIMS Analysis of Oxide Film Depth Profile, Fe-1.0% Mn



Figs.143 & 144. SIMS Analysis of Oxide Film Depth Profile, Fe-1.0% Mn



Figs.145 & 146. SIMS Analysis of Oxide Film Depth Profile, Fe-1.46% Cr

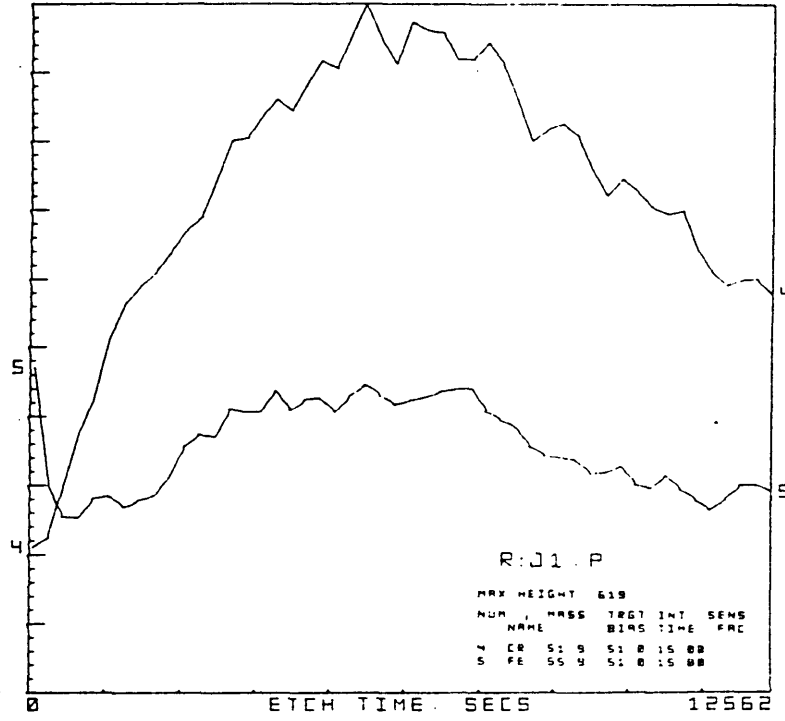


Fig.147. SIMS Analysis of Oxide Film Depth Profile, Fe-1.46% Cr

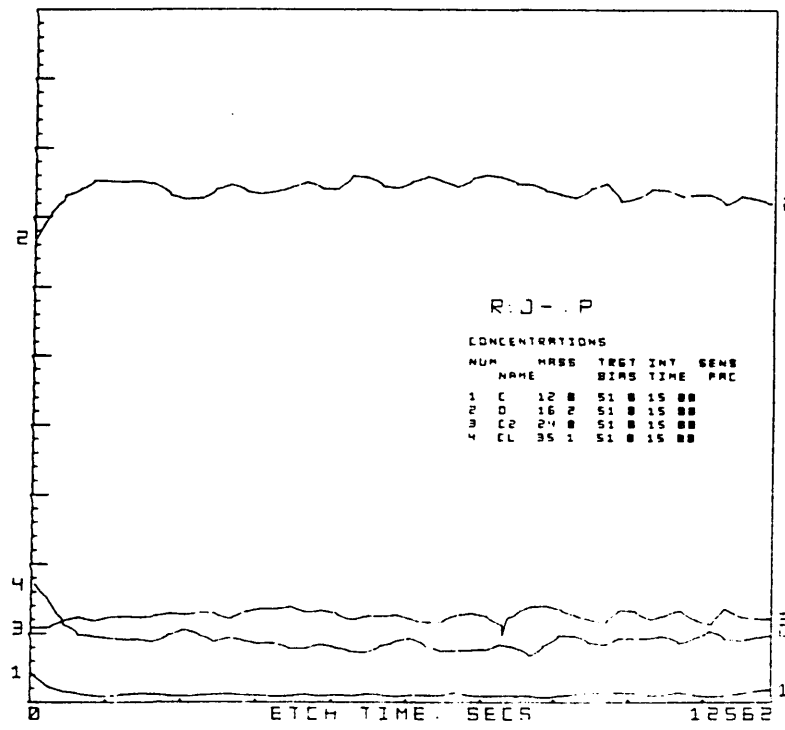
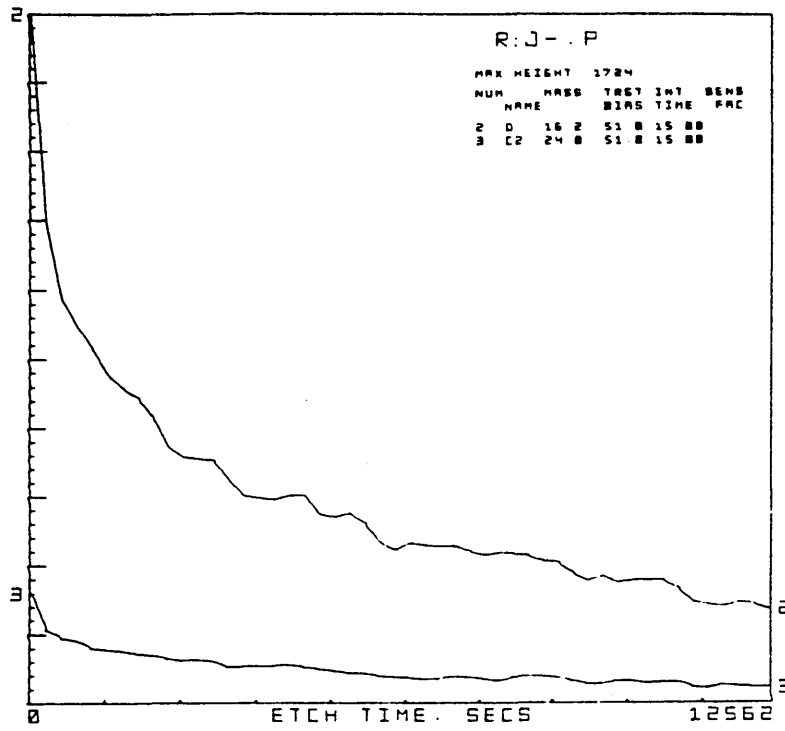
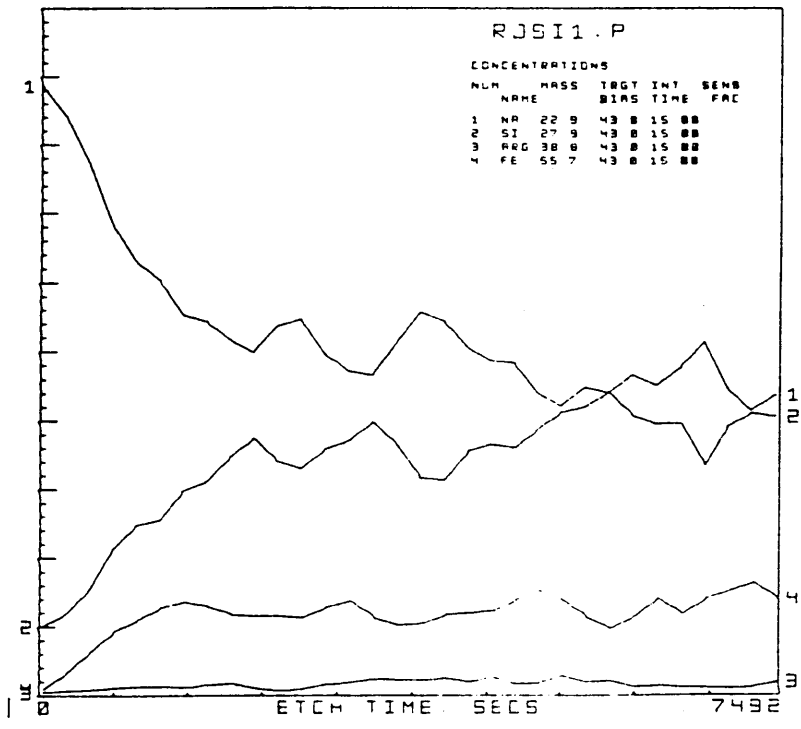
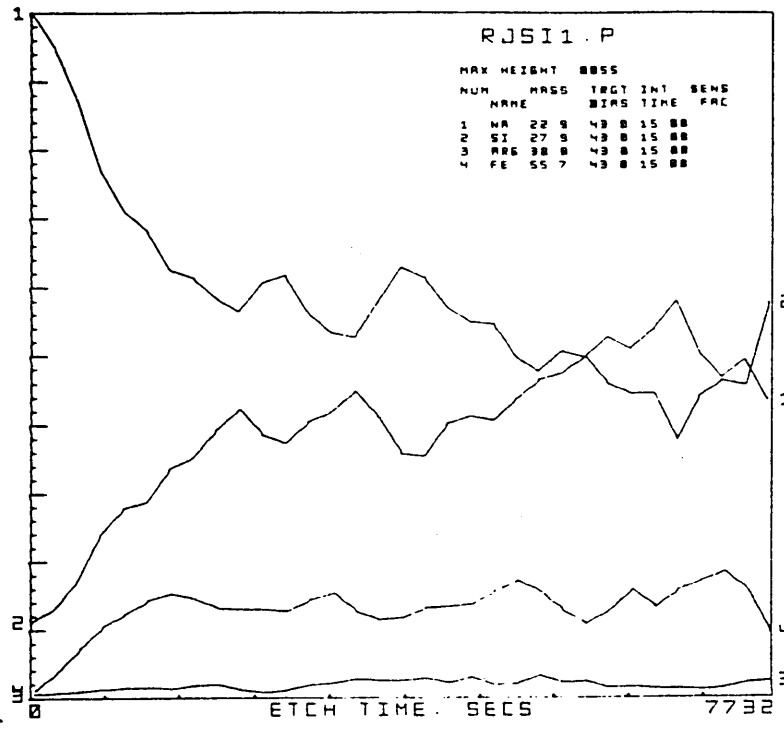


Fig.148 & 149. SIMS Analysis of Oxide Film
Depth Profile, Fe-1.46% Cr



Figs.150 & 151. SIMS Analysis of Oxide Film Depth Profile, Fe-1.33% Si

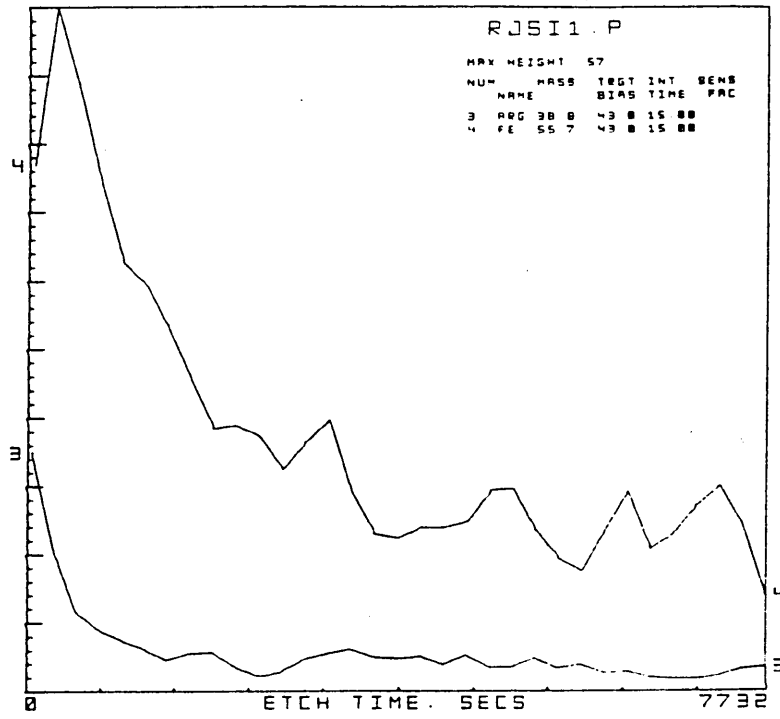
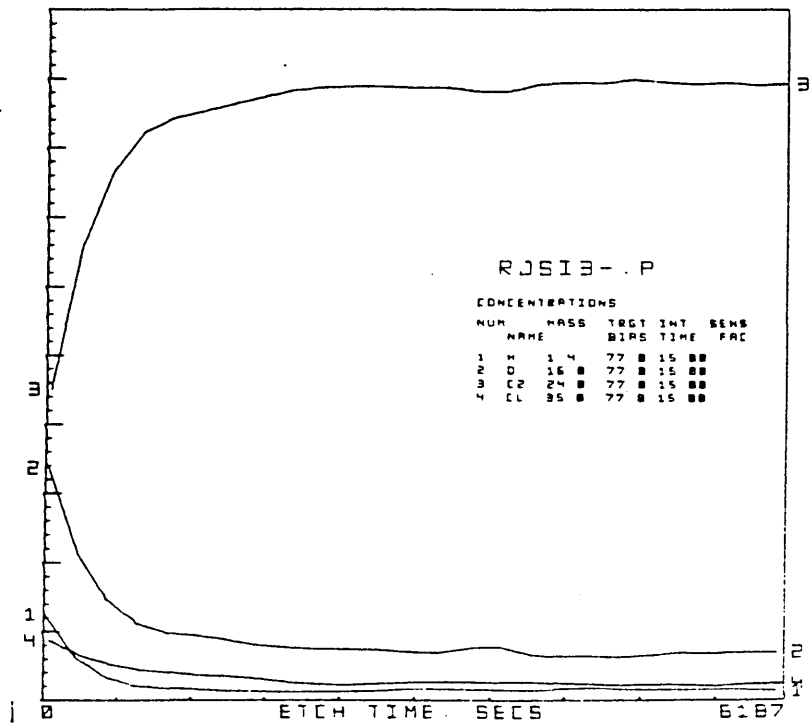
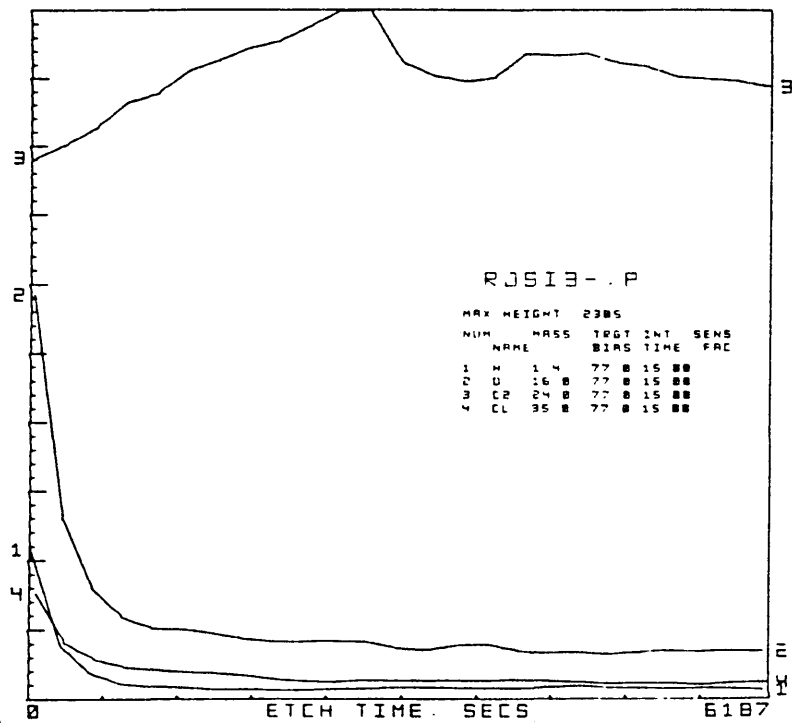


Fig.152. SIMS Analysis of Oxide Film
Depth Profile, Fe-1.33% Si



Figs.153 & 154. SIMS Analysis of Oxide Film Depth Profile, Fe-1.33% Si

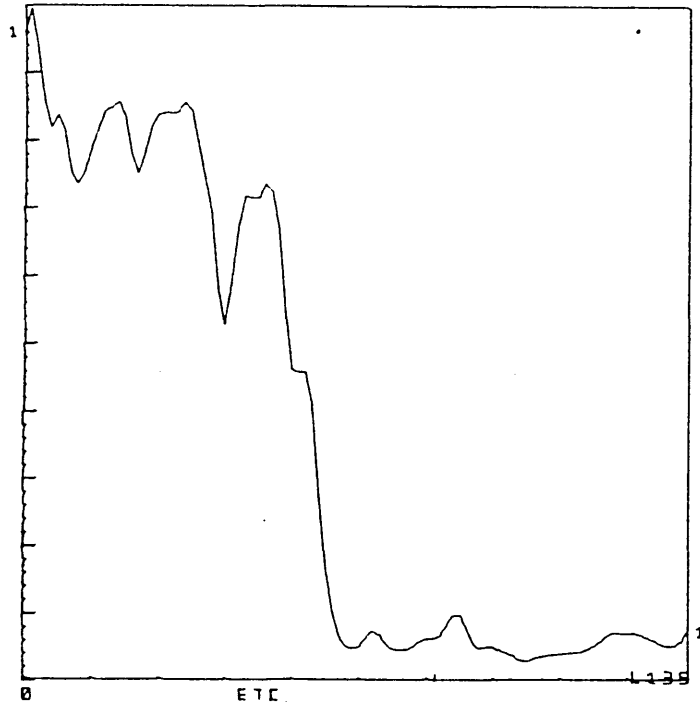
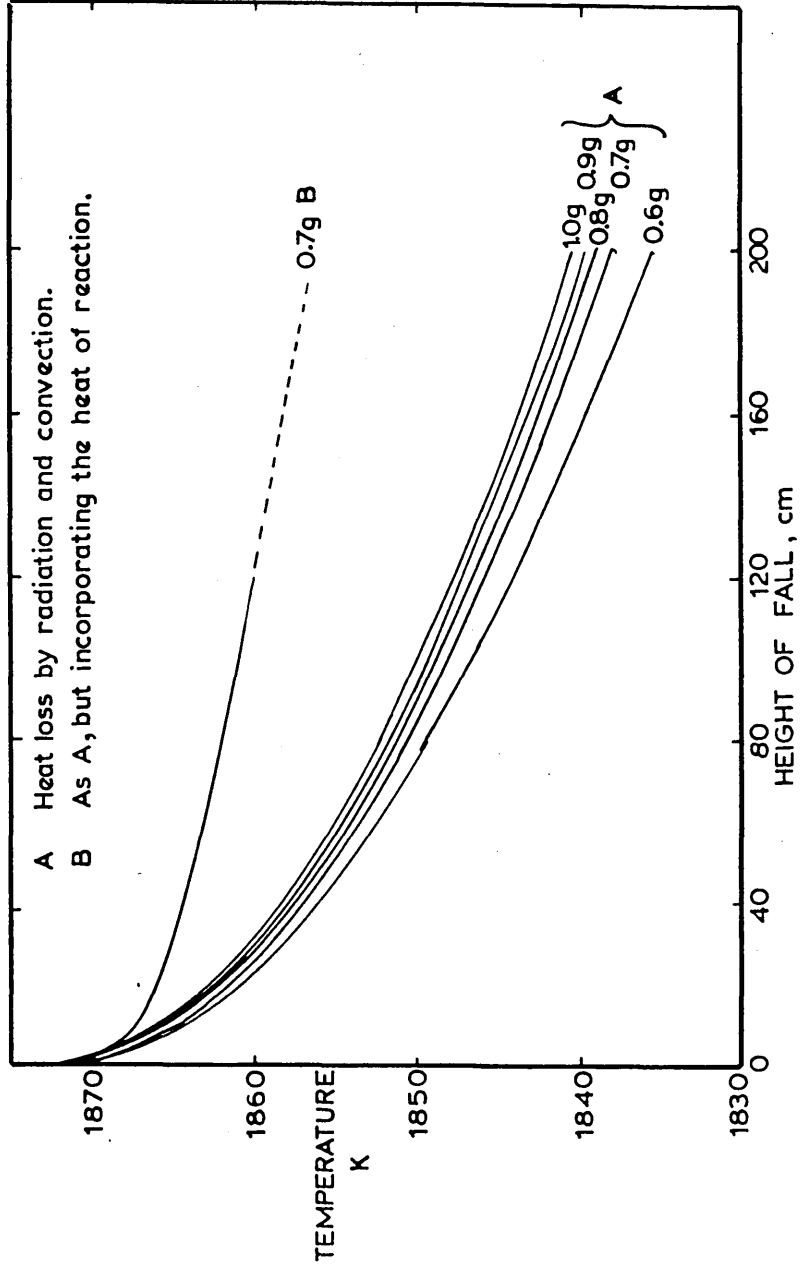


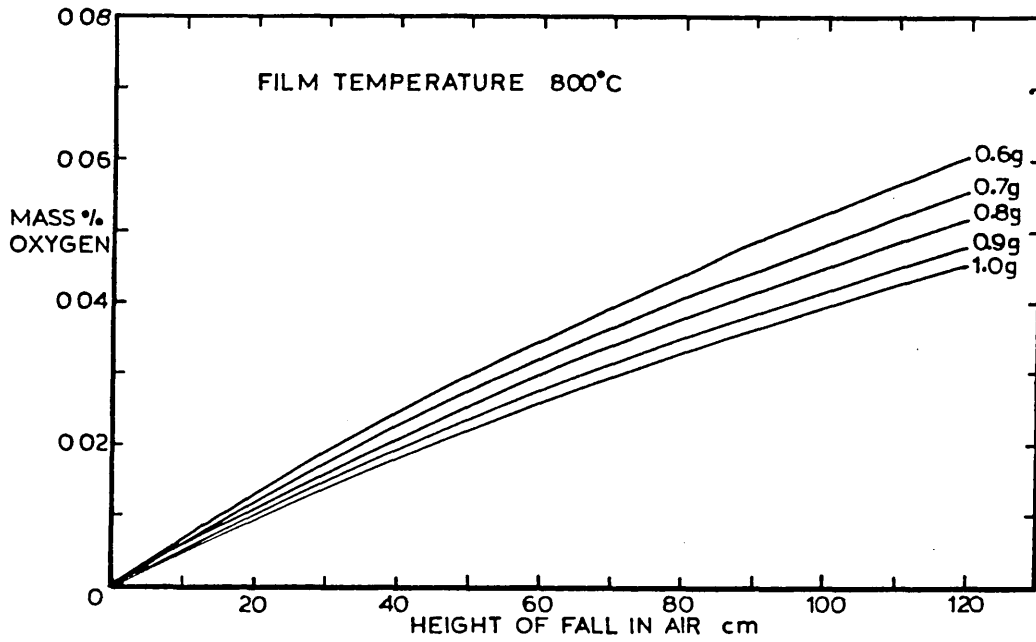
Fig.155. SIMS Analysis of Oxide Film
Depth Profile for Oxygen
Fe-0.5% Mn, Oxidised in air
followed by reduction in hydrogen

Figure 156



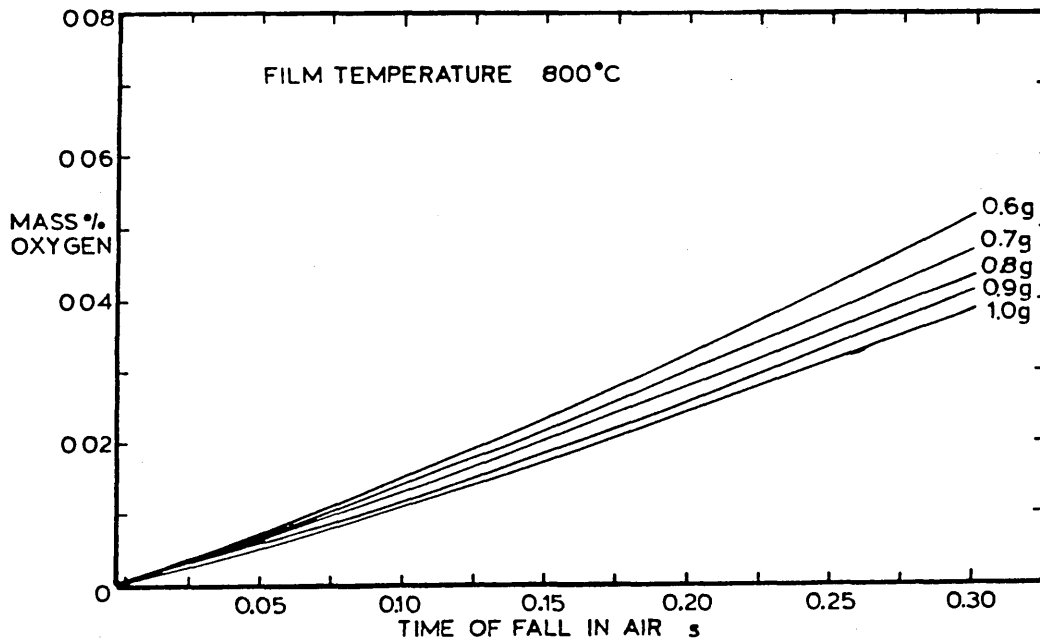
Temperature of Different Sized Droplets as a Function of Height of Fall.

Figure 157



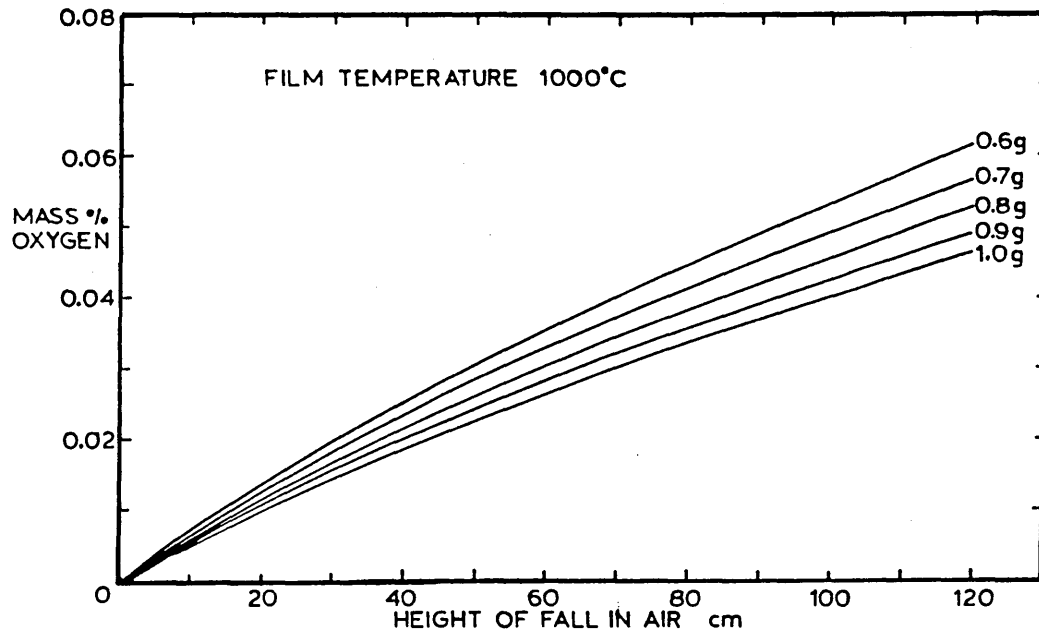
Oxygen level vs Height of fall for Iron Droplets of Different Mass

Figure 158



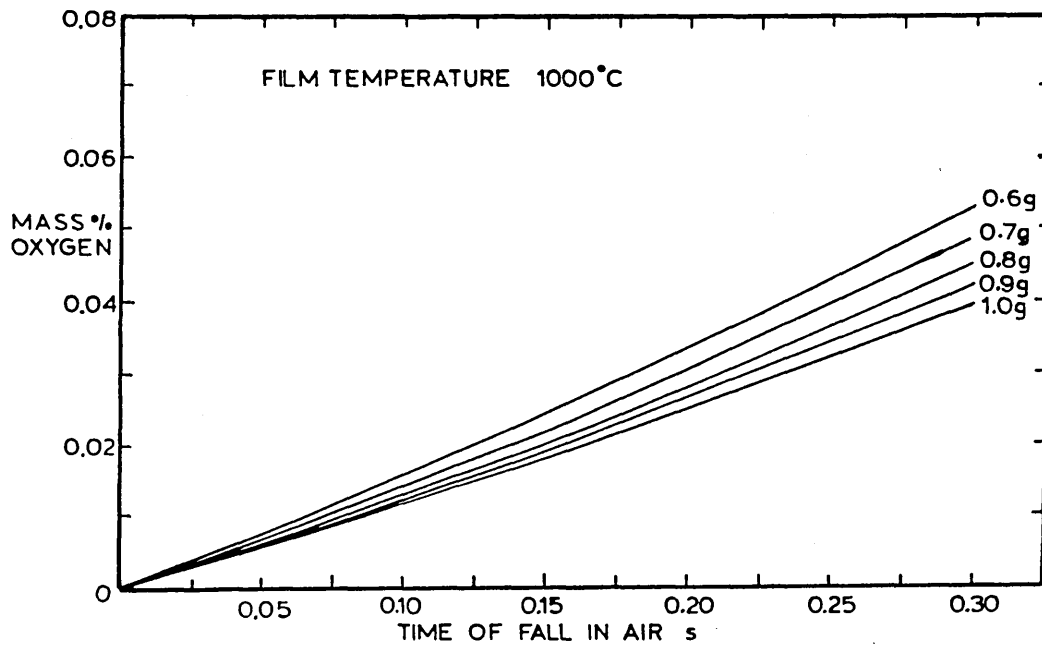
Oxygen level vs Time of fall for Iron Droplets of Different Mass

Figure 159



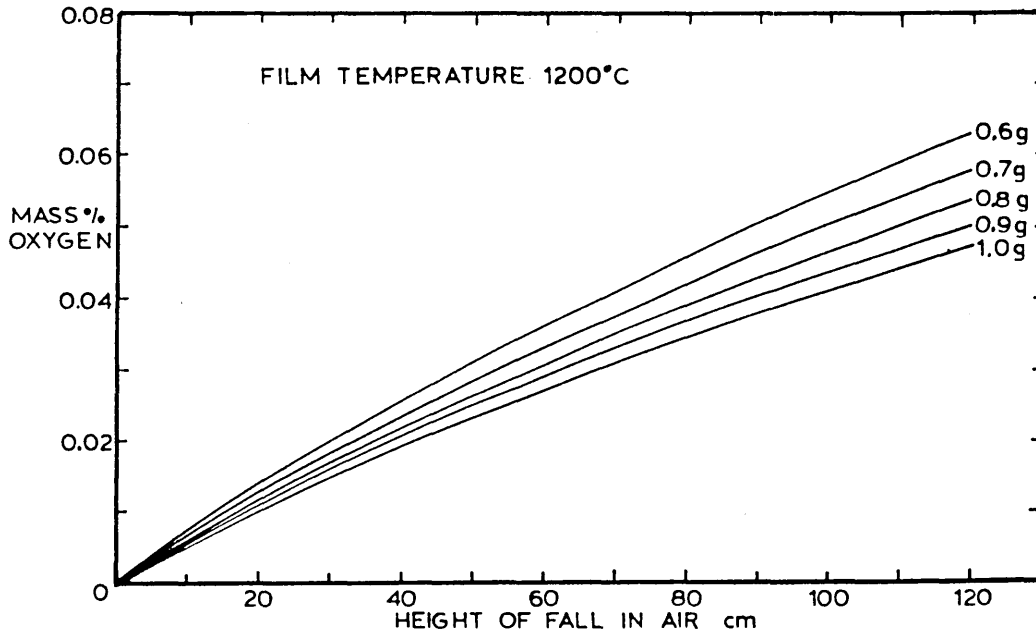
Oxygen level vs Height of fall for Iron Droplets of Different Mass

Figure 160



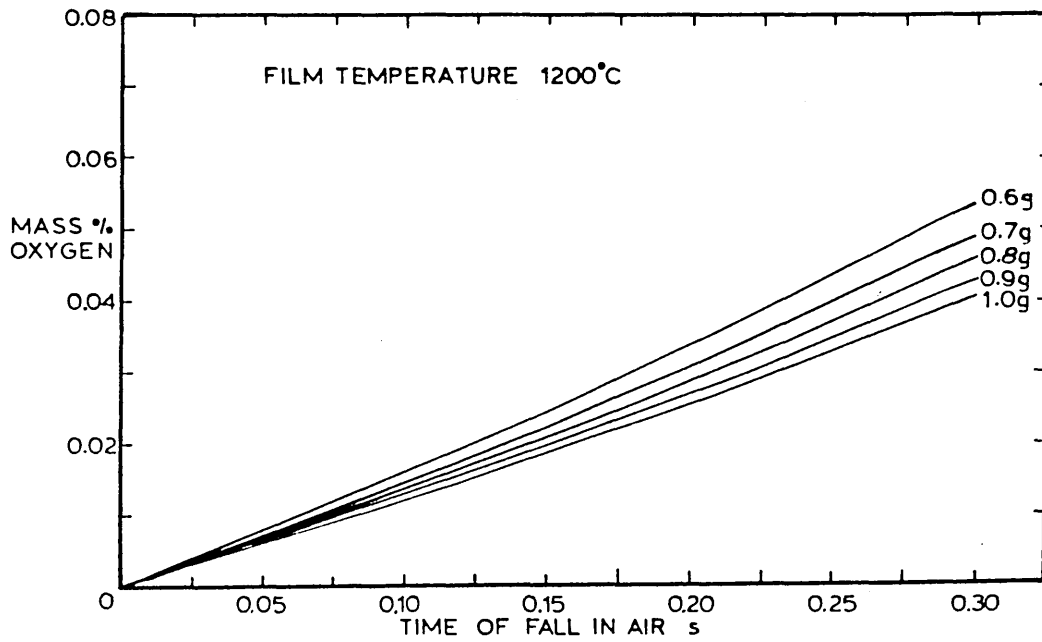
Oxygen level vs Time of fall for Iron Droplets of Different Mass

Figure 161



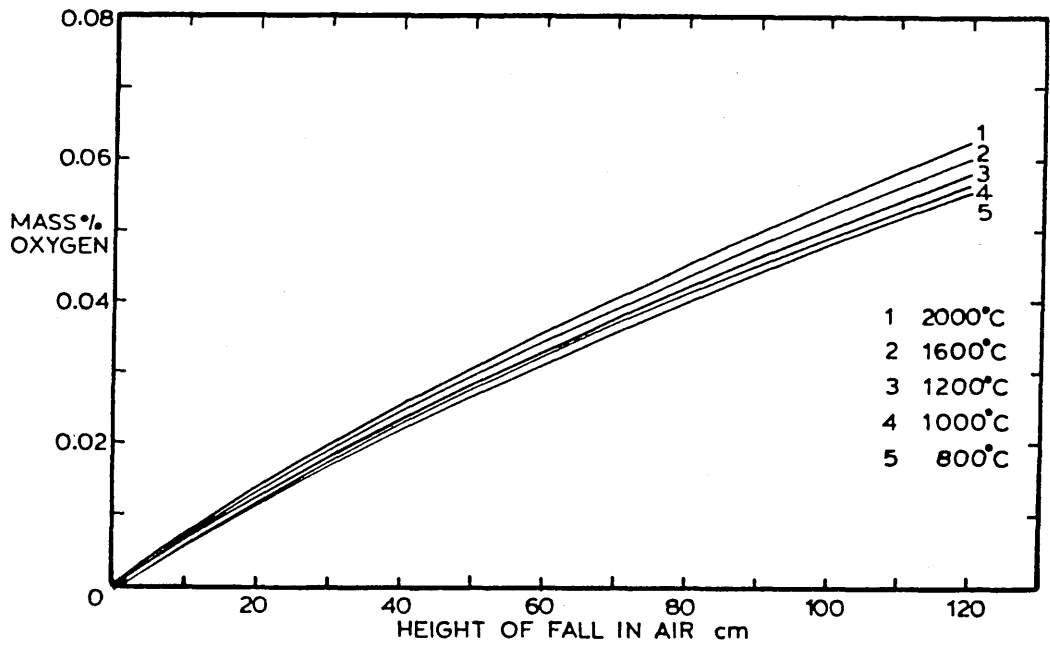
Oxygen level vs Height of fall for Iron Droplets of Different Mass

Figure 162



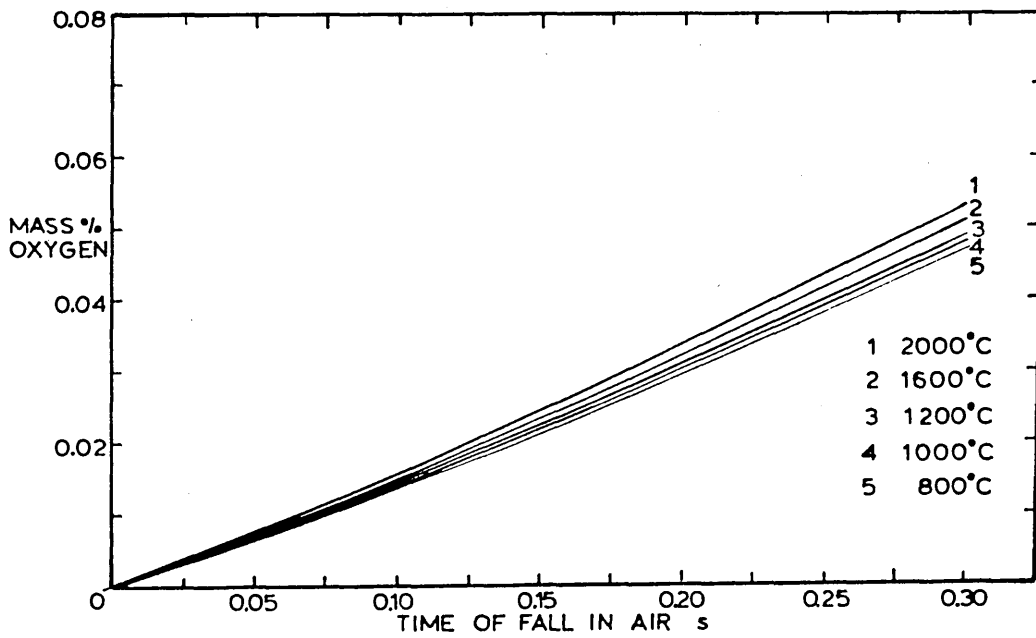
Oxygen level vs Time of fall for Iron Droplets of Different Mass

Figure 163



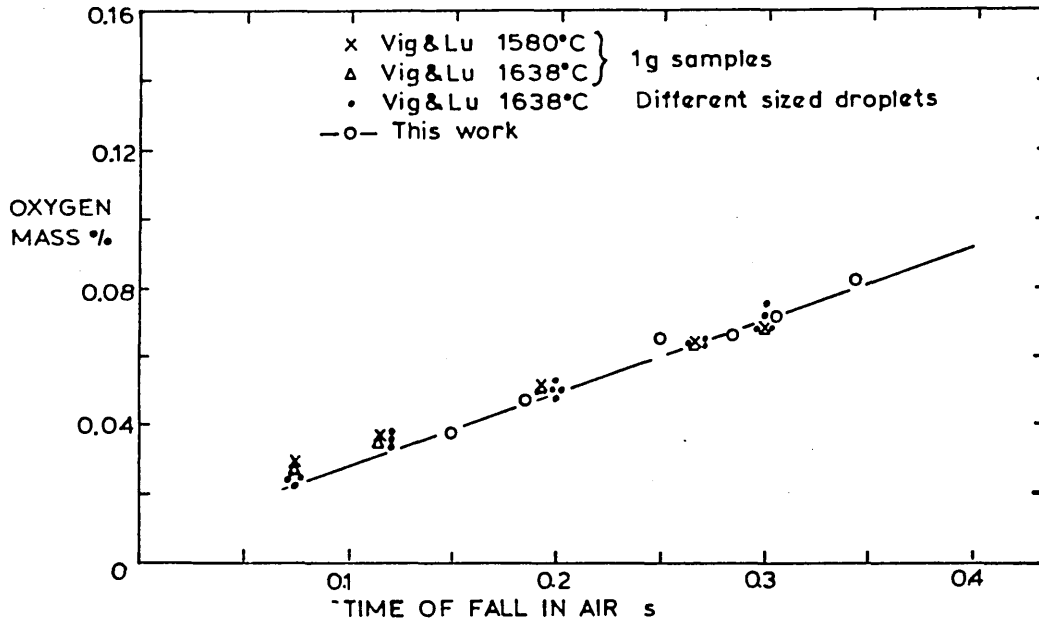
Oxygen level vs Height of fall for 0.7g Iron Droplet for different Film Temperatures

Figure 164



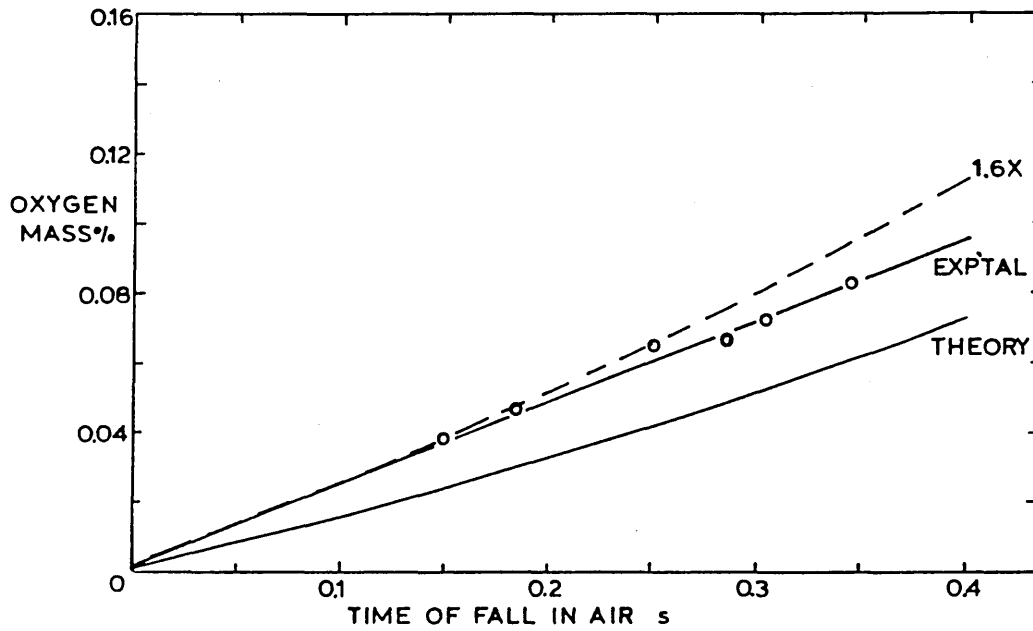
Oxygen level vs Time of fall for 0.7g Iron Droplet for different Film Temperatures

Figure 165



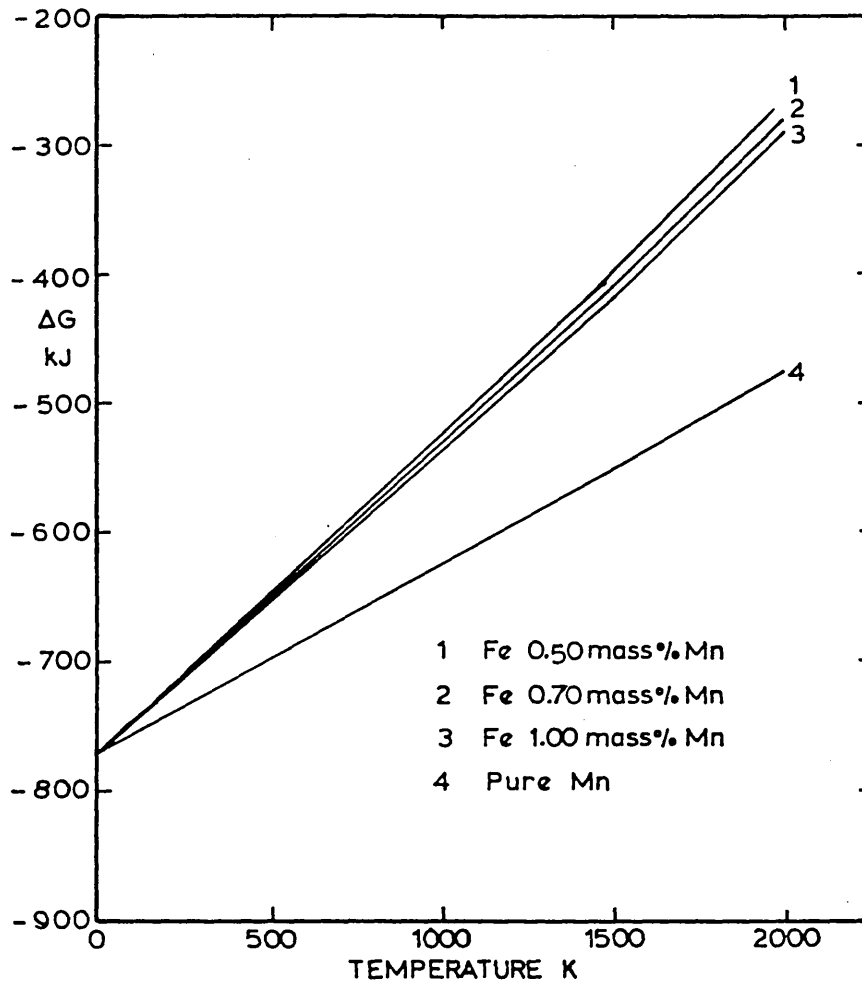
The Rate of Oxidation of Iron

Figure 166



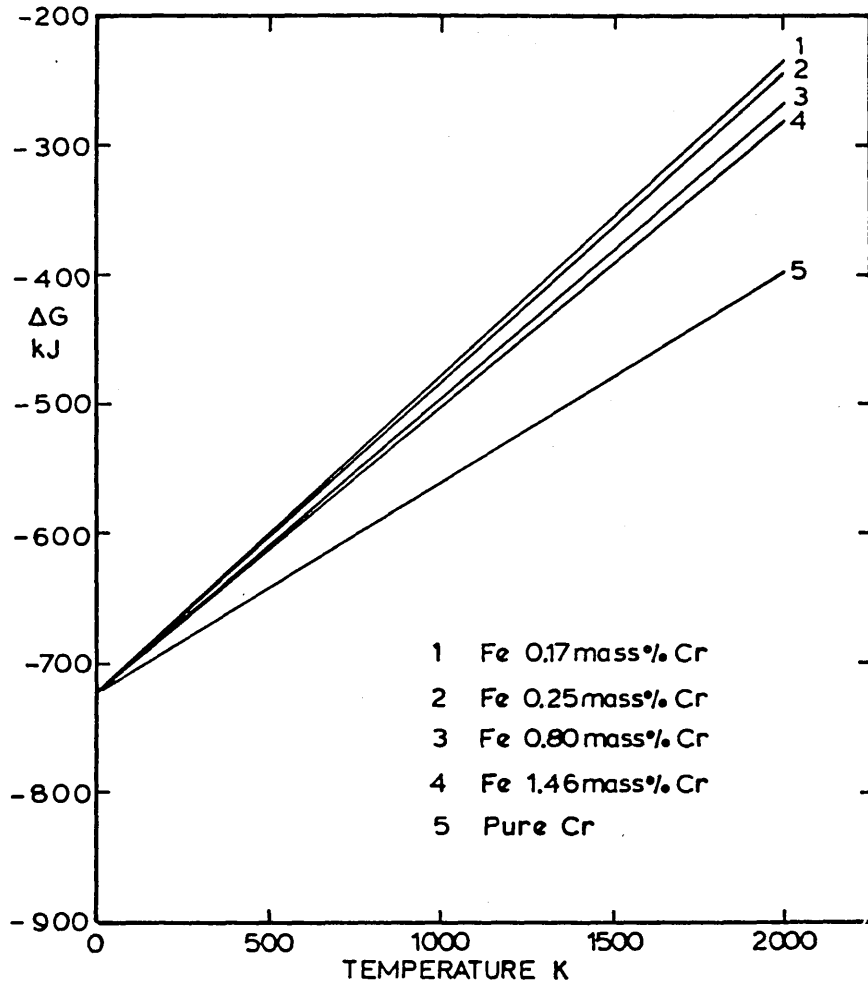
The Rate of Oxidation of Iron at 1600°C

Figure 167



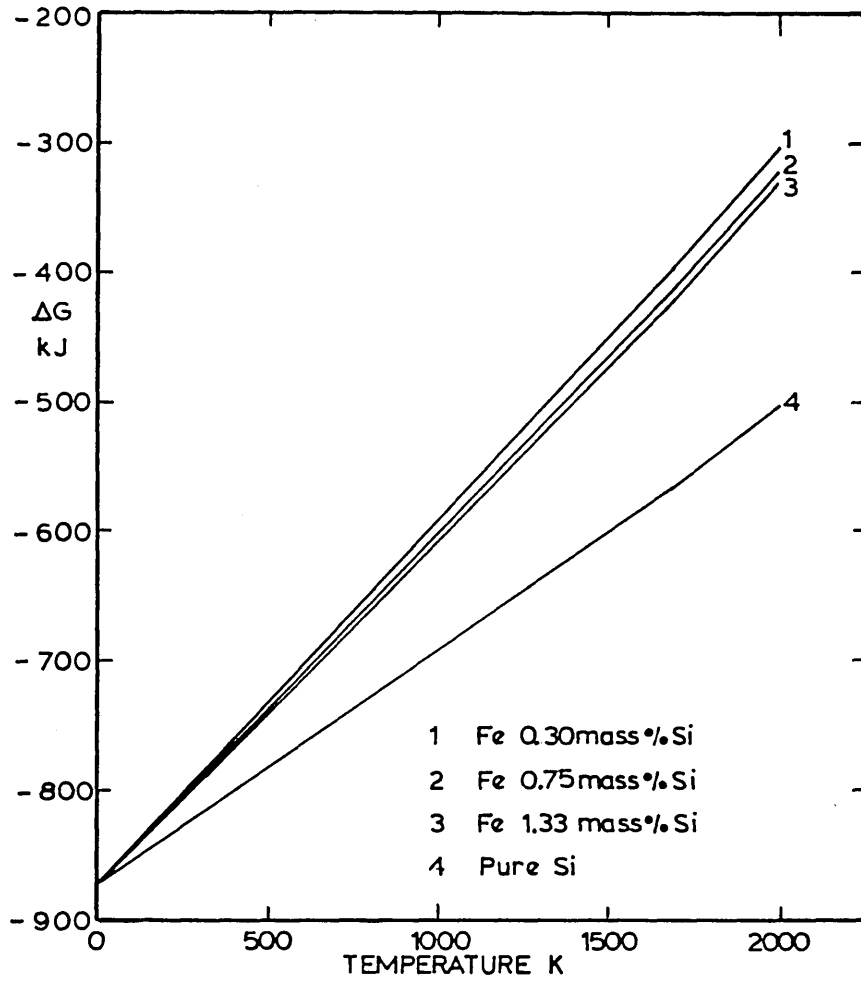
Plot of ΔG vs Temperature for the Reaction $2\text{Mn} + \text{O}_2 = 2\text{MnO}$ for Manganese dissolved in Iron

Figure 168



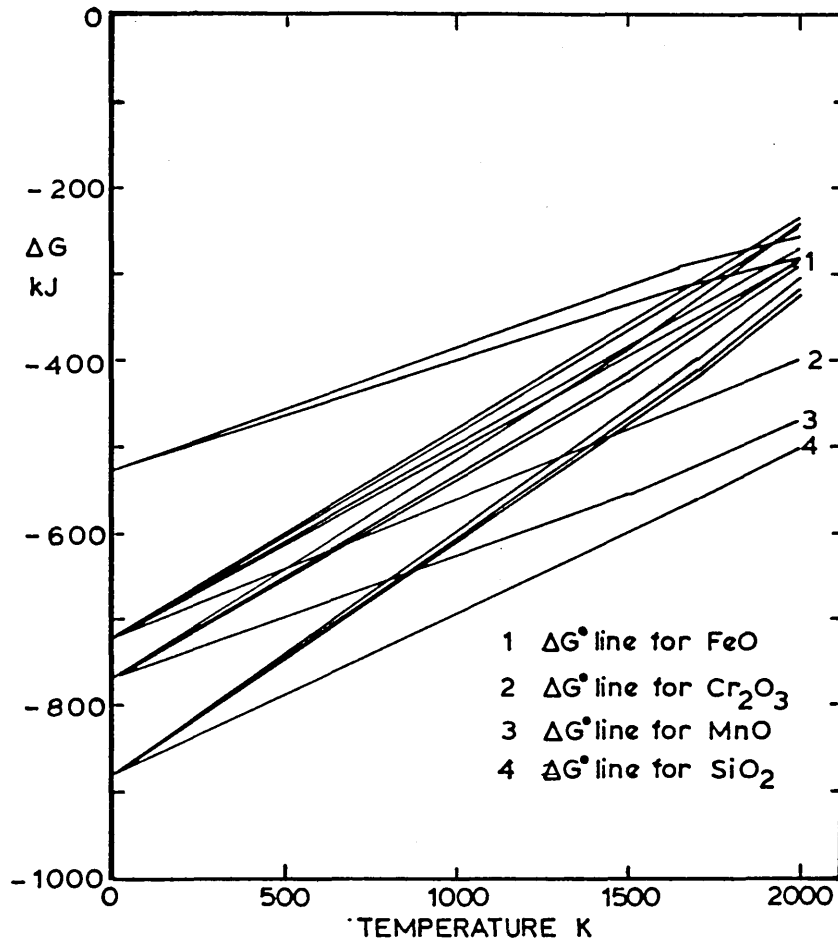
Plot of ΔG vs Temperature for the Reaction $\frac{4}{3}\text{Cr} + \text{O}_2 = \frac{2}{3}\text{Cr}_2\text{O}_3$ for Chromium dissolved in Iron

Figure 169



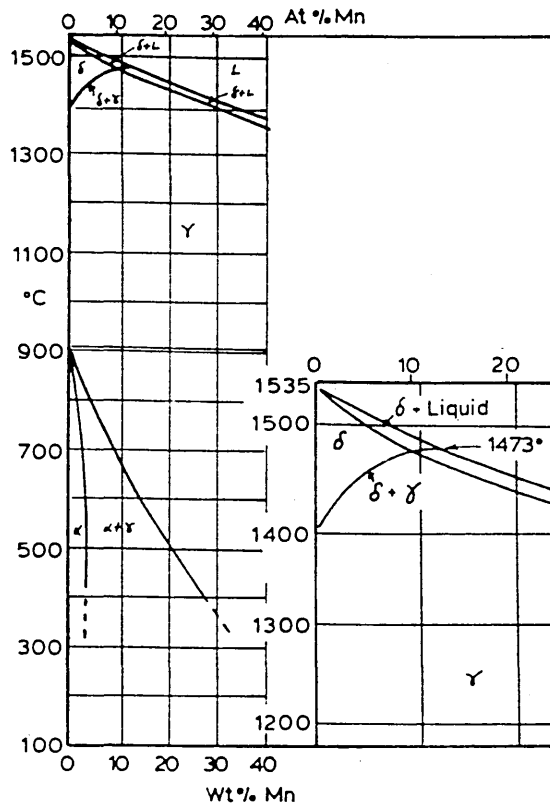
Plot of ΔG vs Temperature for the Reaction $\text{Si} + \text{O}_2 = \text{SiO}_2$ for Silicon dissolved in Iron.

Figure 170



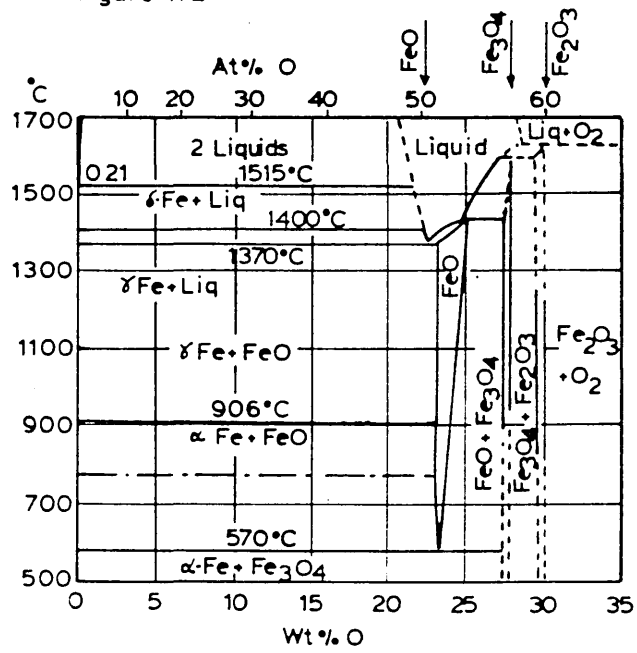
Plot of ΔG vs Temperature for Oxide Systems

Figure 171



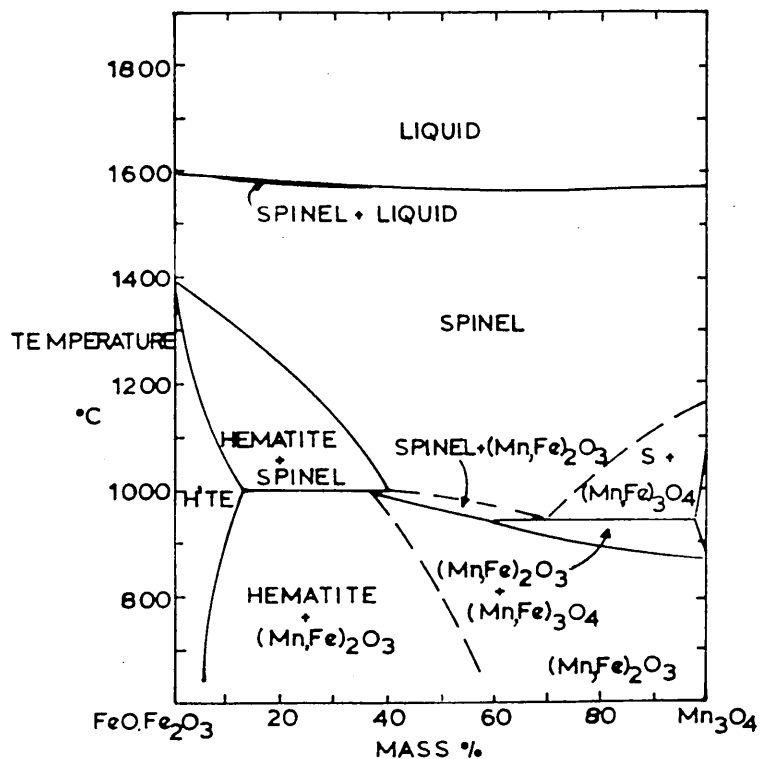
The Fe - Mn Equilibrium Diagram. (125)

Figure 172



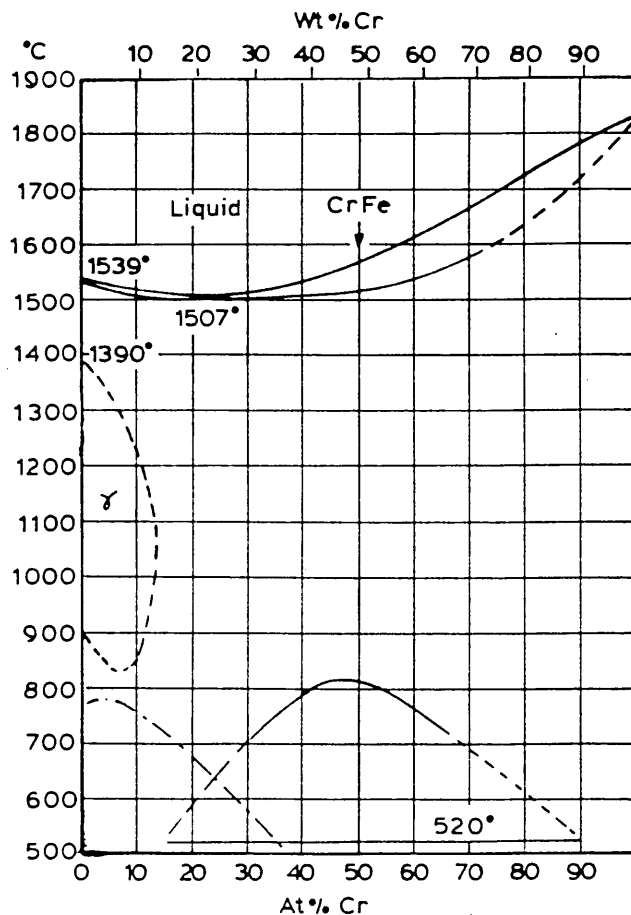
The Fe - O Equilibrium Diagram. (126)

Figure 173



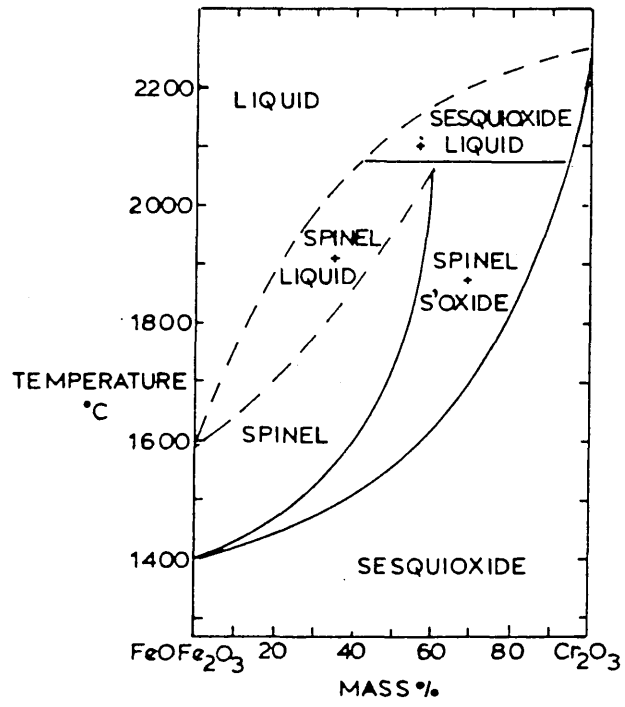
Phase Diagram for the System Iron Oxide - Manganese Oxide in air. (127)

Figure 174



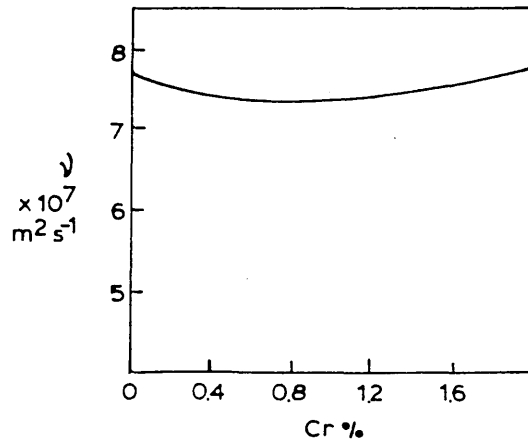
The Fe-Cr Equilibrium Diagram. (126)

Figure 175



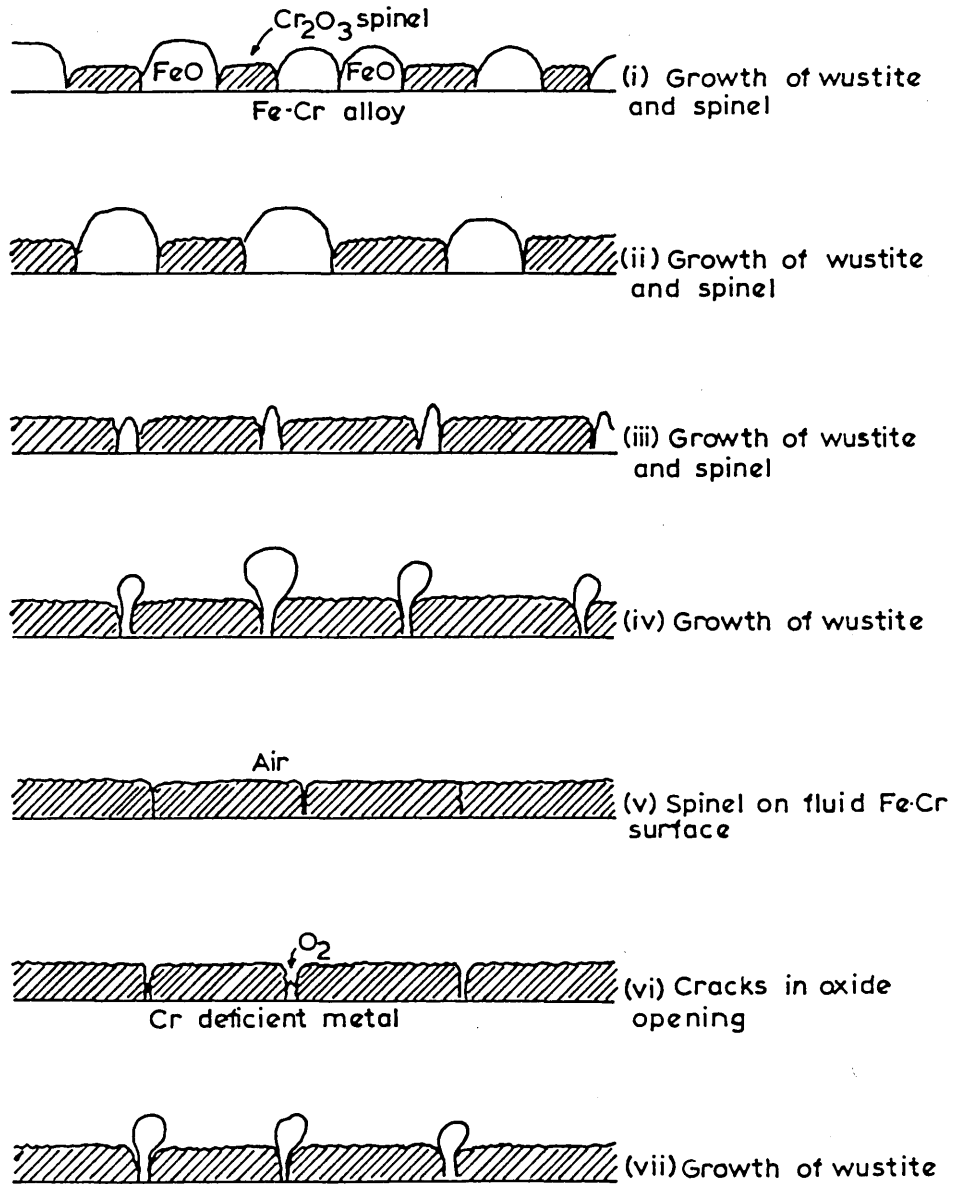
Phase Diagram for the System Iron Oxide - Chromium Oxide in air.⁽¹²⁸⁾

Figure 176



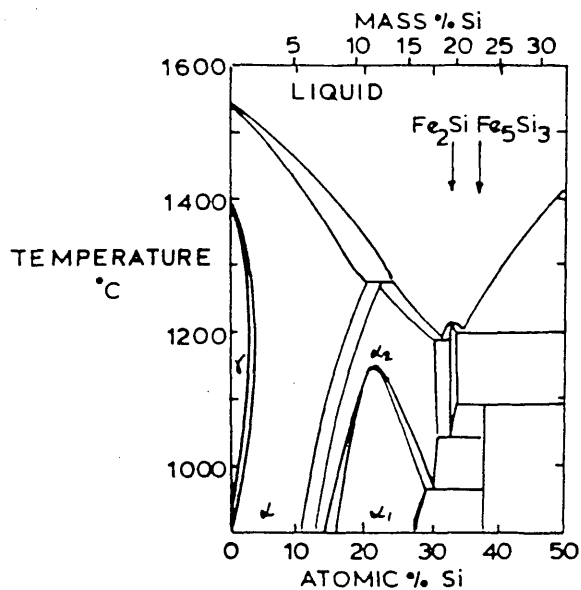
Influence of Chromium on Kinematic Viscosity ν of Pure Iron⁽¹¹⁵⁾

Figure 177



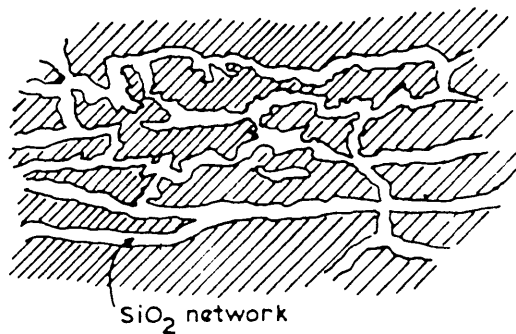
Various Stages in the Growth of Oxide Films on the Surface of Fe-Cr Droplets

Figure 178



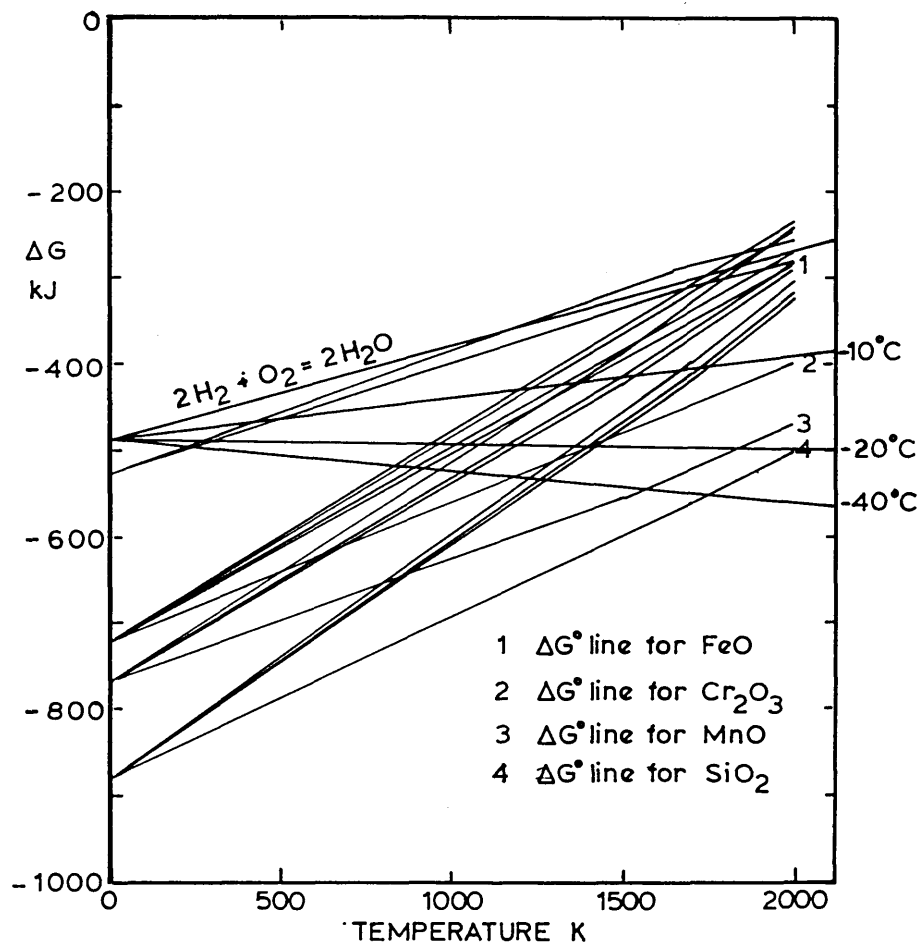
Phase Diagram for the System Iron-Silicon,(129)

Figure 179



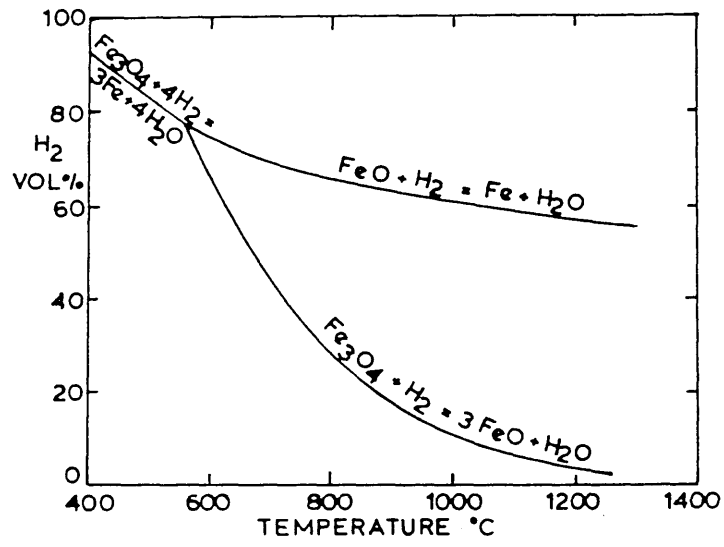
Form of oxide network on Fe-0.3%Si alloy

Figure 180



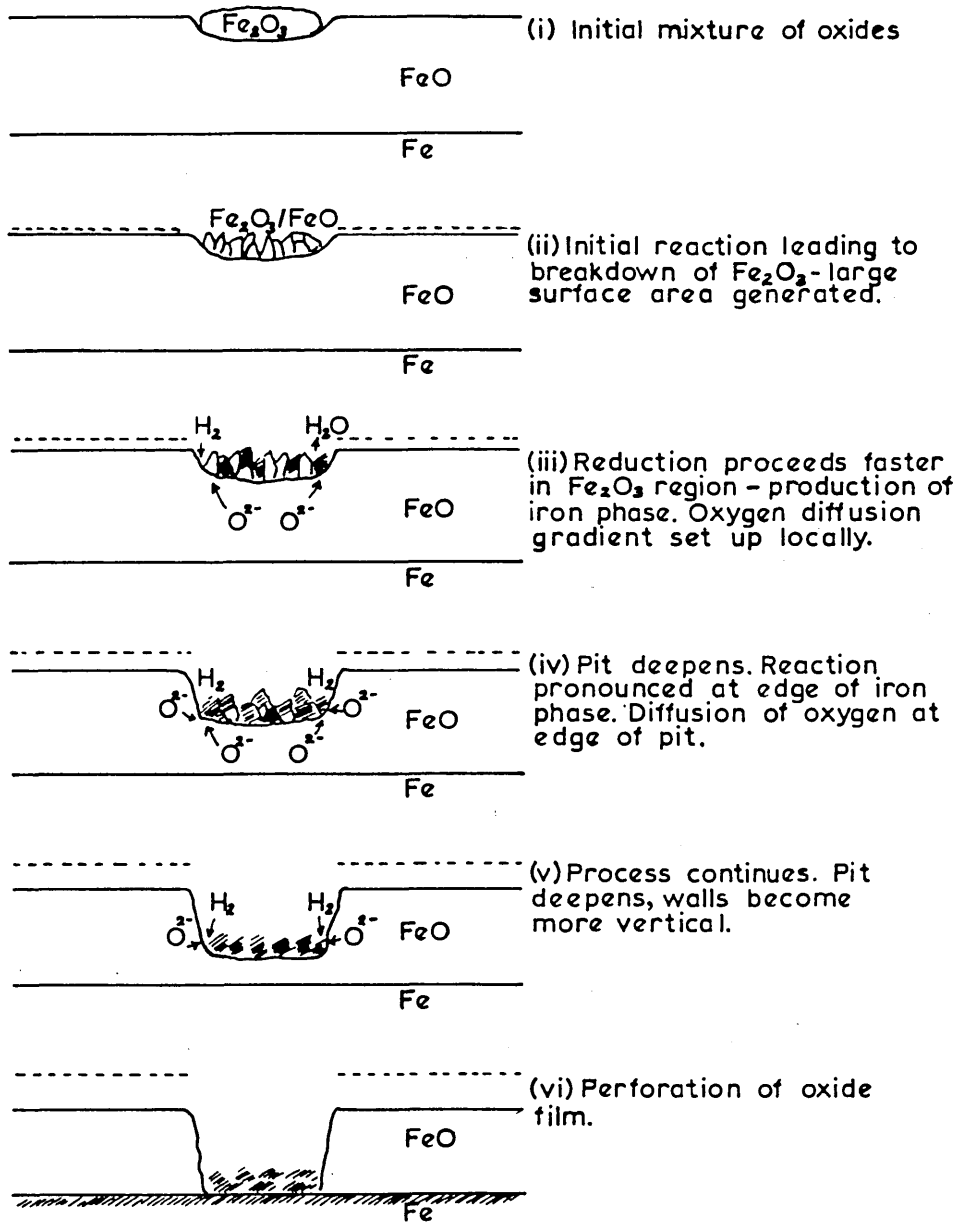
Plot of ΔG vs Temperature for Oxide Systems

Figure 181



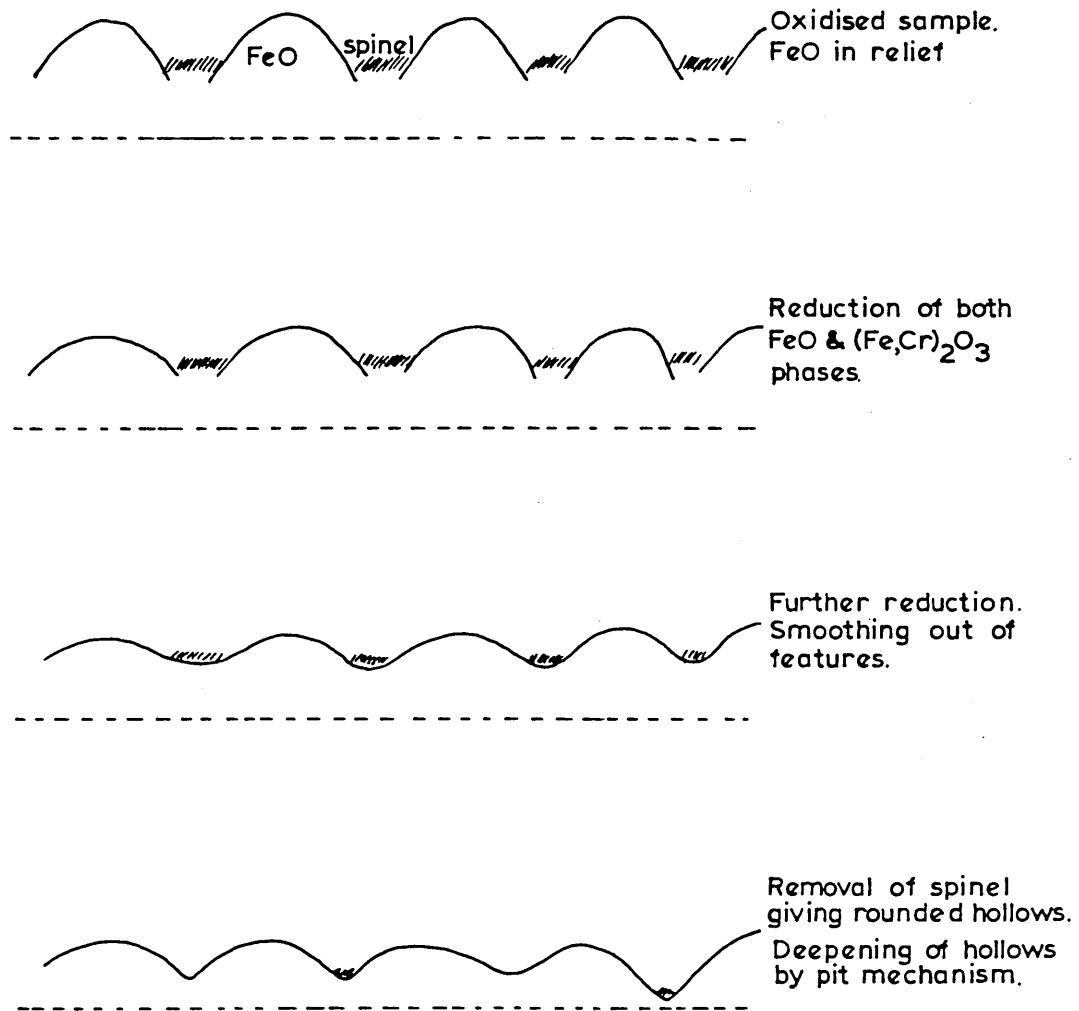
The Fe-H-O Equilibrium. ⁽¹²⁰⁾

Figure 182



Formation of a Pit in an Oxide Film During Reduction in Hydrogen.

Figure 183



Reduction of Wustite & Spinel in low Cr alloys
Producing Pits of Varying Depth.

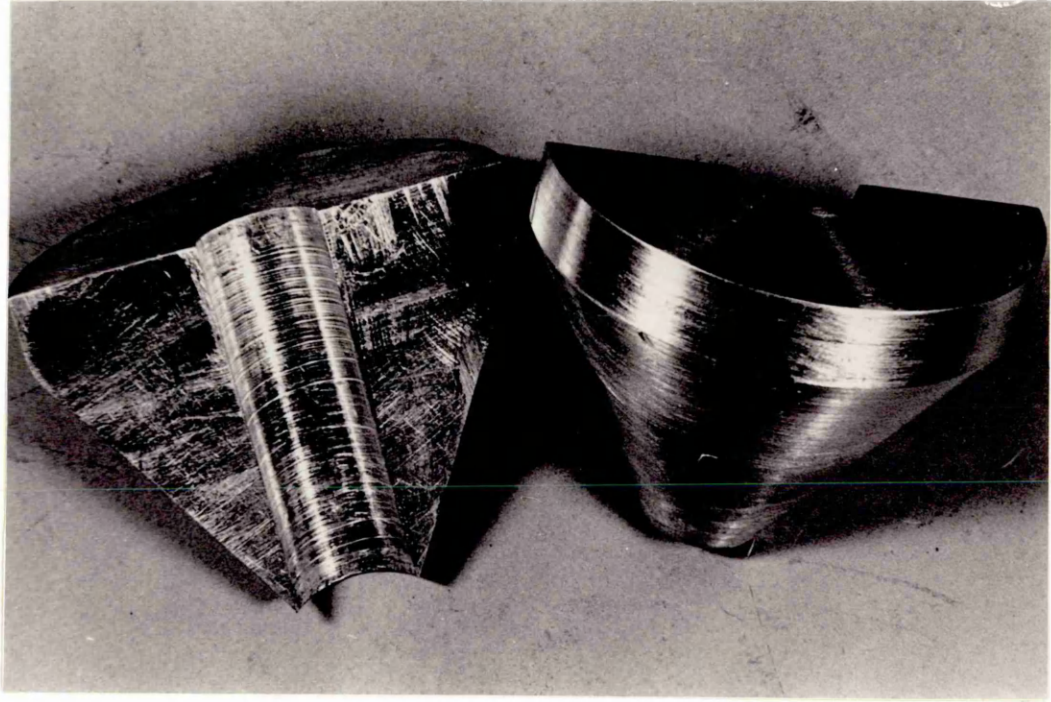
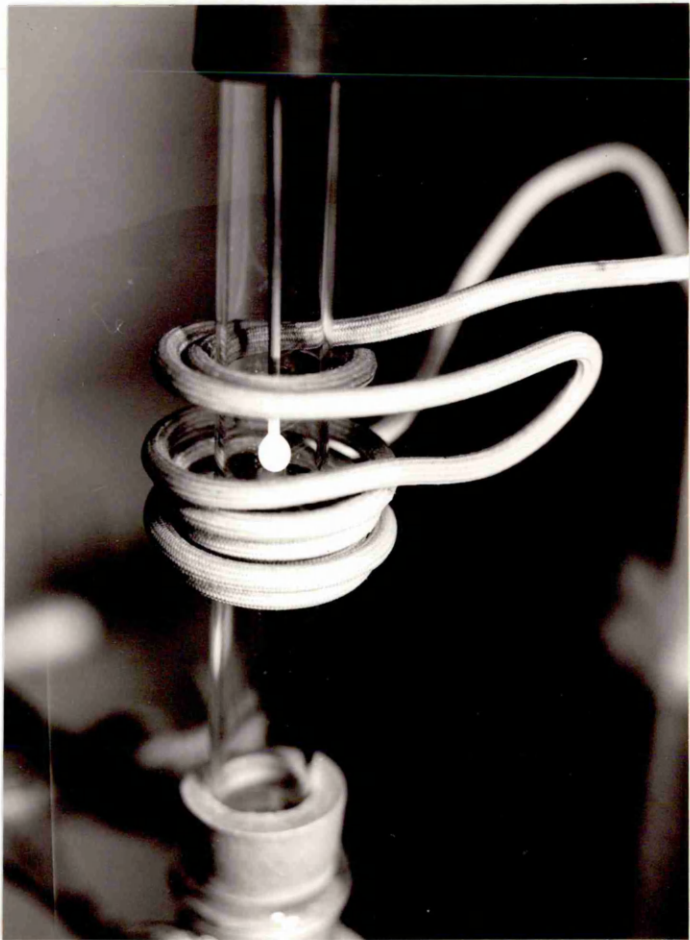
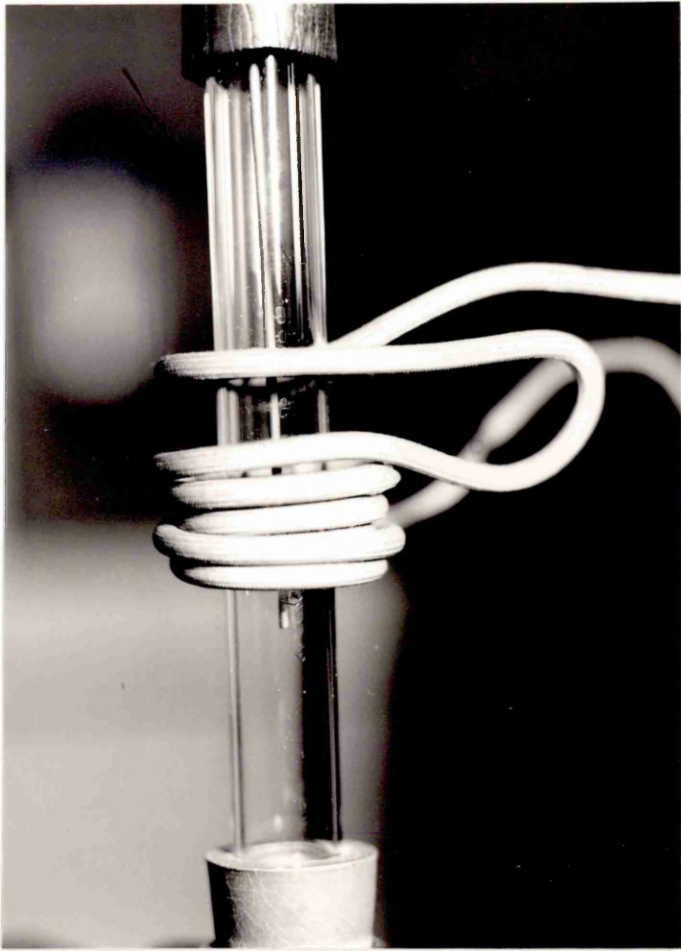


Plate 2 Position of iron wire in the levitation coil.

Plate 3 Formation of a droplet at the end of the iron wire.



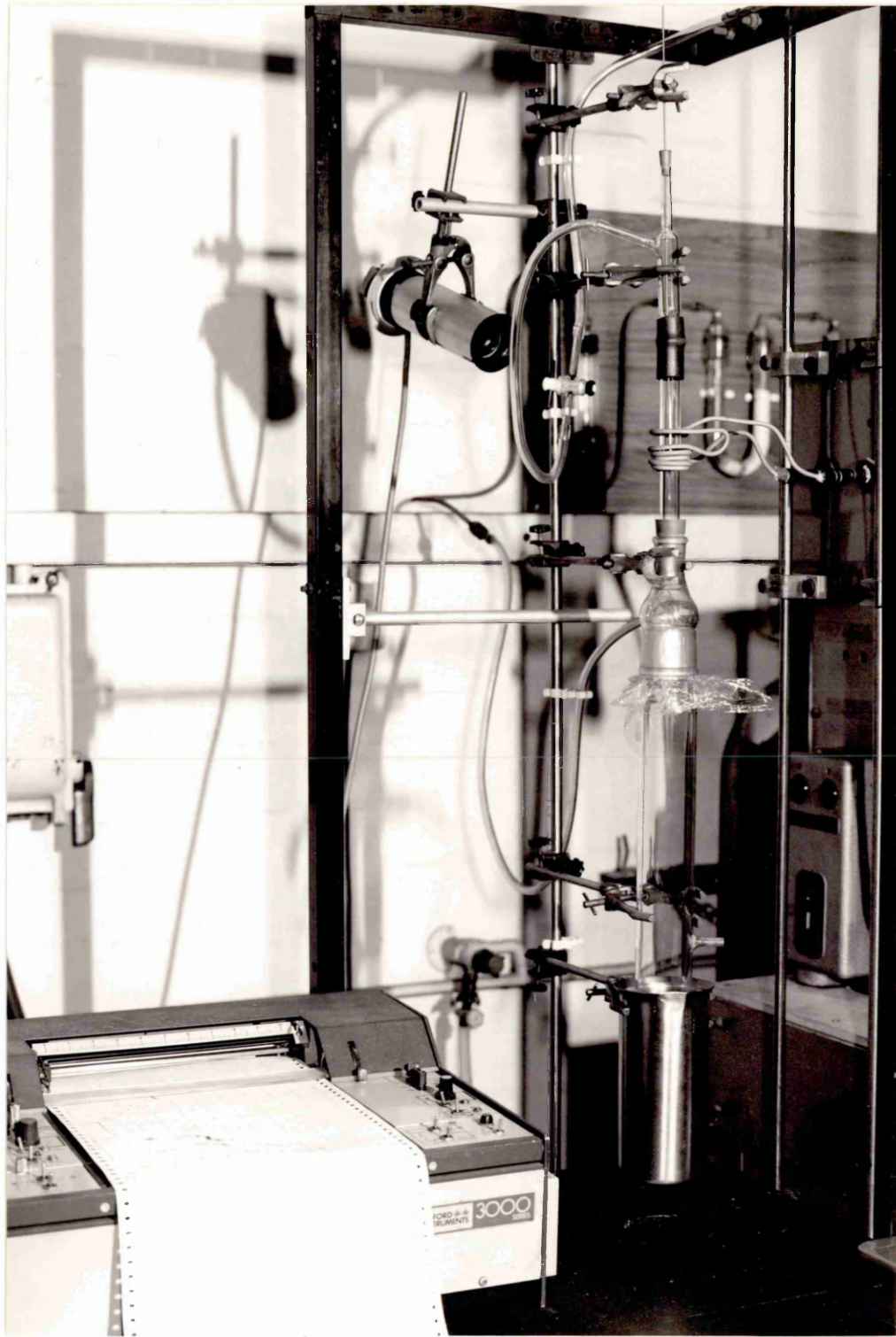


Plate 5

Experimental arrangement for the Droplet-Quench
Media studies

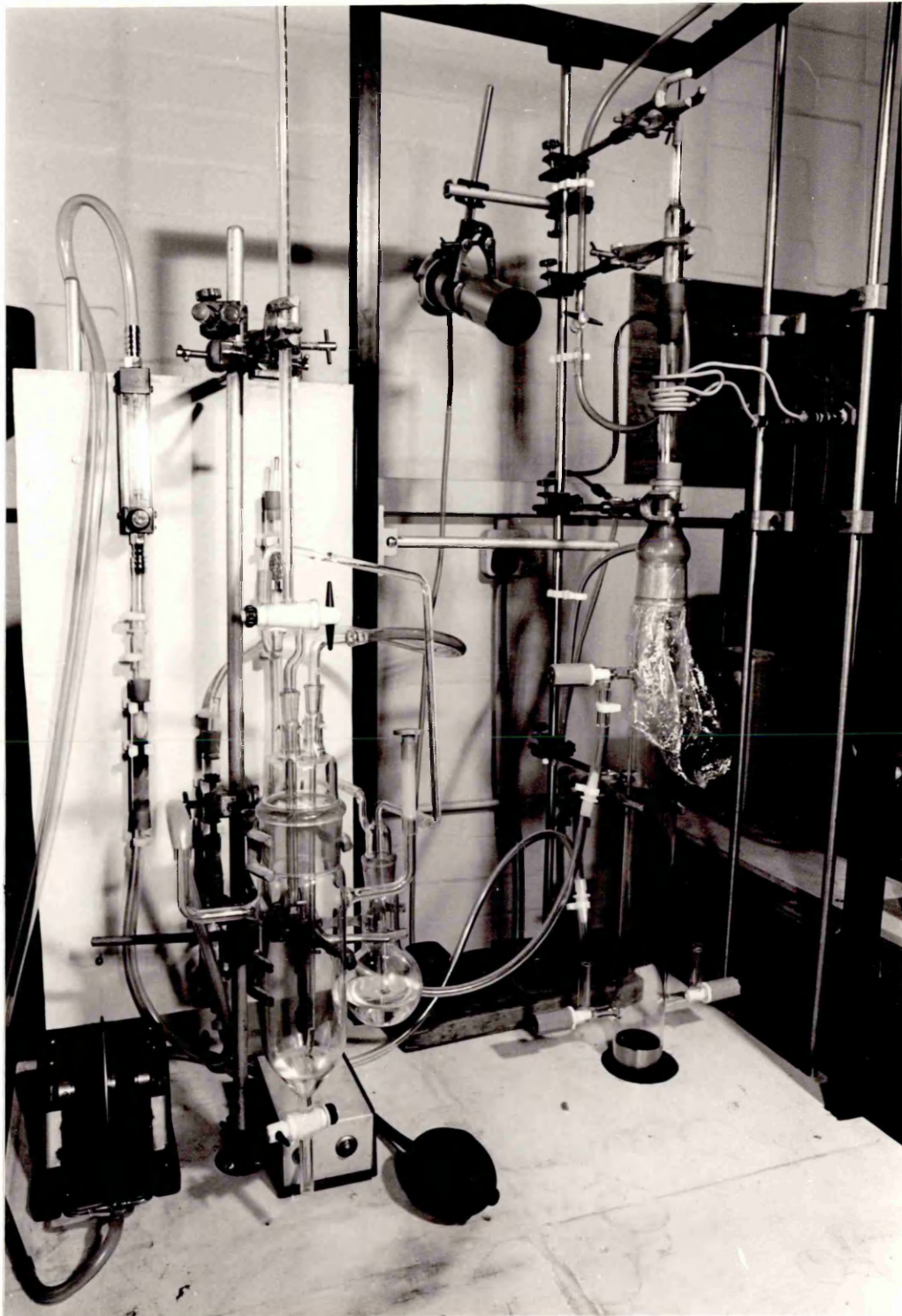


Plate 6

Stanton Massflow Thermobalance and Alnor Dewpoint
Meter.

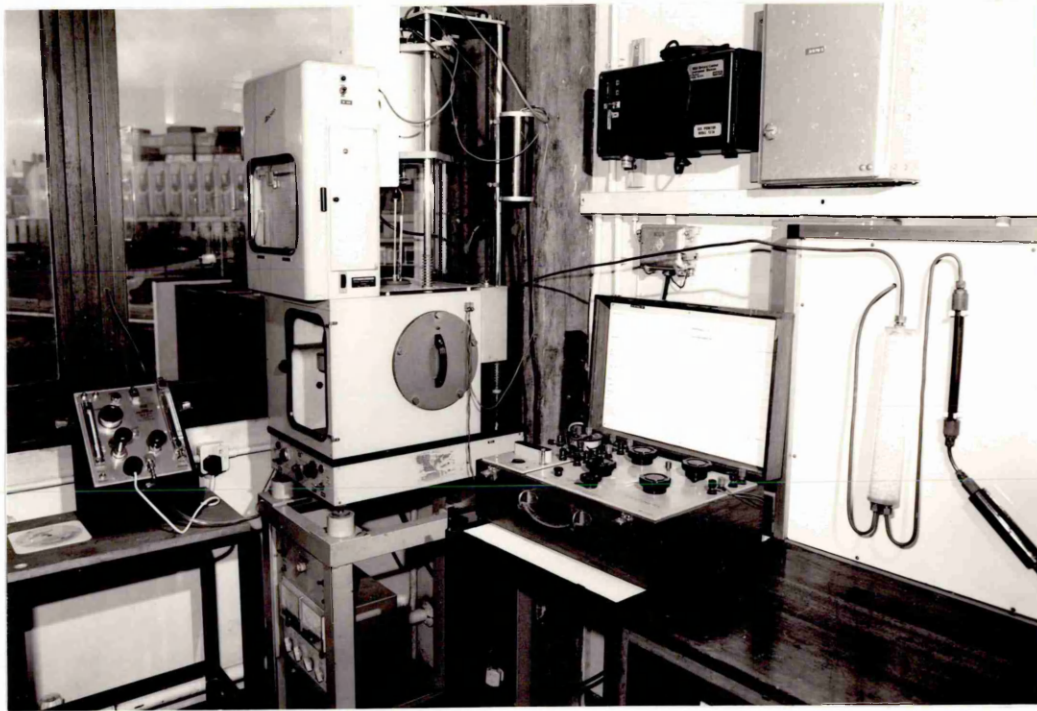


Plate 7

Specimen A43. Pure iron dropped through 50 cm air at 1600°C and quenched in silicone oil.

SEM Micrograph
Magnification 35x

General Topographical details of surface of droplet. Although approximately spherical, the distortion at the horizon is clearly seen, including point of probable ejection. Possible rippling of surface.

Plate 8

Specimen A76. Pure iron dropped through 50 cm air at 1600°C and quenched in de-aerated water.

SEM Micrograph
Magnification 75x

Showing massive nature of oxide formed. Section of oxide has broken away showing nature of surface beneath. Oxide clearly showing grain boundaries. Probable epitaxial growth.

Plate 9

Specimen A76. Pure iron dropped through 50 cm air at 1600°C and quenched in de-aerated water.

SEM Micrograph
Magnification 1175x

Showing detail of oxide formed.

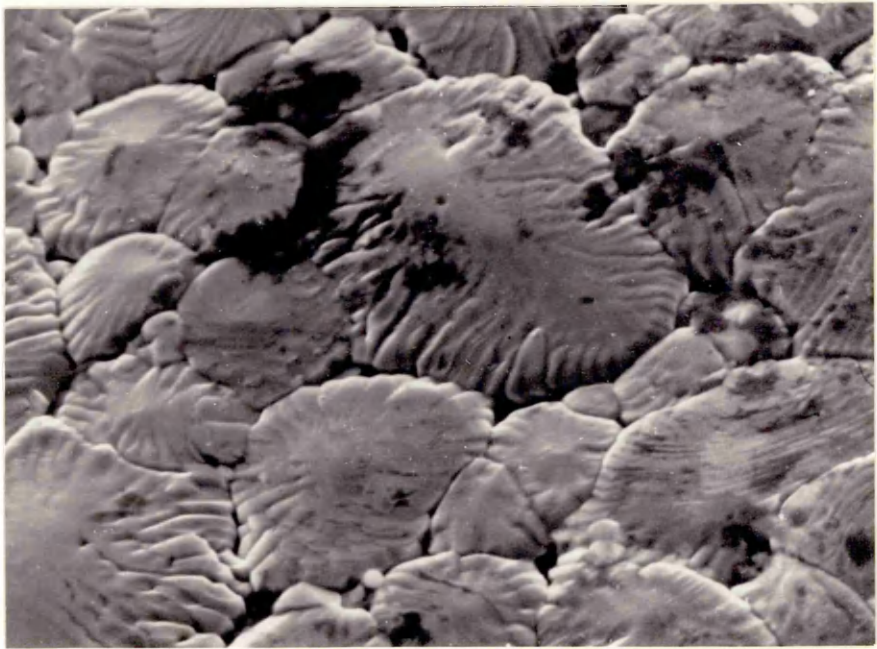
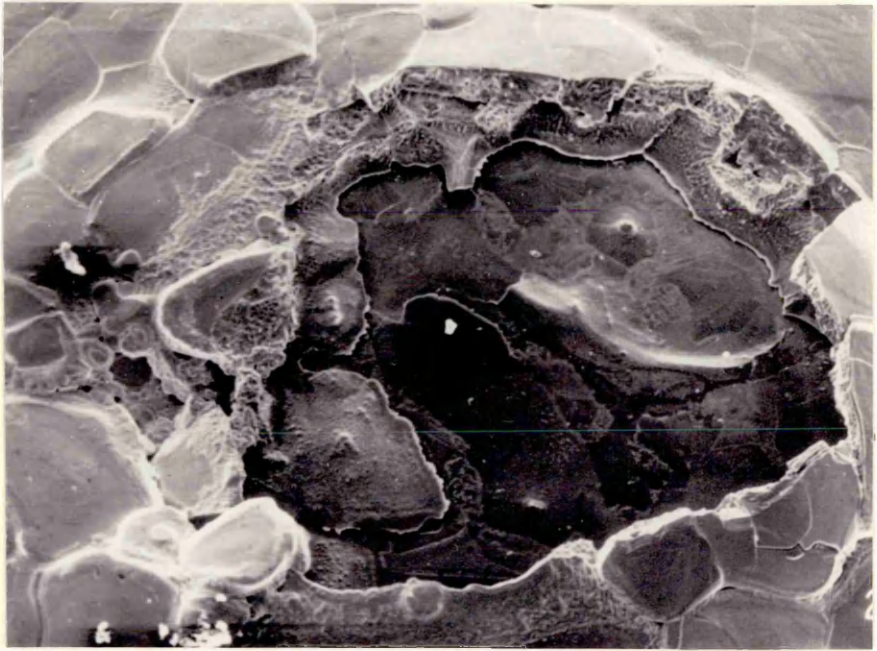


Plate 10

Specimen A283. Pure iron dropped through 100 cm air at 1600°C and quenched in silicone oil.

SEM Micrograph
Magnification 320x

General nature of oxide film showing random wavy pattern, 'sif' type topography. Pattern covers in excess of 90% of surface.

Plate 11

Specimen A283. Pure iron dropped through 100 cm air at 1600°C and quenched in silicone oil.

SEM Micrograph
Magnification 1250x

Oxide film in detail. Surface is a mixture of rough and smooth areas. Large number of small depressions. Possibly some directionality to the surface pattern.



Plate 12

Specimen A282. Pure iron dropped through 100 cm air at 1600°C and quenched in silicone oil. Reduced in hydrogen at 1150°C for 1 hour.

SEM Micrograph
Magnification 320x

Random wavy pattern of original oxide surface still evident. Surface detail has changed. Evidence of a number of pits in the surface.

Plate 13

Specimen A282. Pure iron dropped through 100 cm air at 1600°C and quenched in silicone oil. Reduced in hydrogen at 1150°C for 1 hour.

SEM Micrograph
Magnification 1250x

Many surface features now evident. Characteristic of an etched surface. Evidence of polycrystalline nature. Pits appear to be quite deep with a tapered section.

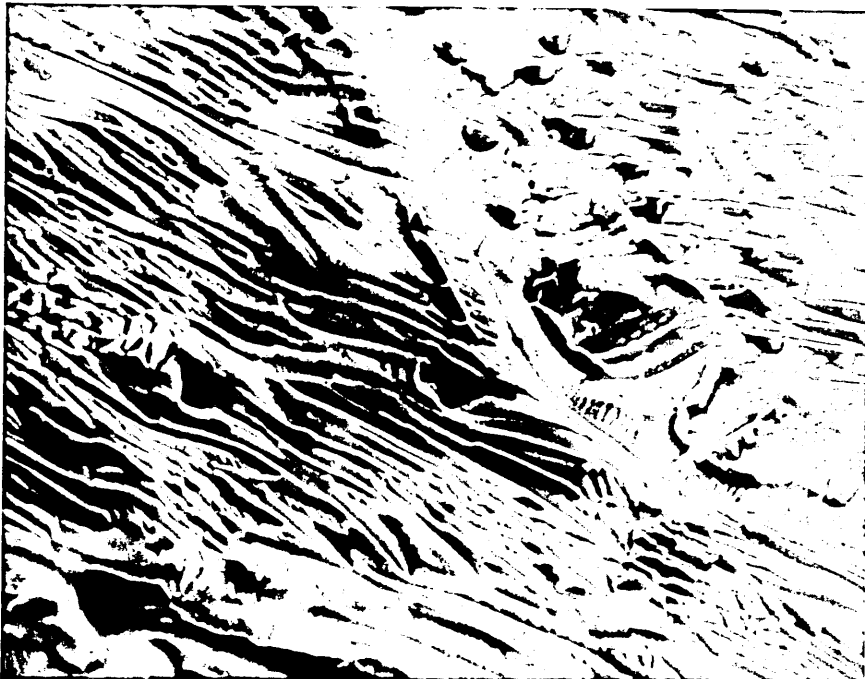
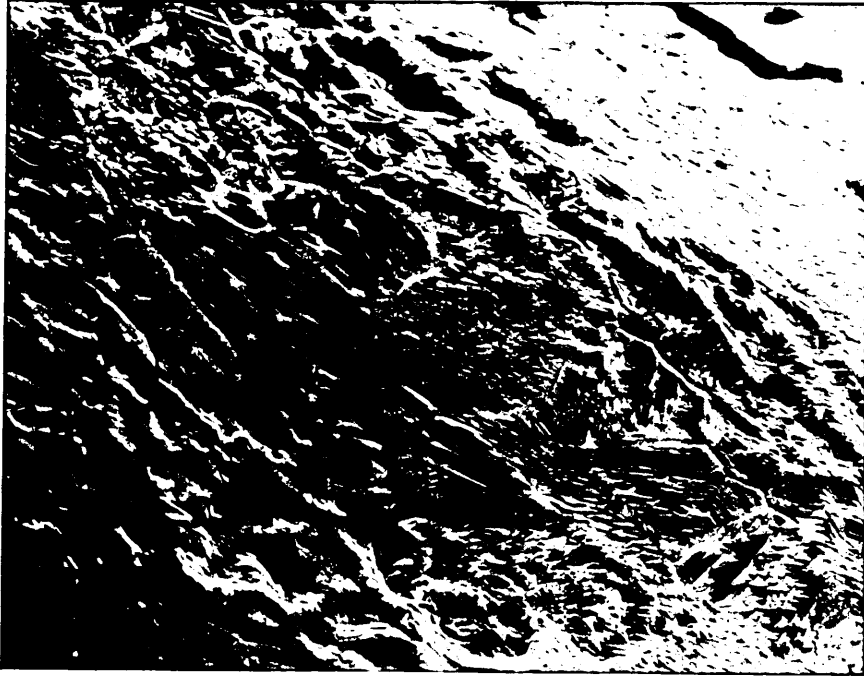


Plate 14

Specimen D78. Fe-0.5% Mn dropped through 50 cm air at 1600°C and quenched in silicone oil.

SEM Micrograph
Magnification 500x

Oxide film appears two-phase. Dominated by stria which are directional. In amongst the stria are pockets of 'wavy' oxide.

Plate 15

Specimen D91. Fe-0.5% Mn dropped through 100 cm air at 1600°C and quenched in silicone oil.

SEM Micrograph
Magnification 2000x

Striated surface in detail. Shows fine mottled detail.

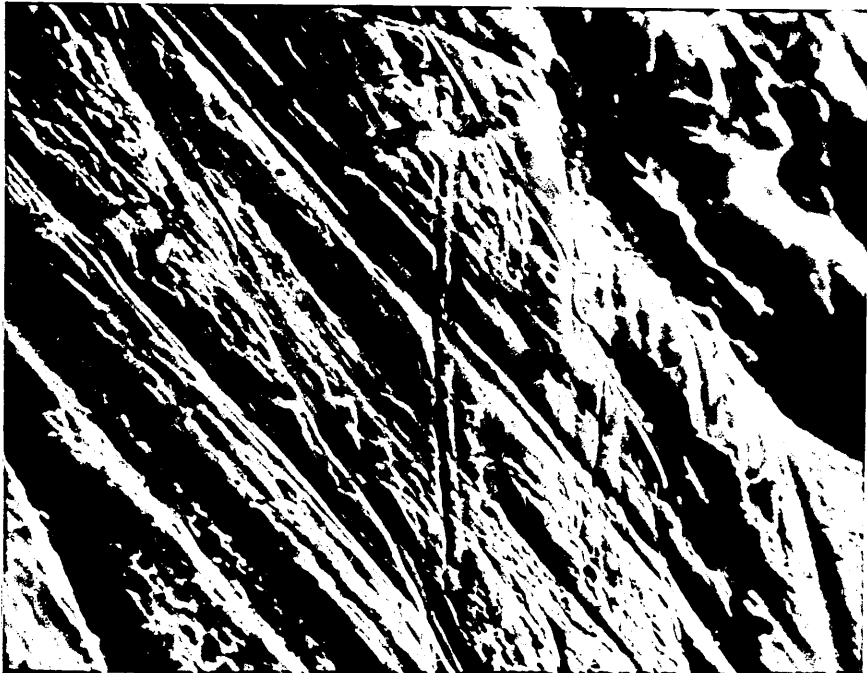
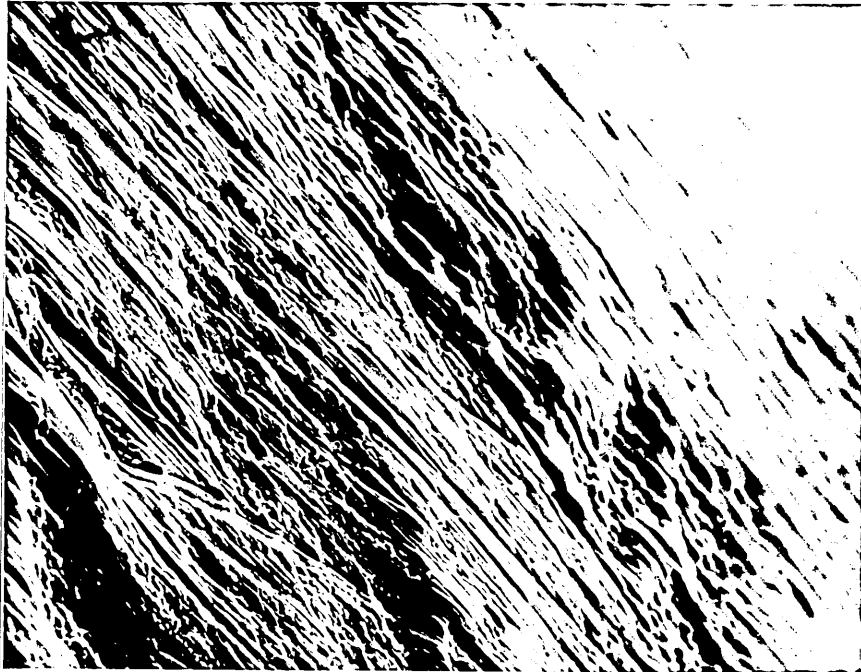


Plate 16

Specimen D92. Fe-0.5% Mn dropped through 100 cm air at 1600°C and quenched in silicone oil. Reduced in hydrogen at 1150°C for 1 hour.

SEM Micrograph
Magnification 500x

Striated surface no longer evident. Surface pitted suggesting removal of material. Evidence of pits joining together to form a surface crack. Suggestion of sub-grain boundaries or fine cracks.

Plate 17

Specimen D77. Fe-0.5% Mn dropped through 50 cm air at 1600°C and quenched in silicone oil. Reduced in hydrogen at 1150°C for 1 hour.

SEM Micrograph
Magnification 2000x

Similar characteristics to previous specimen, shown in more detail. Original oxide film would not have been as thick as that of previous specimen. Many of the surface pits are round; some tend to elongate and join together. There appears to be some degree of directionality in this area. Pits found in valleys and along ridges. Some light marking of surface possibly characteristic of the metal sub-surface.

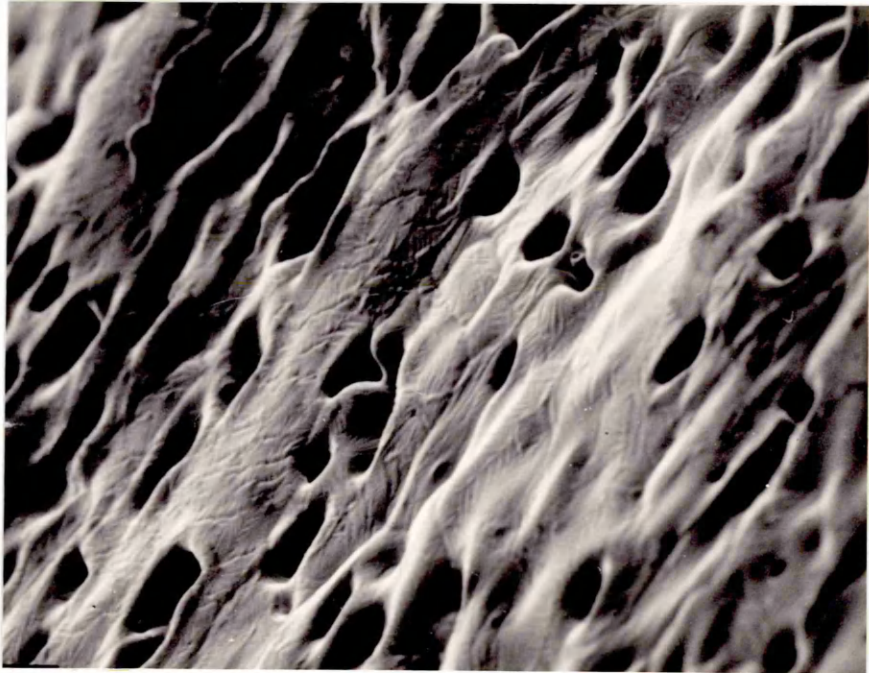
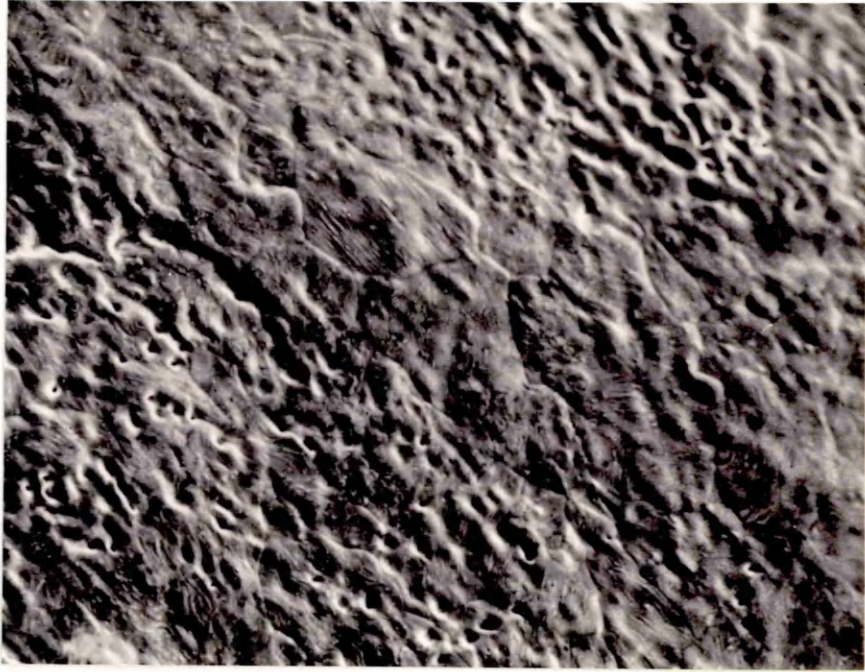


Plate 18

Specimen D91 Fe-0.5% Mn dropped through 100 cm air at 1600°C and quenched in silicone oil. Droplet mounted in bakelite and polished to 6 μm diamond finish.

SEM Micrograph
Magnification 450x

Specimen shows region of porosity immediately behind the droplet surface. The amorphous nature of the oxide film is evident; no surface detail can be seen.

Plate 19

Specimen D92. Fe-0.5% Mn dropped through 100 cm air at 1600°C and quenched in silicone oil. Reduced in hydrogen at 1150°C for 1 hour. Droplet mounted in bakelite and polished to 6 μm diamond finish.

SEM Micrograph
Magnification 900x

Again there is evidence of porosity within the droplet particularly just behind the droplet surface. There is more detail to the oxide film after treatment with hydrogen. Features stand out in relief.



Plate 20

Specimen D33. Fe-0.7% Mn dropped through 100 cm air at 1600°C and quenched in silicone oil.

SEM Micrograph
Magnification 340x

The striated surface of the 0.5% Mn alloy is not as evident. The dominant surface feature appears to be the 'sif' pattern. There are 'smooth' islands in the 'wavy' field.

Plate 21

Specimen D33. Fe-0.7% Mn dropped through 100 cm air at 1600°C and quenched in silicone oil.

SEM Micrograph
Magnification 1350x

Surface shown in more detail. General impression of a smooth textured oxide film; some degree of surface relief.

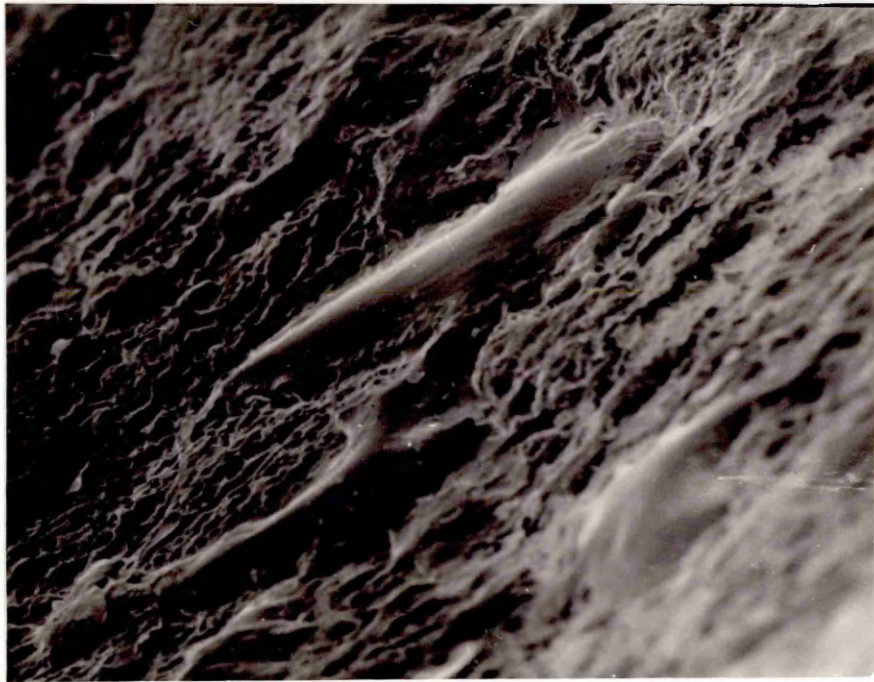
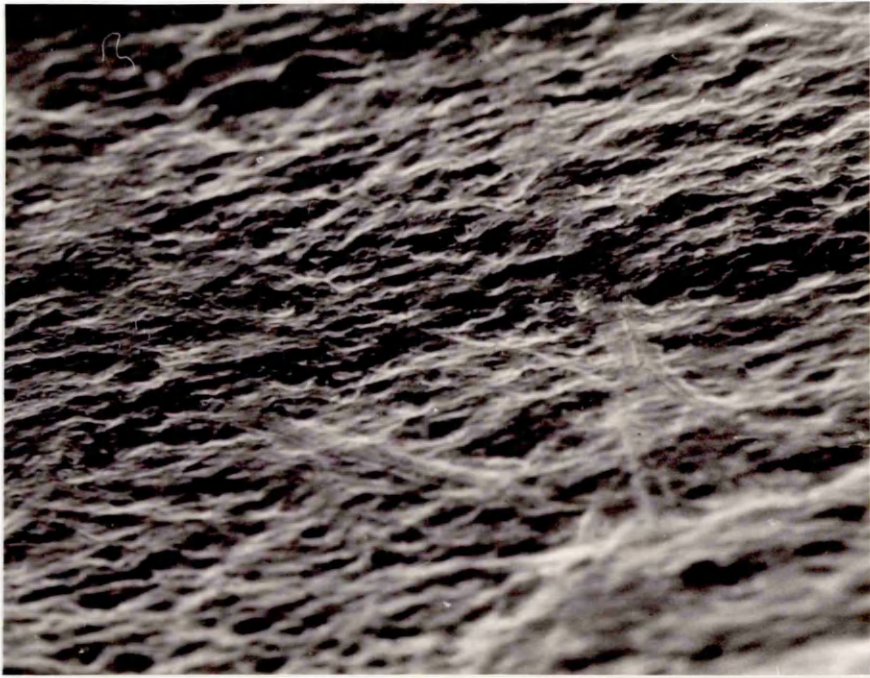


Plate 22

Specimen D32. Fe-0.7% Mn dropped through 100 cm air at 1600°C and quenched in silicone oil. Reduced in hydrogen at 1150°C for 1 hour.

SEM Micrograph
Magnification 340x

Specimen exhibits two types of relief. Firstly, smooth rounded surface showing minute cracks. Secondly, wavy corrugated type of surface where there is only slight pitting evident.

Plate 23

Specimen D32. Fe-0.7% Mn dropped through 100 cm air at 1600°C and quenched in silicone oil. Reduced in hydrogen at 1150°C for 1 hour.

SEM Micrograph
Magnification 1350x

'Sif' relief of small ridges and troughs evident. Appearance of small round pits in the surface. Network of fine 'grain boundaries' or cracks.

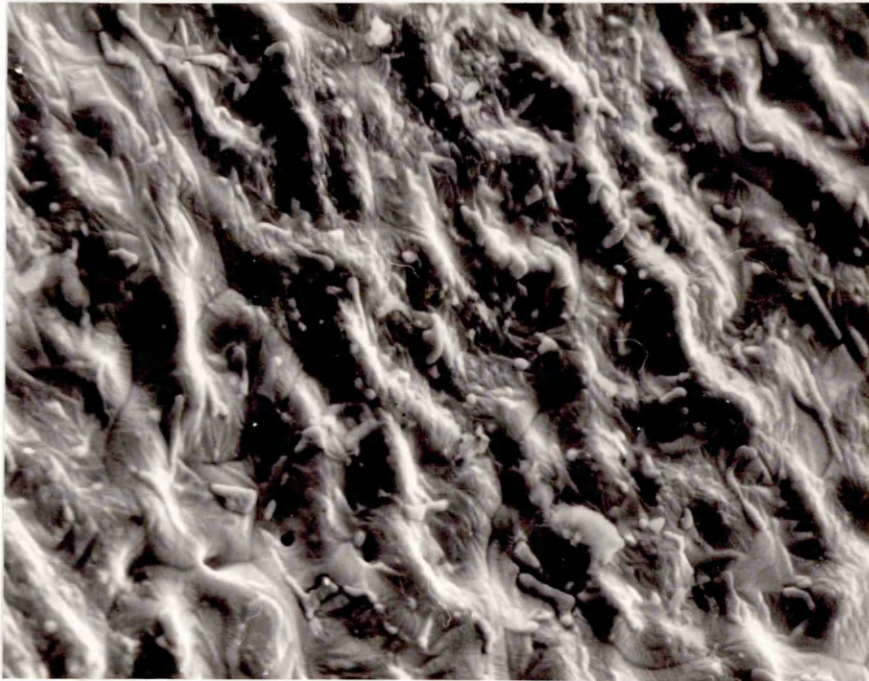
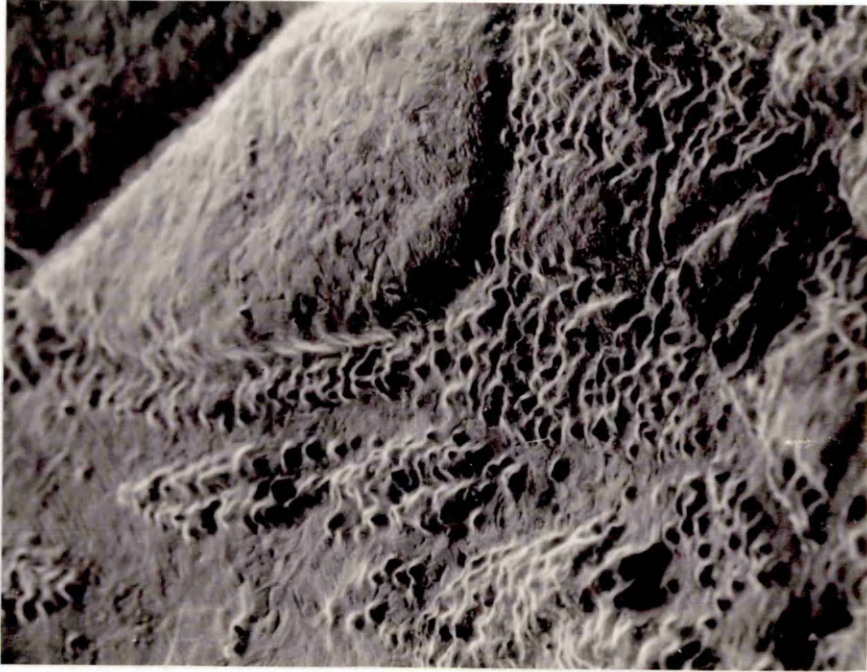


Plate 24

Specimen D90. Fe-1.0% Mn dropped through 100 cm air at 1600°C and quenched in silicone oil.

SEM Micrograph
Magnification 500x

The oxide film on the surface of the droplet showing striated effect. Surface gently undulating. Striations directional. ,

Plate 25

Specimen D95. Fe-1.0% Mn dropped through 50 cm air at 1600°C and quenched in silicone oil.

SEM Micrograph
Magnification 4700x

Detail of surface oxide showing possible duplex nature.

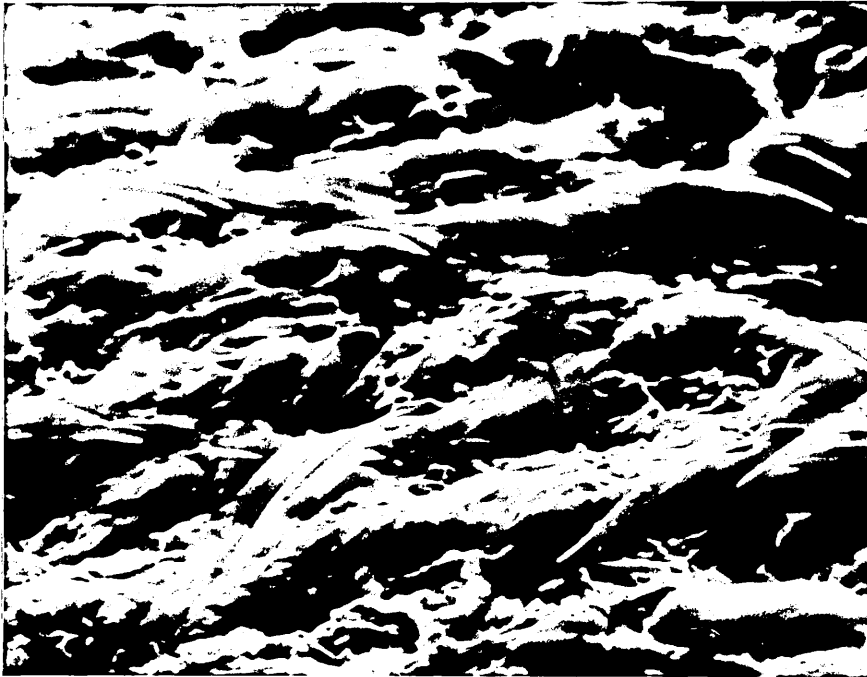
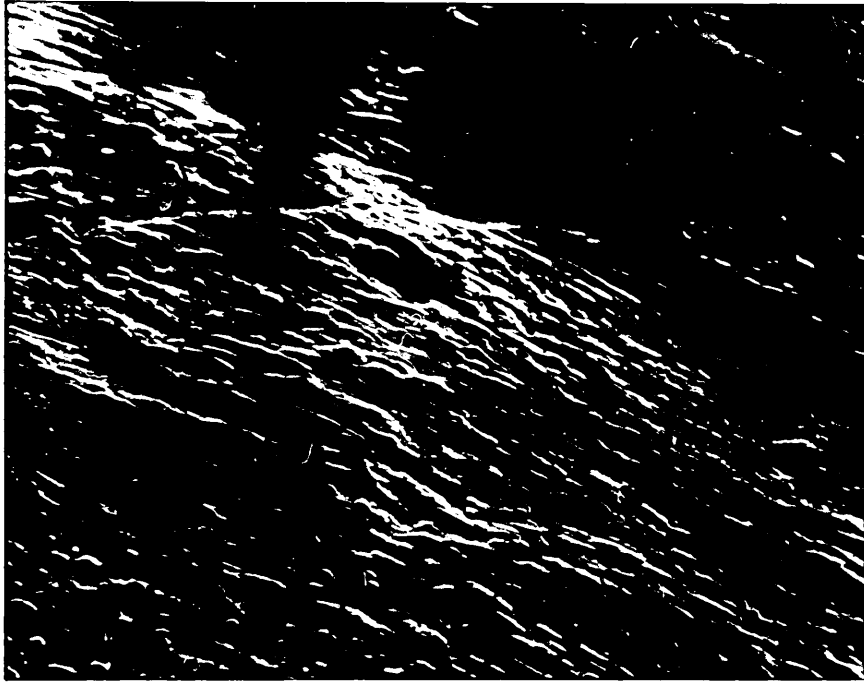


Plate 26

Specimen D96. Fe-1.0% Mn dropped through 50 cm air at 1600°C and quenched in silicone oil. Reduced in hydrogen at 1150°C for 1 hour.

SEM Micrograph
Magnification 550x

Surface contours appear to be smoothed out. Possible traces of striated topography. Some pits evident. Main feature is large network of fine cracks with one very large crack.

Plate 27

Specimen D98. Fe-1.0% Mn dropped through 100 cm air at 1600°C and quenched in silicone oil. Reduced in hydrogen at 1150°C for 1 hour.

SEM Micrograph
Magnification 2350x

Relatively smooth surface. Large number of very small pits. Network of cracks, similar to grain boundaries opening up. Edges of some cracks suggest they are V-shaped by reflection. Possible appearance of dendritic sub-structure in surface film.

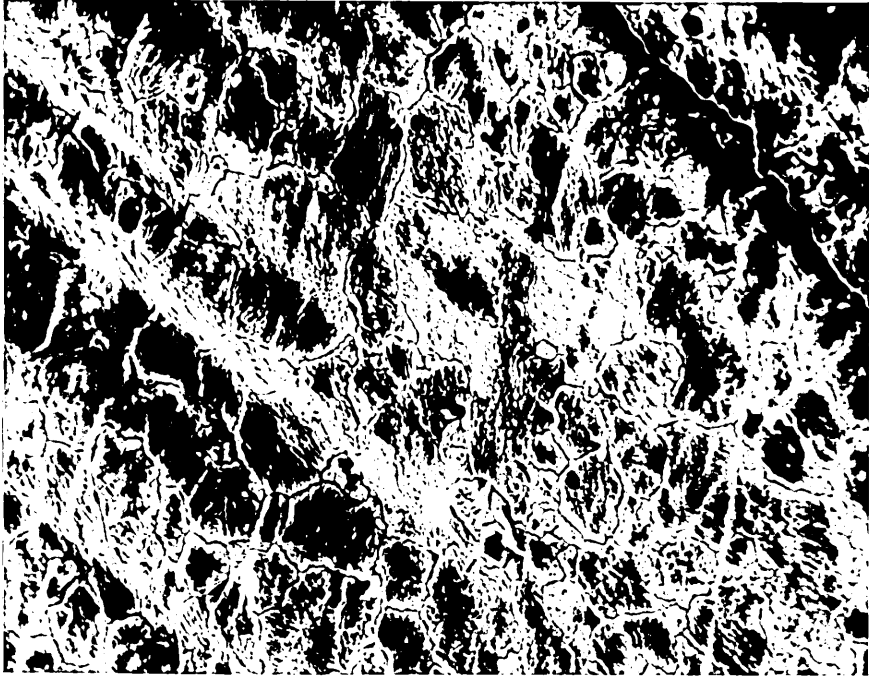


Plate 28

Specimen C134. Fe-0.17% Cr dropped through 100 cm air at 1600°C and quenched in silicone oil.

SEM Micrograph
Magnification 200x

Surface examination reveals duplex structure. Islands of smooth oxide, evenly distributed, standing in a sea of fine 'wavy' oxide. Smooth rounded areas very low in chromium.

Plate 29

Specimen C133. Fe-0.17% Cr dropped through 100 cm air at 1600°C and quenched in silicone oil. Reduced in hydrogen at 1150°C for 1 hour

SEM Micrograph
Magnification 800x

Surface denuded by exposure to the hydrogen. Surface relief appears to be minimised, pockets still remaining containing second oxide. Depressions can be seen in the oxide film; also formation of pits or holes in oxide film.

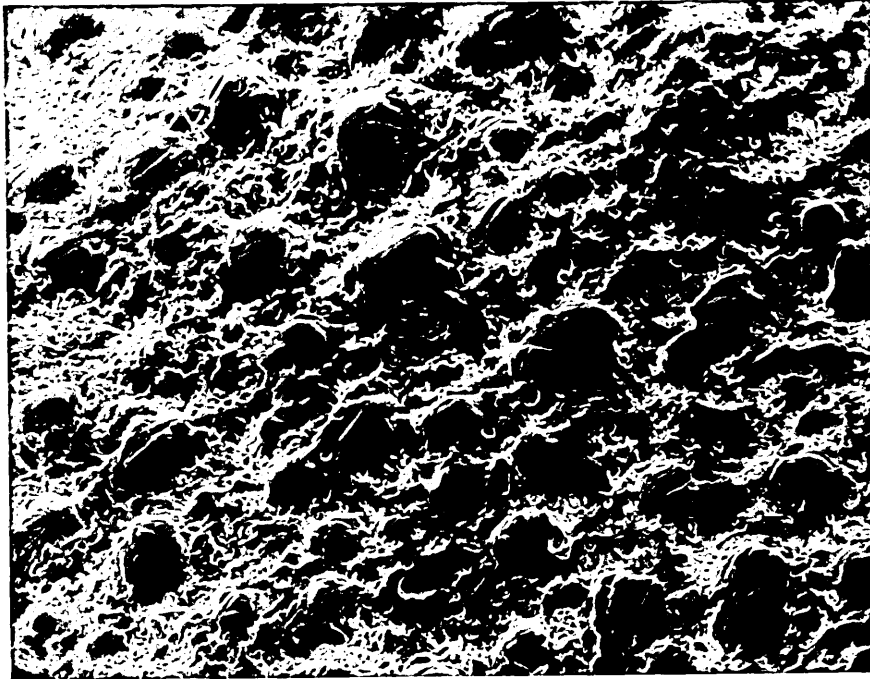


Plate 30

Blank Specimen. Fe-0.25% Cr. Reduced in hydrogen and quenched, unoxidised, in silicone oil.

SEM Micrograph
Magnification 540x

Fine detail of unoxidised surface revealed.
Suggests duplex nature.

Plate 31

Specimen C92. Fe-0.25% Cr dropped through 100 cm air at 1600°C and quenched in silicone oil.

SEM Micrograph
Magnification 450x

Duplex structure similar to specimen 134. One oxide appears as rounded smooth phase standing out in relief with second oxide phase filling in the 'valleys'.

Plate 32

Specimen C91. Fe-0.25% Cr dropped through 50 cm air at 1600°C and quenched in silicone oil. Reduced in hydrogen at 1150°C for 1 hour.

SEM Micrograph
Magnification 800x

Reveals nature of reduced surface. Rounded oxide now not evident. Fine boundaries in evidence. Range of different size tapered pits to be seen both in valley bottoms and in areas of high relief.

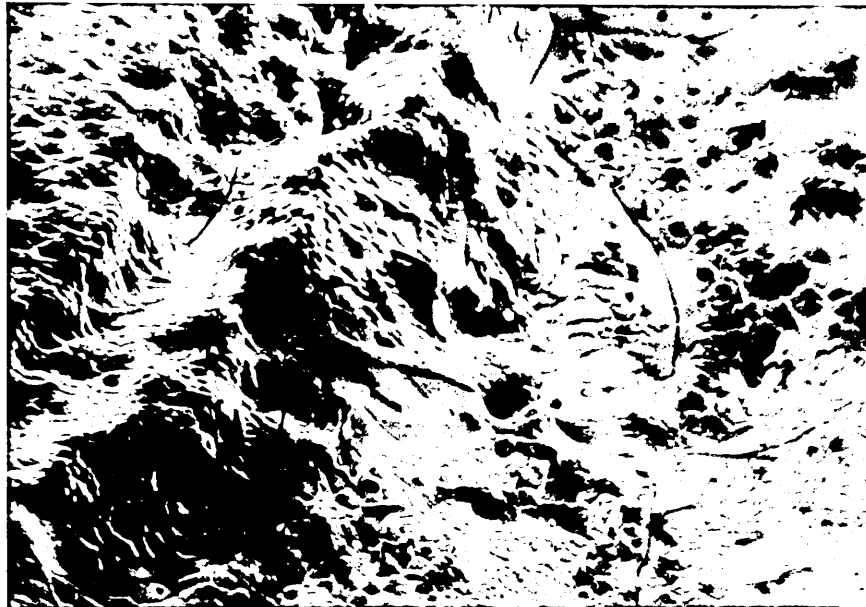
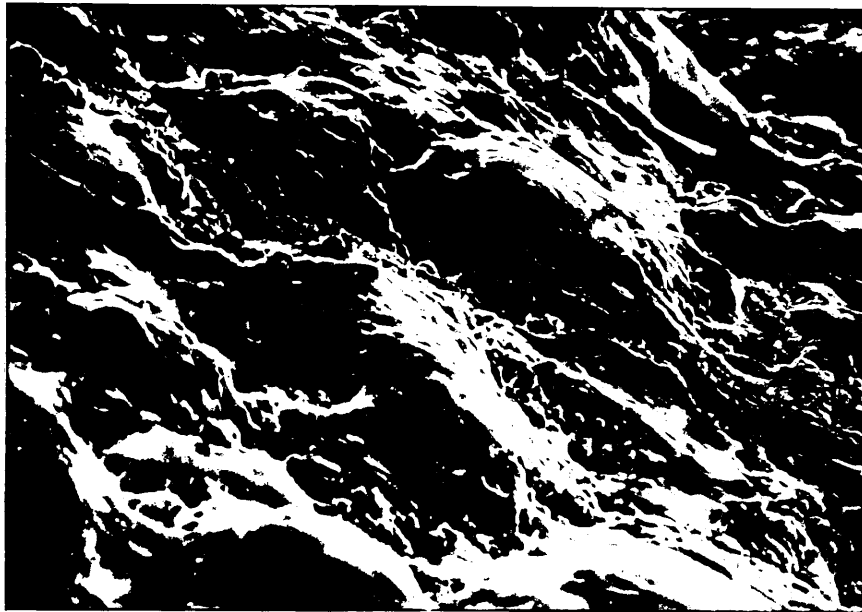
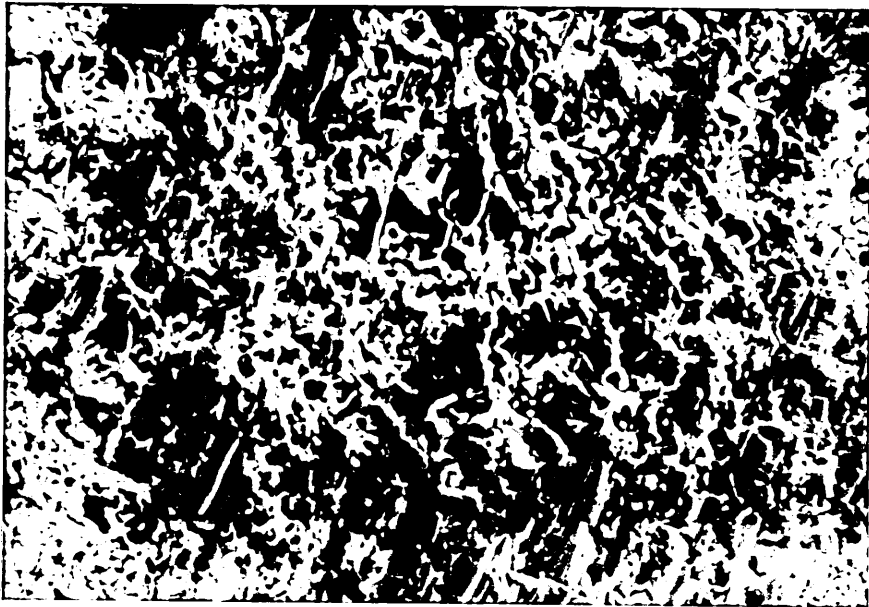


Plate 33

Specimen C26. Fe-0.8% Cr dropped through 100 cm air at 1600°C and quenched in silicone oil.

SEM Micrograph
Magnification 560x

The more massive rounded phase seen in lower chromium alloys is now evident as spheroids on surface. These spheroids contain no chromium. They are small and rounded and distributed evenly over the surface with only odd spheroids growing to any considerable size. The matrix is now the second oxide phase and this predominates.

Plate 34

Specimen C183. Fe-1.46% Cr dropped through 50 cm air at 1600°C and quenched in silicone oil.

SEM Micrograph
Magnification 450x

Surface oxide now completely the fine second oxide with only a trace of smooth oxide. The network covers most of the surface in a closely knit matter.

Plate 35

Specimen C185. Fe-1.46% Cr dropped through 100 cm air at 1600°C and quenched in silicone oil.

SEM Micrograph
Magnification 450x

Shows similar characteristics to the previous specimen. Surface entirely covered with a fine matting of oxide.

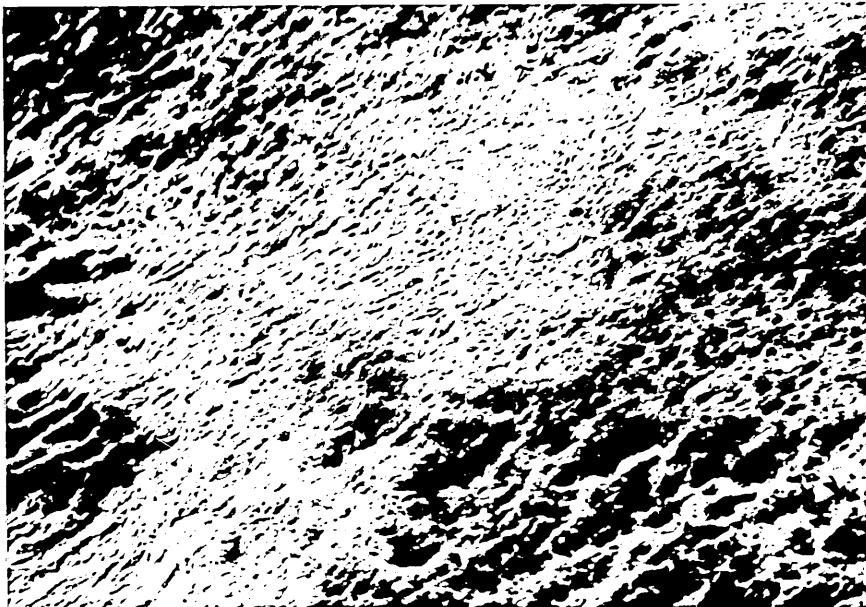
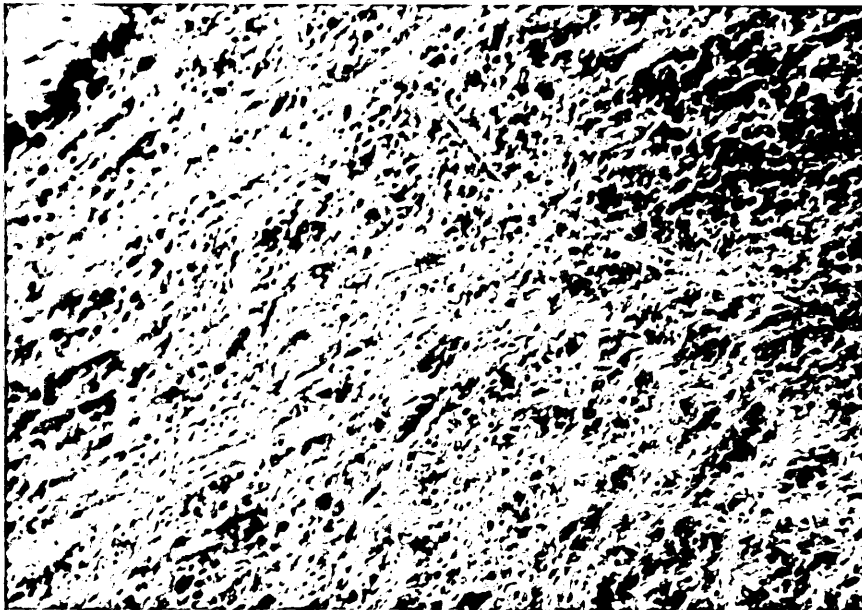
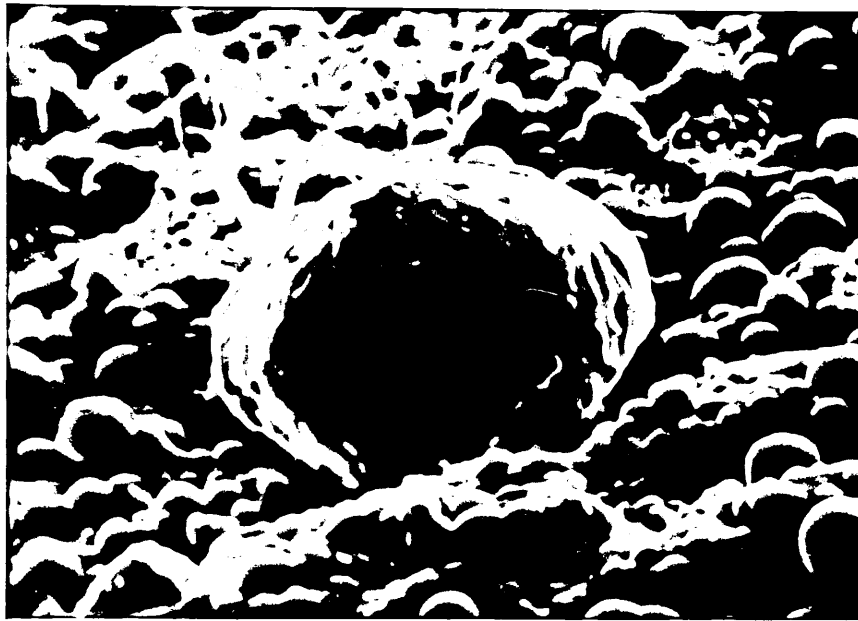


Plate 36

Specimen C184. Fe-1.46% Cr dropped through 50 cm air at 1600°C and quenched in silicone oil. Reduced in hydrogen at 1150°C for 1 hour.

SEM Micrograph
Magnification 900x

Reduction at 1150°C appears to have almost denuded the surface of the oxide film. Traces of light second phase, probably iron, evident. Formation of pits can be seen and a large crack in the surface is in evidence.

Plate 37

Specimen C186. Fe-1.46% Cr dropped through 100 cm air at 1600°C and quenched in silicone oil. Reduced in hydrogen at 1150°C for 1 hour.

SEM Micrograph
Magnification 1800x

This specimen with a thicker oxide film than the previous specimen shows the earlier stages in the reduction process. The oxide film can clearly be seen with the formation of depressions or holes in the film. The possibility of these holes joining up to form a continuous crack in the oxide is evident.

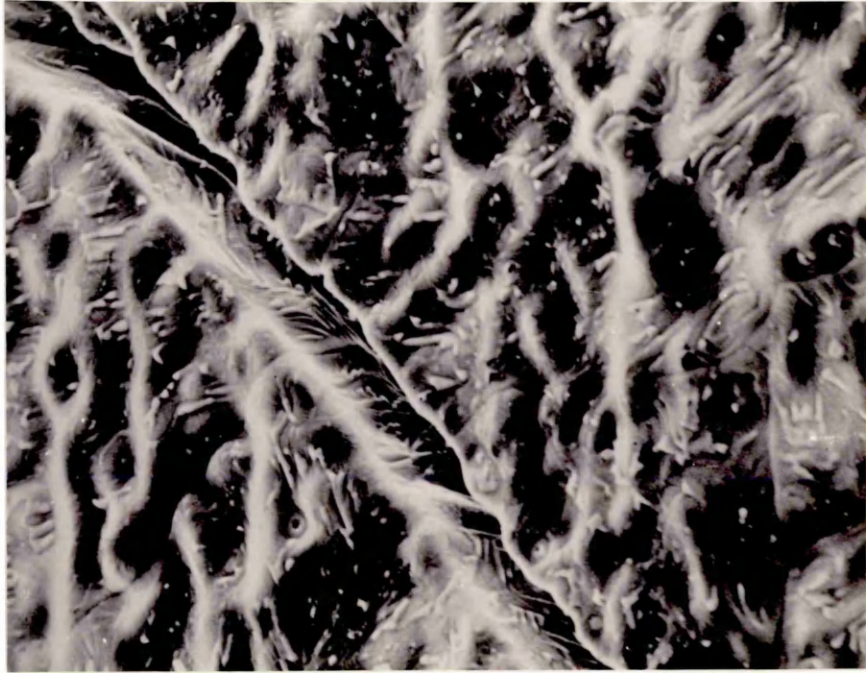


Plate 38

Specimen E1. Fe-0.3% Si dropped through 100 cm air at 1600°C and quenched in silicone oil.

SEM Micrograph
Magnification 540x

General features of nature of oxide film formed on the surface. Very little relief. Oxide appears as a fairly dense network with possibly a few holes or spaces in that network.

Plate 39

Specimen E1. Fe-0.3% Si dropped through 100 cm air at 1600°C and quenched in silicone oil.

SEM Micrograph
Magnification 2160x

Oxide morphology in more detail. Oxide network does not completely cover surface.

Plate 40

Specimen E3. Fe-0.3% Si dropped through 100 cm air at 1600°C and quenched in silicone oil. Reduced in hydrogen at 1150°C for 1 hour.

SEM Micrograph
Magnification 540x

The network of "matted" oxide appears to be breaking down. Small pits are forming in the oxide.

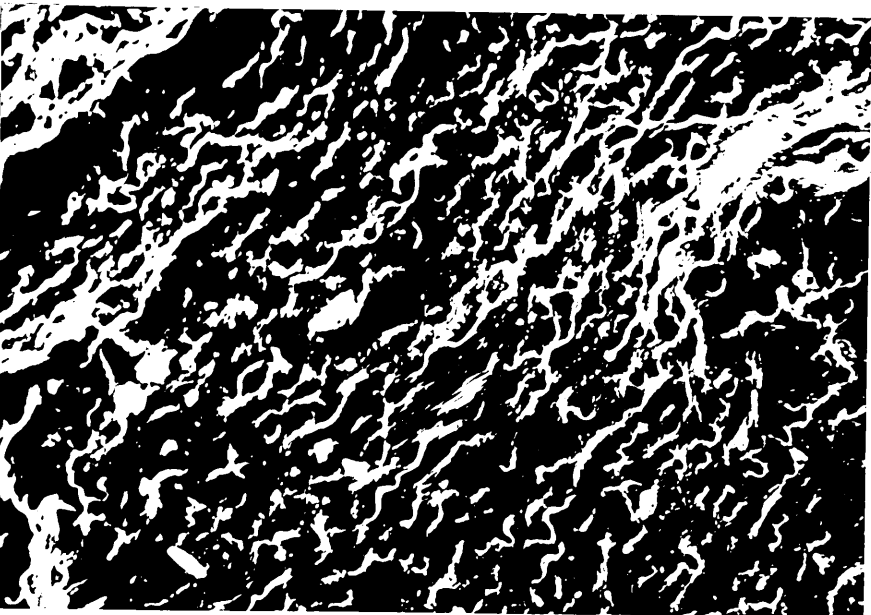
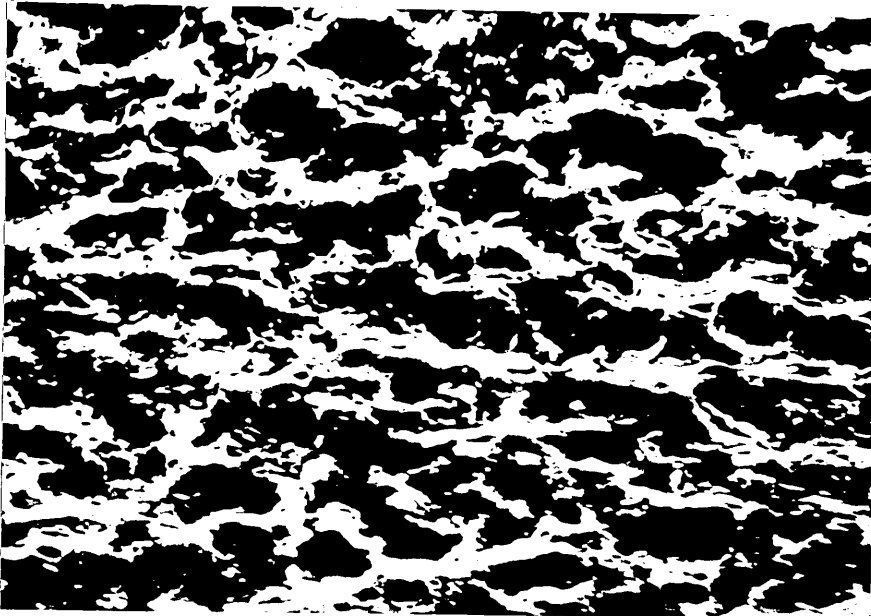
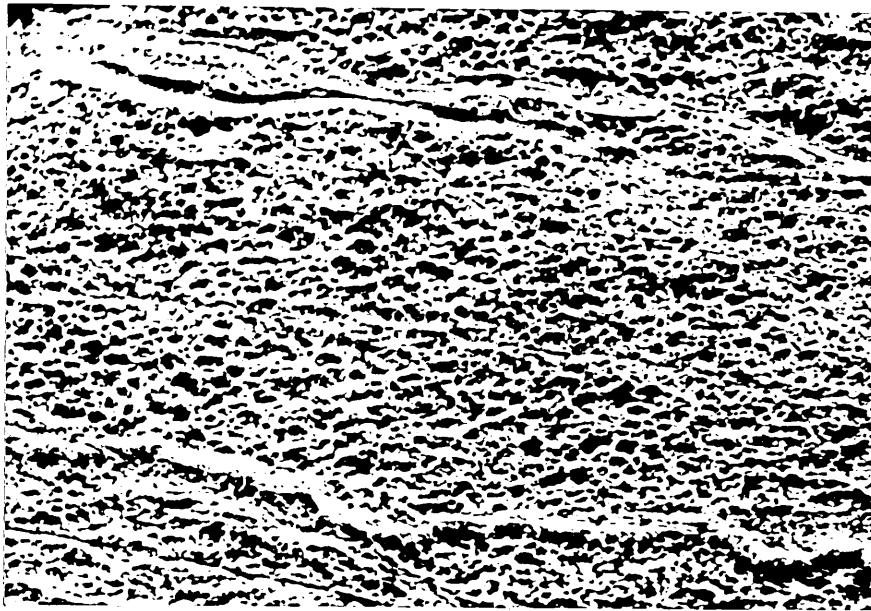


Plate 41

Specimen E65. Fe-0.75% Si dropped through 100 cm air at 1600°C and quenched in silicone oil.

SEM Micrograph
Magnification 1100x

Surface shows similar features to Specimen E1. However, the oxide network appears to be finer. The network is again dense and any holes or gaps in the network are much smaller.

Plate 42

Specimen E62. Fe-0.75% Si dropped through 100 cm air at 1600°C and quenched in silicone oil.

SEM Micrograph
Magnification 540x

The fine network has disappeared and the reduced oxide is perforated by a large number of holes. The surface appears to have a mottled effect. Appearance of more surface relief.

Plate 43

Specimen E62. Fe-0.75% Si dropped through 100 cm air at 1600°C and quenched in silicone oil. Reduced in hydrogen at 1150°C for 1 hour.

SEM Micrograph
Magnification 2160x

Central region magnified. Holes appear to be deep and to perforate oxide film. Mottled effect can be seen to be small "blisters" on the surface.

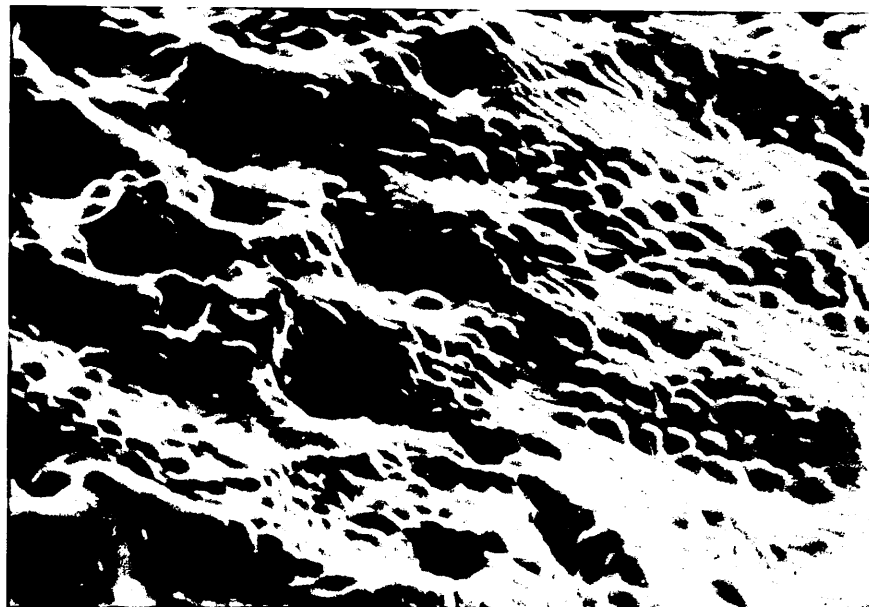
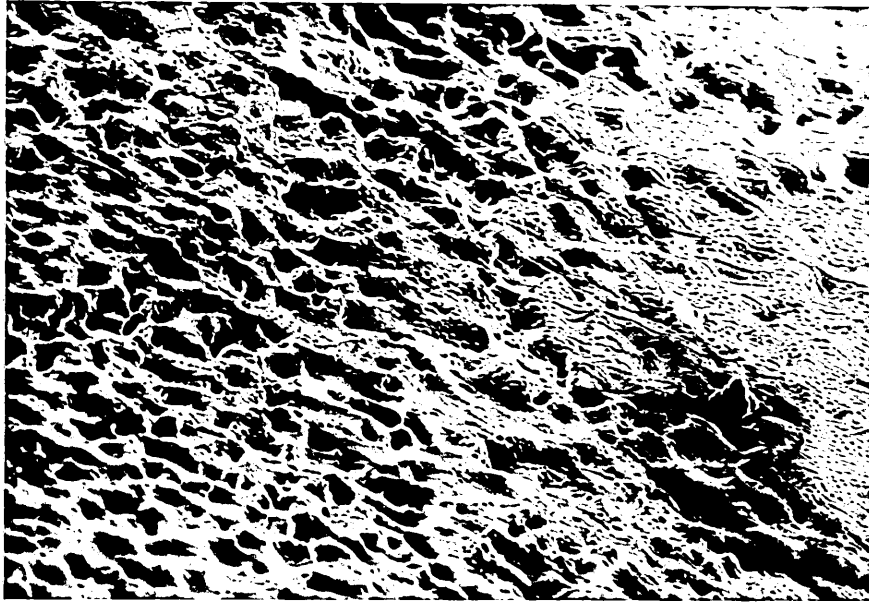
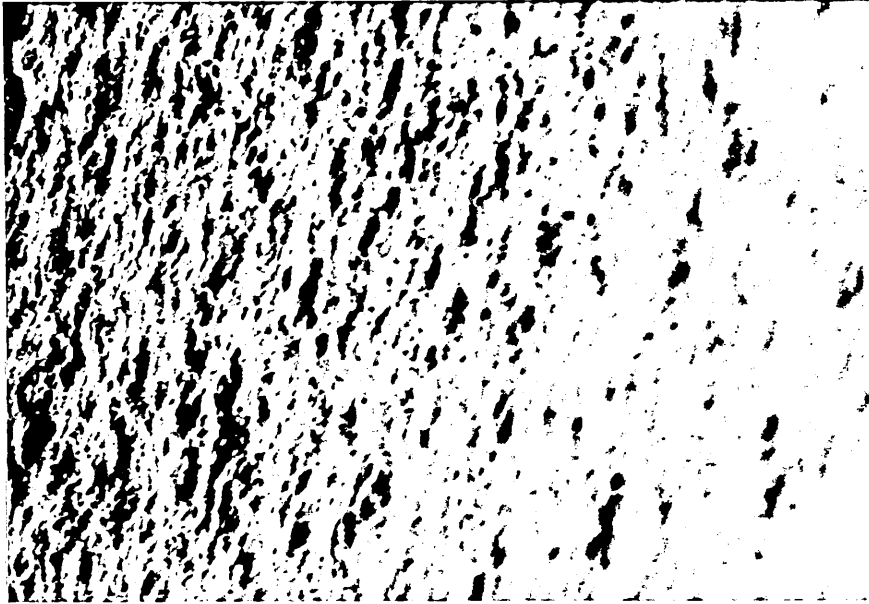


Plate 44

Specimen E5. Fe-1.33% Si dropped through 100 cm air at 1600°C and quenched in silicone oil.

SEM Micrograph
Magnification 540x

Surface again shows the oxide network; there appears to be fewer discontinuities in the oxide film. Perhaps an even finer network structure.

Plate 45

Specimen E5. Fe-1.33% Si dropped through 100 cm air at 1600°C and quenched in silicone oil.

SEM Micrograph
Magnification 2160x

Showing the coverage of the oxide network at higher magnification.

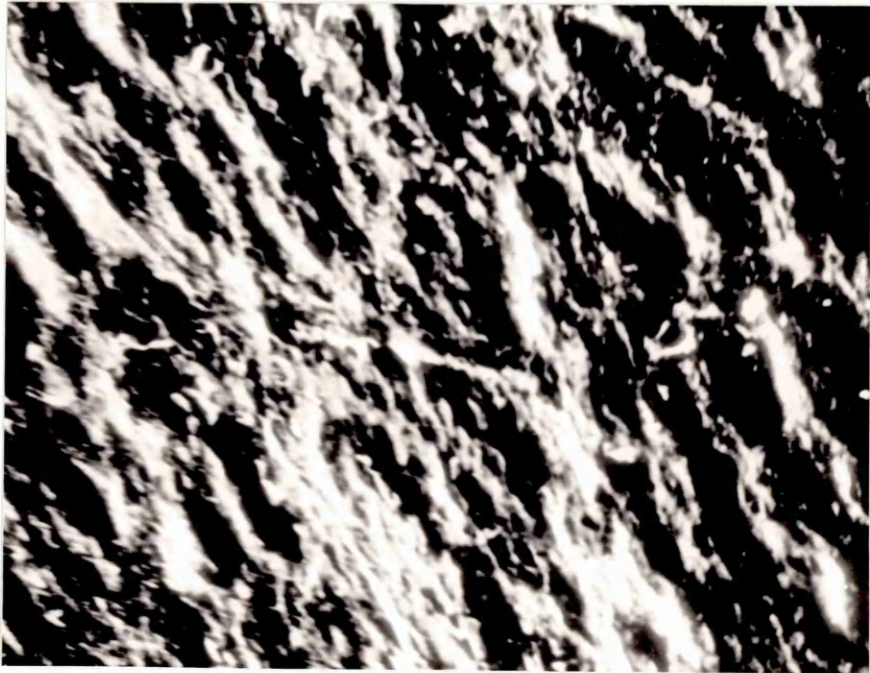
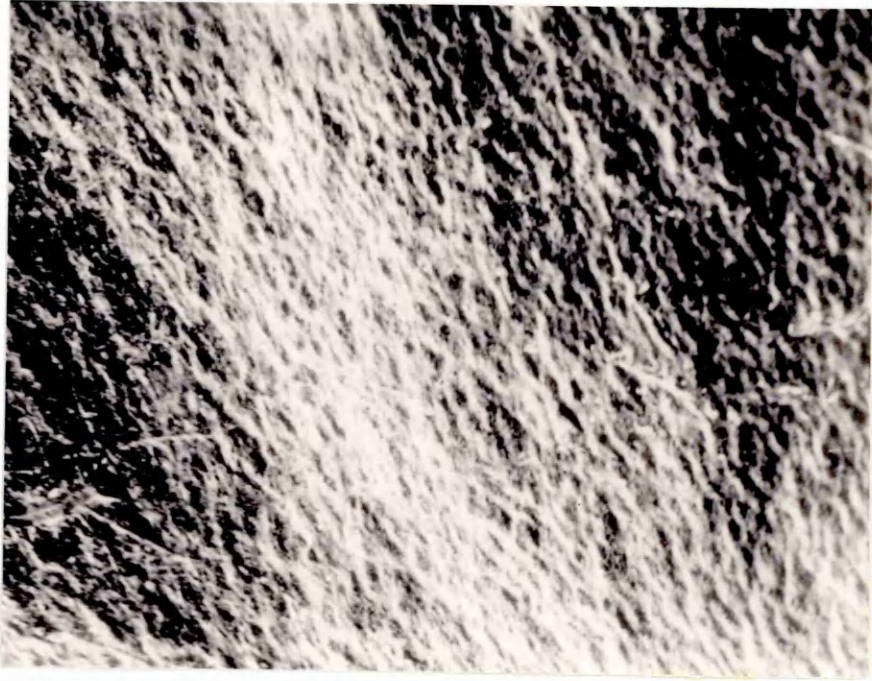


Plate 46

Specimen E5. Fe-1.33% Si dropped through 100 cm air at 1600°C and quenched in silicone oil. Reduced in hydrogen at 1150°C for 1 hour.

SEM Micrograph
Magnification 540x

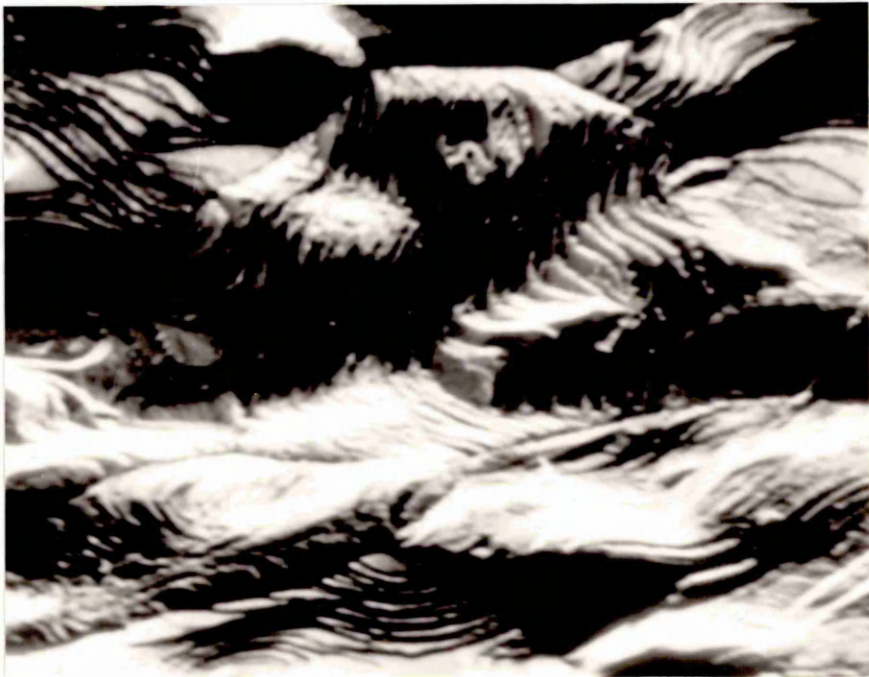
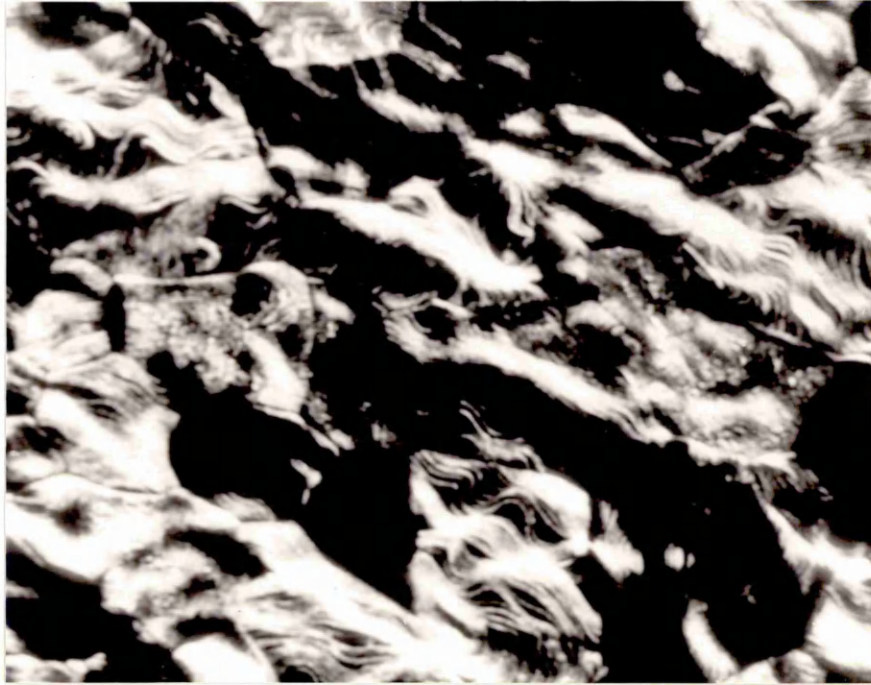
Surface almost completely removed of oxide film. Relatively featureless surface now showing much more relief. Surface also appears to be stepped.

Plate 47

Specimen E5. Fe-1.33% Si dropped through 100 cm air at 1600°C and quenched in silicone oil. Reduced in hydrogen at 1150°C for 1 hour.

SEM Micrograph
Magnification 2160x

Enlargement of central region of previous plate. Shows stratified nature of surface after exposure to hydrogen at 1150°C. Evidence of removal of metal; thermal etching of surface. Pitting of surface not in evidence. Surface suggests removal of oxide evenly over the surface with local relief variations.



APPENDIX I

Interval Estimation and Number of Observations

When there is a range of values it is usually preferable to find an interval estimate. The estimate is constructed in such a way that we have a certain confidence that the interval does contain the unknown parameter. The interval estimate is then called a confidence interval.

Silicone oil quench media.

50 cm fall in air values.

95% C.I. for mean oxygen content.

$$\bar{x} \pm t_{19.975} \frac{s}{\sqrt{n}}$$

where \bar{x} is the mean of the observations

s is the standard deviation of the sample

$$= \sqrt{\left[\sum_{i=1}^n \frac{(x_i - \bar{x})^2}{n-1} \right]}$$

n is the number of observations

x_i is the value of the observation

$t_{19.975}$ is the percentage point of the t distribution

For the results obtained:

$$\bar{x} = 0.0457$$

$$s = 0.0140$$

$$n = 20$$

$$t_{19.975} = 2.093$$

$$\bar{x} \pm t_{19.975} \frac{s}{\sqrt{n}} = 0.0457 \pm 2.093 \times \frac{0.014019}{\sqrt{20}}$$

i.e. 0.0391, 0.0523

To obtain a confidence interval of width 2Δ we require
N observations where:

$$\Delta \approx \frac{2s}{N}$$

$$N \approx \frac{4s^2}{\Delta^2}$$

For $\Delta = 0.005$, $N = 32$

$\Delta = 0.01$, $N = 8$

Above results normalised to 0.7 g equivalent droplet.

$$\bar{x} = 0.0470$$

$$s = 0.0124$$

$$n = 20$$

$$\bar{x} \pm t_{19.975} \frac{s}{\sqrt{n}} = 0.0470 \pm 2.093 \times \frac{0.0124}{\sqrt{20}}$$

i.e. 0.0412, 0.0528

$$\Delta \approx \frac{2s}{\sqrt{N}}$$

$$N \approx \frac{4s^2}{\Delta^2}$$

For $\Delta = 0.005$, $N = 25$

$\Delta = 0.01$, $N = 6$

Reference

C Chatfield Statistics for Technology, Chapman & Hall, 1979.

APPENDIX II

Temperature Profile of a Free Falling Iron Droplet

1. Thermal Losses by Radiation and Convection

The thermal losses by radiation per unit area per unit time are given by the Stefan-Boltzmann law of radiation:

$$\dot{q} = \delta T_s^4 \quad (1)$$

where δ is the Stefan-Boltzmann radiation constant and T_s is the surface temperature.

The above formula is applicable to black body conditions only and must be modified for non-black body conditions by the introduction of the emissivity ϵ of the surface, which is a function of the material, surface properties and temperature.

$$\text{Rate of heat lost by radiation, } \dot{q} = \delta A \epsilon (T_s^4 - T_e^4) \quad (2)$$

for radiation between a finite surface area and its total surroundings, i.e. $F_{12} = 1$,

where A is the surface area of the droplet, and

T_e is the temperature of the environment.

The thermal losses by convection per unit area per unit time are given by:

$$\dot{q} = h (T_s - T_e) \quad (3)$$

where h is the heat transfer coefficient.

In general, the value of h depends on the geometry of the system, droplet velocity and the properties of the gas⁽¹⁾.

Since the properties of the gas are temperature dependent the heat transfer coefficient will also be a function of temperature. In situations which involve the formation of a boundary layer, as in this case, the heat transfer coefficient varies with location along the heat transfer surface.

Under these conditions, where h is dependent on location along the heat transfer surface, it is convenient to define a mean value of the heat transfer coefficient over the entire surface as:

$$\bar{h} = \frac{\int_0^A h \, dA}{\int_0^A dA} \quad (4)$$

The local heat transfer coefficient for convective heat transfer between a spherical particle and a fluid in relative motion can be estimated from the Ranz-Marshall correlation⁽²⁾.

$$N_{Nu} = 2.0 + 0.6 N_{Re}^{\frac{1}{2}} N_{Pr}^{\frac{1}{3}} \quad (5)$$

Figure AII-1 is a typical plot of the variation of local heat transfer coefficient with distance along the perimeter of a sphere⁽³⁾.

From data to be presented later in this section it will be seen that the Reynolds' number for a droplet in flight over a distance of 1.2 metres varies between 70 and 240. In view of this, an average local Nusselt number of 4 would seem reasonable.

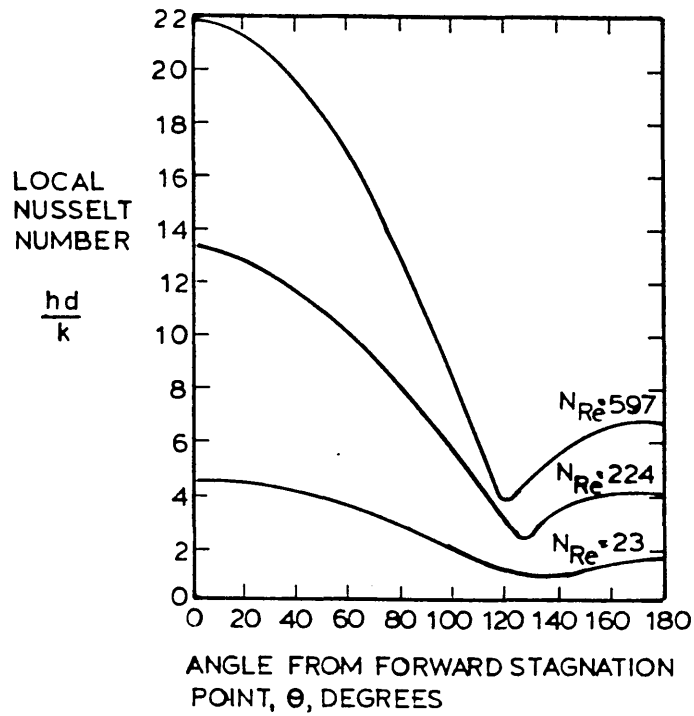
Hence: $N_{Nu} = \frac{hd}{k} = 4$

$\therefore h = \frac{4k}{d}$

where k is the thermal conductivity of the gas. At a mean air temperature of 800°C , the thermal conductivity of air has a value of $57.3 \times 10^{-3} \text{ W m}^{-1} \text{ K}^{-1}$ (4).

Heat transfer coefficient, $h = \frac{4k}{d}$
 $= \frac{4 \times 57.3 \times 10^{-3}}{d} \text{ W m}^{-1} \text{ K}^{-1}$

Figure A II-1



Variation of Local Heat Transfer Coefficient for flow past a sphere. (3)

For a 0.7 g iron droplet

The volume is given by mass \div density. Assuming a spherical droplet and the density of molten iron as 7.10 g cm^{-3} ⁽⁵⁾ the diameter of the droplet is determined as 0.00572 m . Substituting in the above equation,

$$h = 40.0 \text{ W m}^{-2} \text{ K}^{-1}$$

Heat lost from 0.7 g droplet by convection:

$$\dot{q} = hA(T_s - T_e)$$

$$\begin{aligned}\dot{q} &= 40.0 \cdot 4\pi (0.00286)^2 \cdot 1873 - 293 \text{ W} \\ &= \underline{6.50 \text{ W}}\end{aligned}$$

Heat lost from 0.7 g droplet by radiation:

$$\dot{q} = \delta A \varepsilon (T_s^4 - T_e^4)$$

Given that $\delta = 5.670 \times 10^{-8} \text{ W m}^{-2} \text{ K}^{-4}$

$$\varepsilon = 0.37$$

$$\begin{aligned}\dot{q} &= 5.670 \times 10^{-8} \times 0.37 \cdot 4\pi (0.00286)^2 \cdot 1873^4 - 293^4 \\ &= \underline{26.52 \text{ W}}\end{aligned}$$

Determination of heat content of 0.7 g droplet at 1600°C

Specific heat data⁽⁶⁾

(a) Fe(α)	$C_p = 17.49 + 24.77 \times 10^{-3} T$	J mol ⁻¹ K ⁻¹ (273-1033K)
(b) Fe(β)	$C_p = 37.656$	J mol ⁻¹ K ⁻¹ (1033-1181)
(c) Fe(γ)	$C_p = 7.70 + 19.50 \times 10^{-3} T$	J mol ⁻¹ K ⁻¹ (1181-1674)
(d) Fe(δ)	$C_p = 43.93$	J mol ⁻¹ K ⁻¹ (1674-1809)
(e) Fe(l)	$C_p = 41.84$	J mol ⁻¹ K ⁻¹ (1809-1873)

(f)	Fe($\alpha \rightarrow \beta$)	$L_t = 2.761$	$\text{kJ mol}^{-1} \text{K}^{-1}$	1033K
(g)	Fe($\beta \rightarrow \gamma$)	$L_t = 0.921$	$\text{kJ mol}^{-1} \text{K}^{-1}$	1181K
(h)	Fe($\gamma \rightarrow \delta$)	$L_t = 0.879$	$\text{kJ mol}^{-1} \text{K}^{-1}$	1674K
(i)	Fe($\delta \rightarrow \ell$)	$L_f = 15.481$	$\text{kJ mol}^{-1} \text{K}^{-1}$	1809K

$$\Delta H = \int_{T_1}^{T_2} C_p dT + L_t$$

$$\begin{aligned} \Delta H_{\text{Fe}} &= \int_{293}^{1033} (17.49 + 24.77 \times 10^{-3} T) dt + 2761 + \int_{1033}^{1181} 37.656 dT + 921 \\ &+ \int_{1181}^{1674} (7.70 + 19.50 \times 10^{-3} T) dT + 879 + \int_{1674}^{1809} 43.93 dT + 15481 \\ &+ \int_{1809}^{1873} 41.84 dT \\ &= \left[17.49T + 12.39 \times 10^{-3} T^2 \right]_{293}^{1033} + 2761 + \left[37.656T \right]_{1033}^{1181} + 921 \\ &+ \left[7.70T + 9.75 \times 10^{-3} T^2 \right]_{1181}^{1674} + 879 + \left[43.93T \right]_{1674}^{1809} + 15481 \\ &+ \left[41.84T \right]_{1809}^{1873} \\ &= 17.49(1033-293) + 12.39 \times 10^{-3}(1033^2 - 293^2) + 2761 + 37.656(1181-1033) \\ &+ 921 + 7.70(1674-1181) + 9.75 \times 10^{-3}(1674^2 - 1181^2) + 879 + 43.93 \\ &\quad (1809-1674) + 15481 + 41.84(1873-1809) \\ &= 12943 + 12158 + 2761 + 5573 + 921 + 3796 + 13723 + 879 \\ &+ 5931 + 15481 + 2678 \\ &= 76844 \text{ J mol}^{-1} \end{aligned}$$

$$\text{Heat content, } \Delta H = 76.844 \text{ kJ mol}^{-1}$$

$$= \frac{76.844}{55.85} \text{ J mol}^{-1} \text{ g mol}^{-1}$$

$$= 1375.9 \text{ J g}^{-1}$$

For a 0.7 g iron droplet at 1600°C, the heat content of the droplet is given by:

$$\Delta H = 1375.9 \times 0.7$$

$$\underline{\Delta H = 963.13 \text{ J}}$$

Time to fall through one metre = 0.45 s.

Heat lost by droplet in falling through one metre is given by:

$$\text{Heat lost by radiation} = 0.45 \times 26.52$$

$$= 11.93 \text{ J}$$

$$\text{Heat lost by convection} = 0.45 \times 6.50$$

$$= 2.93 \text{ J}$$

$$\text{Total heat lost} = 14.86 \text{ J}$$

$$\begin{aligned} \text{For liquid iron, specific heat capacity, } C_p &= 41.84 \text{ J mol}^{-1} \text{ K}^{-1} \text{ (6)} \\ &= 0.749 \text{ J g}^{-1} \text{ K}^{-1} \end{aligned}$$

Fall temperature of droplet from 1600°C is given by:

$$q = m C_p \Delta T$$

where m is the mass of the droplet

C_p is the specific heat capacity

q is the heat content

ΔT is the temperature change

$$\begin{aligned}\Delta T &= \frac{q}{m C_p} \\ &= \frac{14.86}{0.7 \times 0.749} \\ &= \underline{28.3^\circ\text{C}}\end{aligned}$$

2. Thermal losses offset by heat of reaction

During the fall of the droplet in air, the basic oxidation reaction was considered as $\text{Fe} + \frac{1}{2}\text{O}_2 = \text{FeO}$. The case of the 0.7 gramme iron droplet was considered as data existed for this size of droplet. The amount of oxygen picked up during each 10 cm increment of fall in air was established from Fig.56.

Two assumptions were made. Firstly that the heat of reaction generated at each 10 cm interval offset the fall in temperature in that same interval and secondly the heat generated was evenly dissipated throughout the droplet.

This amount of heat generated was then offset against the thermal losses by radiation and convection in the same interval. The heat generated modified the droplet heat loss; the temperature of the droplet was calculated for each successive 10 cm fall in air.

3. Computer programme to calculate heat losses during fall

The heat losses by radiation and convection from different sized iron droplets falling through air were calculated using a computer programme. The programme calculated the sensible heat of the droplet. The time for the droplet to fall 10 cm intervals was calculated and the heat loss over this interval was determined. The sensible heat of the droplet was adjusted and the temperature at the end of the 10 cm fall obtained. The process was repeated for consecutive intervals up to a total distance of 2 metres for different sized iron droplets in the range 0.6 to 1.0 gramme mass.

The computer programme was modified to take account of the heat of reaction for a 0.7 g iron droplet. The programme and results are presented at the end of this appendix.

References

1. J Szekely and N J Themelis. Rate Phenomena in Process Metallurgy, J Wiley and Sons, 1971.
2. W E Ranz and W R Marshall. Chem. Eng. Prog., 48, 141, 1952, p173.
3. E R G Eckert and R M Drake. Heat and Mass Transfer, McGraw-Hill, 1959.
4. N B Vargaftik. Tables of Thermophysical Properties of Liquids and Gases, 2nd Ed., Hemisphere Publ. Corp., 1975.

5. A Adachi et al. Proc. ICSTIS Suppl. Trans., I.S.I.J.,
11, 1971, 395.
6. O Kubaschewski and E Ll Evans. Metallurgical Thermochemistry,
Pergamon, 1958.

TYPE RADLOSS FORTRAN

```

C PROGRAMME TO CALCULATE THE HEAT LOSS BY RADIATION
C AND CONVECTION FROM DIFFERENT SIZED
C IRON DROPLETS..
C M = MASS OF DROPLET (KG)
C R = RADIUS OF DROPLET(M)
C A = SURFACE AREA OF DROPLET(M2)
C V = VOLUME OF DROPLET(M3)
C S = HEIGHT OF FALL OF DROPLET(M)
C TIM = TIME OF FALL OF DROPLET(S)
C DTIM = TIME INCREMENT BETWEEN 10 CM STEPS
C T = TEMPERATURE OF DROPLET(K)
C SHT = SENSIBLE HEAT OF DROPLET(J)
C HTL = HEAT LOST BY DROPLET(J)
C TO CALCULATE THE VOLUME, AREA AND RADIUS
C OF THE DROPLET.

REAL M
DIMENSION T(25),SHT(25),HTL(25),TIM(25),CON(25),DTIM(25)
DIMENSION M(250),R(250),A(250),V(250),S(250)
DATA S(1),S(2),S(3),S(4),S(5)/0.1,0.2,0.3,0.4,0.5/
DATA S(6),S(7),S(8),S(9),S(10)/0.6,0.7,0.8,0.9,1.0/
DATA S(11),S(12),S(13),S(14),S(15)/1.1,1.2,1.3,1.4,1.5/
DATA S(16),S(17),S(18),S(19),S(20)/1.6,1.7,1.8,1.9,2.0/
DATA (M(J),J=1,6)/0.0005,0.0006,0.0007,0.0008,0.0009,0.0010/
DO 100 J=1,6,1
PI=3.14159
RHO=0.71E+04
V(J)=M(J)/RHO
R(J)=((3*V(J))/(4*PI))**(1./3.)
A(J)=4*PI*(R(J)**2.)
WRITE(6,15)M(J),R(J)
15 FORMAT(//5X,'MASS OF DROPLET = ',F6.4,2X,'KG'/
13X,'RADIUS OF DROPLET = ',F8.6,2X,'METRES'/
21X,'INITIAL TEMPERATURE = 1873K'//)
WRITE(6,20)
20 FORMAT(2X,'HT. OF FALL',2X,'TIME OF FALL',2X,
1'SENSIBLE HEAT',2X,'HEAT LOSS',2X,'TEMP. OF DROPLET'/
24X,'METRES',7X,'SECONDS',8X,'JOULES',7X,'JOULES',
37X,'DEGREES K'//)
C TO CALCULATE THE TIME OF FALL FOR 10 CM INTERVALS.
DO 90 I=1,20,1
G=9.81
T(I)=1873.
TIM(I)=0.
TIM(I)=(2.*S(I)/G)**(1./2.)
C TO CALCULATE THE SENSIBLE HEAT AND HEAT LOSS
C FOR THE IRON DROPLET.THE VALUE OF 1327950 WAS
C OBTAINED FROM CP DATA AND IS THE VALUE OF THE
C HEAT CAPACITY PER KG. OF IRON UP TO THE MELTING
C POINT INCLUDING THE LATENT HEAT. THE VALUE
C OF 249 IS THE HEAT CAPACITY PER KG. OF MOLTEN
C IRON BETWEEN 1809K AND 1873K.

```

```

EMISS=0.37
SIGMA=5.6697E-08
DTIM(I)=TIM(I)-TIM(I-1)
HTC=40.00
CON(I)=(HTC*A(J)*(T(I)-293)*DTIM(I))
SHT(I)=M(J)*(1327950.+749.*(T(I)-1809.))
SHT(I+1)=SHT(I)-HTL(I)
HTL(I)=(SIGMA*A(J)*EMISS*((T(I)**4.)-(293.**4.))*DTIM(I))+CON(I)
T(I+1)=(((SHT(I+1)/M(J))-1327950.)/749.)+1809.
WRITE(6,25)S(I),TIM(I),SHT(I),HTL(I),T(I+1)
25 FORMAT(6X,F4.2,7X,F6.5,7X,F9.4,6X,F6.4,7X,F8.3/)
90 CONTINUE
100 CONTINUE
STOP
END

```

MASS OF DROPLET = 0.0007 KG
 RADIUS OF DROPLET = 0.002866 METRES
 INITIAL TEMPERATURE = 1873K

HT. OF FALL METRES	TIME OF FALL SECONDS	SENSIBLE HEAT JOULES	HEAT LOSS JOULES	TEMP. OF DROPLET DEGREES K
0.10	.14278	963.1201	4.7336	1864.852
0.20	.20193	958.8472	1.9315	1861.526
0.30	.24731	957.1035	1.4730	1858.990
0.40	.28557	955.7742	1.2360	1856.862
0.50	.31928	954.6584	1.0847	1854.996
0.60	.34975	953.6799	0.9772	1853.314
0.70	.37777	952.7979	0.8959	1851.771
0.80	.40386	951.9893	0.8315	1850.342
0.90	.42835	951.2397	0.7789	1849.001
1.00	.45152	950.5369	0.7348	1847.737
1.10	.47356	949.8740	0.6973	1846.538
1.20	.49462	949.2454	0.6648	1845.395
1.30	.51482	948.6462	0.6362	1844.302
1.40	.53425	948.0728	0.6110	1843.251
1.50	.55300	947.5220	0.5884	1842.239
1.60	.57114	946.9915	0.5680	1841.263
1.70	.58871	946.4797	0.5495	1840.319
1.80	.60578	945.9849	0.5326	1839.404
1.90	.62236	945.5051	0.5171	1838.515
2.00	.63855	945.0391	0.5029	1837.651

TYPE RADLOSS FORTRAN

C PROGRAMME TO CALCULATE THE HEAT LOSS BY RADIATION
 C AND CONVECTION FROM DIFFERENT SIZED
 C IRON DROPLETS WHEN HT. OF FORMATION OF FEO ADDED.
 C M = MASS OF DROPLET (KG)
 C R = RADIUS OF DROPLET(M)
 C A = SURFACE AREA OF DROPLET(M²)
 C V = VOLUME OF DROPLET(M³)
 C S = HEIGHT OF FALL OF DROPLET(M)
 C TIM = TIME OF FALL OF DROPLET(S)
 C DTIM = TIME INCREMENT BETWEEN 10 CM STEPS
 C T = TEMPERATURE OF DROPLET(K)
 C SHT = SENSIBLE HEAT OF DROPLET(J)
 C HTL = HEAT LOST BY DROPLET(J)
 C KOX = PERCENT OXYGEN PICKED UP BY DROPLET
 C HTFOR = HEAT OF FORMATION OF FEO (J/KMOL)
 C IFU = KMOL OF OXYGEN PICKED UP AT EACH STAGE
 C TO CALCULATE THE VOLUME, AREA AND RADIUS
 C OF THE DROPLET.

```

REAL M
REAL IFU(25),JXD(25),K(12),S(12)
DIMENSION T(25),SHT(25),HTL(25),TIM(25),CON(25),DTIM(25)
DATA S(1),S(2),S(3),S(4),S(5),S(6)/0.1,0.2,0.3,0.4,0.5,0.6/
DATA S(7),S(8),S(9),S(10),S(11),S(12)/0.7,0.8,0.9,1.0,1.1,1.2/
DATA K(1),K(2),K(3),K(4)/0.014,0.012,0.010,0.008/
DATA K(5),K(6),K(7),K(8)/0.006,0.006,0.005,0.005/
DATA K(9),K(10),K(11),K(12)/0.004,0.004,0.004,0.003/
M=0.0007

```

```

FI=3.14159
RHO=0.71E+04
V=M/RHO
R=((3*V)/(4*PI))**(1./3.)
A=4*PI*(R**2.)
WRITE(6,15)M,R

```

```

15 FORMAT(///5X,'MASS OF DROPLET = ',F6.4,2X,'KG'/
13X,'RADIUS OF DROPLET = ',F8.6,2X,'METRES'/
21X,'INITIAL TEMPERATURE = 1873K'//)

```

```

WRITE(6,20)
20 FORMAT(2X,'HT. OF FALL',2X,'TIME OF FALL',2X,
1'SENSIBLE HEAT',2X,'HEAT LOSS',2X,'TEMP. OF DROPLET'/
24X,'METRES',7X,'SECONDS',8X,'JOULES',7X,'JOULES',
37X,'DEGREES K'//)

```

C TO CALCULATE THE TIME OF FALL FOR 10 CM INTERVALS.

```

DO 90 I=1,12,1
G=9.81
T(1)=1873.
TIM(0)=0.
TIM(I)=(2.*S(I)/G)**(1./2.)

```

C TO CALCULATE THE SENSIBLE HEAT AND HEAT LOSS
 C FOR THE IRON DROPLET.THE VALUE OF 1327950 WAS
 C OBTAINED FROM CP DATA AND IS THE VALUE OF THE
 C HEAT CAPACITY PER KG. OF IRON UP TO THE MELTING

```

C POINT INCLUDING THE LATENT HEAT. THE VALUE
C OF 749 IS THE HEAT CAPACITY PER KG. OF MOLTEN
C IRON BETWEEN 1809K AND 1873K.
  EMISS=0.37
  SIGMA=5.6697E-08
  HTFOR=2.6443E+08
  DTIM(I)=TIM(I)-TIM(I-1)
  IPU(I)=(K(I)/100.)*M/16.
  HTC=40.00
  JXO(I)=IPU(I)*HTFOR
  CON(I)=(HTC*A*(T(I)-293)*DTIM(I))
  SHT(I)=M*(1327950.+749.*(T(I)-1809.))
  HTL(I)=(SIGMA*A*EMISS*((T(I)**4.)-(293.**4.))*DTIM(I))+CON(I)
1-JXO(I)
  SHT(I+1)=SHT(I)-HTL(I)
  T(I+1)=(((SHT(I+1)/M)-1327950.)/749.)+1809.
  WRITE(6,25)S(I),TIM(I),SHT(I),HTL(I),T(I+1)
25 FORMAT(6X,F4.2,7X,F6.5,7X,F9.4,6X,F6.4,7X,F8.3/)
90 CONTINUE
  STOP
  END

```

MASS OF DROPLET = 0.0007 KG
 RADIUS OF DROPLET = 0.002866 METRES
 INITIAL TEMPERATURE = 1873K

HT. OF FALL METRES	TIME OF FALL SECONDS	SENSIBLE HEAT JOULES	HEAT LOSS JOULES	TEMP. OF DROPLET DEGREES K
0.10	.14278	963.1201	3.1140	1867.060
0.20	.20193	960.0051	0.5511	1866.007
0.30	.24731	959.4526	0.3284	1865.378
0.40	.28557	959.1230	0.3252	1864.756
0.50	.31928	958.7969	0.4065	1863.979
0.60	.34975	958.3894	0.2995	1863.404
0.70	.37777	958.0884	0.3343	1862.764
0.80	.40386	957.7524	0.2701	1862.246
0.90	.42835	957.4810	0.3335	1861.607
1.00	.45152	957.1462	0.2894	1861.053
1.10	.47356	956.8557	0.2519	1860.570
1.20	.49462	956.6023	0.3352	1859.928

R;
 RECORD CLOSE

APPENDIX III

Model for the Oxidation of Iron Droplets

1. Mass Transfer by Forced Convection

With reference to the figure below:

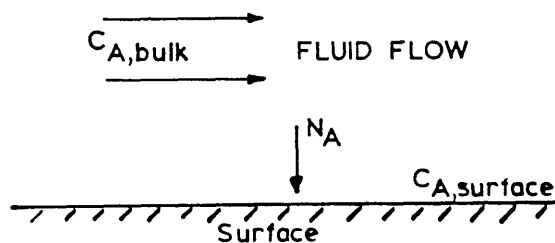
The total flux of a diffusing species relative to a surface may be expressed as⁽¹⁾:

$$N_A = k_d (C_{A,bulk} - C_{A,surface}) \quad (1)$$

where N_A is the molar flux between the bulk fluid and surface.

For a sphere, N_A is the diffusion flux in the radial direction

Figure A III-1



Mass Transfer to a Surface⁽¹⁾

at the sphere surface in $\text{mol.cm}^{-2} \text{s}^{-1}$. k_d is the mass transfer coefficient in cm.s^{-1} . $C_{A,bulk}$ = concentration of species A in the gas phase in mol.cm^{-3} . $C_{A,surface}$ = concentration of species A in the gas phase at the surface of the sphere or droplet in mol.cm^{-3} .

Using the film model for mass transfer and assuming that all resistance to mass transfer is confined to a stagnant layer of

thickness δ adjacent to the surface,

$$N_A = k_d' (X_{A, \text{bulk}} - X_{A, \text{surface}}) \quad (2)$$

where $X_{A, \text{bulk}}$ is the mole fraction of species A in the gas phase at the edge of the concentration boundary layer, and $X_{A, \text{surface}}$ is the mole fraction of species A in the gas phase at the surface of the sphere.

k_d' is a modified transfer coefficient in $\text{mol.cm}^{-2} \text{s}^{-1}$, and is defined:⁽¹⁾

$$k_d' = \frac{c D_{A-B}}{\delta (X_B)_{\text{lm}}} \quad (3)$$

where c = molar density of fluid, moles cm^{-3}

D_{A-B} = binary diffusion coefficient of component A in B,
 $\text{cm}^2 \text{s}^{-1}$

δ = thickness of concentration boundary layer, cm

$(X_B)_{\text{lm}}$ = logarithmic mean of initial and final mole fractions
of component B ($X_B = 1 - X_A$)

$$\text{i.e. } N_A = \frac{c D_{A-B}}{\delta} \frac{(X_{A, \text{bulk}} - X_{A, \text{surface}})}{(X_B)_{\text{lm}}}$$

This can be expressed in terms of molar concentrations of A and B as follows:

$$N_A = \frac{c D_{A-B}}{\delta (C_B)_{\text{lm}}} (C_{A, \text{bulk}} - C_{A, \text{surface}}) \quad (4)$$

where (C_B) is the logarithmic mean concentration of the non-diffusing species B.

Comparison of (4) with (1) shows that:

$$k_d = \frac{c D_{A-B}}{\delta (C_B)_{lm}}$$

when, $C_{A, \text{surface}}, C_{A, \text{bulk}} \ll c$, i.e. at low concentrations of the diffusing species A, then:

$$c = (C_B)_{lm}$$

and therefore:

$$k_d = \frac{D_{A-B}}{\delta}$$

At low concentrations, $X_A \ll 1$, $X_B \approx 1$, and $(X_B)_{lm} \approx 1$

$$\text{i.e. } k'_d = \frac{c D_{A-B}}{\delta}$$

$$\text{and } k'_d = c k_d$$

Now the dimensionless group representing the mass transfer coefficient is the Sherwood number:

$$N_{Sh} = \frac{k_d L}{D_{A-B}}$$

where L is the characteristic length.

Hence, for a spherical droplet:

$$N_{Sh} = \frac{k'_d d_d}{D_{A-B}}$$

where d_d = diameter of droplet in cm.

i.e.
$$N_{Sh_{A-B}} = \frac{k'_d d_d}{c D_{A-B}}$$

hence:
$$k'_d = \frac{N_{Sh_{A-B}} c D_{A-B}}{d_d}$$

Substituting for k'_d in equation (2) gives:

$$N_A = \frac{N_{Sh_{A-B}} c D_{A-B}}{d_d} (X_{A, bulk} - X_{A, surface}) \quad (6)$$

Assuming chemical equilibrium at the gas metal interface it can be shown that $X_{A, bulk}$ is much greater than $X_{A, surface}$ and $X_{A, surface}$ can be ignored, hence:

$$N_A = \frac{N_{Sh_{A-B}} c D_{A-B}}{d_d} X_{A, bulk} \quad (7)$$

Assuming the ideal gas equation,

$$c = \frac{P}{RT}$$

where P is the total pressure of gas in atmospheres,

T is the gas temperature in degrees K,

R is the gas constant = 82.06 cm³.atm.mol⁻¹ K⁻¹

$$N_A = \frac{N_{Sh_{A-B}} D_{A-B} P}{d_d R T} X_{A, bulk} \quad (8)$$

Equation (8) is only strictly applicable to isothermal binary convection in the gas phase.

A steep temperature gradient will exist round the metal droplet. This introduces the problem of choosing an effective temperature to calculate the physical properties of the gas phase.

Hamielec et al⁽²⁾ evaluated gas properties at a film temperature defined by:

$$T_f = \frac{1}{2}(T_{\text{droplet}} + T_{\text{bulk}})$$

and c , the total molar concentration at the edge of the concentration boundary layer was evaluated at an effective temperature, T_E

In general, $T_E \leq T_f$

$$N_A = \frac{N_{\text{Sh}_{A-B,f}} D_{A-B,f} P}{d_d R T_E} X_{A,\text{bulk}} \quad (9)$$

All the terms on the right hand side of equation (9) can be determined from experimental conditions except $N_{\text{Sh}_{A-B,f}}$. This must be either predicted theoretically or obtained from an experimental correlation for convection mass transfer.

Using the Ranz and Marshall formula⁽³⁾ for mass transfer:

$$N_{\text{Sh}} = 2 + 0.60 N_{\text{Re}}^{0.5} N_{\text{Sc}}^{0.33}$$

$$\text{i.e. } N_{\text{Sh}_{A-B,f}} = 2 + 0.60 \left(\frac{d_d u \rho_f}{\mu_f} \right)^{0.5} \left(\frac{\mu_f}{\rho_f D_{A-B}} \right)^{0.33} \quad (10)$$

where u = velocity of the droplet relative to the gas, cm s^{-1}

ρ_f = gas density at the film temperature, g cm^{-3}

μ_f = gas viscosity at the film temperature, $\text{g cm}^{-1} \text{s}^{-1}$

Hence, from (10) N_{Sh} is dependent on relative velocity, u , between

the droplet and gas. Therefore, for an accelerating droplet (under free fall conditions) $N_{Sh_{A-B}}$ will vary with time of fall.

Considering only small droplets of about 1 g mass or less, ($d_p \approx 0.6$ cm) falling under gravity from rest over a short distance, high Reynolds' numbers will not be encountered.

A force balance on an accelerating droplet may be expressed as:

$$M_d \frac{du}{dt} = M_d g - M_f g - F_D \quad (11)$$

where u = velocity of the droplet relative to the gas, $cm\ s^{-1}$

M_d = mass of droplet, g

M_f = mass of gas displaced by droplet, g

g = acceleration due to gravity, $cm\ s^{-2}$

$M_d g$ = gravity force

$M_f g$ = buoyancy force

F_D = drag force

t = time of fall, s

$$\text{Drag force, } F_D = C_D A_d \left(\frac{\rho_f u^2}{2} \right) \quad (12)$$

where C_D = dimensionless drag coefficient

ρ_f = density of the gas, $g\ cm^{-3}$

Using the relationship:

$$C_D = \frac{24}{N_{Re}} + \frac{4}{N_{Re}^3}$$

$$\text{where } N_{Re} = \frac{\rho_f u d_d}{\mu_f}$$

for Reynolds' numbers up to ~ 1000 , then

$$\begin{aligned}
 M_d \frac{du}{dt} &= M_d g - M_f g - F_D \\
 &= M_d g - M_f g - C_D \left(\frac{\pi}{8} d_d^2 \rho_f u^2 \right) \\
 \frac{du}{dt} &= g - \frac{M_f}{M_d} g - \frac{C_D}{M_d} \left(\frac{\pi}{8} d_d^2 \rho_f u^2 \right)
 \end{aligned}$$

If $M_f \ll M_d$

$$\frac{du}{dt} = g - \frac{C_D}{M_d} \left(\frac{\pi}{8} d_d^2 \rho_f u^2 \right)$$

$$\text{But } M_d = V_d \rho_d$$

$$= \frac{1}{6} \pi d_d^3 \rho_d$$

$$\text{Then } \frac{du}{dt} = g - \left(\frac{24}{N_{Re}} + \frac{4}{N_{Re}^{\frac{1}{3}}} \right) \frac{\pi d_d^2 \rho_f u^2}{8 \frac{1}{6} \pi d_d^3 \rho_d}$$

$$= g - \left(\frac{24}{N_{Re}} + \frac{4}{N_{Re}^{\frac{1}{3}}} \right) \frac{3}{4} \frac{\rho_f u^2}{d_d \rho_d}$$

$$= g - 4 \left(\frac{6 N_{Re}^{\frac{1}{3}} + N_{Re}}{N_{Re}^{4/3}} \right) \frac{3}{4} \frac{\rho_f u^2}{d_d \rho_d}$$

$$\text{Now } N_{Re} = \frac{\rho_f u d_d}{\mu_f}$$

$$\text{i.e. } = \frac{d}{dt} N_{Re} = \frac{\rho_f d_d}{\mu_f} \frac{du}{dt}$$

$$\begin{aligned}
\therefore \frac{d N_{Re}}{dt} &= \frac{\rho_f d_d}{\mu_f} \left[g - 3 \frac{\rho_f u^2}{d_d \rho_d} \left(\frac{6 N_{Re}^{\frac{1}{3}} + N_{Re}}{N_{Re}^{4/3}} \right) \right] \\
&= \frac{\rho_f d_d g}{\mu_f} - \frac{3 \rho_f^2 u^2}{f \rho_d} \left(\frac{6 N_{Re}^{\frac{1}{3}} + N_{Re}}{N_{Re}^{4/3}} \right) \\
&= \frac{\rho_f d_d g}{\mu_f} - \frac{3 \rho_f^2 u^3}{f \rho_d N_{Re}^2} \left(6 N_{Re} + N_{Re}^{5/3} \right) \\
&= \frac{\rho_f d_d g}{\mu_f} - \frac{3 \rho_f^2 u^2}{f \rho_d} \left(\frac{f^2}{\rho_f^2 u^2 d_d^2} \right) \left(6 N_{Re} + N_{Re}^{5/3} \right) \\
\frac{d N_{Re}}{dt} &= \frac{\rho_f d_d g}{\mu_f} - \frac{3 \mu_f}{d_d^2 \rho_d} \left(6 N_{Re} + N_{Re}^{5/3} \right) \tag{13}
\end{aligned}$$

Solution of equation (13) will give Reynolds' number or droplet velocity as a function of fall time.

$$\text{Now } u = \frac{dh}{dt} \tag{14}$$

where h is the height of fall in cm.

$$\text{Since } N_{Re} = \frac{\rho_f u d_d}{\mu_f}$$

$$u = \frac{\mu_f}{\rho_f d_d}$$

$$\therefore \frac{dh}{dt} = \frac{\mu_f}{\rho_f d_d} N_{Re} \tag{15}$$

Simultaneous solution of (13) and (15) will give both the droplet Reynolds' number and height of fall as a function of time

$$\text{Now } N_A = \frac{N_{Sh_{A-B,f}} D_{A-B,f} P}{d_d R T_E} X_{A,bulk}$$

where N_A is the molar flux in $\text{mol.cm}^{-2} \text{s}^{-1}$

To determine the pick-up of oxygen by the iron droplet it is necessary to express N_A in terms of mass% oxygen.

$$N[O]_{Fe} = \frac{\frac{d}{dt} (\text{mass\% O}) \rho_d V_d}{100 \text{ M.W. } A_d}$$

where V_d = volume of droplet

A_d = surface area of droplet

M.W. = molecular weight of oxygen [O]

$$\begin{aligned} N[O]_{Fe} &= \frac{\frac{d}{dt} (\text{mass\% O}) \rho_d \frac{4}{3} \pi \frac{d_d^3}{8}}{100 \cdot 16 \cdot 4 \pi \frac{d_d^2}{4}} \\ &= \frac{\frac{d}{dt} (\text{mass\% O}) \cdot \rho_d \cdot d_d}{9600} \end{aligned}$$

$$\therefore \frac{d}{dt} (\text{mass\% O}) = \frac{9600 N_{Sh_{A-B,f}} D_{A-B,f} P}{d_d^2 \rho_d R T_E} X [O], \text{bulk} \quad (16)$$

Using equation (10) to replace $N_{Sh_{A-B,f}}$

$$\frac{d}{dt} (\text{mass\% O}) = \frac{9600 D_{A-B,f} P X [O], \text{bulk}}{d_d^2 \rho_d R T_E} \left(2 + 0.60 N_{Re}^{0.5} N_{Sc}^{0.33} \right)$$

$$\text{Hence: } \frac{d}{dt} (\text{mass\% O}) = \left(\frac{K_1 X [O], \text{bulk}}{d_d^2} \right) \left(2 + K_2 N_{Re}^{0.5} \right) \quad (17)$$

$$\text{where: } K_1 = \frac{9600 P D_{A-B,f}}{\rho_d R T_E}$$

$$\text{and: } K_2 = 0.60 \left(\frac{\mu_f}{\rho_f D_{A-B,f}} \right)^{0.33}$$

To solve equations 13, 15 and 17 simultaneously for small increments of time to give Reynolds' number, droplet fall height and oxygen content in the droplet as a function of time it was necessary to use numerical analysis techniques involving the computer.

The values of the different parameters in the equations and their source of reference are given below.

(i) Density of air⁽⁴⁾

$$\text{Density of air} = \frac{0.001293}{(1 + 0.00367 \theta)}$$

where θ is the temperature in $^{\circ}\text{C}$.

At 800°C , the mean value of the film temperature, the value derived is, $P_{\text{air}} = 0.0003285 \text{ g cm}^{-3}$ which is in good agreement with other data⁽⁵⁾.

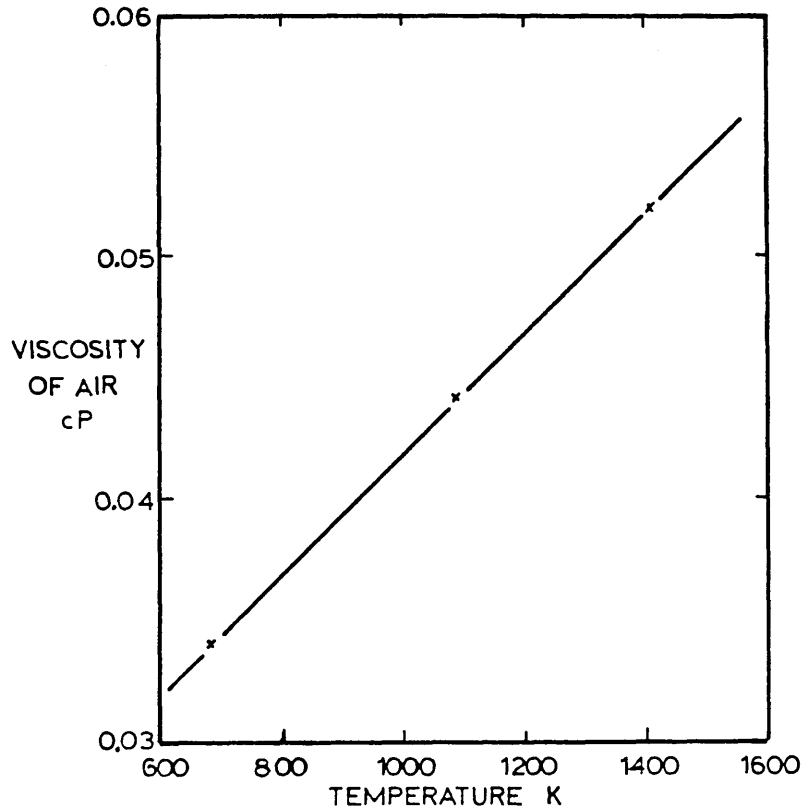
(ii) Density of iron⁽⁶⁾

The temperature of the iron is assumed constant at 1600°C and the value of 7.08 g cm⁻³ is taken.

(iii) Viscosity of air⁽⁷⁾

The data given shows that the viscosity of air over the temperature range 650 K to 1450 K follows a linear relationship. This is plotted in Fig.A III-2.

Figure A III-2



The Viscosity of Air as a Function of Temperature in the Range 600-1500 K⁽¹⁾

The equation of the straight line yields the following:

$$\mu_{\text{air}} = 2.575 \times 10^{-5} T + 0.01588 \text{ cP}$$

This gives a value of 0.0435 cP at 800°C which is in close agreement with other data⁽⁷⁾.

Diffusion Coefficient

For accurate results with simple systems at low pressure and over moderate temperature ranges, Perry⁽⁷⁾ recommends the correlation of Fuller. This relation, an optimised Gilliland-type equation based on data for 153 binary gas pairs, can be expressed as:

$$D_G = \frac{0.0010 T^{1.75}}{P \left[(\sum v_1)^{\frac{1}{3}} + (\sum v_2)^{\frac{1}{3}} \right]^2} \left(\frac{1}{M_1} + \frac{1}{M_2} \right)^{\frac{1}{2}}$$

where T is the absolute temperature,

M_1, M_2 are the molecular masses of the gas

v_1, v_2 are the atomic diffusion volumes for each of the gases

For oxygen and nitrogen at 800°C

$$D_G = \frac{0.00100 (1073)^{1.75}}{1 \left[(16.6)^{\frac{1}{3}} + (17.9)^{\frac{1}{3}} \right]^2} \left(\frac{1}{32} + \frac{1}{28} \right)^{\frac{1}{2}}$$

$$= 1.949 \text{ cm}^2 \text{ s}^{-1}$$

For most gas combinations a convenient reduction formula is given⁽⁵⁾ to reduce the diffusion coefficient to standard temperature and pressure:

$$D = D_o \left(\frac{T}{T_o} \right)^\alpha \frac{P_o}{P}$$

For oxygen in air, the diffusion coefficient D_o is $0.178 \text{ cm}^2 \text{ s}^{-1}$ at standard temperature and pressure.

$$\begin{aligned} \text{At } 800^\circ\text{C} \quad D &= 0.178 \left(\frac{11073}{273} \right)^{1.75} \text{ cm}^2 \text{ s}^{-1} \\ &= 1.953 \text{ cm}^2 \text{ s}^{-1} \end{aligned}$$

This is in good agreement with the Fuller equation⁽⁷⁾. The second equation⁽⁵⁾ was entered into the computer programme because of its easier manipulation.

2. Computer Programme to Solve Mass Transfer Model

The mass transfer model was solved by means of a computer programme based on the Runge-Kutta method for the solution of first order differential equations. The Runge-Kutta method is a step by step process in which an approximation to y_{n+1} is obtained from y_n in such a way that the power series expansion of the approximation would coincide with the actual Taylor series development of $y(x_n + h)$ in powers of h where $h = x_{n+1} - x_n$. No preliminary differentiation is needed and the method also has the advantage that no initial values are needed beyond the prescribed values.

The main uncertainty with the model is the magnitude of the temperature to ascribe to the film temperature. All of the main parameters which are influenced by temperature, notably the density and viscosity of the air and the diffusion of oxygen in air, are written as temperature dependent equations. The programme is so written that it is possible to ascribe any temperature to the film temperature and see its effect on oxygen level in the iron. A

further refinement to the programme is that no oxygen is picked up in the first 15 cm fall as in the actual experimental technique the iron droplet fell 15 cm through argon before it passed through the 'cling' film and entered the air column. During this time, however, the Reynolds' number of the droplet would be increasing. The computer programme is designed to calculate the Reynolds' number and height of fall from the moment the droplet falls out of the levitation coil, but the mass% oxygen picked up by the droplet is calculated from the moment the droplet enters the air column, 15 cm below the levitation coil. In this way, the computer programme reproduces as ideally as possible the experimental conditions. The programme accommodates a variety of droplet sizes, ranging from 0.6 g to 1.0 g.

The programme and results are presented at the end of this appendix.

References

1. J Szekeley and N J Themelis. Rate Phenomena in Process Metallurgy, J Wiley & Sons, 1971.
2. A E Hamielec, W K Lu and J McLean. Can. Met. Quart. 1968, No.7, p27.
3. W E Ranz and W R Marshall. Chem. Eng. Prog., 48, 141, 1952, p173
4. G W C Kaye and T H Laby. Tables of Physical & Chem. Constants, Longmans.

5. D E Gray. American Handbook fo Physics, Colonial Press Inc. 1972.

6. A Adachi et al. Proc. ICSTIS Suppl. Trans., I.S.I.J., 11, 1971, p395.

7. J H Perry and H Chilton. Chemical Engineers Handbook.

FILE: MASS2 FORTRAN A

```
C PROGRAM TO CALCULATE
C (A) REYNOLDS NUMBER AS A FUNCTION OF FALL TIME
C (B) HEIGHT AS A FUNCTION OF REYNOLDS NUMBER
C (C) OXYGEN CONTENT AS A FUNCTION OF REYNOLDS NUMBER
C USING FOURTH ORDER RUNGE KUTTE TECHNIQUE
C RHOA = DENSITY OF AIR, (G./CC.)
C RHOP = DENSITY OF DROPLET, (G./CC.)
C VISC = VISCOSITY OF AIR, (POISE)
C DIFF = DIFFUSION COEFFICIENT, (CM2/S)
C G = ACCELERATION DUE TO GRAVITY, (CM./S2)
C R = GAS CONSTANT, (CC.ATM./MOL.K.)
C TF = FILM TEMPERATURE, (C.)
C D = DIAMETER OF DROPLET, (CM.)
C XOB = MOLE FRACTION OF OXYGEN IN AIR.
C
C
C DIMENSION Y(3),DERY(3),PRMT(5),AUX(8,3)
C EXTERNAL FCT,OUTF,OUTQ
C COMMON A,B,C,S1,S2
C DATA DENS,G,F,VISO,RHOP,DIFO,R,PO,XOB,FI,IANS/0.001293,981.,1.,0.
C !01588,7.08,0.178,82.06,1.,0.21,3.1416,3HYES/
10 WRITE(6,*)'TYPE IN THE VALUE OF THE FILM TEMPERATURE IN DEG.C.'
C READ(5,*) TF
C TF=TF+273.0
C DIFF=DIFO*((TF/273.)**1.75)*PO
C VISC=(VISO+TF*0.00002575)/100.
C RHOA=DENS/(1.+0.00367*(TF-273.))
C Z=0.0
20 Z=Z+1.0
C W=0.55+(Z*0.05)
C D=(6.*W/(RHOP*FI))**(1./3.)
C A=RHOA*D*G/VISC
C B=3.*VISC/((D**2.)*RHOP)
C C=VISC/(RHOA*D)
C S1=9600.*F*DIFF*XOB/(RHOP*R*TF*(D**2.))
C S2=0.6*(VISC/(RHOA*DIFF))**(1./3.)
C Y(2)=0.0
C PRMT(1)=0.0
C PRMT(2)=10.
C PRMT(3)=0.02
C PRMT(4)=0.010
C PRMT(5)=0.0
C DERY(1)=1.0
C DERY(2)=1.0
C DERY(3)=1.0
C NDIM=3
C Y(1)=0.0
C WRITE(6,30) A,B,C,S1,S2,D,W,DIFF
30 FORMAT(///' A = ',F12.6/' B = ',F12.6/' C = ',F12.6/' S1 = ',F1
C !2.6/' S2 = ',F12.6/' D = ',F12.6/' W = ',F12.6/' DIF = ',F12.6/'
C WRITE(6,40)
40 FORMAT(4X,'TIME',6X,'REYNOLDS NO',6X,'HEIGHT',5X,'MASS FRACTION',5X,'I
C !NTEGRAL',3X,'SEC',24X,'CM')
C CALL RKGS(PRMT,Y,DERY,NDIM,INTE,FCT,OUTF,AUX)
C Y(3)=0.0
```

```

PRMT(5)=0.0
CALL RKGS(PRMT,Y,DERY,NDIM,IHLF,FCT,OUTQ,AUX)
IF(W.LT.1.0) GOTO 20
WRITE(6,*)'DO YOU WANT TO RUN ANOTHER VALUE OF THE FILM TEMP.?'
READ(5,50) IREF
50 FORMAT(A3)
IF(IREF.EQ.IANS) GOTO 10
STOP
END
SUBROUTINE OUTP(X,Y,DERY,IHLF,NDIM,PRMT)
DIMENSION Y(3),DERY(3),PRMT(5)
COMMON A,B,C,S1,S2
IF(Y(2).GT.15.0) PRMT(5)=1.0
T=X
WRITE(6,60) T,Y(1),Y(2),IHLF
60 FORMAT(2X,F6.3,7X,F8.3,7X,F7.2,18X,I2)
RETURN
END
SUBROUTINE OUTQ(X,Y,DERY,IHLF,NDIM,PRMT)
DIMENSION Y(3),DERY(3),PRMT(5)
COMMON A,B,C,S1,S2
IF(Y(2).GT.150.0) PRMT(5)=1.0
T=X
WRITE(6,70) T,Y(1),Y(2),Y(3),IHLF
70 FORMAT(2X,F6.3,7X,F8.3,7X,F7.2,5X,F8.4,5X,I2)
RETURN
END
SUBROUTINE FCT(X,Y,DERY)
DIMENSION Y(3),DERY(3)
COMMON A,B,C,S1,S2
DERY(1)=A-B*(6.*Y(1)+(Y(1)**(5./3.)))
DERY(2)=C*Y(1)
DERY(3)=S1*(2.+S2*(Y(1)**(1./2.)))
RETURN
END

```

Compilation completed successfully.
 Loading your program ...
 EXECUTION BEGINS...
 TYPE IN THE VALUE OF THE FILM TEMPERATURE IN DEG.C.
 ?
 800

A = 403.644043
 B = 0.000621
 C = 2.430358
 S1 = 0.021265
 S2 = 0.527154
 D = 0.544970
 W = 0.600000
 DIF= 1.952920

TIME SECONDS	REYNOLDS NO	HEIGHT CM	MASS % O2	IHLF
0.000	0.000	0.00		0
0.020	8.072	0.20		0
0.040	16.144	0.78		0
0.060	24.213	1.77		0
0.080	32.281	3.14		0
0.100	40.346	4.90		0
0.120	48.408	7.06		0
0.140	56.468	9.61		0
0.160	64.525	12.55		0
0.180	72.578	15.88		0
0.000	72.578	15.88	0.0000	0
0.020	80.628	19.61	0.0028	0
0.040	88.675	23.72	0.0057	0
0.060	96.717	28.23	0.0087	0
0.080	104.755	33.12	0.0118	0
0.100	112.789	38.41	0.0150	0
0.120	120.819	44.09	0.0183	0
0.140	128.844	50.15	0.0217	0
0.160	136.864	56.61	0.0251	0
0.180	144.879	63.46	0.0286	0
0.200	152.888	70.70	0.0322	0
0.220	160.893	78.33	0.0358	0
0.240	168.892	86.34	0.0396	0
0.260	176.885	94.74	0.0434	0
0.280	184.873	103.53	0.0472	0
0.300	192.854	112.71	0.0512	0
0.320	200.830	122.28	0.0552	0
0.340	208.799	132.24	0.0592	0
0.360	216.762	142.58	0.0633	0
0.380	224.721	153.31	0.0675	0

A = 424.926758
 B = 0.000560
 C = 2.308631
 S1 = 0.019188
 S2 = 0.527154
 D = 0.573705
 W = 0.700000
 DIF = 1.952920

TIME SECONDS	REYNOLDS NO	HEIGHT CM	MASS % O2	IHLF
0.000	0.000	0.00		0
0.020	8.498	0.20		0
0.040	16.995	0.78		0
0.060	25.490	1.77		0
0.080	33.983	3.14		0
0.100	42.475	4.90		0
0.120	50.963	7.06		0
0.140	59.449	9.61		0
0.160	67.932	12.55		0
0.180	76.411	15.88		0
0.000	76.411	15.88	0.0000	0
0.020	84.888	19.61	0.0026	0
0.040	93.360	23.72	0.0053	0
0.060	101.829	28.23	0.0080	0
0.080	110.294	33.13	0.0109	0
0.100	118.754	38.41	0.0138	0
0.120	127.210	44.09	0.0168	0
0.140	135.662	50.16	0.0199	0
0.160	144.109	56.62	0.0231	0
0.180	152.551	63.47	0.0263	0
0.200	160.988	70.71	0.0296	0
0.220	169.419	78.33	0.0330	0
0.240	177.846	86.35	0.0364	0
0.260	186.266	94.76	0.0399	0
0.280	194.681	103.55	0.0435	0
0.300	203.091	112.73	0.0471	0
0.320	211.494	122.31	0.0508	0
0.340	219.891	132.27	0.0545	0
0.360	228.282	142.61	0.0583	0
0.380	236.666	153.35	0.0621	0

Compilation completed successfully.
 Loading your program ...
 EXECUTION BEGINS...
 TYPE IN THE VALUE OF THE FILM TEMPERATURE IN DEG.C.
 ?
 1000

A = 304.195801
 B = 0.000694
 C = 3.224895
 S1 = 0.024173
 S2 = 0.524307
 D = 0.544970
 W = 0.600000
 DIF = 2.633810

TIME SECONDS	REYNOLDS NO	HEIGHT CM	MASS % O2	IHLF
0.000	0.000	0.00		0
0.020	6.084	0.20		0
0.040	12.166	0.78		0
0.060	18.247	1.77		0
0.080	24.327	3.14		0
0.100	30.405	4.90		0
0.120	36.482	7.06		0
0.140	42.556	9.61		0
0.160	48.628	12.55		0
0.180	54.698	15.88		0
0.000	54.698	15.88	0.0000	0
0.020	60.765	19.61	0.0029	0
0.040	66.829	23.72	0.0059	0
0.060	72.891	28.23	0.0090	0
0.080	78.949	33.12	0.0121	0
0.100	85.005	38.41	0.0154	0
0.120	91.057	44.09	0.0188	0
0.140	97.106	50.16	0.0222	0
0.160	103.152	56.61	0.0257	0
0.180	109.194	63.46	0.0293	0
0.200	115.232	70.70	0.0329	0
0.220	121.267	78.33	0.0366	0
0.240	127.297	86.34	0.0404	0
0.260	133.324	94.75	0.0443	0
0.280	139.346	103.54	0.0482	0
0.300	145.364	112.72	0.0522	0
0.320	151.378	122.29	0.0563	0
0.340	157.387	132.25	0.0604	0
0.360	163.392	142.59	0.0646	0
0.380	169.392	153.33	0.0688	0

A = 320.235107
 B = 0.000626
 C = 3.063373
 S1 = 0.021812
 S2 = 0.524307
 D = 0.573705
 W = 0.700000
 DIF = 2.633810

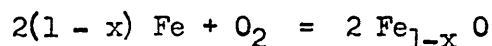
TIME SECONDS	REYNOLDS NO	HEIGHT CM	MASS % O2	IHLF
0.000	0.000	0.00		0
0.020	6.404	0.20		0
0.040	12.808	0.78		0
0.060	19.210	1.77		0
0.080	25.611	3.14		0
0.100	32.010	4.90		0
0.120	38.407	7.06		0
0.140	44.802	9.61		0
0.160	51.195	12.55		0
0.180	57.586	15.88		0
0.000	57.586	15.88	0.0000	0
0.020	63.975	19.61	0.0027	0
0.040	70.360	23.72	0.0054	0
0.060	76.743	28.23	0.0082	0
0.080	83.123	33.13	0.0112	0
0.100	89.500	38.41	0.0142	0
0.120	95.874	44.09	0.0172	0
0.140	102.245	50.16	0.0204	0
0.160	108.612	56.62	0.0236	0
0.180	114.976	63.47	0.0269	0
0.200	121.336	70.71	0.0302	0
0.220	127.692	78.34	0.0337	0
0.240	134.045	86.36	0.0372	0
0.260	140.394	94.76	0.0407	0
0.280	146.738	103.56	0.0443	0
0.300	153.079	112.74	0.0480	0
0.320	159.415	122.32	0.0517	0
0.340	165.746	132.28	0.0555	0
0.360	172.074	142.63	0.0594	0
0.380	178.396	153.36	0.0633	0

APPENDIX IV

Thermodynamic Calculations

(a) The Pure Iron System

Data for the system:



is taken from Richardson⁽¹⁾. The only modification is for the pressure of oxygen in the system not being 1 atmosphere but 0.2 atmosphere.

$$\Delta G = \Delta G^\circ + RT \ln \frac{a_{\text{Fe}_{1-x}\text{O}}^2}{a_{\text{Fe}}^{2(1-x)} P_{\text{O}_2}}$$

For the iron and the oxide in their standard states this reduces to:

$$\begin{aligned} \Delta G &= \Delta G^\circ - RT \ln P_{\text{O}_2} \\ &= \Delta G^\circ + 1.609 RT \\ &= \Delta G^\circ + 13.38 T \end{aligned}$$

For the above system,

(i) In the temperature range 298 - 1644 K

$$\begin{aligned} \Delta G^\circ &= -525900 + 128.41 T \\ \Delta G &= -525900 + 141.79 T \end{aligned}$$

(ii) In the temperature range 1644 - 1808 K

$$\begin{aligned} \Delta G^\circ &= -464800 + 91.25 T \\ \Delta G &= -464800 + 104.63 T \end{aligned}$$

(iii) In the temperature range 1808 - 2000 K

$$\Delta G^{\circ} = -494130 + 107.57 T$$

$$\Delta G = -494130 + 120.95 T$$

where T is in K and ΔG in joules

(b) The Iron-Manganese System

The solutions of manganese in liquid iron have been shown to be ideal from e.m.f. measurements in concentration cells^(2,3). As the solutions are ideal, the free energy of formation of a 1 mass% Mn solution in iron, i.e.

$$[\text{Mn}] = [\text{Mn}]_1 \text{ mass\%}$$

is derived from the activity, where

$$a_{\text{Mn}} = \frac{h_{\text{Mn}}^{\circ} f_{\text{Mn}}^{\circ} M_{\text{Fe}}}{100 M_{\text{Mn}}}$$

Now $f_{\text{Mn}}^{\circ} = 1.0$

Relative atomic mass, Fe = 55.85 g mol⁻¹

Relative atomic mass, Mn = 54.94 g mol⁻¹

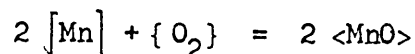
$$a_{\text{Mn}} = 0.010166 \text{ mass\% Mn}$$

$$\Delta G = \Delta G^{\circ} + RT \ln \frac{a_{\text{MnO}}^2}{a_{\text{Mn(Fe)}}^2 P_{\text{O}_2}}$$

$$\Delta G = \Delta G^{\circ} - RT \ln 0.2 (0.010166 \text{ mass\% Mn})^2$$

$$\Delta G = \Delta G^{\circ} - RT \ln 2.06695 \times 10^{-5} (\text{mass\% Mn})^2$$

For the temperature range, 1500 K to 2051 K, for the reaction:

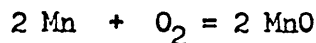


$$\Delta G^{\circ} = -798300 + 164.22 T \text{ joules}^{(1)}$$

The values of ΔG° and ΔG at three different temperatures, 1500 K, 1750 K and 2000 K for the three alloy compositions are given in table IV-1.

Mass% Mn	Temperature K	ΔG° Joules	ΔG Joules
0.50	1500	-551967	-400156
	1750	-510915	-333802
	2000	-469860	-267445
0.70	1500	-551967	-408548
	1750	-510915	-343593
	2000	-469860	-278635
1.00	1500	-551967	-417444
	1750	-510915	-353972
	2000	-469860	-290496

Table IV-1 Values of ΔG° and ΔG for the reaction:



for manganese dissolved in iron

(c) The Iron-Chromium System

The liquid iron-chromium alloys can be considered to be ideal solutions⁽²⁾. As before, the free energy of formation of a 1 mass% Cr solution in iron is derived from the activity, where:

$$a_{\text{Cr}} = \frac{h_{\text{Cr}} f_{\text{Cr}}^{\circ} M_{\text{Fe}}}{100 M_{\text{Cr}}}$$

Now $f_{\text{Cr}}^{\circ} = 1.00$

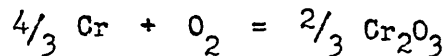
Relative atomic mass, Fe = 55.85 g mol⁻¹

Relative atomic mass, Cr = 52.00 g mol⁻¹

$$a_{\text{Cr}} = \frac{\text{mass\% Cr} \times 55.85}{100 \times 52.00}$$

$$= 0.01074 \text{ mass\% Cr}$$

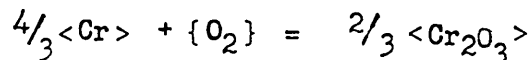
For the reaction,



$$\Delta G = \Delta G^\circ + RT \ln \left(\frac{a_{\text{Cr}_2\text{O}_3}^{\frac{2}{3}}}{a_{\text{Cr}}^{\frac{4}{3}} a_{\text{O}_2}} \right)$$

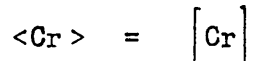
$$\Delta G = \Delta G^\circ - RT \ln (0.2) \times (0.01074 \text{ mass\% Cr})^{\frac{4}{3}}$$

For the temperature range 298 - 2100 K, for the reaction:



$$\Delta G^\circ = -746850 + 173.22 T \text{ joules}^{(4)}$$

However, chromium is solid at the temperatures of interest and the free energy of formation of a solution of chromium in iron from solid chromium is obtained by adding to the above standard free energy of formation the free energy of fusion of chromium i.e. for the reaction:



At the melting temperature the solid and liquid are in equilibrium and the free energy change for the reaction is zero, i.e.

$$\Delta G_f^{\circ} = \Delta H_f^{\circ} - T \Delta S_f^{\circ} = 0$$

$$\text{hence } \Delta H_f^{\circ} = T \Delta S_f^{\circ}$$

The heat of fusion is 19250 J.mol^{-1} at the melting temperature of $2123\text{K}^{(2)}$. Inserting these values into the above equation gives:

$$\begin{aligned} \Delta S_f &= \frac{\Delta H_f}{T} \\ &= \frac{19250}{2123} \\ &= 9.07 \text{ J.mol}^{-1} \text{ K}^{-1} \end{aligned}$$

Hence the free energy of fusion, per mol of chromium at all temperatures is given by:

$$\Delta G_f^{\circ} = 19250 - 9.07 T \text{ J mol}^{-1}(\text{Cr})$$

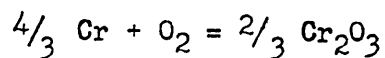
$$\text{For } 4/3 \text{ mol Cr, } \Delta G_f^{\circ} = 25667 - 12.09 T$$

$$\begin{aligned} \therefore \Delta G^{\circ} &= (-746850 + 25667) + (173.22 - 12.09) T \\ &= -721183 + 161.13 T \end{aligned}$$

The values of ΔG° and ΔG for this system at three different temperatures 1000K, 1500K and 2000K for the four alloy compositions are given in Table IV-2.

Mass% Cr	Temperature K	ΔG° Joules	ΔG Joules
0.17	1000	-560053	-476771
	1500	-479488	-354565
	2000	-398923	-232359
0.25	1000	-560053	-481046
	1500	-479488	-360978
	2000	-398923	-240909
0.80	1000	-560053	-493940
	1500	-479488	-380319
	2000	-398923	-266697
1.46	1000	-560053	-500609
	1500	-479488	-390322
	2000	-398923	-280034

Table IV-2 Values of ΔG° and ΔG for the reaction:



for chromium dissolved in iron.

(d) The Iron-Silicon System

The free energy of formation of a 1 mass% Si solution in iron is derived from the activity, where:

$$a_{\text{Si}} = \frac{h_{\text{Si}} f_{\text{Si}}^\circ M_{\text{Fe}}}{100 M_{\text{Si}}}$$

Relative atomic mass of Fe = 55.85 g mol⁻¹

Relative atomic mass of Si = 28.09 g mol⁻¹

$$a_{\text{Si}} = 0.019883 f_{\text{Si}}^\circ \text{mass\% Si}$$

$$\Delta G = \Delta G^\circ + RT \ln \left(\frac{a_{\text{SiO}_2}}{a_{\text{Si(Fe)}} P_{\text{O}_2}} \right)$$

$$\Delta G = \Delta G^{\circ} - RT \ln 0.003977 \text{ mass\% Si } f_{\text{Si}}^{\circ}$$

The value of the Henry's law coefficient for Silicon in iron f_{Si}° at 1600°C is not readily available but can be determined by plotting partial molar free energy values for silicon in iron. In a recent paper Schmid⁽⁵⁾ has calculated the excess Gibbs energy of mixing for liquid solutions of iron and silicon from values determined by a number of investigators. The value given is:

$$\Delta G^{\text{XS}} = X_{\text{Fe}} X_{\text{Si}} \left[X_{\text{Fe}} (-134530 + 16.517 T) + X_{\text{Si}} (-10476 + 32.535 T) + X_{\text{Fe}} X_{\text{Si}} (-174246 + 73.273 T) \right]$$

The integral excess molar quantities are related in the following way:

$$G^{\text{XS}} = G^{\text{M}} - G^{\text{I}}$$

where G^{XS} = integral excess free energy of mixing

G^{M} = integral free energy of mixing

G^{I} = molar free energy of the ideal solution

$$G^{\text{XS}} = G^{\text{M}} - G^{\text{I}}$$

$$G^{\text{XS}} = G^{\text{M}} - RT(X_{\text{Fe}} \ln X_{\text{Fe}} + X_{\text{Si}} \ln X_{\text{Si}})$$

$$\text{i.e. } G^{\text{M}} = G^{\text{XS}} + RT(X_{\text{Fe}} \ln X_{\text{Fe}} + X_{\text{Si}} \ln X_{\text{Si}})$$

The partial molar free energy of mixing of silicon G_{Si}^{M} and hence the activity of silicon (from the relation $G_{\text{Si}}^{\text{M}} = RT \ln a_{\text{Si}}$) can be calculated by using the graphical method of drawing tangents to the curve of G^{M} against X_{Si} .

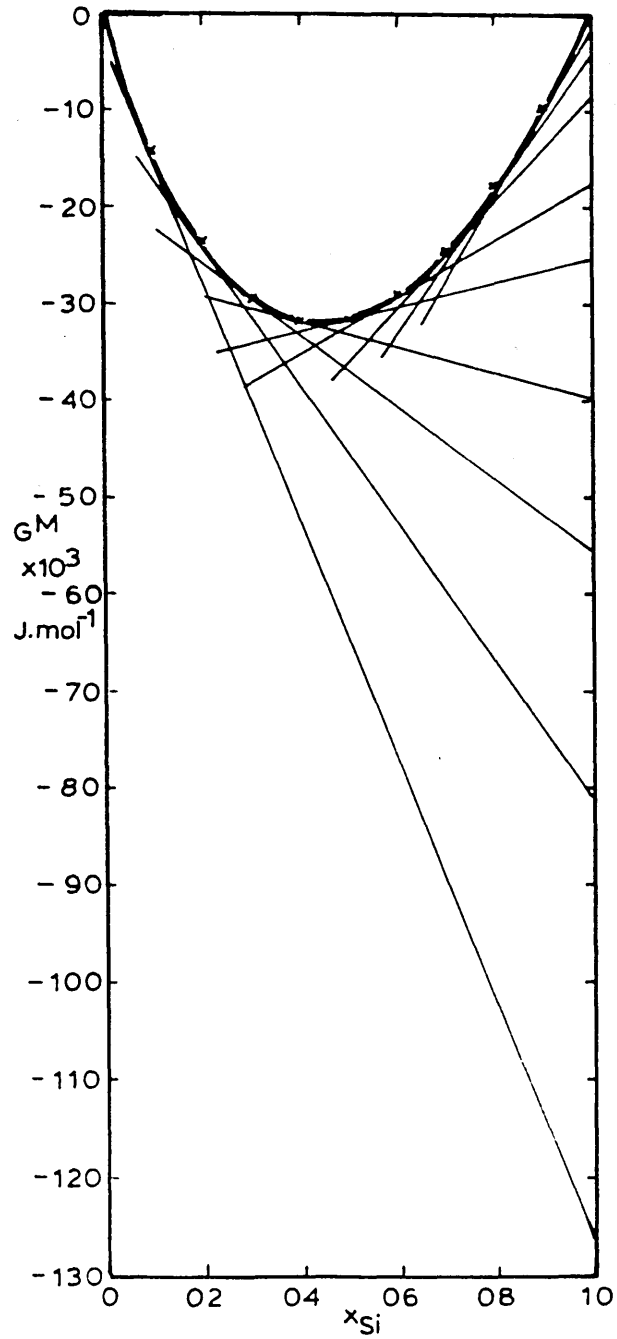
The values of G^{XS} , G^M and G_{Si}^M at 1600°C for the iron silicon system are tabulated in Table IV-3.

X_{Si}	G^{XS} Joules mol ⁻¹	G^M Joules mol ⁻¹	G_{Si}^M Joules mol ⁻¹	a_{Si}
0.01			-150 000	6.6×10^{-5}
0.1	- 9085	-14147	-127 000	2.87×10^{-4}
0.2	-15610	-23402	- 81 000	5.51×10^{-3}
0.3	-19621	-29133	- 55 500	0.028
0.4	-21256	-31736	- 39 800	0.078
0.5	-20740	-31534	- 25 100	0.200
0.6	-18387	-28867	- 17 800	0.319
0.7	-14600	-24112	- 8 600	0.58
0.8	- 9872	-17664	- 4 000	0.77
0.9	- 4782	- 9844	- 1 300	0.90

Table IV-3 Thermodynamic values determined for the
Iron-Silicon System

The values of G^{XS} and G^M were calculated using the above relationships and the values of G_{Si}^M were obtained from Fig. A IV-1.

Figure A IV-1



Plot of Integral Free Energy of Mixing of Iron Silicon Alloys at 1600°C

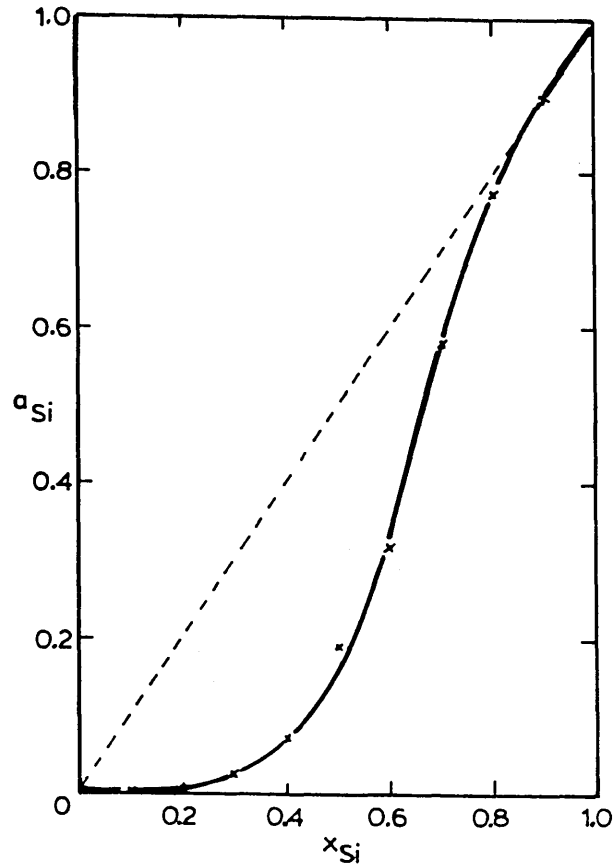
As a result the values of the activity of silicon in iron were derived and these are plotted in Fig. A IV-2.

From the graph the value of f_{Si}^0 is of the order 2.87×10^{-3} (the extrapolation through the $X_{\text{Si}} = 0.1$ to the $X_{\text{Si}} = 1$ axis). The activity coefficient f_{Si}^0 for the infinitely dilute solution can be calculated by applying the relationship:

$$\ln f_{\text{Si}} = \ln f_{\text{Si}}^0 + \epsilon_{\text{Si}}^{\text{Si}} X_{\text{Si}}$$

where ϵ is the interaction coefficient.

Figure A IV-2



The Activity of Silicon in Solution in Molten Iron at 1600°C.

For $\epsilon_{\text{Si}}^{\text{Si}}$ the value is $13^{(6)}$, giving $f_{\text{Si}}^{\circ} = 5.8 \times 10^{-3}$

Substituting for this value,

$$\Delta G = \Delta G^{\circ} - RT \ln 21307 \times 10^{-5} \text{ mass\% Si}$$

The value of ΔG° is readily available⁽¹⁾; the values of ΔG were calculated using the appropriate temperature and mass% Si in the alloy. These values are tabulated below, Table IV-4.

Mass% Si	Temperature K	ΔG° Joules	ΔG Joules
0.30	1773	-548370	-373234
	1873	-527956	-342942
	1973	-507542	-312650
0.75	1773	-548370	-386741
	1873	-527956	-357211
	1973	-507542	-327681
1.33	1773	-548370	-395185
	1873	-527956	-366131
	1973	-507542	-337077

Table IV-4 Values of ΔG° and ΔG for the reaction $\text{Si} + \text{O}_2 = \text{SiO}_2$ for silicon dissolved in iron.

References

1. F D Richardson et al. J.I.S.I. 1948, 160, 261-270
2. M Ohtani. Sci. Rep. Res. Inst., Tohoku Univ., Ser A, 1957, 9, p426.
3. K T Jacob, J P Hajra and M Iwase. Arch. Eisenhüttenwes, 55, 1984, No.9, Sept., p421.

4. O Kubaschewski and E Li Evans. Metallurgical Thermochemistry, Pergamon, 1958.
5. R Schmid. Calphad, vol.4, No.2, 1980, p101.
6. C Bodsworth and H B Bell. Phys. Chem. of Iron and Steel Manufacture, Longman, 1972.